Advanced k.p multiband methods for semiconductor-based spinorbitronics

Duy-Quang To

INSTITUT POLYTECHNIQUE DE PARIS

NNT : 2019IPPAX001

Thèse de doctorat

Advanced multiband k.p methods for semiconductor-based spinorbitronics

Thèse de doctorat de l'Institut Polytechnique de Paris
préparée à l'École polytechnique

École doctorale n°626 Institut Polytechnique de Paris (ED IP Paris)
Spécialité de doctorat : Physique

Thèse présentée et soutenue à Palaiseau, le 11/10/2019, par

DUY-QUANG TO

Composition du Jury :

Jean-Marc JANCU Professeur des Universités, CNRS-UMR 6082, INSA-Rennes	Président
Igor ŽUTIĆ Professeur, University at Buffalo, State University of New York	Rapporteur
Igor ROZHANSKY Professeur, IOFFE Institute, St.Petersburg	Rapporteur
Denis RIDEAU Ingénieur, ST MICROELECTRONICS, Crolles	Examinateur
Virginie TRINITE Ingénieur III-V lab, TRT, Palaiseau	Examinatrice
Henri-Jean DROUHIN Professeur, Ecole Polytechnique, Palaiseau	Directeur de thèse
Henri-Yves JAFFRÈS Directeur de recherche, CNRS-Thales, Palaiseau	Co-directeur de thèse

Acknowledgements

In writing these lines, I would like to give my deepest gratitude to my supervisor Henri-Jean DROUHIN and my co-supervisor Henri-Yves JAFFRÈS. Under their guidance over the years, I have learned from their great minds many things, from how to solve scientific problem to how to make scientific figures or even how to be humorous. Looking back, they have been very nice and very kind to me as well as very patient with my mistakes even though sometimes repeatedly. They always bring their best to support and encourage me. It is extreme honor and fortunate for me to work with two experts like them during three years which is not only an important period in my career but also an unforgettable time in my life.

I would like to give my sincerely thanks to the thesis committee members: Prof. Igor ŽUTIĆ, Prof. Igor ROZHANSKY, Prof. Jean-Marc JANCU, Prof. Denis RIDEAU and Prof. Virginie TRINITE for accepting to be in my jury and spending time to review this thesis as well as for their kindness during my dissertation. I really appreciate their detailed helpful corrections, comments and suggestions. It really enriched this thesis. I have been fortunate to have an opportunity to talk with the leading experts like them. It really helps and broadens my knowledge as well as my vision in spintronics domain.

I believe that research in general and this thesis in particular is a collective work and this thesis would certainly not be completed without the helps and contributions of my collaborators. So that, I am very thankful to Dr. Nguyen Thi Lam Hoai and Dr. Dang Thi Huong for their contributions in this work as well as giving me a chance to meet my supervisor and helping me a lot at the beginning. My sincerely thanks also give to Erina Ekartia, Matthieu Dujany, David Trestini, Gérard Daligou for helping me with some parts in both numerical and analytical calculations in this thesis. I have also learned from them a lot of techniques and skills in analytical and numerical calculations that do help me to do my work.

My friends at LSI Ecole Polytechnique: Annalisa, Benjamin, Imène, Mohamed, Mouad, Nicolò, Pierfrancesco, Rashmi, Simone and Uliana have made my PhD enjoyable. I thank all of you for sharing a happy and memorable time together. Finally, it is my pleasure to acknowledge the director and administration of LSI Ecole Polytechnique, who helped me a lot with administrative procedure during my PhD.

Résumé

Ce travail de thèse est essentiellement consacré au développement de la théorie de transport tunnel **k.p** multibandes (14, 30 et 40 bandes) pour une application à la spinorbitronique avec semiconducteur. La spinorbitronique associe généralement les effets de spin et d'orbite, qui par l'intermédiaire du couplage spin-orbite, introduit des propriétés de transport nouvelles comme les effets Hall de spin et les effets tunnel Hall anormal. Celui-ci se caractérise par une déflection de la trajectoire des porteurs polarisés en spin selon la direction transverse de leur flux. D'autres effets caractéristiques concernent i) les mécanismes de transfert de spin ('spin-transfer' ou 'spin-orbit torque') permettant de commuter une aimantation locale par transfert de moment angulaire, généralisant ainsi les processus de transfert de spin ainsi que ii) la conversion spin-charge aux interfaces médiés par les termes Rashba et/ou Dresselhaus. Dans ce cadre, notre théorie de transport tunnel est adaptable aux hétérostructures semiconductrices, magnétiques ou non, traitant d'une simple interface ou de jonctions tunnel. Elle permet de tenir compte de façon fine des interactions spin-orbite de cœur et d'interface (Rashba, d'interface). Elle utilise de façon générale, l'introduction de bandes hautes supplémentaires, dites fantômes, pour traiter les états spurious inhérents à la théorie **k.p** multibandes. Outre l'introduction de tels états 'fantômes' ne déformant ni la structure électronique, ni le transport polarisé, notre approche utilise la continuité des composantes des fonctions d'onde à chaque interface ainsi que le raccordement des composantes du courant d'onde selon la symétrie particulière des interfaces en considérant soit 1) la continuité des composantes du courant d'onde (extension de la théorie Ben Daniel Duke), 2) les conditions de raccordement correspondant à une symétrie particulière C_{2v} introduisant un certain mélange trous lourds/trous légers dans la bande de valence (conditions d'Ivchenko) ou 3) une discontinuité des bandes p 'hautes'. Nous démontrons, en outre, l'équivalence des conditions de continuité pour le cas de puits quantiques III-V de type AlAs/GaAs/AlAs ce qui représente ainsi une généralisation de résultats précédents développés en 14 bandes.

L'ensemble de ce travail de thèse, analytique et numérique, comportent plusieurs volets et démonstrations à la fois nouveaux et importants. Nous montrons que notre théorie permet de décrire le transport de charge, de spin d'états couplés spin-orbite d'hétérostructures semiconductrices d'axe de croissance [100] ou [110]. Ces résultats sont notamment matérialisés par les calculs les trois composantes du courant de spin dans les barrières semiconductrices III-V (GaAs, AlAs) jouant le rôle de déphaseur de spin. Les calculs que nous développons montrent en effet, comme le prévoit la théorie analytique, une rotation vectorielle de la matrice densité de spin dans l'épaisseur de la barrière et comme prévue par l'application d'un champ e spin-orbite effectif de Dresselhaus parallèle au plan de la barrière.

Notre théorie est également comparée avec succès aux calculs de perturbation multibandes utilisant les fonctions de Green pour le transport pour traiter les mécanismes de l'effet tunnel Hall anormal dans la bande conduction et dans la bande de valences avec des résultats remarquables en terme de fidélité ce qui montre la puissance de la technique utilisée. Nous calculons également les propriétés de courant de spin dans les jonctions tunnel ferromagnétiques de type (Ga,Mn)As/GaAs/(Ga,Mn)As pour en déduire le couple de transfert de spin de d'orbite responsable de la commutation de spin de l'élément ferromagnétique fin dans la tricouche. Nous montrons par exemple, comment les composantes de spin transverses du courant de spin et de spin-orbite représente le paramètre pertinent permettant de commuter une aimantation. Enfin, nous avons adapté notre théorie de transport aux structures confinées III-V pour calculer les états confinés de puits quantiques dans la bande de conduction et bande de valence pour démontrer l'anisotropie optique de l'absorption entre les directions [110] et $[1\bar{1}0]$ pour le champ électrique lorsque la symétrie de l'hétérostructure est réduite à une symétrie C_{2v}. Nous comparons avec succès, nos résultats multibandes à l'état de l'art obtenu précédemment en théorie 6 bandes et 14 bandes.

Abstract

This thesis is essentially devoted to the development of the multiband **k.p** tunneling theory (14, 30 and 40 bands) for spinorbitronic semiconductor application. Spinorbitronic generally associates the effects of spin and orbit, which via spin-orbit coupling, introduces new transport properties such as spin Hall effects and anomalous tunnel Hall effects. This one is characterized by a deflection of the trajectory of the spin polarized carriers according to the transverse direction of their flux. Other characteristic effects concern i) the spin-transfer or spin-orbit torque mechanisms, which make it possible to switch local magnetization by transferring angular momentum, thus generalizing the spin transfer processes as well as ii) spin-charge conversion at interfaces mediated by the terms Rashba and/or Dresselhaus. In this context, our transport theory is adaptable to semiconductor heterostructures, magnetic or not, dealing with a simple interface or tunnel junctions. It allows one to take into account the spin-orbit interactions at the interface (Rashba interaction). It uses in a general way, the introduction of additional high bands, called ghosts, to treat the spurious states inherent to the multiband **k.p** theory. In addition to the introduction of such 'ghost' states, which do not distort the electronic structure or the polarized transport, our approach uses the continuity of the components of the wave functions at each interface as well as the continuity of the components of the wave current according to the particular symmetry of the interfaces considering either 1) the continuity of the components of the wave current (extension of the Ben Daniel Duke theory), 2) the matching conditions corresponding to a particular symmetry C_{2v} introducing a certain mixture of heavy holes/light holes in the valence band (Ivchenko conditions) or 3) a discontinuity of the 'high' bands. We also demonstrate the equivalence of the continuity conditions for the case of AlAs/GaAs/AlAs III-V quantum wells, which represents a generalization of previous results developed in 14 bands.

All of this thesis work, analytical and numerical, includes several components and demonstrations both new and important. We show that our theory can be used to describe the charge-spin transport of spin-orbit coupled states of growth axis semiconductor heterostructures [100] or [110]. These remarkable results are shown by the calculations of the three components of spin current in the III-V semiconductor barrier (GaAs, AlAs) structure acting as spin-phase rotators. The calculations that we are developing show a rotation of the vector spin according to the thickness of the barrier and as analytically predicted by the application of an effective spin-orbit field of Dresselhaus parallel to the plane of the barrier.

Our theory is also successfully compared to multiband perturbation calculations using Green's transport functions to address the mechanisms of anomalous tunnel Hall effect in the conduction and valence bands with remarkable results in terms of chirality showing the power of the technique used. We also calculate the spin current properties in (Ga,Mn)As/GaAs/(Ga,Mn)As ferromagnetic tunnel junctions to derive the orbit spin transfer torque responsible for the magnetization switching of the ferromagnetic element in the trilayer. We show, for example, how the transverse spin components of the spin and spin-orbit currents represent the relevant parameter for switching a magnetization. Finally, we adapted our transport theory to the III-V confined structures to calculate confined states in quantum well for the conduction band and valence band to demonstrate the optical anisotropy of the absorption between the [110] and $[1\bar{1}0]$ directions when the symmetry of the heterostructure is reduced to a C_{2v} symmetry. We successfully compare our state-of-the-art multiband results obtained in theory in 6 bands and 14 bands.

Contents

List of Figures

List of Tables

List of Abbreviations

AHE	**A**nomalous **H**all **E**ffect
ARPES	**A**angular **R**esolved **P**hotoelectron **S**ectroscopy
ATHE	**A**nomalous **T**unnel **H**all **E**ffect
BDD	**B**en **D**aniel **D**uke
BZ	**B**rillouin **Z**one
CB	**C**onduction **B**and
CIMS	**C**urrent **I**nduced **M**agnetization **S**witching
CIP	**C**urrent **I**n-**P**lane
CPP	**C**urrent **P**erpendicular **P**lane
DMI	**D**zyaloshinskii **M**oriya **I**interaction
DOS	**D**ensity **O**f **S**tate
DP	**D**yaknov **P**erel
FMR	**F**erro**m**agnetic **R**esonance
GB	**G**host-**B**and
GF	**G**reen **F**unction
GMR	**G**iant **M**agneto**r**esistance
HH	**H**eavy **H**ole
ISHE	**I**nverse **S**pin **H**all **E**ffect
MRAM	**M**agnetic **R**andom **A**cess **M**emory
MTJ	**M**agnetic **T**unnelm **J**unction
LH	**L**ight **H**ole
QW	**Q**uantum **W**ell
SHE	**S**pin **H**all **E**ffect
SML	**S**pin **M**emory **L**oss
SMR	**S**pin Hall **M**gneto**r**esistance
SO	**S**pin-**O**rbit
SOC	**S**pin-**O**rbit **C**oupling
SOI	**S**pin-**O**rbit **I**nteraction

SOT	**S**pin-**O**rbit **T**orque
STT	**S**pin-**T**ransfer **T**orque
TAMR	**T**unneling **A**nisotropic **M**agneto**r**esistance
THA	**T**unnel **H**all **A**ngle
UC	**U**nit **C**ell
USMR	**U**nidirectional **S**pin Hall **M**agneto**r**esistance
VB	**V**alence **B**and

Physical Constants

Speed of Light	$c_0 = 2.997\,924\,58 \times 10^{8}\,\mathrm{m\,s^{-1}}$
Electron rest mass	$m_e = 9.109 \times 10^{-31}\,\mathrm{kg}$
Proton rest mass	$m_p = 1.672\,621\,923\,69 \times 10^{-27}\,\mathrm{kg}$
Neutron rest mass	$m_p = 1.674\,927\,498\,04 \times 10^{-27}\,\mathrm{kg}$
Electronic charge	$e = 1.6022 \times 10^{-19}\,\mathrm{C}$
Vacuum magnetic permeability	$\mu_0 = 1.256\,637\,062\,12 \times 10^{-6}\,\mathrm{N\,A^{-1}}$
Vacuum electric permittivity	$\epsilon_0 = 8.854\,187\,812\,8 \times 10^{-12}\,\mathrm{F\,m^{-1}}$
Planck constant	$h = 6.626\,070\,15 \times 10^{-34}\,\mathrm{J\,s}$
Reduced Planck constant	$\hbar = 1.054\,571\,817 \times 10^{-34}\,\mathrm{J\,s}$
Boltzmann constant	$k_B = 1.380\,649 \times 10^{-23}\,\mathrm{J\,K^{-1}}$
Bohr magneton	$\mu_B = 9.274\,010\,078\,3 \times 10^{-24}\,\mathrm{J\,T^{-1}}$
Newtonian constant of gravitation	$G = 6.674\,30 \times 10^{-11}\,\mathrm{m^3 kg^{-1} s^{-2}}$
Standard acceleration of gravity	$g = 9.806\,65\,\mathrm{ms^{-2}}$
Stefan–Boltzmann constant	$\sigma = 5.670\,374\,419 \times 10^{-8}\,\mathrm{Wm^{-2}K^{-4}}$
Molar gas constant	$R = 8.314\,462\,618\,\mathrm{J\,mol^{-1}K^{-1}}$
Rydberg constant	$R_\infty = 10\,973\,731.568\,160\,\mathrm{m^{-1}}$
Nuclear magneton	$\mu_N = 5.050\,783\,746\,1 \times 10^{-27}\,\mathrm{J\,T^{-1}}$
Bohr radius	$a_0 = 5.291\,772\,109\,03 \times 10^{-11}\,\mathrm{m}$
Magnetic flux quantum	$\Phi_0 = 2.067\,833\,848 \times 10^{-15}\,\mathrm{Wb}$
Inverse conductance quantum	$G_0^{-1} = 12\,906.403\,72\,\Omega$

List of Symbols

$\mathbf{\Gamma}$	Center of Brillouin zone
E_g	Energy gap
E_F	Fermi energy gap
γ_C	Effecitive mass
γ_D	Dresselhau parameter
$\boldsymbol{S}$	Spin operator
$\boldsymbol{\sigma}$	Pauli operator
$\boldsymbol{B}$	Magnetic field
$\boldsymbol{E}$	Electrical field
$\boldsymbol{L}$	Angular momentum
H_D	Dresselhaus Hamiltonian
H_{SO}	Spin orbit interfaction term in Hamiltonian
H_{exc}	Exchange interaction term in Hamiltonian
θ_{SHE}	Spin Hall angle
t_{l-h}	Heavy-light hole mixing paramters
$\mathbb{I}$	Identity matrix
m_0	Free electron mass
m^*	Effective mass
$\boldsymbol{k}$	Wave vector
$\boldsymbol{p}$	Momentum operator

Introduction, motivation and goals of this thesis

Electrons possess both charge and spin which, until the discovery of Giant Magnetoresistance (GMR) in magnetic multilayers in 1988 in Orsay [1] and Julich [2], have been considered separately. The involvement of spin in devices has opened the way to efficiently control the motion and mobilities of electrons *via* the orientation of magnetization. Those discovery rapidly triggered the development of a new field of research and technology, nowadays referred to Spintronics and brought the 2007 Nobel Prize in Physics to A. Fert and P. Grünberg.

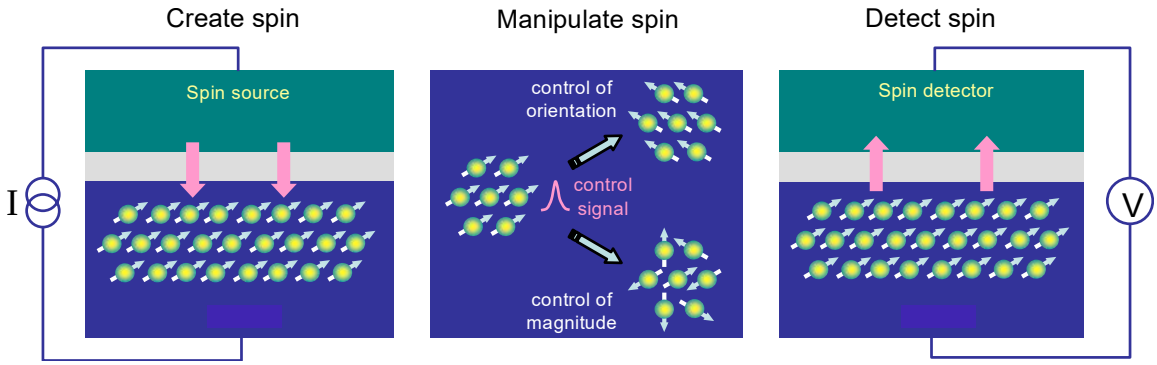

FIGURE 1: Three cornerstones of spintronics: the creation, manipulation and detection of spin polarization. Taken from [3].

Spintronics generally offers better or alternative performances as their conventional *charge-only* counterpart, offering new functionalities like nonvolatility for memories application. Starting from 1988, spintronics get first essentially interest in metals and metallic multilayers with the development of highly-sensitive magnetoresistive devices. In the consecutive years important research efforts toward the control and manipulation of the electron spin in devices have been employed. Fields of studies such as magnetic tunnel junctions and tunnel magnetoresistance phenomena (TMR), spin transfer torque (STT) and STT-based devices and oscillators, and development of materials (bidimentional -2D- materials, Rashba interface states or topological states in particular) strategy and developments have been impressively investigated or employed to boost efficiency and performances. Impressive research achievements enabled to rapidly reach a high technological maturity for the first spintronic based hardware devices leading to the commercialization of hard drives using GMR (IBM, 1997) and TMR (Seagate, 2006), GMR-based galvanic isolators, Magnetic Random Access Memories (MRAM) and in a near future the Spin Transfer Torque Random Access Memories (STT-RAM).

Nowadays, the involvement of spin-orbit interactions (SOI)[2] and potentials in electronic states and related devices makes important scientific step ahead in the novel scientific area named *spinorbitronics*.

[2] In this thesis, the terminologies "spin-orbit interactions" and "spin-orbit coupling" are the same and are used interchangeably.

Since typically beginning 2010, spinorbitronics represents a real emerging multidisciplinary research field thanks to the ability to generate efficient spin-currents without the need of magnetic field or magnetic materials [4]. The use of high spin-orbit metallic or semiconducting materials, heterostructures or interfaces allows to foresee new fundamental issues and prospects. For instance, the use of spin-orbit fields within III-V semiconductors, e. g. involving the (Ga,Mn)As ferromagnetic semiconductors, concerned allows to switch a single thin ferromagnetic layer using the property of angular momentum current [5]. Those currents are now essential to control the magnetization state of a magnet, or moving a domain wall in III-V materials [6–9]. This is made possible *via* the spin-transfer torque generated by a spin-current or by the spin-orbit torque (SOT) generated by the spin-Hall effect possibly involving interfacial Rashba and/or bulk Dresselhaus potentials arising from inversion asymmetry properties of T_d symmetry group [4].

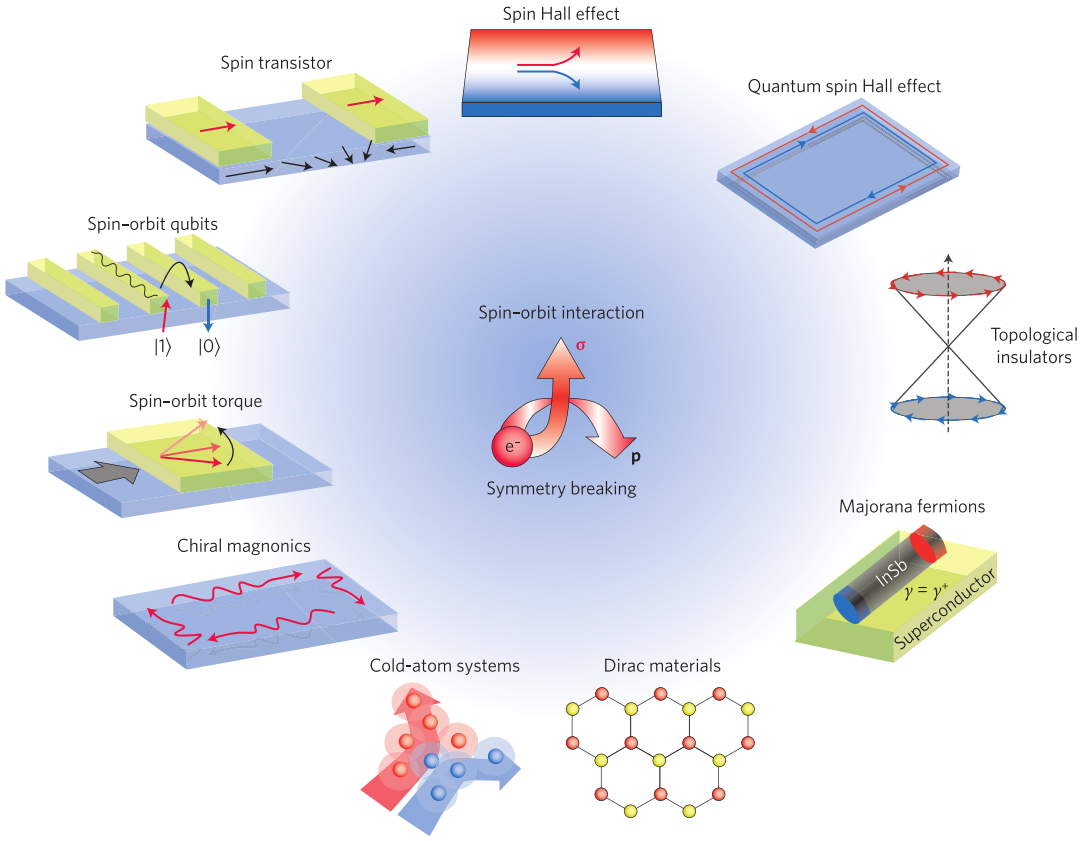

FIGURE 2: The tremendously active field of spinorbitronic: the various sub-fields in which magnetization and spin directions can be manipulated electrically via the spin orbit coupling in systems broken inversion symmetry which reveals novel states of matter. Taken from [10].

From a fundamental point of view, the interplay between particle spin and orbital motion is also at the basis of a new family of effects like spin-galvanic effects or the tunnel anomalous Hall effect [11, 12] leading to transverse (spin) currents at surface or interfaces. Concomitantly with the numerous literature devoted to spin-Hall effects in metals and conductors, a mechanism of tunneling planar Hall effect emerging at ferromagnet FM/TI junctions has recently been proposed. Those qualitatively differ from the SHE in terms of the relevant geometry, the forward/backward scattering in the present case, and/or the magnetization configuration. These phenomena manifest themselves by a left/right asymmetry in the scattering process of spin-polarized carriers along the transverse direction of their flow, giving rise to spin-to-charge conversion and vice versa whose manipulation will become essential in a new generation of devices. Indeed,

those ensemble of properties may offer new functionalities in the next future, like the ability for spin-orbit materials in contact with a thin ferromagnet to emit pulsed THz waves in the time-domain area.

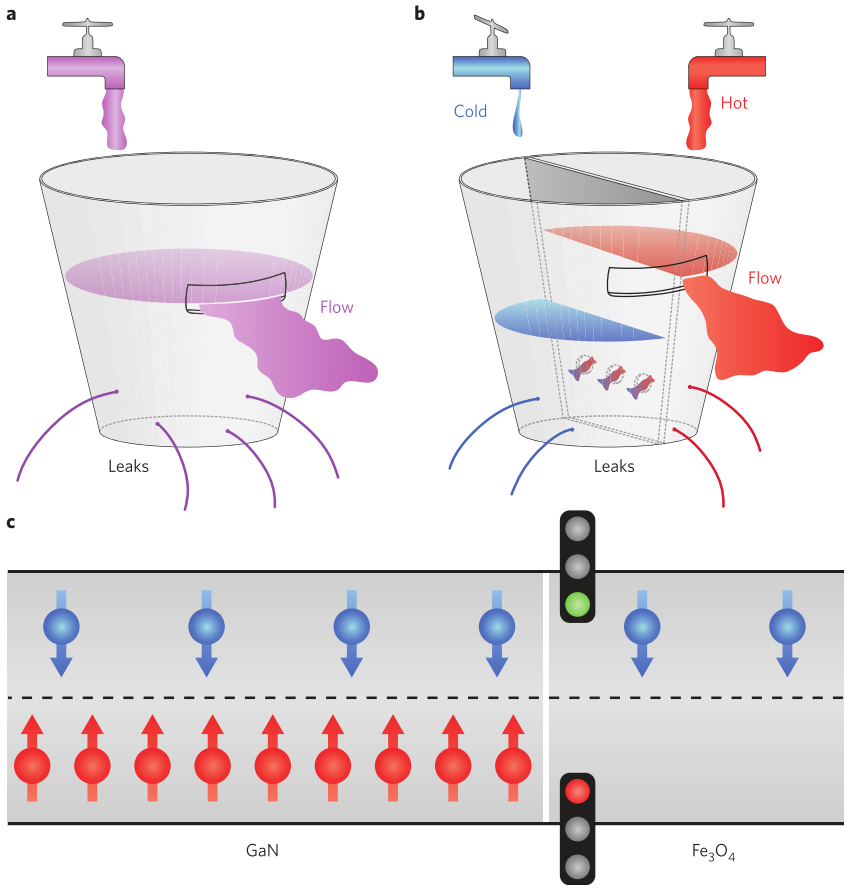

FIGURE 3: The working principle of a spin-laser with a built-in spin filtering mechanism. a, A bucket model of a conventional laser. Water added to the bucket represents the carriers and the water coming out the emitted light. When water is added slowly, the system is analogous to an ordinary light source (spontaneous emission). When water is added at a faster rate the bucket overfills and water pours out. In a semiconductor laser, this regime corresponds to the emission of coherent photons (stimulated emission). b, A bucket model of a spin-laser. The two halves represent two spin populations (hot and cold water in the analogy) and are filled separately. The partition between them is not perfect: spin relaxation can cause the two populations to mix. The difference between uneven water levels represents the spin imbalance in the laser. c, The spin filtering effect at the semiconductor/nanomagnet (GaN/Fe_3O_4) interface is responsible for spin imbalance, even without spin pumping (equal amount of hot and cold water poured in each half in b). The spin-selective interface (here represented by the traffic lights) allows spin-down electrons to move across, while spin-up electrons get stuck behind it, resulting in the spin imbalance of GaN being transferred to the photons to produce polarized emitted light. For such a spin-laser to operate, all nanomagnets have to be aligned in the same direction. This effect is accomplished by applying a magnetic field. Taken from [13]

Besides, even if the science and technology behind passive spintronic devices is well mastered today, the realization of active devices such as spin-orbit based transistors or spin-lasers for optical communication still remains an important challenge. The intense research towards such components is motivated by the potentiality of combining residual magnetic storage of binary information with electronic or optical readout in a single device. One could envisage to propagate the information contained in a magnetic bit over large distances after having converted the spin into light polarization or helicity by using spin-laser devices

[13, 14]. The injection, transport, and detection of spins in such III-V materials, optically active, like (GaAs, InAs) [15] are then the three key points to master. A continuous research effort has been led in that perspective in Spin-Light Emitting Diodes (Spin-LEDs) devices as soon as the 'impedance mismatch' issue between metals and semiconductors was known to be detrimental. The addition of a thin tunneling oxide barrier [16] like played by magnesium oxide (MgO) with efficiency larger than 40%, has been considered at UMϕ CNRS-Thales. *Spin-Light Emitting Diodes* (Spin-LEDs) involves optically active recombination regions (quantum wells) where electrons are injected by electrical means or by optical pumping into an active region where they can recombine radiatively with unpolarized holes to emit preferentially right- or left- circularly polarized light. This information transfer happens through the optical quantum selection rules for dipole radiation associated with the conservation of angular momentum z-projections m_z occurring in confined strained active medium or Quantum Wells (QWs) [17]. In that type of experiments, the degree of circular-polarization of the light emitted serves as a fingerprint of the initial spin-polarization of carrier injected electrically. The first functional Spin-LED was proposed by Fiederling et al. in 1999 [18]. Such carrier-to-photon angular momentum transfer and information conversion have been demonstrated now e.g. in Naval Research Lab (Washington) Hanover, Bochum [19]. The device must provide a coherent light emission with switchable polarization state and an output polarization degree as high as possible in order for instance to robustly encode a bit of information [20–22]. *spin-lasers* (spin-VECSELs) are devices using the same properties but with the enhanced quality of a coherent light emitted (spatially and temporally). The amplification effects induced by the combination of a gain medium and a resonant optical cavity give a unique opportunity to maximize the conversion efficiency of the carrier spin-information into light polarization information. On the other hands, Spin-lasers would provide a number of advantages over conventional VCSELs for future optical communication systems such as spin driven reconfigurable optical interconnects [23], fast modulation dynamics [23], polarization control [24, 25] as well as higher performances such as laser threshold reduction [25, 26], improved laser intensity, and polarization stability. In terms of device implementation, III-V semiconductor based Vertical Cavity Surface Emitting Lasers (VCSEL) emerged as perfect candidates for a Spin-Laser implementation thank to their vertical geometry. Additionally, they exhibit a polarization emission much more isotropic than the conventional side-emitting laser diodes. Outstanding optical [24, 25] and electrical [25, 27] spin-injection results were already achieved in monolithic VCSEL structures in the past few years. From a physical fundamental point of view, a detailed knowledge, of the electronic and photonic spin-current profiles (polarized electromagnetic wave) and this information transfer by relevant optical selection rules in active media embedded in a multilayer structure is generally required to gain in performance. The latter calculations should take into account all the physical ingredients that are e.g. circular dichroism, circular and anisotropic gain, linear birefringence and local strain field at surfaces and interfaces. These ingredients are generally needed to model the light emission in semiconducting multilayers inside optical cavities constituted by one or two Bragg mirrors and/or external mirror (1/2 VECSEL). However, concerning spin-lasers functionalities, additional in-plane linear anisotropies strongly impact the performance and properties of spin operations. Theoretical as well as experimental investigations have allowed experimentalists to separate several different contributions [28]: i) a linear birefringence originating from interfaces between ternary quantum wells and barriers and ii) possible local surface strain of III-V materials after surface crystal reconstruction and iii) a magneto-optical anisotropy. However, a full theoretical physical description of such in-plane linear anisotropies is still missing today.

Overall, the ensemble of those complex phenomena mentioned above, requires now a clear description of the spin-currents anatomy with advanced calculation tools and modeling platforms. This can be hardly fulfilled by ab-initio methods because of the needs to treat multilayered systems. In term of semiconductor based structure, an alternative method for ab-intitio is the **k.p** technique since a convenient and efficiency

method it is for the treatments of multilayered systems. Therefore, this thesis is devoted to the theoretical, analytical and computational study of III-V based interfaces from fundamentals to experiments understandings and analyses associated with multiband **k.p** method. In particular, we focus on theoretical study of the electronic and photonic spin-currents profiles in hybrid heterostructures by taking into account the relevant spin-orbit potentials involved. Together with the analytical development in this manuscript, we have developed numerical calculations tools and platform based on $\boldsymbol{k.p}$ methods for tunneling and adapted to many type of multilayers. Beside the 2×2 CB and 6×6 VB effective models describing for example the GaAs and related material band structure and hetererostructure, the simultaneous treatment of electrons and holes needs a 8-band $\boldsymbol{k.p}$ whereas the inclusion of odd-parity symmetry effect requires at least a 14×14 bands $\boldsymbol{k.p}$ treatment [29] and for a full Brillouin zone description which is useful for the indirect band gap semiconductor like silicon, one needs to deal with 30×30 [29] or 40×40 bands $\boldsymbol{k.p}$ Hamiltonian. However, the difficulty to treat with a multiband like 8-, 14-, 30- and 40-band $\boldsymbol{k.p}$ model for spin transport is to get rid of the well-known unphysical spurious electronic states making the tunneling calculation unfeasible due to tunneling shortcuts within the first Brillouin zone. One of the real peculiarity and difficulty is to treat correctly the tunneling elastic transport in heterostructures occurring at a constant energy, and not at a constant wavevector $\boldsymbol{k}$. Generally, it allows for a spurious or unphysical character being away from the validity zone of the $\boldsymbol{k.p}$ treatment. Thus, this makes the tunneling problem to become much more complex than the electronic band structure calculations as well as band to band optical transition estimations. This work, therefore, provides one of the most advanced implementation of numerical $\boldsymbol{k.p}$ tunneling transport codes (from 14-, up to 30- and 40- band) to investigate the spin-orbit field effects in carrier transport in a new class of spintronic and spinorbitronic structures possibly involving also Si and Ge and their group IV semiconductor alloys.

The organization of this thesis

This manuscript is organized as follows:

The first parts of this thesis is devoted to six chapters starting with chapter 1 where we review the fundamental material properties of the III-V semiconductors and related materials. In this chapter, we start firstly with the concept of spin and spin-orbit interaction of electron in crystal lattice. Afterward, the properties of III-V semiconductor compounds like GaAs or (Ga,Mn)As is presented and linked to the symmetry of crystal. Then, the chapter discusses the spin Hall phenomenal via spin-orbit interaction in semiconductors as well as the generation of spin polarization for spin injection into a semiconductor. Finally, this chapter closes by giving some main points for the spin relaxation mechanisms in semiconductors.

Chapter 2 describes in details the electronic band structure of O_h and T_d semiconductors using the $\boldsymbol{k.p}$ technique. This chapter starts, first, with the description of $\boldsymbol{k.p}$ method and then discusses the way how to build $\boldsymbol{k.p}$ Hamiltonians for the case of O_h and T_d semiconductors from the general symmetry point of view. Afterward, the chapter is devoted to a "novel Ghost-band method" which allows one to remove spurious states in multiband $\boldsymbol{k.p}$ Hamiltonians from 14- up to at least 40-band $\boldsymbol{k.p}$ Hamiltonians. Finally, the chapter reviews some detail on the effective Hamiltonian, exchange interaction and strain field within the $\boldsymbol{k.p}$ framework.

Chapter 3 considers the quantum matching conditions fulfilled by the electronic wavefunctions and current waves at the various interfaces within multilayer structure. From the standard matching condition to the matching condition in the case involving the surface potential as well as the matching condition for the effective Hamiltonian along [110] direction, this chapter gives a set of consistent matching conditions for each case which allows one to describe the tunneling properties of electron through heterostructures such as the resonant tunneling, bound state or quasi bound state in quantum well. As an example of matching

condition with surface potential, the chapter discusses the properties of wavefunction and splitting energy in quantum well with matching condition proposed by Ivchenko et al. [30] and Durnev et al. [31].

Chapter 4 is devoted to the Green function technique which is a very useful mathematical and physical tool for studying the electronic, optical and transport properties of materials. In this chapter the comparison between the numerical calculation with 30 bands **k.p** and perturbation calculation with Green function for spin dephasing of an electron in the conduction band tunnels through [110] barrier structure, is also implemented.

Chapter 5 and 6 contain the main focus of this thesis's work. Chapter 5 starts with the definition of spin current and then discuss on the spin transfer torques with (Ga,Mn)As/GaAs/(Ga,Mn)As in antiparallel configuration of magnetization. Afterward, this chapter gives in details the anomalous tunnel Hall effect in CB and VB with perturbation calculation based on Green function as well as numerical calculations based on multiband $\boldsymbol{k.p}$ technique. Chapter 6 starts with the introduction to spin lasers then discusses the experiment study of surface and interfacial optical anisotropy by ellipsometry method. Finally, this chapter gives a theoretical study of optical anisotropy which is induced by the symmetry breaking at the interface of semiconductor heterostructure as well as the segregation effect based on **k.p** technique together with the matching condition.

Afterward, the last part of this thesis is devoted to conclusion and perspective of this thesis's work as well as four appendices giving in details of all methods and techniques using in this work: explicit matrix representation of multiband **k.p** in a consistent basis set, the error estimation of ghost band method, transfer and scattering matrices formalism and the calculations of the oscillator strength and optical anisotropy for heavy and light holes.

CHAPTER 1

III-V semiconductors and related materials based structure for spintronics and optoelectronics

Contents

In this work, the main materials subject to investigation are III-V based ferromagnetic semiconductors which attract much attention in Spintronics and Spinorbitronics for decades [32–40], thank to their particular magnetic and spin-orbital properties. In particular, we focus on (Ga,Mn)As material. Like (Ge,Mn)As for group IV semiconductors, (Ga,Mn)As remains a unique prototype group III-V semiconductor which demonstrates non-zero exchange interactions and carrier-mediated ferromagnetism [33]. This makes possible the development of spinorbitronics devices with their particular interest and properties appearing as soon as both exchange strengths and spin-orbit interactions (SOI) come into play. From a fundamental point of view, the ferromagnetic semiconductor (Ga,Mn)As provided new opportunities to study spin-polarized transport phenomena in semiconductor heterojunctions [41]. One of the interests in (Ga,Mn)As lies in the wealth and varieties of its electronic valence band structure, location of exchange interactions, and strong spin-orbit coupling. In this vein, advantage of semiconductor tunnel junction are fourfold: (1) III-V heterostructures can be epitaxially grown in a wide variety of tunnel devices with abrupt interfaces and with atomically controlled layer thicknesses; (2) junctions can be easily integrated with other III-V structures and devices; (3)many structural and band parameters are controllable, like barrier thickness and barrier height, allowing the engineering of any band profile; and (4) one can introduce quantum heterostructures much more easily than in any other material system.

Throughout this present work, several kinds of III-V (Ga,Mn)As based tunnel junctions are used hereafter, including thin GaAs layer or (In,Ga)As quantum well, for theoretical consideration of spin transport and spin laser problems. A full understanding of the spin properties and dynamics requires knowledge of the fundamental material properties, this chapter is, therefore, devoted to a brief discussion on the material characteristics and the fabrication of these semiconductors and related materials. First of all, this chapter starts with a concept of the spin degree of freedom and spin-orbit interaction, the relativistic coupling of the spin to the movement of electrons in an electric field generated by an atom or a crystal lattice, which has sparked a rich variety both of fundamental research in spin physics and of new spin-based applications in technology. Then the Thomas factor which is the correction factor due to the acceleration motion of the electron, is also obtained from two different ways: the relativistic kinetic point of view and the common way with Dirac equation. In the next part, this chapter gives a basic discussion on a fabrication of III-V semiconductor and their alloys using Molecular Beam Epitaxy (MBE) technique which may provide very pure crystal structure, as well as the fabrication of a ferromagnetic semiconductor by doping the semiconductor with magnetic transition metals. From the fact that a crucial point to understand the spin transport phenomena in semiconductor and related structure is to understand the spin orbit interaction relating to the symmetry of certain structure since the SOI plays a very important role in various spin transport processes. For example, the interplay of electron motion and SOI may generate a spin polarization in a non-magnetic material due to Spin Hall Effect or a combination of SOI and ferromagnetic materials may give rise a spin-to-charge conversion which will be given in details in chapter 5. Therefore, one part of this chapter gives an introduction to SOI in III-V semiconductor which is the core of this work and link it to the symmetry of crystal. Then, the chapter discusses the spin Hall family phenomena via spin-orbit interaction in semiconductors. One of a key parts in spintronic device prospects is ascribed to the spin field effect transistor (FET), a famous proposal of Datta and Das in 1990 [42]. Their concept requires the creation of spin polarization injected from magnetized contacts into a normal semiconductor which may be done with two common mechanism: electrical and optical spin injection being reviewed in the following part. However, in contrast with spin polarization generation in semiconductor, the spin orientation is not conserved due to the SOI since it will relax into thermal equilibrium after a certain spin relaxation time. This chapter will close with four relaxation mechanisms which are of great importance in semiconductor spinorbitronics.

1.1 Electron spin and spin-orbit interaction

1.1.1 Electron spin

Spin is an intrinsic magnetic dipole moment μ carried by elementary particles (such as electron), composite particles (hadrons), and atomic nuclei [43] . The existence of spin is inferred from experiments, such as the Stern-Gerlach experiment where the silver atoms were observed to possess two opposite angular momenta whereas no orbital angular momentum [43].

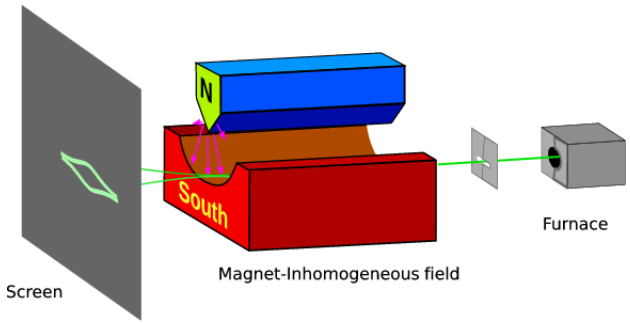

FIGURE 1.1: Stern Gerlach experiment: Silver atoms traveling through an inhomogeneous magnetic field, and being deflected up or down depending on their spin.

In quantum mechanic, the spin quantity is derived from the relativistic Dirac equation [44] and known as one of two types of the angular momentum as internal degree of freedom beside the orbital angular momentum [43]. The spin operator is defined as:

$$\boldsymbol{S} = \frac{1}{2}\boldsymbol{\sigma} \tag{1.1}$$

where $\boldsymbol{\sigma}$ is the Pauli operator which acts on the up and down spin states respectively as:

$$\begin{aligned} \sigma_x |\uparrow\rangle &= |\downarrow\rangle, \quad \sigma_y |\uparrow\rangle = i |\downarrow\rangle, \quad \sigma_z |\uparrow\rangle = |\uparrow\rangle \\ \sigma_x |\downarrow\rangle &= |\uparrow\rangle, \quad \sigma_y |\downarrow\rangle = -i |\uparrow\rangle, \quad \sigma_z |\uparrow\rangle = -|\uparrow\rangle \end{aligned} \tag{1.2}$$

This also refers to the electron spin $\frac{1}{2}$ as only two states $|\uparrow\rangle$ and $|\downarrow\rangle$ respectively. Generally, for the case of spin $\frac{1}{2}$ system (the case of electrons), $\sigma_x, \sigma_y, \sigma_z$ are the three Pauli matrices, given by:

$$\sigma_x = \begin{pmatrix} 0 & 1 \\ 1 & 0 \end{pmatrix} \qquad \sigma_y = \begin{pmatrix} 0 & -i \\ i & 0 \end{pmatrix} \qquad \sigma_z = \begin{pmatrix} 1 & 0 \\ 0 & -1 \end{pmatrix} \tag{1.3}$$

1.1.2 Spin-orbit interactions

The magnetic moment of the electron relates to its spin:

$$\boldsymbol{\mu} = -\frac{1}{2} g \mu_B \boldsymbol{\sigma} \tag{1.4}$$

where $\mu_B = \frac{|e|\hbar}{2m_e}$ is the Bohr magneton and $g = 2.0023 \simeq 2$.

In a uniform magnetic field $\boldsymbol{B}$, this magnetic moment is submitted to a torque like:

$$\boldsymbol{M} = \boldsymbol{\mu} \times \boldsymbol{B} \tag{1.5}$$

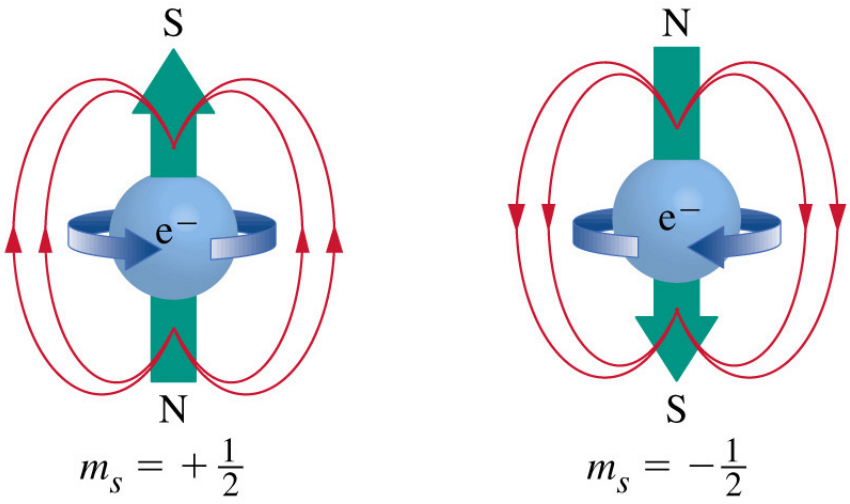

FIGURE 1.2: Schematic diagram depicting the spin of electron. Taken from [45]

Thus, the energy of a magnetic moment in a uniform magnetic field is described by

$$H = -\boldsymbol{\mu}.\boldsymbol{B} = \frac{1}{2} g \mu_B \boldsymbol{\sigma}.\boldsymbol{B} \tag{1.6}$$

which is called *Zeeman* Hamiltonian [46]. When the electron moves in a magnetic field gradient, such as in the famous case of the Stern-Gerlach experiment, the electron interacts with magnetic field through its magnetic dipole moment by the force given by [46]:

$$\boldsymbol{F} = \nabla (\boldsymbol{\mu}.\boldsymbol{B}) = (\boldsymbol{\mu}.\nabla)\, \boldsymbol{B} \tag{1.7}$$

Electrons with different spin orientations are therefore deflected in two opposite directions. Moreover, the spin interacts also with electric fields. This is the case for example when an electron moves in the electric field $\boldsymbol{E}$ generated by the atoms or a crystal lattice. Here, if we assume that the atom or the crystal lattice is at rest in the inertial system. Then the electron will experience in its own rest system not only a pure electric field, but also a magnetic field which, in the lowest order in v/c, can be written as

$$\boldsymbol{B'} = \frac{1}{c^2} \boldsymbol{v} \times \boldsymbol{E} \tag{1.8}$$

due to the relativistic transformation of the electromagnetic fields. Here we have denoted the primed variables as the quantities in the coordinate system in which the electron is at rest. The magnetic moments in the lab frame and in the electron's rest frame are the same to first order in v/c. The magnetic field $\boldsymbol{B'}$ couples to the magnetic dipole moment of the electron, i.e., to the spin, via the *Zeeman* interaction and we have in the lowest order in v/c

$$H'_{SO} = g \mu_B \boldsymbol{B'}.\boldsymbol{S'} = -g \mu_B \frac{1}{c^2} (\boldsymbol{v} \times \boldsymbol{E}) .\boldsymbol{S} = H_{SO} \tag{1.9}$$

The above argument is incomplete as it neglects complications arising due to the acceleration of the electron leading to the so-called Thomas precession. If the term is exactly derived from the relativistic Dirac equation by taking the non-relativistic limit, the result is

$$H_{SO} = -\frac{g \mu_B}{2} \frac{1}{c^2} (\boldsymbol{v} \times \boldsymbol{E}) .\boldsymbol{S} = \frac{g \hbar}{4 c^2 m_e^2} (\nabla V(\boldsymbol{r}) \times \boldsymbol{p}) .\boldsymbol{S} \tag{1.10}$$

where g is the Lande factor, m_e the electron mass. This exact expression differs only by a factor $1/2$, the so-called Thomas factor, from the expression obtained from the classical expansion. It is the nature of this spin-orbit interaction that the electron feels an effective magnetic field oriented normal to both its direction of motion and to the external electric field.

The Thomas factor [47]

We are now going to present a major idea of Kroemer which allows one to derive the Thomas precession factor in the value of spin orbit strength in the framework of the relativistic kinematics. The details can be found in Ref.[47] where the main points are:

♣ When an electron moves with a velocity $\boldsymbol{v}$ through space in the presence of an electric field $\boldsymbol{E}$, the electron will experience in its own frame of reference an effective magnetic field $\boldsymbol{B'}$. However, one cannot use a Lorentz-transformed magnetic field $\boldsymbol{B'}$ given by the familiar expression:

$$\boldsymbol{B'} = \frac{(\boldsymbol{E} \times \boldsymbol{v})/c^2}{\sqrt{1-(v/c)^2}}_{v \ll c} \Longrightarrow \frac{(\boldsymbol{E} \times \boldsymbol{v})}{c^2} \tag{1.11}$$

in such a simple way since the electron's rest frame is not an inertial reference frame. Indeed an electric field with a component perpendicular to the electron velocity causes an additional acceleration of the electron along the direction perpendicular to its instantaneous velocity, leading a curved trajectory. In a rotating frame of reference, this leads to an additional precession of the electron which is called the Thomas precession. Beyond, one may observe from a Lorentz transformation that the transformation $\boldsymbol{E} \rightarrow \boldsymbol{B'}$ mus be linear in $\boldsymbol{E}$, and $\boldsymbol{E}$ may occur only in the combination $\boldsymbol{E} \times \boldsymbol{v}$ which reflects the fact that only the component of $\boldsymbol{E}$ perpendicular to the velocity $\boldsymbol{v}$ can play a role. In other word, $\boldsymbol{B'}$ must be perpendicular to both $\boldsymbol{E}$ and $\boldsymbol{v}$. Generally, the magnetic field transformation admits the following form:

$$\boldsymbol{B'} = \alpha \frac{(\boldsymbol{E} \times \boldsymbol{v})}{c^2} \tag{1.12}$$

or in the case of a magnetic field $\boldsymbol{B}$ present in the initial frame, Eq.1.12 may be generalized to:

$$\boldsymbol{B'} = \alpha \frac{\boldsymbol{E} \times \boldsymbol{v}}{c^2} + \beta \boldsymbol{B} \tag{1.13}$$

where α and β are scalar factors which depend on the velocity but not on either $\boldsymbol{E}$ or the magnetic field $\boldsymbol{B}$ in the initial frame.

♣ In order to obtain the correct magnetic field acting on the electron in its rest frame (determining the coefficient α and β in Eq.1.13), one can use the Lorentz transformation by taking into account the influence of a rotating frame by considering the case in which an electron moves in crossed electric field $\boldsymbol{E}$ and magnetic field $\boldsymbol{B}$ chosen such that the electric Coulomb force is balanced by the magnetic Lorentz force. For that: (i) the electron will move along a straight line with an uniform velocity. The electron's rest reference becomes an inertial reference frame and therefore the Lorentz transformation can be applied to obtain the magnetic field $\boldsymbol{B'}$ experienced by the electron in this reference frame; (ii) the term which corresponds to the magnetic field $\boldsymbol{B}$ will play the role of the rotating frame in the case of a curved motion of the electron in the presence of a pure electric field $\boldsymbol{E}$.

Particularly, we are now considering a specific combination both electric and magnetic fields such that

$$\boldsymbol{E} = -\boldsymbol{v} \times \boldsymbol{B} \tag{1.14}$$

where $\boldsymbol{v}$ is the velocity of the electron, and $\boldsymbol{B}$ is chosen perpendicular to $\boldsymbol{v}$. Without loss of generality, one may choose a Cartesian coordinate system such that the velocity is along the x direction, the magnetic field is directed along the z direction, and the electric field is in the y direction to give:

$$E_y = v_x B_z \tag{1.15}$$

Using the Lorentz transformation to obtain the magnetic field B_z' in the uniformly moving electron frame:

$$B_z' = \frac{B_z - E_y v_x/c^2}{\sqrt{1-(v_x/c)^2}} \tag{1.16}$$

Expanding the right hand side of Eq. 1.16 in powers of v_x, we obtain:

$$B_z' = B_z + \frac{B_z v_x^2}{c^2}\left[\frac{1}{2} + \frac{3}{8}\left(\frac{v_x}{c}\right)^2\right] - \frac{E_y v_x}{c^2}\left[1 + \frac{1}{2}\left(\frac{v_x}{c}\right)^2\right] + ... \tag{1.17}$$

Using the relation 1.15, Eq. 1.17 can be re-written as:

$$B_z' = B_z - \frac{E_y v_x}{c^2}\left[\frac{1}{2} + \frac{1}{8}\left(\frac{v_x}{c}\right)^2\right] + ... \tag{1.18}$$

In the limit $v \ll c$, one gets:

$$B_z' = B_z - \frac{1}{2}\frac{E_y v_x}{c^2} \tag{1.19}$$

or in a three-dimensional vector form, it yields:

$$\boldsymbol{B}' = \boldsymbol{B} + \frac{1}{2}\frac{\boldsymbol{E}\times\boldsymbol{v}}{c^2} \tag{1.20}$$

which is required from Eq. 1.13 with $\alpha = \frac{1}{2}$ and $\beta = 1$. Finally, we get the Thomas's factor $\alpha = \frac{1}{2}$ which is good agreement with the literature. As noted in Ref. [47] the central assumption of this derivation is that proportionality between $\boldsymbol{B}'$ to $\boldsymbol{E}\times\boldsymbol{v}$ carried over to a rotating frame of reference. Beside, the term $B_z v_x^2$ in Eq. 1.17 plays an important role since this term replaces the rotating frame corrections in the case of a pure electric field. Neglecting it would be exactly equivalent to neglecting the effects of a rotating frame of reference for a general choice of fields [47]. The assemble of those general arguments developed here will also serve as the derivation of some general properties dealing with spin-orbital properties at surface or interfaces spinorbitronics materials like developed further in this manuscript.

1.1.3 Relativistic Dirac equation [44]

As mentioned above, the electron spin was theoretically predicted by application of the special relativity principles to the quantum mechanics. It appears naturally in Dirac equation as a result of Lorentz covariance leading to a deep connection between spin and Lorentz invariance that is obscure in non relativistic quantum mechanics [48]. Now we present here the Dirac equation (without presenting how to derive it) and establish the expression of spin-orbit interaction from this equation by an approach introduced by Sakurai [43] and by Winkler [44]. First of all, let us recall the Dirac equation for an electron [43]:

$$(i\hbar\gamma^\mu\partial_\mu - e\gamma^\mu A_\mu - m_0 c)\psi = 0 \tag{1.21}$$

Comparing to Schrödinger equation:

$$i\hbar\frac{\mathrm{d}}{\mathrm{d}t}\psi = H\psi \tag{1.22}$$

one may re-write Eq. 1.21 in term of:

$$i\hbar\frac{\partial}{\partial t}\psi = H_D\psi \tag{1.23}$$

where $H_D = \boldsymbol{\alpha}\cdot(\boldsymbol{p}-e\boldsymbol{A})c+\beta m_0c^2+eV$. Here we have used four-dimensional Einstein summation together with following notations

$$\boldsymbol{\alpha} = \begin{bmatrix} 0 & \boldsymbol{\sigma} \\ \boldsymbol{\sigma} & 0 \end{bmatrix},\ \beta = \begin{bmatrix} I_2 & 0 \\ 0 & I_2 \end{bmatrix},\ \gamma^0 = \beta,\ \gamma^i = \beta\alpha^i \tag{1.24}$$

$$p^\mu = i\hbar\frac{\partial}{\partial x^\mu},\ A^\mu = (V/c, \boldsymbol{A}) \tag{1.25}$$

A solution of Eq. 1.23 is a four-component spinor which can be decomposed into two two-component spinor with the normalized factor as following:

$$\psi = e^{-i\frac{m_0c^2t}{\hbar}}\begin{bmatrix}\phi \\ \chi\end{bmatrix} \tag{1.26}$$

Substituting 1.26 to 1.23, one finds:

$$i\hbar\frac{\partial}{\partial t}\begin{bmatrix}\phi \\ \chi\end{bmatrix} = \begin{bmatrix} eV & c\boldsymbol{\sigma}\cdot(\boldsymbol{p}-e\boldsymbol{A}) \\ c\boldsymbol{\sigma}\cdot(\boldsymbol{p}-e\boldsymbol{A}) & -2m_0c^2+eV \end{bmatrix}\begin{bmatrix}\phi \\ \chi\end{bmatrix} = \mathcal{H}\begin{bmatrix}\phi \\ \chi\end{bmatrix} \tag{1.27}$$

For the stationary state, one obtains

$$\mathcal{H}\begin{bmatrix}\phi \\ \chi\end{bmatrix} = E\begin{bmatrix}\phi \\ \chi\end{bmatrix} \tag{1.28}$$

Solving this equation, one has:

$$\chi = \frac{c\vec{\sigma}\cdot(\boldsymbol{p}-e\boldsymbol{A})}{E-eV+2m_0c^2}\,\phi \tag{1.29}$$

$$[\boldsymbol{\sigma}\cdot(\boldsymbol{p}-e\boldsymbol{A})]\frac{c^2}{E-eV+2m_0c^2}[\boldsymbol{\sigma}\cdot(\boldsymbol{p}-e\boldsymbol{A})]\,\phi = (E-eV)\phi \tag{1.30}$$

To the zeroth order:

$$\frac{E-eV}{2m_0c^2} \propto \frac{v^2}{c^2} \tag{1.31}$$

Finally, we obtain the well-known equation of Pauli [43]

$$\left[\frac{(\boldsymbol{p}-e\boldsymbol{A})^2}{2m_0}+eV-\frac{e\hbar}{2m_0}\boldsymbol{\sigma}\cdot\boldsymbol{B}\right]\phi = E\phi \tag{1.32}$$

Besides, to the first order, one has

$$\frac{c^2}{E-eV+2m_0c^2} \approx \frac{1}{2m_0}\left(1-\frac{E-V}{2m_0c^2}+\ldots\right) \tag{1.33}$$

giving the following equation, which is not an eigenvalue equation:

$$[\boldsymbol{\sigma}\cdot(\boldsymbol{p}-e\boldsymbol{A})]\frac{1}{2m_0}\left(1-\frac{E-V}{2m_0c^2}\right)[\boldsymbol{\sigma}\cdot(\boldsymbol{p}-e\boldsymbol{A})]\,\phi = (E-eV)\phi \tag{1.34}$$

Applying the renormalization for the wavefunction 1.26, we have:

$$\begin{aligned} 1 &= \int \left(\phi^\dagger\phi + \chi^\dagger\chi\right) \mathrm{d}x^3 = \int \left[\phi^\dagger\phi + \left(\frac{\boldsymbol{\sigma}\cdot(\boldsymbol{p}-e\boldsymbol{A})}{2m_0c}\phi\right)^\dagger \left(\frac{\boldsymbol{\sigma}\cdot(\boldsymbol{p}-e\boldsymbol{A})}{2m_0c}\phi\right)\right] \mathrm{d}x^3 \\ &= \int \phi^\dagger \left[1 + \frac{\sum_{ij}(p_i - eA_i)^\dagger(p_j - eA_j)\sigma_i^\dagger\sigma_j}{4m_0c^2}\right] \phi \, \mathrm{d}x^3 = \int \phi^\dagger \left[1 + \frac{(\boldsymbol{p}-e\boldsymbol{A})^2}{4m_0c^2}\right] \phi \, \mathrm{d}x^3 \end{aligned} \tag{1.35}$$

We renormalize then ϕ in the following way (to the first order):

$$\tilde{\phi} = \Omega\phi = \left[1 + \frac{(\boldsymbol{p}-e\boldsymbol{A})^2}{8m_0^2c^2}\right]\phi \tag{1.36}$$

$$\phi = \Omega^{-1}\tilde{\phi} = \left[1 - \frac{(\boldsymbol{p}-e\boldsymbol{A})^2}{8m_0^2c^2}\right]\tilde{\phi} \tag{1.37}$$

Substituting to the Pauli's equation to obtain:

$$\Omega\left[\boldsymbol{\sigma}\cdot(\boldsymbol{p}-e\boldsymbol{A})\right]\frac{1}{2m_0}\left(1 - \frac{E-V}{2m_0c^2}\right)\left[\boldsymbol{\sigma}\cdot(\boldsymbol{p}-e\boldsymbol{A})\right]\Omega^{-1}\tilde{\phi} = (E-eV)\tilde{\phi} \tag{1.38}$$

This expression can then be rewritten, after many simplifications to the order of v^2/c^2 [49]

$$\begin{aligned} \Bigg[\frac{(\boldsymbol{p}-e\boldsymbol{A})^2}{2m_0} + eV + \frac{e\hbar}{2m_0}\boldsymbol{\sigma}\cdot\boldsymbol{B} - \frac{e\hbar\,\boldsymbol{\sigma}\cdot(\boldsymbol{p}-e\boldsymbol{A})\times\boldsymbol{\mathcal{E}}}{4m_0^2c^2} - \frac{e\hbar^2}{8m_0^2c^2}\boldsymbol{\nabla}\cdot\boldsymbol{\mathcal{E}} \\ - \frac{(\boldsymbol{p}-e\boldsymbol{A})^4}{8m_0^3c^2} - \frac{e\hbar(\boldsymbol{p}-e\boldsymbol{A})^2}{4m_0^3c^2}\boldsymbol{\sigma}\cdot\boldsymbol{B} - \frac{(e\hbar B)^2}{8m_0^3c^2}\Bigg]\tilde{\phi} = E\tilde{\phi} \end{aligned} \tag{1.39}$$

where $\boldsymbol{\mathcal{E}} = \frac{1}{e}\nabla V$ is the electric field; $\boldsymbol{B} = \nabla\times\boldsymbol{A}$ is the magnetic field.

The different terms in Eq. 1.39 can be interpreted as [44]

1. $(\boldsymbol{p}-e\boldsymbol{A})^2/2m_0 + eV$: free electron term.
2. $e\hbar/2m_0\boldsymbol{\sigma}\cdot\boldsymbol{B}$: Zeeman term.
3. $-e\hbar\,\boldsymbol{\sigma}\cdot(\boldsymbol{p}-e\boldsymbol{A})\times\boldsymbol{\mathcal{E}}/4m_0^2c^2$: spin-orbit coupling.
4. $-(e\hbar^2/8m_0^2c^2)\boldsymbol{\nabla}\cdot\boldsymbol{\mathcal{E}}$: Darwin term.
5. $-(\boldsymbol{p}-e\boldsymbol{A})^4/8m_0^3c^2 - (e\hbar(\boldsymbol{p}-e\boldsymbol{A})^2/4m_0^3c^2)\boldsymbol{\sigma}\cdot\boldsymbol{B} - (e\hbar B)^2/(8m_0^3c^2)$: relativistic corrections to kinetic energy and Zeeman term.

Note that, mainly in the following, we are interested in the spin-orbit coupling since it introduces non-linear coupling terms in the absence of external magnetic field. In framework of $\boldsymbol{k.p}$ method, the spin-orbit coupling can be treated as a perturbation with the fact that this term is strictly zero when there is an inversion symmetry in the crystal [44].

1.2 The III-V semiconductors and related materials (ferromagnetic (Ga,Mn)As): the art of state

We now will discuss main properties dealing with III-V ferromagnetic semiconductors. Typically, we will focus on (Ga,Mn)As material.

1.2.1 The III-V semiconductors and their alloys: Generalities

The III-V semiconductors such as GaAs, AlAs and InAs are the basis materials for the structures considered in this work. The Molecular Beam Epitaxy which provides crystal structures with sharp layer boundaries, and negligible thickness variations of the layer, is a method to fabricate them.

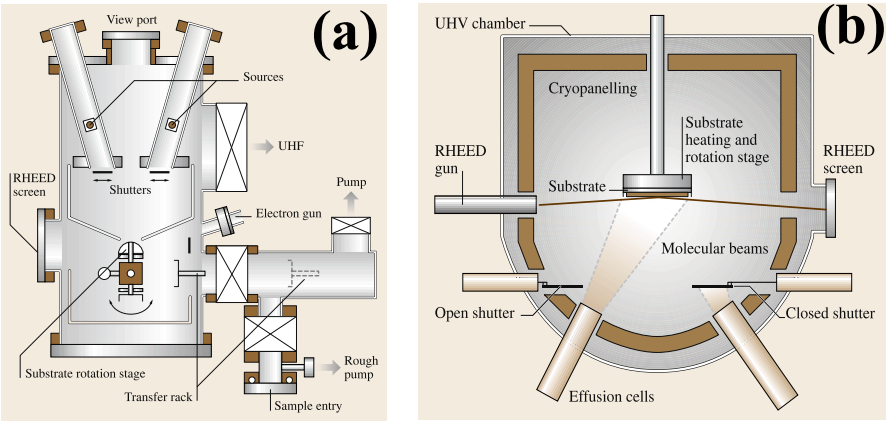

FIGURE 1.3: a) Schematic of a simple molecular beam epitaxial system for the growth of semiconductors. b) Schematic diagram of a MBE growth chamber, showing the effusion cells and shutters, the substrate stage, and the arrangement of the Reflection High-Energy Electron Diffraction (RHEED) system, taken from Ref. [50].

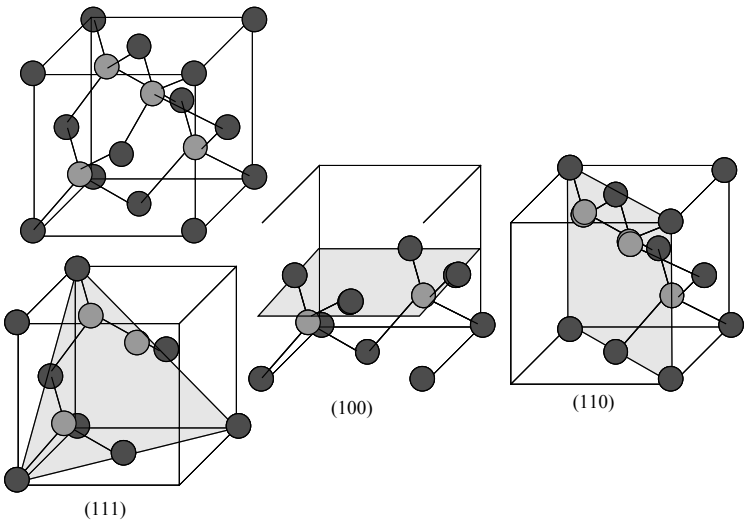

FIGURE 1.4: The unit cell and crystallographic planes of GaAs, taken from Ref. [51].

Figure 1.3 depicts a basis setup of a MBE chamber where the pure materials evaporate from effusion cells setting in a ultrahigh vacuum chamber. Due to the ultrahigh vacuum which is supported by cryogenic

cooling shields to freeze out impurity atoms, the molecules do not interact with each other until they eventually condense on a substrate. This method provides a slow deposition rate allowing epitaxial growth which means that the deposited layer is congruent to the substrate. The relative fluxes out of the effusion cells is controlled by mechanical shutters, and the growth is monitored with the high energy electron diffraction technique.

Using the MBE technique, one can fabricate III-V semiconductor structures such as GaAs-based heterosstructure which consists of tetrahedral covalent bonds by each Ga(As) atom formed with four As (Ga) atoms [51]. Hence, the two interpenetrating face centered cubic (fcc) lattices of the two atom types are forming a zinc blende crystal depicted in Fig. 1.4. The space group symmetry of such crystal is symmorphic and labeled $F\bar{4}3m$ or T_d^2 [52] which contains 24 symmetry operations: the identity, eight C_3 operations (rotation by 120^0), two C_2 operations (rotation by 180^0), six S_4 operations (rotation followed by a reflection perpendicular to the rotation axis), and six σ operations (reflection with respect to a plane) [53].

Unlike the O_h group, the T_d group possesses no inversion center or inversion symmetry which leads to a small potential asymmetry in the lattice potential in T_d group $V_{T_d} = V_{sym} + V_{antisym}$ where $V_{antisym}$ can be considered as a perturbation [29]. When SOI, Eq. 1.10, is taken into account, the lack of inversion symmetry causes an effective internal magnetic field, experienced by the electrons and described by the Dresselhaus terms H_D in the conduction band (CB) [52]:

$$H_D = \gamma_D \left[\sigma_x k_x (k_y^2 - k_z^2) + \sigma_y k_y (k_z^2 - k_x^2) + \sigma_z k_z (k_x^2 - k_y^2)\right] \tag{1.40}$$

where γ_D is the Dresselhaus parameter, k_x, k_y and k_z are three components of wave vector $\boldsymbol{k}$ along x-, y- and z-direction respectively.

One has to emphasize that the H_D contributes odd terms in the electron wave vector $\boldsymbol{k}$ and is responsible for a number of fascinating and important effects being actively studied recently in semiconductors and spintronic [31] such as spin filtering effect without ferromagnetism [54], spin dephasing in barrier grown along [110] direction [55], spin injection via [110] grown semiconductor barrier [56], or anomalous tunnel Hall effect which will be largely described throughout this manuscript [11, 12, 57].

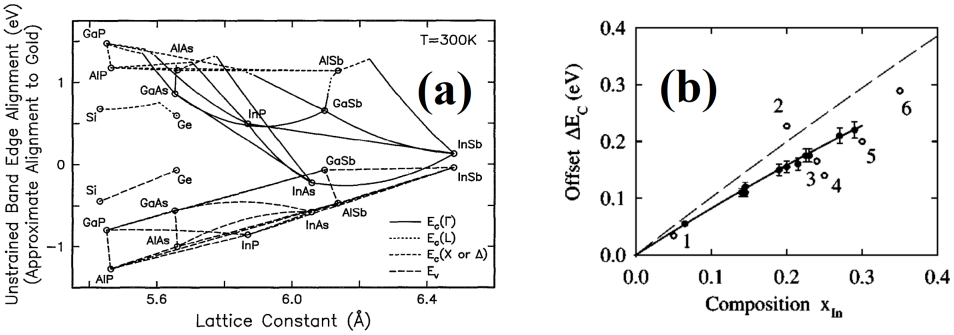

FIGURE 1.5: (a): Energy gap vs. lattice parameter at temperature 300K (taken from Ref. [58]). (b) Conduction band offsets in strained $In_xGa_{1-x}As/GaAs$ QWs as function of In composition (taken from Ref. [59])

The MBE technique also allows one to fabricate the ternary alloys such as $In_xGa_{1-x}As$. In these structures, one of the two fcc-lattices consists of As atoms and the other is occupied by In and Ga atoms. Because GaAs forms a band gap $E_G^{(GaAs)} = 1.42eV$ larger than InAs $E_G^{(InAs)} = 0.35eV$, the band gap of the alloy may be designed by changing the content of In_x [60]: $E_g = xE_g(InAs) + (1-x)E_g(GaAs) - x(1-x)C$ where C accounts for the deviation from a linear interpolation between the two binaries GaAs and InAs which is the so-called bowing parameter, in the range of 0.45-0.5 eV [60]. It has also been proposed that

the bowing depends on the temperature, being almost flat below 100K and decreasing rapidly at higher temperatures [60]. The energy gap as a function of the lattice parameter at room temperature for several III-V alloys is shown in Fig. 1.5a whereas 1.5b gives the band offset of $In_xGa_{1-x}As$. Because of the difference between the gap of GaAs and InAs, one can grow heterostructures with different potential landscapes, such as quantum wells or semiconductor barrier by stacking such layers with different band gaps. These structures are known as type I heterostructures, where the higher VB edge and the lower CB edge are both in the material with the smaller band gap.

1.2.2 Ferromagnetic semiconductors: Exchange interactions in GaMnAs

There is no magnetic order in a III-V semiconductor. However, ferromagnetism was introduced in III-V, [61, 62] and II-VI [63, 64] semiconductors based on proposal of Furdyna [65]: doping the semiconductors with magnetic transition metals, yielding the so-called diluted magnetic semiconductor where the magnetic moments are distributed randomly in the host, allows one to explore the physics of ferromagnetism in semiconductors [32]. In such a material as (Ga,Mn)As, the Mn atoms may substitute ideally a Ga atom in the lattice or locate between the atom sites in the lattice. There are different possibilities for a Mn atom to incorporate into the lattice: two tetrahedral positions between four Ga/As atoms or hexagonal positions between three Ga/As atoms. In the (Ga,Mn)As crystal, manganese plays the role of an acceptor, since Mn has an electron less than Ga in the 4p shell ($Mn = [Ar]\,3d^5 4s^2$; $Ga = [Ar]\,3d^5 4s^2 p^1$ and $As = [Ar]\,3d^5 4s^2 p^3$) [37]. However, this acceptor behavior may be partially or fully compensated due to interstitial Mn impurities. The 3d shell of a Mn atom is only half occupied, yielding a magnetic moment of $\frac{5}{2}\mu_B$ [37, 43]. Because these electrons are not involved in the atomic bonding, the magnetic moment is conserved in the macroscopic material.

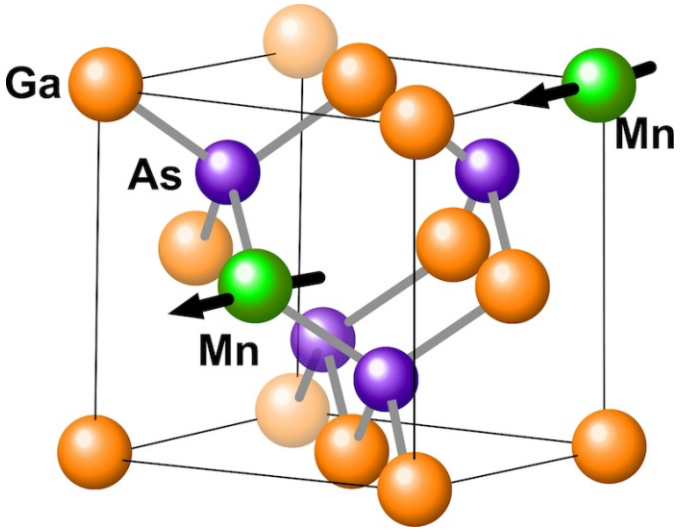

FIGURE 1.6: Crystal structure of (Ga,Mn)As. Mn ions substituting Ga possesses a magnetic moment, and the magnetic moment of each Mn ion aligns along the same direction. This implies ferromagnetism of (Ga,Mn)As. Taken from Ref.[66].

Commonly, the MBE growth temperature for GaAs is high to ensure a pure crystal growth, however, the low solubility of Mn in GaAs would cause segregation at this high temperature, yielding a Mn accumulation on the surface [67]. Therefore, low temperatures are necessary to incorporate the Mn atoms, but also, are giving rise to the implementation of defects. The combination of growth temperature and the Mn concentration, thus, will determine the alloy's state.

Below the Curie temperature, ferromagnetic materials posses a non-vanishing spontaneous magnetization $\boldsymbol{M}$ even in the absence of an external magnetic field. In this regime the magnetic moments are oriented parallel to each other within magnetic domains, and an external magnetic field may align the magnetization directions of the domains. Above the Curie temperature on the contrary, the magnetic moments are randomly oriented in the paramagnetic phase in such a way that the total energy consisting of the exchange energy and the kinetic energy is minimized, yielding an energy splitting in the density of states of two spin orientations. A simple model to describe ferromagnetism is the Heisenberg model in which the two nearest neighbor spins couple ferromagnetically according to the Heisenberg Hamiltonian [68]:

$$H_H = \sum_{i,j} J_{i,j} \boldsymbol{S}_i . \boldsymbol{S}_j \tag{1.41}$$

where $\boldsymbol{S}_{i,j}$ are two nearest neighbor spins and $J_{i,j}$ is the exchange integral which is responsible for the exchange interaction. It exists various kinds of exchange interactions. For example, in the common 3d transition metals, the ferromagnetism is based on the direct exchange interaction, which is an interplay between the Coulomb interaction and the Pauli principle. In (Ga,Mn)As, due to the dilute incorporation, the average distance between the localized magnetic moments is too large to allow a direct exchange coupling, since the overlap of the wave functions of the involved spins is too small. Moreover, Ohno et al. [61, 62] observed a ferromagnetic order in (Ga,Mn)As for Mn concentration higher than 1% which indicates that the ferromagnetism in (Ga,Mn)As is caused by an indirect exchange interaction. In this case, the carriers get spin polarized and couple with other carriers by localized magnetic moments (Zener-type ferromagnetism). Consequently, the exchange integral in Eq. 1.41 possesses an oscillatory behavior $J_{i,j} \propto \frac{cos(k_F r_{i,j})}{r_{i,j}^3}$, where k_F is here the Fermi wave vector and $r_{i,j}$ the distance between the two coupled magnetic moments. For the case of metallic (Ga,Mn)As, with Mn concentration in the 1% – 12% range, the distances are small enough to assume only antiferromagnetic coupling [32]. Thus, the holes couple antiferromagnetically with the localized 3d electron spins (p-$d$interactions), yielding a local ferromagnetic coupling between two Mn magnetic moments. In the case where the hole concentration is large enough, the hole impurity band merges with the GaAs valence band, and the holes, which are freely propagating, align the Mn spins all over the sample. We now discuss the main properties of the p-d exchange interactions within the (Ga,Mn)As compound in both a atomic picture and in a mean-field approach.

Atomic and chemical picture

From general group-theory arguments, in the effective mass approximation [69–71], non-magnetic shallow acceptors like played by Mn atoms can be described by hydrogenic states of fundamental symmetry term $1S_{3/2}$ of binding energy equal to 28 meV for GaAs. In a spherical approximation, these are characterized by a total angular momentum $\mathbf{F} = \mathbf{L} + \mathbf{J} = 3/2$ which is a constant of motion where $\mathbf{L}$ is the angular momentum of the envelope wavefunction. The result is that the fundamental $1S_{3/2}$ wavefunction is $\Phi(S_{3/2}) = f_0(r)\,|L = 0, J = 3/2, F = 3/2, F_z\rangle + g_0(r)\,|L = 2, J = 3/2, F = 3/2, F_z\rangle$. However, according to optical studies, Mn is known to form a shallow acceptor center in GaAs with Mn level of about A^0=d^5+h and electronic configuration characterized by a binding energy [72] of 110 meV due to the consideration of the central potential correction term, and an energy difference of the order of 10 ($\pm$3) meV between the $J = 1$ and $J = 2$ h-d^5 states.

In this picture, the $J = S + j$ quantum number constant of motion is the sum of the d^5 Mn spin angular momentum $S = 5/2$ and the $j = 3/2$ hole angular momentum. In the $S-j$ exchange coupling scheme where the exchange interaction is $J_{exc}\ \mathbf{S} \cdot \mathbf{j}$, the energy difference between the extrema $J = 1$ and $J = 4$ states is equal to $9J_{exc}$ whereas it gives $2J_{exc}$ between the two successive $J = 1$ and $J = 2$ states. It follows that

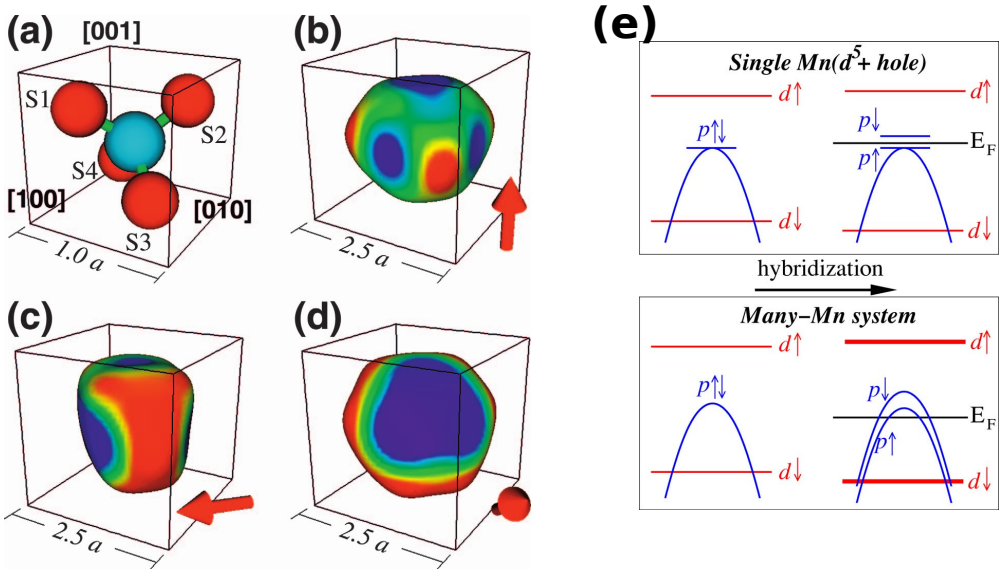

FIGURE 1.7: (a) Atomic structure near a substitutional Mn dopant (blue) in the GaAs lattice (red atoms are As). The As atoms are labeled by S1, S2, S3, and S4. (b-d) Contour surfaces of the LDOS of acceptor level at 10 % if the peak value at the Mn site. The Mn spin is aligned with the (b)[001], (c) [110], or (d) [111] axis of the GaAs lattice. The symmetry is (b) D_{2d}, (c) C_{2v}, or (d) C_{3v}. The LDOS at each atomic site is spatially distributed according to a normalized Gaussian with a 2.5 Å width. The box outlines are aligned with the cubic lattice and have widths in units of the lattice constant a = 5.65 Å, taken from [73]. (e) Electron-picture cartoon: splitting of the isolated Mb acceptor level (top panel) and of the top of the valence-band in the many-Mn system (bottom panel) due to p-d hybridization, taken from [74].

the energy difference between the states corresponding to the spin of the bound hole respectively parallel and antiparallel to the Mn spin can be estimated to be 45 meV. This relative small p-d exchange energy originates from the relative long extent of the bound hole wavefunction where the Mn d states are mostly localized within an effective Bohr radius $a_0^* \propto \epsilon/m^* \simeq 0.8$ nm (ϵ is dielectrical constant) and corresponding to an effective volume of 3 nm^3 as well as an effective Mn concentration approaching $x_{loc} = 1.35\%$. A direct consequence is that the average exchange integral Δ_{exc} is expected to be enhanced with increasing the Mn content x above this threshold Mn concentration $x_{loc} = 1.35\%$.

In the metallic regime and in the **S-s** exchange coupling scheme, the average exchange interaction in $\left(Ga_{(1-x)}, Mn_x\right) As$ reads $\Delta_{exc} = -5/2 x N_0 \beta$, where N_0 is the concentration of cations and $N_0\beta = -(16/S)\left(\frac{1}{-\Delta_{eff}+U_{eff}} + \frac{1}{\Delta_{eff}}\right) \times \left(\frac{1}{3} pd\sigma - \frac{2\sqrt{3}}{9} pd\pi\right)^2 < 0$ is the exchange integral found by treating the p-d hybridization as a perturbation in the configuration interaction picture [75] giving rise to antiferromagnetic interactions between p and d shells. Here, S is the localized d spin, U_{eff}=E(d^{n-1})+E(d^{n+1})-2E(d^n) is the characteristic 3d-3d Coulomb interaction, Δ_{eff}=E($\underline{L}d^n$)-E(d^{n-1}) is the ligand-to-3d charge transfer energy. On the other hand, $(pd\sigma)$ and $(pd\pi)$ are the characteristic Slater-Koster hopping integrals [76]. The value of $N_0\beta = -1.2$ eV ($\beta = -54$ meV.nm^3) is generally admitted from core level photoemission measurements for (Ga,Mn)As with a T_C close to 60 K [77] corresponding to an effective acceptor concentration $x_{eff} \simeq 4\%$ where $x_{eff} = x_0 - 2x_D$ (x_0: minimal doping; x_D: double donors). Figure. 1.8 displays the 4-different exchange-split (Ga,Mn)As subbands calculated for a hole density p=1.7 $\times$ 10^{20} cm^{-3} and an average exchange energy between up and down hole spin of $\Delta_{exc} = 120$ meV.

From a point of view of experiments and material properties, questions remain on the general trends of Tunneling magnetoresistance (TMR) *vs.* exchange interactions $\Delta_{exc} = -5/2 x N_0 \beta$ where xN_0 is the concentration of Mn atoms as well as hole band filling within (Ga,Mn)As. Also, what are the possible effects

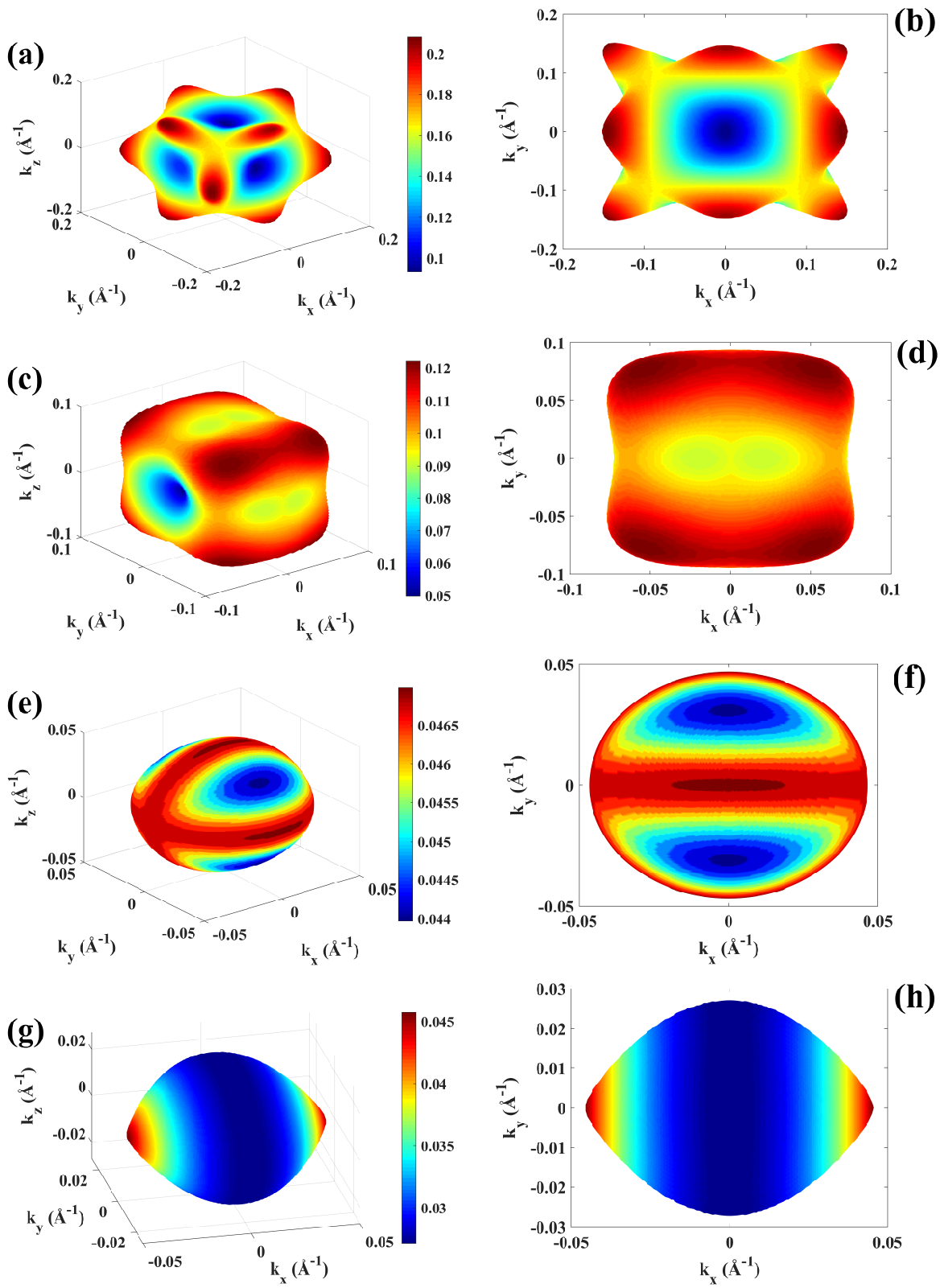

FIGURE 1.8: The four different Fermi surfaces heavy hole up (a) and down (c) and light hole up (e) and down (f) of (Ga,Mn)As calculated in the **k.p** formalism for a Fermi energy equal -135 meV counted from the top of the valence band ($p = 1.7 \times 10^{20}\ cm^{-3}$) and an exchange interaction $\Delta_{exc} = 120 MeV$ (calculated without strain). The magnetization is along the [100] direction. The color code scales the Fermi wavevactor (in nnm^{-1}) along the corresponding crystalline axis. Corrpespondingly, figures (b, d, f, h) are the xy plane projection of figures (a, c , e) and (g).

of the low-temperature (L-T) growth procedure used for the synthesis of these MTJs on the band lineup, valence band offset and related barrier heights of heterostructures integrating (Ga,Mn)As? Remarkably and as shown by non-linear I-V characteristics recorded on junctions both (Ga,As) and (In,Ga)As materials play the role of a tunnel barrier for holes injected from/into (Ga,Mn)As [7, 78]. The same qualitative feature have been demonstrated through optical measurement of the hole chemical potential in ferromagnetic (Ga,Mn)As/GaAs heterostructures by photoexcited resonant tunneling [79]. These results favor a band-edge discontinuity due to the smaller band gap of (Ga,Mn)As compared to GaAs [80] and indicate a pinning of the Fermi level deep inside the band gap of the (Ga,As) host. A part of the answer lies in the incorporation of *n*-type double-donor As antisites during the low temperature growth procedure that partly governs the pinning of the Fermi level at a higher energy position than expected, neighboring the midgap of GaAs. The second reason is due to the positive coulombic-exchange potential experienced by holes and introduced by Mn species playing the role of hydrogen centers for holes orbiting around it. This is at the origin of an impurity-band formation at smaller or intermediate doping level in the host bandgap and an intense debate remains about the position of the Fermi level relative to the impurity band [81]. While infrared measurements [82] as well as magnetic circular dichroism (MCD) [83] experimental and theoretical studies [84] seem to support the scenario of a detached impurity band, recent low-temperature conductivity measurements [85] validate the approach of a VB picture more compatible with a $\boldsymbol{k.p}$ treatment of its electronic properties.

Averaging in media: mean-field approach

In 2000, Dietl et al developed a mean field Zener model to describe the ferromagnetism in (Ga,Mn)As in detail in Ref. [86, 87]. In this approach, the p-d interaction is considered as an effective magnetic field which causes a spin splitting in the valence band. In the picture given by Dietl, the exchange interaction with the hole and *p-d* hybridization is described by [87]:

$$H_{exc} = \frac{\beta \boldsymbol{s}.\boldsymbol{M}}{g\mu_B} = 3B_G \boldsymbol{s}.\boldsymbol{M} \tag{1.42}$$

where β is the average exchange integral, $\boldsymbol{s}$ is the electron spin, $\boldsymbol{M}$ is a localized spin, g is the Landé factor, and μ_B is the Bohr magneton. For the sake of simplicity, in this work we will assume that Eq. 1.42 can be applied to the exchange interaction between electrons and localized magnetic moments.

1.3 Spin-orbit interactions and their symmetry in semiconductors: Larmor frequency

We now turn on the description of specific spin-orbital properties of III-V semiconductor and related materials. In the structure of semiconductors belonging to the O_h group, there is an existing space inversion symmetry which implicates that the spin up and spin down states are degenerate. This can be understood as the consequence of the time-reversal symmetry and space inversion symmetry.

In the system lacking of a space inversion center, the spin degeneracy is lifted because of the presence of an electric field which results from an asymmetric charge distribution inside the semiconductor unit cell, or an electric field applied along a certain crystal axis [29, 37]. According to Eq 1.10, the potential gradient would lead to a spin splitting in the energy dispersion of electron in the conduction band even in the absence of any external magnetic field. An external magnetic field would break the time inversion symmetry and therefore would cause a Zeeman splitting in the energy dispersion. The SO splitting may be considered

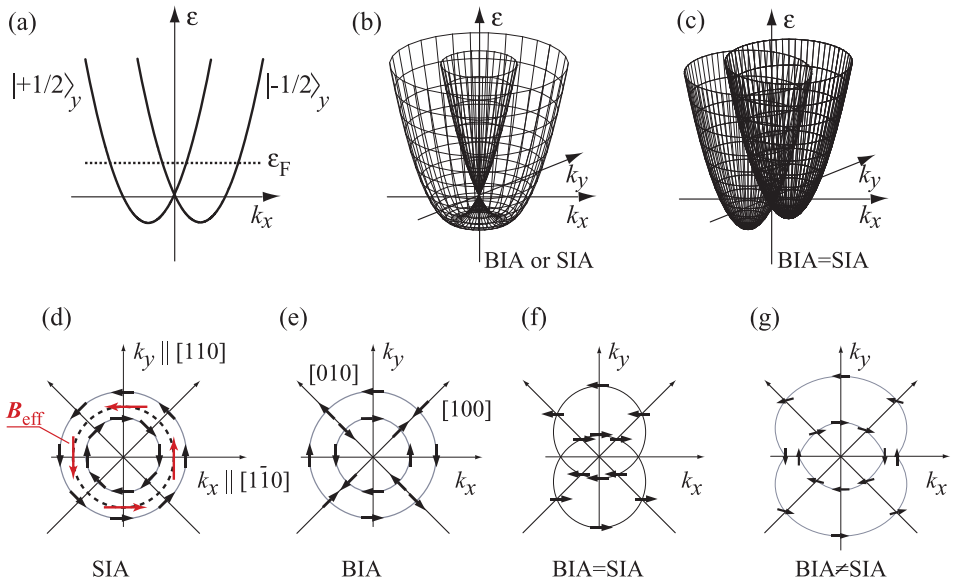

FIGURE 1.9: Panels (a) illustrates the SIA/BIA spin splitting, here $|\pm 1/2\rangle_y$ label the eigenstates with fixed y spin components. Panels (b) and (c) show schematic 2D band structure with k-linear terms for C_{2v} symmetry. The energy ε is plotted as a function of k_x and k_y in (b) with only one type of inversion asymmetry, BIA or SIA, and in (c) for equal strength of the BIA and SIA terms in the Hamiltonian. The bottom panels (d–g) show the distribution of spin orientations at the Fermi energy for different strengths of the BIA and SIA terms. Taken from [88].

as an intrinsic effective $\boldsymbol{k}$ dependent magnetic field $\boldsymbol{B_{eff}(k)}$ in which an electron spin precesses with the Larmor frequency. Consequently, we can re-write 1.10 as:

$$H_{SO} = \frac{\hbar}{2}\boldsymbol{\Omega(k).\sigma} \tag{1.43}$$

where $\boldsymbol{\Omega(k)} = \frac{g\mu_B}{\hbar}\boldsymbol{B_{eff}(k)}$ is the Larmor frequency. The effective SO field must vanish at $k = 0$ because Kramer's theory requires that $\boldsymbol{\Omega(k)} = \boldsymbol{\Omega(-k)}$ thus, leading to no spin splitting at $\boldsymbol{k} = 0$. When $\boldsymbol{k} \neq 0$, the splitting energy is $\Delta E_{SO} = 2\hbar|\boldsymbol{\Omega(k)}|$.

There exist several kinds of space inversion asymmetries:

♣ The bulk inversion asymmetry BIA.

♣ The structure inversion asymmetry SIA.

♣ The natural interface asymmetry NIA.

In the following, we are going to discuss on BIA and SIA which represent very common space inversion asymmetries in III-V semiconductor heterostructures considered in this work.

1.3.1 Bulk inversion asymmetry

In III-V semiconductors of a zinc blende structure, there is no inversion center which gives rise to the BIA. In 1955, G. Dresselhaus used general group theoretical arguments to give an expression for the spin splitting in zinc blende structures [89]. In this case, the Larmor precession vector can be written in the form which is also well known as Dresselhaus field (Eq. 1.40) according to:

$$\boldsymbol{\Omega(k)}_{BIA} = \frac{\gamma_D}{\hbar}\left[k_x\left(k_y^2 - k_z^2\right), k_y\left(k_z^2 - k_x^2\right), k_z\left(k_x^2 - k_y^2\right)\right] \tag{1.44}$$

where the $x-direction$ is along the [100] direction; $y-$ the direction along [010]; $z-$ the direction along [001] and the spin-splitting parameter γ_D is expressed as [37, 90, 91]

$$\gamma_D = \frac{\alpha\hbar^3}{m^*\sqrt{2m^*E_g}} \tag{1.45}$$

here m^* is the electron effective mass, and E_g is the energy gap. One may observe that the magnitude of the Dresselhaus SOI depends on the material and is expressed through a dimensionless parameter α_D. In the literature, there exist several publications which have determined the value of γ_D for the bulk semiconductors like shown in Table 1.1.

$\gamma_D(eV.\text{Å}^3)$	Vurgaftman et al. [60]	Jancu et al. [92]	Perel et al [54]	T.H.Dang et al. [93]
GaAs	17.4-26	24.4	24	23.5
GaSb	185	176	187	180
InAs	-	48.6	130	130
InSb	226	465	220	335
AlAs	-	11.2	11.4	17

TABLE 1.1: Dresselhaus parameter of some bulk semiconductors taken from literature.

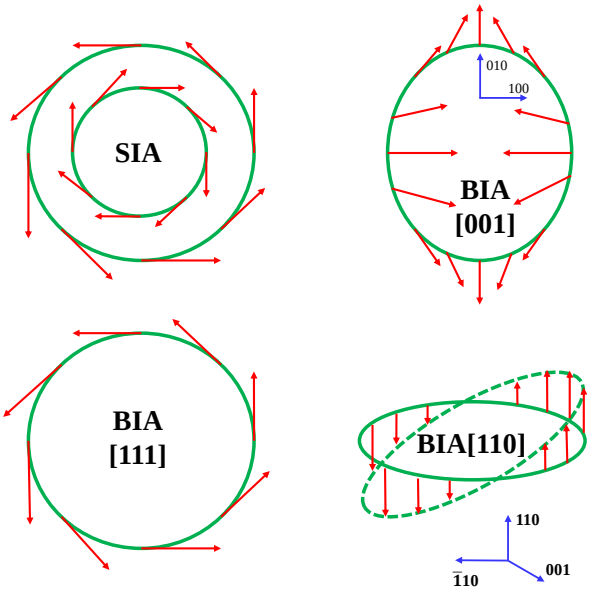

FIGURE 1.10: Vector fields $\boldsymbol{\Omega(k)}$ on the Fermi surface (circle) for the structure inversion asymmetry (SIA) and bulk inversion asymmetry (BIA). Since $\boldsymbol{\Omega(k)}$ is also the spin quantization axis, the vector pattern is also the pattern of the spin on the Fermi surface. As the opposite spins have different energies, the Fermi circle becomes two concentric circles with opposite spins. This is shown here only for the SIA case, but the analogy extends to all examples. The field for BIA [110] lies perpendicular to the plane, with the magnitude varying along the Fermi surface. All other cases have constant fields lying in the plane. Taken from Ref. [37]

In the 2-dimensional electron system, γ_D depends on the confinement energy in the quantum well. The value of γ_D decreases as the confinement energy increases. Moreover, the penetration of the wave function in the barrier material also results in a change of the parameter γ_D [44]. The sign of the parameter is determined by the coordinate system we use. For example, in the case of GaAs in which the cation Ga is

placed at the origin of a GaAs primitive cell and the anion As is located at $a\left(\frac{1}{4},\frac{1}{4},\frac{1}{4}\right)$, γ_D is negative [94]. The confinement of the electron wavefunction in 2D semiconductor systems implicates that the quantization of the momentum is along the growth direction (z-direction). In the first order perturbation theory, the terms k_z and k_z^2 in Eq 1.44 may be replaced by their expectation values. The shape and orientation of the Dresselhaus field now depends on the direction of the quantization axis as depicted in figure 1.10 [37, 91].

In the case of [110]-grown quantum well, one may re-write the Eq.1.44 in a coordinate system $x\|[1\bar{1}0], y\|[00\bar{1}, z\|[110]]$ with a special attention that in quantum wells, since $\langle k_z^2\rangle$ is much larger than the in-plane momentum $k_\|^2$ [91], thus one may neglect the term $\left(k_x^2 - 2k_y^2\right)$ in comparison with $\langle k_z^2\rangle$ to get:

$$\mathbf{\Omega}_{\boldsymbol{D}}^{[110]}(\boldsymbol{k}) = \frac{2\beta}{\hbar}[0,0,k_x] \tag{1.46}$$

where $\beta = \gamma_D\langle k_z^2\rangle$ is the so-called the Dresselhaus parameter. Furthermore, the other components are obtained by cyclic permutation of the indices and one may easily obtain the Dresselhaus fields for both [001] and [111] direction given by [37, 91, 95]:

$$\mathbf{\Omega}_D^{[001]}(\boldsymbol{k}) = \frac{\beta}{\hbar}\left[-k_x, k_y, 0\right] \tag{1.47}$$

$$\mathbf{\Omega}_D^{[111]}(\boldsymbol{k}) = \frac{2\beta}{\sqrt{3}\hbar}\left[k_y, -k_x, 0\right] \tag{1.48}$$

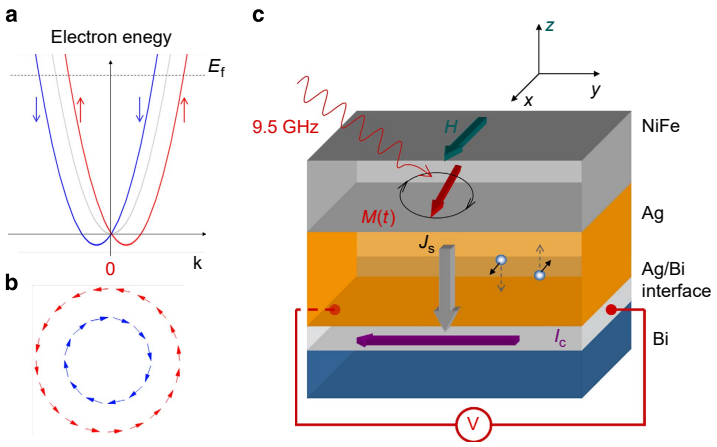

FIGURE 1.11: Electronic structure of interfacial Rashba states and principle of experiments. (a) Typical spin-split dispersion curves of a Rashba 2DEG for $\alpha_R > 0$ (adapted from Nechaev et al. [96]) and (b) typical Fermi contours. An electron flow (that is, a shift of the Fermi contour in the direction of the flow) automatically induces a nonzero spin density or Rashba Edelstein effect (REE). Inversely, a nonzero spin density generated by spin injection induces an electron flow or Inverse Rashba Edelstein effect (IREE)[1]. (c) Scheme of the NiFe/Ag/Bi samples under resonance. The radio frequency (RF) field is along y, and the DC field along x; J_S is the vertical DC spin current injected into the Ag/Bi interface states (back flow included), and converted into a horizontal DC charge current I_C by the IREE. In an open circuit situation I_C is balanced by the current associated to the DC voltage V. Taken from Ref.[97].

[1]We will use the terminologies "Rashba Edelstein" and "Inverse Rashba Edelstein" effects later in the thesis but one has to note here that these effects seem to have previously discovered by other authors, but having more complicated last names, a common author is Lyanda-Geller, [98, 99]. The inverse effect was studied even earlier [100].

1.3.2 Structure inversion asymmetry

In a heterostructure such as quantum well or semiconductor barrier, an external or internal electric field may break the space inversion symmetry [101, 102] resulting in the Bychlov-Rashba spin-orbit interaction which is proportional to the average of the sum of the external and internal field [103]. Moreover, the confinement potential is described in the first order, by an electric field $\boldsymbol{E}$. Thus, similarly to the BIA, the contribution of the SIA to the Hamiltonian in 1.43 can be considered as an effective field, which can be expressed in the lowest order in $\boldsymbol{k}$ and $\boldsymbol{E}$ like [44, 104]

$$\boldsymbol{\Omega}_{BR}(\boldsymbol{k}) = \frac{2\alpha_0}{\hbar}\boldsymbol{k} \times \boldsymbol{E} \tag{1.49}$$

where α_0 is a material parameter ($\alpha_0 = 5.2eA^2$ for GaAs [44]). Typically, the electric field and the material parameters are averaged over barrier and quantum well, if $\boldsymbol{E} = (0, 0, E_z)$ and we put $\alpha = \langle \alpha_0 E_z \rangle$ to find:

$$\boldsymbol{\Omega}_{BR}(\boldsymbol{k}) = \frac{\alpha}{\hbar}[k_y, -k_x, 0] \tag{1.50}$$

This gives a spin splitting in the conduction band $\Delta E_{BR} = \alpha k_{\parallel}$ which is linear in $k_{\parallel} = (k_x, k_y, 0)$ and E_z for small $k_{\parallel}$. The Rashba field 1.49 does not depend on the growth direction of the heterostructure. It is always oriented in the plane and along the direction orthogonal to the electron in plane wavevector. When $k_{\parallel}$ becomes large, the parabolic approximation of the band structure does not hold anymore, and consequently, the spin splitting converges towards a constant [104],

1.4 Spin Hall phenomena via spin-orbit interaction in semiconductors

The Spin Hall Effect, which is a member of the Hall family (see figure 1.12), was predicted by M. I. Dyakonov and V. I. Perel in 1971 [105] and was observed in semiconductors in 2004 by using Kerr notation microscopy technique [106, 107]. This effect consists in the appearance of a spin accumulation on the lateral surfaces of an electric current-carrying sample, the signs of the spin directions being on the opposite boundaries. Therefore, an electrical current flowing through a sample may lead to a spin transport along the direction perpendicular direction as well as a spin accumulation at lateral boundaries. These purely electrical mechanisms do not require neither external magnetic field nor ferromagnets and can be observed in materials with strong spin-orbit as the SO coupling acts like an effective magnetic field on the spin of the electrons. Eventually, SHE gives us the way to generate a spin accumulation like a source of pure spin currents needed for spin injection.

1.4.1 Spin Hall effects

The spin Hall effect originates from the spin-orbit interaction which couples the electron spin to the orbital motion [109]. The origin of the SHE is classified as:

- ♣ *Intrinsic* if SO effects on the wavefunctions of the conducting band are predominant.
- ♣ *Extrinsic* if SO effects originates from the scattering potential of impurities or defects.

In a nonmagnetic conductor, the SOI generates a pure spin current J_{spin} which is orthogonal to the charge current J_{charge}. The conversion efficiency of the charge current density into spin current density is characterized by the spin Hall angle θ_{SHE} given by:

$$\theta_{SHE} = \frac{J_{spin}}{J_{charge}} \tag{1.51}$$

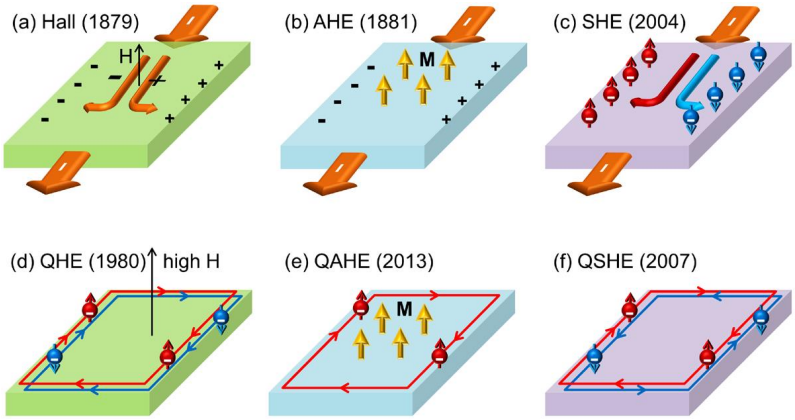

FIGURE 1.12: Members of the Hall family: (a) Hall effect. (b) Anomalous Hall effect. (c) Spin Hall effect. (d) Quantum Hall effect. (e) Quantum Anomalous Hall effect. (f) Quantum Spin Hall effect. Numbers in parentheses indicate the years of each discovery. H is the external magnetic field, M is the intrinsic spontaneous magnetization, and S denotes spin. Taken from Ref.[108].

The use of SHE, eventually, leads to the development of experiments and concepts involving the switching of magnetization in ferromagnetic materials via spin-transfer torque or spin-orbit torque [110], spin torque ferromagnetic resonance [111] and the SHE transistors [112].

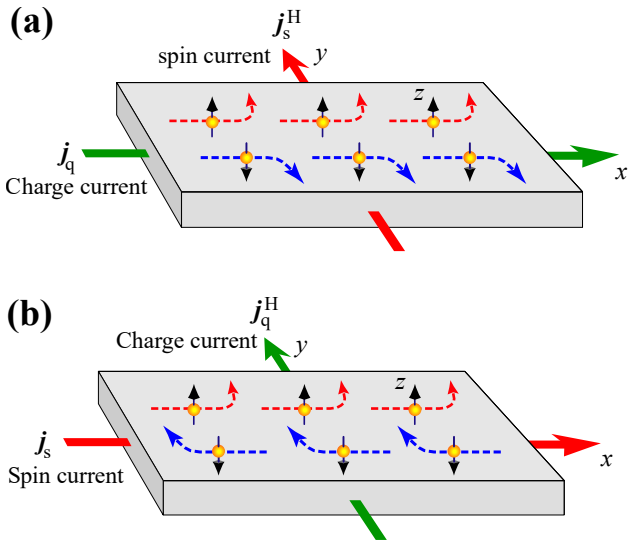

FIGURE 1.13: (a) Charge-current-induced Spin Hall effect (SHE) in which the charge current j_q along the x-direction induces the spin current j_s^H in the y-direction with the polarization parallel to the z-axis. (b) Inverse Spin Hall effect (ISHE) in which the spin current j_s flowing along the x-direction with the polarization parallel to the z-axis induces the charge current j_q^H in the y-direction, taken from Ref.[113].

1.4.2 *Inverse Spin Hall effects and Tunneling Anomalous Hall Effects*

The inverse spin-Hall effect (ISHE), displaying in figure 1.13a, qualifies the mechanism reciprocal to the SHE in which a pure spin current can be converted into a charge current and a charge accumulation. The

ISHE is caused by the bending of electron orbits of up and down spins into opposite directions normal to their group velocity, owing to the spin-orbit interactions [114, 115].

Furthermore, the interplay of SOI and exchange interactions at interfaces and tunnel junctions may result in a large difference of transmission for carriers, depending on the sign of their incident in-plane wavevector: this leads to interfacial skew-tunneling effects that are referred to as anomalous tunnel Hall effect (ATHE) [12, 57] or tunnel anomalous Hall effect (TAHE) [11] which allows one to convert pure spin currents to charge currents as well. Anomalous Tunnel Hall effect based on ferromagnetic semiconductors is one of the main focus of this work and will be discussed in detail in Chapter 5.

1.5 Generation of spin polarization for spin injection into a semiconductor

In conventional (non-magnetic) semiconductors, spin up and spin down populations are balanced, macroscopically since they are randomly oriented. Finding an effective manner to generate a spin imbalance has been a great challenge in the spintronics and semiconductor community.

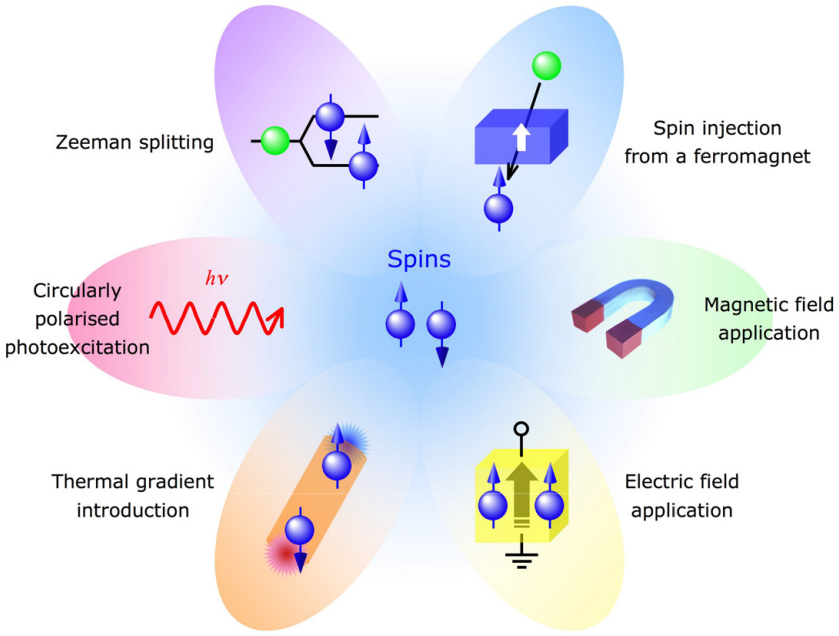

FIGURE 1.14: Techniques to generate spin-polarized electrons in a non-magnetic medium. Taken from [116].

A common way to proceed is an electrical spin injection from a ferromagnetic electrode or via optical pumping with a circularly polarized light source (laser). There are also other ways to create a spin imbalance based on the Spin Seebeck effect [117], where the spin imbalance arises due to the generation of a thermal gradient, or the spin Hall effect [109], where an electrical current driven through a material with a strong spin orbit interaction yields a spin imbalance at the edges of the conducting channel (see section 1.4).

1.5.1 Electrical injection

The electrical injection is well known for a wide application in spintronics devices because of its ability for integrating in the compact devices. This method has already been realized experimentally by Clark

and Feher [118], who drove a direct current through a sample of InSb inthe presence of a constant applied magnetic field. Then, Aronov [119, 120], and Aronov and Pikus [121] established several key concepts in electrical spin injection giving the way to inject a spin polarization from a ferromagnet into a semiconductor, electrically.

In a ferromagnetic material, the exchange interaction causes the spin up and spin down subbands to be split, yielding the differential density of states at the Fermi energy for the two spin subbands. This leads to a strong difference in the mobility of the two spin species. The total current through a ferromagnet, thus, can be described by two independent currents [122, 123] with different mobilities, leading to a net spin polarization injected into a semiconductor layer [124–128].

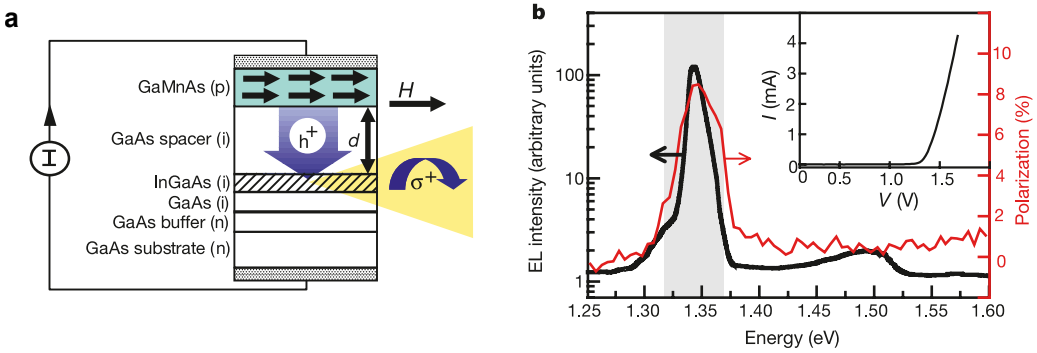

FIGURE 1.15: (a)Electrical spin injection in an epitaxially grown ferromagnetic semiconductor heterostructure, based on GaAs.a, Spontaneous magnetization develops below the Curie temperature T_C in the ferromagnetic p-type semiconductor (Ga,Mn)As, depicted by the black arrows in the green layer. Under forward bias, spin-polarized holes from (Ga,Mn)As and unpolarized electrons from the n-type GaAs substrate are injected into the (In,Ga)As quantum well (QW, hatched region), through a spacer layer with thickness d, producing polarized EL. (b) Total electro-luminescence (EL) intensity of the device (d = 20 nm) under forward bias at temperature T = 6 K and magnetic field H = 1 Oe is shown (black curve) with its corresponding polarization (red curve). Current I = 1.43 mA. Note that the polarization is largest at the QW ground state (E = 1.34 eV). The EL and polarization are plotted on semi-log and linear scales, respectively. Inset, a current-voltage plot characteristic of a 20-nm spacer layer device. Taken from [129].

However, the conductivity mismatch between a ferromagnetic material and a semiconductor leads to a very low spin-injection efficiency [130–132]. A solution for this issue is to introduce a spin dependent interface resistance by using tunnel barriers in which the transmission is proportional to the product of the density of states on both sides [127, 133]. Thus, the resistivity for majority spin is lower than for minority spin, leading to a dependence of spin accumulation on the polarization at the tunnel barrier [68, 127, 134, 135]. Various kinds of tunnel barriers have been proposed, such as the "vacuum" tunnel barriers proposed by Alvaro et al. [136] with an efficiency about 30 %, or Schottky barriers which are naturally formed between a semiconductor and metal [137–139]. Analyzing degree of the circular polarization of the observed electroluminescence, Hanbicki et al [138] observed the spin efficiency up to 32 % for the Fe/AlGaAs contact. However, intermixing between a ferromagnetic material and semiconductor layer during growth process might lead to reduced interface quality, which plays an important role in spin injection. Therefore, the tunnel barrier which is created by inserting an isolating material between ferromagnetic contact and semiconductor may be an alternative solution. Motsynie et al [140] used Al_2O_3 as insulating material which shows very high spin injection efficiency even at room temperature: 21 % and 16 % at 80 K and 300 K, respectively. Beside, a MgO tunnel barriers seem to be very an attractive way for spin injection into a semiconductor since the spin polarization reaches 57 % at 100 K and 47 % at 290 K, respectively [141].

Finally, a different approach to solve the conductivity mismatch problem is to use device based on ferromagnetic semiconductor/semiconductor like (Ga,Mn)As/GaAs Esaki zener diode structure [142] where the spin polarization could be achieved up to 80 % [143–146]. This approach has attracted tremendous attention [67, 143, 147–149] for decades and is one of the mains theoretical focus of this work. For that, one needs to know the band structure of the involved materials. Typically, a complex band structure needs to be considered together with the matching conditions of the wavefunction at the interface. Note that the parallel components of the wavevectors $k_{||}$ of the electrons are preserved during tunneling process, and in the case of (Ga,Mn)As/GaAs based structure, only states close to the Γ-point with matching $k_{||}$ are involved in the tunneling. Sankowski et al. [150] showed that the spin polarization increases as $k_{||}$ increases and achieves the maximum value when $k_{||}$ is parallel to the magnetization $\boldsymbol{M}$. Hence, rising the Mn content and the doping concentration would increase the spin polarization. However, in contrast, the spin lifetime in the GaAs decreases for high doping concentration leading to a decrease of spin polarization. Thus, in order to get high spin polarization, one needs to optimize the parameters to obtain the proper doping concentration.

1.5.2 Optical spin injection

Beside the electrical injection, the optical injection is also widely used for devices because of its simple design and allowance for a uniform carrier excitation over a large area of active region as well as an absorption in a broad wavelength region. The physical basis of optical injection is based on the interaction of light with a semiconductor crystal which may be described through the transition probabilities between two states given by Fermi's golden rule [43]:

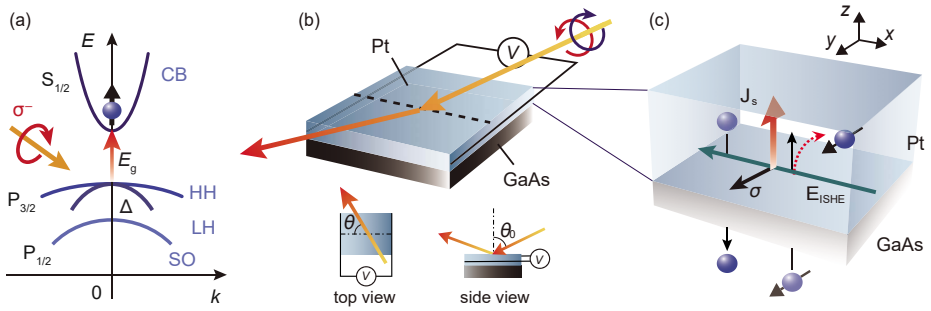

FIGURE 1.16: (a) A schematic illustration of the band structure of GaAs and spin-polarized electrons generated by the absorption of circularly polarized light. (b) A schematic illustration of the Pt/GaAs hybrid structure. θ is the in-plane angle between the incident direction of the illumination and the direction across the two electrodes attached to the Pt layer; $\theta = 65^0$ is the angle of the light illumination to the normal axis of the film plane. (c) A schematic illustration of the inverse spin Hall effect induced by photoexcited pure spin currents in the Pt/GaAs system. Taken from [151].

$$w_{i\to f} = \frac{2\pi}{\hbar}\sum_{f}|\langle f|V_{fi}|i\rangle|^2\delta(E_f - E_i \pm \hbar\omega) \tag{1.52}$$

where $|i\rangle$ and $|f\rangle$ are the initial and final states and V_{fi} is the perturbation operator. The delta function term indicates the conservation of energy, where an incident photon creates an electron-hole pair in conduction and valence bands for $\hbar\omega \geq E_g$. Because the momentum of the photon is small compared to the electron momentum, then one has $k_e \approx k_h$ which implicates a vertical transition in $\boldsymbol{k}$-space. In the first order, V_{ij} may be approximated by an electrical dipolar potential, which does not depend on the spin, in the limit of weak SOI given by:

$$V_{fi} = \vec{d}.\vec{E} = d_xE_x + d_yE_y + d_zE_z \tag{1.53}$$

where $\vec{d}$ is the dipole moment and $\vec{E}$ is the electric field of the light wave in which the components of the electric field E_x, E_y and E_z are considered constant as the electric field variations are small compared to the periodical variation of the lattice potential; the vector $\vec{d}$ is expressed as a spherical tensor $d_\pm$ for $\sigma^\pm$ optical transition. The conservation of angular momentum in interband transitions leads to selection rules applying for the total angular momentum $J = 0, \pm 1$ and its projection on the quantization axis $m_J = \pm 1$, providing a way to directly convert a circularly polarized light to spin-polarized carriers. Typically, these selection rules are satisfied by left σ^+ or right σ^- circularly polarized photons incident along the quantization axis which are emitted from a $\Delta m_J = -1$ transition.

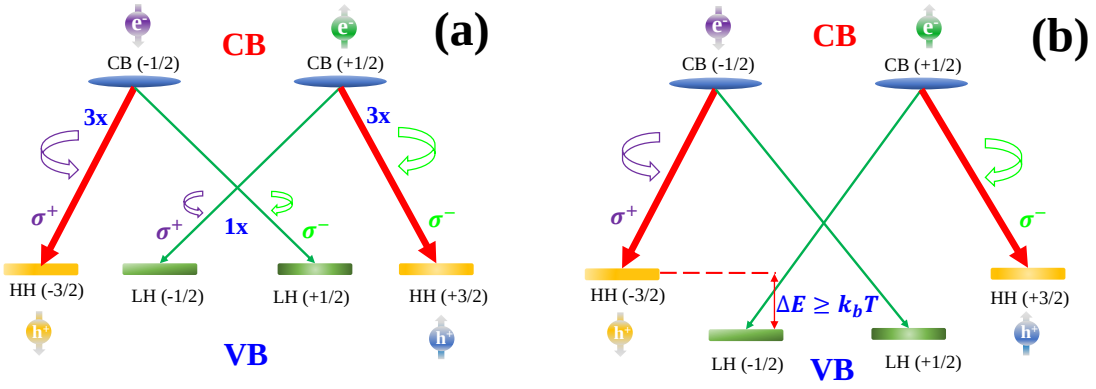

FIGURE 1.17: Optical selection rules for dipole radiation: (a) In the case of a bulk active medium, the HH-band and LH-band are degenerated and (b) a $e \rightarrow h$ recombination in a quantum well structure , the epitaxial strain and quantum confinement lift the degeneracy between the HH-band and LH-band.

Figure 1.17 depicts the relative transition probabilities for $\sigma^\pm$ light in a bulk semiconductor and quantum well active medium at the Γ-point where the CB-HH transitions are three times greater than the CB-LH transition regardless to the active medium. In a bulk semiconductor, the HH and the LH bands are degenerated at the Γ-point leading to a limitation of the spin polarization injected into devices. The maximum of the spin polarization can in this case , theoretically, reach about 50 %. Whereas, the spatial confinement in quantum well may lift the degeneracy of HH and LH bands leading to very high spin polarization efficiency. Theoretically, 100 % of polarization could be achieved. One has to note that the optical selection rules are only strictly valid at the Γ-point. Moving away from this point may lead to an admixture of HH and LH yielding reduced net spin polarization. Nevertheless, the optical circular polarization in the active medium is not immediately converted to a spin polarization since this process is governed by a recombination time and the depolarization mechanism occurring during the transport which would provide a limit value for the spin injection efficiency.

In terms of (Ga,Mn)As materials based structures, Endres et al. [152] has demonstrated that an efficient optical spin injection can be achieved with unpolarized light by illuminating a p-n junction where the p-type region consists of a (Ga,Mn)As ferromagnet semiconductor (see Fig. 1.18b, c). If one illuminates a p-n junction based on GaAs (Fig 1.18a) by photons with an energy exceeding the band gap, electron-hole pairs are generated and will be separated in the built-in electric field of the p-n junction giving rise to a photo-voltage (photo-current). In a device employing the ferromagnetic semiconductor (Ga,Mn)As on the p-side, a highly doped n-side will result in a narrow depletion zone and enables tunneling across the gap. The band bending region of this structure is mostly confined to the n-GaAs because of the heavily p-doped (Ga,Mn)As. If such a p-n junction is illuminated, the resulting photo-current will mostly consist of photoexcited electrons from the n-GaAs side and thus only a small fraction of spin-polarized electrons is created in the (Ga,Mn)As leading to the small spin polarization of the photo-current [152]. The charge

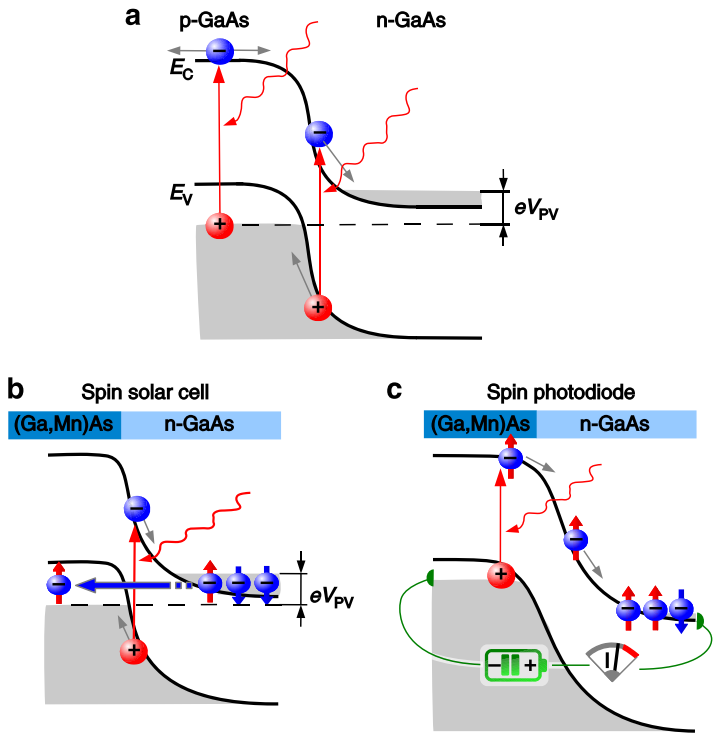

FIGURE 1.18: (a) Schematic of an illuminated GaAs p-n junction showing the conduction and valence band edge E_C and E_V across the junction. Electron-hole pairs are separated in the electric field of the space charge region (see grey arrows) and generate a photo-voltage V_{PV} . Grey areas indicate occupied states. (b) Working principle of the spin solar cell (open circuit condition): the light-induced photo-voltage drives an electron tunneling current (blue arrow) across the gap resulting in a spin accumulation on the n-GaAs side. Photoexcited electrons are only weakly polarized. (c) Working principle of the spin photodiode (biased circuit condition): at reverse bias the width of the tunnel barrier (depletion zone) increases and tunneling is suppressed. As a consequence, photoexcited electrons from the (Ga,Mn)As, which are spin-polarized, are drifting to the n-GaAs conduction band and generate an oppositely oriented spin accumulation. Taken from [152]

accumulation in the n-GaAs leads to a photo-voltage which in turn causes electrons to tunnel across the narrow barrier into the (Ga,Mn)As. Due to the different tunneling probabilities for spin-up and spin-down electrons, spins accumulate in the n-GaAs, that is, light-induced spin extraction occurs (Fig 1.18b) that overcompensates the photo-current-induced spin accumulation [152]. This leads to the central working principle of spin solar cell in this case: the energy of the incident light is not only converted into a voltage (current) but also into a spin accumulation [152]. In not too highly n-doped junctions where tunneling is suppressed in reverse direction leading to another mode of operation, depicted in Fig. 1.18c. When a negative voltage is applied to the p-side of the junction (reverse bias), this would increase the depletion width and suppresses tunneling. Photoexcited electrons on the p-side are, due to the spin-dependent density of states in the valence band, spin-polarized and drift in the electric field of the junction into the conduction band of n-GaAs. This spin photodiode effect was theoretically predicted in 2001 by Žutić et al. [153, 154] and also results in a spin accumulation, however, with the spin orientation reversed in comparison to the spin solar cell effect. Consequently, light-induced spin injection occurs. This spin photodiode effect and its related phenomenon are under theoretical and experimental efforts in the studies in our group at LSI Ecole Polytechnique and CNRS Thales as well.

1.6 Spin relaxation mechanisms in semiconductors

Spin relaxation is of great importances for spintronics since a spin polarization in a nonmagnetic material returns to its thermal equilibrium within the spin lifetime. In the case of III-V semiconductors, one may expect four mechanisms for spin relaxation of conduction electrons: Elliott-Yafet mechanism; D'yakonov-Perel' mechanism; Bir-Aronov-Pikus mechanism; and Hyperfine interaction. The details of these four mechanisms can be found in Ref. [37]. Here, we just present the main points and consequences of these mechanisms.

1.6.1 Elliott-Yafet mechanism

In this mechanism, the spin relaxation is induced by the ordinary momentum scattering requiring a spin orbit interaction to couple the electron spin wavefunction with the lattice wavefunction. The SO coupling is described by:

$$V_{SO} = \frac{\hbar}{4m^2c^2}\left(\nabla V_{SC} \times \boldsymbol{p}\right).\boldsymbol{\sigma} \tag{1.54}$$

where m is the free-electron mass, V_{SC} is the scalar periodic lattice potential, $\boldsymbol{p}$ is the linear momentum operator and $\boldsymbol{\sigma}$ are the Pauli matrices. The Bloch wavefunctions are not the eigenstates of σ_z but a combination of Pauli spin up $|\uparrow\rangle$ and spin down $|\downarrow\rangle$ states. In the case of III-V semiconductors, the spin relaxation of conduction electron with energy $E_{\boldsymbol{k}}$ is characterized by a spin lifetime $\tau_s\left(E_{\boldsymbol{k}}\right)$ given by [37]

$$\frac{1}{\tau_s\left(E_{\boldsymbol{k}}\right)} = A\left(\frac{\Delta_{SO}}{E_g + \Delta_{SO}}\right)^2\left(\frac{E_{\boldsymbol{k}}}{E_g}\right)^2\frac{1}{\tau_p\left(E_{\boldsymbol{k}}\right)} \tag{1.55}$$

where $\tau_p\left(E_{\boldsymbol{k}}\right)$ is the momentum scattering time at energy $\left(E_{\boldsymbol{k}}\right)$, E_g is the energy gap, and Δ_{SO} is the spin-orbit splitting of the valence band. The coefficient A depends on the dominant scattering mechanism.

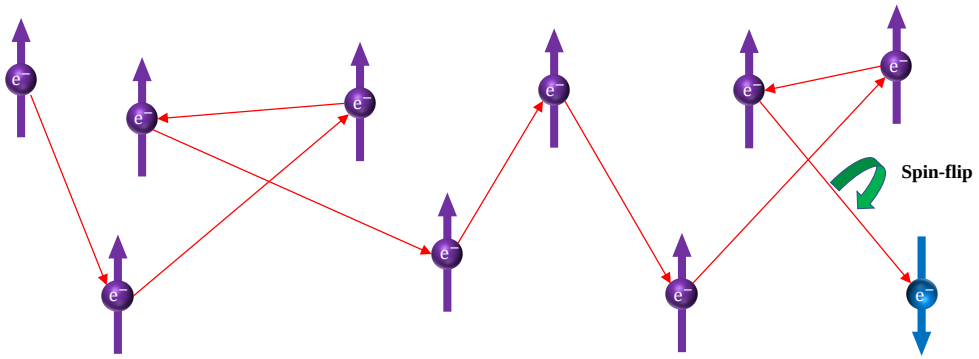

FIGURE 1.19: Schematic of Elliott-Yafet mechanism: relaxation by diffusion on impurities or phonons.

Equantion 1.55 implicates that the Elliott-Yafet mechanism is important for small-gap semiconductor with large SO interaction. For a degenerate semiconductor, $E_{\boldsymbol{k}} = E_f$ whereas for a nondegenerate semiconductor $E_{\boldsymbol{k}} \simeq k_BT$. However, $\tau_s \sim \tau_p$ in both cases. Besides, the temperature dependence of τ_s and τ_p are similar for degenerate semiconductors, while for a non degenarate semiconductor, one has $\frac{1}{\tau_s(T)} \sim \frac{T^2}{\tau_p(T)}$ except in the case of scattering by charged impurities: $\frac{1}{\tau_s(T)} \sim T^{1/2}$ and $\tau_p(T) \sim T^{3/2}$ [37].

1.6.2 D'yakonov-Perel' mechanism

The D'yakonov-Perel' mechanism is a particular mechanism of spin relaxation of systems lacking inversion symmetry such as the bulk III-V semiconductors or the interfaces between different materials. In these systems, the two spin up and spin down states are split: $E_{\boldsymbol{k}\uparrow} \neq E_{\boldsymbol{k}\downarrow}$. This splitting can be described by introducing the intrinsic effective $\boldsymbol{k}$-dependent field (see section 1.3) which is well known as D'yakonov-Perel' effective field. The corresponding Hamiltonian describing the precession of electrons in the conduction band is given by Eq. 1.43 with the Larmor frequency defined in Eq. 1.44.

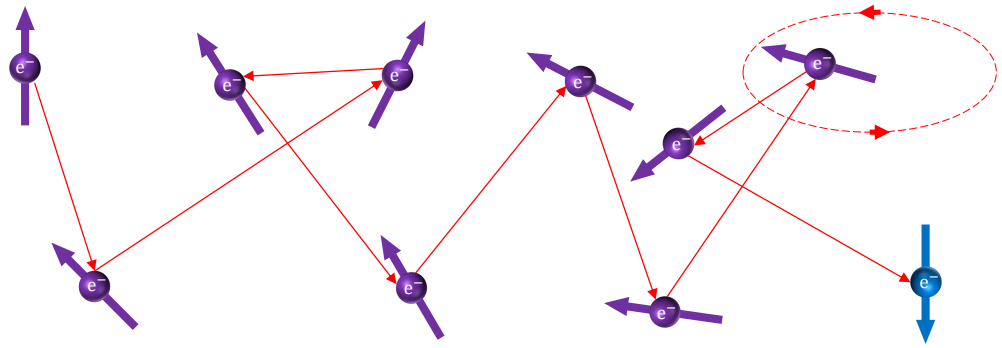

FIGURE 1.20: Schematic of D'yakonov-Perel' mechanism: relaxation by spin precession around the effective $\boldsymbol{k}$-dependent SO magnetic field as well as by diffusion on the crystalline network

If we characterize the momentum scattering by momentum relaxation time τ_p and put Ω_{av} as the average magnitude of Larmor frequency, then one may consider two limiting cases:

♣ $\tau_p\Omega_{av} \geq 1$: In this limit, the spin dephasing rate is proportional to the bandwidth $\Delta\Omega$ of the Larmor frequencies such that $\frac{1}{\tau_s} \approx -\Delta\Omega$ leading to $\tau_s \sim \tau_p$ [37].

♣ $\tau_p\Omega_{av} \leq 1$: In this case, one has $\frac{1}{\tau_s} = \Omega_{av}^2\tau_p$, or in other word, the spin lifetime is inversely proportional to the momentum relaxtion time[37].

In comparision with the Elliott-Yafet mechanism, one observes that the relation of the dephasing rate to the momentum scattering time is opposite. Additionally, in the Elliott-Yafet mechanism the relaxation takes place during the scattering event, whereas in the D'yakonov-Perel' mechanism, the relaxation is between the scattering events.

1.6.3 Bir-Aronov-Pikus mechanism

The electron-hole exchange scattering, which was first shown by Bir et al. in 1975, may also cause spin relaxation [155, 156]. This mechanism is very important, typically for p-doped semiconductors at low temperature. The exchange interaction between electrons and holes is given by the following Hamiltonian [37]:

$$H_{BAP} = A_x \boldsymbol{S}.\boldsymbol{J}_h\delta(\boldsymbol{r}) \tag{1.56}$$

where A_x is proportional to the matrix element of the Coulomb exchange interaction between conduction and valence band states. $\boldsymbol{S}$ is the electron spin operator and $\boldsymbol{J}_h$ is the operator of the total angular momentum of the hole, $\delta(\boldsymbol{r})$ depicts the relative position of the electron and hole.

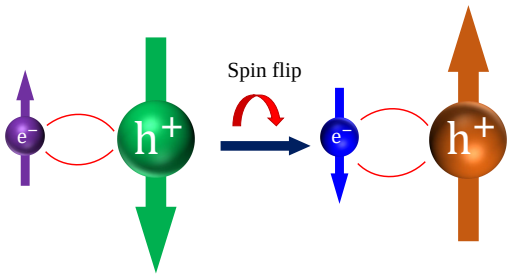

FIGURE 1.21: Schematic of Bir-Aronov-Pikus mechanism: Electron-Hole exchange interaction leading to fast spin relaxation through Elliot-Yafet mechanism

This exchange interaction acts like an effective magnetic field and entails a spin exchange during the scattering process. Consequently, the long range interaction provides the spin-flip since the SOI induces the splitting of the valence band. The spin-flip scattering probability, thus, depends mainly on the states of holes, then, results in the spin relaxation.

For a non degenerate hole system, the spin relaxation resulting from Bir-Aronov-Pikus mechanism is given by [37, 103, 156]:

$$\frac{1}{\tau_s} = \frac{2}{\tau_0} N_a a_B^3 \frac{v_{\boldsymbol{k}}}{v_B} \left[\frac{P}{N_a} |\psi(0)|^4 + \frac{5}{3} \frac{N_a - P}{N_a} \right] \tag{1.57}$$

where N_a is the density of acceptor, $a_B = \frac{\hbar^2 \epsilon}{e^2 m_c}$ the exciton Bohr radius, m_c is the effective mass of electron in the conduction band, p is the density of free holes, τ_0 is an exchange splitting parameter: $\frac{\hbar}{\tau_0} = \frac{3\pi}{64} \frac{\Delta_{ex}^2}{E_B}$ (with $E_B = \frac{\hbar^2}{2 m_c a_B^2}$ is the Bohr exciton energy and Δ_{ex} is the exchange splitting of the excitonic ground state), and $v_B = \frac{\hbar}{m_c a_B}$; $|\psi(0)|^2$ is the Sommerfeld's factor, which enhances the free hole contribution and is given by:

$$|\psi(0)|^2 = \frac{2\pi}{\kappa} \left[1 - exp\left(-\frac{2\pi}{\kappa} \right) \right]^{-1} \tag{1.58}$$

for an unscreened Coulomb potential, where $\kappa = \frac{E_k}{E_B}$ ($|\psi(0)|^2 = 1$ for a completely screened potential)

For a degenerate hole system, the spin dephasing rate is given by [37, 103]

$$\frac{1}{\tau_s} = \frac{3}{\tau_0} p a_B^3 \frac{\langle v_k \rangle}{v_B} \frac{k_B T}{E_{Fh}} \tag{1.59}$$

where E_{Fh} is the hole Fermi energy and $|\psi(0)|^2 = 1$ for degenerate holes. Note that Bir-Aronov-Pikus mechanism dominates in n-doped 2D heterostructures with optical spin injection [157, 158] where the Bir-Aronov-Pikus dephasing rate is proportional to the hole density which is proportional to the laser intensity in the case of optical spin injection.

1.6.4 Hyperfine interaction

The hyperfine interaction comes from the exchange interaction between the spin of electrons and nuclear spin of atoms in the crystalline lattice where the total nuclear spin is non-zero $S_n \neq 0$ [37]. The effective Hamiltonian for the hyperfine interaction is given by [37]:

$$H = \frac{8\pi}{3} \frac{\mu_0}{4\pi} g_0 \mu_B \sum_i \hbar \gamma_{n,i} \boldsymbol{S}.\boldsymbol{I_i} \delta(\boldsymbol{r} - \boldsymbol{R_i}) \tag{1.60}$$

where μ_0 is the vacuum permeability, $g_0 = 2.0023$ is the free electron g factor, μ_B is the Bohr magneton, $\boldsymbol{i}$ is the label for nuclei at positions $\boldsymbol{R_i}$, $\boldsymbol{S}$ and $\boldsymbol{I_i}$ are electron and nuclear spin operators, respectively, expressed in the units of $\hbar$, and $\gamma_{n,i}$ is the nuclear gyromagnetic ratio. The Hamiltonian 1.60 implicates that the spin of an electron experiences an effective magnetic field, which is generated by the hyperfine interaction, given by [37]

$$\boldsymbol{B}_n = \frac{2\mu_0}{3}\frac{g_0}{g}\mu_B \sum_i \hbar\gamma_{n,i}\boldsymbol{S}\boldsymbol{I}_i\delta(\boldsymbol{r} - \boldsymbol{R}_i) \tag{1.61}$$

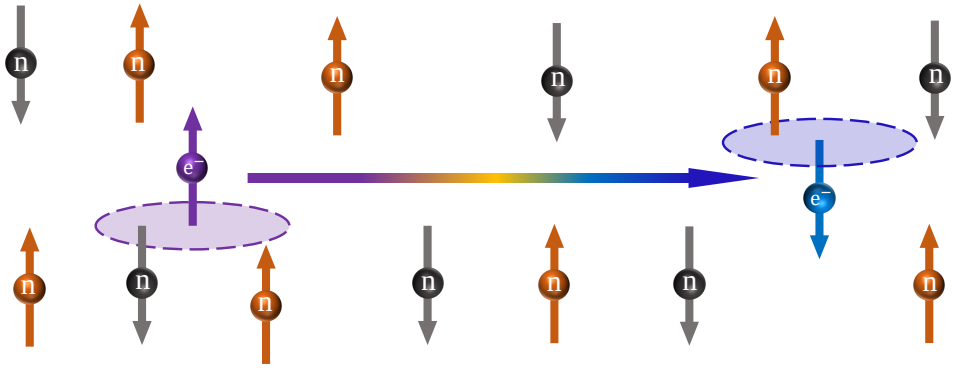

FIGURE 1.22: Schematic of Hyperfine interaction mechanism: Electron-Nucleus exchange interaction.

Commonly in semiconductors, the influence of the hyperfine interaction on the global spin relaxation is small compared to the impact of mechanisms originating from SO like Elliott-Yafet mechanism or D'yakonov-Perel' mechanism. However, its contribution may become significant when the nucleus polarization increases in case of optical pumping.

CHAPTER 2

O_h and T_d semiconductors: The electronic band structure

Contents

Calculating the electronic structure and band dispersion of a single and many body systems (multilayers) is a very complex task which still requires modern computer hardware. Commonly, material science computational methods for the band structure calculation fall into two general approaches [53]:

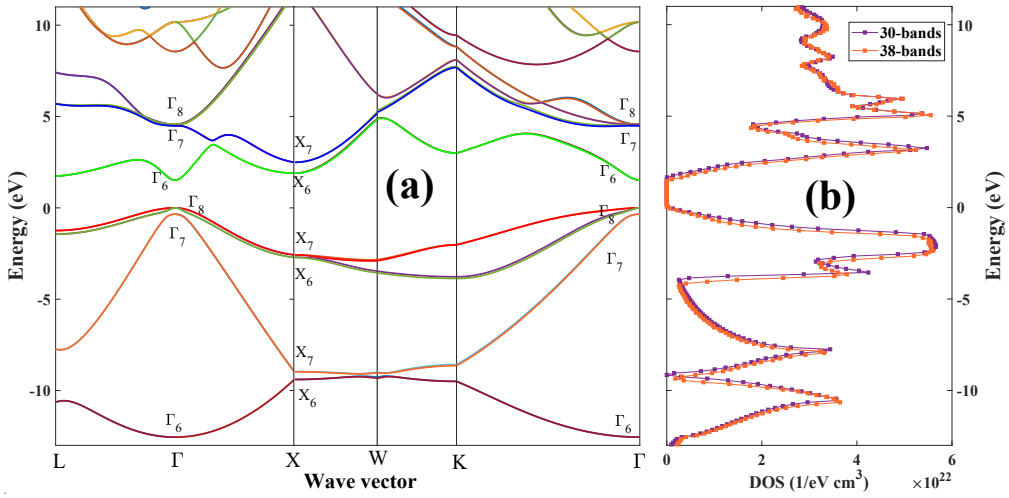

FIGURE 2.1: (a) Band structure of GaAs (belongs to T_d group) calculated in framework of 30-band $\boldsymbol{k.p}$ model. The energy at the top of the filled valance bands has been taken to be zero. (b) Density of states (DOS) calculated with native 30-band $\boldsymbol{k.p}$ method and 38-band (30 bands + 8 ghost-bands detailed hereafter) which shows that the ghost-band weakly affects the DOS which is in good agreement with the experimental results and numerical results, calculated by Density Functional Theory in Ref.[46].

♣ The first approach involves ab-initio methods, such as Density Functional Theory (DFT) or Hartree-Fock method from first principle techniques without the need of empirical parameters except in a LSDA + U approach [159].

♣ The second approach, less consuming, consists of far more computationally efficient semi-empirical methods such as the empirical pseudopotential method (EPM) [160, 161], Tight-binding (TB) and the $\boldsymbol{k.p}$ method, according to which energy band structure is obtained from a set of parameters: the energy gaps at Γ point, the momentum matrix elements and the strength of the spin-orbit (SO) coupling. The number of energy bands (or levels) effectively implemented is related to the precision chosen for the results.

In the present work, our main focus is to develop a multiband $\boldsymbol{k.p}$ framework to describe the electronic structure within the Brillouin zone (BZ) of semiconductors and related heterostructures. It consists in applying a perturbation approach from the unique knowledge of those parameters at the Γ point.

We first describe the main issues of DFT fundamentals before discussing the semi-empirical tight-binding and $\boldsymbol{k.p}$ schemes. The $\boldsymbol{k.p}$ method is largely employed in this work and manuscript.

Description of the k.p method First, we start with the description of the $\boldsymbol{k.p}$ method and obtain the $\boldsymbol{k.p}$ equation for the envelope function by using the Bloch theorem. We then discuss the way how to build $\boldsymbol{k.p}$ Hamiltonians for O_h and T_d semiconductors from the point of view of symmetry using Linear Combination of Atomic Orbital (LCAO) and Tight-Binding (TB) principle. To exactly match the true band structure, one has to work with an infinite basis set (infinite dimensional Hamiltonian) which has to be restricted to a finite number of bands: 2-band effective model may be employed to describe the conduction states near the Γ point whereas a 6-band Luttinger model may describe the valence band of p-symmetry in an effective Hamiltonian approach using the Luttinger parameters [162]. Furthermore, a 8-band $\boldsymbol{k.p}$ model is needed to describe the coupling between the conduction and valence bands, whereas

a 14-band $\boldsymbol{k.p}$ model becomes mandatory to property describe spin-orbit interactions (SOI) coupled to the absence of inversion symmetry involving Dresselhaus terms [94]. Beyond, a 30-band $\boldsymbol{k.p}$ or 40-band $\boldsymbol{k.p}$ is mandatory to describe the spin injection properties in the full BZ, as required for an indirect band gap group IV semiconductors like Si, Ge, and their compounds alloys and related heterostructures. These finite multiband Hamiltonians are detailed in this chapter and Appendix A.

However, the price to pay for such simplification within finite dimensional basis like pointed out in Ref. [163], is that spurious or unphysical states emerge at large wave vectors as a consequence of the truncation of the remote bands necessary to recover the Bloch periodicity. These states are unphysical and have to be removed in the electronic structure to restore the relevant physical properties. We suggest here a new method based on an extension to Kolokolov's proposal [164] and called "Ghost band" method. We will show that this novel method is very robust and can be adapted to very wide cases, from 8-band up to, at least, 40 band $\boldsymbol{k.p}$ Hamiltonian.

Finally, we review some detail on the effective Hamiltonian for both CB and VB (conduction and valence bands) by including SOI and the effect of exchange interactions within possible strain field accounted for the framework of $\boldsymbol{k.p}$ theory before investigating the main transport properties.

2.1 Density Functional Theory (DFT)

We give here some insight about the Density Functional Theory (DFT) technique which is a powerful technique to solve many-body problems in solid state physics by reducing the complexity to an effective single-particle equations. The advantage of DFT is that, unlike the $\boldsymbol{k.p}$ method, it represents an ab initio technique without any further needed input than atomic parameters (and positions) which makes it straightforwardly applicable to many systems with high predictivity. The representation of the a priori unknown exchange-correlation functional, described hereafter, has been improved from the local density via the generalized gradient approximation to more sophisticated functions allowing for an accurate description of strongly correlated systems [165, 166].

Born-Oppenheimer approximation

In detail, the general free Schrödinger Hamiltonian describing the full interactions of the electronic system, which constitutes a complex many-body problem, cannot, generally, be solved numerically nor analytically. In this case, the well-known Born-Oppenheimer approximation makes an important simplification. Here, the assumption is that the motion of atomic nuclei and electrons in a molecule can be treated separately. Accordingly, the nuclei coordinates are fixed within the Born-Oppenheimer approximation and the Hamiltonian is solved for that particular set of atomic positions.

Hohenberg-Kohn theorems

The basic idea of DFT has been developed in the 1960 by Hohenberg and Kohn [167]. They proved for a system with a non-degenerate groundstate that the potential and therefore the Hamiltonian is a unique functional of the electron density $n(\boldsymbol{r})$ alone. A generalized proof was given by Levy [168]. This yields the famous Hohenberg-Kohn theorem:

♣ All ground state properties of a given many-body system are unique functionals of the electron density $n(\boldsymbol{r})$.

♣ The total energy functional $E[n]$ underlies the variational principle:

$$\frac{\partial E[n]}{\partial n(\boldsymbol{r})} = \mu \tag{2.1}$$

where μ is a Lagrange-multiplicator and that will correspond to the Femi level, consuming the particle conversation

$$N - \int n(\boldsymbol{r})d\boldsymbol{r} = 0 \tag{2.2}$$

and where the ground state density n_0 minimizes the energy functional:

$$E[n] \geq E[n_0] = E_0 \tag{2.3}$$

Kohn-Sham equation

The basic idea of Kohn and Sham [169] is to represent an interacting system by a non-interacting system with the same electron density to obtain a good approximation for the contribution of the kinetic energy to the energy functional E[n]. The functional E[n] 2.3 then can be split into several parts and written as [170]:

$$E[n] = T_0[n] + \int\int d\boldsymbol{r}d\boldsymbol{r}'\frac{n(\boldsymbol{r})n(\boldsymbol{r})'}{|\boldsymbol{r}-\boldsymbol{r}'|} + E_{xc}[n] + \int d\boldsymbol{r}n(\boldsymbol{r})V_{ext}(\boldsymbol{r}) \tag{2.4}$$

where $n(\boldsymbol{r})$ is the electron density, V_{ext} is the external potential, and $T_0[n]$ describes the kinetic energy of a system of non-interacting particles with the same electron density. The second term denotes the Coulomb interaction of the electrons in the Hartree approximation and E_{xc} is the exchange correlation energy arising due to the exchange and correlation effects of the electron density itself.

For the following discussion it is intuitive to introduce a wave-function representation. Then the electron density can be expressed by:

$$n(\boldsymbol{r}) = \sum_{i=1}^{N} |\phi_i(\boldsymbol{r})|^2 \tag{2.5}$$

where the summation extends over the N orbitals with the lowest eigenvalues. The functional for the kinetic energy T_0 reads in that basis:

$$T_0[n] = \sum_{i=1}^{N} \int \nabla\phi_i^*(\boldsymbol{r})\nabla\phi_i(\boldsymbol{r})d\boldsymbol{r} \tag{2.6}$$

The next important step is to apply the variational principle, which is stated in the Hohenberg-Kohn theorems, to the energy functional 2.4 under the Lagrange constraint that the normalization of the wave-function ϕ_i is conserved:

$$\sum_i \epsilon_i \left(\int \phi_i^*(\boldsymbol{r})\phi_i(\boldsymbol{r})d\boldsymbol{r} - 1 \right) \tag{2.7}$$

where ϵ_i are the Lagrange-parameters. The variation of the energy functional $E[n]$ then yields the pseudo Schrödinger equation according to:

$$\left(-\nabla^2 + V_{eff}[n]\right)\phi_i = \epsilon_i\phi_i \tag{2.8}$$

The effective potential V_{eff} covers all previously discussed contributions to the energy and reads:

$$V_{eff}[n] = \int \frac{n(\boldsymbol{r}')}{\boldsymbol{r}'-\boldsymbol{r}}d\boldsymbol{r}' + V_{ext}(\boldsymbol{r}) + \frac{\partial E_{xc}[n]}{\partial n} \tag{2.9}$$

and the determination of the kinetic energy T_0:

$$T_0[n] = \sum_{i=1}^{N} \epsilon_i - \int V'_{eff}[n']n(\boldsymbol{r})d\boldsymbol{r} \tag{2.10}$$

where V'_{eff} is the effective potential for a trial electron density n'. The total energy functional then reads:

$$E[n] = \sum_{i=1}^{N} \epsilon_i - \int V'_{eff}(\boldsymbol{r}) n(\boldsymbol{r}) + \int V_{ext}(\boldsymbol{r}) n(\boldsymbol{r}) + \int\int \frac{n(\boldsymbol{r}) n(\boldsymbol{r}')}{|\boldsymbol{r} - \boldsymbol{r}'|} + E_{xc}[n] \tag{2.11}$$

where the first term accounts the single-particle contribution.

It is worth to point out that the eigenvectors ϕ_i of the Kohn-Sham equation 2.8 have to be obtained self-consistently as the effective potential is a functional of the density itself.

Spin-density functional theory

For the purpose of incorporating magnetic effects, DFT has to be generalized for two spin channels. Going a step beyond the Hohenberg-Kohn approach, independently Hedin [166] and Pant and Rajagopal [171] extended the method by including spin-dependent electron densities or alternatively a magnetization density $m(\boldsymbol{r})$ and generalized the Hohenberg-Kohn theorem to the spin-polarized case. Within the later notation the variational principle becomes:

$$E[n(\boldsymbol{r}), m(\boldsymbol{r})] \geq E[n_0(\boldsymbol{r}), m_0(\boldsymbol{r})] = E_0 \tag{2.12}$$

where the electron and magnetization density are defined by:

$$n(\boldsymbol{r}) = n^{\uparrow}(\boldsymbol{r}) + n^{\downarrow}(\boldsymbol{r}) \tag{2.13}$$

$$m(\boldsymbol{r}) = n^{\uparrow}(\boldsymbol{r}) - n^{\downarrow}(\boldsymbol{r}) \tag{2.14}$$

where $n^{\uparrow}$ and $n^{\downarrow}$ are spin up and spin down densities, respectively.

In general, the two-component Pauli spinors or the spin-density matrix $\rho_{\alpha,\beta}$ as originally proposed [166, 171] are used to derive the spin-dependent Kohn-Sham equations. Analogously the derivations of the Kohn and Sham for DFT [169], the basic equations of SDFT turn out to be effective single-particle Pauli-Schrödinger equations:

$$\left\{-\nabla^2 + V^{\sigma}_{eff}[n, m]\right\} \phi^{\sigma}_i = \epsilon^{\sigma}_i \phi^{\sigma}_i \tag{2.15}$$

where the two components ϕ^{σ} are coupled to each other and optionally to an external magnetic field, which can enter the effective potential V_{eff}. It is important to note that we did not take into account here any possible non-collinearity or relativistic effects like spin-orbit coupling.

Exchange-interaction potential.

The most important approaches to find accurate approximations to the exchange-correlation potential are the local-density approximation (LDA) and the generalized gradient approximation (GGA).

In the LDA - or, in the spin-polarized case, local spin density approximation (LSDA) - the function E^{LDA}_{xc} is assumed to be locally approximated by the exchange-correlation energy of a homogeneous electron gas of the density $n(\boldsymbol{r})$ [172]. This procedure is similar to the Thomas-Fermi-approximation for the kinetic energy of an inhomogeneous electron system. Integrating the locally defined function of spin dependent electron densities over then whole space yields the total exchange-correlation energy according to:

$$E^{LSD}_{xc}[n_{\uparrow}(\boldsymbol{r}), n_{\downarrow}(\boldsymbol{r})] = \int \left[\epsilon^{hom}_x(n_{\uparrow}(\boldsymbol{r}), n_{\downarrow}(\boldsymbol{r})) + \epsilon^{hom}_c(n_{\uparrow}(\boldsymbol{r}), n_{\downarrow}(\boldsymbol{r}))\right] d\boldsymbol{r} \tag{2.16}$$

While the exchange energy ϵ^{hom}_x is known exactly for the homogeneous electron liquid, developing a parametrization of the correlation energy ϵ^{hom}_c is a highly non-trivial problem.

Due to the fact that any real system has a spatially varying electron density, the LSDA approach can be improved by considering gradient corrections to give

$$E_{xc}^{GGA}[n_\uparrow(\boldsymbol{r}), n_\downarrow(\boldsymbol{r})] = \int f(n_\uparrow(\boldsymbol{r}), n_\downarrow(\boldsymbol{r}), \nabla n_\uparrow(\boldsymbol{r}), \nabla n_\downarrow(\boldsymbol{r}))d\boldsymbol{r} \tag{2.17}$$

There are many different ways to construct the function f, one of the most reliable ones has been developed by Perdew et al. [173]. Besides this most commonly used LDA and GGA functionals, part of the additional correlation effects can be described within the LDA + U - approach [174].

2.2 The tight-binding method [175]

We are now going to review the general procedure of the Tight-Binding (TB) method. The ideas of TB are closely related to the Linear Combination of Atomic Orbitals (LCAO) method which is based on the superposition of wavefunctions of isolated atoms located at each atom site in the lattice. If we assume that $V(\boldsymbol{r})$ is the periodic potential which is formed by the atoms in the lattice, then in the framework of TB method, $V(\boldsymbol{r})$ may be written as a sum of atomic potentials at each site and the potentials from neighbors [46, 76, 176]:

$$V(\boldsymbol{r}) \simeq \sum_m U(\boldsymbol{r} - \boldsymbol{R_m}) + \sum_{l \neq m} U(\boldsymbol{r} - \boldsymbol{R_l}) \tag{2.18}$$

here, $U(\boldsymbol{r} - \boldsymbol{R_m})$ is the atomic potential at $\boldsymbol{r}$ contributed by an atom which is located at $\boldsymbol{R_m}$ and $\sum_{l \neq m} U(\boldsymbol{r} - \boldsymbol{R_l})$ is the potential from its neighbors which is considered as perturbative potential.

The Schrödinger equation for an electron in the crystal is given by:

$$\left[-\frac{\hbar^2}{2m}\nabla^2 + V(\boldsymbol{r})\right]\psi(\boldsymbol{r}) = E\psi(\boldsymbol{r}) \tag{2.19}$$

Substituting 2.18 to 2.19 one may re-write Eq.2.19 in terms of:

$$\left[-\frac{\hbar^2}{2m}\nabla^2 + \sum_m U(\boldsymbol{r} - \boldsymbol{R_m}) + \sum_{l \neq m} U(\boldsymbol{r} - \boldsymbol{R_l})\right]\psi(\boldsymbol{r}) = E\psi(\boldsymbol{r}) \tag{2.20}$$

Equation 2.19 gives rise a meaning that the electron at each side feels not only the atomic potential at the same side but also the potential from its neighbors which is given by the perturbative potential $\sum_{l \neq m} U(\boldsymbol{r} - \boldsymbol{R_l})$.

Let us now assume that the solutions for the Schrödinger equation of the free atoms that form the crystal:

$$\left[-\frac{\hbar^2}{2m}\nabla^2 + U(\boldsymbol{r})\right]\chi_i(\boldsymbol{r}) = E_i\chi_i(\boldsymbol{r}) \tag{2.21}$$

are known, where $U(\boldsymbol{r})$ is the atomic potential of a free atom and $\chi_i(\boldsymbol{r})$ is the eigentstate of an electron in the atomic energy level E_i.

If there are a atoms in the primitive cell and their coordinates are given by:

$$\boldsymbol{R_m} + \boldsymbol{r_\alpha} \tag{2.22}$$

where $\boldsymbol{r_\alpha}$ represents the position of one atom inside the primitive cell. Then Eq.2.20 or Eq.2.19 may admit a solution in the form of linear combination of Bloch function which can be constructed as [176]:

$$\psi_{n,\boldsymbol{k}}(\boldsymbol{r}) = \frac{1}{\sqrt{N}}\sum_{n=1}^{N}\sum_{\alpha=1}^{a} e^{i\boldsymbol{k}.\boldsymbol{R_m}}\chi_n(\boldsymbol{r} - \boldsymbol{R_m} - \boldsymbol{r_\alpha}) \tag{2.23}$$

where N is the number of primitive cells in the crystal, $\boldsymbol{k}$ is the wavevector within the first Brillouin zone whose values are determined by the periodic boundary conditions. However, the atomic orbitals $\chi_j(\boldsymbol{r})$ on different atomic sites are not orthogonal to one another. Thus, Löwdin et al. [177] has proposed an orthogonal set which is obtained from this nonorthogonal one in Eq.2.23 in such a way it preserves the symmetry properties of the original set. The relation between Löwdin functions and 2.23 functions is given by the transformation [176]:

$$f_n\left(\boldsymbol{r}-\boldsymbol{R_l}-\boldsymbol{r_\alpha}\right)=\sum_{i,\boldsymbol{R_m}} S^{1/2}_{j\boldsymbol{R_l},i\boldsymbol{R_m}}\chi_{i,\boldsymbol{R_m}} \tag{2.24}$$

where S is the overlap matrix which has a greater extent in space than the atomic orbitals, implying that the Hamiltonian matrix will have elements significantly different from zero between atoms that are second or third nearest neighbors. The orthogonal basis set for building TB Hamiltonian can then be formed from these Löwdin functions as:

$$\Phi_{n,\boldsymbol{k}}=\frac{1}{\sqrt{N}}\sum_m\sum_\alpha e^{i\boldsymbol{k}.\boldsymbol{R_m}} f_n\left(\boldsymbol{r}-\boldsymbol{R_m}-\boldsymbol{r_\alpha}\right) \tag{2.25}$$

The wavefunction of an electron in crystal can be written in terms of basis set 2.25 as:

$$\Psi_{m,\boldsymbol{k}}=\sum_m c_{mn}\Phi_{n,\boldsymbol{k}} \tag{2.26}$$

Note that, the matrix elements of the TB Hamiltonian built from the Löwdin functions are not the same as the atomic energies. However, this is not important since after all, the tight-binding Hamiltonian is formed in a parametrization scheme. Using the Löwdin functions to replace the atomic orbitals, the orthogonality properties are fullfilled. Therefore, substituting Eq.2.26 and Eq.2.25 to Eq.2.19, multiplying by $\Psi^*_{\boldsymbol{k}}$ from the left and integrating over space, gives the coupled equations for the expansion coefficients $c_{m,n}$ as:

$$\sum_{m,n}\left(H_{mn,m'n'}-E(\boldsymbol{k})\delta_{mm'}\delta_{nn'}\right)c_{m',n'}(\boldsymbol{k})=0 \tag{2.27}$$

where:

$$H_{mn,m'n'}=\frac{1}{N}\sum_{m,m'} e^{i(\boldsymbol{R_m}-\boldsymbol{R_{m'}})}\int f(\boldsymbol{r}-\boldsymbol{R_m}-\boldsymbol{r_n})Hf(\boldsymbol{r}-\boldsymbol{R_{m'}}-\boldsymbol{r_{n'}})d\boldsymbol{r} \tag{2.28}$$

The $H_{mn,m'n'}$ depend on the overlap integral of the Löwdin functions on the different sites which up to the nearest neighbors is good enough to give satisfactory results for some cases, but sometime one has to include the next nearest neighbors also to get more accurate results.

2.3 The k.p methods [29, 163]

In 1970, Bir and Pikus [29, 178, 179] observed an interesting result that, first of all, only the neighborhoods of the band extrema are important for the semiconductors because their electronic properties like transport are governed by the shape of the extrema of the various energy band. Second, the qualitative physics should be governed by the shape of those energy surface which means that a property should be readily obtainable from symmetry arguments. The first observation has led to the common view of the $\boldsymbol{k.p}$ scheme as a perturbation theory which was developed by Dresselhaus et al. [89] and Kane [180]. The second observation has manifested itself through the power of symmetry analysis like in the method of invariants introduced by Luttinger [162]. In fact, one can treat well beyond the neighborhood of band extrema which was already demonstrated by Cardona and Pollak in 1966 [181]. In this work, they obtained realistic band structure for Si and Ge using a full-zone $\boldsymbol{k.p}$ theory. However, due to the fact that the $\boldsymbol{k.p}$ method is a

consequence of basic equations of quantum mechanic, therefore in the following, we will review the general case of an electron in a crystal which is described by a Schrödinger equation admitting Bloch solutions to get the general equation for the $\boldsymbol{k.p}$ method.

2.3.1 Schrödinger equation and Bloch theorem. General views of k.p method

Starting with the Schrödinger equation for one electron in the crystal's structure involving spin-orbit interactions 1.10 one has:

$$H\Psi = E\Psi \tag{2.29}$$

where the Hamiltonian H writes:

$$H = \frac{p^2}{2m_0} + V(\boldsymbol{r}) + \frac{g\hbar}{4c^2m_0^2}(\nabla V(\boldsymbol{r}) \times \boldsymbol{p})\,\boldsymbol{\sigma} \tag{2.30}$$

here $V(\boldsymbol{r})$ represents the periodic potential within the crystal, m_0 is the effective mass of electron in the crystal, $\boldsymbol{p}$ is the momentum operator, $\boldsymbol{\sigma}$ the Pauli operator, and g the Lande factor.

$$V(\boldsymbol{r}) = V(\boldsymbol{r} + \boldsymbol{R_j}) \tag{2.31}$$

for a set of translation vectors $\{\boldsymbol{R_j}\}$ of the lattice.

Note that, concerning the tunneling issue (elastic process) within an inhomogeneous heterostructure, in order to construct the overall heterostructure wavefunction, one has to match, at interfaces, the states of different symmetry at the same elastic energy E and same component of wavefunction parallel to the interface $\boldsymbol{k}_{||}$ [163]. Therefore, it is necessary to calculate the different eigenstates in the bulk materials for fixed E and $\boldsymbol{k}_{||}$. Possible values of the wave vector perpendicular to the interfaces $\boldsymbol{k}_{\perp}$, are generally found. For convenience of notation, throughout the manuscript, we will use the symbol k_z to refer to the normal component of the wave vector and the symbol $\boldsymbol{k}$ to refer to a three dimensional wave vector.

Complex values of k_z corresponding to evanescent states, are also possible. We will refer to this issue as the generalized "complex band-structure problem". To solve this problem, a basis set $\{\Phi_{n,\boldsymbol{k}}(\boldsymbol{r})\}$ is chosen, and the solutions of the equation 2.29 are sought by expanding in terms of the basis set according to [163]:

$$\Psi_{m,\boldsymbol{k}} = \sum_n C_{mn}\Phi_{n,\boldsymbol{k}} \tag{2.32}$$

For the usual band structure determination, wavevectors are generally fixed, the energies E and wavefunctions $\Psi_{m,\boldsymbol{k}}$ are found via a diagonalisation procedure. This problem leads to the usual form of an eigenvalue equation. In the complex band structure problem, given E and $\boldsymbol{k}_{||}$, different values of k_z and wavefunctions $\Psi_{m,\boldsymbol{k}}$ are found. This problem does not immediately lead to the usual form of an eigenvalue equation depending on the form of the matrix elements:

$$\overline{H}_{nn'}(\boldsymbol{k}) = \left\langle \Phi_{n,\boldsymbol{k}} | H | \Phi_{n',\boldsymbol{k}} \right\rangle \tag{2.33}$$

However, it may be possible to cast 2.29 into a form of an eigenvalue equation. It becomes mandatory to build a numerically efficient method to solve the complex band structure problem. Let us consider three possible forms for the basis set [163].

(1) *The plane wave basis* :

$$\Phi_{\boldsymbol{Gk}} = \frac{1}{\sqrt{\mathcal{V}}} e^{[i(\boldsymbol{k}+\boldsymbol{G})\boldsymbol{r}]} \tag{2.34}$$

(2) *The basis of Bloch functions* :

$$\Phi_{n,\boldsymbol{k}} = \frac{1}{\sqrt{N}} e^{(i\boldsymbol{k}.\boldsymbol{r})} \psi_{n,\boldsymbol{k}}(\boldsymbol{r}) \tag{2.35}$$

(3) *The basis of Tight − binding functions*

$$\Phi_{n,\boldsymbol{k}} = \frac{1}{\sqrt{N}} \sum_j \sum_\alpha e^{(i\boldsymbol{k}.\boldsymbol{R_j})} f_n(\boldsymbol{r} - \boldsymbol{R_j} - \boldsymbol{r_\alpha}) \tag{2.36}$$

Here $\mathcal{V}$ is the sample volume, N the number of unit cells, $\boldsymbol{G}$ is a reciprocal lattice vector, and $\psi_{n,\boldsymbol{k}}$ is a Bloch function; r_α specifies an atomic position within the unit cell (j is the unit cell index), f_n is a local function centered at the atom located at r_α. The tight-binding basis functions posses the property:

$$\Phi_{\boldsymbol{k}+\boldsymbol{G}} = \Phi_{\boldsymbol{k}} \tag{2.37}$$

unlike the plane waves and Bloch function basis functions. Using a tight binding basis, the individual Hamiltonian matrix elements satisfy

$$\overline{H}_{nn'}(\boldsymbol{k} + \boldsymbol{G}) = \overline{H}_{nn'}(\boldsymbol{k}) \tag{2.38}$$

unlike plane waves and Bloch function basis. Using plane waves and Bloch function basis, the infinite dimensional matrices $H(\boldsymbol{k} + \boldsymbol{G})$ and $H(\boldsymbol{k})$ are related by a unitary transformation [163]. Using a plane wave basis, $H(\boldsymbol{k} + \boldsymbol{G})$ is related to $H(\boldsymbol{k})$ by relabeling rows and columns. Thus the infinite dimensional matrices $H(\boldsymbol{k} + \boldsymbol{G})$ satisfy translation property invariance in all three basis sets. However, once the basis sets are truncated, $H(\boldsymbol{k} + \boldsymbol{G})$ and $H(\boldsymbol{k})$ become no longer equivalent, unlike the tight-binding basis because each individual matrix element satisfies here Eq. 2.38. As a result, in the last case using a truncated tight-binding basis, the solutions will be still periodic,

$$\Psi_{n,\boldsymbol{k}+\boldsymbol{G}} = \Psi_{n,\boldsymbol{k}} \tag{2.39}$$

unlike truncated plane wave and Bloch function bases. For the usual band structure issue, this lack of periodicity is not a major problem. The mesh in $k-values$ is fixed in the first Brillouin zone whereas enough basis functions are chosen for eigenfunctions so that eigenenergies be accurately determined in the energy range of interest. For the complex band structure problem, the lack of periodicity causes major difficulties. In principle, solutions in which k_z takes a value such that $\boldsymbol{k}(= [\boldsymbol{k}_{||}, k_z])$ lies outside the Brillouin zone map onto an equivalent solution inside of Brillouin zone. However, because of the lack of the periodicity, such mapping does not occur in the truncated plane wave and Bloch function bases. As a result, out-of-zone spurious solutions occur in the complex band structure calculations. Those spurious solutions have caused considerable confusion in the application of pseudopotential and $\boldsymbol{k}.\boldsymbol{p}$ methods (based on plane waves and Bloch functions bases respectively), applied to superlattice and interface problems [163]. Similar difficulties occur when one uses other basis sets that do not satisfy 2.37 and whose Hamiltonian matrix elements therefore do not satisfy 2.38. Solving the equation 2.29 with the Bloch functions basis set 2.35, after several transformations, Eq.2.29 becomes:

$$\left[H_{SC} + \check{k}^2 + \frac{\hbar^2}{m_0} \boldsymbol{k}.\boldsymbol{p} + \frac{\hbar^2}{4m_0^2 c^2} (\nabla V \times \boldsymbol{k}) \boldsymbol{\sigma} \right] \psi_{n,\boldsymbol{k}}(\boldsymbol{r}) = E_{n,\boldsymbol{k}} \psi_{n,\boldsymbol{k}}(\boldsymbol{r}) \tag{2.40}$$

where $\check{k}^2 = \frac{\hbar^2}{2m_0^2} k^2$ and

$$H_{SC} = \frac{p^2}{2m_0} + V + \frac{\hbar}{4m_0^2 c^2} (\nabla V \times \boldsymbol{p}) .\boldsymbol{\sigma} \tag{2.41}$$

Besides, as pointed out in a work of Kane et al. in Ref. [182], we may neglect the term $\frac{\hbar^2}{4m_0^2c^2}(\nabla V \times \boldsymbol{k}).\boldsymbol{\sigma}$ on the left hand of Eq.2.40 since it turns out to be very small in the far interior of the atom where most of the spin-orbit interaction occurs in T_d group [182]. Afterward, we obtain Eq.2.40 in the form:

$$\left[H_{SC} + \check{k}^2 + \frac{\hbar^2}{m_0}\boldsymbol{k}.\boldsymbol{p}\right]\psi_{n,\boldsymbol{k}}(\boldsymbol{r}) = E_{n,\boldsymbol{k}}\psi_{n,\boldsymbol{k}}(\boldsymbol{r}) \tag{2.42}$$

Note: When $\boldsymbol{k} \longrightarrow 0$ then $H_{\boldsymbol{k}.\boldsymbol{p}} \longrightarrow H_{SC}$ where $H_{\boldsymbol{k}.\boldsymbol{p}} = H_{SC} + \check{k}^2 + \frac{\hbar^2}{m_0}\boldsymbol{k}.\boldsymbol{p}$, so we can consider the term $\check{k}^2 + \frac{\hbar^2}{m_0}\boldsymbol{k}.\boldsymbol{p}$ as the perturbed term of $H_{\boldsymbol{k}.\boldsymbol{p}}$ in the vicinity of the point $\boldsymbol{k} = 0$. For a number of semiconductor materials, the extreme point is located at the Γ point or the center of Brillouin zone corresponding to $\boldsymbol{k} = 0$. Furthermore, the group of the Γ point corresponds to the point group of the crystal. By analyzing the symmetry of the wave function at the Γ point in framework of LCAO, we can derive the suited basis function $\psi_{n,\boldsymbol{k}}$ to construct the Hamiltonian $H_{\boldsymbol{k}.\boldsymbol{p}}$ (we will discuss in detail in the next section).

Assuming that the functions $\psi_{m,\boldsymbol{k}}(\boldsymbol{r})$ at $\boldsymbol{k} = 0$ are well known and denoting $\psi_m = \psi_{m,\boldsymbol{k}=0}(\boldsymbol{r})$ as well as the energies $E_m = E_{m,\boldsymbol{k}=0}$, one obtains $H_{SC}\psi_m = E_n\psi_m$. The functions $\psi_{n,\boldsymbol{k}}(\boldsymbol{r})$ with $\boldsymbol{k} \neq 0$ can be expanded onto the basis ψ_m as:

$$\psi_{n,\boldsymbol{k}}(\boldsymbol{r}) = \sum_m C^m_{n,\boldsymbol{k}}\psi_m \tag{2.43}$$

Then the equation 2.42 can be re-written as:

$$\left[H_{SC} + \check{k}^2 + \frac{\hbar^2}{m_0}\boldsymbol{k}.\boldsymbol{p}\right]\left(\sum_m C^m_{n,\boldsymbol{k}}\psi_m\right) = E_{n,\boldsymbol{k}}\left(\sum_m C^m_{n,\boldsymbol{k}}\psi_m\right) \tag{2.44}$$

In an ideal case, the dimension of the basis set $\{\psi_m\}$ is infinite and the Hamiltonian H_{SC} together with its eigenfunctions satisfy the periodicity properties of the crystal. It results that one can restrict ourself to the resolution of 2.44 to the unit cell region only. We multiply both sides of 2.44 by ψ_n^* and integrate over the unit cell using the following orthonormality properties $\oint \psi_n^*\psi_m dV = \langle\psi_n|\psi_m\rangle = \delta_{n,m}$. We thus obtain the equation determining the $C^m_{n,\boldsymbol{k}}$ coefficients according to:

$$\sum_m \left[\left\langle\psi_n\left|H_{SC} + \frac{\hbar}{m_0}\boldsymbol{k}.\boldsymbol{p}\right|\psi_m\right\rangle + \check{k}^2\delta_{n,m} - E_{n,\boldsymbol{k}}\delta_{n,m}\right]C^m_{n,\boldsymbol{k}} = 0 \tag{2.45}$$

which corresponds to the secular equation to solve.

Note that the sum in 2.45 is generally infinite so that an infinite set of equations has to be fulfilled for the determination of $\psi_{n,\boldsymbol{k}}(\boldsymbol{r})$ in 2.43. It results that the energies E for every bands are the solution of the following secular equation:

$$det\,[H - E\mathbb{I}] = 0 \tag{2.46}$$

where $\mathbb{I}$ is the identity matrix and the matrix elements of H are determined by:

$$\overline{H}_{nm} = \left\langle\psi_n\left|H_{SC} + \frac{\hbar}{m_0}\boldsymbol{k}.\boldsymbol{p}\right|\psi_m\right\rangle + \check{k}^2\delta_{n,m} \tag{2.47}$$

For our purpose with the choice of solving the complex band structure where values of $\boldsymbol{k}_{||}$ and E are fixed and values of k_z have to be found, it is convenient to rewrite 2.47 according to the more general following form:

$$\overline{H}_{nm} = \overline{H}^2_{nm}k_z^2 + \overline{H}^1_{nm}k_z + \overline{H}^0_{nm} \tag{2.48}$$

Then the secular equation 2.46 becomes:

$$det\left[H^2k_z^2 + H^1k_z + H^0 - E\mathbb{I}\right] = 0 \tag{2.49}$$

and the Eq 2.45 can be cast in a matrix block form, as a equation for k_z by:

$$\begin{bmatrix} 0 & 1 \\ -(H^2)^{-1}\left(H^0 - E\mathbb{I}\right) & -(H^2)^{-1}H^1 \end{bmatrix} \begin{pmatrix} C \\ k_z C \end{pmatrix} = k_z \begin{pmatrix} C \\ k_z C \end{pmatrix} \tag{2.50}$$

One observes that the matrix in Eq 2.50 is non-Hermitian. Therefore the k-eigenvalues may be complex numbers. These complex values of k correspond to evanescent solutions which do not result from the truncation of the basis set. Besides, the form of H^j ($j = 1,2,3$) in Eq. 2.49 implies that if k_z satisfy Eq 2.49 then k_z^* does also (see also in the references [183, 184]). We thus have the important result that complex eigenvalues always occur in pairs, k_z and k_z^*. That is, evanescent states come in growing and decaying pairs with identical real part of k and imaginary parts of k with opposite signs. On the other hand, solving the eigenvalue equation 2.50 for fixed $\boldsymbol{k}_{||}$ and E determines the possible values of k_z and the expansion coefficients $C^m_{n,\boldsymbol{k}}$. Relationships between k_z and k_z^* and the corresponding eigenvectors are discussed in detail in Ref. [184].

Note that, in framework of $\boldsymbol{k.p}$ method, the solutions for $\boldsymbol{k}$ will not satisfy periodicity conditions for a finite basis set [163]. This means that for whatever a finite basis set is, spurious states will always appear in the band structure calculated from $\boldsymbol{k.p}$ Hamiltonian. If a larger basis set is used, the periodicity conditions are maintained to somewhat larger values of k. However, they eventually break down completely. Moreover, as the basis set is expanded, even more such spurious states occur [163].

2.3.2 k.p Hamiltonian for O_h and T_d semiconductors

In order to solve the secular equation 2.46 to obtain the electronic band structure of materials, one needs to choose a proper basis set $\{|\psi_n\rangle\}$ at $\boldsymbol{k} = 0$ and then determines the matrix elements 2.47. It can be performed by analogy to LCAO and Tight-Binding methods based on symmetry arguments. This section is devoted to the description of the basis set to construct the $\boldsymbol{k.p}$ Hamiltonian for semiconductors belonging to the O_h or T_d group.

Structure of O_h and T_d groups

Crystals of diamond or zinc-blende semiconductors are constructed from two face-centered cubic (fcc) sub-lattice (A) and (B), shifted by one forth of the cube main diagonal. The atoms are placed at each sub-lattice point. If we take the three Ox, Oy and Oz axes and their corresponding unit vectors $\boldsymbol{e_x}$, $\boldsymbol{e_y}$ and $\boldsymbol{e_z}$, respectively, parallel to the [100], [010] and [001] directions of the crystal, an atom of sub-lattice (A) at the point $\boldsymbol{R_j'} = \boldsymbol{R_j} + \boldsymbol{a}$ possesses four nearest neighbors at sites $\boldsymbol{R_j} + \boldsymbol{a_n}$ where $\boldsymbol{a} = a\left(\frac{1}{4},\frac{1}{4},\frac{1}{4}\right)$; $n = 0,1,2,3$; $\boldsymbol{a_0} = \boldsymbol{0}$, $\boldsymbol{a_1} = a\left(\frac{1}{2},\frac{1}{2},0\right)$, $\boldsymbol{a_2} = a\left(\frac{1}{2},0,\frac{1}{2}\right)$, $\boldsymbol{a_3} = a\left(0,\frac{1}{2},\frac{1}{2}\right)$, where a is the length of the unit cell (see Fig. 2.2).

If the two atoms in the two sub-lattices are identical, one obtains the diamond structure. In that case, an inversion center exists in the middle of the segment joining these two atoms. These semiconductors belong to the O_h group. This is the case of semiconductors of group IV such as silicon, germanium and carbon. Otherwise, if the two atoms are different, one obtains the zinc-blende structure. This is the case of III-V compounds such as GaAs, AlAs, InAs or II-VI such as ZnTe. These structures belong to the T_d group, where the inversion symmetry is removed. The reciprocal lattice of this structure is the body centered cubic

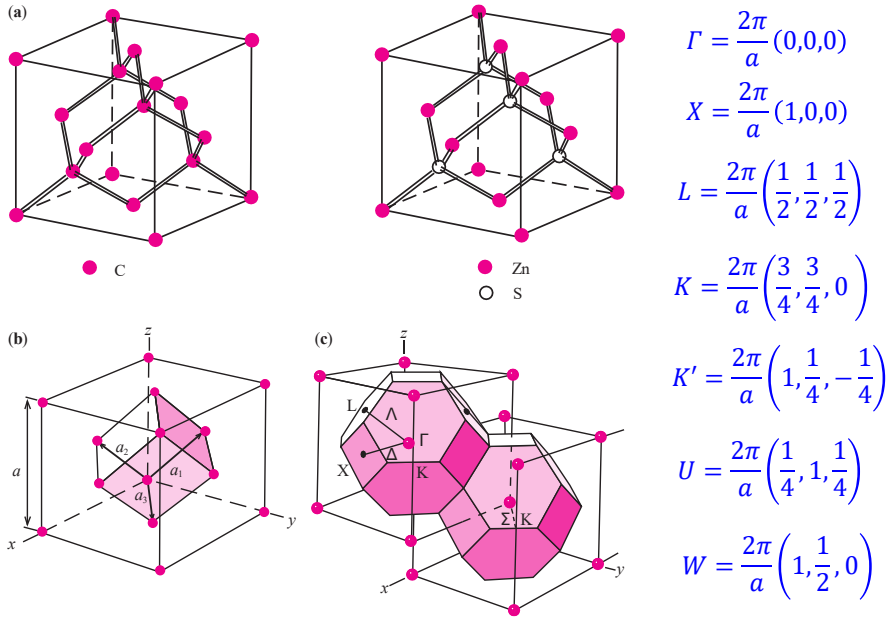

FIGURE 2.2: (a)The crystal structure of diamond and zinc-blende (ZnS). (b) the fcc lattice showing a set of primitive lattice vectors. (c) The reciprocal lattice of the fcc lattice is shown with the first Brillouin zone. Special high-symmetry points are denoted by Γ, X and L, while high-symmetry lines joining some of these points are labeled as Δ, taken from Ref.[53]

lattice (bcc) describing the common first Brillouin zone of O_h and T_d groups, bounded by eight regular hexagonal faces and six square faces. The symmetry points are defined as in Fig 2.2 where the Γ point is the center of the Brillouin zone. The other symmetry points: K, K' and U points are equivalent from the point of view of crystallography. The Δ line connecting Γ and X, the Λ line connecting Γ and L, and the Σ line connecting Γ and K are three principal directions.

Wavefunction at the Γ point. Basis set for k.p Hamiltonians

In order to build up the $\boldsymbol{k.p}$ Hamiltonian, the basis set $\{\psi_m\}$ in 2.43 has to be known. Note that ψ_m is the wave function at $\boldsymbol{k} = 0$ (Γ point) where the symmetry group matches with the symmetry group of the crystal itself.

The unit cell of O_h and T_d groups contains two atoms. Therefore in the framework of LCAO and Tight-Binding methods, the wavefunction at the center of the Brillouin zone is a linear combination of the wavefunctions of the two atoms which, in the present case, results from the overlap and hybridization of s and p atomic orbitals. We first consider two identical atoms of respective energy state E_s and E_p and corresponding to atomic wavefunctions or orbitals s_a and $p_a = x_a, y_a, z_a$ of the form $|n\rangle = f(r)\mathcal{Y}_{lm}(\theta,\phi)$ where $l = 0,1,2,3,...$; $m = -l,...,l$ and $\mathcal{Y}_{lm}(\theta,\phi)$ is the spherical harmonic given by [43]:

$$\mathcal{Y}_{lm}(\theta,\phi) = (-1)^{\frac{m+|m|}{2}}\sqrt{\left(\frac{2l+1}{4\pi}\right)\frac{(l-|m|)!}{(l-|m|)!}}P_l^m(cos\theta)e^{im\phi} \tag{2.51}$$

where $P_l^m(cos\theta)$ are Associated Legendre Functions:

$$P_l^m(cos\theta) = sin^m\theta\frac{d^m}{d(cos\theta)^m}P_l(cos\theta) \tag{2.52}$$

TABLE 2.1: $|j,m\rangle$ states developed on $|l,s\rangle$ basis

$\|3/2,3/2\rangle = \|\mathcal{Y}_{11}\uparrow\rangle$	$\|3/2,-3/2\rangle = \|\mathcal{Y}_{1-1}\downarrow\rangle$
$\|3/2,1/2\rangle = \left\|\sqrt{\frac{2}{3}}\mathcal{Y}_{10}\uparrow + \frac{1}{\sqrt{3}}\mathcal{Y}_{11}\downarrow\right\rangle$	$\|1/2,1/2\rangle = \left\|\frac{1}{\sqrt{3}}\mathcal{Y}_{10}\uparrow - \sqrt{\frac{2}{3}}\mathcal{Y}_{11}\downarrow\right\rangle$
$\|3/2,-1/2\rangle = \left\|\frac{1}{\sqrt{3}}\mathcal{Y}_{1-1}\uparrow + \sqrt{\frac{2}{3}}\mathcal{Y}_{10}\downarrow\right\rangle$	$\|1/2,-1/2\rangle = \left\|\sqrt{\frac{2}{3}}\mathcal{Y}_{1-1}\uparrow - \frac{1}{\sqrt{3}}\mathcal{Y}_{10}\downarrow\right\rangle$

with:

$$P_l(cos\theta) = \sqrt{\frac{\theta}{sin\theta}}cos\left(\left(l+\frac{1}{2}\right)\theta + \frac{\pi}{4}\right) + O\left(l^{-1}\right) \tag{2.53}$$

The angular dependence of the s- and p-state wavefunctions are related to spherical harmonics according to:

$$\mathcal{Y}_{00} = \frac{1}{\sqrt{4\pi}} = s \tag{2.54}$$

$$\mathcal{Y}_{10}(\theta,\phi) = \sqrt{\frac{3}{4\pi}}cos\theta = \sqrt{\frac{3}{4\pi}}\frac{z}{r} = iz_a \tag{2.55}$$

$$\mathcal{Y}_{1\pm1}(\theta,\phi) = \mp\sqrt{\frac{3}{4\pi}}sin\theta e^{\pm i\phi} = \mp\sqrt{\frac{3}{4\pi}}\frac{x \pm iy}{r} = i\frac{(x_a) \pm iy_a}{2} \tag{2.56}$$

Note that the spherical harmonics do not include the spin degree of freedom. When the spin $\boldsymbol{s} = 1/2$ is considered, then the total angular momentum is defined as $\boldsymbol{j = l + s}$. The projection of $\boldsymbol{j}$ on the z axis takes the respective values $m = j_z \in \{-j,...,j\}$. It is more convenient to use the $|j,m\rangle$ states which satisfy:

$$|j,m\rangle = \sqrt{j(j+1) - m(m-1)}|j,m-1\rangle \tag{2.57}$$

where

♠ For s_a, $l = 0$ and $j = 1/2$ to obtain $|s+\rangle = |1/2,1/2\rangle_s$ and $|s-\rangle = |1/2,-1/2\rangle_s$.

♠ For $l = 1$, then four states $|3/2,-3/2\rangle$, $|3/2,-1/2\rangle$, $|3/2,1/2\rangle$ and $|3/2,3/2\rangle$ corresponding to $j = 3/2$ and two states $|1/2,-1/2\rangle$, $|1/2,1/2\rangle$ corresponding to $j = 1/2$ where exact expressions are given in Table 2.1.

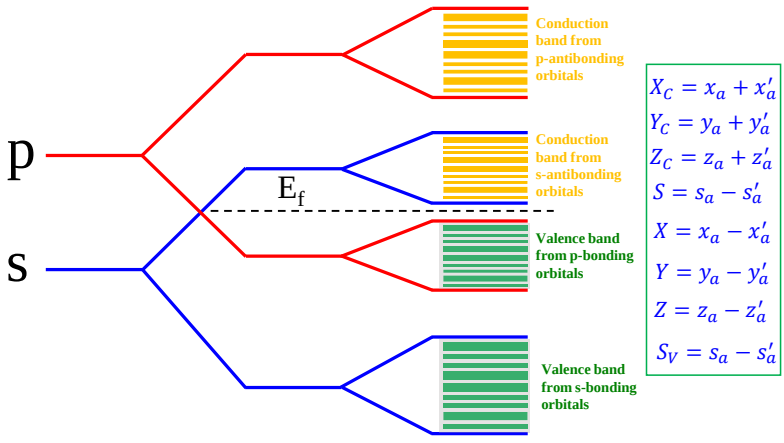

FIGURE 2.3: Schematic of evolution of the atomic s- and p-states, to form the conduction and valence bands in semiconductor and the wave function at the Brillouin zone center.

When two identical atoms, A and A', are put in contact closely, their wavefunctions overlap and consequently, new energies levels are formed with the final wavefunctions becoming linear a combinations of the atomic functions s_a and p_a, respectively. The wavefunctions at the zone center are displayed in Fig. 2.3 where the S, X_C, Y_C and Z_C functions of the CB are fully antisymmetric, whereas the S_V, X, Y and Z functions are fully symmetric in the O_h group. It is well known that in the O_h group, the S function possesses an xyz symmetry (the three axes play the same role), changing their sign when $\boldsymbol{r}$ is changed into $-\boldsymbol{r}$. X, Y and Z functions possess respectively yz, zx and xy symmetry, respectively, keeping their sign when $\boldsymbol{r}$ is changed into $-\boldsymbol{r}$. The function S_V has the s symmetry whereas the X_C, Y_C and Z_C functions have x, y and z symmetry under O_h operations. For the T_d group, where the centro-symmetry no longer exists, wavefunctions are identical to those of O_h except an additional part of orbital mixing arising from the perturbation asymmetric potential. The Table 2.2 gathers the different wavefuntions and their symmetry where ϵ is a small mixing coefficient. This coefficient represents the effect of the spatial antisymmetric potential contribution V_a with $V = V_S + V_a$ ($V_S(\boldsymbol{r}) = V_S(-\boldsymbol{r})$ symmetric part in both O_h and T_d, $V_a(\boldsymbol{r}) = -V_a(-\boldsymbol{r})$ for T_d only) originating from the non-identical A and A' atoms.

TABLE 2.2: Wavefunctions at zone center in the T_d group, takem from Ref. [29].

Function	LCAO	Group	Symmetry
X_C	$(x_a + x'_a) + \epsilon(x_a - x'_a)$	Γ_5	$x + \epsilon yz$
Y_C	$(y_a + y'_a) + \epsilon(y_a - y'_a)$	Γ_5	$y + \epsilon zx$
Z_C	$(z_a + z'_a) + \epsilon(z_a - z'_a)$	Γ_5	$z + \epsilon xy$
S	$(s_a - s'_a) + \epsilon(s_a + s'_a)$	Γ_1	$xyz + \epsilon s$
X	$(x_a - x'_a) + \epsilon(x_a + x'_a)$	Γ_5	$yz + \epsilon x$
Y	$(y_a - y'_a) + \epsilon(y_a + y'_a)$	Γ_5	$zx + \epsilon y$
Z	$(z_a - z'_a) + \epsilon(z_a + z'_a)$	Γ_5	$xy + \epsilon z$
S_V	$(s_a + s'_a) + \epsilon(s_a - s'_a)$	Γ_1	$s + \epsilon xyz$

The $X_C, Y_C, Z_C, S, X, Y, Z$ and S_V states above do not include the spin degree of freedom and, moreover, the electron now does not possess a true orbital momentum l as in the case of single atom but only a pseudo-orbital momentum "L". The S function corresponds to $\boldsymbol{L} = 0$ while X, Y and Z correspond to $\boldsymbol{L} = 1$. When the spin is taken into account, the sum $\boldsymbol{J} = \boldsymbol{L} + \boldsymbol{S}$ is, now, no longer well defined. However, starting with $\boldsymbol{L} = 0$ we can write $\boldsymbol{J} = 1/2$ for the Γ_6 band, and for $\boldsymbol{L} = 1$ we can define $\boldsymbol{J} = 1/2$ for the Γ_7 and $\boldsymbol{J} = 3/2$ for the Γ_8 band [185]. By analogy with atomic physics, one can construct the wavefunctions for the two atoms in the unit cell by replacing the spherical harmonic $\mathcal{Y}_{lm}$ by cubic harmonics Y_{lm}, the atomic functions x_a, y_a and z_a being replaced by the X, Y and Z functions. Therefore, we define:

$$Y_{10} = iZ; \quad Y_{11} = -i\frac{X + iY}{\sqrt{2}}; \quad Y_{1-1} = i\frac{X - iY}{\sqrt{2}} \tag{2.58}$$

And similarly to the $|j, m\rangle$ functions given in the case of single atom, we can write down the functions used as the basis set $\{\psi_m\}$ in 2.43 to expand the $\boldsymbol{k.p}$ matrix elements as in the Table 2.3. Thus the $|J, M\rangle$ basis set is usually used to build the $\boldsymbol{k.p}$ Hamiltonian [29, 53, 179]. However, the $|L, S\rangle$ basis is sometimes more convenient if one considers formulation and analyses involving boundary conditions at interfaces of heterojunctions [29–31]. The table 2.3 gives the relationship between the $|J, M\rangle$ and $|L, S\rangle$ basis set allowing the unitary transformation from one representation to the other. Note that, the matrix elements of $\boldsymbol{k.p}$ Hamiltonian built from cubic harmonic functions Y_{lm} are not the same as atomic energies. However, again, it is not a big issue since after all, like tight-binding technique, the $\boldsymbol{k.p}$ Hamiltonian is formed in parametrization scheme from DFT calculations or from experimental measurements.

TABLE 2.3: $|j,m\rangle$ states for kp matrix elements [29]

$\left\|\frac{3}{2},\frac{3}{2}\right\rangle_{\Gamma_{8C}} = \left\|i\left[-\frac{1}{\sqrt{2}}(X_C+iY_C)\uparrow\right]\right\rangle$	$\left\|\frac{3}{2},\frac{1}{2}\right\rangle_{\Gamma_{8C}} = \left\|i\left[\sqrt{\frac{2}{3}}Z_C\uparrow-\frac{1}{\sqrt{6}}(X_C+iY_C)\downarrow\right]\right\rangle$
$\left\|\frac{3}{2},\frac{-1}{2}\right\rangle_{\Gamma_{8C}} = \left\|i\left[\frac{1}{\sqrt{6}}(X_C-iY_C)\uparrow+\sqrt{\frac{2}{3}}Z_C\downarrow\right]\right\rangle$	$\left\|\frac{3}{2},\frac{-3}{2}\right\rangle_{\Gamma_{8C}} = \left\|i\left[\frac{1}{\sqrt{2}}(X_C-iY_C)\downarrow\right]\right\rangle$
$\left\|\frac{1}{2},\frac{1}{2}\right\rangle_{\Gamma_{7C}} = \left\|i\left[\frac{1}{\sqrt{3}}Z_C\uparrow+\sqrt{\frac{2}{3}}(X_C+iY_C)\downarrow\right]\right\rangle$	$\left\|\frac{1}{2},\frac{-1}{2}\right\rangle_{\Gamma_{7C}} = \left\|i\left[\frac{1}{\sqrt{3}}(X_C-iY_C)\uparrow-\frac{1}{\sqrt{3}}Z_C\downarrow\right]\right\rangle$
$\|+\rangle = \|S\uparrow\rangle$	$\|-\rangle = \|S\downarrow\rangle$
$\left\|\frac{3}{2},\frac{3}{2}\right\rangle_{\Gamma_8} = \left\|i\left[-\frac{1}{\sqrt{2}}(X+iY)\uparrow\right]\right\rangle$	$\left\|\frac{3}{2},\frac{1}{2}\right\rangle_{\Gamma_8} = \left\|i\left[\sqrt{\frac{2}{3}}Z\uparrow-\frac{1}{\sqrt{6}}(X+iY)\downarrow\right]\right\rangle$
$\left\|\frac{3}{2},\frac{-1}{2}\right\rangle_{\Gamma_8} = \left\|i\left[\frac{1}{\sqrt{6}}(X-iY)\uparrow+\sqrt{\frac{2}{3}}Z\downarrow\right]\right\rangle$	$\left\|\frac{3}{2},\frac{-3}{2}\right\rangle_{\Gamma_8} = \left\|i\left[\frac{1}{\sqrt{2}}(X-iY)\downarrow\right]\right\rangle$
$\left\|\frac{1}{2},\frac{1}{2}\right\rangle_{\Gamma_7} = \left\|i\left[\frac{1}{\sqrt{3}}Z\uparrow+\sqrt{\frac{1}{3}}(X+iY)\downarrow\right]\right\rangle$	$\left\|\frac{1}{2},\frac{-1}{2}\right\rangle_{\Gamma_7} = \left\|i\left[\frac{1}{\sqrt{3}}(X-iY)\uparrow-\frac{1}{\sqrt{3}}Z\downarrow\right]\right\rangle$

2.4 Evanescent states and spurious states elimination in the framework of the multiband k.p method (14, 30, and 40 bands)

2.4.1 Simple example of 2-band toy model without spin:

In order to give an insight on the appearance and impact of the spurious states on the electric band structure and tunneling properties, we are going to consider firstly a simple 2-band $\boldsymbol{k.p}$ toy model involving a single CB and VB states coupled by the off-diagonal $\boldsymbol{k.p}$ terms. In this model, the 2-band Hamiltonian then writes:

$$H = \frac{\hbar^2k^2}{2m_0}\mathbb{I} + \begin{pmatrix} E_G & Pk \\ Pk & 0 \end{pmatrix} = \begin{array}{c} \\ |C\rangle \\ |V\rangle \end{array}\begin{array}{c} \begin{array}{cc} |C\rangle & |V\rangle \end{array} \\ \begin{pmatrix} E_G+\check{k}^2 & Pk \\ Pk & \check{k}^2 \end{pmatrix} \end{array} \tag{2.59}$$

where the energy origin is at the top of the valence band, E_G is band gap and $P = \frac{\hbar}{m_0}\langle C|\boldsymbol{p}|V\rangle$, the coupling parameter between $|C\rangle$ and $|V\rangle$. The energy E, solution of the secular equation 2.46 then reads:

$$E = \check{k}^2 + \frac{E_G \pm \sqrt{E_G^2 + 4E_P\check{k}^2}}{2} \tag{2.60}$$

with $E_P = \frac{2m_0}{\hbar^2}P^2$.

When k is very small, one may neglect the term P^2k^2 since $P^2k^2 \ll E_G^2$ to get $E = \check{k}^2\left(1+\frac{E_P}{E_G}\right)+E_G$ for electrons in the CB and $E = \check{k}^2\left(1-\frac{E_P}{E_G}\right)$ for holes in the VB. Usually, the term $\frac{E_P}{E_G}$ is of the order of 10, and the electron effective mass $m_e^* = (1+E_P/E_G)^{-1}$ is positive whereas the hole effective mass $m_h^* = (1-E_P/E_G)^{-1}$ is negative as expected.

However when k becomes large enough, the term k^2 increases faster than the $\sqrt{E_G^2+4E_P\check{k}^2}$ term which makes the energy in the VB to increase before crossing the band gap as depicts in Fig. 2.4. These unphysical states are called "spurious states". They appear as a natural consequence of the truncation of the remote bands necessary to recover the overall Bloch periodicity. Spurious states with large real wave vectors are problematic since they mix and interact with real states, making then difficult to identify and remove them in numerical calculations. Spurious states with larger imaginary wave vector components are rapidly decaying and therefore harmless. Back to the solution 2.60, when k is purely imaginary, i.e, $k = iK$,

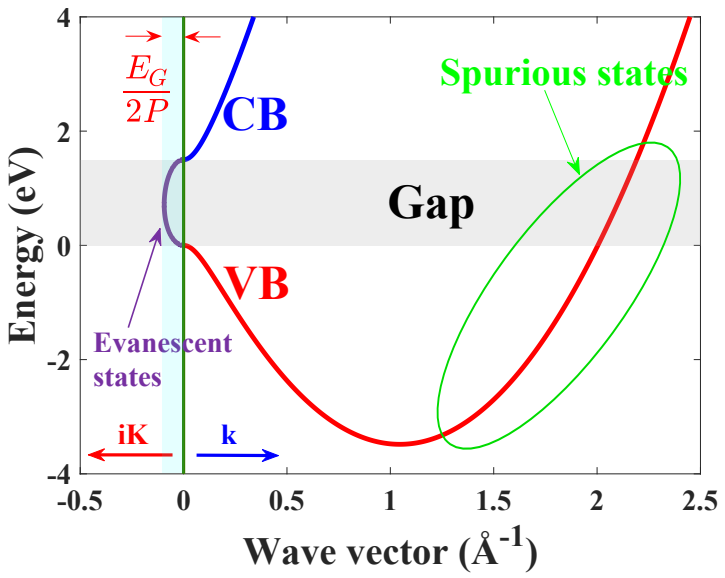

FIGURE 2.4: Spurious and Evanescent states in 2 band toy model. The spurious states cross the band gap at $k = 2\text{Å}^{-1}$ and the evanescent states are located within $K = [0, \frac{E_G}{2P}]$

where K is real, then:

$$E = -\frac{\hbar^2}{2m_0}K^2 + \frac{E_G \pm \sqrt{E_G^2 - 4P^2K^2}}{2} \tag{2.61}$$

Note that E is real only if $|K| \leq \frac{E_G}{2P}$. Then if this condition is satisfied, evanescent solutions exist as depicts in Fig. 2.4. For GaAs, $P = 9.3\ eV.\text{Å}$ and $E_G = 1.52\ eV$ then $|K| \leq 0.1\ \text{Å}^{-1}$. The evanescent states are localized within about $0.1\ \text{Å}^{-1}$, i.e., the evanescent states are confined within a small region of the k-space (Fig. 2.4).

2.4.2 *Method of spurious states elimination in multiband k.p method*

Spurious states [186] have been more than a numerical headache for researchers in the community of theoretician of semiconductors, particularly because it appears difficult to discriminate them from true physical states [164, 186–190].

Furthermore, the wavefunction mixing between real and spurious states renders the envelope functions approach useless in calculating dipole matrix elements because of the unphysical oscillatory features. This is also particularly true for transport properties. More generally, the spurious solutions with large imaginary k are related to the wing-band solutions discussed in Ref. [191]. The wing-band solutions are rapidly decaying in nature and therefore considered to be harmless in contrast to the oscillatory solutions with large real k, which are the main issues of this section. The problem is not new but no fully satisfactory fixed and widely used solutions exist. So far, several approaches have been suggested.

The first is to modify the Hamiltonian by discarding the terms responsible for the spurious solutions [191–194]. This costs some accuracy in the band structure, since it is no longer possible to fit all experimental effective masses correction. The idea of Foreman [186, 188] to avoid this trouble is that one just sets some of the coefficients of the k^2 term in the conduction band matrix elements to zero and fits the CB mass using a spatially varying momentum matrix elements as well as the coefficients of the k^2 term in VB. The other idea from Kolokolov et al. [164] is instead of modifying the coefficient of k^2, to introduce additional off-diagonal terms $i\alpha k^2$ in the Hamiltonian. This supplementary coupling will contribute to a positive term

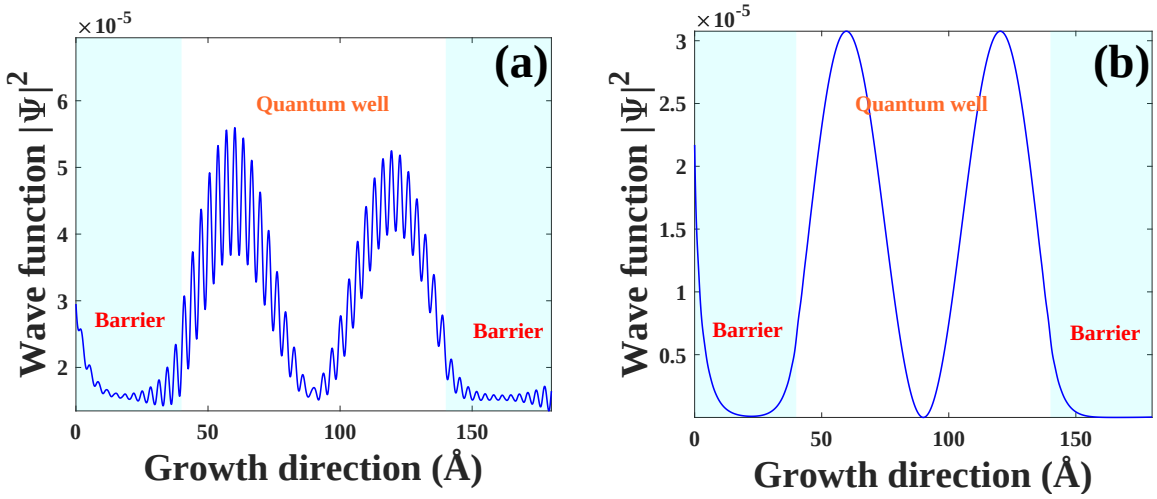

FIGURE 2.5: Envelope functions in GaAs/AlAs 10 nm quantum well before removing spurious states: figure (a) where the spurious state makes envelope function to oscillate and after removing spurious states: figure (b) : the unphysical oscillatory features no longer appear. Results calculated by 30-band $\boldsymbol{k.p}$ model.

$\alpha^2 k^4$ in the dispersion relation able to pull down the valence band structure at large wavevector, removing thus the spurious characters. This technique has been applied to the 8-bands $\boldsymbol{k.p}$ method [164] and adapted to 14-band by Dang et al. [93]. However, when one increases the number of bands, e.g., dealing with the 30-band $\boldsymbol{k.p}$ method, the number of spurious states increases as well, with the result that the perturbations on the conduction band caused by the additional terms becomes more and more significant, making the method to be no longer accurate enough to deal with indirect band gap semiconductors like Silic for example.

A second possibility is to keep the original Hamiltonian (that is accurate near the Γ point) but reject the unphysical large k-solutions [193, 195–198]. This technique is problematic in heterostructures, since the discarded solutions are needed to be considered to satisfy the general boundary conditions. It would become unclear to determine which boundary conditions should be eliminated for mathematical consistency.

A third approach therefore consists in retaining all solutions on the grounds that spurious bands admit negligible influence on the properties of bound-state eigenfunctions [199]. This is better justified but still runs into trouble with oscillatory modes [186].

In the next part, we review the major idea of Kolokolov et al. [164] and then propose to extend this proposal to our novel ghost-band method in order to adapt it to both 30-band and 40-band $\boldsymbol{k.p}$ models.

Adding off diagonal terms: the Kolokolov method [164]

Coming back to the 2-band toy model and Eq. 2.60, ideally to pull down the VB in the large wavevector region, one would need to increase the value of $E_G^2 + 4E_P\check{k}^2$ by possibly adding a positive term $\alpha^2 k^4$ larger than P^2k^2 [164]. This is the role of the off-diagonal supplementary term $i\alpha k^2$ giving an overall Hamiltonian

$$H = \begin{array}{c} \begin{matrix} |C\rangle & |V\rangle \end{matrix} \\ \begin{pmatrix} E_G + \check{k}^2 & Pk - i\alpha k^2 \\ Pk + i\alpha k^2 & \check{k}^2 \end{pmatrix} \end{array} \tag{2.62}$$

We assume that $E_G^2 + 4E_P\check{k}^2 \ll \alpha^2 k^4$ in the large wavevector region. The eigenenergy for the VB becomes now:

$$E_{hole} = \left(\frac{\hbar^2}{2m_0} - \alpha\right) k^2 \tag{2.63}$$

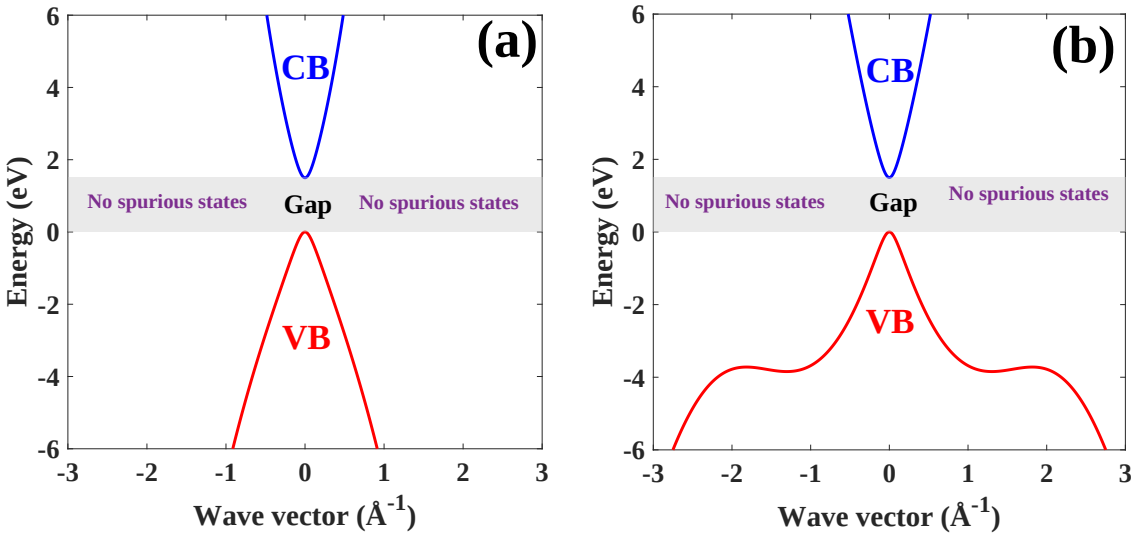

FIGURE 2.6: Spurious states elimination in 2 band toy model with two different methods: (a) off-diagonal term method [164] with supplementary term $\alpha = \frac{5\hbar^2}{8m_0}$. (b) ghost-band method with supplementary term $\alpha = \frac{\hbar^2}{4m_0}$ and the ghost band energy $E_\Phi = 10eV$. The band structure near the Γ point in both cases remains identical.

If $\alpha > \hbar^2/2m_0$, the hole effective mass is always negative as expected. With the supplementary terms, one obtains, from the energy, the electron effective mass at small wavevectors according to:

$$\begin{aligned} E_{electron} &= \check{k}^2 + \frac{\sqrt{E_G^2 + 4E_P\check{k}^2 + \alpha^2k^4}}{2} + \frac{E_G}{2} \approx \check{k}^2 + \frac{E_G}{2}\left(1 + \frac{4E_P\check{k}^2 + \alpha^2k^4}{E_G^2}\right)^{0.5} + \frac{E_G}{2} \\ &= E_G + \check{k}^2 + \frac{E_P}{E_G}\check{k}^2 + \frac{\alpha^2}{4E_G}k^4 \end{aligned} \tag{2.64}$$

Since $\alpha^2k^4/E_G \ll k^2$ and because of the k^4 dependence, the electron effective mass weakly depends on the added terms. We can derive similar results for the hole band. This method was improved to remove the spurious states within the 8 -band $\boldsymbol{k.p}$ model [164] and has been adapted recently to 14 band $\boldsymbol{k.p}$ model by Dang et al. [93].

In this work, we also managed to remove spurious states by adapting the so-called $ghost-band$ method which appears as an extension of the original idea of Kolokolov [164]. We discuss now in much details, the Ghost-band method employed here.

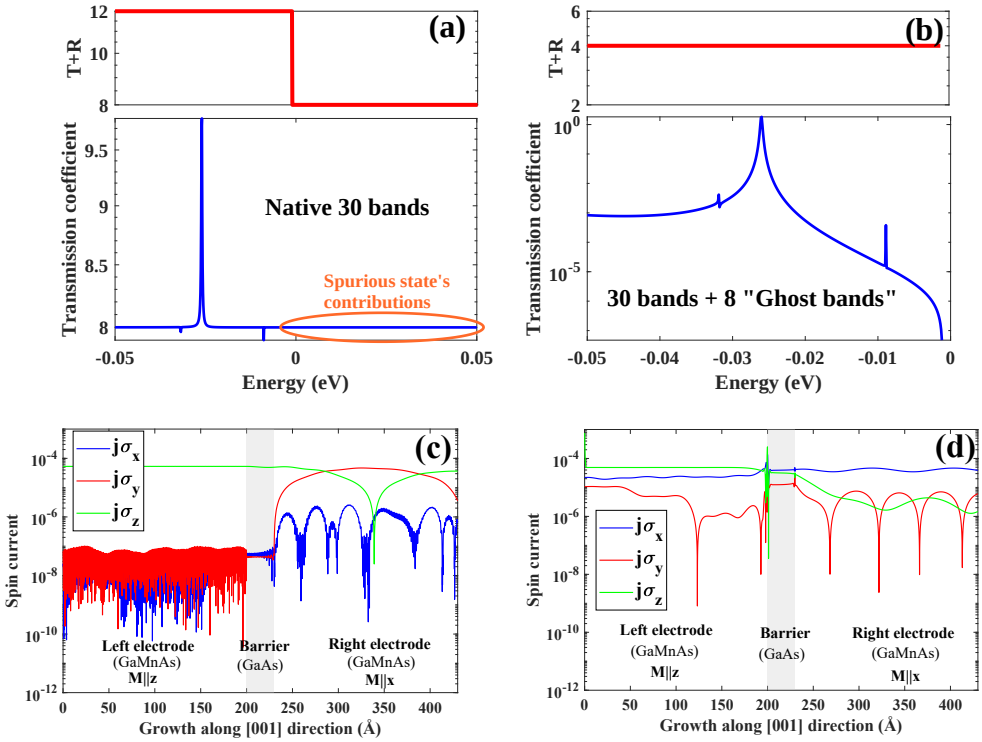

FIGURE 2.7: (a) Resonant tunneling with spurious states: the appearance of spurious states allows the transmission coefficient to be different of zero in the band gap (blue curve). The red curve is the sum of transmission and reflection coefficients (= number of bands) involving spurious states. (b) The same calculation after having removed spurious states by ghost-band method. (c) The three components of the spin current calculated through the (Ga,Mn)As/GaAs/(Ga,Mn)As structure where the magnetization is along z direction in the left electrode and along the x direction in the right electrode with spurious, and (d) without spurious states.

Our novel ghost-band approach.

The appearance of spurious states at large $\boldsymbol{k}$ in the $\boldsymbol{k.p}$ scheme naturally arises from the inherent truncation procedure. In order to extend the procedure of Ref. [164] to a wider region in the k space away from Γ to almost cover the full Brillouin zone, we propose the so-called *ghost-band* method (see the detailed introduction of this method in the appendix B). It consists in adding supplementary fictitious upper bands (ghost-band) and off-diagonal coupling terms of the form:

$$H_\Phi = \left[\begin{array}{c|ccccc} \Phi & 0 & \cdots & 0 & \cdots & 0 \\ \hline & 0 & \cdots & 0 & \cdots & 0 \\ & \vdots & \vdots\vdots & \vdots & \vdots\vdots & \vdots \\ 0 & 0 & \cdots & 0 & \cdots & 0 \\ & \vdots & \vdots\vdots & \vdots & \vdots\vdots & \vdots \\ & 0 & \cdots & 0 & \cdots & 0 \end{array}\right]; \quad \hat{V}_{off} = \left[\begin{array}{c|ccccc} 0 & i\hat{\alpha}k^2 & & & & \\ \hline & 0 & \cdots & 0 & \cdots & 0 \\ & \vdots & \vdots\vdots & \vdots & \vdots\vdots & \vdots \\ -i\hat{\alpha}^\dagger k^2 & 0 & \cdots & 0 & \cdots & 0 \\ & \vdots & \vdots\vdots & \vdots & \vdots\vdots & \vdots \\ & 0 & \cdots & 0 & \cdots & 0 \end{array}\right] \tag{2.65}$$

in the extended $N \times N$ (N=14, 30 or 40) hamiltonian *via* a set of α^{ij} parameters and ghost band energy levels Φ conveniently chosen. The spirit is to extend the *off-diagonal* k^2 formalism [164] at the edge of the first Brillouin zone with chosen parameters α^{ij} perturbing the less the correct electronic band structure. In order to do that one must minimize the perturbation at specific k points (A) where the supplementary $\hat{V}_{off} = \alpha^{ij}k^2$ off diagonal terms are being operated. Then, the set of α^{ij} matrices (parameters) may be

conveniently chosen by the optimization procedure for energies (depicts in figure 2.9)and wavefunctions. We describe here the main issues:

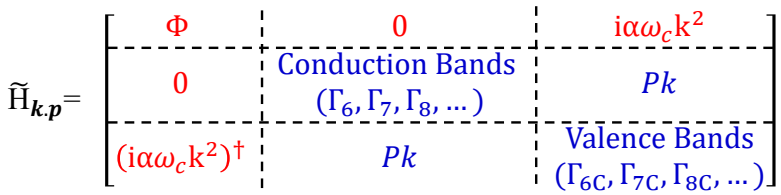

FIGURE 2.8: Schematic of the Hamiltonian including the ghost band to remove the spurious states. The off diagonal terms couple ghost bands and valence bands only in second order to pull down the valence band structure at large wave vector k.

(1) Supplementary fictitious bands (8 supplementary bands in the case of the 30-band method, 18 in the case of the 40-band method), the so-called "ghost-bands" (GB) of adequate symmetry, are introduced in the basis states in order to branch on the off-diagonal coupling ($\hat{V}_{off}$). The coupling strength is calculated so as to leave unchanged the physical bands in the vicinity of the different CB valleys (Γ, X, or L valleys) and at the VB, Γ-valley, all relevant for the carrier transport. In short, the GB represent the average of all the other remote bands truncated by a finite size Hamiltonian. Their mean position in energy lies in a region higher than the S-type CB by approximately 15 eV without the need of a strong accuracy. The $\hat{V}_{off}$ coupling allows to invert the concavity of the spurious bands in the VB at large k avoiding thus any gap-crossing.

(2) New $\boldsymbol{k.p}$ Hamiltonian $\mathcal{H}_{k.\,p}$ including the ghost-bands has form:

$$\mathcal{H}_{k.\,p} = \left[\begin{array}{c|c} \Phi & 0 \\ \hline 0 & H_{\boldsymbol{k.p}} \end{array}\right] \tag{2.66}$$

where $H_{\boldsymbol{k.p}}$ is the original $\boldsymbol{k.p}$ Hamiltonian which involves the spurious states. The new $\boldsymbol{k.p}$ Hamiltonian $\mathcal{H}_{k.\,p}$ is then changed into a perturbed Hamiltonian $\tilde{\mathcal{H}}_{k.p}$ with $\tilde{\mathcal{H}}_{k.p} = \mathcal{H}_{k.\,p} + C_{k_c}\hat{V}_{off}C_{k_c}^{-1}$ where C_{k_c} is the unitary matrix of eigenstates of the new Hamiltonian 2.66 calculated at a certain point k_c close to the Brillouin zone (where $\hat{V}_{off}$ operates). The shape of new Hamiltonian 2.66 (the ghost-band Φ is uncoupled) make it possible to write C_{k_c} in the form:

$$C_{k_c} = \begin{bmatrix} I & 0 & \dots & 0 \\ 0 & & & \\ \vdots & & \hat{\omega}_{k_c} & \\ 0 & & & \end{bmatrix} \tag{2.67}$$

where $\hat{\omega}_k$ is also a unitary matrix and I is the unit matrix with the same dimension as ghost-band Φ; k_c may be found by minimization procedure without the need of a very high accuracy because leading to only moderate errors on the effective mass and tunneling current properties. It can be shown that the procedure leaves unchanged the electronic structure of the conduction band at this particular k_c point by our construction method.

(3) The $\alpha^{ij}k^2$ coupling leaves unchanged the bare Hamiltonian at the Γ point ($k = 0$) because of its specific k^2 form. By an effective Hamiltonian analysis (see more detail in Appendix B), the Hamiltonian is only slightly perturbed by the coupling (perturbation $\hat{V}_{off}$ varying like k^q with $q \geqslant 4$ by construction):

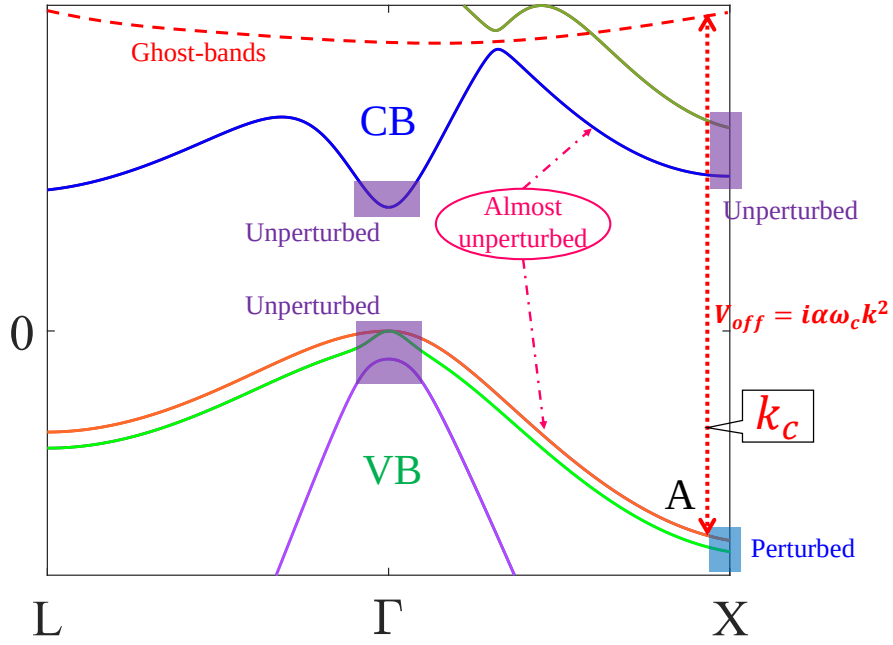

FIGURE 2.9: Schematic of band structure of Hamiltonian in Fig 2.8, the ghost bands are included at higher energy than the first conduction band for perturbation minimization. At the A point, the ghost bands only couple with the VBs and ensure that at Γ and A points, the CBs is weakly affected

⋆ At the first order of the theory of perturbation:

$$\Delta\epsilon^{(1)}_{CB} = \langle CB|V_{off}|CB\rangle = \left\langle CB\middle|\left(C^{-1}_{k_c}\right)_{c\nu} V^{off}_{\nu\Phi}\left(C_{k_c}\right)_{\Phi c}\middle|CB\right\rangle + .c.c = 0 \tag{2.68}$$

because $(C)_{\Phi c} = 0$ (see Eq.2.67). Similarly, one has the same for the first order of energy in VB:

$$\Delta\epsilon^{(1)}_{VB} = \langle VB|V_{off}|VB\rangle = 0 \tag{2.69}$$

⋆ At the second order of the theory of perturbation:

$$\Delta\epsilon^{(2)}_{CB} = \frac{\langle CB|V_{off}|\Phi\rangle\langle\Phi|V_{off}|CB\rangle}{E_\Phi - E_C} = \sum_\Phi \frac{\left\langle CB\middle|\left(C^{-1}_{k_c}\right)_{c\nu}\alpha_{\nu\Phi}\middle|\Phi\right\rangle\langle\Phi|\alpha_{\Phi\nu}\left(C_{k_c}\right)_{\nu c}|CB\rangle}{E_\Phi - E_C}k^4 \tag{2.70}$$

with $\left|\left(C_{k_c}\right)_{\nu c}\right| < 1$ and $\left|\left(C^{-1}_{k_c}\right)_{c\nu}\right| < 1$, and:

$$\Delta\epsilon^{(2)}_{VB} = \sum_\Phi \frac{\left\langle VB\middle|\left(C^{-1}_{k_c}\right)_{V\nu}\alpha_{\nu\Phi}\middle|\Phi\right\rangle\langle\Phi|\alpha_{\Phi\nu}\left(C_{k_c}\right)_{\nu V}|VB\rangle}{E_\Phi - E_V}k^4 \tag{2.71}$$

(the effective Hamiltonian is analyzed in detail in Appendix B).

(4) The α^{ij} parameters are chosen to leave unchanged the current-operator $(1/\hbar)(\partial\hat{H}/\partial k_z)$ (here k_z is directed along the current flow (z is the crystal growth direction) for a geometry of perpendicular spin-polarized current) at the Γ point and mostly unchanged near the Γ point from the $2\alpha^{ij}k \ll P$ relationship at small k where P is the dipolar coupling energy term.

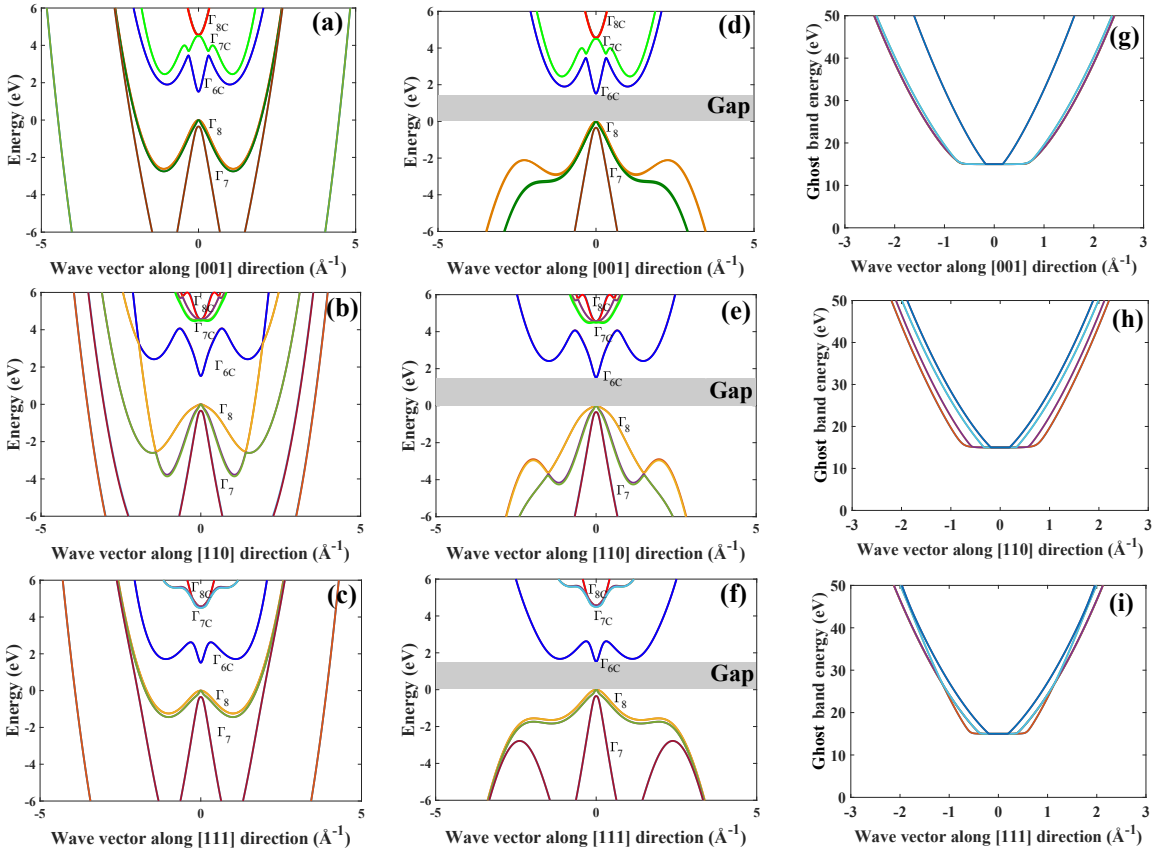

FIGURE 2.10: Electronic band structures of GaAs near the band gap along three characteristic directions with native 30 band $\boldsymbol{k.p}$ method (a,b,c) and 30 bands + 8 ghost bands method (d,e,f). Figure (g,h) and (i) are the 8-ghost bands corresponding to three characteristic directions. The effective mass and band dispersion along the different crystal graphic directions are leaved unchanged.

(5) Due to *(3)*, the effective mass is left unchanged near the Γ point, the perturbative Hamiltonian varying like k^q with $n \geqslant 4$. This property favors the treatment of the tunneling process due to the fact that the evanescent waves are mostly kept unchanged by the perturbation applied: the relevant evanescent waves that expand near the Γ point are the ones corresponding to the smaller imaginary wavevectors lying rather close to the Γ point.

(6) The ensemble of the previous points (1)-(5) can be rigourously demonstrated from the derivation of an effective Hamiltonian at the second order of the perturbation theory close to the Γ point for the respective valence band and conduction bands. Those demonstrations are given in Appendix B. The effective perturbative Hamilonian $\mathcal{H}_{off}$, arising from a perturbative potential α, and projected on a reduced block basis Γ_n writes in the present case:

$$\left(\mathcal{H}_{off}\right)_{m,m'} = \frac{k^4}{2}\left[\frac{\alpha_{\Gamma_m\Gamma_l}\alpha_{\Gamma_l\Gamma_{m'}}}{\mathcal{E}_{\Gamma_m} - \mathcal{E}_{\Gamma_l}} + \frac{\alpha_{\Gamma_m\Gamma_l}\alpha_{\Gamma_l\Gamma_{m'}}}{\mathcal{E}_{\Gamma_{m'}} - \mathcal{E}_{\Gamma_l}}\right] \tag{2.72}$$

where $\mathcal{E}_\Gamma$ is the energy of the corresponding block that are $\{m,m'\} = \{\Gamma_{7,8}\}$ and where the l subscript represents all the other blocks. This leads to a k^4 variation because of the cancellation of the first order energy term in k^2.

And consequently, it results that:

⋆) The electronic and transport properties are not affected at the vicinity of the Γ point for all the CB, VB, HH, LH, and SO bands by V_{off}.

⋆) The electronic and transport properties of the CB are not affected at the vicinity of the point where V_{off} is introduced (close to the first Brillouin zone edge). The tunneling current mediated by a finite evanescent wave-vectors will be only weakly affected by the present treatment method. Those *ghost-band evanescent states* correspond to very large evanescent wave-vectors.

We can expect that the tunneling transport properties corresponding to the involvement of evanescent states from the bottom of the CB to the top of the VB (Γ point) will be only weakly affected and particularly to the 30-band or 40-band case. Then the interest of this procedure is that one can readily transpose the method to a full multiband approach where spurious states originating from the VB arise in the first BZ boundary (the L valley of Ge, or nearly the X valleys of Si). The symmetry of the corresponding states at the first BZ boundary generally admits a well defined character possibly rendering the correction more convenient. Note that the Hamilonian in the CB is unchanged at the A point depicts in Fig.2.9.

The cost to pay for the method is the necessity to introduce at least two different coupling at two points $+\boldsymbol{k}$ (A^+) and $-\boldsymbol{k}$ (A^-) instead of a single one for the BZ center treatment since the different eigenvectors symmetry corresponding to $+\boldsymbol{k}$ and $-\boldsymbol{k}$.

In the figure 2.10, we show the band structure of GaAs along 3 characteristic directions [001], [110] and [111] calculated with native 30 bands $\boldsymbol{k.p}$ method (Fig 2.10 a,b,c) and 30 bands + 8 ghost bands (Fig 2.10 d,e,f). The spurious states at large wavevector $\boldsymbol{k}$ in native 30 band $\boldsymbol{k.p}$ method are then removed after using our novel ghost band method which keeps the band structure almost unchanged within the first Brillouin zone. Figure 2.10 (g,h,i) are the 8 ghost bands along 3 characteristic directions [001], [110] and [111]. These ghost band energies are proportional to k^n where $n \geq 5$ since the coupling terms of the phantom band are proportional to k^2.

Estimation of the error on the effective mass introduced by the ghost-band method

In order to check validity of our 30- and 40-band 'ghost-band' approaches, we consider several situations:

First, we have calculated the in-plane energy dispersion of holes along the X, K directions in an AlAs/GaAs/AlAs quantum well (QW) grown along the [001] directions (Fig 2.11a) with our 30-band **k.p** tunneling code with parameters extracted from Richard et al. [200, 201]. Those are compared with the results obtained with an effective 6-band **k.p** model for the two X and K directions [202] *with a resulting excellent agreement*. We focus on the particular point that the AlAs barriers admit an indirect gap along the X-valley which is perfectly taken into account in our modified 30-band **k.p** tunneling model. The same calculations for the AlAs/GaAs/AlAs quantum well grown along [110] (Fig 2.11b) and [111] (Fig 2.11c) directions are also done in comparison with 6-band model in Ref.[203] giving good agreements.

Moreover, we presently consider the tunneling transmission of electrons and holes in the GaAs/GaAs/GaAs structure, by adding a fictitious potential for the central GaAs layer for the sake of simplicity, *vs.* the GaAs barrier thickness d for the respective CB (see Fig 2.12 a) and VB (see Fig 2.12 b). We have performed the calculations for different "ghost-spurious" coupling strength $|\alpha_{ij}|$ varying in the range of $1-2\ eV.\text{Å}^{-2}$ and $1.5-1.7\ eV.\text{Å}^{-2}$ for the 30 and 40-band method, respectively. The results are that the carrier transmission and tunneling effective mass, extracted from the slope of transmission vs. d $\left(\frac{\sqrt{2m^*\Phi}}{\hbar} = -\frac{\partial \log_e T}{\partial d}\right)$, either for electrons or holes, is not affected by the off-diagonal coupling strength α. One can show that the calculations are also robust *vs.* the exact application of the coupling point k_c. With the following procedure, the effective mass in the CB is correctly found to be $m^*_{e,30b} = 0.06$ and $m^*_{e,40b} = 0.064$ for the respective 30 and 40-band method near the Γ point at about 0.2 eV above the gap. In the same way, the extracted light hole effective mass was found $m^*_{LH,30b} =\simeq m^*_{LH,40b} = 0.07$ very close

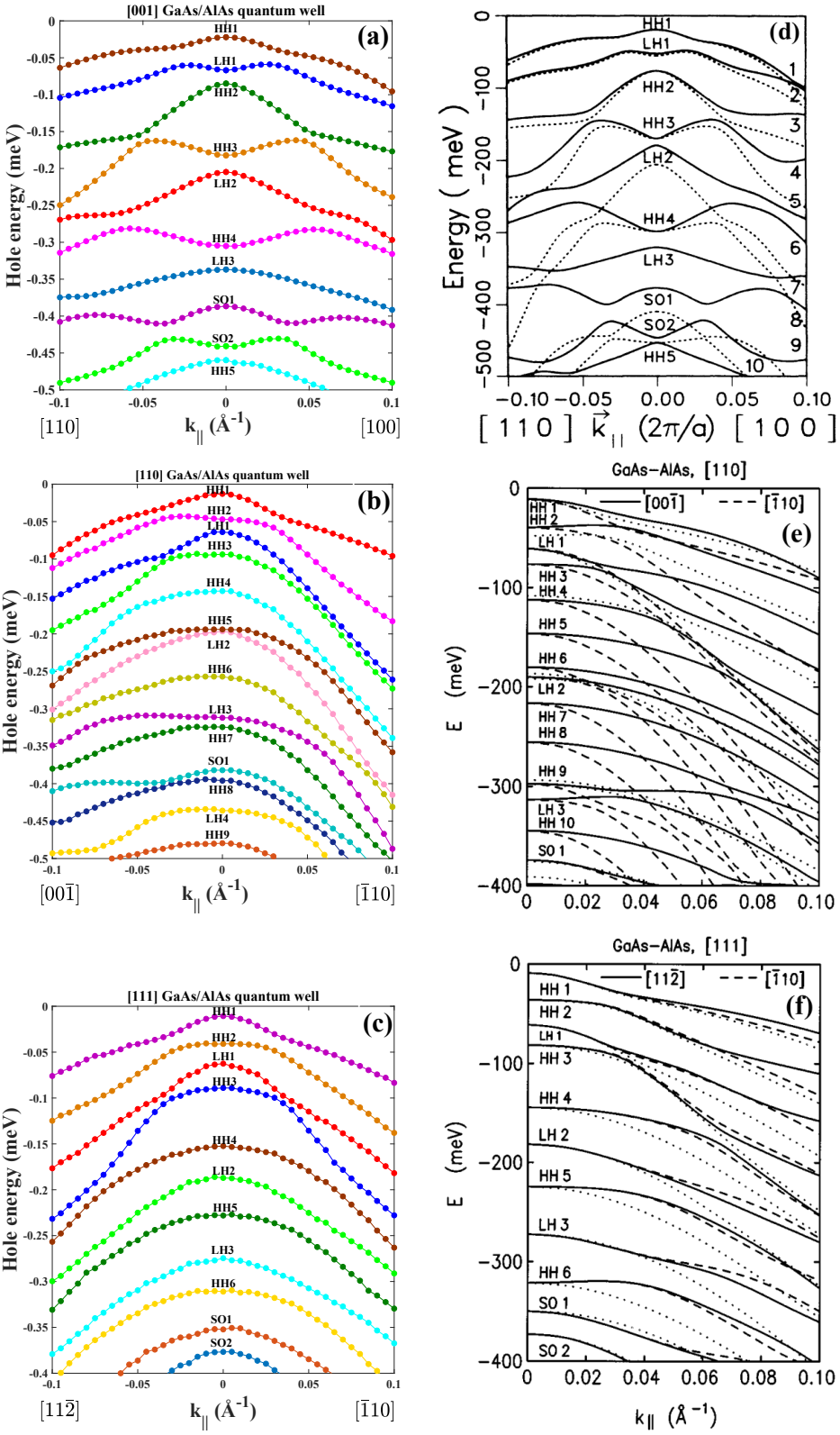

FIGURE 2.11: Hole dispersions in AlAs/GaAs 6nm quantum well calculated by a 30-band $\boldsymbol{k.p}$ model using ghost-band method for the three respective growth directions [001] [110] and [111], Fig. (a), (b) and (c) respectively, in comparison with the result calculated by Eppenga et al. [202] with 6-band $\boldsymbol{k.p}$ model, Fig. (d), and Winkler et al. [203], Fig. (e) and (f).

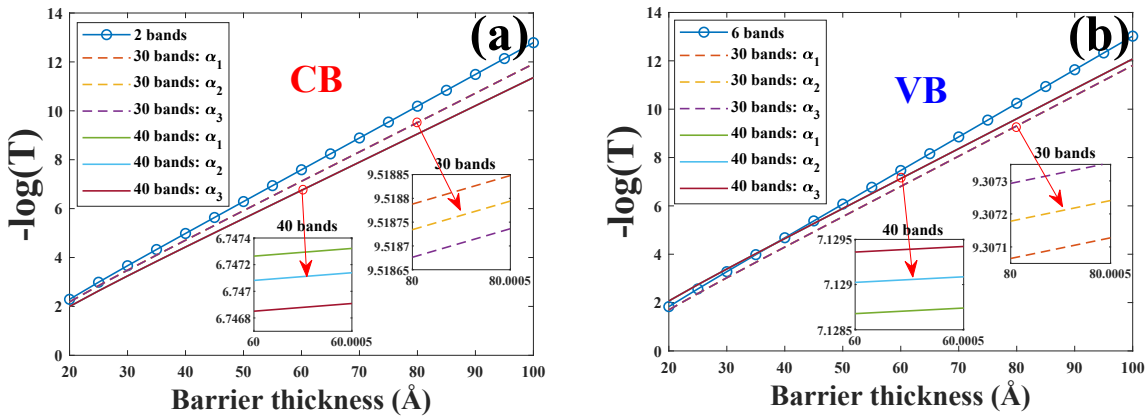

FIGURE 2.12: Transmission of carriers (in log. scale) vs. the barrier thickness d in fictitious GaAs/GaAs/GaAs trilayer barrier (a fictitious barrier height has been added in the central GaAs of -0.2eV) calculated in the CB (Fig. (a)) and VB (Fig. (b)) within an extended 30- and 40- band $\boldsymbol{k.p}$ framework for strictly normal incidence ($k_{||} = 0$). The slope of the transmission in log. scale vs d is related to the tunneling effective mass which remains robust under ghost-spurious coupling strength α: $\left\{\alpha_1 = 1eV.\text{Å}^{-2}; \alpha_2 = 1.5eV.\text{Å}^{-2}; \alpha_3 = 2eV.\text{Å}^{-2}\right\}$ for 30-band $\boldsymbol{k.p}$ model and $\left\{\alpha_1 = 1.5eV.\text{Å}^{-2}; \alpha_2 = 1.6eV.\text{Å}^{-2}; \alpha_3 = 1.7eV.\text{Å}^{-2}\right\}$ for 40 band $\boldsymbol{k.p}$ model.

to the expectation values 0.08. The relative errors calculated on the dispersion of the effective mass at the Γ point (barrier height of -0.2 eV) and introduced by the perturbative spurious-ghost band procedure are the following ones:

	m_e^*/m_0		$\delta m_e^*/m_e^*$	m_{LH}^*/m_0		$\delta m_{LH}^*/m_{LH}^*$
	Cal.	Lit.		Cal.	Lit.	
Si	-	-	-	0.1652	0.16	1.6×10^{-5}
Ge	-	0.041	-	0.0417	0.043	5.6×10^{-6}
GaAs	0.064	0.063	1.5×10^{-5}	0.07	0.082	4×10^{-5}
InAs	0.0238	0.023	1.4×10^{-7}	0.0258	0.026	1.6×10^{-6}
AlAs	-	0.16	-	0.1749	0.18	1×10^{-4}
$In_{0.25}Ga_{0.75}As$	0.0617	-	2.9×10^{-6}	0.0733	-	1.8×10^{-5}
InSb	0.0144	0.014	1×10^{-7}	0.0161	0.015	3×10^{-6}
InP	0.0703	0.08	3.6×10^{-7}	0.0904	0.089	1×10^{-6}
GaP	-	0.09	-	0.1504	0.14	6×10^{-5}

TABLE 2.4: Effective mass at the Γ point of several semiconductors extracted from our numerical calculations (Cal.) in comparison with literature (Lit.) (taken from Ref.[53]) and the relative error of our numerical calculations induced by the phantom treatment.

$$\left(\frac{\Delta m_e^*}{m_e^*}\right)_{30b} \simeq 2.3\times10^{-6}, \left(\frac{\Delta m_e^*}{m_e^*}\right)_{40b} \simeq 1.5\times10^{-5},$$
$$\left(\frac{\Delta m_{LH}^*}{m_{LH}^*}\right)_{30b} \simeq 1.5\times10^{-5}, \left(\frac{\Delta m_{LH}^*}{m_{LH}^*}\right)_{40b} \simeq 4.0\times10^{-5} \quad (2.73)$$

where LH stands here for the *light-hole* index corresponding to the smaller hole tunneling wavevector as discussed previously. In Table 2.4, we show that the effective mass and the errors which were done in the

same way as in GaAs, for different materials. Note that, the errors in the Table 2.4 are the relative differences between the effective mass calculated with different ghost-band coupling strength, not the relative differences between the effective mass calculated with our method and the literature value. One can observe that those errors remain very small leading to the fact that the ghost-band method weakly affect on the effective mass which is very important quantity for the tunneling problems. We are now going to compare these results on the effective mass (extracted by numerical calculation) with analytical calculations.

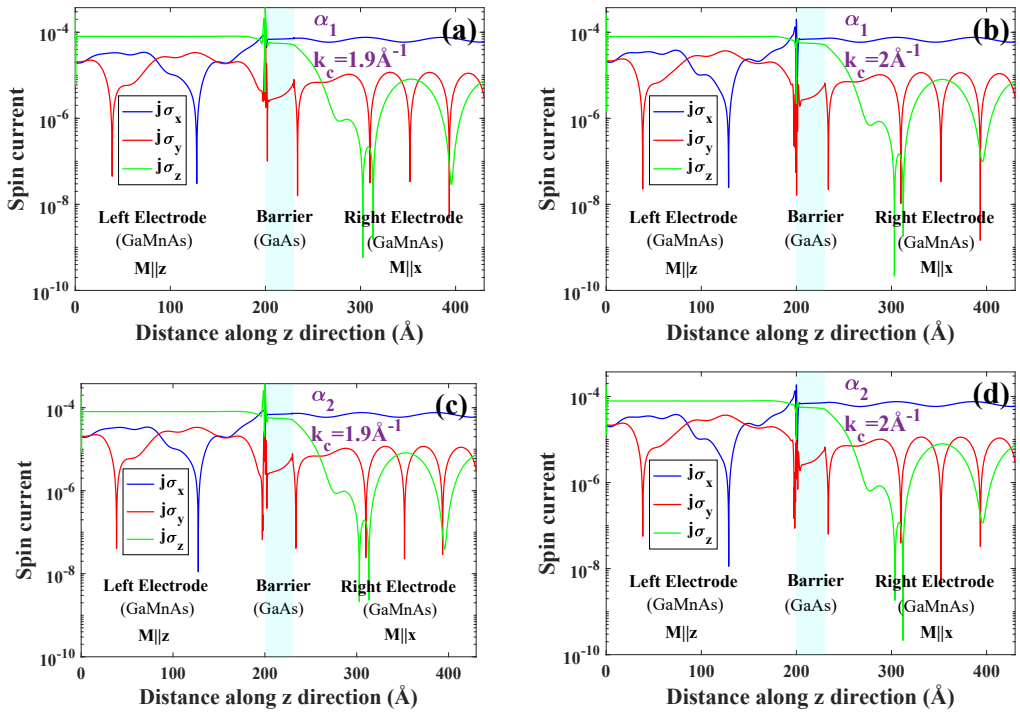

FIGURE 2.13: The 3 spin-current components through GaMnAs/GaAs/GaMnAs trilayer structure, the magnetization in the left and in the right electrode are aligned respectively along the z and x directions, within an extended 30-band ***k.p*** framework calculated for strictly normal incidence ($k_{||} = 0$) and for different ghost-spurious coupling strength α: $\alpha_1 = 1.5eV.\text{Å}^{-2}$ Figs. (a,b) and $\alpha_2 = 2eV.\text{Å}^{-2}$ Figs. (c,d) and at different coupling points k_c as depicted in the figure.

We consider here the energy dispersion up to the second order of the theory of perturbation, one has:

$$\epsilon = \frac{\hbar^2 k^2}{2m_0^*} + \frac{\alpha^2 |\omega_{k_c}|^2 k^4}{E_\Phi - E_S} = \frac{\hbar^2 k^2}{2m^*} \tag{2.74}$$

where m^* is the effective mass:

$$\frac{1}{m^*} = \frac{1}{\hbar^2}\frac{\partial^2 \epsilon}{\partial k^2} = \frac{1}{m_0^*} + \sum_\Phi \frac{12\alpha^2 |\omega_{k_c}|^2 k^2}{\hbar^2 (E_\Phi - E_S)} \tag{2.75}$$

$$\frac{1}{m^*} - \frac{1}{m_0^*} \approx \frac{m_0^* - m^*}{\left(m_0^*\right)^2} = \sum_\Phi \frac{12\alpha^2 |\omega_{k_c}|^2 k^2}{\hbar^2 (E_\Phi - E_S)} \tag{2.76}$$

When considering the tunneling through simple barrier structure, one has $\frac{\hbar^2 k^2}{2m_0^*} \cong \Delta$ the barrier height in the gap or $k^2 = \frac{2m_0^* \Delta}{\hbar^2}$.

$$\frac{\Delta m^*}{m^*} \simeq \frac{m_0^* - m^*}{m_0^*} = \sum_{\Phi} \frac{24\left(m_0^*\right)^2 \Delta}{E_\Phi - E_S} \frac{\alpha^2 |\omega_{k_c}|^2}{\hbar^2} \tag{2.77}$$

If we call N_Φ: number of ghost bands, then one has:

$$\frac{\Delta m^*}{m^*} < N_\Phi \frac{24\left(m_0^*\right)^2 \Delta}{|E_\Phi - E_S|} \frac{\alpha^2 |\omega_{k_c}|^2}{\hbar^2} = N_\Phi |\omega_{k_c}|^2 \frac{24\Delta}{|E_\Phi - E_S|} \left(\frac{m\alpha}{\hbar}\right)^2 \tag{2.78}$$

For the numerical calculations based on 30-band $\boldsymbol{k.p}$ model above, one has: $N_\Phi = 8$; $|\omega_{k_c}|^2 \simeq 1$ (since ω_{k_c} is unitary matrix); $\Delta = 0.2eV$; $|E_\Phi - E_S| \approx 15eV$; $\alpha = 1.5eV.\text{Å}^{-2}$ and $m^* \simeq m_0$ then, one can get the result that:

$$\frac{\Delta m^*}{m^*} < 10^{-5} \tag{2.79}$$

which is in very good agreement with the numerical results in Table 2.4.

Finally, figure. 2.13 shows that the calculated profiles of the charge and spin-current components remain mostly unchanged by the procedure adopted (see Fig 2.13). This makes our calculation scheme and strategy extremely robust.

2.4.3 *Evanescent states*

While a real wavevector and corresponding Bloch state describe a propagating state, a complex wave vector describes an evanescent state [185]. Such states are localized close to the crystal surface or interface or in the forbidden band gap of a bulk semiconductor [55, 183, 185]. In the 2-band toy model, the evanescent states appear when the wave vector is complex. In the $\boldsymbol{k.p}$ framework, the evanescent states are found by solving the secular equation 2.49 where the wavevector $\boldsymbol{k}$ now possesses an imaginary part. Heine [205] has studied the properties of the real energy lines for the diamond structure (O_h group) in the framework of the group theory. He proved several theorems for these real energy lines and observed that neither the real-energy lines can branch nor terminate, nor can they coalesce more than one time. Moreover, they can cross each other only at real wave vector $\boldsymbol{k}$. Energies at the crossing point are extrema of E when plotted in the real wave-vector space. The conclusion of Heine is that there are only two possibilities for the evanescent states, one is that the real energy line crosses the bandgap, connecting the maximum of one band to the minimum of a higher band, another is that these lines monotonically vary and run to infinity. This prediction was confirmed by Jones [206] with a numerical calculation for determining the evanescent states of silicon, taking into account only the bands in the neighborhood of the band gap. Using the tight-binding method, Chang [207] has calculated the structure of the evanescent states in several materials with diamond structure (O_h) or with zinc-blende structure (T_d), but without taking into account the spin-orbit coupling. In 1985's, Schuurmans and 't Hooft [208] studied the band structure of GaAs and AlAs (T_d) using the Kane model. The spin orbit coupling was taken into account, but these authors supposed that the contribution of k^3 terms to the bands structure is minor, and they disregarded the linear k term in the band dispersion. That means GaAs and AlAs were considered as if they belonged to the O_h group. Consequently, the evanescent states are spin degenerated, no splitting is found for evanescent states in any direction.

The spin-orbit coupling and the absence of inversion symmetry were both considered for the first time by Richard et al. [201, 204] and Rougemaille et al. [209] using the 14×14 and 30×30 $\boldsymbol{k.p}$ matrices. A more recent discussion can be found in Ref. [184]. Here we recovered the calculation of Richard et al. with our 30×30 band $\boldsymbol{k.p}$ method in Fig. 2.14 where the original topology of evanescent states is found along the $[tan\theta, 0, i]$ k-direction with $\theta = \xi/K$ defined in the figure. Our result is in good agreement

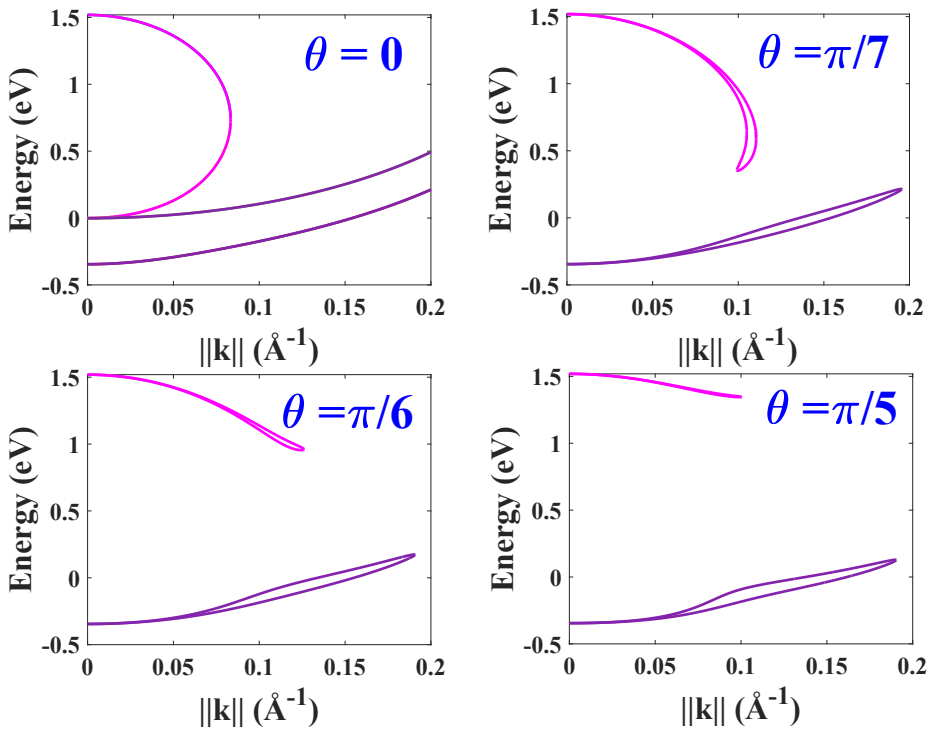

FIGURE 2.14: Plot of the real energy line inside the gap for $\boldsymbol{k} = [\xi, 0, iK] = [tan\theta, 0, i]\,k$ where ξ and K are real and positive and $\theta = \frac{\xi}{K}$. The calculations were performed using our 30×30 $\boldsymbol{k.p}$ model. The presence of the spin-orbit coupling and the lack of an inversion center lead to a splitting in the complex band structure when $\theta \neq 0$. These results are in good agreement with results of Richard et al. in Ref.[204].

with the results of these authors [55, 183, 185, 201, 204]. According to these numerical calculations, the evolution of the evanescent lines is depending on θ. Along the [001] direction when $\theta = 0$, one observes an evanescent loop connecting the Γ_6 conduction band and Γ_8 light-hole bands, with two-fold degeneracy. When increasing θ ($\theta > 0$ but still small), the appearance of D'yakonov-Perel' field leads to a small energy splitting. The evanescent line is, then, represented by a loop that connects two spins subbands inside the forbidden band gap. The splitting between these two evanescent subbands increases as θ increases, until $\theta = \pi/6$, an angle beyond which the evanescent state extension starts to decrease. An energy region exists in the band gap where no states are allowed: a forbidden band gap appears inside the bandgap and the evanescent loop no longer reaches the valence band [185]. At larger θ, one observes a smaller extension of the evanescent loops in wave vector space and energy. The loop totally disappears at the value $\theta = \pi/2$ [185, 201, 204]. Such band diagrams are the consequence of the spin-orbit coupling and the lack of inversion symmetry [183]. For a complex wave vector $\boldsymbol{k}$ we have $E(\boldsymbol{k}^*) = [E(\boldsymbol{k})]^*$ [205]. Then, with Kramers 's conjugate, one finds four states corresponding to $\boldsymbol{k}$, $-\boldsymbol{k}^*$, $\boldsymbol{k}^*$ and $-\boldsymbol{k}$ at the same energy.

Finally, figure 2.15 shows the calculations of the evanescent states along three characteristic direction in the whole first Brillouin zone with native 30 bands and 38 bands (8 ghost bands) $\boldsymbol{k.p}$ method. The evanescent band structures calculated by native 30 bands and 38 bands are the same in the region close to the Γ point where k is small. This shows that the tunneling processes inside the barrier are the same for both approaches, i.e, using the complex band structure calculated by a native 30 bands $\boldsymbol{k.p}$ Hamtilonian or by a 30 bands + 8 ghost bands method. Besides, at larger wave vector k, there are additional bands which are the consequences of converting the spurious solutions with larger real k to the spurious solutions with large imaginary k in the framework of ghost-band theory. However, this is less important since the states corresponding to well larger imaginary wavevectors are harmless in their possible tunneling contributions

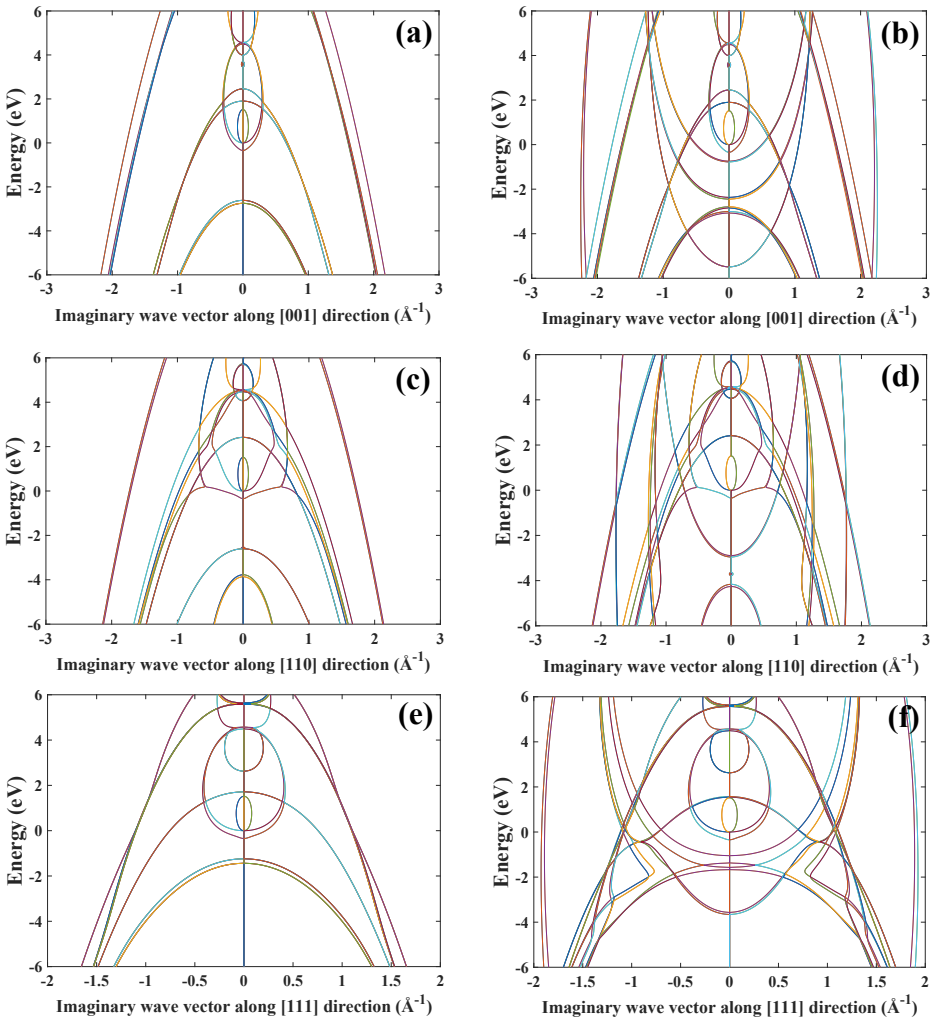

FIGURE 2.15: Evanescent band structure of GaAs within native 30-band (a), (c), (e) and 38-band (8 ghost-band) (b), (d) and (f) calculated for three characteristic direction [001], [110] and [111]. In comparison to native 30-band, there are additional evanescent bands at far away from Γ point in the calculation with 38-band method. As mentioned in Ref. [164], these additional bands are the consequences of converting the spurious solutions with large real k to the spurious solution with large imaginary k which, as commented earlier, are harmless in the calculations. The imaginary k landscape remains unchanged close to the Γ point.

because they will decay very quickly.

2.5 *The envelope function approximation and Burt-Foreman Approach [179]*

The **k.p** theory or the theory of Luttinger-Kohn describing an effective equation for the wavefunction of a Bloch electron is generally valid in the presence of a slowly-varying perturbative potential. In the presence of atomically-abrupt heterostructures, the potentials are no longer slowly varying and the questions arises to develop more refined models accounting for the presence of potentials confined at the vicinity of the interfaces. Those potentials however needs not to be local in space although close to the interface. In that view, in heterostructures, the material is position dependent and its properties do not generally commute with the spatial differential operators appearing in the 'effective mass' approach (**k.p** method) and in the

envelope function approximation (EFA) [210–212]. Unlike those two latter approaches requiring rules for operator ordering process, the more recent envelope-function theory of Burt and Foreman [213–215] attempts to derive an effective Hamiltonian from first principles.

2.5.1 Envelope function approximation (EFA) [212]:

The main idea of the EFA is to consider that, in each separate layer of any heterostructures (typically named A and B), the wavefunction can be expanded in terms of the periodic part of the Bloch functions (cellular part) at a given wavevector k_0 (e.g. at the Γ point), of the type [210–212]:

$$\psi(\boldsymbol{r}) = \sum_n f_n^{(A,B)}(\boldsymbol{r}) u_{n\boldsymbol{k}_0}^{(A,B)}(\boldsymbol{r}) \tag{2.80}$$

and then match the solutions across boundaries. This method, largely developed in the present manuscript, is exact in the case where the perturbation varies slowly in the landscape of the junctions. The boundary conditions for the wavefunctions, which generally corresponds to abrupt potential leads to specific matching conditions which can largely depart from the BenDaniel-Duke ones as one involves the local potentials thus describing an effective interfacial Hamiltonian. We largely discuss those specific matching condition in this manuscript. In the EFA method, we assume that the periodic (cellular) functions in the layers are the same. This appears to be a good approximation, in particular, if the chemical species belongs to the same column (Ga, As, Al) or similar and if the crystalline structure is the same (Oh or Td symmetry group). Moreover, it also comes that the dipolar coupling terms remain almost unchanged for III-V elements with the result that the main available or free parameters from material to material are the different energy gaps between energy levels and band offsets.

In the quasi one dimensional tunneling problem, one can use Bloch periodicity in term of:

$$f_n^{(A,B)}(\boldsymbol{r}) = f_n^{(A,B)}(\boldsymbol{r}_{||}, z) = \frac{1}{\sqrt{S}} e^{i\boldsymbol{k}_{||}\boldsymbol{r}_{||}} \chi_n^{(A,B)}(z) \tag{2.81}$$

where z-direction is the tunneling direction, $\boldsymbol{r}_{||}$ is a position vector in the in-plane and S is the surface area in this plane. This theory was used at length for quantum well structure by Bastard et al. [210–212] giving rise an accuracy up to 0.3eV or 10% of the first Brillouin zone for GaAs/AlAs quantum well structures. Note that, in terms of the envelope functions, they are continuous but their first derivatives may be not. For example, in a material system whereby the effective mass changes sign, there are discontinuities in the first derivatives of the envelope functions at the interfaces.

2.5.2 Burt-Foreman Theory [213–215]:

A first-principle envelope function theory was firstly formulated by Burt in the 1980 [214, 215], followed more recently by B. Foreman [213], which makes the advantage of not imposing a particular symmetrization of the effective 6-band and 8-band multiband Hamiltonian. Before discussing some details of the theory, the main difference between the previous EFA approaches and that one is the ability to consider, from the first principles, the exact effect of the local varying potentials (effective interface Hamiltonian) on the wave function itself more than in the boundary conditions.

The essence of the theory is that the wavefunction can be written as an envelope-function expansion according to:

$$\psi(z) = \sum_n F_n(z) U_n(z) \tag{2.82}$$

where $F_n(z)$ is the envelope function which has to be a smooth continuous function with Fourier-component lying in the first Brillouin zone (FBZ) and the $U_n(z)$ represents a complete set of orthogonal periodic function, strongly localized, over the whole structure.

Like in the EPM approach, one starts by expanding the wave function in terms of plane waves according to:

$$\psi(z) = \sum_{kG} \tilde{\psi}_G(k) e^{i(k+G)z} \tag{2.83}$$

where k is the wavevector in the FBZ and G is vector of the reciprocal space. We have to consider now the fact that a plane-wave expansion is unique and complete on the Burt-Foreman basis. Indeed, since $U_n(z)$ are periodic functions, they can be writtetn as a sum in the Fourier space according to:

$$U_n(z) = \sum_{G} U_{nG} e^{iGz} \tag{2.84}$$

If the $U_n(z)$ are chosen complete and linearly independent, plane waves can be uniquely expanded in terms of them to give:

$$e^{iGz} = \sum_{n} \left(U^{-1}\right)_{Gn} U_n(z) \tag{2.85}$$

where:

$$\sum_{G} U_{nG} \left(U^{-1}\right)_{Gm} = \delta_{nm} \tag{2.86}$$

We have then

$$F_n(z) = \sum_{kG} \tilde{\psi}_G(k) e^{ik_z} \left(U^{-1}\right)_{Gn} \tag{2.87}$$

showing that the $F_n(z)$ are uniquely determined by a Fourier expansion of plane waves within the FBZ and furthermore we can show that this expansion is unique as well [179].

Starting from the Schrödinger equation for one dimensional tunneling along z-direction:

$$-\frac{\hbar^2}{2m_0}\frac{d^2\psi}{dz^2} + V(z)\psi = E\psi \tag{2.88}$$

we are now going to perform the equation for the envelope function 2.82 by considering separately kinetic and potential terms as following.

2.5.3 *Kinetic Energy:*

Using the envelope function expansion 2.82, the kinetic energy term becomes:

$$-\frac{\hbar^2}{2m_0}\frac{\partial^2\psi}{\partial z^2} = -\frac{\hbar^2}{2m_0}\sum_{n}\left[F_n^{"}U_n + 2F_n^{'}U_n^{'} + F_nU_n^{"}\right] \tag{2.89}$$

where one has the periodicities of $U_n^{'}$ and $U_n^{"}$:

$$U_n^{'}(z+a) = U_n^{'}(z) \tag{2.90}$$

$$U_n^{"}(z+a) = U_n^{"}(z) \tag{2.91}$$

leading to:

$$-i\hbar\frac{\partial U_n}{\partial z} = \sum_{m} p_{mn}U_m \tag{2.92}$$

One can now obtain the coefficients P_{mn} by multiplying each side of equation by U_n^* integrate over z, and use orthonormality. Besides, one has:

$$\begin{aligned}\int \frac{dz'}{a} \sum_m U_m^*(z') \left(-i\hbar \frac{dU_n(z')}{dz'}\right) U_m(z) &= \int \frac{dz'}{a} \left(-i\hbar \frac{dU_n(z')}{dz'}\right) \sum_m U_m^*(z') U_m(z) \\ &= \int \frac{dz'}{a} \left(-i\hbar \frac{dU_n(z')}{dz'}\right) \delta(z-z') = -i\hbar \frac{dU_n}{dz}\end{aligned} \tag{2.93}$$

yielding an alternative solution for the Eq 2.92 if we define:

$$p_{mn} = \int \frac{dz}{a} U_m^*(z) \left(-i\hbar \frac{\partial}{\partial z}\right) U_n(z) \tag{2.94}$$

Similarly, one can define:

$$T_{mn} = \int \frac{dz}{a} U_m^*(z) \left(-\frac{\hbar^2}{2m_0} \frac{\partial^2}{\partial z^2}\right) U_n(z) \tag{2.95}$$

and show that:

$$\sum_m T_{mn} U_m = -\frac{\hbar^2}{2m_0} \frac{\partial^2 U_n}{\partial z^2} \tag{2.96}$$

Then, the kinetic energy term for envelope function can be obtained as:

$$-\frac{\hbar^2}{2m_0} \frac{d^2\psi}{dz^2} = \sum_n \left[-\frac{\hbar^2}{2m_0} \frac{d^2F_n}{dz^2} - \frac{i\hbar}{m_0} \sum_m p_{nm} \frac{dF_m}{dz} + \sum_m T_{nm} F_m\right] U_n \tag{2.97}$$

2.5.4 Potential energy:

We start by Fourier transforming the These can then be compared to those obtained starting from the bulk Luttinger–Kohn Hamiltonian. potential V(z) (the periodic part and possible non periodic part close to the interface) and expanding $\psi(z)$ in the envelope function expansion and also replace the envelope function $F_n(z)$ and $U_n(z)$ by their respective Fourier transform to derive:

$$V(z)\psi(z) = \sum_n \left[\sum_m \int dz' V_{nm}(z,z') F_m(z')\right] U_n(z) \tag{2.98}$$

where:

$$V_{nm}(z,z') = \frac{1}{L} \sum_{kk'} \sum_{GG'} U_{n,G+G'}^* \tilde{V}_{G-G'}(k) U_{mG'} e^{i(kz+k'z'+)} \tag{2.99}$$

and

$$\tilde{V}_{G-G'}(k) = \int_L \frac{dz}{L} V(z) e^{-i(k+G)z} \tag{2.100}$$

is the Fourier components of the potential.

2.5.5 Envelope function equation and effective Hamiltonian:

Putting the kinetic energy and potential energy terms into Schrödinger equation, one has:

$$\sum_n \left[-\frac{\hbar^2}{2m_0} \frac{\partial^2 F_n}{\partial z^2} - \frac{i\hbar}{m_0} \sum_m p_{nm} \frac{\partial F_m}{\partial z} + \sum_m T_{nm} F_m + \sum_m \int dz' V_{nm}(z,z') F_m(z')\right] U_n = E \sum_n F_n(z) U_n(z) \tag{2.101}$$

giving rise exact envelope function equation:

$$-\frac{\hbar^2}{2m_0}\frac{\partial^2 F_n}{\partial z^2}-\frac{i\hbar}{m_0}\sum_m p_{nm}\frac{\partial F_m}{\partial z}+\sum_m\int dz' H_{nm}(z,z')F_m(z')=EF_n(z) \tag{2.102}$$

where:

$$H_{nm}(z,z')=T_{nm}\delta(z-z')+V_{nm}(z,z') \tag{2.103}$$

This envelope-function equation can be simplified to reproduce multiband Hamiltonians for arbitrary nanostructures as we will see in the next chapter dealing with matching conditions for tunneling within heterostructures.

2.6 Effective Hamiltonian in the k.p framework involving spin-orbit interactions (relation to the envelope function approximation (EFA)).

In many physical systems and in particular for the investigation of physical effects related to the relativistic spin-orbit coupling in bulk semiconductors or at their interfaces, building an effective reduced Hamiltonian projected on a smaller block may reveal particularly interesting. The advantage of such Hamiltonian reduced within a smaller size on blocks of particular symmetry (e.g. 2×2 CB Hamiltonian or 4×4 or 6×6 VB Hamiltonian) is the ability to handle with the envelope function approximation (EFA) for describing wavefunction symmetries and developing analytical algebra methods for solving particular transport issues and phenomena. The EFA method also allows to describe electron and hole states in the presence of electric fields that vary slowly on the length scale of the lattice constant. Those fields can be internal, such as the crystal field, or external by means of the application of an electric field e.g. a gate voltage. This generally leads to a system of coupled differential equations, the eigenstates of which are the multi-component envelope functions or spinors-like functions described within the manuscript.

The standard method to realize the projection of the starting $N\times N$ multiband k.p Hamiltonian on a reduced basis states of a given Bloch symmetry is called the Löwdin perturbation theory like described in many textbooks [29, 44]. It will result that, in the reduced basis, the $\boldsymbol{k.p}$ interactions with the remote bands that are not taken exactly into account will, in counterpart, lead to new terms at higher order of k (typically k^2 terms), and connected to the effective mass of carriers.

Moreover, the reduction of a multiband Hamiltonian of size $N\times N$ to a reduced size, is also interesting from the symmetry point-of-view. Indeed, another complementary approach for the construction of a finite size Hamiltonian is based on the theory of invariants (Ref. [44]). This approach utilizes, the fact, that independently of any microscopic details, the Hamiltonian must be invariant under all the symmetry operations, and thus associated to well-known representation forms for its corresponding block Hamiltonian part of given point-group symmetries. This also serves to check the final form of the application of Löwdin's perturbation techniques in a subset of the corresponding levels.

2.6.1 The effective Hamiltonian in the conduction band of T_d symmetry group semiconductors

The effective Hamiltonian for the electrons in the first CB is:

$$H_C=\frac{\hbar^2}{2m^*}k^2\mathbb{I}+H_D \tag{2.104}$$

where m^* is the electron effective mass in the crystal, $\mathbb{I}$ is the identity matrix, H_D is the Dresselhaus Hamiltonian 1.40:

$$H_D = \gamma_D \begin{bmatrix} k_z\left(k_x^2 - k_y^2\right) & k_x\left(k_y^2 - k_z^2\right) - ik_y\left(k_z^2 - k_x^2\right) \\ k_x\left(k_y^2 - k_z^2\right) + ik_y\left(k_z^2 - k_x^2\right) & -k_z\left(k_x^2 - k_y^2\right) \end{bmatrix} \tag{2.105}$$

with

$$\gamma_D = \gamma_D^{(3)} + \gamma_D^{(4)} \tag{2.106}$$

$\gamma_D^{(3)}$ represents here the Dresselhaus coefficient obtained to the third-order perturbation series, whereas $\gamma_D^{(4)}$ corresponds to the fourth-order contribution [31]. Both terms originate from antisymmetric coupling terms P' and Δ' present in the T_d group and are zeros in the O_h group. According to the parameters in the literature [92], $|\gamma_D^{(4)}|$ is much larger than $|\gamma_D^{(3)}|$, meaning that, counterintuitively, the contribution of the fourth-order term is larger than the third order one. This nontrivial property makes then difficult to anticipate the consequence of a truncation, possible higher-order development could give significant Dresselhaus contributions. One need to note that the SOI in an effective Hamiltonian model originates from the core spin-orbit potential (Δ and Δ^C) and from the lack of inversion center (Δ' and P') [31]. In the O_h group, $P' = 0$ and $\Delta' = 0$ resulting in $\gamma_D^{(3)} = 0$, $\gamma_D^{(4)} = 0$ and more generally $\gamma_D^{(n)} = 0$ resulting in the cancellation of the Dresselhaus interaction.

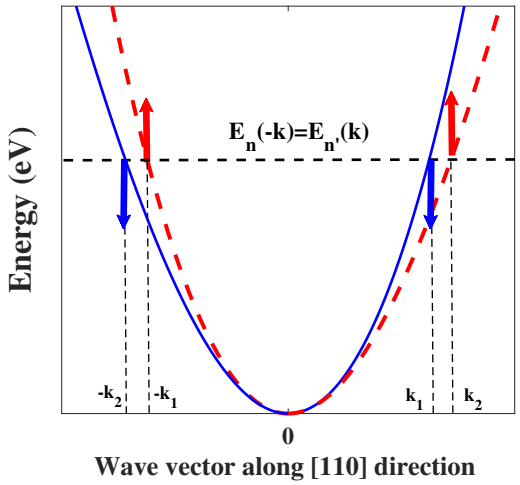

FIGURE 2.16: Energies of ↑ spin (red line) and ↓ spin (blue line) states generated by Dresselhaus terms.

For the sake of convenience, we define the $\boldsymbol{\chi}$ vector, $\boldsymbol{\chi} = (\chi_x, \chi_y, \chi_z)$ where, $\chi_x = k_x(k_y^2 - k_z^2)$, $\chi_y = k_y(k_z^2 - k_x^2)$, $\chi_z = k_z(k_x^2 - k_y^2)$. The Dresselhaus Hamiltonian admits then the form:

$$H_D = -\gamma_D \boldsymbol{\chi}.\boldsymbol{\sigma} = -2\gamma_D \boldsymbol{\chi}.\boldsymbol{S} = -\gamma \begin{bmatrix} \chi_z & \chi_x - i\chi_y \\ \chi_x + i\chi_y & -\chi_z \end{bmatrix} \tag{2.107}$$

where $\boldsymbol{S} = \frac{\boldsymbol{\sigma}}{2}$. The H_D in Eq.2.107 is the so-called the D'akonov-Perel's Hamiltonian [90, 105, 109]. The expression of H_D shows that the electron spin experiences a magnetic field proportional to $\boldsymbol{\chi}$, which depends on the $\boldsymbol{k}$-direction. Therefore, $\boldsymbol{\chi}$ is called the internal magnetic field or D'yakonov-Perel's field. The internal magnetic field varies both in magnitude and direction and this is known to lead to a spin relaxation mechanism of conduction electrons (D'yakonov-Perel's mechanism). The electron's energies in

the CB are eigenvalues of the Hamiltonian 2.104 can be written in different ways:

$$\varepsilon = \frac{\hbar^2}{2m^*}k^2 \pm \gamma_D\sqrt{\chi_x^2 + \chi_y^2 + \chi_z^2} \tag{2.108}$$

or equivalently:

$$\begin{aligned}\varepsilon &= \frac{\hbar^2}{2m^*}k^2 \pm \gamma_D\sqrt{k_z^2(k_x^2 - k_y^2)^2 + k_x^2(k_y^2 - k_z^2)^2 + k_y^2(k_z^2 - k_x^2)^2} \\ &= \frac{\hbar^2}{2m^*}k^2 \pm \gamma_D\sqrt{k^2(k_x^2k_y^2 + k_y^2k_z^2 + k_z^2k_x^2) - 9k_x^2k_y^2k_z^2}\end{aligned} \tag{2.109}$$

The degeneracy of the conduction band is lifted along some peculiar directions but , e.g., neither along the [001] nor the [111] directions. Along the [110] direction, $\varepsilon = \frac{\hbar^2}{2m^*}k^2 \pm \gamma_D k^3$, is associated to the maximum spin-splitting [94].

This effective Hamiltonian model in the CB is known to be convenient for analytical development adapted to III-V semiconductors. However, situations possibly involving interfaces and/or heterostructures with III-V can be much more complex to solve and implement due to the appearance of higher order terms. For example, if one considers tunneling along the [110] direction, the appearance of k cubic terms leads to the discontinuity of the envelope function and requires a re-definition of the current operator and current flux at the interface in an effective Hamiltonian approach [56, 183, 185]. Generally, it is not easy to find the new relevant matching conditions for the wavefunction and/or current for electrons tunneling along the [110] direction.

In order to illustrate that particular point, we will address now several examples and situations involving III-V heterostructures with Dresselhaus interactions in the CB that we can list as below.

Spin-orbit effect in T_d symmetry group materials: The Dresselhaus Hamiltonian [54]

When the quantization direction is along [001], the two terms $\sigma_x k_x \left(k_y^2 - k_z^2\right)$ and $\sigma_y k_y \left(k_z^2 - k_x^2\right)$ are called in-plane Dresselhaus components, whereas the term $\sigma_z k_z \left(k_x^2 - k_y^2\right)$ is the out-of-plane Dresselhaus component. In almost all previous work concerning spin filtering effects working with small oblique incidences leading to a small value of inplane wave vector k_x^2 and k_y^2 in comparison to k_z^2, the Dresselhaus Hamiltonian in Eq. 2.107 is simplified, getting rid of the out-of plane to give [54]**:**

$$\hat{H}_D = \gamma_D\left[\sigma_x k_x - \sigma_y k_y\right]\frac{\partial^2}{\partial z^2}, \tag{2.110}$$

corresponding to a perfect two-dimensional electron gas (2D electron gas) or at the limit of a grazing incidence of electrons. Up to now, this reduced Dresselhaus form has been used to study the spin-dependent tunneling [11, 56, 216, 217]. Note that, in Eq. 2.110, the out-of-plane Dresselhaus component has been totally neglected. In Chapter 5, we will show that the out-of plane Dresselhaus component plays an important role in the Anomalous Tunnel Hall Effect (ATHE) [11, 12, 57] and is connected to a new type of chiral phenomena.

The quantized direction of ↑- and ↓-spins for various directions of the in-plane electron wavevectors $\mathbf{k}_\parallel$ in the crystal are shown in Fig. 2.17. If $\mathbf{k}_\parallel$ is directed along a cubic crystal axis ([100] or [010]) then the spins are parallel (or antiparallel) to $\mathbf{k}_\parallel$, while the spin directions are perpendicular to $\mathbf{k}_\parallel$ if the in-plane wavevector is directed along the $[1\bar{1}0]$ or [110] axes.

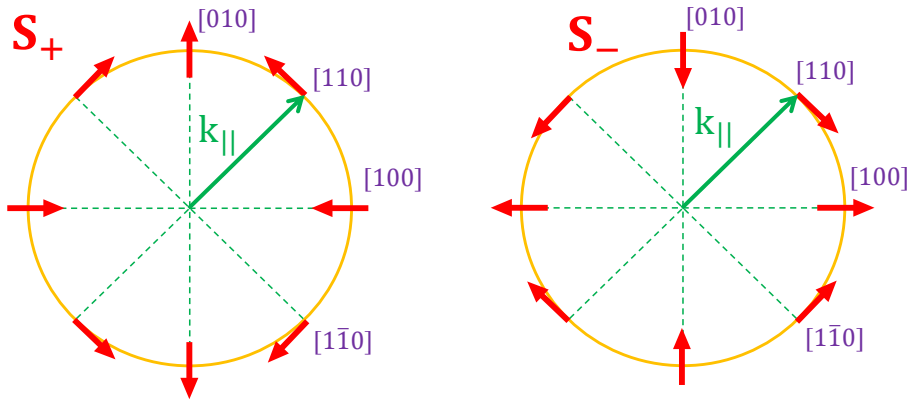

FIGURE 2.17: Quantized directions of ↑ and ↓ eigenstates as a function of the orientation of the in-plane electron wave vector $k_{||}$. Taken from Ref.[54].

Spin filtering effect without ferromagnetism [54]

The Dresselhaus interaction allows one to get a polarized spin current free of the application of external magnetic field by considering the case of spin-dependent tunneling transmission in the presence of a spin-orbit Dresselhaus field (Fig.2.17) localized within a "thin" tunnel barrier, (Fig. 2.18) [54].

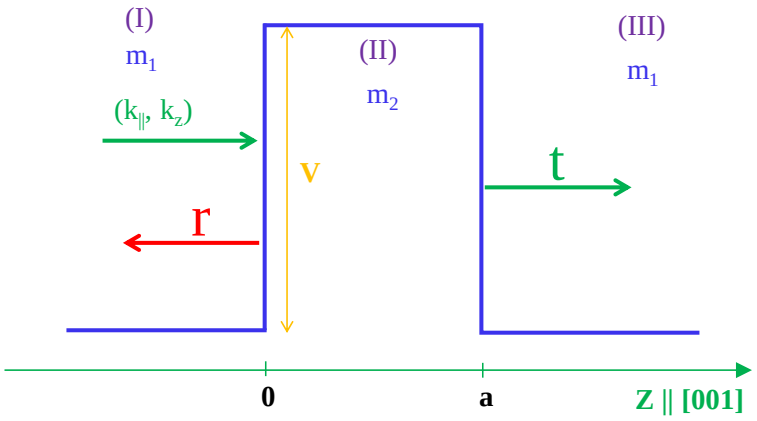

FIGURE 2.18: Sketch of a three-dimensional model of electron tunneling. Transmission of electrons with the wave vector $\boldsymbol{k} = (k_{||}, k_z)$ through the potential barrier V of width a grown along z. Taken from Ref.[54]

We present here the ideas of Perel'et al of spin-filtering effect. In 2003, Perel' et al. [54] studied the electronic transmission with an initial wavevector $\mathbf{k} = (\mathbf{k}_{\|}, k_z)$ through a rectangular barrier grown along the $z\|[001]$ direction. For the sake of simplicity, the authors assumed that the inversion symmetry is broken only inside the barrier. The eigenvectors of Eq. 2.110 read:

$$\chi_{\pm} = \frac{1}{\sqrt{2}}\begin{pmatrix} 1 \\ \mp e^{i\varphi} \end{pmatrix}, \tag{2.111}$$

where $\mathbf{k} = (k_x \cos\varphi, k_y \sin\varphi, k_z)$. This introduces a correction to the effective mass for ↑- and ↓- spins in the barrier according to

$$m_{\pm} = m_2 \left(1 \pm \frac{2\gamma_D k_{\|} m_2}{\hbar^2}\right)^{-1} \tag{2.112}$$

where m_2 is the electron effective mass in the barrier with no SOI included. The energy and in-plane wavevector are conserved upon electron tunneling. The electronic wave functions are,

$$\Psi_{\pm}(\mathbf{r}) = u_{\pm}(z)\exp(i\mathbf{k}_{\parallel}\rho), \tag{2.113}$$

where $\mathbf{k}_{\parallel} = \mathbf{k}_x + \mathbf{k}_y$, and $\rho = (\mathbf{x}, \mathbf{y})$. The functions $u_{\pm}(z)$ are solutions of the Schrödinger equations in each layer: left electrode, barrier, and right electrode according to:

$$\begin{aligned} u_{\pm}^{(I)}(z) &= \exp(ik_z z) + r_{\pm}\exp(ik_z z), & (2.114)\\ u_{\pm}^{(II)}(z) &= A_{\pm}\exp(-q_{\pm}z) + B_{\pm}\exp(q_{\pm}z), & (2.115)\\ u_{\pm}^{(III)}(z) &= t_{\pm}\exp(ik_z z), & (2.116) \end{aligned}$$

where $q_{\pm}$ are the wavevectors in the barrier for the spin $\uparrow$ and spin $\downarrow$ populations, respectively:

$$\begin{aligned} q_{\pm} &= \sqrt{\frac{2m_{\pm}V}{\hbar^2} - k_z^2\frac{m_{\pm}}{m_1} - k_{\parallel}^2\left(\frac{m_{\pm}}{m_1} - 1\right)}, & (2.117)\\ q_{\pm} &= \sqrt{\left(\frac{2m_2V}{\hbar^2} - k_z^2\frac{m_2}{m_1}\right)\left(1 \pm \frac{2\gamma_D k_{\shortparallel} m_2}{\hbar^2}\right)^{-1} - k_{\parallel}^2\left[\frac{m_2}{m_1}\left(1 \pm \frac{2\gamma_D k_{\shortparallel} m_2}{\hbar^2}\right)^{-1} - 1\right]}. & (2.118) \end{aligned}$$

In the limit where $\left(2\gamma k_{\parallel} m_2/\hbar^2\right) \ll 1$, we get:

$$\begin{aligned} q_{\pm} &\approx \sqrt{\left(\frac{2m_2V}{\hbar^2} - k_z^2\frac{m_2}{m_1}\right)\left(1 \pm \frac{2\gamma_D k_{\shortparallel} m_2}{\hbar^2}\right)^{-1} - k_{\parallel}^2\left(\frac{m_2}{m_1} - 1\right)\left(1 \pm \frac{2\gamma_D k_{\shortparallel} m_2}{\hbar^2}\right)^{-1}}, & (2.119)\\ q_{\pm} &\approx \sqrt{\left(\frac{2m_2V}{\hbar^2} - k_z^2\frac{m_2}{m_1}\right) - k_{\parallel}^2\left(\frac{m_2}{m_1} - 1\right)}\left(1 \pm \frac{2\gamma_D k_{\shortparallel} m_2}{\hbar^2}\right)^{-1/2} = q_0\left(1 \pm \frac{2\gamma_D k_{\shortparallel} m_2}{\hbar^2}\right)^{-1/2} & (2.120) \end{aligned}$$

where $q_0 = \sqrt{\left(\frac{2m_2V}{\hbar^2} - k_z^2\frac{m_2}{m_1}\right) - k_{\parallel}^2\left(\frac{m_2}{m_1} - 1\right)}$ is the wavevector in the barrier when the Dresselhaus term is neglected.

To anticipate the discussions on the matching conditions needed for the description of interface crossing, the BenDaniel Duke (BDD) [218] matching conditions are used here in the case of the CB: u and $(1/m)(\partial u/\partial z)$ are continuous at the interface. Note that the small spin-dependent renormalization of the effective mass induced by the Dresselhaus Hamiltonian can be neglected in the boundary conditions, since it produces only a small correction to the pre-exponential factor in the final expressions, thus leading to:

$$\begin{aligned} t_{\pm} &= -4i\frac{m_2}{m_1}\frac{k_z q_{\pm}}{(q_{\pm} - ik_z m_2/m_1)}\exp(-q_{\pm}a - ik_z a) & (2.121)\\ &\approx -4i\frac{m_2}{m_1}\frac{k_z q_0}{(q_0 - ik_z m_2/m_1)}\exp(-q_0 a - ik_z a)\exp\left(\pm\frac{\gamma_D k_{\shortparallel} m_2}{\hbar^2}\right)\\ &\approx t_0\exp\left(\pm\frac{\gamma_D k_{\shortparallel} m_2}{\hbar^2}\right), \end{aligned}$$

where

$$t_0 = -4i\frac{m_2}{m_1}\frac{k_z q_0}{(q_0 - ik_z m_2/m_1)^2}\exp(-q_0 a - ik_z a), \tag{2.122}$$

is the transmission amplitude when the SOI is neglected in the barrier. Equation. 2.121 presents the difference of transmission between ↑- and ↓- spin electrons. The spin polarization [54] is then:

$$P = \frac{|t_+|^2 - |t_-|^2}{|t_+|^2 + |t_-|^2} = \tanh\left(2\gamma_D \frac{m_2 k_{\shortparallel}}{\hbar^2} a q_0\right). \tag{2.123}$$

which clearly depends on the barrier thickness. Using a systematic expansion to the first order in γ, Nguyen et al. [183] considered that Dresselhaus terms do not re-normalize the effective masses of ↑- and ↓- spinors in the barrier but a renormalization of effective mass alters the wavevectors. In the limit of a small in-plane wavevector they recovered Eq. 2.123. From these results, it is possible to state that the in-plane Dresselhaus components play a very important role for spin filtering, whereas the out-of-plane component may be neglected in this particular case. In contrast, the latter one will make the specificity of the Anomalous Tunnel Hall effect (transmission asymmetry of opposite in-plane wavevectors) via a new type of chiral phenomena, that we will discuss in the next part. We now turn on to the case and description of the VB admitting also an effective Hamiltonian up to the second order of the perturbation (or higher).

2.6.2 The effective Hamiltonian in the valence band [29]

We now describe the effective model in the valence band that we need to describe spin-transport phenomena in (Ga,Mn)As based heterostructure. Similarly to the conduction band, the second order *Löwdin's* perturbation method in $\{\Gamma_7, \Gamma_8\}$ described by a 6×6 $\boldsymbol{k.p}$ Hamiltonian for VB in $|J, M\rangle = \{|3/2\rangle, |1/2\rangle, |-1/2\rangle, |-3/2\rangle, |7/2\rangle, |-7/2\rangle\}$ leads to the following Hamiltonian form [29, 53, 93, 185]

$$H_{VB} = \begin{array}{c} \begin{matrix} |3/2\rangle & |1/2\rangle & |-1/2\rangle & |-3/2\rangle & |7/2\rangle & |-7/2\rangle \end{matrix} \\ \begin{pmatrix} -\gamma_1 \check{k}^2 + \mathfrak{U} & \mathfrak{B} & \mathfrak{C} & 0 & \frac{1}{\sqrt{2}}\mathfrak{B}_\Delta & \sqrt{2}\mathfrak{C}_\Delta \\ cc & -\gamma_1 \check{k}^2 - \mathfrak{U} & 0 & \mathfrak{C} & -\sqrt{2}\mathfrak{U}_\Delta & -\sqrt{\frac{3}{2}}\mathfrak{B}_\Delta \\ cc & cc & -\gamma_1 \check{k}^2 - \mathfrak{U} & -\mathfrak{B} & -\sqrt{\frac{3}{2}}\mathfrak{B}^*_\Delta & \sqrt{2}\mathfrak{U}_\Delta \\ cc & cc & cc & -\gamma_1 \check{k}^2 + \mathfrak{U} & -\sqrt{2}\mathfrak{C}^*_\Delta & \frac{1}{\sqrt{2}}\mathfrak{B}^*_\Delta \\ cc & cc & cc & cc & -\Delta - \gamma_{\Delta 1}\check{k}^2 & 0 \\ cc & cc & cc & cc & cc & -\Delta - \gamma_{\Delta 1}\check{k}^2 \end{pmatrix} \end{array} \tag{2.124}$$

where the Luttinger parameters in the matrix 2.124 are introduced in Ref [29]. These Luttinger parameters in the VB possess no specific contribution arising from the lack of inversion center. It means that this effective Hamiltonian applies for both O_h and T_d symmetry groups as well. In this picture, the SOI in VB is introduced through the core spin-orbit parameter Δ. This particular shape of the 6×6 projected Hamiltonian was firstly proposed by Luttinger-Kohn from general arguments of invariant theory [219]. Note that one can also use the effective Hamiltonian for VB in the $|L, S\rangle = |X\uparrow\rangle, |Y\uparrow\rangle, |Z\uparrow\rangle, |X\downarrow\rangle, |Y\downarrow\rangle, |Z\downarrow\rangle$ basis set given by the transformation:

$$\begin{pmatrix} |3/2\rangle \\ |1/2\rangle \\ |-1/2\rangle \\ |-3/2\rangle \\ |7/2\rangle \\ |-7/2\rangle \end{pmatrix} = i \begin{bmatrix} -\frac{1}{\sqrt{2}} & -\frac{i}{\sqrt{2}} & 0 & 0 & 0 & 0 \\ 0 & 0 & \sqrt{\frac{2}{3}} & -\frac{1}{\sqrt{6}} & -\frac{i}{\sqrt{6}} & 0 \\ \frac{1}{\sqrt{6}} & -\frac{i}{\sqrt{6}} & 0 & 0 & 0 & \sqrt{\frac{2}{3}} \\ 0 & 0 & 0 & \frac{1}{\sqrt{2}} & -\frac{i}{\sqrt{2}} & 0 \\ 0 & 0 & \frac{1}{\sqrt{3}} & \sqrt{\frac{2}{3}} & i\sqrt{\frac{2}{3}} & 0 \\ \frac{1}{\sqrt{3}} & -\frac{i}{\sqrt{3}} & 0 & 0 & 0 & -\frac{1}{\sqrt{3}} \end{bmatrix} \begin{pmatrix} |X\uparrow\rangle \\ |Y\uparrow\rangle \\ |Z\uparrow\rangle \\ |X\downarrow\rangle \\ |Y\downarrow\rangle \\ |Z\downarrow\rangle \end{pmatrix} \tag{2.125}$$

Sometimes for convenience, we also use the transformation below:

$$\begin{pmatrix} |3/2\rangle \\ |1/2\rangle \\ |-1/2\rangle \\ |-3/2\rangle \\ |7/2\rangle \\ |-7/2\rangle \end{pmatrix} = i \begin{bmatrix} -\frac{1}{\sqrt{2}} & 0 & -\frac{i}{\sqrt{2}} & 0 & 0 & 0 \\ 0 & -\frac{1}{\sqrt{6}} & 0 & -\frac{i}{\sqrt{6}} & \sqrt{\frac{2}{3}} & 0 \\ \frac{1}{\sqrt{6}} & 0 & -\frac{i}{\sqrt{6}} & 0 & 0 & \sqrt{\frac{2}{3}} \\ 0 & \frac{1}{\sqrt{2}} & 0 & -\frac{i}{\sqrt{2}} & 0 & 0 \\ 0 & \sqrt{\frac{2}{3}} & 0 & i\sqrt{\frac{2}{3}} & \frac{1}{\sqrt{3}} & 0 \\ \frac{1}{\sqrt{3}} & 0 & -\frac{i}{\sqrt{3}} & 0 & 0 & -\frac{1}{\sqrt{3}} \end{bmatrix} \begin{pmatrix} |X\uparrow\rangle \\ |X\downarrow\rangle \\ |Y\uparrow\rangle \\ |Y\downarrow\rangle \\ |Z\uparrow\rangle \\ |Z\downarrow\rangle \end{pmatrix} \tag{2.126}$$

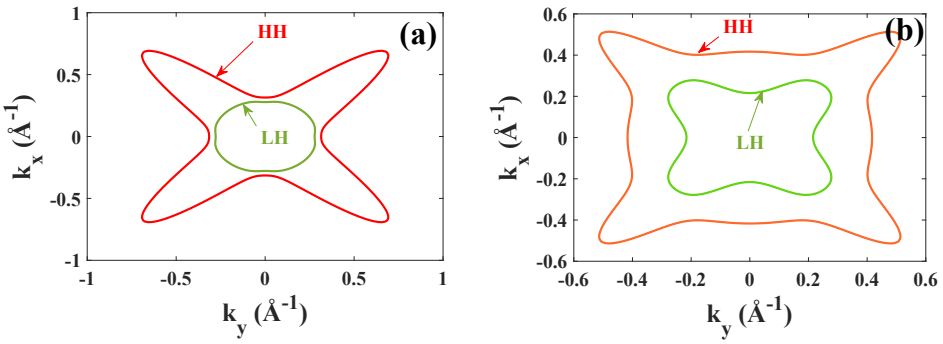

FIGURE 2.19: Constant energy surface of Heavy Holes (HH) and Light Holes (LH) in the GaAs band structure with $E_f = -0.1\ eV$ and $E_f = -1\ eV$, Figure (a) and (b) respectively.

One observes that, within the small k regime, the matrix 2.124 may be divided into two matrices comprising an upper left 4×4 matrix and lower right 2×2 matrix [53, 220] since the blocks of 2×4 give rise to an error of the order of $\frac{k^4}{\Delta}$. The 2×2 matrix gives the energy of the doubly degenerate $J = \frac{1}{2}$ (Γ_7 band) as [53]

$$E_{so} = \frac{\hbar^2 k^2}{2m} + \frac{1}{3}(2M' + L')k^2 - \Delta_0 = -\Delta_0 + \frac{\hbar^2 k^2}{2m}\left[1 - \frac{2}{3}\left(\frac{P^2}{m(E_0 + \Delta_0)} + \frac{2Q^2}{m(E_0' + \Delta_0)}\right)\right] \tag{2.127}$$

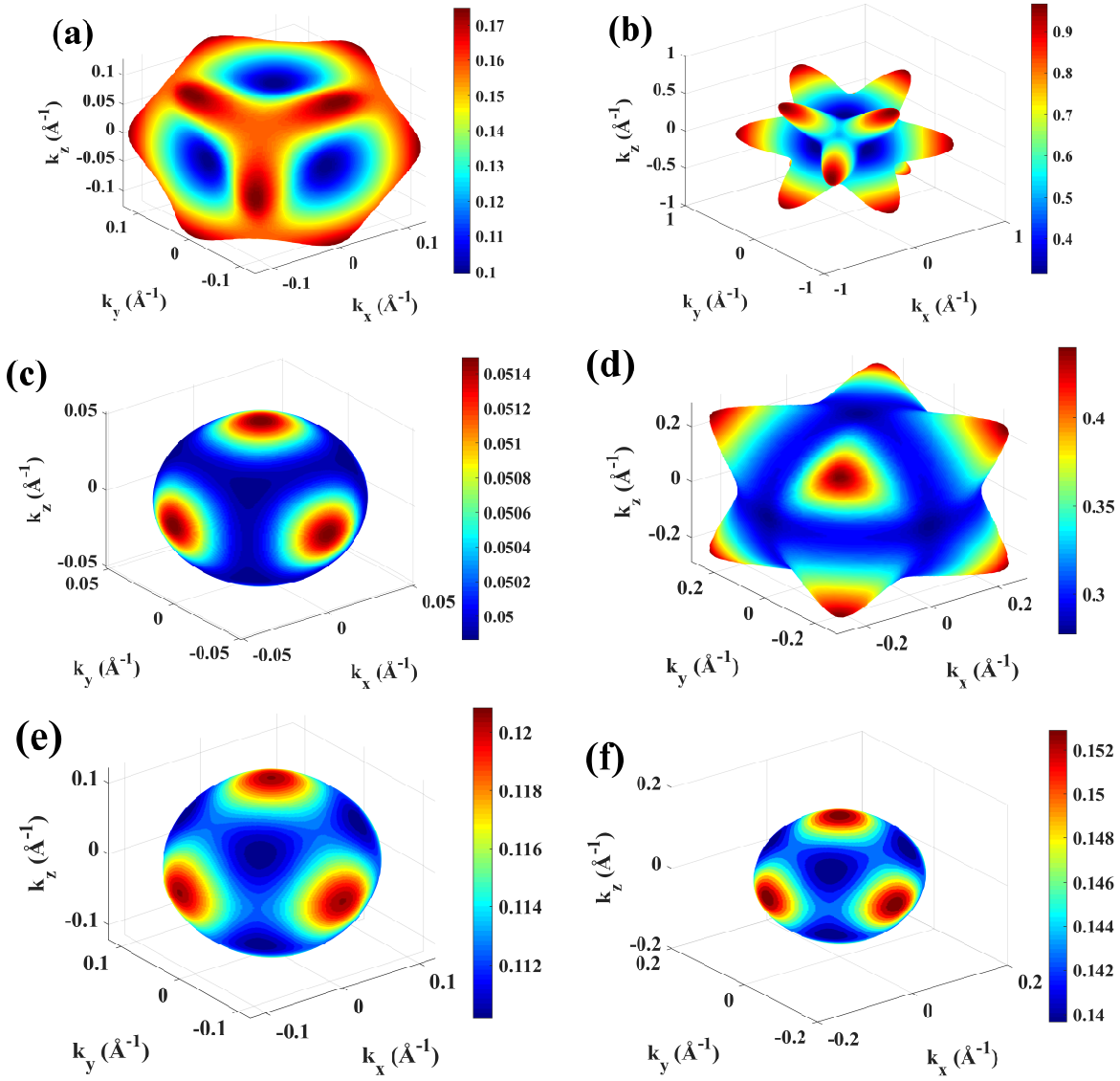

FIGURE 2.20: Fermi surface of heavy hole (a,c), light hole (b,d) and SO band (e,f) with $E_f = -0.1eV$ (a,b), $E_f = -1eV$ (b,d,e) and $E_f = -1.5eV$ (f).

TABLE 2.5: Valence band parameters A and B in units of $\frac{\hbar^2}{2m}$. Taken from [53].

	A	B	$\|C\|^2$	$\Delta_0(eV)$	m_{HH}/m_0	m_{LH}/m_0
Si	-4.28	-0.68	24	0.044	0.50	0.15
Ge	-13.38	-8.5	173	0.295	0.43	0.041
GaP	-4.05	-0.98	16	0.08	0.51	0.16
GaAs	-6.9	-4.4	43	0.341	0.73	0.08
GaSb	-13.3	-8.8	230	0.75	0.98	0.04
InP	-5.15	-1.9	21	0.11	0.44	0.11
InAs	-20.04	-16.6	167	0.38	0.4	0.026
InSb	-36.41	-32.5	43	0.81	0.48	0.013

Thus, the constant energy surface for the $j = \frac{1}{2}$ split-off valence band is spherical and the band dispersion parabolic. The 4×4 matrix gives the solution for energy:

$$E_{\pm} = Ak^2 \pm \left[B^2k^4 + C^2\left(k_x^2k_y^2 + k_y^2k_z^2 + k_z^2k_x^2\right)\right] \tag{2.128}$$

The Eq. 2.128 was first derived by Dresselhaus et al. [89]. Here, the constants A, B and C in 2.128 are related to the electron momentum matrix elements and energy gaps which are given by [53]

$$\begin{aligned}
\frac{2m}{\hbar^2}A &= 1 - \frac{2}{3}\left[\frac{P^2}{mE_0} + \frac{2Q^2}{mE_0'}\right] \\
\frac{2m}{\hbar^2}B &= \frac{2}{3}\left[-\frac{P^2}{mE_0} + \frac{Q^2}{mE_0'}\right] \\
\left(\frac{2m}{\hbar^2}C\right)^2 &= \frac{16P^2Q^2}{3mE_0mE_0'}
\end{aligned} \tag{2.129}$$

For convenience, one may define the constants A, B and C in the units of $\hbar^2/2m$. In the table 2.5, we have listed the values of the constants A, B and C for several semiconductors taken from [53].

Equation 2.128 gives the dispersion of the Γ_8 bands near the zone center Γ and valids only for energies small compared to the spin-orbit splitting. Moreover, from Eq.2.129 both A and B are negative since the leading term in Eq. 2.129 is $\frac{2P^2}{3mE_0} \gg 1$. Consequently, the effective masses of those bands are negative. Since the valence band represented by E_+ in Eq 2.128 is characterized by a smaller dispersion and hence a larger mass, it is generally referred to as the heavy hole band, while the band represented by E_- in Eq. 2.128 is known as the light hole band [29, 53]. We now denote these two hole bands energies as E_{HH} and E_{LH} given by:

$$E_{HH} = -Ak^2 - \left[B^2k^4 + C^2\left(k_x^2k_y^2 + k_y^2k_z^2 + k_z^2k_x^2\right)\right] \tag{2.130}$$

$$E_{LH} = -Ak^2 + \left[B^2k^4 + C^2\left(k_x^2k_y^2 + k_y^2k_z^2 + k_z^2k_x^2\right)\right] \tag{2.131}$$

The constant energy surfaces of heavy hole and light hole for GaAs calculated by $\boldsymbol{k.p}$ method are shown in Fig 2.19, where k_x, k_y and k_z are along [100], [010] and [001] directions, respectively. The shape of these constant energy surfaces are referred to as warped spheres [53]. This warping occurs along the [100] and [111] directions because of the cubic symmetry of the zinc-blende crystal. One may argue that these warped spheres are the only possible shapes for constant energy surfaces described by a second-order equation in cubic crystals. The hole band dispersion along the [100] and [111] directions are parabolic, however, the

hole effective masses are different along the two directions. For the [100] direction, one has:

$$\frac{1}{m_{HH}} = \frac{2}{\hbar^2}(-A+B) \tag{2.132}$$

$$\frac{1}{m_{LH}} = \frac{2}{\hbar^2}(-A-B) \tag{2.133}$$

whereas along the [111] direction, one has:

$$\frac{1}{m_{HH}} = \frac{2}{\hbar^2}\left[-A+B\left(1+\frac{|C|^2}{3B^2}\right)^{\frac{1}{2}}\right] \tag{2.134}$$

$$\frac{1}{m_{LH}} = \frac{2}{\hbar^2}\left[-A-B\left(1+\frac{|C|^2}{3B^2}\right)^{\frac{1}{2}}\right] \tag{2.135}$$

One observes that the warping of the valence bands is caused by the term $|C|^2$, which is proportional to Q^2. If the term B^2 is much larger than $|C|^2/3$, then the warping can be neglected and one obtains $m_{LH} \approx 3m_c^*/2$. Note that Q^2 is crucial to m_{HH}, because if one puts $Q^2 = 0$ then we obtain the incorrect result $m_{HH} = -m_0$. For simplicity, one may assume that the valence band masses are isotropic [53]. In such cases, average heavy and light hole masses m^*_{HH} and m^*_{LH} can be obtained by averaging 2.133 and 2.135 over all possible directions of $\boldsymbol{k}$ to obtain:

$$\frac{1}{m^*_{HH}} = \frac{1}{\hbar^2}\left[-2A+2B\left(1+\frac{2|C|^2}{15B^2}\right)\right] \tag{2.136}$$

$$\frac{1}{m^*_{LH}} = \frac{1}{\hbar^2}\left[-2A-2B\left(1+\frac{2|C|^2}{15B^2}\right)\right] \tag{2.137}$$

The constant energy surfaces for the valence bands as described by Eq.2.128 possess inversion symmetry: $E(\boldsymbol{k}) = E(-\boldsymbol{k})$ (see Figure 2.20), even though the crystal may not posses such symmetry. This is a consequence of time reversal symmetry: two Bloch waves corresponding to $\boldsymbol{k}$ and $-\boldsymbol{k}$ wavevector, admit the same energy [29]. Furthermore, in the four-band approximation, only the heavy holes and light holes are taken into account while the spin orbit-off bands are neglected. This four-band model has been proved to be a very good approximation for not only the optical matrix elements but also the energy levels in GaAs/AlGaAs quantum well structure [221]. This because in GaAs/AlGaAs quantum well, the spin-orbit splitting energy Δ_0 is larger than the quantum confinement energy of holes. However, the effect of SO bands should be incorporated for rigorous calculations of the valence band structure. This effect becomes significant in strained quantum wells such as InGaAs/GaAs quantum well [221].

Finally, one has to point out that there is an alternative approach to describe the valence band dispersion for diamond and zinc-blende semiconductors which was proposed by Luttinger. Using the group theory, Luttinger derived an effective $\boldsymbol{k.p}$ Hamiltonian appropriate for the Γ_4 valence bands:

$$H_L = \frac{\hbar^2}{2m}\left[\left(\gamma_1+\frac{5}{2}\gamma_2\right)\boldsymbol{\nabla}^2 - 2\gamma_3(\boldsymbol{\nabla}.\boldsymbol{J})^2 + 2(\gamma_3-\gamma_2)\left(\nabla_x^2 J_x^2 + c.p\right)\right] \tag{2.138}$$

where γ_1, γ_2 and γ_3 are the well known Kohn-Luttinger parameters; $\boldsymbol{J} = (J_x, J_y, J_z)$ is an operator whose effects on the Γ_8 valence bands are identical to those of the pseudo-angular momentum operator on the $J = 3/2$ atomic states, and c.p stands for cyclic permutations. The first two terms in 2.138 possess spherical symmetry while the last one represents the effect of the lower, cubic symmetry. One may observe that the warping of the valence band is directly proportional to the difference between γ_2 and γ_3. The Kohn-Luttinger parameters are related to the coefficients A, B and C in Eq.2.128 by:

$$\frac{\hbar^2}{2m}\gamma_1 = -A \tag{2.139}$$

$$\frac{\hbar^2}{2m}\gamma_2 = -B/2 \tag{2.140}$$

$$\frac{\hbar^2}{2m}\gamma_3 = \left[\frac{B^2}{4} + \frac{C^2}{12}\right]^{1/2} \tag{2.141}$$

2.7 Exchange interactions and strain field.

We have already described the p-d exchange interactions in chap 1. In the following section, we present here the mathematical and physical description of the interactions of p-d exchange which is compatible with **k.p** platform technique largely used in this work.

2.7.1 Exchange interactions

The $p-d$ exchange interactions appearing in the VB are introduced through the Hamiltonian matrix as proposed by Dietl *et al*. [87] as well as in [222] in different approaches:

$$H_{exc} = 3B_G \boldsymbol{s}.\boldsymbol{m} \tag{2.142}$$

In this work, we expand the model proposed by Dietl in Ref.[87] for electrons in the CB with different values of B_G like classically considered. Using the Bloch functions basic set based on $|j,m\rangle$ states, one may write the exchange Hamiltonian in $n-band$ $\boldsymbol{k.p}$ model as:

$$H_{exc} = \begin{bmatrix} H_{exc}^{CB} & 0 \\ 0 & H_{exc}^{VB} \end{bmatrix} \tag{2.143}$$

where H_{exc}^{CB} is the block exchange Hamiltonian in the CB and H_{exc}^{VB} is the block exchange Hamiltonian in VB.

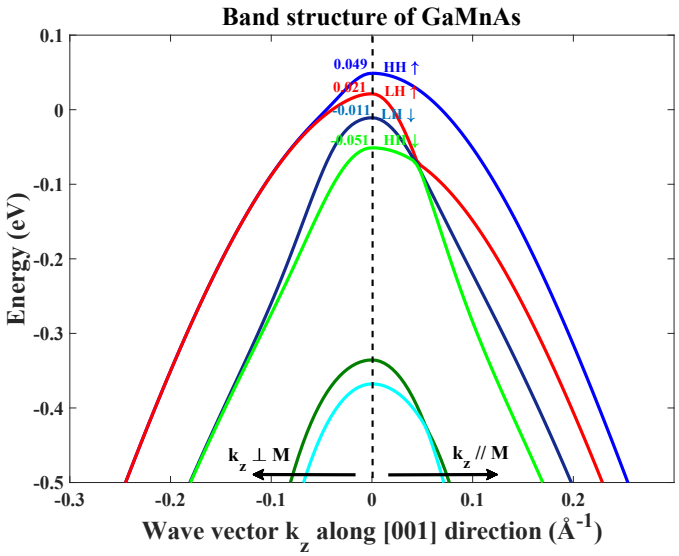

FIGURE 2.21: Valence band structure of GaMnAs along [001] direction via 30 – *band* $\boldsymbol{k.p}$ model with exchange energy equal 0.05 eV for two cases of magnetization direction: perpendicular and parallel to the growth direction.

For instance, if we write the exchange Hamiltonian in the $14-band\ \boldsymbol{k.p}$ model, then:

$$H_{exc}^{CB} = \begin{bmatrix} H_{exc}^{\Gamma_{5C}} & 0 \\ 0 & H_{exc}^{\Gamma_1} \end{bmatrix} \tag{2.144}$$

and

$$H_{exc}^{VB} = H_{exc}^{\Gamma_5} \tag{2.145}$$

where $H_{exc}^{\Gamma_{5C}}$ is the block exchange Hamiltonian in the Γ_{5C} subspace, $H_{exc}^{\Gamma_1}$ is the block exchange Hamiltonian in the Γ_1 subspace, and $H_{exc}^{\Gamma_5}$ is the block exchange Hamiltonian in the Γ_5 space. If we write:

$$\boldsymbol{sm} = (s_- m_+ + s_+ m_-) + s_z m_z \tag{2.146}$$

after having defined $s_\pm = \frac{(s_x \pm i s_y)}{2}$ and $m_\pm = (m_x \pm i m_y)$ then the exchange Hamiltonian in Γ_5 acting on the spin degree of freedom can read:

$$H_{exc}^{\Gamma_5} = B_G^{\Gamma_5} \begin{array}{c} \begin{matrix} |3/2\rangle & |1/2\rangle & |-1/2\rangle & |-3/2\rangle & |7/2\rangle & |-7/2\rangle \end{matrix} \\ \begin{pmatrix} 3m_z & \sqrt{3}m_- & 0 & 0 & -\sqrt{6}m_- & 0 \\ \sqrt{3}m_+ & m_z & 2m_- & 0 & 2\sqrt{2}m_z & -\sqrt{2}m_- \\ 0 & 2m_+ & -m_z & \sqrt{3}m_- & \sqrt{2}m_+ & 2\sqrt{2}m_z \\ 0 & 0 & \sqrt{3}m_+ & -3m_z & 0 & \sqrt{6}m_+ \\ -\sqrt{(6)}m_+ & 2\sqrt{2}m_z & \sqrt{2}m_- & 0 & -m_z & -m_- \\ 0 & -\sqrt{2}m_+ & 2\sqrt{2}m_z & \sqrt{6}m_- & -m_+ & m_z \end{pmatrix} \end{array} \tag{2.147}$$

whereas the exchange Hamiltonian in Γ_1 is

$$H_{exc}^{\Gamma_1} = B_G^{\Gamma_1} \begin{array}{c} \begin{matrix} |S\uparrow\rangle & |S\downarrow\rangle \end{matrix} \\ \begin{pmatrix} 3m_z & 3m_- \\ 3m_+ & -3m_z \end{pmatrix} \end{array} = 3B_G^{\Gamma_1} \begin{array}{c} \begin{matrix} |S\uparrow\rangle & |S\downarrow\rangle \end{matrix} \\ \begin{pmatrix} m_z & m_- \\ m_+ & -m_z \end{pmatrix} \end{array} \tag{2.148}$$

The exchange Hamiltonian in the second CB is similar to Eq.2.147 but we replace the coefficient $B_G^{\Gamma_5}$ by $B_G^{\Gamma_{5C}}$. Furthermore, one can easily extend this model in the same way for $30-band$ or $40-band\ \boldsymbol{k.p}$ Hamiltonian model. Figure 2.21 displays the band structure of GaMnAs calculated via 30-band $\boldsymbol{kp}$ giving the same results in comparison to via 6-band model [223].

2.7.2 Description of the strain field [224]

Today's semiconductor industry is facing lots of critical challenges such as the high gate leakage current for very thin gate dielectrics, or the high power dissipation for small transistors, etc. Therefore, an innovative techniques like strain engineering could be used to solve or circumvent the arising problems. The influence of strain on the intrinsic mobility of Si was first investigated in the early 1950 [225] and demonstrated that n-channel MOSFETs on a strained Si substrate, exhibit a 70% higher effective mobility than those on unstrained substrates, in 1992 by Welser et al.[226]. Since then, semiconductor industry has adapted several different technologies to introduce strain in the Si channel of MOSFETs. In the context of spintronics and spinorbitronics, using strain to control spin-polarized current has attracted much attention. Recently, the possibility of using strain to control electron-spin precession in zinc-blende structure semiconductors has been demonstrated [107, 227]. The spatial part of the conduction electron wavefunction is modified in the presence of strain, which affects the electron spin degrees of freedom due to spin-orbit coupling [228–230].

Theoretically, the effect of strain in semiconductor can be easily included in framework of **k.p** method and this section is devoted to do that. In particular, we now present the approach to treat the effect of an

homogeneous strain within the $\boldsymbol{k.p}$ framework [224]. It is worth to note that one may not treat the strain effect as a perturbation because it is not really small and besides, strain changes the periodicity of the crystal [176]. In the uniformly deformed crystal, the potential is still periodic except that the function $V(\boldsymbol{r})$ is a different potential from the undeformed potential $V_0(\boldsymbol{r})$ and the difference $V_0(\boldsymbol{r}) - V(\boldsymbol{r})$ can be of the order of $V_0(\boldsymbol{r})$ [29, 176, 179, 224]. On the other hand, in perturbation theory, the wavefunction of the perturbed system is expressed as a superposition of the wavefunctions of the unperturbed system. These two sets of wavefunctions satisfy the same boundary conditions defined by the lattice periodicity. However, strain would change the lattice periodicity, and, consequently, changes the periods of the lattice periodic functions $\psi_{\boldsymbol{k}}(\boldsymbol{r})$ in Bloch waves. Therefore, to avoid these difficulties, Pikus and Bir [176] have used a coordinate transformation to make the deformed and undeformed crystals to have the same boundary conditions. Under strain represented by the strain tensor $\bar{\bar{\epsilon}}$, the coordinates of the deformed and undeformed crystal are linked by the transformation [29, 176, 179, 224]

$$r_i^{'} = r_i + \sum_j \epsilon_{ij} r_j \tag{2.149}$$

where $r_i, r_j = x, y, z$. In the vector form, one has:

$$\boldsymbol{r}^{'} = (1 + \bar{\bar{\epsilon}})\boldsymbol{r} \tag{2.150}$$

and the inverse transformation is given by:

$$\boldsymbol{r} = (1 - \bar{\bar{\epsilon}})\boldsymbol{r}^{'} \tag{2.151}$$

Correspondingly, the transformation for the reciprocal vectors is given by:

$$\boldsymbol{k} = (1 + \bar{\bar{\epsilon}})\boldsymbol{k}^{'} \tag{2.152}$$

Using the above transformation, $V(\boldsymbol{r'})$ can be expressed as a function of $\boldsymbol{r}$ with the same boundary conditions as those of $V_0(\boldsymbol{r})$:

$$V(\boldsymbol{r'}) = V[(1 + \bar{\bar{\epsilon}})\boldsymbol{r}] = V_0(\boldsymbol{r}) + \sum_{i,j} V_{ij}\epsilon_{ij} \tag{2.153}$$

where

$$V_{ij} = \lim_{\epsilon \to 0} \frac{V[(1 + \bar{\bar{\epsilon}})\boldsymbol{r}] - V_0(\boldsymbol{r})}{\epsilon_{ij}} = \frac{\partial V}{\partial \epsilon_{ij}} \tag{2.154}$$

that is related to deformation potentials. The crystal potential $V(\boldsymbol{r})$ is assumed to be the sum of the potentials of the individual ions, and the deformation of the lattice causes only a displacement of lattice site $\boldsymbol{R_n}$, without distorting their potentials. Thus,

$$\begin{aligned} V[(1 + \bar{\bar{\epsilon}}).\boldsymbol{r}] - V_0(\boldsymbol{r}) &= \sum_n V_a[(1 + \bar{\bar{\epsilon}})(\boldsymbol{r} - \boldsymbol{R_n})] - V_a(\boldsymbol{r} - \boldsymbol{R_n}) \\ &= \sum_n \sum_{i,j} \frac{\partial V_a(\boldsymbol{r} - \boldsymbol{R_n})}{\partial r_i} \epsilon_{ij} (\boldsymbol{r} - \boldsymbol{R_n})_j \end{aligned} \tag{2.155}$$

to give:

$$V_{ij} = \frac{1}{2} \sum_n \left[\frac{\partial V_a(\boldsymbol{r} - \boldsymbol{R_n})}{\partial r_i} (\boldsymbol{r} - \boldsymbol{R_n}) + \frac{\partial V_a(\boldsymbol{r} - \boldsymbol{R_n})}{\partial r_j} (\boldsymbol{r} - \boldsymbol{R_n}) \right] \tag{2.156}$$

here $V_a(\boldsymbol{r} - \boldsymbol{R_n})$ is the atomic potential for an ion located at $\boldsymbol{R_n}$. It is appropriate to assume that $V_a(\boldsymbol{r})$ possesses a spherical symmetry, and thus the derivative of it with respect to r_i, is an odd function of r_i.

Since

$$\frac{\partial}{\partial r_i^{'}} = \sum_j \frac{\partial r_j}{\partial r_i^{'}} \frac{\partial}{\partial r_j} = \frac{\partial}{\partial r_i} - \sum_j \epsilon_{ij} \frac{\partial}{\partial r_j} \tag{2.157}$$

we have:

$$\boldsymbol{p}^{'} = \boldsymbol{p}(1 - \bar{\bar{\epsilon}}) \tag{2.158}$$

and

$$p^{'2} = p^2 - 2 \sum_{ij} p_i \epsilon_{ij} p_j \tag{2.159}$$

We now consider the transformation of the *Schrödinger* equation 2.29 in the form

$$\left[\frac{P^2}{2m_0} + V(\boldsymbol{r}) + \frac{\hbar}{2c^2 m_e^2} (\nabla V(\boldsymbol{r}) \times \boldsymbol{p}) . \boldsymbol{S} \right] \Psi_{m,\boldsymbol{k}}(\boldsymbol{r}) = E \Psi_{m,\boldsymbol{k}}(\boldsymbol{r}) \tag{2.160}$$

under the strain.

In the new coordinate system, we have:

$$\left[\frac{P^{'2}}{2m_0} + V(\boldsymbol{r'}) + \frac{\hbar}{2c^2 m_e^2} \left(\nabla^{'} V(\boldsymbol{r'}) \times \boldsymbol{p'} \right) . \boldsymbol{S} \right] \Psi_{m,\boldsymbol{k}}(\boldsymbol{r'}) = E \Psi_{m,\boldsymbol{k}}(\boldsymbol{r'}) \tag{2.161}$$

The goal is to re-express Eq. 2.161 in terms of unstrained coordinates and new terms linear in the strain tensor by using Bloch function basic set in the new coordinate system as:

$$\Psi_{m,\boldsymbol{k}}(\boldsymbol{r'}) = \sum_n C_{mn} \Phi_{n,\boldsymbol{k}}(\boldsymbol{r'}) \tag{2.162}$$

with

$$\Phi_{n,\boldsymbol{k}}(\boldsymbol{r'}) = e^{i\boldsymbol{k}.\boldsymbol{r}^{'}} \psi_{n\boldsymbol{k}}(\boldsymbol{r'}) \tag{2.163}$$

Then one gets:

$$\begin{aligned} &\left[\frac{P^{'2}}{2m_0} + V(\boldsymbol{r'}) + \frac{\hbar}{4m_0^2 c^2} \left(\boldsymbol{\sigma} \times \boldsymbol{\nabla}^{'} V(\boldsymbol{r'}) \right) . \boldsymbol{p'} + \frac{\hbar}{m_0} \boldsymbol{k} . \left(\boldsymbol{p'} + \frac{\hbar}{4m_0 c^2} \left[\boldsymbol{\sigma} \times \boldsymbol{\nabla}^{'} V(\boldsymbol{r'}) \right] \right) \right] \psi_{n\boldsymbol{k}}(\boldsymbol{r'}) \\ &= \left[E_n(\boldsymbol{k}) - \frac{\hbar^2 k^2}{2m_0^2} \right] \psi_{n\boldsymbol{k}}(\boldsymbol{r'}) \end{aligned} \tag{2.164}$$

As we argued previously, one may neglect the term $\frac{\hbar^2}{4m_0^2 c^2 \boldsymbol{k}} \left(\boldsymbol{\sigma} \times \boldsymbol{\nabla}^{'} V(\boldsymbol{r'}) \right)$ in comparison with $\frac{\hbar}{4m_0^2 c^2} \left(\boldsymbol{\sigma} \times \boldsymbol{\nabla}^{'} V(\boldsymbol{r'}) \right) . \boldsymbol{p'}$; moreover, using Eq. 2.153, Eq. 2.158 and Eq. 2.159, after doing some calculations and neglecting spin-orbit effects in the strain energy for sake of simplicity we can re-write Eq. 2.164 as:

$$\left[H_0 + \frac{\hbar}{m_0} \boldsymbol{k}.\boldsymbol{p} + \frac{\hbar^2 k^2}{2m_0} + \frac{\hbar}{4m_0^2 c^2} (\nabla V \times \boldsymbol{p}) \boldsymbol{\sigma} + H_\epsilon + H_{\epsilon k} \right] \psi_{n\boldsymbol{k}}(\boldsymbol{r'}) = E_n(\boldsymbol{k}) \psi_{n\boldsymbol{k}}(\boldsymbol{r'}) \tag{2.165}$$

where

$$H_0 = \frac{p^2}{2m_0} + V(\boldsymbol{r}) \tag{2.166}$$

$$H_\epsilon = \sum_{ij} \left(-\frac{1}{m_0} p_i p_j + V_{ij} \right) \epsilon_{ij} \tag{2.167}$$

$$H_{\epsilon k} = -\frac{2\hbar}{m_0}\sum_{ij} k_i \epsilon_{ij} p_j \tag{2.168}$$

The term $H_{\epsilon k} = -\frac{2\hbar}{m_0}\sum_{ij} k_i\epsilon_{ij}p_j$ in Eq. 2.165 accounts for the interaction between the strain and the momentum of the carriers, whereas the deformation potential operator $H_\epsilon = \sum_{ij}\left(-\frac{1}{m_0}p_i p_j + V_{ij}\right)\epsilon_{ij}$ describes the change in the potential and the kinetic energy of carriers due to the strain itself [29, 176, 179]. In this work, although we did not consider the effect of strain field but one may easily include the strain field in our 30 or 40 multiband $\boldsymbol{k.p}$ platform and we plan to do it in the short future.

2.8 Density of states and Fermi energy

In the following, we are going to give some insights into important definitions and notions of the electronic band structure and correlated physical parameters that we use throughout the manuscript, the density of sates and Fermi level.

2.8.1 Density of states

Together with the shape of constant energy surfaces shown in Fig.2.20, the density of states is often an important quantity entering a number of physical properties. The general definition of the density of states is:

$$\mathcal{D}(E) = \frac{1}{V}\sum_{n,\boldsymbol{k},\sigma}\delta\left(E - E_{n\boldsymbol{k}\sigma}\right) \tag{2.169}$$

where V is the volume of the crystal, n is the band index, $\boldsymbol{k}$ is the wave vectors and σ is the spin quantum number. The quantity $\mathcal{D}(E)dE$ describes the number of quantum states in the energy interval $[E, E+dE]$ normalized to the volume. The functional form of the density of states depends only on the dispersion relation $E_{n\boldsymbol{k}\sigma}$.

Integrating the density of states over energy up to a maximum energy bound results in the total number of states (per unit volume):

$$\int_{-\infty}^{E} dE'\mathcal{D}(E') = \frac{1}{V}\int_{-\infty}^{E} dE' \sum_{n,\boldsymbol{k},\sigma}\delta\left(E - E_{n\boldsymbol{k}\sigma}\right) = \frac{1}{V}\sum_{n,\boldsymbol{k}\sigma||E_{n\boldsymbol{k}\sigma}<E} 1 = \mathcal{N}(E) \tag{2.170}$$

correspondingly,

$$\mathcal{D}(E) = \frac{d\mathcal{N}(E)}{dE} \tag{2.171}$$

This relation is frequently used for analytical calculations of the density of states when the dispersion relation is well known.

Otherwise, Eq. 2.169 can be solved numerically by the procedure depicted in Fig. 2.22: dividing the k-space and energy, at each $\boldsymbol{k}$, one can obtain all possible values of energy E_n then counts the number of E_n between $[E, E+\delta E]$.

2.8.2 Fermi level

The electron concentration n_c in thermal equilibrium is expressed as:

$$n_c = \int_0^{\infty} \mathcal{D}(E) f(E) dE \tag{2.172}$$

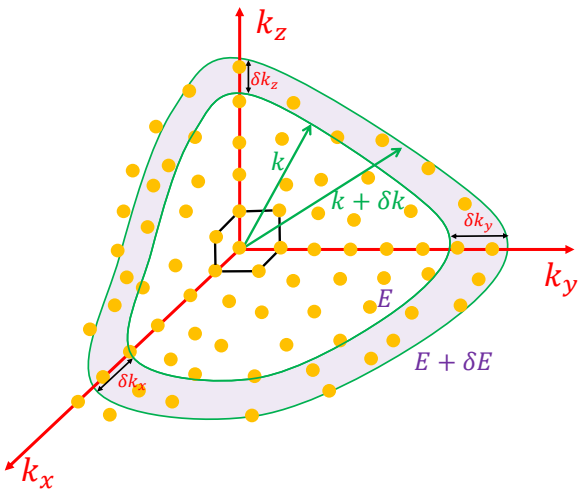

FIGURE 2.22: Scheme of construction in k-space to calculate the density of states in three dimensions. The shells have radii k and $k + \delta k$ corresponding to energies E and $E + \delta E$.

where $f(E)$ is the Fermi-Dirac distribution under thermal equilibrium (in general, $f(E)$ is the temperature dependent occupation probability under thermal nonequilibrium when one considers the electron concentration under thermal nonequilibrium) which becomes unity at absolute zero when E is less than E_F and zero when E is greater than E_F:

$$f(E) = \frac{1}{e^{\frac{E-E_F}{k_B T}} + 1} \tag{2.173}$$

The Fermi-Dirac distribution implies that at absolute zero (ground state of a system), the largest Fermion states (electron, holes, etc.) are filled up to an energy which is called the Fermi energy. Here we specifically define the Fermi energy at absolute zero. Finally, Figure 2.23 displays the DOS of GaAs and the Fermi level as function of carrier concentration in this semiconductor. These calculations were done in framework of 30-band $\boldsymbol{k.p}$ model showing good agreement with DFT calculation in Ref [46].

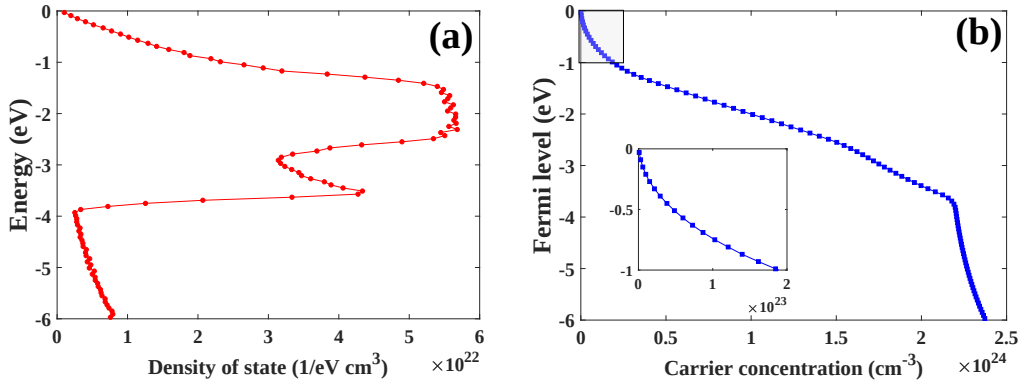

FIGURE 2.23: The density of states (DOS) and Fermi level vs carrier concentration calculated for GaAs in framework of 30-band $\boldsymbol{k.p}$ method.

CHAPTER 3

Modeling of spin-polarized transport within semiconductor heterostructures in a k.p multiband picture

Contents

In this chapter and following subsections, we consider the quantum matching conditions fulfilled by the electronic wavefunctions and electronic current at the various interfaces within multilayer structures. The set of matching conditions arises from the resolution of the Schrödinger equation within each layer with correct boundary conditions depending on the particular interface properties and related symmetries such as the $T_d \rightarrow C_{2v}$ reduction at the scale of some unit cells [44]. The physical issues related to wavefunction and electronic current matching are of a primary importance, because the issue of interface crossing for carriers (electrons or holes) is encountered for the correct description of the quantum states of materials; *e. g.* to describe correctly optical properties of optically active regions (or quantum wells) as well as spin-resolved Boltzmann diffusion equations for both in-plane and out-of-plane diffusion transport [231–234]. More generally, the particular matching conditions are to be generalized in order to take into account the local spin-orbit field starting from a simple 2×2 spinor vision towards a multiband approach involving the orbital degree of freedom. The reason is that the interface crossing (or scattering) derives from a pure quantum-mechanical process where spin-polarized carriers mainly behave more like waves than particles. These observations partly explain the choice of dedicating a full chapter to the matching conditions.

For the case of semiconducting heterostructures largely developed in the present manuscript, we have chosen to consider the standard multiband matching conditions possibly involving *extrinsic SO surface potentials* although, in the particular case of T_d compounds, interfaces break the bulk symmetry group into the C_{2v} symmetry responsible for the mixing between heavy holes and light holes. These particular matching conditions for the C_{2v} symmetry have been proposed at the IOFFE institute in 1996 [30] in a first 4-band and 6-band approach before their generalization to a 14-band treatment very recently [31]. These particular matching conditions have been implemented in our 14-, 30- and 40-band ***k.p*** codes without high complexity. After having given a set of consistent matching conditions for quantum wavefunctions and current waves at each interface, one may easily describe the properties of an electron tunneling through multilayered structures such as resonant tunneling, bound states and quasi bound states in quantum well structures via transfer or scattering matrix approach. Besides, the well known Landauer formalism gives the relation between the electrical conductance and scattering properties of the system in the simple form.

In the following, we first describe the matching conditions for unpolarized electrons in the CB before generalizing to the case of the spin-polarized multiband transport involving both the CB and VB of semiconductor heterostructures. Then we discuss the matching conditions involving interface potentials and the matching condition for an effective Hamiltonian of electrons in the CB tunneling through a [110] barrier structure under normal incidence as in Ref.[183]. In order to valid our multiband **k.p** platforms for a consideration of tunneling of an electron through a heterostructure, we will demonstrate the cancellation of the interference terms for the current as well as the negligible contributions of ghost bands on the current. Then an important Landauer formula will be recovered from the expression of the wave current performed by **k.p** technique. As an example of heterostructure to be considered, we present a calculation method for resonant tunneling through GaAs/AlAs quantum well structure and give descriptions of bound states as well as quasi bound states in this quantum well structure via scattering matrix approach developed in Appendix C. For matching condition with surface potential at the interfaces, we consider the structure with reduction from $T_{2d} \rightarrow C_{2v}$ and adapt the matching conditions proposed by Ivchenko et. al and Durnev et al. in the framework of 6-band and 14-band ***k.p*** model, to our multiband (30- and 40-band) calculations. Noting that the matching conditions should satisfy the fact that the current is conserved within whole structure, we then give a limit for the application of Durnev's matching conditions within multiband **k.p** Hamiltonian. Afterward, we discuss the properties of wavefunctions and splitting energy in quantum wells from our numerical calculations in comparison with the results of Ivchenko [30] and Durnev [31].

3.1 Matching conditions for tunneling within heterostructures

Tunneling and electronic transport is a starting point but it is however a complex problem in fundamental quantum physics, which is important for application. For example, electrons can be transmitted through a tunnel barrier whose the first accessible propagating electronic states lies at an energy higher than the incoming electron energy. Let us consider for instance free electrons tunneling in one dimension, for which the Hamiltonian in the whole space is written: [218]

$$H = \frac{p^2}{2m_0} + V_0\theta(x) = -\frac{\hbar^2}{2m_0}\frac{\partial^2}{\partial x^2} + V_0\theta(x) \tag{3.1}$$

where m_0 is free electron mass, V_0 is a certain constant potential and $\theta(x)$ is the Heaviside function.

A possible approach is first to establish the continuity of the wave function derivative by integration of the *Schrödinger* equation 3.1:

$$\begin{aligned} &\int_{-\epsilon}^{+\epsilon}\left[-\frac{\hbar^2}{2m_0}\frac{\partial^2}{\partial x^2} + V_0\theta(x)\right]\Psi(x)dx = \int_{-\epsilon}^{+\epsilon}\varepsilon\Psi(x)dx \\ \Leftrightarrow &\int_{-\epsilon}^{+\epsilon} -\frac{\hbar^2}{2m_0}\frac{\partial^2}{\partial x^2}\Psi(x)dx = \int_{-\epsilon}^{+\epsilon}\left[\varepsilon - V_0\theta(x)\right]\Psi(x)dx \end{aligned} \tag{3.2}$$

Taking the limit when $\epsilon \to 0$, because of the term $\varepsilon - V_0\theta(x)$ is bounded, we obtain:

$$\lim_{\epsilon\to 0}\int_{-\epsilon}^{+\epsilon}\left[\varepsilon - V_0\theta(x)\right]\Psi(x)dx = 0 \tag{3.3}$$

Then, the Eq. 3.2 becomes:

$$\lim_{\epsilon\to 0}\left[\frac{\partial}{\partial x}\Psi(x)\right]_{-\epsilon}^{+\epsilon} dx = 0 \tag{3.4}$$

Eventually, the probability current has to be continuous, *i.e*,

$$\boldsymbol{J}^f[\Psi] = Re\left[\Psi^*\frac{\boldsymbol{p}}{m_0}\Psi\right] = \frac{\hbar}{m_0}Im\left[\Psi^*\frac{\partial}{\partial x}\Psi\right] = const \tag{3.5}$$

Consequently, a sufficient condition for the charge current conservation is now given by $[\Psi]_{x=0} = 0$ which provides us the standard matching condition, namely the continuity of the envelope function and of its derivative.

However, the problem becomes more complex when an electron propagates through an heterostructure made of different or inhomogenous materials, where in each medium, the system is described by its own bulk Hamiltonian. We then need to define the proper matching conditions at each boundary. In this situation, the standard matching condition is known to be the simplest one to be considered [218]. Let us introduce the BDD ideas for the matching conditions in one dimension. Suppose that an electron tunnels through an interface delimiting two different media at $x < 0$ and $x > 0$. As mentioned before, each medium is characterized by its own Hamiltonian and one must find a solution of *Schrödinger's* equation, made of eigenvectors of relevant bands in the two bulk materials, ensuring the continuity of the probability current at the origin. In this sense, the problem is analogous to a scattering problem, where the wave functions are determined only at some distance of the scattering potential. Proper matching conditions rely on the

extension of the bulk envelope function over the whole space. In an effective mass point of view, the BDD proposed to write the Hamiltonian in the whole space as:

$$H(x) = \frac{p_x^2}{2m_{(x)}} + V(x) = p_x \left[\frac{1}{2m_{(x)}} p_x \right] + V(x) = \frac{1}{2} p_x \frac{\partial H}{\partial p_x} + V(x) \tag{3.6}$$

where $m_{(x)}$ is the effective position-dependent mass and $V(x)$ is the potential in each medium. This procedure yields a symmetric Hermitian Hamiltonian which is mandatory. The integration of the Hamiltonian in Eq. 3.6 around the boundary automatically ensures the continuity of the probability, provided that both $\Psi(x)$ and electronic current $\left(\frac{\partial H}{\partial p_x}\right)\Psi$ are continuous. The BDD matching conditions are well known as standard matching conditions for electrons in the CB and have been applied with success to a variety of situations. However one must note that these conditions are not valid in the systems described by Hamiltonians including terms with momentum operator power of order larger than two, along the flux direction as well as surface potentials.

When one works with a complex system including $e.g.$ k^3 terms, corresponding to Dresselhaus interactions in an effective Hamiltonian approach, it is, generally, no longer possible to treat the transport in the standard way. The general solution is to increase the number of bands to consider in the general Hamiltonian form so that each matrix element of the Hamiltonian only involves off-diagonal k coupling terms with power strictly lower than three. In a special case when the k^3 terms are perturbations, such as the case of an electron in CB tunneling through [110] at normal incidence, one may redefine the matching conditions as in the work of Nguyen et al. [183].

3.1.1 Standard matching or boundary conditions

We now discuss the standard matching conditions in framework of the multiband $\boldsymbol{k.p}$ methods where it is possible to include SOI and exchange interactions. This peculiar issue arises when one considers the crossing of ferromagnetic/spin-orbit layers in semiconductors as well as metallic spintronics systems like recently emphasized in papers dealing with the problem of spin-orbit transport and Spin-Orbit Torque (SOT) via the Spin Hall effect (SHE) as well as Spin-Hall magneto resistance (SMR). As mentioned before, the SOI associated to the lack of inversion center leads to the appearance of a cubic term, $i.e$, Dresselhaus terms, in the conduction band. It implies to modify the standard matching conditions or consider the cubic term as perturbation. Another solution, which is adopted in the present work, is to work within a larger set of basis functions to decrease the order of the momentum, for example, using 6 bands or 8 bands (not possible to describe the odd term without including perturbation of higher bands) or 14 bands, 30 bands, and 40 bands (mandatory to describe the odd potential term) model instead of a 2-band effective model. In this point of view, it becomes necessary to redefine the proper matching condition for multiband transport. Let us start with the Hamiltonian without exchange interaction given by:

$$H = \frac{P^2}{2m_0} + V + \frac{\hbar}{4m_0^2c^2} \left(\nabla V \times \boldsymbol{p}\right).\boldsymbol{\sigma} \tag{3.7}$$

For convenient, we re-write Hamiltonian 3.7 in the more general form [183, 235–237]

$$H = \sum_j a_j \boldsymbol{p_j} + \sum_{j,k} b_{jk} \boldsymbol{p_j} \boldsymbol{p_k} \tag{3.8}$$

where $\boldsymbol{p_j}$ and $\boldsymbol{p_k}$ are the components of momentum $\boldsymbol{p}$; whereas a_j and b_{jk} (j, k refer to Cartesian coordinates) are $n \times n$ Hermitian matrices operating with the spin space and invariant under permutation of j, k. To describe the potentials independent of the momentum, e.g., the exchange potential or external magnetic field, as well as surface potential, we introduce H_0 as a supplementary term in Eq. 3.8.

We have intentionally chosen to give the exact derivation for the current and spin current operators in a multiband approach. From *Schrödinger* equation, we obtain:

$$i\hbar\frac{\partial|\Psi\rangle}{\partial t} = H|\Psi\rangle = \sum_j a_j \boldsymbol{p_j}|\Psi\rangle + \sum_{j,k} b_{jk}\boldsymbol{p_j}\boldsymbol{p_k}|\Psi\rangle + H_0|\Psi\rangle \tag{3.9}$$

Taking the Hermitian conjugate, we have:

$$-i\hbar\frac{\partial\langle\Psi|}{\partial t} = \sum_j \langle\boldsymbol{p_j}\Psi|a_j + \sum_{j,k}\langle\boldsymbol{p_j}\boldsymbol{p_k}\Psi|b_{jk} + \langle\Psi|H_0 \tag{3.10}$$

The conservation equation related to the density of probability or 'continuity equation' follows quite straight-forwardly from the following development:

$$\begin{aligned} i\hbar\frac{\partial\langle\Psi|\Psi\rangle}{\partial t} &= i\hbar\left[\left\langle\Psi\middle|\frac{\partial\Psi}{\partial t}\right\rangle + \left\langle\frac{\partial\Psi}{\partial t}\middle|\Psi\right\rangle\right] \\ &= \sum_j\langle\Psi|a_j\boldsymbol{p_j}|\Psi\rangle + \sum_{j,k}\langle\Psi|b_{jk}\boldsymbol{p_j}\boldsymbol{p_k}|\Psi\rangle - \sum_j\langle\boldsymbol{p_j}\Psi|a_j\Psi\rangle - \sum_{j,k}\langle\boldsymbol{p_j}\boldsymbol{p_k}\Psi|b_{jk}\Psi\rangle \\ &= \left[\sum_j\langle\Psi|a_j\boldsymbol{p_j}|\Psi\rangle - \sum_j\langle\boldsymbol{p_j}\Psi|a_j\Psi\rangle\right] + \left[\sum_{j,k}\langle\Psi|b_{jk}\boldsymbol{p_j}\boldsymbol{p_k}|\Psi\rangle - \sum_{j,k}\langle\boldsymbol{p_j}\boldsymbol{p_k}\Psi|b_{jk}\Psi\rangle\right] \end{aligned} \tag{3.11}$$

Since $\langle\boldsymbol{p_j}\Psi|a_j\Psi\rangle = \langle\Psi|a_j\boldsymbol{p_j}|\Psi\rangle^*$ and $\langle\boldsymbol{p_j}\boldsymbol{p_k}\Psi|b_{jk}\Psi\rangle = \langle\Psi|b_{jk}\boldsymbol{p_j}\boldsymbol{p_k}|\Psi\rangle^*$ we get:

$$\frac{\partial\langle\Psi|\Psi\rangle}{\partial t} = \frac{2}{\hbar}Im\left[\sum_j\langle\Psi|a_j\boldsymbol{p_j}|\Psi\rangle + \sum_{j,k}\langle\Psi|b_{jk}\boldsymbol{p_j}\boldsymbol{p_k}|\Psi\rangle\right] \tag{3.12}$$

Moreover, let us demonstrate that:

$$\frac{2}{\hbar}Im\left[\sum_j\langle\Psi|a_j\boldsymbol{p_j}|\Psi\rangle + \sum_{j,k}\langle\Psi|b_{jk}\boldsymbol{p_j}\boldsymbol{p_k}|\Psi\rangle\right] = -\sum_j\boldsymbol{\nabla}_j\left(Re\langle\Psi|\boldsymbol{J}_j|\Psi\rangle\right) \tag{3.13}$$

where $\boldsymbol{J}_j$ is the j^{th} component of wave current operator $\boldsymbol{J}$ [235, 238]:

$$\boldsymbol{J}_j = \frac{\partial H}{\partial \boldsymbol{p}_j} = a_j + 2\sum_k b_{jk}\boldsymbol{p}_k \tag{3.14}$$

One obtains:

$$Re\langle\Psi|\boldsymbol{J}_j|\Psi\rangle = \sum_k\left\langle\left(\frac{a_j}{2} + b_{jk}\boldsymbol{p}_k\right)\Psi\middle|\Psi\right\rangle + \sum_k\left\langle\Psi\middle|\frac{a_j}{2} + b_{jk}\boldsymbol{p}_k\middle|\Psi\right\rangle \tag{3.15}$$

to give

$$\boldsymbol{\nabla}_j\left(Re\langle\Psi|\boldsymbol{J}_j|\Psi\rangle\right) = \boldsymbol{\nabla}_j\left\{\sum_k\left\langle\left(\frac{a_j}{2} + b_{jk}\boldsymbol{p}_k\right)\Psi\middle|\Psi\right\rangle + \sum_k\left\langle\Psi\middle|\frac{a_j}{2} + b_{jk}\boldsymbol{p}_k\middle|\Psi\right\rangle\right\} \tag{3.16}$$

Note that $\boldsymbol{\nabla}_j = \frac{i}{\hbar}\boldsymbol{p}_j$ and $(a_j)^+ = a_j, (b_{jk})^+ = b_{jk}$. We first consider the derivation of the first order components in 3.16:

$$\begin{aligned} A_1 &= \boldsymbol{\nabla}_j \left\{ \left\langle \Psi \middle| \frac{a_j}{2}\Psi \right\rangle + \left\langle \frac{a_j}{2}\Psi \middle| \Psi \right\rangle \right\} = \frac{i}{\hbar}\boldsymbol{p}_j\boldsymbol{p}_j\langle\Psi|a_j\Psi\rangle = \frac{i}{\hbar}\left\{ \left\langle \Psi \middle| \frac{a_j}{2}\Psi \right\rangle + \left\langle \frac{a_j}{2}\Psi \middle| \Psi \right\rangle \right\} \\ &= \frac{i}{\hbar}\boldsymbol{p}_j\langle\Psi|a_j\Psi\rangle = \frac{i}{\hbar}\{\langle\Psi|a_j\boldsymbol{p}_j\Psi\rangle - \langle\boldsymbol{p}_j\Psi|a_j\Psi\rangle\} = -\frac{2}{\hbar}Im\langle\Psi|a_j\boldsymbol{p}_j\Psi\rangle \end{aligned} \tag{3.17}$$

And the derivation of the second order components in 3.16:

$$\begin{aligned} A_2 &= \boldsymbol{\nabla}_j \left\{ \sum_k \left[\langle\Psi|b_{jk}\boldsymbol{p}_k\Psi\rangle + \langle b_{jk}\boldsymbol{p}_k\Psi|\Psi\rangle \right] \right\} = \frac{i}{\hbar}\sum_k \boldsymbol{p}_j \left\{ \langle\Psi|b_{jk}\boldsymbol{p}_k\Psi\rangle + \langle b_{jk}\boldsymbol{p}_k\Psi|\Psi\rangle \right\} \\ &= \frac{i}{\hbar}\sum_k \left\{ \langle\Psi|b_{jk}\boldsymbol{p_j}\boldsymbol{p_k}\Psi\rangle - \langle\boldsymbol{p_j}\Psi|b_{jk}\boldsymbol{p}_k\Psi\rangle - \langle b_{jk}\boldsymbol{p_j}\boldsymbol{p_k}\Psi|\Psi\rangle + \langle b_{jk}\boldsymbol{p_k}\Psi|\boldsymbol{p_j}\Psi\rangle \right\} \\ &= \frac{i}{\hbar}\sum_k \left(\langle\Psi|b_{jk}\boldsymbol{p_j}\boldsymbol{p_k}\Psi\rangle - \langle b_{jk}\boldsymbol{p_j}\boldsymbol{p_k}\Psi|\Psi\rangle \right) + \frac{i}{\hbar}\sum_k \left(\langle b_{jk}\boldsymbol{p}_k\Psi|\boldsymbol{p}_j\Psi\rangle - \langle\boldsymbol{p_j}\Psi|b_{jk}\boldsymbol{p}_k\Psi\rangle \right) \\ &= -\frac{2}{\hbar}\sum_k Im\langle\Psi|b_{jk}\boldsymbol{p_j}\boldsymbol{p_k}\Psi\rangle + \frac{i}{\hbar}\sum_k \left(\langle b_{jk}\boldsymbol{p}_k\Psi|\boldsymbol{p}_j\Psi\rangle - \langle\boldsymbol{p_j}\Psi|b_{jk}\boldsymbol{p}_k\Psi\rangle \right) \end{aligned} \tag{3.18}$$

Then, from Eq 3.17 and 3.18:

$$\boldsymbol{\nabla}_j \left(Re\langle\Psi|\boldsymbol{J}_j|\Psi\rangle \right) = -\frac{2}{\hbar}\sum_k Im\langle\Psi|(a_j\boldsymbol{p}_j + b_{jk}\boldsymbol{p_j}\boldsymbol{p_k})\Psi\rangle + \frac{i}{\hbar}\sum_k \left(\langle b_{jk}\boldsymbol{p}_k\Psi|\boldsymbol{p}_j\Psi\rangle - \langle\boldsymbol{p_j}\Psi|b_{jk}\boldsymbol{p}_k\Psi\rangle \right) \tag{3.19}$$

to get:

$$\sum_j \boldsymbol{\nabla}_j \left(Re\langle\Psi|\boldsymbol{J}_j|\Psi\rangle \right) = -\frac{2}{\hbar}\sum_{j,k} Im\langle\Psi|(a_j\boldsymbol{p}_j + b_{jk}\boldsymbol{p_j}\boldsymbol{p_k})\Psi\rangle + \frac{i}{\hbar}\sum_{j,k} \left(\langle b_{jk}\boldsymbol{p}_k\Psi|\boldsymbol{p}_j\Psi\rangle - \langle\boldsymbol{p_j}\Psi|b_{jk}\boldsymbol{p}_k\Psi\rangle \right) \tag{3.20}$$

Because:

$$\sum_{j,k}\langle b_{jk}\boldsymbol{p}_k\Psi|\boldsymbol{p}_j\Psi\rangle = \sum_{j,k}\langle\boldsymbol{p}_k\Psi|b_{jk}\boldsymbol{p}_j\Psi\rangle = \sum_{j,k}\langle\boldsymbol{p_j}\Psi|b_{jk}\boldsymbol{p}_k\Psi\rangle \tag{3.21}$$

hence

$$\sum_{j,k} \left(\langle b_{jk}\boldsymbol{p}_k\Psi|\boldsymbol{p}_j\Psi\rangle - \langle\boldsymbol{p_j}\Psi|b_{jk}\boldsymbol{p}_k\Psi\rangle \right) = 0 \tag{3.22}$$

Combining Eq. 3.12 and Eq.3.20 we get:

$$\frac{\partial\langle\Psi|\Psi\rangle}{\partial t} = -\sum_j \boldsymbol{\nabla}_j \left(Re\langle\Psi|\boldsymbol{J}_j|\Psi\rangle \right) \tag{3.23}$$

Thus, for a stationary regime (time-independent):

$$\boldsymbol{\nabla}_j \left(Re\langle\Psi|\boldsymbol{J}_j|\Psi\rangle \right) = 0 \tag{3.24}$$

where:

$$\sum_j \boldsymbol{\nabla}_j \left(Re\langle\Psi|\boldsymbol{J}_j|\Psi\rangle \right) = -\frac{2}{\hbar}\sum_{j,k} Im\langle\Psi|(a_j\boldsymbol{p}_j + b_{jk}\boldsymbol{p_j}\boldsymbol{p_k})\Psi\rangle \tag{3.25}$$

Equation 3.24 demonstrates that the current $\langle\Psi|\boldsymbol{J}_j|\Psi\rangle$ is conserved, at least in each layers of the heterostructures separately. In the next section, we will show that is also true within the whole heterostructure upon requirement to define the proper current operator from the Hamiltonian and the correct boundary

conditions. And finally, the continuity of both wavefunction Ψ and current wave $\boldsymbol{J}_j\Psi$ are sufficient conditions which ensure that the probability current is continuous at an interface. We will show, afterwards, that the charge current remains constant in heterostructures independently of the electron coordinate within the heterostructure.

3.1.2 Extended matching conditions with surface potentials at interfaces

In this part, we discuss the matching conditions to be used in quantum wells and heterostructures involving possible surface potential at a given interface. The surface potentials may arise from Rashba effect [37], strain [176] or symmetry breaking at the interface [30, 31] and are essential to be taken into account because they represent the effects of the electronic wavefunction originating from a possible strong potential present in the lattice at the scale on typically a few atomic cells from the interfaces in the heterostructure.

The Tight-Binding picture

Such peculiarity can be more easily observed if one adopts a tight-binding scheme for an electron moving close to the interface between two materials A and B. For the tight binding Hamiltonian in the second quantization form:

$$H_{TB} = \sum_{i,j} t_{ij}\delta(x)\hat{a}_j^+\hat{a}_i \tag{3.26}$$

where $\hat{a}_i$ and $\hat{a}_j^+$ are the annihilation and creation operators for the sites (i) and (j) respectively, and from the expression of the density operator:

$$\rho = \sum_i \hat{a}_i^+\hat{a}_i \tag{3.27}$$

the divergence of the current operator reads:

$$\frac{d\rho}{dt} = -\frac{i}{\hbar}\left[H_{TB},\rho\right] = -\frac{i}{\hbar}\left[\sum_{i,j} t_{ij}\delta(x)\hat{a}_j^+\hat{a}_i, \sum_k \hat{a}_k^+\hat{a}_k\right] \tag{3.28}$$

For the $i^{th}-component$ of current operator:

$$\frac{d\rho_i}{dt} = -\nabla\boldsymbol{J}_i = \frac{i}{\hbar}\sum_j t_{ij}\delta(x)\hat{a}_j^+\hat{a}_i - c.c = \frac{i}{\hbar}H_{TB}^i - c.c \tag{3.29}$$

where $c.c$ is the complex conjugate; H_{TB}^i is the local surface potential at the interface (i), giving after integration:

$$\boldsymbol{J}_i^{left} - \boldsymbol{J}_i^{right} = \frac{2i}{\hbar}H_{TB}^i \tag{3.30}$$

that is the expression given above in the second quantization formalism.

The k.p picture

Generally, we can write any surface potential at a given interface defined by x_0 like:

$$H_{surface} = \sum_j V_j\delta(x_j - x_0) \tag{3.31}$$

where V_j is a amplitude of surface potential along jth direction. Note that the values of V_j may be different for different directions, but however independent of the jth component of momentum. Then the total Hamiltonian is:

$$H_{total} = H + H_{surface} \tag{3.32}$$

where H was introduced in 3.8, the $Schrödinger$ equation now can be re-written as:

$$i\hbar\frac{\partial|\Psi\rangle}{\partial t} = H_{total}|\Psi\rangle = H|\Psi\rangle + \sum_j V_j\delta(x_j - x_0)|\Psi\rangle \tag{3.33}$$

Taking the Hermitian conjugate of this equation, one gets:

$$-i\hbar\frac{\partial\langle\Psi|}{\partial t} = \langle H\Psi| + \sum_j \langle V_j\Psi|\delta(x_j - x_0) \tag{3.34}$$

The equation of conservation for the present Hamiltonian becomes now:

$$\begin{aligned}\frac{\partial\langle\Psi|\Psi\rangle}{\partial t} &= \left\langle\frac{\partial\Psi}{\partial t}\middle|\Psi\right\rangle + \left\langle\Psi\middle|\frac{\partial\Psi}{\partial t}\right\rangle = \frac{1}{i\hbar}\left(\langle\Psi|H\Psi\rangle - \langle H\Psi|\Psi\rangle\right)\\ &+ \frac{1}{i\hbar}\left[\sum_j\langle\Psi|V_j\delta(x_j - x_0)|\Psi\rangle - \sum_j\langle V_j\Psi|\delta(x_j - x_0)|\Psi\rangle\right]\end{aligned} \tag{3.35}$$

Since:

$$\frac{1}{i\hbar}\left(\langle\Psi|H\Psi\rangle - \langle H\Psi|\Psi\rangle\right) = -\sum_j \boldsymbol{\nabla}_j\left(Re\left\langle\Psi\middle|\frac{\partial H}{\partial \boldsymbol{p_j}}\middle|\Psi\right\rangle\right) \tag{3.36}$$

One obtains within the $\boldsymbol{k.p}$ framework:

$$\begin{aligned}&\frac{1}{i\hbar}\left[\sum_j\langle\Psi|V_j\delta(x_j - x_0)|\Psi\rangle - \sum_j\langle V_j\Psi|\delta(x_j - x_0)|\Psi\rangle\right]\\ &= \sum_j\frac{-i}{\hbar}\langle\Psi|V_j\delta(x_j - x_0)|\Psi\rangle + c.c = \sum_j Re\left\langle\Psi\middle|\frac{-2i}{\hbar}V_j\delta(x_j - x_0)\middle|\Psi\right\rangle\end{aligned} \tag{3.37}$$

Using the fact that $\delta(x_j - x_0) = \frac{\partial\Theta(x_j - x_0)}{\partial x_j}$ where Θ is the Heaviside function, this yields:

$$\frac{\partial\langle\Psi|\Psi\rangle}{\partial t} = \sum_j \boldsymbol{\nabla}_j Re\left[-\left\langle\Psi\middle|\frac{\partial H}{\partial \boldsymbol{p}_j} - \frac{2i}{\hbar}V_j\Theta(x_j - x_0)\middle|\Psi\right\rangle\right] = -\frac{1}{\hbar}\sum_j \boldsymbol{\nabla}_j Re\left[\left\langle\Psi\middle|\frac{\partial H}{\partial \boldsymbol{k}_j} + 2iV_j\Theta(x_j - x_0)\middle|\Psi\right\rangle\right] \tag{3.38}$$

When the Hamiltonian is time-independent, one obtains thus:

$$\sum_j \boldsymbol{\nabla}_j Re\left[\left\langle\Psi\middle|\frac{\partial H}{\partial \boldsymbol{k}_j} + 2iV_j\Theta(x_j - x_0)\middle|\Psi\right\rangle\right] = 0 \tag{3.39}$$

Or:

$$\sum_j \boldsymbol{\nabla}_j Re\left[\left\langle\Psi\middle|\boldsymbol{J}_j + 2iV_j\Theta(x_j - x_0)\middle|\Psi\right\rangle\right] = 0 \tag{3.40}$$

where $\boldsymbol{J}_j = \frac{\partial H}{\partial \boldsymbol{k}_j}$ is the jth space component of the current operator to match at interfaces. This important relationship allows one to give a formal definition of the current operator to be used in each media of the heterostructure. It provides a generalization of the correct expression to use in the case of a general surface potential possibly involving Rashba, Desselhaus, exchange interactions and all other types of spin-orbit

interactions.

This development then yields the new matching conditions which is used as far as $Re\left[\left\langle\Psi\left|\boldsymbol{J}_j + 2iV_j\Theta(x_j - x_0)\right|\Psi\right\rangle\right]$ is continuous at the interface. It can be ensured by the continuity of the wavefunction $|\Psi\rangle$ and electronic wave like term $\left[\boldsymbol{J}_j + 2iV_j\Theta(x_j - x_0)\right]|\Psi\rangle$ at the interface.

Because of the properties of the Θ Heaviside function: $\Theta(x_j - x_0) = 0$ if $(x_j - x_0) \leq 0$ and $\Theta(x_j - x_0) = 1$ if $(x_j - x_0) > 0$, therefore, one can say that the new boundary conditions to adapt are the continuity of the wave function and a certain discontinuity of the electronic current at the interfaces. In particular, we derived the system of equations describing the boundary conditions to be used hereafter namely:

$$\begin{aligned} |\Psi\rangle^{left} &= |\Psi\rangle^{right} \\ \left[\boldsymbol{J}_j^{left}\right]|\Psi\rangle^{left} &= \left[\boldsymbol{J}_j^{right} + 2iV_j\right]|\Psi\rangle^{right} \end{aligned} \tag{3.41}$$

where "left" and "right" labels refer to the wavefunction and current operator on the left and on the right interfaces respectively; V_j is the surface potential at the interfaces which might be a scalar quantity (potential step) or spin-dependent operator in general. We will come back to this boundary condition in the next part for a typical case symmetry breaking.

3.1.3 *Specificity of the matching conditions for the effective Hamiltonian along the [110] growth direction [183]*

In this section, we deal with the matching conditions along the [110] direction for an effective Hamiltonian in the conduction band including a Desselhaus contribution. These developments will be used in the description of the spin-dephasing effects (or spin rotation effects) which are described in detail in Chap.4. This will reveal to be an unusual problem [183] because of the appearance of a higher order term (k^3 term) originating from the bulk Dresselhaus terms for electrons propagating along the [110] direction. To describe this novel situation, we consider the tunneling problem through a simple barrier grown along the [110] direction, as depicted in the Figure 3.1

It was shown by Nguyen et al. [183, 185] that even in the simplest case, under a normal incidence, no solution can be calculated in the usual way assuming that the wavefunction and its derivative are both continuous. The energies ($\mathcal{E}_\uparrow$ and $\mathcal{E}_\downarrow$) of the electrons along the [110] axis with normal incidence $\mathbf{k} = k(1/\sqrt{2})[110]$ are respectively for spin $\uparrow$ and spin $\downarrow$:

$$\text{for} \quad \uparrow \quad \text{-spin} \; \mathcal{E}_\uparrow = \gamma_c k^2 + \frac{1}{2}\gamma_D k^3, \tag{3.42}$$

$$\text{for} \quad \downarrow \quad \text{-spin} \; \mathcal{E}_\downarrow = \gamma_c k^2 - \frac{1}{2}\gamma_D k^3. \tag{3.43}$$

where $\gamma_C = \frac{\hbar}{2m^*}$ and γ_D is the Dresselhaus parameters ($eV\text{Å}^3$). Respectively, their eigenvectors satisfy two equations in parallel

$$\left[-\gamma_c\frac{\partial^2}{\partial z^2} + \frac{1}{2}i\gamma_D\frac{\partial^3}{\partial z^3}\right]\Psi_\uparrow = [\mathcal{E} - V(z)]\,\Psi_\uparrow, \tag{3.44}$$

$$\left[-\gamma_c\frac{\partial^2}{\partial z^2} - \frac{1}{2}i\gamma_D\frac{\partial^3}{\partial z^3}\right]\Psi_\downarrow = [\mathcal{E} - V(z)]\,\Psi_\downarrow, \tag{3.45}$$

where $V(z) = V$ when $0 \leq z \leq a$ and $V(z) = 0$ outside. If the in-plane wavevector in the barrier is purely imaginary, $\pm iK$, the respective energy $-\gamma_c K^2 \mp \frac{1}{2}i\gamma_D K^3$ will not be real. Therefore, the wavevectors in the

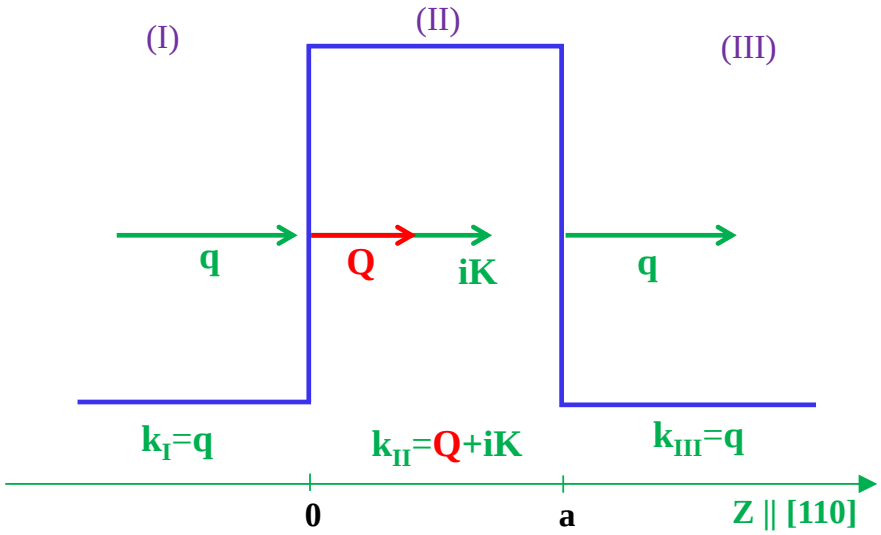

FIGURE 3.1: Sketch of the tunnel geometry with notations. The spin-orbit-split barrier material of thickness a (medium II is located between two free-electron like materials (media I and III). The tunnel axis, normal to the barrier, is the z axis. In the free-electron like materials, the real normal incident electron wave vector in the z direction is referred to as $\boldsymbol{q}$. In the barrier material, the evanescent wave vector along the z axis is referred to as $\boldsymbol{Q}+\boldsymbol{iK}$, where $\boldsymbol{Q}$ and $\boldsymbol{K}$ are real quantities. The transverse wave-vector component is in the barrier plane. Then, the overall wave vectors in the three media are, respectively, $\boldsymbol{k_I = k_{III} = q}$ and $\boldsymbol{k_{II} = Q + iK}$.

barrier are complex quatities, *i.e.*, $Q \pm iK$ where a real part (Q) has been added. Let us write $\Uparrow = \uparrow e^{iQz}$ and $\Downarrow = \downarrow e^{iQz}$. We first try to deal with this situation according to the usual procedure. The wavefunction is in each part of the heterostructures:

$$\Psi = \begin{cases} \Psi_I(z) = \left(A_1 e^{iqz} + B_1 e^{-iqz}\right) \uparrow + \tilde{B}_1 e^{-iqz} \downarrow \ (z < 0), \\ \Psi_{II}(z) = \left(A_2 e^{-Kz} + B_2 e^{Kz}\right) \Uparrow + \left(\tilde{A}_2 e^{-Kz} + \tilde{B}_2 e^{Kz}\right) \Downarrow \ (0 \le z \le a), \\ \Psi_{III}(z) = A_3 e^{iqz} \uparrow + \tilde{A}_3 e^{iqz} \downarrow \ (z > a). \end{cases} \tag{3.46}$$

Applying the BDD [218] matching conditions for $\downarrow$- spin states, we find:

$$\begin{cases} \tilde{B}_1 = \tilde{A}_2 + \tilde{B}_2, \\ q\tilde{B} = (Q - iK)\,\tilde{A}_2 + (Q + iK)\,\tilde{B}_2, \\ \tilde{A}_2 e^{-i(Q-iK)a} + \tilde{B}_2 e^{-i(Q+iK)a} = \tilde{A}_3 e^{iqa}, \\ (Q - iK)\tilde{A}_2 e^{-i(Q-iK)a} + (Q + iK)\tilde{B}_2 e^{-i(Q+iK)a} = -q\tilde{A}_3 e^{iqa}. \end{cases} \tag{3.47}$$

These equations have a non zero solution when

$$\left(q^2 - Q^2 - K^2\right) \sinh Ka + 2iKq \cosh Ka = 0. \tag{3.48}$$

The only solution is $K = 0$ but it is not relevant to our problem.

As introduced above, the Dyakonov Perel term was obtained by a perturbation method, therefore we will look for a solution of the effective Schrödinger equation to the first order in γ only, *e.g.* for $\uparrow$- spin $\Psi_\uparrow = \Psi^{(0)} + \Psi^{(1)}_\uparrow$ where $\Psi^{(0)}$ is a solution when the Dresselhaus terms are neglected. The Schrödinger equation for $\uparrow$- spin in Eq. 3.44 becomes

$$\left[-\gamma_c \frac{\partial^2 \Psi_\uparrow}{\partial z^2} + \frac{1}{2} i\gamma_D \frac{\partial^3 \Psi^{(0)}}{\partial z^3}\right] = [\mathcal{E} - V(z)]\,\Psi_\uparrow. \tag{3.49}$$

Integrating this equation from one side of the interface to the other, one obtains:

$$\lim_{\varepsilon \longrightarrow 0} \left[-\gamma_c \frac{\partial \Psi_\uparrow}{\partial z}\Big|_{z_0-\varepsilon}^{z_0+\varepsilon} + \frac{1}{2} i \gamma_D \frac{\partial^2 \Psi^{(0)}}{\partial z^2}\Big|_{z_0-\varepsilon}^{z_0+\varepsilon} \right] = 0. \tag{3.50}$$

Note that, in the electrodes, if the incident wave possesses a wavevector q, the reflected wave will possess wavevector $-q'$, where $\gamma_c q^2 + \frac{1}{2}\gamma_D q^3 = \gamma_c q'^2 - \frac{1}{2}\gamma_D q'^3$. It leads to $\delta q = q' - q$ being a second order term in γ_D so that this term can be neglected. This means there is no spin splitting in the electrodes. In the case of free electrons, one may prove that:

$$\frac{\partial^2 \Psi^{(0)}}{\partial z^2}\Big|_{z_0-\varepsilon}^{z_0+\varepsilon} = \left(K^2 + q^2\right) \Psi^{(0)}(z_0). \tag{3.51}$$

From Eqs.3.50 and 3.51, we have

$$\lim_{\varepsilon \longrightarrow 0} \left(\frac{\partial \Psi_\uparrow}{\partial z}\Big|_{z_0-\varepsilon}^{z_0+\varepsilon} \right) = \frac{i\gamma_D}{2\gamma_c} \left(K^2 + q^2\right) \Psi^{(0)}(z_0) \approx 2iQ_\uparrow \Psi^{(0)}(z_0). \tag{3.52}$$

Equation. 3.52 clearly shows the discontinuity of the derivative of the wavefunction at an interface grown along the [110] direction in the presence of DP field. Now, the solutions of the Schrödinger equation have to satisfy the new matching conditions, *e.g.* for ↑-spin that are:

$$\Psi \text{ continuous, and } \lim_{\varepsilon \longrightarrow 0} \left(\frac{\partial \Psi_\uparrow}{\partial z}\Big|_{z_0-\varepsilon}^{z_0+\varepsilon} \right) = 2iQ_\uparrow \Psi^{(0)}(z_0). \tag{3.53}$$

We write $Q_\uparrow = Q$ for ↑-spin and $Q_\downarrow = -Q$ for ↓-spin. The solution of the Schrödinger equation is calculated to the first order in γ in the form

$$\Psi = \varphi^s + \varphi^{\hat{s}}, \tag{3.54}$$

where

$$\varphi^s = \begin{cases} \varphi^s_I(z) = a_1 e^{iqz} + b_1 e^{-iqz} & (z < 0), \\ \varphi^s_{II}(z) = \left(a_2 e^{-Kz} + b_2 e^{Kz}\right) e^{iQz} & (0 < z < a), \\ \varphi^s_{III}(z) = a_3 e^{iqz} e^{iQz} & (a < z), \end{cases} \tag{3.55}$$

and

$$\varphi^{\hat{s}} = \begin{cases} \varphi^{\hat{s}}_I(z) = \beta_1 Q e^{-iqz} & (z < 0), \\ \varphi^{\hat{s}}_{II}(z) = Q\left(\alpha_2 e^{-Kz} + \beta_2 e^{Kz}\right) e^{iQz} & (0 < z < a), \\ \varphi^{\hat{s}}_{III}(z) = \alpha'_3 Q e^{iqz} & (a < z). \end{cases} \tag{3.56}$$

The new matching conditions for the effective Hamiltonian along the [110] direction are the following:

(i) φ^s and $\varphi^{\hat{s}}$ are continuous at the interfaces,

(ii) $\lim_{\varepsilon \longrightarrow 0} \left(\frac{\partial(\varphi^s + \varphi^{\hat{s}})}{\partial z}\Big|_{z_0-\varepsilon}^{z_0+\varepsilon} \right) = iQ\Psi^{(0)}_{II}(z_0)$.

The conclusion of this section is that it seems very difficult to find the exact analytical solution for electron tunneling through a heterostructure grown along [110] direction. This peculiarity of the [110] direction has been also emphasized by Alekseev [56] as well as Durnev [31]. In the simplest model, the incoming electron at normal incidence was treated to the first order in γ. The difficulties do not only originate from the mathematical techniques but also from the physical point of view; the discontinuity of the derivative of the wave function caused by the **k** cubic term highlights the crucial role of the matching conditions. The consequence is that numerical computational techniques, *e.g.* using advanced **k**.**p** methods, like 14-band, 30-band or 40 band tunneling codes, become mandatory in order to analyze the new properties brought by spin-orbit effects over the Brillouin zone (BZ). The techniques we have employed and developed beyond

the state of the art, will also appear to be perfect numerical tools to check some analytical developments based on perturbation technique approaches.

3.2 Current within heterostructures: Landauer Büttiker Formalism

3.2.1 Current within heterostructures

In this section, we will demonstrate that the application of the matching conditions derived in the previous sections and applied to each interface within a given heterostructure, simple interfaces, tunnel junctions, quantum wells, double-barrier structures, are always associated to a conserved charge-current profile along the transport direction. This is one of the main issues to fulfill. The demonstration will be made taking into account the properties of the S- scattering matrix within the multilayers. On the other hand, the same conclusions cannot be generalized to the case of the spin current profile once either bulk or interface potentials admit an Hamiltonian term not commuting with the spin operators (Pauli matrices). This effect should lead to the re-examination of the calculations of the spin-mixing conductance (real part and imaginary part) for systems involving Rashba interactions at interfaces [239].

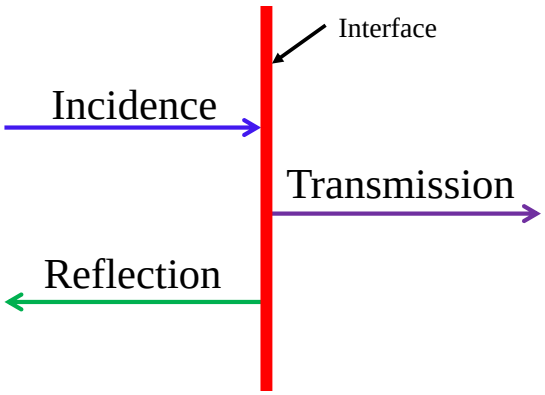

FIGURE 3.2: Scheme of continuity of wave current at the interface of heterostructure.

Considering an interface between two materials and assuming that the electron is moving from the left to the right, then the wavefunction at some distance on the right interface can be a simple a linear combination of eigenstates of the asymptotic Hamiltonian, or, equivalently, a linear combination of transmitted waves at the right interface, namely:

$$\Psi_R = \sum_n t_{in,n} \Phi_{n,k_n}(\boldsymbol{r}) \tag{3.57}$$

where $t_{in,n}$ are complex numbers. Note that the total Hamiltonian may also have evanescent modes, however at some distance (far enough) from the interface, these modes posses zero contribution to the wavefunction since they decay quickly with the distance from the interface.

At some distance to the left interface, the electrons are scattered at the interface then go back to the left. We thus get a solution without contribution from evanescent modes as:

$$\Psi_L = \Phi_{in}(\boldsymbol{r}) + \sum_n r_{in,n} \Phi_{n,k_n}(\boldsymbol{r}) \tag{3.58}$$

involving all possible reflected waves which admit the same energy as the incoming wave. Here $\Phi_{in}(\boldsymbol{r}) = \sum_{i=1}^{N_i} C_i \Phi_{i,k_i}(\boldsymbol{r})$, N_i is the number of band used to describe the incident wave, C_i are normalization coefficients (normally $C_i = 1$), and $\{\Phi_{i,k_i}(\boldsymbol{r}\}$ (or $\{\Phi_{n,k_n}(\boldsymbol{r}\}$) is the basis function set.

Let us assume that the matching conditions at the interfaces are the continuity of the wavefunction Ψ and of the electronic current $Re\langle\Psi|\mathbf{J}|\Psi\rangle$ where $\mathbf{J} = \partial H/\partial\mathbf{p}$. These are the matching conditions that we consider throughout the present work.

The probability current at the left of the interface is:

$$Re\langle\Psi_L|\mathbf{J}|\Psi_L\rangle = Re\left\langle\Phi_{in} + \sum_n r_{in,n}\Phi_{n,k_n}\middle|\mathbf{J}\middle|\Phi_{in} + \sum_n r_{in,n}\Phi_{n,k_n}\right\rangle \tag{3.59}$$

$$= Re\langle\Phi_{in}|\mathbf{J}|\Phi_{in}\rangle + \sum_n \left|r_{in,n}\right|^2 Re\left\langle\Phi_{n,k_n}\middle|\mathbf{J}\middle|\Phi_{n,k_n}\right\rangle + \sum_n Re\left\langle r_{in,n}\Phi_{n,k_n}\middle|\mathbf{J}\middle|\Phi_{in}\right\rangle \tag{3.60}$$

$$+ \sum_n Re\langle\Phi_{in}|\mathbf{J}\left|r_{in,n}\Phi_{n,k_n}\right\rangle + \sum_{nm(n\neq m)} Re\left\langle r_{in,n}\Phi_{n,k_n}\,|\mathbf{J}|\,r_{in,m}\Phi_{n,k_m}\right\rangle.$$

where the following contribution

$$\left\langle r_{in,n}\Phi_{n,k_n}\middle|\mathbf{J}\middle|\Phi_{in}\right\rangle = \left\langle\mathbf{J}^+ r_{in,n}\Phi_{n,k_n}\middle|\,\Phi_{in}\right\rangle = \langle\Phi_{in}|\mathbf{J}\left|r_{in,n}\Phi_{n,k_n}\right\rangle^* = -\left\langle\mathbf{J}\Phi_{in}|\,r_{in,n}\Phi_{n,k_n}\right\rangle^*. \tag{3.61}$$

and

$$\left\langle r_{in,n}\Phi_{n,k_n}\,|\mathbf{J}|\,r_{in,m}\Phi_{n,k_m}\right\rangle \tag{3.62}$$

with $n \neq m$ are called the interference term in reflection.

From Eq. 3.61, it must obey:

$$Re\left\langle r_{in,n}\Phi_{n,k_n}\middle|\mathbf{J}\middle|\Phi_{in}\right\rangle = 0. \tag{3.63}$$

Equations 3.61 and 3.63 show that the interference terms in Eq. 3.59 are canceled

$$\sum_n Re\left\langle r_{in,n}\Phi_{n,k_n}\middle|\mathbf{J}\middle|\Phi_{in}\right\rangle + \sum_n Re\langle\Phi_{in}|\mathbf{J}\left|r_{in,n}\Phi_{n,k_n}\right\rangle = 0. \tag{3.64}$$

as well as :

$$\sum_{nm(n\neq m)} Re\left\langle r_{in,n}\Phi_{n,k_n}\,|\mathbf{J}|\,r_{in,m}\Phi_{n,k_m}\right\rangle = 0 \tag{3.65}$$

and this point is particularly interesting when we deal with Green's function technique in chapter 4.

Then, we get:

$$\langle\Psi_L|\mathbf{J}|\Psi_L\rangle = \langle\Phi_{in}|\mathbf{J}|\Phi_{in}\rangle + \sum_n \left|r_{in,n}\right|^2 \left\langle\Phi_{n,k_n}\middle|\mathbf{J}\middle|\Phi_{n,k_n}\right\rangle. \tag{3.66}$$

The probability current at the right of the interface is:

$$Re\langle\Psi_R|\mathbf{J}|\Psi_R\rangle = \left\langle\sum_n t_{in,n}\Phi_{n,k_n}\middle|\mathbf{J}\middle|\sum_n t_{in,n}\Phi_{n,k_n}\right\rangle = \sum_n \left|t_{in,n}\right|^2 \left\langle\Phi_{n,k_n}\middle|\mathbf{J}\middle|\Phi_{n,k_n}\right\rangle. \tag{3.67}$$

The continuity of the probability current gives:

$$\langle\Phi_{in}|\mathbf{J}|\Phi_{in}\rangle + \sum_n \left|r_{in,n}\right|^2 \left\langle\Phi_{n,k_n}\middle|\mathbf{J}\middle|\Phi_{n,k_n}\right\rangle = \sum_n \left|t_{in,n}\right|^2 \left\langle\Phi_{n,k_n}\middle|\mathbf{J}\middle|\Phi_{n,k_n}\right\rangle \tag{3.68}$$

or

$$1 + \sum_n \left|r_{in,n}\right|^2 \frac{\left\langle\Phi_{n,k_n}\middle|\mathbf{J}\middle|\Phi_{n,k_n}\right\rangle}{\langle\Phi_{in}|\mathbf{J}|\Phi_{in}\rangle} = \sum_n \left|t_{in,n}\right|^2 \frac{\left\langle\Phi_{n,k_n}\middle|\mathbf{J}\middle|\Phi_{n,k_n}\right\rangle}{\langle\Phi_{in}|\mathbf{J}|\Phi_{in}\rangle} \tag{3.69}$$

Cancellation of the interference terms for the current: where does it come from?

We now demonstrate the cancellation of the interference terms (Eq. 3.61) for both reflection and transmission in the framework of the ***k.p*** theory. In order to do that, we write the Hamiltonian in the form [163]: $H = \hat{A}k_z^2 + \hat{B}k_z + \hat{C}$ and the current operator is then: $\mathbf{J} = \hat{A}k_z + \frac{1}{2}\hat{B}$. We assume that the nth eigenvector at a constant tunneling energy is $|n\rangle$ which corresponds to positive or negative incidence. Since the wavefunction can be a linear combination of these egenvectors, thus, in order to prove 3.61, one needs to calculate the interference terms of the current in the form of $\langle n|\mathbf{J}|m\rangle$ to show that $Re\left(a\langle m|\mathbf{J}|n\rangle + a^*\langle n|\mathbf{J}|m\rangle\right) = 0$, where a is the expansion coefficient where $|n\rangle$ and $|m\rangle$ are two different bands (n and m) at the same elastic energy ϵ and described by two different wave vectors k_n and k_m, respectively.

So, we start with:

$$\langle m\,|\boldsymbol{J}|\,n\rangle = \left\langle m\left|\hat{A}k_z^{(n)} + \frac{\hat{B}}{2}\right|n\right\rangle \tag{3.70}$$

$$\langle n\,|\boldsymbol{J}|\,m\rangle = \left\langle n\left|\hat{A}k_z^{(m)} + \frac{\hat{B}}{2}\right|m\right\rangle \tag{3.71}$$

$$\langle n\,|\boldsymbol{J}|\,m\rangle^* = \left\langle n\left|\hat{A}k_z^{(m)*} + \frac{\hat{B}}{2}\right|m\right\rangle \tag{3.72}$$

One has:

$$\langle n|\mathbf{J}|m\rangle^* + \langle m|\mathbf{J}|n\rangle = \left\langle n\left|\hat{A}\left(k_z^{(n)} + k_z^{(m)*}\right) + \hat{B}\right|m\right\rangle \tag{3.73}$$

$$= \left\langle n\left|\hat{A}\left(k_z^{(n)} + k_z^{(m)*}\right) + \hat{B}\right|m\right\rangle \times \frac{k_z^{(n)} - k_z^{(m)*}}{k_z^{(n)} - k_z^{(m)*}} \tag{3.74}$$

$$= \frac{1}{k_z^{(n)} - k_z^{(m)*}}\left\langle n\left|\hat{A}\left(k_z^{(n)^2} - k_z^{(m)*^2}\right) + \hat{B}\left(k_z^{(n)} - k_z^{(m)*}\right)\right|m\right\rangle \tag{3.75}$$

$$= \frac{1}{k_z^{(n)} - k_z^{(m)*}}\left[\left\langle n\left|\hat{A}k_z^{(n)^2} + \hat{B}k_z^{(n)} + \hat{C}\right|m\right\rangle - \left\langle n\left|\hat{A}k_z^{(m)*^2} + \hat{B}k_z^{(m)*} + \hat{C}\right|m\right\rangle\right] \tag{3.76}$$

$$= \frac{1}{k_z^{(n)} - k_z^{(m)*}}\left[\left\langle n\left|\hat{A}k_z^{(n)^2} + \hat{B}k_z^{(n)} + \hat{C}\right|m\right\rangle - \left\langle m\left|\hat{A}k_z^{(m)^2} + \hat{B}k_z^{(m)} + \hat{C}\right|n\right\rangle\right] \tag{3.77}$$

$$= \frac{\epsilon_n - \epsilon_m}{k_z^{(n)} - k_z^{(m)*}}\langle m|n\rangle \tag{3.78}$$

So that

$$\langle n|\mathbf{J}|m\rangle^* + \langle m|\mathbf{J}|n\rangle = \frac{\epsilon_n - \epsilon_m}{k_z^{(n)} - k_z^{(m)*}}\langle m|n\rangle \tag{3.79}$$

♣ Case 1: $k_z^{(n)}$ and $k_z^{(m)}$ are real, then $\epsilon_n = \epsilon_m$ (elastic tunneling), we have:

$$\langle n|\mathbf{J}|m\rangle^* + \langle m|\mathbf{J}|n\rangle = 0 \tag{3.80}$$

Or

$$\langle n|\mathbf{J}|m\rangle^* = -\langle m|\mathbf{J}|n\rangle \tag{3.81}$$

$$\left(a^*\langle n|\mathbf{J}|m\rangle\right)^* = -a\langle m|\mathbf{J}|n\rangle \tag{3.82}$$

And finally, we get:

$$Re\left(a\langle m|\mathbf{J}|n\rangle + a^{*}\langle n|\mathbf{J}|m\rangle\right) = 0 \tag{3.83}$$

Or one can say that the interference terms for propagating waves are canceled in both the reflection and transmission region.

♣ Case 2: $k_z^{(n)}$ is purely real and $k_z^{(m)}$ is pure imaginary or mixed (real + imaginary) then we reach the same conclusion as in the previous case: there remains no interference term in the current.

♣ Case 3: $k_z^{(n)}$ and $k_z^{(m)}$ are both complex (evanescent states) and $k_z^{(n)} \neq k_z^{(m)*}$ then no interference term exists in the current.

♣ Case 4: $k_z^{(n)}$ and $k_z^{(m)}$ are both complex (evanescent states) and $k_z^{(n)} = k_z^{(m)*}$ then:

$$\langle n|\mathbf{J}|m\rangle^{*} + \langle m|\mathbf{J}|n\rangle \neq 0 \tag{3.84}$$

In this case, the interference term results in tunneling current inside the barrier as expected.

The two equations 3.83 and 3.84 become mandatory to derive a general expression for the multiband and multilayer Green function as we will show in Chap 4. It will allow one to connect the value of a proper wavefunction at a point z' of the multilayer to the knowing wavefunction in a given point z in another part of the multilayer. These treatments developed here are specific in the sense that one is able to find a correlation between $\langle n|\mathbf{J}|m\rangle^{*}$ and $\langle m|\mathbf{J}|n\rangle$ for the case where $|n\rangle$ and $|m\rangle$ are Bloch function or evanescent waves corresponding to the same elastic energy ϵ but different wave vectors $\boldsymbol{k}$ (or iK). In that sense, we proved here the generalization of the validity of the $\boldsymbol{k}.\boldsymbol{p}$ framework to the case of tunneling waves involving evanescent wave [240].

Interference terms of spin current

Doing the same for spin current $\boldsymbol{j}_s$ defined by:

$$\boldsymbol{j}_s = \frac{1}{2}\left[\boldsymbol{\sigma}\frac{\partial H}{\partial k_z} + \frac{\partial H}{\partial k_z}\boldsymbol{\sigma}\right] \tag{3.85}$$

where $\frac{\partial H}{\partial k_z} = 2\hat{A}k_z + \hat{B}$, or we get:

$$\boldsymbol{j}_s = \left(\boldsymbol{\sigma}\hat{A} + \hat{A}\boldsymbol{\sigma}\right)k_z + \frac{1}{2}\left(\boldsymbol{\sigma}\hat{B} + \hat{B}\boldsymbol{\sigma}\right) \tag{3.86}$$

As the same as electric current, we are now trying to calculate:

$$\begin{aligned}
&\left\langle m\left|\boldsymbol{j}_s\right|n\right\rangle + \left\langle n\left|\boldsymbol{j}_s\right|m\right\rangle^{*} \\
&= \left\langle m\left|\left[\left(\boldsymbol{\sigma}\hat{A} + \hat{A}\boldsymbol{\sigma}\right)k_z^{(n)} + \frac{1}{2}\left(\boldsymbol{\sigma}\hat{B} + \hat{B}\boldsymbol{\sigma}\right)\right]\right|n\right\rangle + \left\langle n\left|\left[\left(\boldsymbol{\sigma}\hat{A} + \hat{A}\boldsymbol{\sigma}\right)k_z^{(m)} + \frac{1}{2}\left(\boldsymbol{\sigma}\hat{B} + \hat{B}\boldsymbol{\sigma}\right)\right]\right|m\right\rangle^{*} \\
&= \left\langle m\left|\left[\left(\boldsymbol{\sigma}\hat{A} + \hat{A}\boldsymbol{\sigma}\right)k_z^{(n)} + \frac{1}{2}\left(\boldsymbol{\sigma}\hat{B} + \hat{B}\boldsymbol{\sigma}\right)\right]\right|n\right\rangle + \left\langle m\left|\left[\left(\boldsymbol{\sigma}\hat{A} + \hat{A}\boldsymbol{\sigma}\right)k_z^{(m)*} + \frac{1}{2}\left(\boldsymbol{\sigma}\hat{B} + \hat{B}\boldsymbol{\sigma}\right)\right]\right|n\right\rangle \\
&= \left\langle m\left|\left[\left(\boldsymbol{\sigma}\hat{A} + \hat{A}\boldsymbol{\sigma}\right)\left(k_z^{(n)} + k_z^{(m)*}\right) + \left(\boldsymbol{\sigma}\hat{B} + \hat{B}\boldsymbol{\sigma}\right)\right]\right|n\right\rangle
\end{aligned} \tag{3.87}$$

Since we have:

$$\left[\hat{A}(k_z^{(n)})^2 + \hat{B}k_z^{(n)} + \hat{C}\right]|n\rangle = \epsilon_n|n\rangle \tag{3.88}$$

$$\left[\hat{A}(k_z^{(m)})^2 + \hat{B}k_z^{(m)} + \hat{C}\right]|m\rangle = \epsilon_m|m\rangle \tag{3.89}$$

then:

$$\begin{aligned}
&\left(k_z^{(n)} - k_z^{(m)*}\right)\left(\langle m|\boldsymbol{j}_s|n\rangle + \langle n|\boldsymbol{j}_s|m\rangle^*\right) \\
&= \left\langle m\left|\left[\left(\boldsymbol{\sigma}\hat{A} + \hat{A}\boldsymbol{\sigma}\right)\left(\left(k_z^{(n)}\right)^2 - \left(k_z^{(m)*}\right)^2\right) + \left(\boldsymbol{\sigma}\hat{B} + \hat{B}\boldsymbol{\sigma}\right)\left(k_z^{(n)} - k_z^{(m)*}\right)\right]\right|n\right\rangle \\
&= \left\langle m\left|\left[\left(\boldsymbol{\sigma}\hat{A} + \hat{A}\boldsymbol{\sigma}\right)\left(\left(k_z^{(n)}\right)^2 - \left(k_z^{(m)*}\right)^2\right) + \left(\boldsymbol{\sigma}\hat{B} + \hat{B}\boldsymbol{\sigma}\right)\left(k_z^{(n)} - k_z^{(m)*}\right) + 2\boldsymbol{\sigma}\hat{C} - 2\hat{C}\boldsymbol{\sigma} + 2\hat{C}\boldsymbol{\sigma} - 2\boldsymbol{\sigma}\hat{C}\right]\right|n\right\rangle \\
&= \left\langle m\left|2\boldsymbol{\sigma}\hat{A}\left(k_z^{(n)}\right)^2 + 2\boldsymbol{\sigma}\hat{B}k_z^{(n)} + 2\boldsymbol{\sigma}\hat{C}\right|n\right\rangle + \left\langle m\left|\left(\hat{A}\boldsymbol{\sigma} - \boldsymbol{\sigma}\hat{A}\right)\left(k_z^{(n)}\right)^2 + \left(\hat{B}\boldsymbol{\sigma} - \boldsymbol{\sigma}\hat{B}\right)k_z^{(n)} + \hat{C}\boldsymbol{\sigma} - \boldsymbol{\sigma}\hat{C}\right|n\right\rangle \\
&- \left\langle m\left|2\boldsymbol{\sigma}\hat{A}\left(k_z^{(m)*}\right)^2 + 2\boldsymbol{\sigma}\hat{B}k_z^{(m)*} + 2\boldsymbol{\sigma}\hat{C}\right|n\right\rangle - \left\langle m\left|\left(\hat{A}\boldsymbol{\sigma} - \boldsymbol{\sigma}\hat{A}\right)\left(k_z^{(m)*}\right)^2 + \left(\hat{B}\boldsymbol{\sigma} - \boldsymbol{\sigma}\hat{B}\right)k_z^{(m)*} + \hat{C}\boldsymbol{\sigma} - \boldsymbol{\sigma}\hat{C}\right|n\right\rangle \\
&= \frac{2}{\hbar}\left\{\epsilon_n\langle m|\boldsymbol{\sigma}|n\rangle - \epsilon_m\langle m|\boldsymbol{\sigma}|n\rangle\right\} + \frac{1}{\hbar}\left\{\langle m|[H_n,\boldsymbol{\sigma}]|n\rangle + \langle m|[H_m,\boldsymbol{\sigma}]|n\rangle\right\}
\end{aligned} \tag{3.90}$$

Since:

$$\left(k_z^{(n)} - k_z^{(m)*}\right)\left(\langle m|\boldsymbol{j}_s|n\rangle + \langle n|\boldsymbol{j}_s|m\rangle^*\right) = i\partial_z\left(\langle m|\boldsymbol{j}_s|n\rangle + \langle n|\boldsymbol{j}_s|m\rangle^*\right) \tag{3.91}$$

then, one obtains:

$$i\partial_z\left(\langle m|\boldsymbol{j}_s|n\rangle + \langle n|\boldsymbol{j}_s|m\rangle^*\right) = \frac{2}{\hbar}(\epsilon_n - \epsilon_m)\langle m|\boldsymbol{\sigma}|n\rangle - i\left\{\frac{i}{\hbar}\langle m|[H_n,\boldsymbol{\sigma}]|n\rangle + \frac{i}{\hbar}\langle m|[H_m,\boldsymbol{\sigma}]|n\rangle\right\} \tag{3.92}$$

In case $\epsilon_n = \epsilon_n$ and $k_z^{(n)} \neq k_z^{(m)*}$, one obtains:

$$i\partial_z\left(\langle m|\boldsymbol{j}_s|n\rangle + \langle n|\boldsymbol{j}_s|m\rangle^*\right) = -\frac{i}{\hbar}\left\{\langle m|[H_n,\boldsymbol{\sigma}]|n\rangle + \langle m|[H_m,\boldsymbol{\sigma}]|n\rangle\right\} \tag{3.93}$$

This relationship shows that the spin current is not always conservation quantity.

Cancellation of ghost-band currents

To anticipate the discussions on the matching conditions given in the previous section, we adopt here the continuity of the wavefunction and electronic current (the standard matching conditions) to study the consequence of the ghost-band treatment. Our conclusion will be that, through standard matching conditions, the ghost-band treatment is truly relevant to describe the full (spin-dependent) transport properties in the main conduction valleys: *i.e.,* Γ valley for direct-gap semiconductors for both electrons and holes, L valleys for the CB in the case of indirect-gap semiconductors (*e.g.* AlAs). We have already checked (without formal proofs) that the symmetry of both the wavefunction, the wave current and the spin current remain almost unchanged at the relevant valleys following the ghost-band approach.

We decompose the wave function Ψ into a form

$$\Psi_T = \begin{pmatrix}\Psi_P \\ \bar{\Psi}_G\end{pmatrix}, \tag{3.94}$$

where Ψ_T is over all full wavefunction oof the complete Hamiltonian, Ψ_P refers to the physical components and $\bar{\Psi}_G$ to the unphysical ghost part.

The boundary conditions now read: (i) The continuity of the wavefunction means that Ψ_T is continuous at each interface indicating that both of the Ψ_P and $\bar{\Psi}_G$ parts are continuous. Ψ_P is then continuous (necessary condition) at each interface and at each energy.

(ii) The continuity of the electronic current means that $\boldsymbol{J}(\Psi_T)$ is continuous at each interface which, however, does not necessary imply that $\boldsymbol{J}\Psi_P$ and $\boldsymbol{J}\bar{\Psi}_G$ are both continuous separately at each energy because of the supplementary coupling introduced.

However this important property remains true near the extrema of the valleys involved in the transport because the symmetry is conserved for both wavefunction and electronic current in these regions (derivation of the supplementary coupling is equal to zero).

Let us write the current operator in the form:

$$\boldsymbol{J} = \boldsymbol{J}_P + \boldsymbol{J}_G, \tag{3.95}$$

where $\boldsymbol{J}_P$ is a nb×nb matrix which has n×n non-zero components and dealing with the original n×n **k**.**p** Hamiltonian, and all the other blocks concerning ghost-band being zero near the Γ point.

The (spin-dependent) current flux is written at the first order in wave vector k (because of the highest order in k of coupling terms is k^2 even between the physical and phantom bands):

$$\begin{aligned} Re\langle\Psi_T|\boldsymbol{J}|\Psi_T\rangle &= Re\left\langle \Psi_P \quad \bar{\Psi}_G \left| \boldsymbol{J} \right| \begin{matrix}\Psi_P\\ \bar{\Psi}_G\end{matrix} \right\rangle \\ &= Re\left\langle \Psi_P \quad 0 \left| \boldsymbol{J}_P \right| \begin{matrix}\Psi_P\\ 0\end{matrix} \right\rangle + Re\left\langle 0 \quad \bar{\Psi}_G \left| \boldsymbol{J}_G \right| \begin{matrix}0\\ \bar{\Psi}_G\end{matrix} \right\rangle, \end{aligned} \tag{3.96}$$

By principle (matching conditions), $\mathrm{Re}\langle\Psi_T|\boldsymbol{J}|\Psi_T\rangle$ is continuous over the multilayer structure which means that the sum of the two terms are continuous but not necessary each term separately.

The current of the supplementary ghost-bands:

$$Re\left\langle 0 \quad \bar{\Psi}_G \left| \boldsymbol{J}_G \right| \begin{matrix}0\\ \bar{\Psi}_G\end{matrix} \right\rangle = \sum_{n,m} \frac{\epsilon_n^G - \epsilon_m^G}{k_z^{(n,G)} - k_z^{(m,G)*}} \langle m_G|n_G\rangle\, e^{i\left(k_z^{(n,G)} - k_z^{(m,G)*}\right)} \tag{3.97}$$

where G indicates the ghost band quantities, $k_z^{(n,G)}$ and $k_z^{(m,G)*}$ are both pure complexities; $|m_G\rangle$ and $|n_G\rangle$ describe here the ghost-band components of the total wavefunction. By increasing the ghost band energies, one may increase $k_z^{n,G}$ and $k_z^{m,G}$ as well. This results in the term $e^{i\left(k_z^{(n,G)} - k_z^{(m,G)*}\right)} \to 0$, thus one may neglect the contributions originating from the ghost-band, once the ghost-bands are sufficiently high in energy compared to the bottom of the CB. So that we obtain

$$Re\langle\Psi_T|\hat{J}|\Psi_T\rangle \simeq Re\langle\Psi_P|\hat{J}_P|\Psi_P\rangle. \tag{3.98}$$

The proof for the spin-dependent tunneling current can be considered but, by simple arguments, one can estimate that the result is equivalent so that one neglects the evanescent current contribution originating from the lower spurious VBs, which is generally the case.

Note that those rules derived here mainly concern charge current, they are generally not applicable to the case of spin-currents because of the non-zero commutation between Hamiltonian and Pauli matrices.

3.2.2 *Landauer formula from the expression of the wave current*

Ballistic transport.

In mesoscopic physics, ballistic transport relates to the transport of charge carriers in a small structure where one may assume that the charge carriers move elastically, through the active medium without scattering except for a possible reflection from a barrier. In this ballistic transport, the motion of carriers is simply described by the classical Newton second law. The ballistic transport may be observed in the system where

the mean free path of the carriers (typically the electrons) is much lager than the dimensions of the system. To that goal, together when reducing the system size, one has to increase the mean free path of electrons by reducing the impurities in the system or by lowering the temperature. In this regime, the conductance of the system may be described in the framework of Landauer Büttiker formalism which gives the relationship between the electrical resistance and the scattering properties of the system, and is going to be presented in the following.

Landauer formalism [241]

In order to derive the Landauer formula, let us now calculate the current across a given surface S perpendicular to the direction x of global electron flow, carried by the wave $\Psi_{ik_i}(\boldsymbol{r})$. Starting with the expectation value of the current density operator $\hat{\boldsymbol{i}}(\boldsymbol{r})$ over the state $|\Psi_{ik_i}\rangle$, one has:

$$\boldsymbol{j}(\boldsymbol{r}) = \langle\Psi_{ik_i}|\hat{\boldsymbol{i}}(\boldsymbol{r})|\Psi_{ik_i}\rangle = \frac{\hbar}{2im}\left[[\Psi_{ik_i}(\boldsymbol{r})]^* \frac{\partial\Psi_{ik_i}(\boldsymbol{r})}{\partial x} - \Psi_{ik_i}(\boldsymbol{r})\frac{\partial[\Psi_{ik_i}(\boldsymbol{r})]^*}{\partial x}\right] \tag{3.99}$$

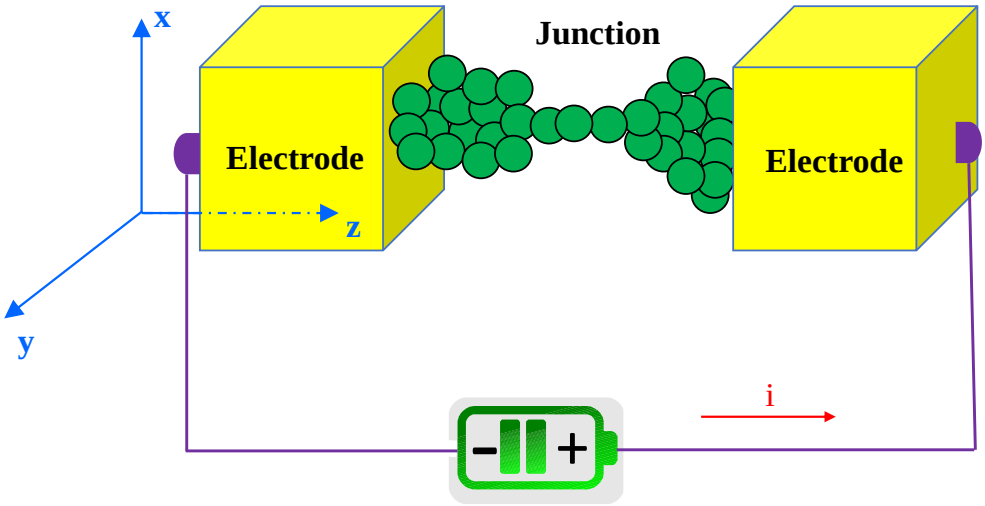

FIGURE 3.3: Scheme of a closed system, electron source plus electrode-junction-electrode structure. The electrodes are assumed to confine electrons in the x-y direction.

Integrating over a plane (x,y) perpendicular to the z direction, one observes the average current $I(E_i)$ which is carried by the state at energy E_i:

$$I(E_i) = e\int_{-\infty}^{\infty} dx \int_{-\infty}^{\infty} dy\, \boldsymbol{j}(\boldsymbol{r}) = \frac{e\hbar}{2im}\int_{-\infty}^{\infty} dx \int_{-\infty}^{\infty} dy \left[[\Psi_{ik_i}(\boldsymbol{r})]^* \frac{\partial\Psi_{ik_i}(\boldsymbol{r})}{\partial x} - \Psi_{ik_i}(\boldsymbol{r})\frac{\partial[\Psi_{ik_i}(\boldsymbol{r})]^*}{\partial x}\right] \tag{3.100}$$

Let us assume that our system is in a steady state. Therefore, the current does not depend on the position of the surface at which we evaluate it. Thus, one may evaluate it deep into the left electrode or deep into the right electrode, equivalently, and the resulting currents must be identical. Deep into the left and deep into the right electrode, the wave function $\Psi_{ik_i}(\boldsymbol{r})$ becomes:

$$\Psi_{ik_i}(\boldsymbol{r}) \rightarrow \Phi_{ik_i}(\boldsymbol{r}) + \sum_{f=1}^{N_c^L} r_{if}\Phi_{fk_f}(\boldsymbol{r}) \tag{3.101}$$

$$\Psi_{ik_i}(\boldsymbol{r}) \rightarrow \sum_{f=1}^{N_c^R} t_{if}\Phi_{fk_f}(\boldsymbol{r}) \tag{3.102}$$

where N_c^L and N_c^L are number of channels on the Left and Right electrode, respectively.

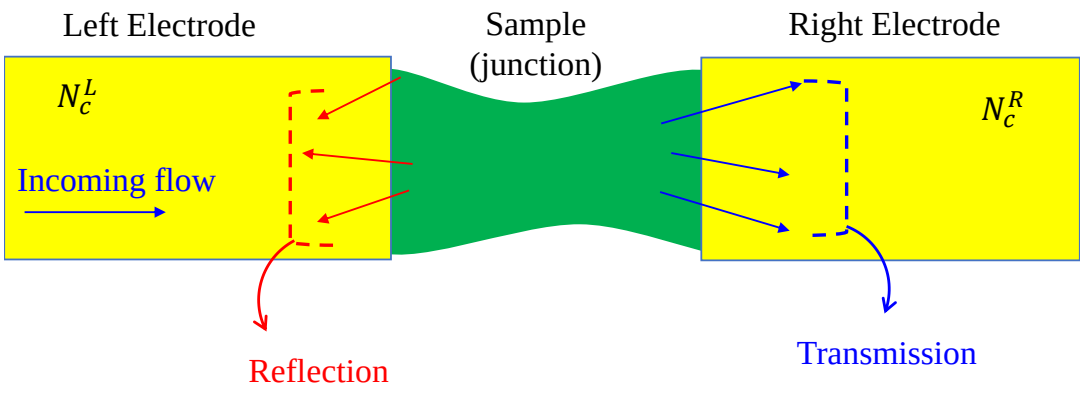

FIGURE 3.4: Reflected and transmitted wave at the junction.

Deep into the left electrode, we replace 3.101 into 3.100 to obtain:

$$I_L(E_i) = I_i(E_i) + \sum_{f=1}^{N_c^L} |r_{if}|^2 I_f(E_i) \tag{3.103}$$

where :

$$\begin{aligned} I_i(E_i) &= \frac{e\hbar}{2im}\int_{-\infty}^{\infty} dx \int_{-\infty}^{\infty} dy \left[[\Phi_{ik_i}(\boldsymbol{r})]^* \frac{\partial \Phi_{ik_i}(\boldsymbol{r})}{\partial x} - \Phi_{ik_i}(\boldsymbol{r}) \frac{\partial [\Phi_{ik_i}(\boldsymbol{r})]^*}{\partial x} \right] \\ &= \frac{v_i(k_i)}{L} \end{aligned} \tag{3.104}$$

and

$$\begin{aligned} I_f(E_i) &= \frac{e\hbar}{2im}\int_{-\infty}^{\infty} dx \int_{-\infty}^{\infty} dy \left[[\Phi_{fk_f}(\boldsymbol{r})]^* \frac{\partial \Phi_{fk_f}(\boldsymbol{r})}{\partial x} - \Phi_{fk_f}(\boldsymbol{r}) \frac{\partial [\Phi_{fk_f}(\boldsymbol{r})]^*}{\partial x} \right] \\ &= \frac{v_f(k_f)}{L} \end{aligned} \tag{3.105}$$

where $v_j(k_j)$ is the group velocity of an electron in j^{th} channel and L is the volume of the system [43]. Due to the fact that in this case, all wavevectors k_f are in the negative z direction with the opposite sign than the incident current I_i. So, if we introduce the quantity:

$$R_{if}(E_i) = |r_{if}|^2 \frac{|I_f(E_i)|}{|I_i(E_i)|} \tag{3.106}$$

as the reflection probability for a wave incident on the nanostructure with momentum $\hbar k_i$ to be scattered back into the left electrode in a state with momentum $\hbar k_f$ while the energy is conserved, then one obtains:

$$I_L(E_i) = I_i(E_i) - \sum_{f=1}^{N_c^L} |r_{if}|^2 |I_f(E_i)| = I_i(E_i)\left(1 - \sum_{f=1}^{N_c^L} R_{if}(E_i)\right) \tag{3.107}$$

Doing the same calculation deep into the right electrode, one obtains:

$$I_R(E_i) = \sum_{f=1}^{N_c^R} |t_{if}|^2 |I_f(E_i)| = I_i(E_i) \sum_{f=1}^{N_c R} T_{if}(E_i) \tag{3.108}$$

where:

$$T_{if}(E_i) = |t_{if}|^2 \frac{|I_f(E_i)|}{|I_i(E_i)|} \tag{3.109}$$

is the transmission probability that the wave with initial momentum $\hbar k_i$ is transmitted across the nanojunction into the right electrode in a final state with momentum $\hbar k_f$ at the same energy. We remind again that in a steady state, the two currents $I_L(E_i)$ and $I_R(E_i)$ have to be identical. Therefore, one finds the relation between the reflection and transmission coefficients for a wave incident from the left electrode:

$$\sum_{f=1}^{N_c^R} T_{if}(E_i) + \sum_{f=1}^{N_c^L} R_{if}(E_i) = 1 \tag{3.110}$$

which complies with the general result of Eq. 3.69. Since the motion of electrons is ballistic, then the channels are independent and the total current in the system is afterwards calculated as the sum of all currents carried by all states (channels) at all energies. Thus, one needs to integrate in energy, multiply by the density of states (number of channels per unit energy) for each momentum direction, and sum over all incident channels (both right and left motions). Since each channel represents a one-dimensional problem, the density of states per spin for the momentum $\hbar k_i$ of given direction is simply:

$$D_i(E_i) dE_i = \frac{L}{2\pi} dk_i \tag{3.111}$$

or

$$D_i(E_i) = \frac{L}{2\pi} \frac{dk_i}{dE_i} = \frac{L}{2\pi\hbar} \frac{1}{v_i(k_i)} \tag{3.112}$$

where $v_i(k_i)$ is the group velocity of an electron in i^{th} channel.

Assuming that the electro-chemical potential Δ at the left and the right electrodes respectively, are μ_L and μ_R, the local equilibrium distribution appropriate to the corresponding to the left and right electrodes are:

$$f_L(E) = \frac{1}{e^{\frac{E-\mu_L}{k_B t}} + 1} \tag{3.113}$$

$$f_R(E) = \frac{1}{e^{\frac{E-\mu_R}{k_B t}} + 1} \tag{3.114}$$

Note that we are dealing with a steady state, therefore, it is possible to calculate this current anywhere in space. At an arbitrary point deep into the right lead, one gets the total current:

$$
\begin{aligned}
I &= 2e \int dE \left\{ \sum_{i=1}^{N_c^L} \sum_{f=1}^{N_c^R} f_L(E) D_i(E) I_i(E) T_{if}(E) - \sum_{i=1}^{N_c^R} f_R(E) D_i(E) I_i(E) \left[1 - \sum_{f=1}^{N_c^L} R_{if}(E) \right] \right\} \\
&= 2e \int dE \left\{ \sum_{i=1}^{N_c^L} \sum_{f=1}^{N_c^R} f_L(E) D_i(E) I_i(E) T_{if}(E) - \sum_{i=1}^{N_c^R} \sum_{f=1}^{N_c^L} f_R(E) D_i(E) I_i(E) T_{if}(E) \right\} \\
&= \frac{2e}{2\pi\hbar} \int dE \left[f_L(E) T_{LR}(E) - f_R(E) T_{RL}(E) \right]
\end{aligned}
\tag{3.115}
$$

where from Eqs. 3.104, 3.105 and 3.112 one has

$$
D_i(E) I_i(e) = \frac{1}{2\pi\hbar} \tag{3.116}
$$

and we have defined the total transmission coefficient at a given energy as:

$$
T_{RL}(E) = \sum_{i=1}^{N_c^R} \sum_{f=1}^{N_c^L} T_{if}(E) = \sum_{i=1}^{N_c^R} \tilde{T}_i(E) \tag{3.117}
$$

and

$$
T_{LR}(E) = \sum_{i=1}^{N_c^L} \sum_{f=1}^{N_c^R} T_{if}(E) = \sum_{i=1}^{N_c^L} T_i(E) \tag{3.118}
$$

where

$$
\tilde{T}_i(E) = \sum_{f=1}^{N_c^L} T_{if}(E) \tag{3.119}
$$

and

$$
T_i(E) = \sum_{f=1}^{N_c^R} T_{if}(E) \tag{3.120}
$$

Since the particle flux must be conserved, the total transmission coefficient from left to right must be equal to the total transmission coefficient from right to left.

$$
T_{RL}(E) = T_{LR}(E) \equiv T(E) \tag{3.121}
$$

Combining 3.115 and 3.121 one gets:

$$
I = \frac{e}{\pi\hbar} \int dE \left[f_L(E) - f_R(E) \right] T(E) \tag{3.122}
$$

The zero-bias limit:

In the limit of zero bias or $(\mu_R - \mu_L) \to 0$ where μ_L and μ_R are equilibrium fermi energy on the left and right electrodes respectively, one may use the approximation:

$$
f_R(L) - f_R(E) = -\frac{\partial f_R(E)}{\partial E} (\mu_L - \mu_R) + O\left[(\mu_L - \mu_R)^2 \right] \tag{3.123}
$$

Then the 3.122 can be written to the first order in $(\mu_L - \mu_R)$ as:

$$I = \frac{e}{2\pi\hbar}(\mu_L - \mu_R)\int dE \left(-\frac{\partial f_R(E)}{\partial E}\bigg|_{\mu_R}\right) T(E) \tag{3.124}$$

If we now consider the limit when the temperature $T \to 0$, then the local Fermi-Dirac distribution $f_R(E)$ becomes a step function and its energy derivative becomes a δ function centered at the right electro-chemical potential μ_R. The equation 3.124 then becomes:

$$I = \frac{e}{2\pi\hbar}(\mu_L - \mu_R)T(\mu_R) = \frac{e}{2\pi\hbar}T(\mu_R)V \tag{3.125}$$

where the transmission coefficient is evaluated at the right electro-chemical potential. Equivalently, one may choose to expand the right local Fermi-Dirac distribution to get:

$$I = \frac{e}{2\pi\hbar}(\mu_L - \mu_R)T(\mu_L) = \frac{e^2}{2\pi\hbar}T(\mu_L)V \tag{3.126}$$

where now the transmission coefficient is evaluated at the left electrochemical potential. These two equations 3.125 and 3.126 are both correct since we are working in the limit in which μ_L and μ_R differ only sightly from each other. One can assume that they both differ negligibly from the Fermi energy E_F of the electron gas at equilibrium, with μ_L an infinitesimal energy ϵ above and μ_R an infinitesimal energy ϵ below the Fermi energy:

$$\mu_L \approx E_F + \epsilon \tag{3.127}$$

$$\mu_R \approx E_F - \epsilon \tag{3.128}$$

The transmission coefficient evaluated at the left or the right electrochemical potential is thus:

$$T(\mu_L) = T(E_F + \epsilon) \approx T(E_F - \epsilon) = T(\mu_R) \approx T(E_F) \tag{3.129}$$

with this approximation, one finally gets:

$$I = \frac{e^2}{\pi\hbar}T(E_F)V \tag{3.130}$$

which is well known as the Landauer formula giving the conductance:

$$G = \frac{e^2}{\pi\hbar}T(E_f) \tag{3.131}$$

3.3 Calculation method for the tunneling problem within semiconductor heterostructures

As examples of using multiband **k.p** platforms in the tunneling problem through a heterostructure, we describe in this part the details of the calculation techniques implemented for investigating the electronic properties of spin-orbit-split semiconductors and multilayers. These calculation techniques are based on the transfer or scattering matrix formalism which will be described in detail in section C.1. The readers

may refer to this section (section C.1) concerning the relevant definitions and notations of the scattering (or transfer) matrix.

3.3.1 Resonant tunneling

A typical device under investigation is a quantum well embedded between barriers with different energy gaps including possible surface potentials. Such structure displays in Fig.3.5, will be the focus of the following calculations performed using an 30- and 40-band tunneling platform codes.

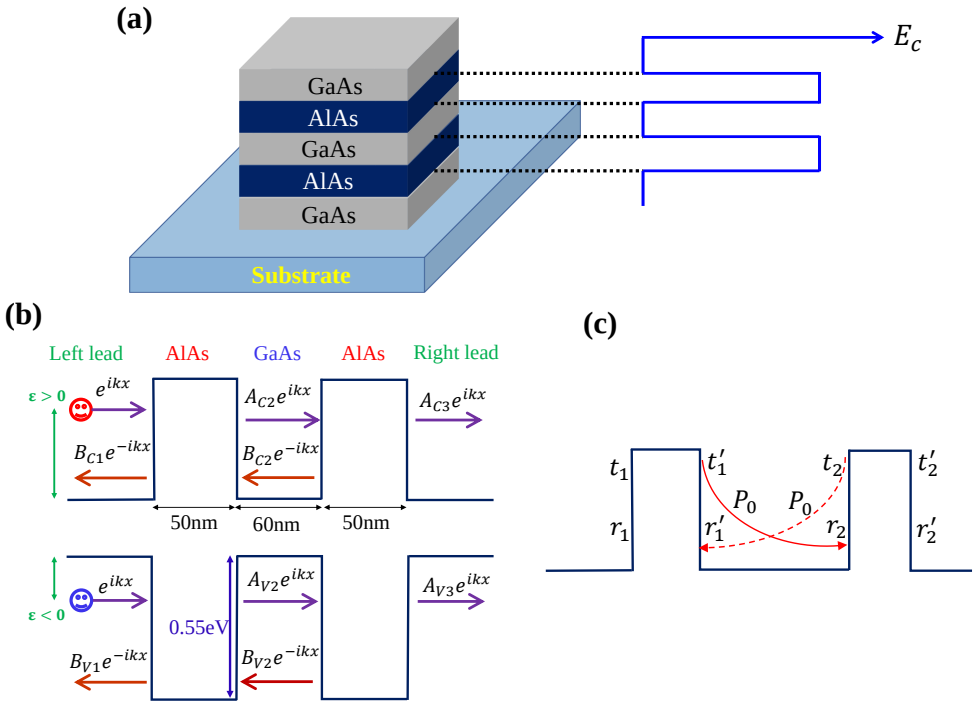

FIGURE 3.5: (a) Scheme of GaAs/AlAs quantum well structures by sandwiching the middle GaAs layer between two AlAs barriers. (b) Resonant tunneling through GaAs/AlAs quantum well structure together with the corresponding amplitude of the waves. (c) Indication of transmission and reflection coefficients as well as propagation inside the considered quantum well structure.

Concerning resonant tunneling problems, one has to consider the transmission coefficient of an electron tunneling through a quantum well structure. In figure 3.6c, we indicate the transmission and reflection coefficients as well as the propagation within the considered GaAs/AlAs quantum well structure. If we denote the transfer matrix of left and right barriers as T_1 and T_2 respectively, the propagation matrix within quantum well as Q and the total transfer matrix of the structure as T, then one has:

$$T_1 = \begin{bmatrix} t_1^{-1} & -t_1^{-1}r_1^{'} \\ r_1 t_1^{-1} & t_1^{'} - r_1 t_1^{-1} r_1^{'} \end{bmatrix} \tag{3.132}$$

$$T_2 = \begin{bmatrix} t_2^{-1} & -t_2^{-1}r_2^{'} \\ r_2 t_2^{-1} & t_2^{'} - r_2 t_2^{-1} r_2^{'} \end{bmatrix} \tag{3.133}$$

$$Q = \begin{bmatrix} P_0^{-1} & 0 \\ 0 & P_0 \end{bmatrix} \tag{3.134}$$

and

$$T = \begin{bmatrix} t^{-1} & -t^{-1}r' \\ rt^{-1} & t' - rt^{-1}r' \end{bmatrix} \tag{3.135}$$

Note that, using the multipliable properties of transfer matrix, for whole structure, the transfer matrix T

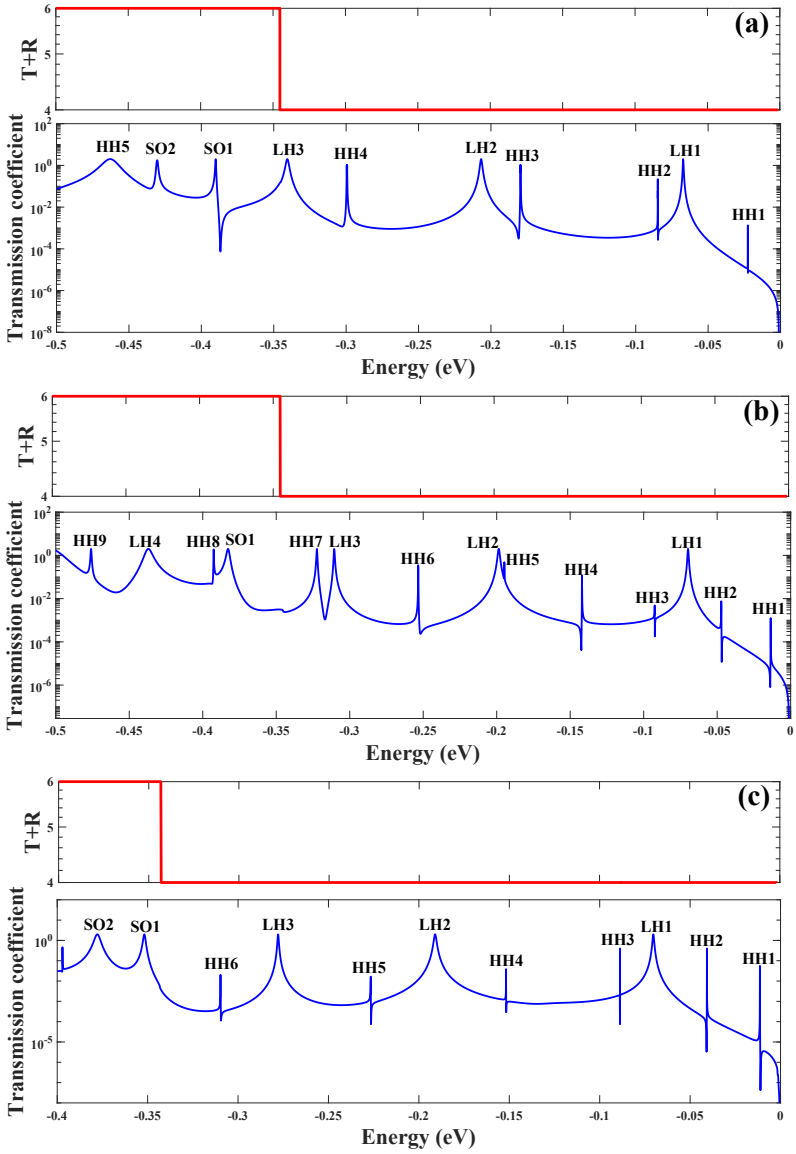

FIGURE 3.6: Calculation of transmission coefficient (blue) and sum of transmission and reflection coefficient (red) for resonant tunneling through GaAs/AlAs quantum wells with growth directions along three characteristic directions: [001], [110] and [111] (figures (a), (b) and (c) respectively) with normal incidence $k_{||} = 0$ via 30-band ***k.p*** method.

can be constructed from T_1, T_2 and Q as following:

$$T = T_1 * Q * T_2 \tag{3.136}$$

leading to a relationship:

$$\begin{bmatrix} t^{-1} & -t^{-1}r' \\ rt^{-1} & t' - rt^{-1}r' \end{bmatrix} = \begin{bmatrix} t_1^{-1} & -t_1^{-1}r_1' \\ r_1t_1^{-1} & t_1' - r_1t_1^{-1}r_1' \end{bmatrix} \begin{bmatrix} P_0^{-1} & 0 \\ 0 & P_0 \end{bmatrix} \begin{bmatrix} t_2^{-1} & -t_2^{-1}r_2' \\ r_2t_2^{-1} & t_2' - r_2t_2^{-1}r_2' \end{bmatrix} \tag{3.137}$$

giving:

$$t^{-1} = t_1^{-1} P_0^{-1} \left[\mathbb{I} - P_0 r_1^{'} P_0 r_2 \right] t_2^{-1} \tag{3.138}$$

where $\mathbb{I}$ is the identity matrix.

Finally, one obtains the transmission coefficient equation for an electron tunnel through the quantum well structure in terms of transmission and refection elements of barriers as well as propagation within quantum well as following:

$$t = t_2 \left[\mathbb{I} - P_0 r_1^{'} P_0 r_2 \right]^{-1} P_0 t_1 \tag{3.139}$$

Equation 3.139 gives rise the conditions for resonant tunneling through a quantum well structure:

$$det \left[\mathbb{I} - P_0 r_1^{'} P_0 r_2 \right] = 0 \tag{3.140}$$

This is a well-known Fabry–Pérot condition for resonant mode in optical cavity [242, 243].

Figure 3.6 displays the typical electronic resonance occurring in the valence band under normal incidence ($k_{||} = 0$) for the three different growth directions [001], [110] and [111] of GaAs/AlAs 6nm QWs calculated by 30 bands **k.p** method. The zero-energy is chosen at the top of VB. One may observe resonances in transmission corresponding to resonant levels (or quantized) states in the quantum well (HH1, LH1, HH2, HH3,...). We also checked that the sum of the reflection (R) and transmission (T) coefficient $T + R = N$ where N is the number of incoming channels (propagating waves). This relation $T + R = N$ shows a physical requirement that the current is ensured to be conserved.

3.3.2 Bound states and quasi bound states

Bound states

In classical mechanics, bounded motion is always possible for a particle near a point of stable equilibrium. However, in quantum mechanics, a bound state is not necessarily allowed, even though the potential energy function may describe an attractive force. Since the method of solution for a particular problem will often depend on whether the energy spectrum is discrete or continuous, it is useful to know in advance whether bound state exist. In this section, we are now going to describe bound state in quantum well structure from physical point of view with transmitted and reflected wave as well as from mathematical point of view with scattering or transfer matrix approach and a good agreement between the two.

Physical point of views

A bound state of an electron in a quantum well can be figured out as the confinement of the electron emitting from an inner source within a quantum well structure (depicted in Fig 3.7). Without loss of general, we may assume that the source is close to the right barrier and for convenience we consider here the one dimensional problem. At a certain time, the source emits an electron heading to the right barrier. This electron reflects at right barrier then propagates to the left barrier and reflects again at left barrier and finally propagates back to the initial position close to the source.

The condition for a bounded motion or a bound state of the electron is that the phase of wavefunction of the electron at the initial and the ending states at right barrier are the same. If we call Ψ_{int} the initial wavefunction of the electron, then the wavefunction of the electron at the end of the process can be determine by following relation:

$$\Psi_{end} = \left[P_0 r_1^{'} P_0 r_2 \right] \Psi_{int} \tag{3.141}$$

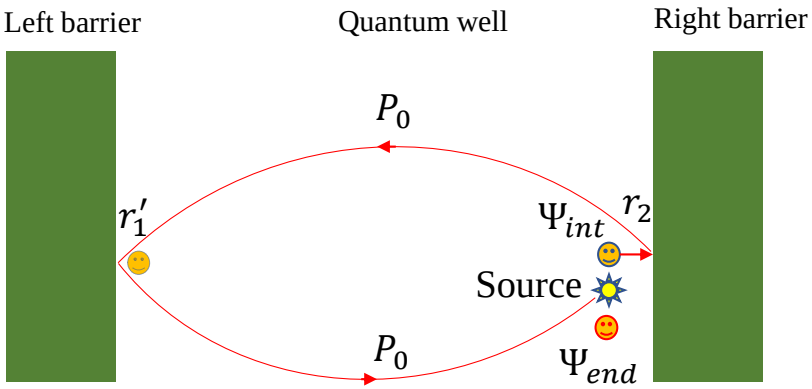

FIGURE 3.7: Scheme of bounded motion or bound state of an electron in a quantum well structure. Ψ_{int} is the initial wavefunction of the electron and Ψ_{end} is the ending wavefunction of the electron after one (or many) period of motion; $r_1^{'}$ and r_2 are the reflection coefficient of the left barrier and right barrier, respectively; P_0 is the propagation within quantum well (thank to the inversion time symmetry, the propagation from left to right and from right to left are the same and denoted by P_0).

giving rise the conditions for bound state:

$$\left[P_0 r_1^{'} P_0 r_2\right] \Psi_{int} = \Psi_{int} \tag{3.142}$$

or equivalently:

$$\left[\mathbb{I} - P_0 r_1^{'} P_0 r_2\right] \Psi_{int} = 0 \tag{3.143}$$

yielding non trivial solutions if:

$$det\left[\mathbb{I} - P_0 r_1^{'} P_0 r_2\right] = 0 \tag{3.144}$$

The wavefunction Ψ_{int} can be obtained as a linear combination of eigenfunctions of $\left[\mathbb{I} - P_0 r_1^{'} P_0 r_2\right]$ and the bound state wavefunction within whole quantum well structure then can be constructed from Ψ_{int} via scattering or transfer matrix method.

Description of bound state in quantum well via transfer and scattering matrix

One of the main interests of the scattering (or transfer) matrix method is that one may characterize the bound state of quantum-well structures or more complex heterostructures to calculate accurately the bound state energy and exact eigenvector symmetry components in a multiband approach [244, 245]. We propose the readers to refer to section C.1 for the fulfill definitions of the amplitude of the wavefunction $\boldsymbol{a}_0$ and $\boldsymbol{b}_N$ as well as scattering (or transfer) matrix.

The key point in this case is that the wavefunction decays on both sides of potential profile formed by the structure leading to a so-called outgoing wavefunction solution [245]. Then we may obtain the correct solution of bound states in quantum wells by considering $\boldsymbol{a}_0 = [0]$ and $\boldsymbol{b}_N = [0]$ (depicted in Fig. 3.8) where $[0]$ indicates the vector zero. In the framework of transfer matrix $\boldsymbol{T}(0,n)$ method, one obtains (see section C.1 for the definitions of vectors $\boldsymbol{a}_0$, $\boldsymbol{b}_N$ and $\boldsymbol{T}(0,n)$ transfer matrix):

$$\begin{bmatrix} 0 \\ \boldsymbol{b}_0 \end{bmatrix} = \boldsymbol{T}(0,N) \begin{bmatrix} \boldsymbol{a}_N \\ 0 \end{bmatrix} = \begin{bmatrix} T_{11} & T_{12} \\ T_{21} & T_{22} \end{bmatrix} \begin{bmatrix} \boldsymbol{a}_N \\ 0 \end{bmatrix} \tag{3.145}$$

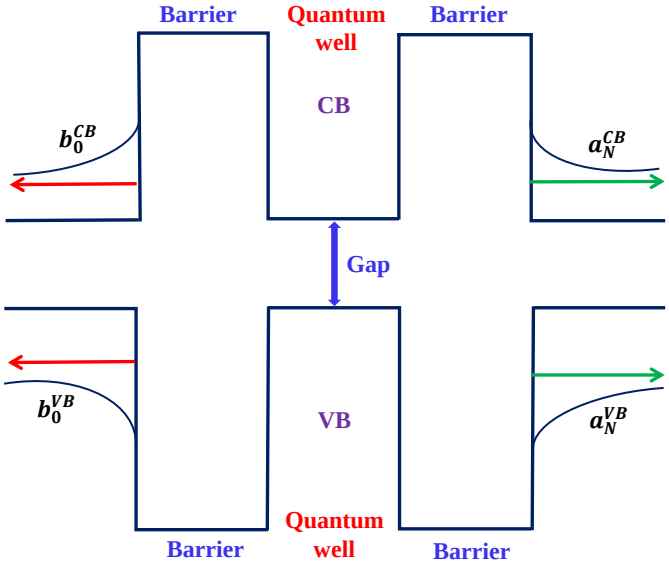

FIGURE 3.8: Scheme of bound state wavefunction in quantum well. Outside of quantum well, the wave function decays exponentially which means that $\boldsymbol{a}_0 = \boldsymbol{b}_N = [0]$.

The coefficients $\boldsymbol{a}_N$ and $\boldsymbol{b}_0$ may be eliminated from above equation to give:

$$T_{11}\boldsymbol{a}_N = 0 \tag{3.146}$$

$$T_{21}\boldsymbol{a}_N - \boldsymbol{b}_0 = 0 \tag{3.147}$$

leading to:

$$\begin{bmatrix} T_{11} & 0 \\ T_{21} & -1 \end{bmatrix} \begin{bmatrix} \boldsymbol{a}_N \\ \boldsymbol{b}_0 \end{bmatrix} = 0 \tag{3.148}$$

The non trivial solutions of Eq. 3.148 yield to a determination equation [245]

$$det \begin{bmatrix} T_{11} & 0 \\ T_{21} & -1 \end{bmatrix} = 0 \tag{3.149}$$

or

$$Det[T_{11}] = 0 \tag{3.150}$$

If we use transfer matrix $\boldsymbol{T}(n,0)$ defined in section C.1, then we might obtain the equivalent equation for bound state as following:

$$Det[\overline{T}_{22}] = 0 \tag{3.151}$$

Note that, in the framework of the scattering matrix formalism, it becomes more difficult to use the $\boldsymbol{S}(0,n)$ scattering matrix to describe the bound states since this requires the value of $\boldsymbol{a}_0$ and $\boldsymbol{b}_n$ that are presently unknown quantities (to describe scattering wave). Therefore, in this case, one needs to switch to the scattering matrix $\boldsymbol{S}(n,0)$ describing the scattering process for outgoing waves to obtain:

$$\begin{bmatrix} 0 \\ 0 \end{bmatrix} = \boldsymbol{S}(n,0) \begin{bmatrix} \boldsymbol{a}_N \\ \boldsymbol{b}_0 \end{bmatrix} \tag{3.152}$$

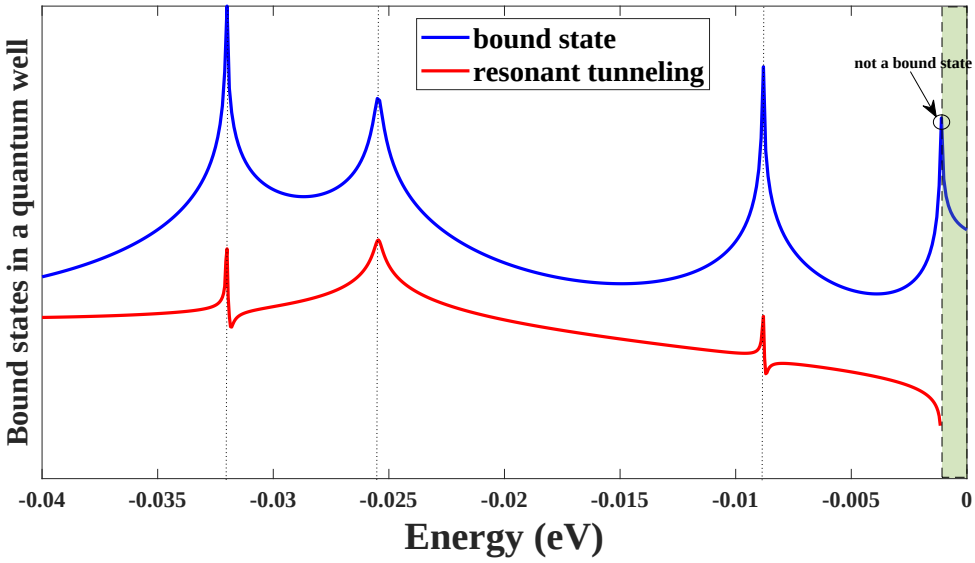

FIGURE 3.9: Resonant tunneling (red curve) and $Det[S(0,N)]$ (blue curve) in arbitrary units as the functions of energy of an electron in (In,Ga)As/GaAs 10 nm quantum well structure. The positions of the maximum points corresponding to the bound state solutions of blue curve are exactly the same as the resonant peaks of red curve excepts the first maxima (of blue curve) which is not a bound state solution, but a tuning point of current from pure evanescent to propagating states.

since $\boldsymbol{a}_0 = [0]$ and $\boldsymbol{b}_N = [0]$. This gives:

$$Det[\boldsymbol{S}(N,0)] = 0 \tag{3.153}$$

Using the relation C.26 and the properties of determinants:

$$Det[X + AB] = Det[X]Det[I + AX^{-1}B] \tag{3.154}$$

where I is identity matrix, one might show that 3.150, 3.151 and 3.153 are equivalent. After solving the equation 3.150 or 3.153, we can extract the eigenenergies that is the quantized energy of bound states in the quantum well and build up the bound state wavefunction afterward.

The equivalence between the physical point of views and scattering matrix description of bound state in quantum well

In order to make above descriptions united, let us now prove that the Eq. 3.150 is equivalent to Eq.3.144. Indeed, from Eq. 3.138 we have:

$$T_{11} = t_1^{-1}P_0^{-1}\left[\mathbb{I} - P_0 r_1^{'} P_0 r_2\right] t_2^{-1} \tag{3.155}$$

then the conditions for bound states 3.150 can be re-written:

$$det\left\{t_1^{-1}P_0^{-1}\left[\mathbb{I} - P_0 r_1^{'} P_0 r_2\right] t_2^{-1}\right\} = det\left[t_1^{-1}P_0^{-1}\right] * det\left[\mathbb{I} - P_0 r_1^{'} P_0 r_2\right] * det\left[t_2^{-1}\right] = 0 \tag{3.156}$$

leading to:

$$det\left[\mathbb{I} - P_0 r_1^{'} P_0 r_2\right] = 0 \tag{3.157}$$

In the other words, we obtain a fact that the physical point of view of bound state and transfer (or scattering) matrix description of bound state in quantum well are the same as expected.

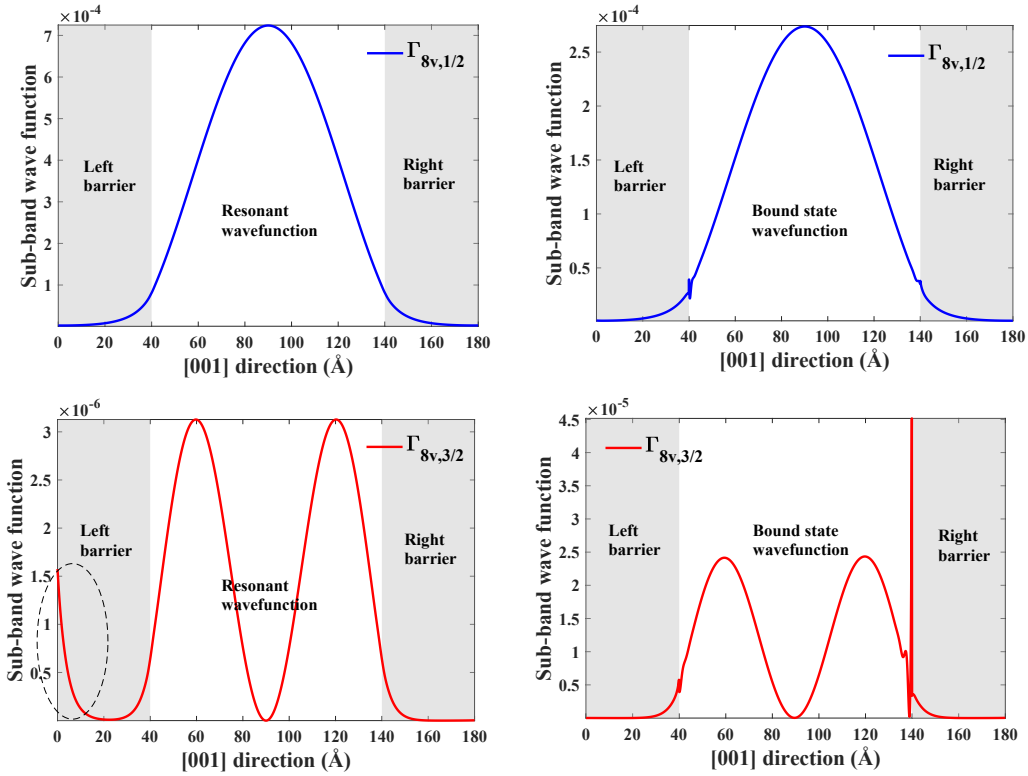

FIGURE 3.10: Scattering wavefunction (left pannel) and bound state wavefunction (right pannel) correspond to lh1 energy level in (In,Ga)As/GaAs 10 nm quantum well. The blue curves are the $\Gamma_{8v,1/2}$ subband wavefunction and the red curves are the $\Gamma_{8v,3/2}$ subband wavefunction.

Nummerical calculations of bound state for an electron in quantum well based on multiband k.p method

Note that from a numerical point of view, we can solve 3.153 by varying the energy and find the local minimum of $Det[S(N,0)]$ or local maximum of $\frac{1}{Det[S(N,0)]} = Det[S(0,N)]$ v.s energy (the same for 3.144, 3.150 or 3.151). However, the accuracy to find the numerical local extreme points depends on the variable resolution (in particular, the energy). Therefore, these numerical local extreme points are, sometime, not accurate enough to describe the solutions of 3.153. In order to calculate $\boldsymbol{a}_N$ and $\boldsymbol{b}_0$, numerically, one notices that if $Det[S(N,0)] = 0$, then, it is possible for a zero eigenvalue of $S(N,0)$ to exist, with that $\boldsymbol{a}_N$, $\boldsymbol{b}_0$ can be linear combination of eigenvectors corresponding to this zero eigenvalue. Thus, numerically, a_N and b_0 are determined by solving the general eigenvalue problem:

$$S(N,0) * \tilde{u} = \lambda \tilde{u} \tag{3.158}$$

where $\tilde{u}$ and λ are the eigenvector and eigenvalue of $S(N,0)$, respectively. Our method then, consists in extracting the eigenvalue λ and choosing the absolute minimum one λ_{min} as well as the corresponding eigenvectors. One can then consider that $\boldsymbol{a}_N$, $\boldsymbol{b}_0$ correspond to those eigenvectors.

Figure 3.9 shows a comparison between resonant tunneling (red curve) and $Det[S(0,N)]$ (blue curve) in arbitrary units as the functions of energy of an electron in (In,Ga)As/GaAs 10 nm quantum well structure. One observed that excepts the first maximum point of blue curve, the positions of three other maximum points corresponding to a bound state solutions of blue curve are exactly the same as the resonant peaks of red curve (as expected). One need to note that, mathematically, a bound state solutions will satisfy the condition 3.153 but not vice versa. Therefore one has to eliminate the bad solutions for bound states of Eq.

3.153 (by comparing with resonant tunneling). In this case, the first maxima of blue curve is not a bound state solution, but a tuning point of current from pure evanescent state inside the barrier to propagating state within the quantum well. Figure 3.10, on the other hand, shows the scattering wavefunction (from resonant tunneling) and bound state wavefunction corresponding to the LH1 energy level in (In,Ga)As/GaAs 10 nm quantum well. Except the amplitudes, the shapes of $\Gamma_{8v,1/2}$ subband wavefunctions are the same in both scattering and bound state calculations, but however the $\Gamma_{8v,3/2}$ subband wavefunctions within the left barrier are different. This can be understandable since the wavefunction from scattering method is not a true bound state wavefunction.

Quasi bound states

A quasi bound state may exist in a quantum well limited by thin barriers. The electron in its fundamental state is temporarily trapped in the quantum well with a maximum of occupation probabilities at the middle of quantum well, and then escapes to the leads at a certain moment via quantum tunneling phenomena (this is very similar to alpha decay phenomena) [43, 246].

In a semi-classical point of view, one can imagine the following scheme: The electron is temporarily confined between the two barriers. It moves back and forth and collides to the two barriers, however, each time the electron hits the barriers, it may tunnel through the barriers with a small probability making the state of electron in quantum well to be a quasi-bound state instead of a truly bound state [244, 246, 247].

In order to estimate the probability of an electron tunneling through a barrier to consider a quasi bound state in quantum well structure, we assume that the barrier thickness is thick enough to make the electron to feel as if it is moving between two infinite thick barriers, and therefore, the motion of an electron in quantum well possesses stable state (constructive interference). The simplest approximation to calculate the corresponding state in a confined region is to use the Bohr-Summerfeld quantization principle giving the energy spectrum of electrons in a quantum well in a familiar formula as following[43, 244]

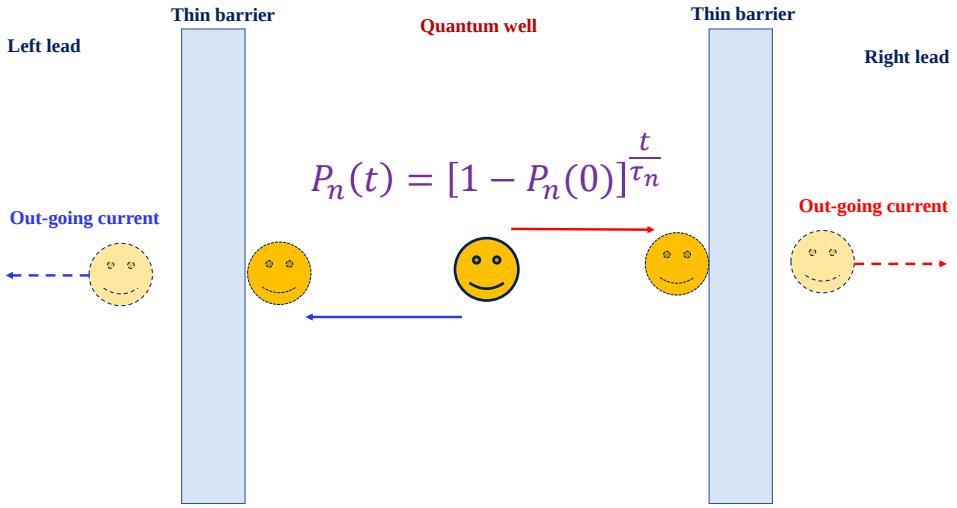

FIGURE 3.11: Scheme of a quasi-bound state in a quantum well structure. An electron with maximum occupation probabilities at the middle of quantum well decrease with time since each time the electron hits the barriers, it may tunnel through barrier with a small probability.

$$E_n = \frac{\hbar\pi^2 n^2}{2md^2} \tag{3.159}$$

Now let us consider an electron in the n^{th} state associating to the classical momentum $p_n = \hbar k_n = \frac{\hbar \pi n}{d}$ and classical velocity $v_n = \frac{p_n}{m}$ between the two barriers. Each time when the electron hits the barrier's wall, it may tunnel through the barrier with a probability given by the WKB (named after Wentzel, Krammers, and Brillouin) approximation [43, 244]

$$P_n = exp\left\{-\int_{x_1}^{x_2} |q(x)|dx\right\} \tag{3.160}$$

where x_1 and x_2 are the classical tuning points, $q(x)$ is the imaginary wave number in classically forbidden. The period of motion is $\tau_n = \frac{d}{v_n}$. After the period of time t, the number of collision is $N \approx \frac{t}{\tau_n}$ then the probability to find the electron in quantum well can be estimated as:

$$P_n(t) = [1 - P_n(0)]^{\frac{t}{\tau_n}} \tag{3.161}$$

From a quantum mechanical point of view, one can describe this phenomena by assuming that the electron can be described by a wavefunction with a generalized imaginary energy part, however much smaller than its real part [246–248]. The existence of a imaginary part in the energy makes the probability to find the electron in quantum well decreasing exponentially with time according to Eq. 3.160. We emphasize that the imaginary part is much smaller than the real part and plays the role of a perturbation in order to ensure the stable state of the electron.

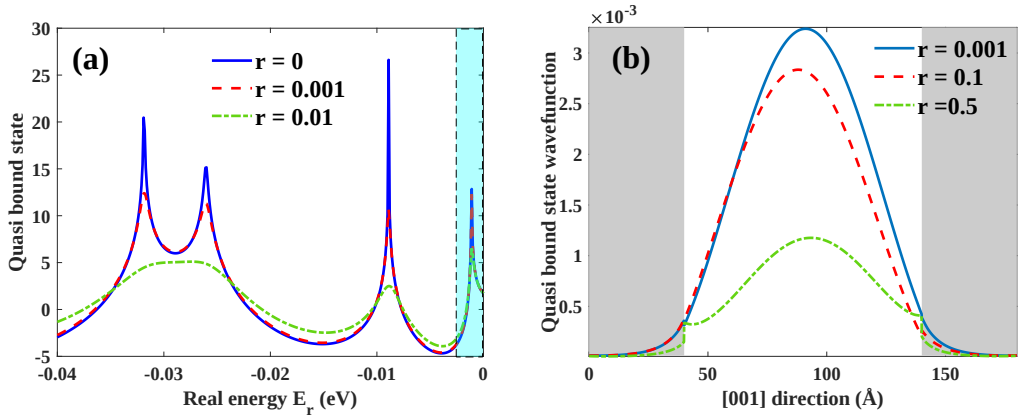

FIGURE 3.12: (a) The $Det[S(0,N)]$ as function of energy with different ratios $r = \frac{E_r}{E_i}$ where E_r and E_i are the real and imaginary part of generalized energy E, respectively, of an electron in (In,Ga)As/GaAs 10 nm quantum well structure. As the same as previous argument with bound state solutions, the first maximum of the curves here are not bound state solutions. (b) The quasi bound state wavefunction corresponding to the lh1 energy level in (In,Ga)As/GaAs 10 nm quantum well structure with different values of r.

By a similar argument, we can state that the quasi bound state in a quantum well can be described by 3.150 or 3.153 but with the imaginary part in energy. From a numerical calculation point of view, we can solve 3.150 by varying the energy $E = E_r + iE_i$ and find the local minimum of $Det[S(N,0)]$ or local maximum of $\frac{1}{Det[S(N,0)]} = Det[S(0,N)]$. Here E_r and E_i are the real part and imaginary part of the generalized energy, respectively. Figure 3.12 displays the $Det[S(0,N)]$ as function of energy (a) and the wavefunction (b) of an electron in a (In,Ga)As/GaAs 10 nm quantum well with different ratios $r = \frac{E_r}{E_i}$. It shows that when one increases the value of r then the stable of quasi bound state decreases since the local maximum of $Det[S(0,N)]$ v.s energy become smaller leading to the smaller occupation probabilities (the wavefunction

in Fig 3.12b) of the electron in quantum well as expected from above argument: the imaginary part in the energy makes the probability to find the electron in quantum well decreasing with time.

3.3.3 Structures with symmetry reduction from T_d (D_{2d}) to C_{2v} at the interfaces

We have considered transport properties of the electrons through a heterostructure based on III-V semiconductors like GaAs/AlAs quantum well structures made by sandwiching the middle GaAs layer between two AlAs barriers, but by far, neglected all interface effects. Note that the point group of III-V bulk semiconductors such as GaAs, AlAs, InAs, is the T_d group, however, the interfaces of related heterostructures, e.g., GaAs/AlAs quantum wells grown along [001] direction (z direction), depicted in Fig. 3.13, possess a lower symmetry , which is C_{2v} [30]. The C_{2v} symmetry is lower than T_d because a rotation which transforms Ga into Al is missing (see Fig 3.13). Particularly, the reduced symmetry from T_d to C_{2v} at the interface of heterostructure leads to the mixing of the heavy hole (HH) $|\pm\frac{3}{2}\rangle$ and light hole (LH) $|\pm\frac{1}{2}\rangle$ states with the same parity (the parity with respect to the element S_{4z} of the group T_d). We are now going to consider the consequence of this resulting mixing on the boundary conditions at the interface.

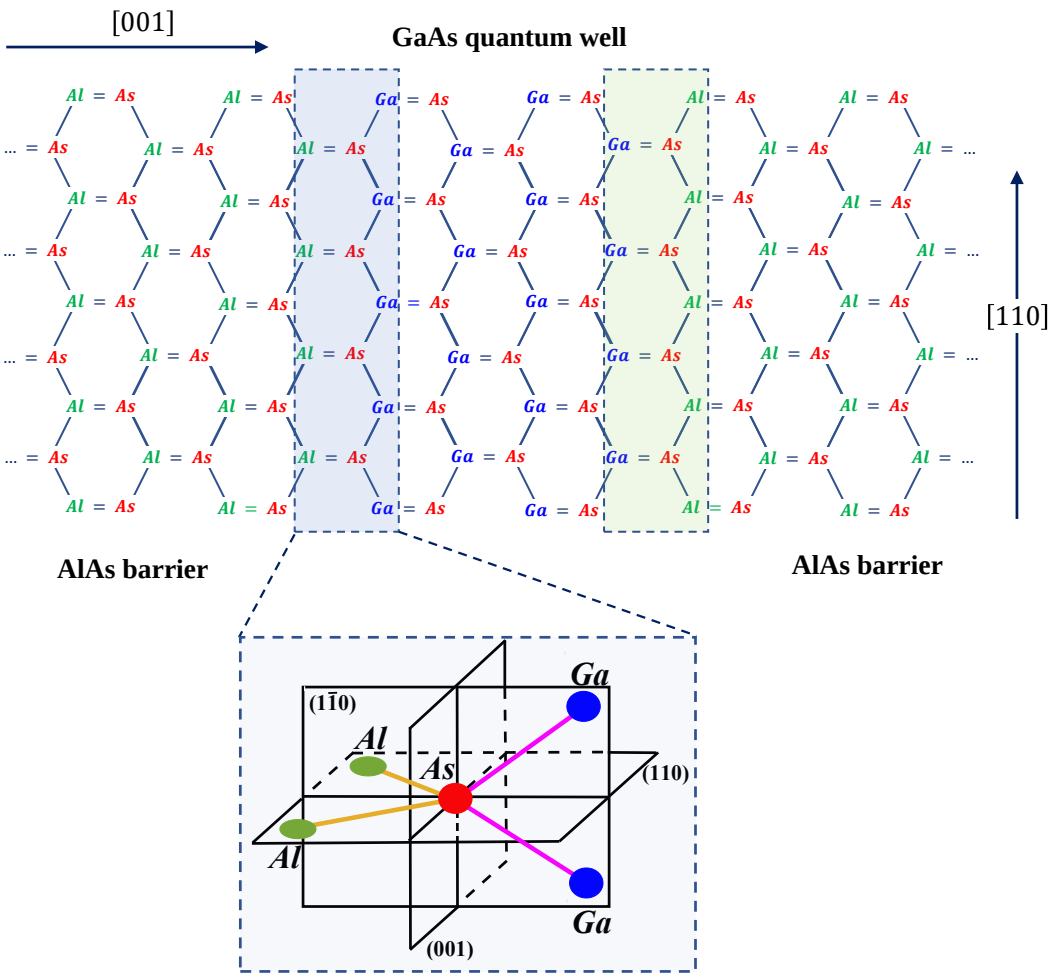

FIGURE 3.13: Schematics of the nearest neighbors of an As interface atom of GaAs/AlAs quantum well structure where the point symmetry C_{2v} of a single heterosjunction contains the twofold rotation axis C_2 parallel to the growth direction [001] and two mirror planes [110] and $[1\bar{1}0]$

Within the envelope function theory presented in section 2.5.1, the wavefunction of an electron in the quantum structure can be expanded in the $|J,M\rangle$ and $|L,S\rangle$ basis as:

$$\Psi(\boldsymbol{r}) = \frac{e^{i\boldsymbol{k}_{||}\boldsymbol{\rho}}}{\sqrt{\mathfrak{A}}} \sum_{L,S} f_{L,S}|L,S\rangle = \frac{e^{i\boldsymbol{k}_{||}\boldsymbol{\rho}}}{\sqrt{\mathfrak{A}}} \sum_{J,M} F_{J,M}|J,M\rangle \tag{3.162}$$

Here, z is the growth axis, $\boldsymbol{k}_{||}$ is the in-plane wave vector with two components (k_x, k_y) and $\mathfrak{A}$ is the normalization area, $\boldsymbol{r} = \boldsymbol{\rho} + \boldsymbol{z}$ with $\boldsymbol{\rho} = \boldsymbol{x} + \boldsymbol{y}$. Note that $\boldsymbol{k}_{||}$ is supposed to be conserved within the whole heterostructure and the envelope functions $f_{L,S}$ or $F_{J,M}$ depend only on the coordinate z. Thus, the standard matching condition for wavefunction [218] may be written , now, in the framework of the envelope function theory according to:

$$\begin{aligned} \boldsymbol{f}_A &= \boldsymbol{f}_B \\ (\boldsymbol{J}_z \boldsymbol{f})_A &= (\boldsymbol{J}_z \boldsymbol{f})_B \end{aligned} \tag{3.163}$$

for the envelope $f_{L,S}$ function, where $\boldsymbol{f}$ is the column vector with the components $f_{L,S}$ and:

$$\begin{aligned} \boldsymbol{F}_A &= \boldsymbol{F}_B \\ (\boldsymbol{J}_z \boldsymbol{F})_A &= (\boldsymbol{J}_z \boldsymbol{F})_B \end{aligned} \tag{3.164}$$

for the envelope $F_{J,M}$ functions, where $\boldsymbol{F}$ is the column vector with the components $F_{J,M}$. The subscripts A, B indicate the different materials on the left and the right interfaces, say AlAs or GaAs; $\boldsymbol{J}_z = \frac{1}{\hbar}\frac{\partial H}{\partial k_z}$ is the z component of the current operator.

*Ivchenko's boundary conditions within 6 – band **k**.**p** model [30]*

In the framework of 6-band $\boldsymbol{k}.\boldsymbol{p}$ model, the HH-LH mixing, or mixing between X and Y orbital states, can be described by the following coupling Hamiltonian which, written in $|L,S\rangle$ basis reads [30]:

$$H_{X-Y} = \pm \frac{\hbar^2 t_{X-Y}}{m_0 a_0} \begin{bmatrix} \{I_x, I_y\} & 0 \\ 0 & \{I_x, I_y\} \end{bmatrix} \delta(z - z_i) \tag{3.165}$$

where $\{I_x, I_y\}$ is the symmetrized product of the angular momentum $I = 1$:

$$\{I_x I_y\} = \frac{1}{2}(I_x I_y + I_y I_x) = \frac{1}{2} \begin{bmatrix} 0 & -1 & 0 \\ -1 & 0 & 0 \\ 0 & 0 & 0 \end{bmatrix} \tag{3.166}$$

which is an invariant under C_{2v} and the $\delta - function$ with z_i being the coordinate of the interface. The sign ± refers to BA or AB interfaces and the pre-factor with Planck's constant $\hbar$, free electron mass m_0, and lattice constant a_0 (assumed to be the same for A and B) has been introduced to characterize the X-Y orbital mixing by the dimensionless real parameter t_{X-Y}. Taking into account H_{X-Y} and using Eq. 3.41 for the surface potential terms, then the standard boundary conditions for envelope function $f_{L,S}$ have then to be changed by adding the term:

$$i \frac{\hbar t_{X-Y}}{m_0 a_0} \begin{bmatrix} 2\{I_x I_y\} & 0 \\ 0 & 2\{I_x I_y\} \end{bmatrix} \boldsymbol{f} \tag{3.167}$$

to $(\boldsymbol{J}_z \boldsymbol{f})_B$ on the right hand side of Eq. 3.163 to give:

$$\begin{aligned} \boldsymbol{f}_A &= \boldsymbol{f}_B \\ (\boldsymbol{J}_z \boldsymbol{f})_A &= \left(\left\{ \boldsymbol{J}_z + i \frac{\hbar t_{X-Y}}{m_0 a_0} \begin{bmatrix} 2\{I_x I_y\} & 0 \\ 0 & 2\{I_x I_y\} \end{bmatrix} \right\} f \right)_B \end{aligned} \tag{3.168}$$

Or equivalently, the new matching conditions for the envelope $F_{J,M}$ functions which take into account the HH-LH mixing, have form:

$$\begin{aligned} \boldsymbol{F}_A &= \boldsymbol{F}_B \\ (\boldsymbol{J}_z \boldsymbol{F})_A &= (\boldsymbol{J}_z \boldsymbol{F})_B - \frac{2}{3} i \frac{\hbar}{a_0 m_0} t_{X-Y} R \boldsymbol{F}_B \end{aligned} \tag{3.169}$$

Here R is the following 6×6 matrix:

$$R = \begin{bmatrix} \{J_x J_y\} & 3U_{xy} \\ 3U_{xy}^{\dagger} & 0 \end{bmatrix} \tag{3.170}$$

composed of angular momentum matrices J_α ($\alpha = x, y, z$) for $J = 3/2$ and 4×2 matrix U_{xy} and being the corresponding C_{2v} symmetry group [44]

$$\{J_x, J_y\} = \frac{i}{2} \begin{bmatrix} 0 & 0 & -\sqrt{3} & 0 \\ 0 & 0 & 0 & -\sqrt{3} \\ \sqrt{3} & 0 & 0 & 0 \\ 0 & \sqrt{3} & 0 & 0 \end{bmatrix} \tag{3.171}$$

$$U_{xy} = \frac{i}{\sqrt{6}} \begin{bmatrix} 0 & 1 \\ 0 & 0 \\ 0 & 0 \\ 1 & 0 \end{bmatrix} \tag{3.172}$$

Then we get [44]

$$R = \frac{3}{2} \begin{bmatrix} 0 & 0 & \frac{-i}{\sqrt{3}} & 0 & 0 & i\sqrt{\frac{2}{3}} \\ 0 & 0 & 0 & \frac{-i}{\sqrt{3}} & 0 & 0 \\ \frac{i}{\sqrt{3}} & 0 & 0 & 0 & 0 & 0 \\ 0 & \frac{i}{\sqrt{3}} & 0 & 0 & i\sqrt{\frac{2}{3}} & 0 \\ 0 & 0 & 0 & -i\sqrt{\frac{2}{3}} & 0 & 0 \\ -i\sqrt{\frac{2}{3}} & 0 & 0 & 0 & 0 & 0 \end{bmatrix} \tag{3.173}$$

If the hole energy E is small compared to the spin-orbit splitting Δ_{so}, then the mixing between the Γ_8 and Γ_7 subspaces can be neglected and we retain in Eq. 3.169 only the first four components F_j and R in the 4×4 block $\{J_x J_y\}$. In this case the boundary conditions then read [30]

$$\begin{aligned} (F_j)_A &= (F_j)_B \\ (\nabla^j F_j)_A &= (\nabla^j F_j)_B + \frac{2}{\sqrt{3}} t_{l-h} \{J_x, J_y\}_{jj'} (F_{j'})_B \end{aligned} \tag{3.174}$$

where $\{J_x J_y\}$ is pure imaginary. By considering the following relationship:

$$t_{l-h} = \frac{1}{\sqrt{3}} t_{X-Y} \tag{3.175}$$

Here, we have defined the two gradient operators acting respectively on heavy and light holes:

$$\nabla^{\pm 3/2} = a_0 \frac{m_0}{m_{HH}} \frac{\partial}{\partial z} \tag{3.176}$$

$$\nabla^{\pm 1/2} = a_0 \frac{m_0}{m_{LH}} \frac{\partial}{\partial z} \tag{3.177}$$

and we used the notations m_{HH}, m_{LH} for the effective masses of heavy and light holes. For convenience, one can re-write 3.174 in the form:

$$\begin{aligned} (F_j)_A &= (F_j)_B \\ M_A^{-1} \left(\frac{\partial F}{\partial z} \right)_A &= M_B^{-1} \left(\frac{\partial F}{\partial z} \right)_B + \frac{2}{\sqrt{3}} t_{l-h} \{J_x, J_y\} (F)_B \end{aligned} \tag{3.178}$$

where the matrix M is diagonal and includes the values of the heavy-hole $m_{HH} = \frac{m_0}{\gamma_1 - 2\gamma_2}$ and the light-hole $m_{LH} = \frac{m_0}{\gamma_1 + 2\gamma_2}$, respectively. Those boundary conditions may be applied to our 30×30, and 40×40 multiband Hamiltonian in the corresponding reduced 6×6 blocks of the $p - symmetry$ components (e.g. VB). Following the general arguments developed above, the charge current will be shown to be conserved by adopting such boundary conditions.

Durnev's boundary conditions within 14-band k.p model [31]

We remind here that the boundary conditions to adopt have to i) conserve the charge flux (current) and ii) make allowance for the heavy-to-light hole mixing in Eq. 3.169 or 3.178. We are now interested to investigate the boundary conditions proposed by Durnev et al. [31] in the framework of the 14-multiband ***k.p*** theory. In 2014, Durnev et al. proposed a boundary condition which is: the continuity of the wavefunction and discontinuity of the current-wave by Ivchenko [30] in the 6×6 block of the VB may be replaced by the continuity of wave current, the five envelope functions $f_{L,S}$ corresponding to $\mathcal{S}, \mathcal{X}, \mathcal{Y}, \mathcal{Z}, \mathcal{Z}'$, and the discontinuity of the wavefunctions of the level of the Γ_{5C} p-type symmetry band as follows:

$$\begin{aligned} (\hat{f}_{\mathcal{X}'})_A &= (\hat{f}_{\mathcal{X}'})_B + \tilde{t} (\hat{f}_{\mathcal{X}})_B \\ (\hat{f}_{\mathcal{Y}'})_A &= (\hat{f}_{\mathcal{Y}'})_B + \tilde{t} (\hat{f}_{\mathcal{Y}})_B \end{aligned} \tag{3.179}$$

where $\tilde{t}$ is a real dimensionless interface - mixing parameter and the two component spinor envelopes in 3.179 are defined as:

$$\hat{f}_L = \begin{bmatrix} f_{L,1/2} \\ f_{L,-1/2} \end{bmatrix} \tag{3.180}$$

where L refers to $\mathcal{X}', \mathcal{X}, \mathcal{Y}', \mathcal{Y}, \ldots$ ($\mathcal{X}, \mathcal{Y}$ correspond to Γ_{5v} and $\mathcal{X}', \mathcal{Y}'$ to Γ_{5c}). They have also showed that the proposed conditions 3.179 are in agreement with the flux continuity which is given for a 14-component envelope functions f_{LS} by [31]:

$$\boldsymbol{S} = \frac{1}{\hbar} \sum_{L'S', LS} f^*_{L'S'} \frac{\partial \mathcal{H}^{14}_{L'S', LS}(\boldsymbol{k})}{\partial \boldsymbol{k}} f_{LS} \tag{3.181}$$

or explicitly one has, e.g., for the flux z component [31]

$$S_z = \frac{i}{\hbar}\left[P(\hat{f}^{\dagger}_{\mathcal{Z}}\hat{f}_{\mathcal{S}} - \hat{f}^{\dagger}_{\mathcal{S}}\hat{f}_{\mathcal{Z}}) + P'(\hat{f}^{\dagger}_{\mathcal{Z}'}\hat{f}_{\mathcal{S}} - \hat{f}^{\dagger}_{\mathcal{S}}\hat{f}_{\mathcal{Z}'}) + Q(\hat{f}^{\dagger}_{\mathcal{X}'}\hat{f}_{\mathcal{Y}} - \hat{f}^{\dagger}_{\mathcal{Y}}\hat{f}_{\mathcal{X}'} + \hat{f}^{\dagger}_{\mathcal{Y}'}\hat{f}_{\mathcal{X}} - \hat{f}^{\dagger}_{\mathcal{X}}\hat{f}_{\mathcal{Y}'})\right] \tag{3.182}$$

where P, P' and Q are the coupling strength [31].

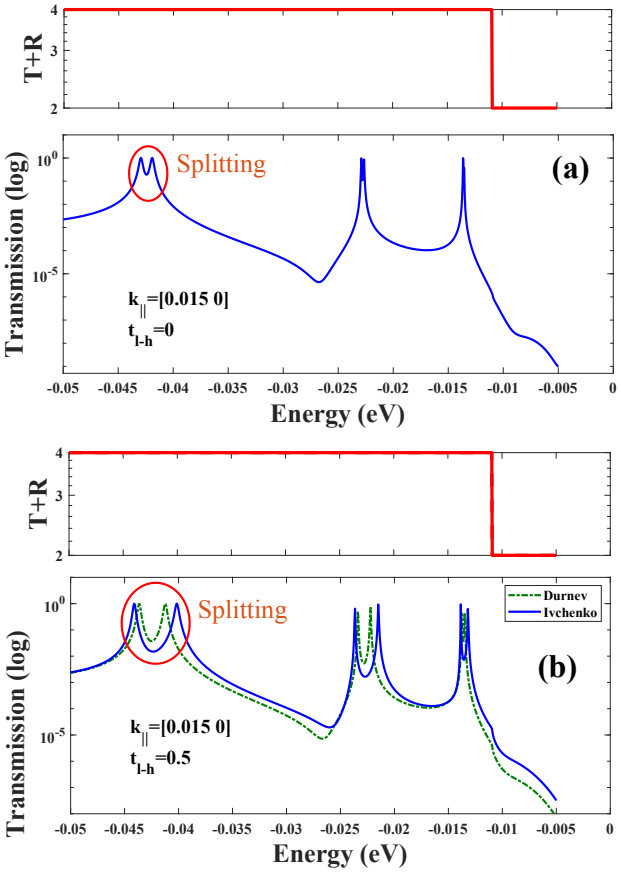

FIGURE 3.14: Spin splitting in resonant tunneling through GaAs/GalAs quantum well structures [31] where the mixing between the heavy hole and light hole in figure (b) (t_{lh} = 0.5) allows splitting to become larger than the splitting caused only by Dresselhaus term in figure (a) (t_{lh} = 0). In figure (b) are the calculations with two boundary conditions proposed by Durnev [31] and Ivchenko [30] which were adapted to 30-band ***k.p*** model. The sum of transmission and reflection coefficients (red curve) for both two adapting boundary condition in 30-band ***k.p*** model are almost constantly and are equal to number of bands included in tunneling. This mean that the wave current is conserved.

Note that one can readily prove the conservation of charge flux by applying the boundary condition 3.179 directly to flux equation 3.182. Furthermore, the boundary conditions 3.169 or 3.178 can be obtained from Eq. 3.179 taking into account that the $Q\hat{k}_z$ off-diagonal matrix elements in the 14×14 Hamiltonian couple $\hat{f}_{\mathcal{X}'}$ with $\hat{f}_{\mathcal{Y}}$ and $\hat{f}_{\mathcal{Y}'}$ with $\hat{f}_{\mathcal{X}}$ according to:

$$\hat{f}_{\mathcal{X}'} = -\frac{Q}{E_{c'} - E_{nj}}\frac{\partial \hat{f}_{\mathcal{Y}}}{\partial z} \tag{3.183a}$$

$$\hat{f}_{\mathcal{Y}'} = -\frac{Q}{E_{c'} - E_{nj}}\frac{\partial \hat{f}_{\mathcal{X}}}{\partial z} \tag{3.183b}$$

Here $E_{c'}$ is the energy position of $\Gamma_{15}^{'}$ conduction band, E_{nj} the energy in the nth electronic subband, and we replaced $\hat{k}_z$ by $-i\frac{\partial}{\partial z}$ acting on the smooth envelopes. Substituting $\hat{f}_{X'}$, $\hat{f}_{Y'}$ from 3.183 into Eq. 3.179, transforming it into Γ_8 basis and making use of the explicit forms of Luttinger-Kohn parameters, we arrive in the linear k_z approximation to the second boundary condition 3.178 with the heavy-light hole mixing coefficient:

$$t_{l-h} = \frac{2m_0 a_0}{\sqrt{3}\hbar^2} Q\tilde{t} \tag{3.184}$$

Figure 3.14 displays the splitting of the resonant peaks in GaAs/GalAs quantum well structure [31] where the mixture of the heavy hole and light hole (figure 3.14b), described via the $t_{lh} = 0.5$ parameter, allows a larger splitting than the ones caused only by Dresselhaus terms ($t_{lh} = 0$) in figure 3.14b. These calculations were done with the boundary conditions proposed by Durnev [31] and Ivchenko [30] adapting to 30 band $\boldsymbol{k.p}$ model which are now going to be discussed in the following section.

Adapting the Ivchenko's and Durnev's boundary conditions to the 30- and 40-multiband k.p models

Let us now develop the boundary conditions which allow one to describe the symmetry reduction from T_d to C_{2v} at the interface of III-V semiconductor heterostructure within the multiband **k.p** platforms. In order to do that we try to adapt the boundary conditions proposed by Ivchenko et al. [30] and Durnev et al. [31] to multiband $\boldsymbol{k.p}$ Hamiltonian, typically for $30-band$ and $40-band$ $\boldsymbol{k.p}$ models where the details of them can be found in Appendix A.

First of all, for convenience we rewrite the boundary conditions proposed by Ivchenko et al. given in Eq. 3.169 in the matrix form as the following:

$$\begin{bmatrix} \boldsymbol{F}_A \\ (\boldsymbol{J}_z\boldsymbol{F})_A \end{bmatrix} = \begin{bmatrix} \hat{I}_{6\times6} & 0 \\ -\frac{2}{3}\frac{i\hbar}{a_0 m_0} t_{X-Y} R & \hat{I}_{6\times6} \end{bmatrix} \begin{bmatrix} \boldsymbol{F}_B \\ (\boldsymbol{J}_z\boldsymbol{F})_B \end{bmatrix} \tag{3.185}$$

where $\hat{I}_{6\times6}$ is the 6×6 identity matrix and R was defined in Eq. 3.173. The matching conditions adapted from Ivchenko's boundary conditions to the 30- and 40-band $\boldsymbol{k.p}$ models then, may be given in a following form:

$$\begin{bmatrix} \boldsymbol{F}_A \\ (\boldsymbol{J}_z\boldsymbol{F})_A \end{bmatrix} = \begin{bmatrix} \hat{I}_{(nb+22)\times(nb+22)} & 0 & 0 & 0 \\ 0 & \hat{I}_{6\times6} & 0 & 0 \\ 0 & -\frac{2}{3}\frac{i\hbar}{a_0 m_0} t_{X-Y} R & \hat{I}_{6\times6} & 0 \\ 0 & 0 & 0 & \hat{I}_{(nb-28)\times(nb-28)} \end{bmatrix} \begin{bmatrix} \boldsymbol{F}_B \\ (\boldsymbol{J}_z\boldsymbol{F})_B \end{bmatrix} \tag{3.186}$$

where $\hat{I}_{(nb+22)\times(nb+22)}$ and $\hat{I}_{(nb-28)\times(nb-28)}$ are $(nb+22)\times(nb+22)$ and $(nb-28)\times(nb-28)$ identity matrices, respectively, with $nb = 30$ for $30-band$ and $nb = 40$ for $40-band$ $\boldsymbol{k.p}$ models.

The boundary conditions 3.186 show that in framework of $30-band$ and $40-band$ $\boldsymbol{k.p}$ models, one has the continuity of the wavefunctions at the interface, the discontinuity of 6 components of the wave current corresponding to 6 valence sub-bands $HH\uparrow$, $HH\downarrow$, $LH\uparrow$, $LH\downarrow$, $SO\uparrow$, $SO\downarrow$; and the continuity of the remaining components of the wave current. Here, we keep the same terms responsible for the discontinuity of current as in 6×6 band model. One can easily observe that this extended boundary conditions also ensure the conservation of the charge current. Indeed, note that the term $Re\left[\boldsymbol{F}^*\left(-\frac{2}{3}\frac{i\hbar}{a_0 m_0} t_{X-Y} R\right)\boldsymbol{F}\right] = 0$ which can easily be proven by multiplying both side of Eq.3.186 with $\boldsymbol{F}^*$ on the left.

Doing the same treatments for Durnev's boundary conditions, one may also adapt these boundary conditions for $30-band$ and $40-band$ $\boldsymbol{k.p}$ models with the matching conditions defined by:

$$\begin{bmatrix} \boldsymbol{F}_A \\ (\boldsymbol{J}_z\boldsymbol{F})_A \end{bmatrix} = \begin{bmatrix} \hat{I}_{14\times14} & 0 & 0 & 0 \\ 0 & \hat{D}_{14\times14} & 0 & 0 \\ 0 & 0 & \hat{I}_{(nb-28)\times(nb-28)} & 0 \\ 0 & 0 & 0 & \hat{I}_{nb\times nb} \end{bmatrix} \begin{bmatrix} \boldsymbol{F}_B \\ (\boldsymbol{J}_z\boldsymbol{F})_B \end{bmatrix} \tag{3.187}$$

where $\hat{I}_{14\times14}$ and $\hat{I}_{nb\times nb}$ are 14×14 and $nb\times nb$ identity matrices respectively; $\hat{D}_{14\times14} = R.M_t.R^{-1}$, here R is a matrix which transforms the $|J,M\rangle$ basis set to $|L,S\rangle$ basis set and M_t is 14×14 matrix such that the diagonal elements are equal to ones: $M_t(i,i) = 1$ (i=1:14); and $M_t(1,9) = M_t(2,10) = M_t(3,11) = M_t(4,12) = \tilde{t}$ and the remaining terms are equal to zero.

Conveniently, one may re-write Eqs 3.186 and 3.187 as:

$$\begin{bmatrix} \boldsymbol{F}_A \\ (\boldsymbol{J}_z\boldsymbol{F})_A \end{bmatrix} = M_{mixing} \begin{bmatrix} \boldsymbol{F}_B \\ (\boldsymbol{J}_z\boldsymbol{F})_B \end{bmatrix} \tag{3.188}$$

where:

$$M_{mixing} = \begin{bmatrix} \hat{I}_{(nb+22)\times(nb+22)} & 0 & 0 & 0 \\ 0 & \hat{I}_{6\times6} & 0 & 0 \\ 0 & -\frac{2}{3}\frac{i\hbar}{a_0 m_0} t_{X-Y} R & \hat{I}_{6\times6} & 0 \\ 0 & 0 & 0 & \hat{I}_{(nb-28)\times(nb-28)} \end{bmatrix} \tag{3.189}$$

for Ivchenko's boundary conditions and

$$M_{mixing} = \begin{bmatrix} \hat{I}_{14\times14} & 0 & 0 & 0 \\ 0 & \hat{D}_{14\times14} & 0 & 0 \\ 0 & 0 & \hat{I}_{(nb-28)\times(nb-28)} & 0 \\ 0 & 0 & 0 & \hat{I}_{nb\times nb} \end{bmatrix} \tag{3.190}$$

for Durnev's boundary conditions.

Finally, These boundary conditions can be involved in the scattering and transfer matrix approaches by modifying the interfacial matrix in Eq. C.14 as:

$$\boldsymbol{IM}(n+1) = \left(M_{mixing} * \begin{bmatrix} \psi_n^1(k_n^1) & .... & \psi_n^1(k_n^{2m}) \\ . & . & . \\ . & . & . \\ . & . & . \\ \psi_n^m(k_n^1) & ... & \psi_n^m(k_n^{2m}) \\ J_z\psi_n^1(k_n^1) & .... & J_z\psi_n^1(k_n^{2m}) \\ . & . & . \\ . & . & . \\ . & . & . \\ J_z\psi_n^m(k_n^1) & .... & J_z\psi_n^m(k_n^{2m}) \end{bmatrix} \right)^{-1} \begin{bmatrix} \psi_{n+1}^1(k_{n+1}^1) & .... & \psi_{n+1}^1(k_{n+1}^{2m}) \\ . & . & . \\ . & . & . \\ . & . & . \\ \psi_{n+1}^m(k_{n+1}^1) & ... & \psi_{n+1}^m(k_{n+1}^{2m}) \\ J_z\psi_{n+1}^1(k_{n+1}^1) & .... & J_z\psi_{n+1}^1(k_{n+1}^{2m}) \\ . & . & . \\ . & . & . \\ . & . & . \\ J_z\psi_{n+1}^m(k_{n+1}^1) & .... & J_z\psi_{n+1}^m(k_{n+1}^{2m}) \end{bmatrix} \tag{3.191}$$

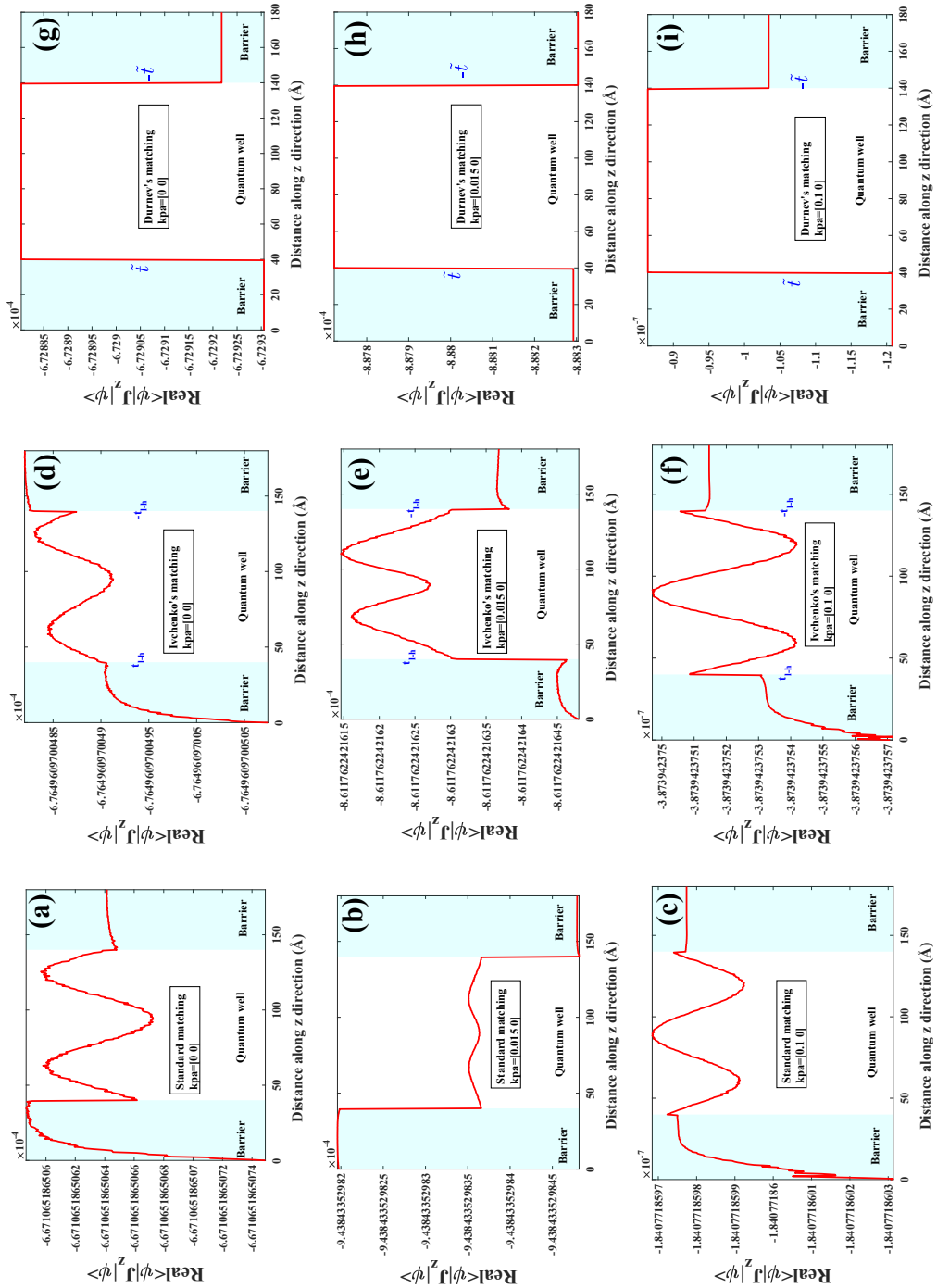

FIGURE 3.15: The current wave through GaAs/AlAs quantum well with different matching conditions: (a,b,c) standard matching condtion. (d,e,f) Ivchenko's matching condition, $t_{l-h} = 0.5$. (g, h,i) Durnev's matching condition $\tilde{t} = 0.07$ and with different in-plane wave vectors $k_{||}$ (kpa) depict in the figure.

It is worth noting that, in the framework of 30- and 40-band ***k.p*** models, and unlike the extended Ivchenko's matching conditions which is easy to see that the conservation of charge current is ensured, the extended Durnev's matching conditions are more difficult to analyze. Figure 4.1.1 displays the wave current through a GaAs/AlAs quantum well structure for different matching conditions calculated with the 30-band ***k.p*** framework. One observes that the extended Durnev's matching conditions are just accurate in the vicinity of the Γ point where the in-plane wave vector $\boldsymbol{k}_{||}$ is small and becomes inaccurate when $\boldsymbol{k}_{||}$ increases. Therefore, in this work, we just use the extended Durnev's matching conditions for restricted cases where $\boldsymbol{k}_{||}$ is small enough (typically less than 0.015Å^{-1}).

3.4 Symmetry of wavefunctions in Quantum Wells of T_d semiconductor groups in a 30-band k. p approach and linear energy Splitting in Quantum wells

3.4.1 Symmetry of wavefunctions in Quantum Wells of T_d semiconductors in a 30-band k.p approach

In this section, we describe the specific symmetry of the electrons and holes wavefunctions in III-V semiconductors quantum wells (AlAs/GaAs QW(10 nm)/AlAs) calculated in our 30-band (or 40-band) ***k.p*** multiband scheme. We compare our results to the 14-band model as discussed by Durnev et al [31]. Hereafter, we will discuss calculations and modeling of the linear energy splitting *vs.* the in-plane electronic wavevector $k_{\|}$.

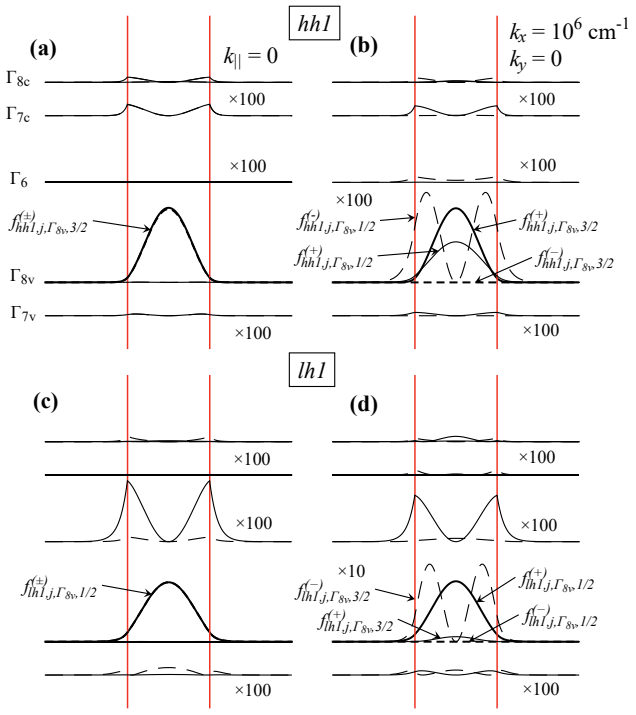

FIGURE 3.16: The envelope function $\left|f^{(+)}_{nj,N}\right|^2$ (solid lines) and $\left|f^{(-)}_{nj,N}\right|^2$ (dashed lines) for $n = hh1(HH1)$ (a,b) and $n = lh1(LH1)$ (c,d) in $GaAs/Al_{0.35}Ga_{0.75}As$ 100 Å quantum well. Here, (+) and (−) are labeled for spin up and spin down and the calculations was done for $k_{||}$ =[0 0] (a,c) and $k_{||}$ = [$10^6 cm^{-1}$ 0] (b,d) and for t_{l-h} = 0 for all. Taken from Ref.[249]

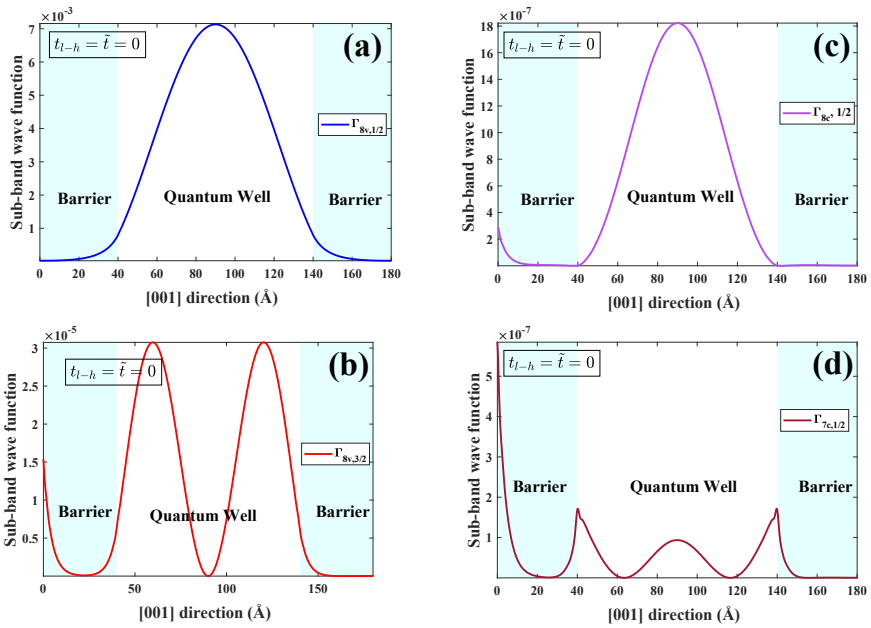

FIGURE 3.17: The envelope functions in a GaAs/AlAs quantum well calculated in the framework of 30-band $\boldsymbol{k}.\boldsymbol{p}$ theory with standard matching condition ($t_{l-h} = \tilde{t} = 0$) and normal incidence $\boldsymbol{k}_{||} = 0$ for corresponding LH_1 (h+) energy level. The calculated wavefunctions are the scattered waves propagating from left to right.

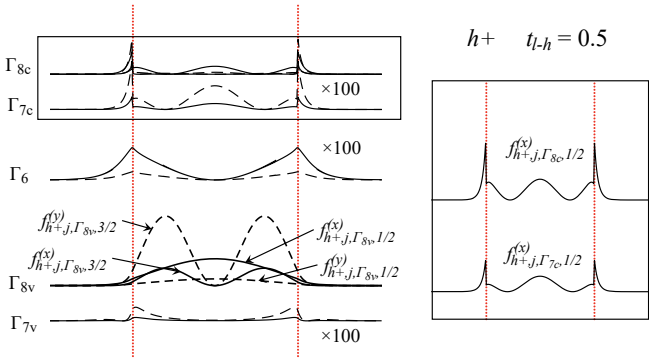

FIGURE 3.18: The envelope function $\left|f^{(+)}_{nj,N}\right|^2$ (solid lines) and $\left|f^{(-)}_{nj,N}\right|^2$ (dashed lines) for LH_1 (h+) with $t_{lh} = 0.5$ and $k_{||} = 0$ in $GaAs/Al_{0.35}Ga_{0.75}As$ 100 Å quantum well. In the right panel enlarged images of two envelopes of the upper conduction band are shown. Taken from Ref.[249]

We will discuss respectively the different matching conditions, the hypotheses arising from the C_{2v} interfaces that are of three types:

$\mathbb{A}$) Without heavy-to-light hole mixing.

$\mathbb{B}$) Ivchenko's boundary's conditions corresponding to a discontinuity of the Γ_{5v} hole bands.

$\mathbb{C}$) Durnev's boundary conditions (discontinuity of the Γ_{5c} conduction bands).

Figs 3.17 displays the typical wavefunction profiles (scattered wave) corresponding to the first light hole states (LH_1) within the GaAs QW and in the barriers without any mixing and calculated for $k_{||} = 0$, at normal incidence. The wavefunctions components corresponding to the $\Gamma_{8v,1/2}$, $\Gamma_{8c,1/2}$, $\Gamma_{8v,3/2}$, and $\Gamma_{7c,1/2}$ represented here are all continuous along the coordinate z as required by the matching conditions of type $\mathbb{A}$. Moreover, those calculations are in pretty good agreement with the results published by Durnev et

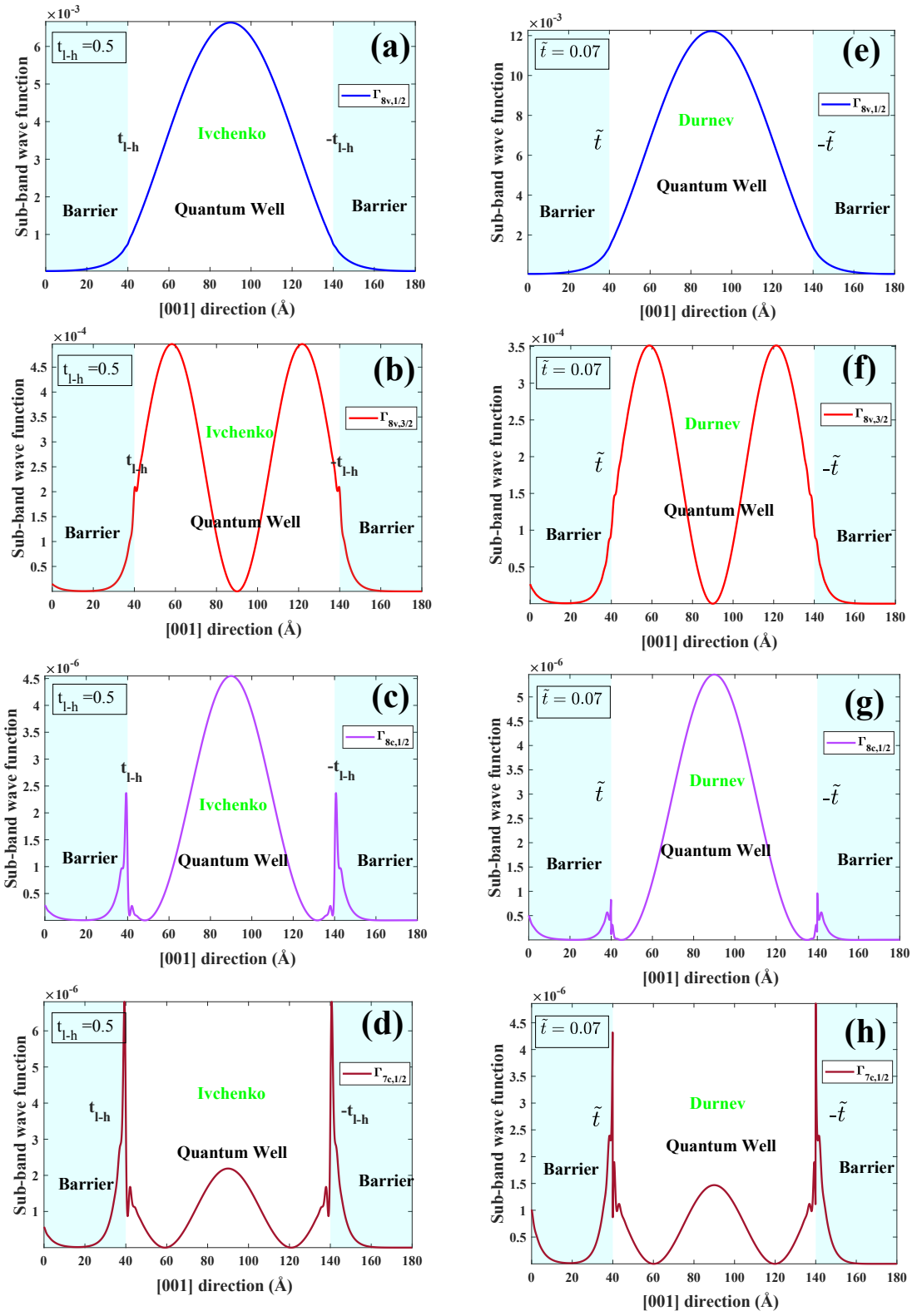

FIGURE 3.19: The envelope functions in a GaAs/AlAs quantum well calculated in the framework of 30-band $\boldsymbol{k.p}$ theory with Ivchenko's matching conditions $t_{l-h} = 0.5$ (a-d) and Durnev's matching condition $\tilde{t} = 0.07$ (c-f) with normal incidence $\boldsymbol{k}_{||} = 0$ for corresponding LH_1 (h+) energy level. The calculated wavefunctions are the scattered waves propagating from left to right.

al. and displayed in Fig. 3.16. One can observe that under oblique incidence, the $LH1$ state is mainly of the $\Gamma_{8v,1/2}$ symmetry as expected but acquires other symmetry components (only $\Gamma_{8c,1/2}$, $\Gamma_{8v,3/2}$ and $\Gamma_{7c,1/2}$ are represented here) arising from the off-diagonal coupling and characterized by a different shape of the envelope function that we will discuss hereafter.

In the same way, Fig 3.19 displays the equivalent wavefunction components profiles (symmetry-projected electron density components) corresponding to $\Gamma_{8v,1/2}$, $\Gamma_{8c,1/2}$, $\Gamma_{8v,3/2}$, and $\Gamma_{7c,1/2}$ for the $LH1$ level by adapting type $\mathbb{B}$ and type $\mathbb{C}$ matching conditions and where $\Gamma_{8v,1/2}$ acquires the larger weight. Those curves should be compared to the 14 – *band* ***k.p*** results published by Durnev in Fig. 3.18 and are in good agreement. Note that the component-dependent electron (hole densities) of $\Gamma_{7c,1/2}$ and $\Gamma_{8c,1/2}$ are characterized by a discontinuity at each QW/barrier interface due to the heavy-to-light-hole mixing on the current-wave (type $\mathbb{B}$ boundary conditions) or on the Γ_{5c} states (type $\mathbb{C}$ boundary conditions). One notes also a strong increase of the $\Gamma_{8v,3/2}$ density in the case of type $\mathbb{B}$ and type $\mathbb{C}$ conditions due to such mixing terms. The impact of the 30-band ***k.p*** treatment on the electronic density calculation is a much better precision owing to the introduction of large evanescent wave components of the high energy states (levels) leading to the appearance of contributions characterized by rapid oscillations close to interfaces. Moreover, the off-diagonal parts (*e. g.* $\Gamma_{8v,3/2}$ contributions to the $\Gamma_{8v,1/2}$) are calculated with much more accurate precision in this 30-multiband approach.

3.4.2 *Linear energy splitting due to heavy-light hole mixing in quantum wells [31]*

We discuss now the energy splitting for the $HH1$ and $LH1$ and $HH2$ doublets in the same type of (AlAs/GaAs QW(10 nm)/AlAs) as discussed by Durnev et al. [31].

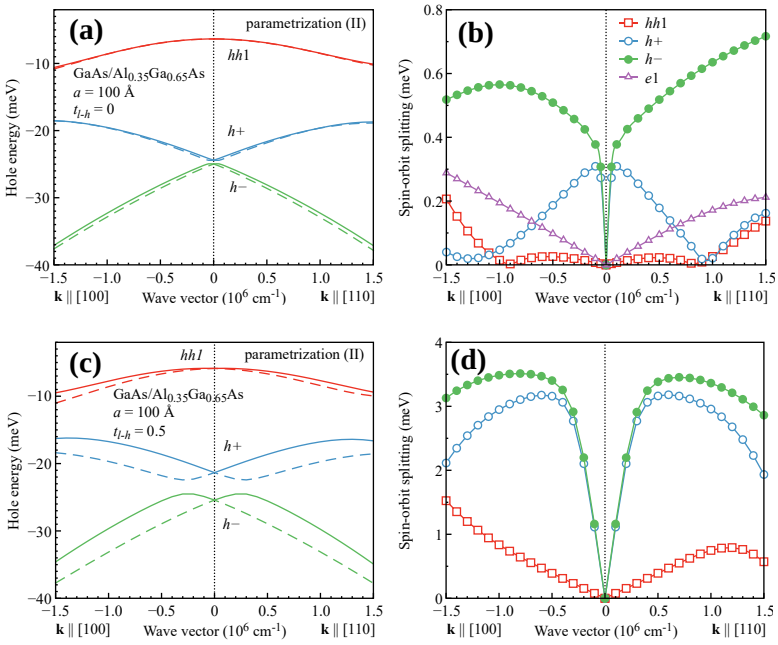

FIGURE 3.20: Dispersion (a, c) and spin splitting (b, d) of valence subbands for GaAs/$Al_{0.35}Ga_{0.65}As$ 10nm QW. The calculations are done for two cases: mixing parameter t_{l-h} = 0 [panels (a) and (b)] and t_{l-h} = 0.5 [panels (c) and (d)]. The spin splitting of conduction subband e1 is presented in (b) for comparison. Taken from Ref.[31].

Figures 3.20 display the results of 14-band ***k.p*** calculations performed by Durnev and corresponding

respectively to: *(i)* band energy dispersions of $HH1$ and $LH1$ and $HH2$ levels along the [100] and [110] k-lines within the reciprocal space, together with *ii)* the energy splitting observed *vs.* $k_{\|}$. Such splitting, with a value reaching possibly 3 to 4 meV, results from the native Dresselhaus term due to the T_d bulk symmetry group of the GaAs QW and/or the effects of the heavy-to-light hole mixing terms. As discussed by Durnev, one generally notes an enhancement of the hole splitting when type $\mathbb{C}$ (or type $\mathbb{B}$) boundary conditions are used, *e. g.*, by considering subsequent heavy-to-light hole mixing, like discussed in the last section. Such enhancement of the k-linear energy splitting for the doublet set (hh^+ and hh^- are almost degenerated in energy for a 10 nm QW) ranges from 0.6 to 4 meV.

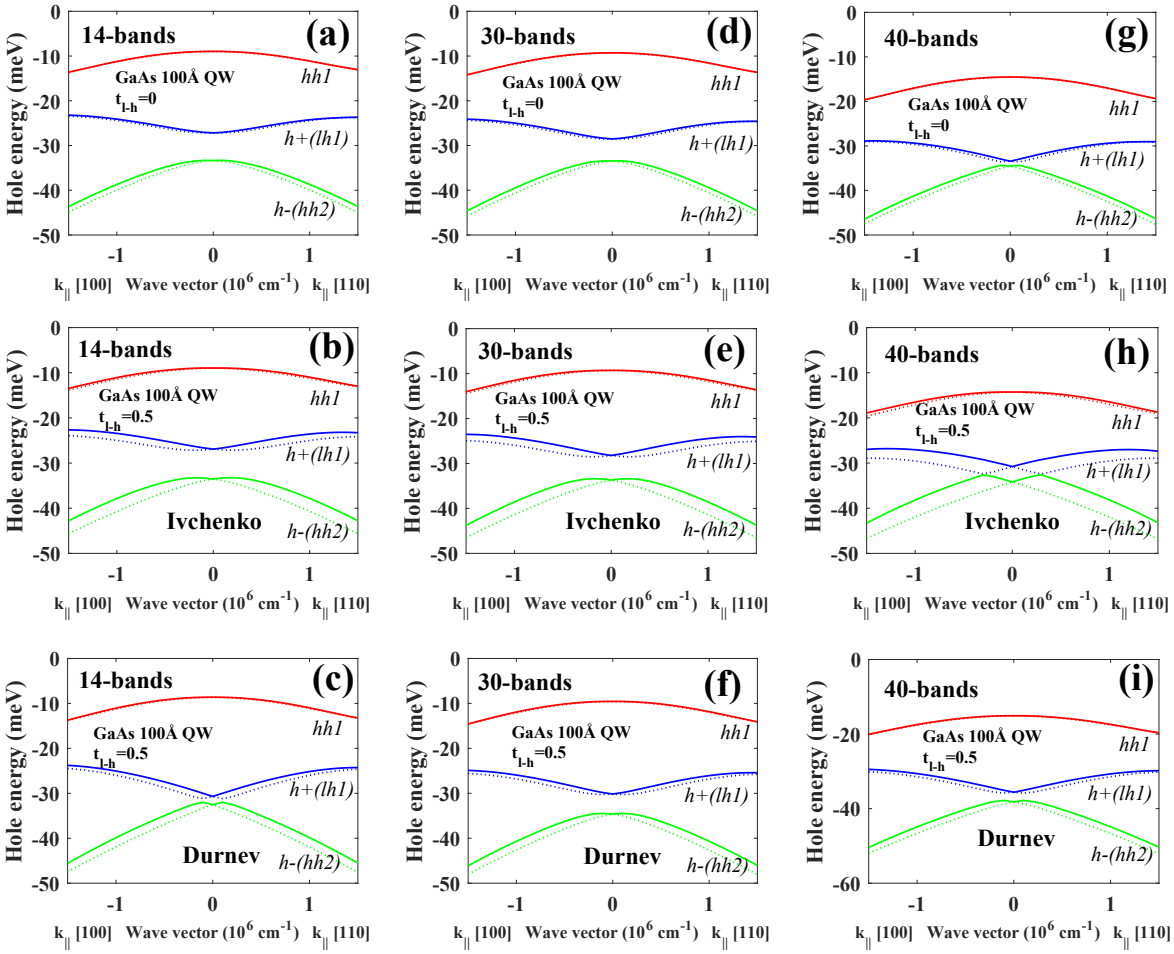

FIGURE 3.21: Valence subbands dispersion in GaAs/AlAs 10nm QW calculated with different ***k.p*** platforms (indicated in the figures), for two values of the mixing term t_{l-h} = 0 and t_{l-h} = 0.5 with two sets of boundary conditions proposed by Ivchenko et al. [30] and Durnev et al. [31].

In order to check our 14×14, 30×30 and 40×40 multiband tunneling code, we have operated to same kind of calculations by extracting the typical resonance energy of $HH1$ and $LH1$ and $HH2$ levels using electronic scattering waves (tunneling waves and not outgoing waves -bonding states-) boundary conditions. We have then extracted the main energy peaks in resonance together with their splitting ΔE_{SO1}. Figs. 3.21 (a-i) show the energy dispersions calculated along the respective [100] and [110] k-lines in the different situations with a pretty good agreement with the results of Durnev. Figs. 3.22 (a-i) display the characteristic energy splitting extracted in each calculation and one can note that the different platforms give consistent results with each others, confirming thus the power of our ***k.p*** treatment.

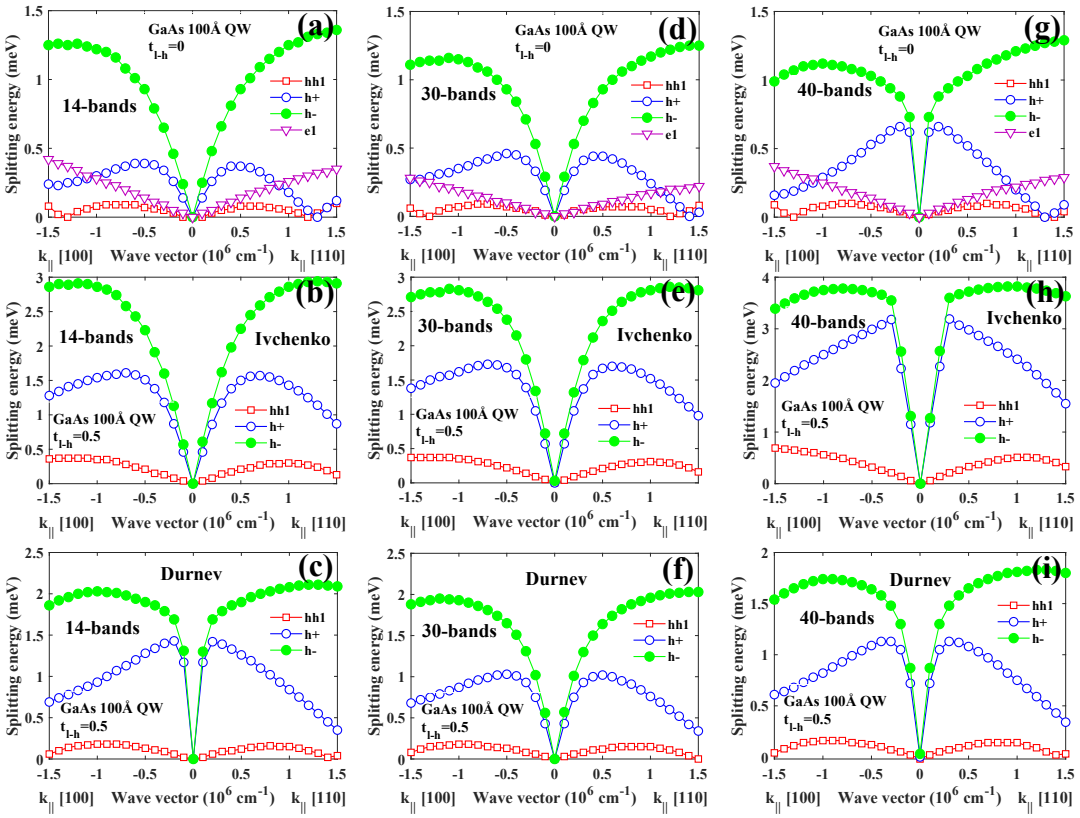

FIGURE 3.22: Splitting of valence subbands in GaAs/AlAs 10nm QW calculated with different ***k.p*** platforms (depicted in the figure), for two values of the mixing term $t_{l-h} = 0$ and $t_{l-h} = 0.5$ with two sets of boundary conditions proposed by Ivchenko et al. [30] and Durnev et al. [31].

In Figs. 3.23 (a-c), we have reported the results of calculations for the valence band splitting as a function of the interface mixing strength (t_{lh}) for a 8.5 nm GaAs QW embedded in GaAs (Figs. 3.23a) and AlAs (Figs. 3.23b) barriers for the respective $HH1$, $LH1$ and $HH2$ levels. One can observe that the splitting parameter β_1, defined as $\Delta E_{SOI} = \beta_1 k_{\|}$ increases firstly linearly with t_{l-h} and more strongly for $t_{lh} > 1$. The intercept of these curves with $t_{lh} = 0$ correspond to the native Dresselhaus splitting (positive or negative depending on the convention) whereas the values of ΔE_{SOI} acquired for $t_{lh} > 0$ from its value at origin correspond to the heavy-to-light hole mixing terms (C_{2v} interface symmetry). These calculations and results reinforce the energy splitting enhancement by the mixing of the hole characters arising also at pure normal incidence. In agreement with the calculations of Durnev (Fig. 3.24), our multiband ***k.p*** platform also exhibits a drop of the splitting coefficient β_1 *vs.* QW thickness d from typical values of $20 - 60$ or 200 meV.Å at $d = 5$ *nm* to vanish for $d > 15$ *nm*. This feature is due to a rapid decrease of the electron charge density at the C_{2v} interface when the QW width increases.

3.4.3 30×30 and 40×40 multiband k.p modeling of the energy splitting in the VB

As largely discussed by Durnev et al. [31, 250], the large hole energy splitting in the valence band, of the order of 1-4 meV that is beyond the k^3-Dresselhaus term, originates from the combined action of the heavy-to-light hole mixing term at oblique incidence and the surface potential at C_{2v} interfaces H_s. Under oblique incidence, the heavy-to-light hole $k-$linear mixing is a consequence of the complex valence band structure and is related to the off-diagonal elements of the Luttinger Hamiltonian H and H^*, here $H = -3\hbar^2\gamma_3/m_0(k_x - ik_y)k_z$, and $k = (k_x,\ k_y)$ is the in-plane wave vector of the hole. Here, γ_i $(i = 1, 2, 3)$

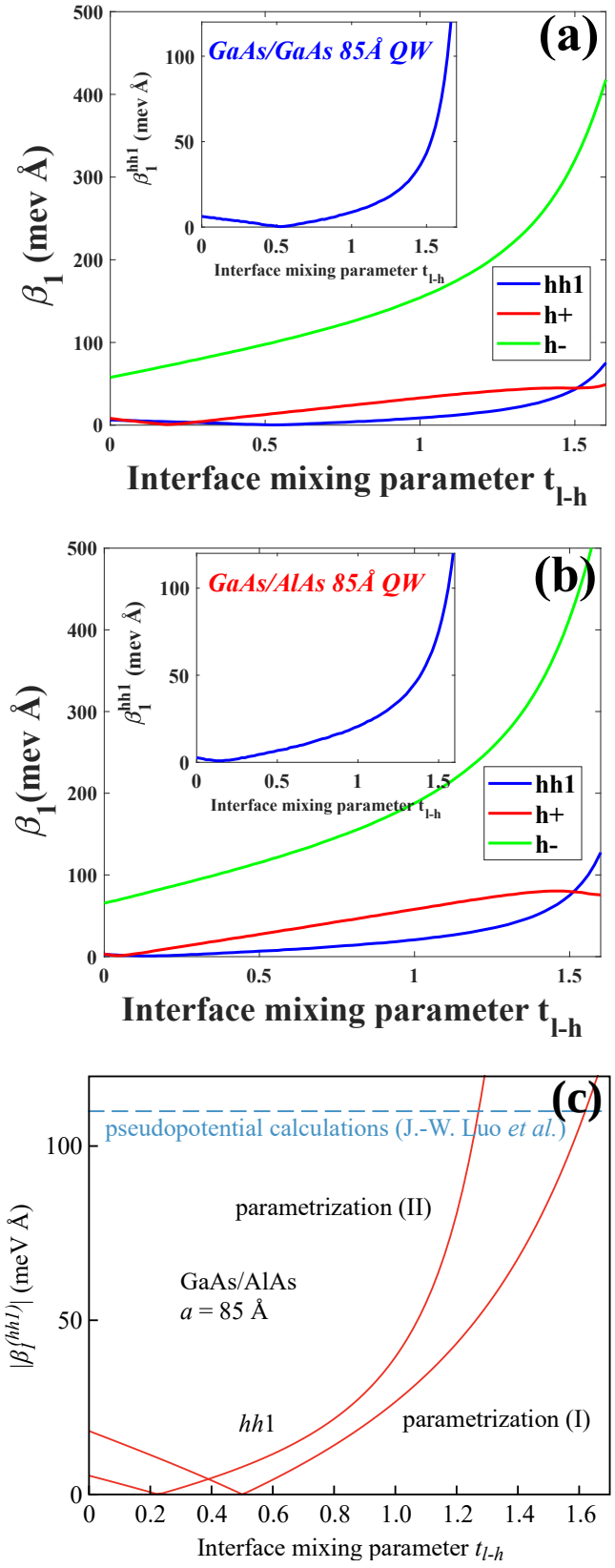

FIGURE 3.23: The results of calculations for valence subbands spin splitting as a function of the interface mixing strength for GaAs/GaAs and GaAs/AlAs 85 Å quantum well (a,b) respectively. The insets in (a,b) present heavy-hole (HH1) spin splitting for comparison with the result from Durnev et al. in figure (c) [31].

are the Luttinger parameters in an effective Hamiltonian approach, and z is the operator of the z-component of the hole wave vector. The mixing results in the following form for the ground-state heavy-hole and light-hole wavefunctions [250]

$$\Psi_{\pm}^{(L)} = C_L(z)\,|\pm 1/2\rangle \mp i(k_{\mp}d)\mathcal{S}_L(z)\,|\pm 3/2\rangle\,, \tag{3.192}$$

$$\Psi_{\pm}^{(H)} = C_h(z)\,|\pm 3/2\rangle \pm i(k_{\pm}d)\mathcal{S}_H(z)\,|\pm 1/2\rangle\,, \tag{3.193}$$

here $C_L(z) \equiv |LH\rangle$ (C like cos, and $\mathcal{S}$ like sin functions) and $C_H(z) \equiv |HH\rangle$ are the envelopes of hole motion along the z axis at $k = 0, \pm 1/2$, $\pm 3/2$ are the Bloch functions, $k_{\pm} = k_x \pm ik_y$, and d is the well width.

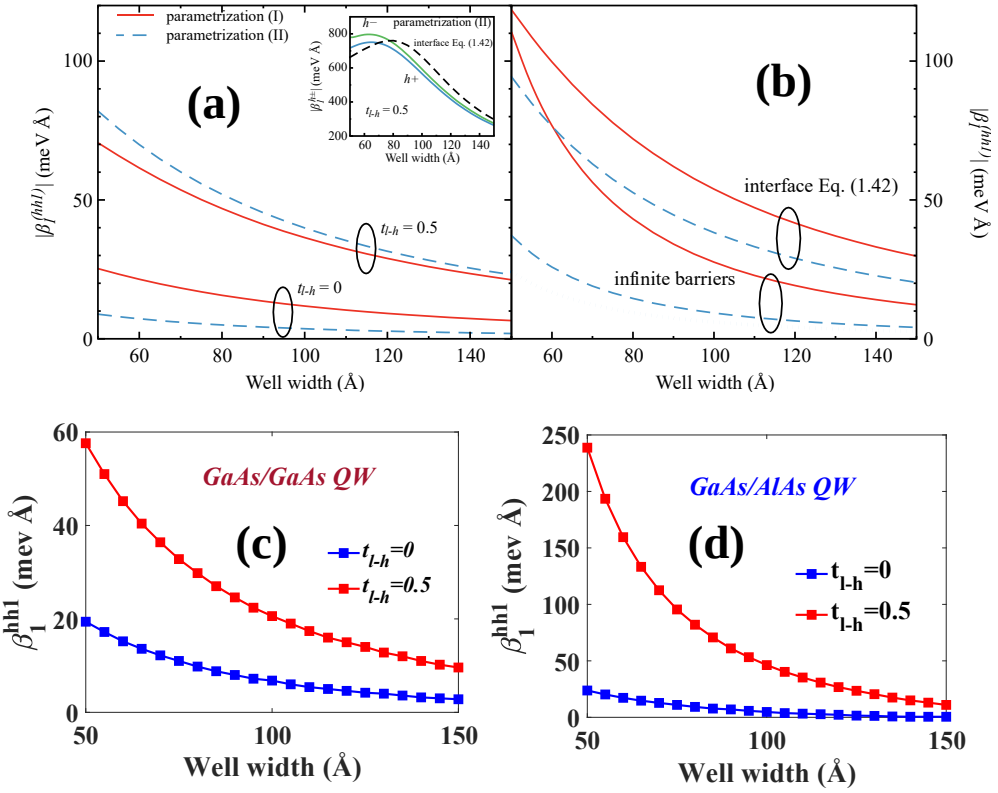

FIGURE 3.24: Spin-orbit k-linear term β_1 for the HH1 subband in a $GaAs/Al_{0.35}Ga_{0.65}As$ QW. (a) 14-band numerical calculation is shown for two sets of parameters (solid and dashed lines) and for two values of the interface mixing parameter: t_{l-h} = 0 and 0.5. The inset represents the results for h+ and h- subbands at t_{l-h} = 0 for the parametrization (I); (b) Analytical calculation of β_1 . Three bottom curves are obtained in the limit of infinitely-high barriers from Eq.(8) of Ref. [251] the solid curve represents the parametrization (I), the dotted and dashed curves are calculated for the parametrization (II). (c,d) Numerical calculations for GaAs/GaAs and GaAs/AlAs QW respectively, with Ivchenko's matching condition, mixing paramter t_{l-h} = 0 and 0.5, in the framework of a 30-band ***k.p*** method.

Envelopes $C_{L,H}(z)$ satisfy the Schrödinger equation corresponding to a normal incidence: This reads

$$C_{L,H}(z) = \mathcal{N}_{L,H} \begin{cases} \cos(k_{L,H}.z) \text{for} |z| < d/2 \\ \cos(k_{L,H}.a/2)\exp^{-\kappa_{L,Z}(|z|-a/2)} \text{for } |z| > d/2 \end{cases} \tag{3.194}$$

where

$$k_{L,H} = \sqrt{\frac{2m_0\varepsilon_{L,H}}{\hbar^2(\gamma_1 \pm 2\gamma_2)}},\ \mathrm{K}_{L,H} = \sqrt{\frac{2m_0(V_0 - \varepsilon_{L,H})}{\hbar^2(\gamma_1 \pm 2\gamma_2)}}. \tag{3.195}$$

$\mathcal{N}_{L,H}$ is the normalization factor, ε_L and ε_H are the energies of $|LH\rangle$ and $|HH\rangle$ states, $V(z) = 0$ at $|z| < d/2$ and $V(z) = V_0$ at $|z| > d/2$ is the confinement potential of the well. The barrier height V_0 is equal to the valence band offset at heterointerfaces. Boundary conditions for $C_{L,H}$ and $\mathcal{S}_{L,H}$ at the well interfaces are obtained from the continuity of $\Psi_{\pm}^{(L,H)}$ and $v_z\Psi_{\pm}^{(L,H)}$ columns with $\hat{v}_z$ being the velocity operator. Envelopes $S_{L,H}(z)$ are odd in z and satisfy the following equation [250]:

$$\left[-\frac{\hbar^2}{2m_0}\frac{\partial}{\partial z}(\gamma_1 \mp 2\gamma_2)\frac{\partial}{\partial z} + V(z) - \epsilon_{L,H}\right]\mathcal{S}_{L,H}(z) = -\frac{3\hbar^2}{m_0 d}\left\{\gamma_3\frac{\partial}{\partial z}\right\}\mathcal{S}_{L,H}(z) \tag{3.196}$$

Here, the upper and lower signs correspond to S_L and S_H respectively and curly brackets define the symmetrized product $\left\{\gamma_3\frac{\partial}{\partial z}\right\} = \frac{1}{2}\left(\gamma_3\frac{\partial}{\partial z} + \frac{\partial}{\partial z}\gamma_3\right)$. If one is interested to find the solution for S_H, one obtains: $S_H = A_1^H \sin\left(k_H\sqrt{\nu}z\right) + A_2^H \sin\left(k_H.z\right)$ in the quantum well where $\nu = \frac{\gamma_1 - 2\gamma_2}{\gamma_1 + 2\gamma_2}$ and where the coefficient $A_2^H = -\frac{\sqrt{3}\gamma_3}{2k_h d\gamma_2}\mathcal{N}_h$ and where the value of A_1^H ensures the relevant continuity equations at the interface with the barriers. One thus finds that, under oblique incidence, the heavy-hole level acquires a small light-hole component, proportional to $k_{\|}$ and with a different symmetry for the envelope amplitude.

From the energy point of view, the involvement of a surface potential term of the form $H_s = \frac{2}{\sqrt{3}}\frac{t_{lh}}{a_0 m_0}\{J_x J_y\}_s$ leads to an energy splitting $\Delta E_{SOI} = \beta_1 k_{\|} = \frac{2t_{lh}\hbar^2}{m_0 a_0} d\Psi_H \mathcal{S}_L$ for the $HH1$ [31]. The same occurs for the $LH1 - HH2$ doublet.

3.4.4 Conclusions of the section

Finally a short conclusion of this section is that an appropriate modification of the matching conditions previously proposed for 6x6 and 14x14 multiband Hamiltonians by Ivchenko and Durnev el al. [30, 31] accounting for the heavy and light hole mixing at the interface for the first time have been extended to 30x30 and 40x40 multiband **k.p** models in this thesis. The comparison of the wavefunction profile and valence band dispersion as well as spin splitting in a GaAs/AlAs quantum well structure for these different numerical models have been presented showing a good agreement. Thus, the implementation of the 30x30 and 40x40 multiband numerical algorithm developed in the thesis has been verified. This is very important point as in the next part, we will apply these matching condition in framework of 30 or 40 bands **k.p** Hamiltonian to describe an optical anisotropy (in spin lasers system) arising from broken symmetry at interfaces between ternary quantum wells and barriers of such structure like (In,Ga)As/GaAs quantum well.

CHAPTER 4

Green function techniques for multiband perturbative spin-orbit transport in heterostructures

Contents

The single-particle and two-particle Green functions (GF) are very useful mathematical and physical tools for studying the electronic, optical and transport properties of materials and multilayers because they can be used to express all the quantum observables of the system [252] thanks to their specific structures. Indeed, beyond the knowledge of the wavefunctions, the determination of the single particle GF allows for:

(i) An efficient treatment of complex systems, starting from idealized ones to *e.g.* interfaces and multilayered systems by handling the complexity as a perturbation involving *e. g* spin-orbit interactions. Moreover, in order to obtain the electronic structure of a periodic system with a localized impurity or defect, one can start from the GF method to treat the impurity (also like played by an interface) and subsequent SOI and spin-dependent electronic diffusion as perturbations to increasing order. Similarly, the presence of a surface can be considered to be a perturbation to the GF of an infinite medium. That way, we may introduce a GF treatment for mixed propagating and evanescent waves within tunnel junctions considering the spin-orbit interactions in a localized volume (tunnel barrier) or in semi-infinite half-spaces as a perturbation to investigate the properties of the scattered waves in the ground state taken at the zeroth order. This provides us a way to generalize the investigations dealing with spin polarized currents in GMR systems [253] by the involvement of the spin-orbit interactions in both current geometry (CIP and current-perpendicular to plane - CPP -).

(ii) More generally, the GF techniques are very useful for the calculation of the response of a system to an external field within the linear response regime thanks to the well-established Kubo's formula [254] like *e.g.* the conduction properties within multilayers [255] as well as the optical response of a system *via* the knowledge of the optical indexes, optical susceptibility or density matrix (optical gain).

For all those reasons, the ability to calculate the GF of a single interface or of a multilayered system with an arbitrary potential shaped barrier becomes mandatory as soon as the complete resolution of the Schrödinger equation of a complex system is not feasible. For an homogeneous media, the GF may be evaluated locally using unperturbed wavefunctions as a basis or may be calculated quite straightforwardly in the real space by matrix inversion technique like explored within a tight-binding approach. Similarly, the GF for an infinite periodic system may be obtained by matrix inversion in the reciprocal space. Nevertheless, in the case of semi-infinite or inhomogeneous systems, *e.g.* an infinite periodic system with surfaces or interfaces or involving two reservoirs (possibly ferromagnetic), one encounters the specific problem of the matching conditions for the GFs which have been largely discussed and debated in a series of papers [253, 256–258]. Those works deal with finding the proper general expressions for the GF describing the multilayer structures from the 'bulk' ones and involving the relevant transmissions and reflections coefficients at each interface. In this chapter, we will start to give an expression of the spin-polarized GF corresponding to a simple potential step in the energy range of an evanescent transmission from pure spin-up channel to pure spin-down channel without SOI before adapting and generalizing to multilayers and multiband hamiltonian.

Although we mostly deal with the development of the GF methods adapted to spin-orbit-assisted skew tunneling for an interface or a tunnel junction, it is worth to mention a few applications without however giving a full comprehensive view out-of-scope of the present manuscript. For that physical issues, the GF formalism with spin-orbit extension has been employed with great success to study transport through mesoscopic devices, exchange coupling, GMR [255] as well as tunneling magnetoresistance [259], surface and interface states, as well as spin-Hall effect of heavy-metal/transition metal alloys [260].

4.1 Green functions techniques for transport calculations.

4.1.1 Green functions and Lippman-Schwinger equation

The scattering presented here theory is essentially a time-independent perturbation theory applied to the case of a continuous spectrum. That means that we know that it exists a complete eigenstates set (propagating or evanescent) corresponding to the full Hamiltonian for every possible energy, $\mathcal{E}$. At this given energy $\mathcal{E}$, one may be interested to find the perturbed eigenstates $|\Psi(\mathcal{E})\rangle$. There exist usually some degenerate eigenstates for any given energy. So, the question becomes which of the presumably infinitely degenerate full-eigenstates we are trying to compute? The answer originates from the causality; we want to be able to completely specify the probability current amplitude incoming *in* from $\boldsymbol{r} \longrightarrow \infty$, and we want the theory to give us the corresponding outgoing current amplitude. The way we do this is picking an unperturbed eigenstate which has the desired incoming current amplitude. At this stage we do not need to worry what the outgoing current amplitude of the unperturbed state is. The second step is to make sure that our perturbation theory generates no contribution and no changes on the incoming currents, which we accomplish by considering such condition, under the argument of causality. As we will see, this means that the resulting *full eigenstates* set will have desired incoming current amplitudes. We recall that solving a partial differential equation requires first to specify the boundary conditions, which is exactly what the standard scattering theory formalism is designed to do.

We first consider a spin-polarized particle free of any orbital moment and described by a 2−component spinor. The Hamiltonian only involves 2×2 identity and Pauli matrices. Typically, the scattering formalism is described within the following approach: an incident particle in the state $|\Psi_0\rangle$ is scattered by the 2×2 potential V, resulting in a scattered state $|\Psi_s\rangle$. The incident state $|\Psi_0\rangle$ is assumed to be an eigenstate of the host Hamiltonian H_0, with the eigenvalue $\mathcal{E}$. This is mathematically expressed as:

$$(\mathcal{E} - H_0)\,|\Psi_0\rangle = 0, \tag{4.1}$$

The potential $V(\mathbf{r})$ is assumed to be *localized* (without however being always a necessary condition), so that

$$\lim_{\boldsymbol{r}\longrightarrow\infty} V(\mathbf{r}) = 0. \tag{4.2}$$

The goal of the scattering theory is then to solve the full eigenvalue problem

$$(\mathcal{E} - H_0 - V)\,|\Psi\rangle = 0, \tag{4.3}$$

where $|\Psi\rangle$ is the eigenstate of the full Hamiltonian $H = H_0 + V$ of the system with the energy $\mathcal{E}$. It should be clear that there is a different $|\Psi_0\rangle$ and correspondingly a different $|\Psi\rangle$ for each energy $\mathcal{E}$, even though our notation does not indicate this explicitly. We start by defining the scattered state $|\Psi_s\rangle$ *via*

$$|\Psi_s\rangle = |\Psi\rangle - |\Psi_0\rangle\,. \tag{4.4}$$

The full Schrödinger equation (Eq. 4.3) may be written as

$$(\mathcal{E} - H_0)\,|\Psi\rangle = V\,|\Psi\rangle\,, \tag{4.5}$$

which, after substituting $|\Psi\rangle = |\Psi_s\rangle + |\Psi_0\rangle$ and making use of Eq. 4.1, this gives:

$$(\mathcal{E} - H_0)\,|\Psi_s\rangle = V\,|\Psi\rangle\,, \tag{4.6}$$

otherwise,

$$|\Psi_s\rangle = (\mathcal{E} - H_0)^{-1} V |\Psi\rangle , \tag{4.7}$$

by adding $|\Psi_0\rangle$ to both sides of Eq. 4.7, one obtains:

$$|\Psi\rangle = |\Psi_0\rangle + (\mathcal{E} - H_0)^{-1} V |\Psi\rangle . \tag{4.8}$$

This is well known as the Lippman-Schwinger equation. It is often expressed in a slightly more compact notation by introducing the concept of Green's function, defined as:

$$G_0^{\pm} = \lim_{\epsilon \longrightarrow 0} (\mathcal{E} - H_0 \pm i\epsilon)^{-1} . \tag{4.9}$$

G_0^+ (G_0^-) is called retarded (advanced) Green function. The term $i\epsilon$ is added to enforce causality by making sure that $|\Psi_s\rangle$ has no incoming probability current associated with it. It makes sense that scattered waves propagate away from the source, and not other way around. In our work, as we only consider the retarded Green function, for simplicity we use G_0 instead of G_0^+. Using this definition, the Lippman-Schwinger equation takes its standard form:

$$|\Psi\rangle = |\Psi_0\rangle + G_0 V |\Psi\rangle . \tag{4.10}$$

Solving the Lippman-Schwinger equation for $|\Psi\rangle$ is formally very simple. This yields:

$$|\Psi\rangle = (1 - G_0 V)^{-1} |\Psi_0\rangle . \tag{4.11}$$

The Born series give:

$$|\Psi\rangle = |\Psi_0\rangle + G_0 V |\Psi_0\rangle + G_0 V G_0 V |\Psi_0\rangle + ... \tag{4.12}$$

and, to the first order,

$$|\Psi\rangle = |\Psi_0\rangle + G_0 V |\Psi_0\rangle . \tag{4.13}$$

Written as an integral equation, Eq. 4.13 becomes

$$\Psi(\boldsymbol{r}) = \Psi_0(\boldsymbol{r}) + \int G_0(\boldsymbol{r}, \boldsymbol{r}')_0 V(\boldsymbol{r}') \Psi_0(\boldsymbol{r}') d\boldsymbol{r}', \tag{4.14}$$

where $\langle \boldsymbol{r} \ |\Psi\rangle = \Psi(\boldsymbol{r})$, and $G_0(\boldsymbol{r}, \boldsymbol{r}') = \langle \boldsymbol{r}| \, G_0 \, |\boldsymbol{r}'\rangle$. The GF, $G_0(\boldsymbol{r}, \boldsymbol{r}')$, is a solution of Eq. 4.9.

$$(\mathcal{E} - H_0) \, G_0(\boldsymbol{r}, \boldsymbol{r}') = \delta(\boldsymbol{r} - \boldsymbol{r}') . \tag{4.15}$$

The respective retarded and advanced Green functions $G_0^{\pm}$ for homogeneous host materials of eigenvalues $\mathcal{E}$ and eigenvectors Ψ_k, with a certain translational invariance involving Bloch $\mathbf{k}$ states, and satisfying $(\mathcal{E} - H_0)\Psi_k(\boldsymbol{r}) = 0$ at the energy $\mathcal{E}$, is generally determined according to the general formula:

$$G_0^{\pm}(\mathcal{E}, \boldsymbol{r}, \boldsymbol{r}') = \sum_k \frac{\Psi_k(\boldsymbol{r}) \Psi_k^*(\boldsymbol{r}')}{\mathcal{E} - \mathcal{E}_k \pm i\eta}, \tag{4.16}$$

where $\mathcal{E}_k$ is the energy of the state $|k\rangle$.

Generally, in the multiband, one has [261]:

$$G_0^{\pm}(\mathcal{E}, \boldsymbol{r}, \boldsymbol{r}') = \sum_k \sum_j \frac{\Psi_k^j(\boldsymbol{r}) \left(\Psi_k^j(\boldsymbol{r}')\right)^*}{\mathcal{E} - \mathcal{E}_k^j \pm i\eta^j} \tag{4.17}$$

to find the bulk or in heterostructures where η ($\eta > 0$) represents an infinitesimal value needed for convergence; η ensures that the electronic waves coming from the left (right) side remains finite over the whole host volume after a given propagation time τ. $|k_j\rangle$ is the state of wavevector k and band j; $\mathcal{E}_k^j$ is the energy of such sate. The equivalent Green function $G_0^{\pm}$ to be derived for a junction composed of two semi-infinite media or for a tunnel junction is often more complex to obtain. We present here a general method developed for spin-unpolarized particles based on some references [253, 256–258] before its generalization to spin-polarized particles.

4.1.2 Green function and the scattering matrix

It is possible to relate the Green function directly to the scattering matrix that is developed in details in Appendix C [262]. This relation is very convenient as it will allow one to write the total transmission coefficient as well as the wavefunction in a compact form containing the total Green function. Let us now discuss an effective way to connect the Green function and scattering matrix formalism. In order to get some insights, we consider firstly a single band green function with single layer and then go to a general case with multiband Green function in multilayer structure.

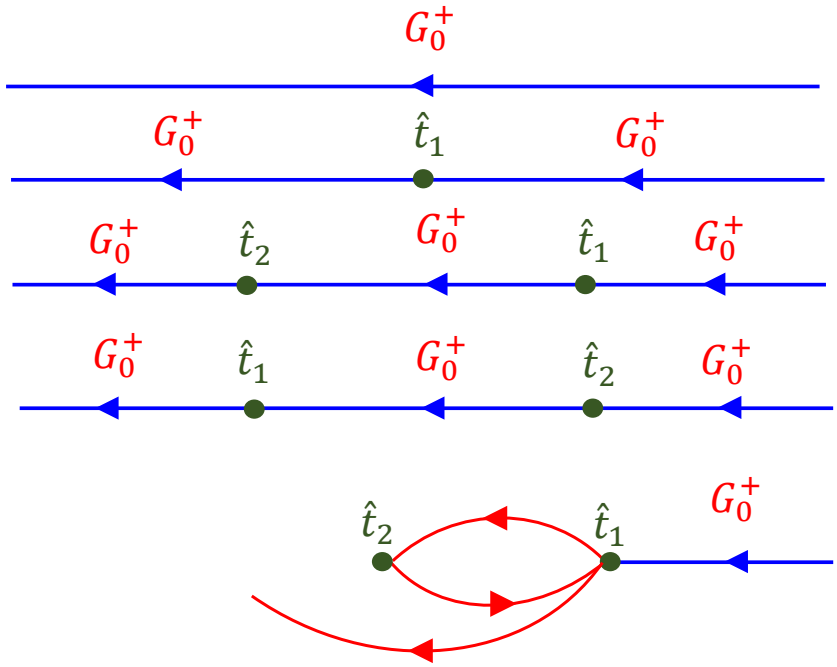

FIGURE 4.1: Scheme of Green function where $\hat{t}_1$ and $\hat{t}_2$ symbols design scattering evens.

A single layer.

Considering a single layer contacting with left and right electrodes with a point $\boldsymbol{r}_L$ inside the left electrode where the amplitudes of the scattering matrix are evaluated, and an equivalent point $\boldsymbol{r}_R$ inside the right electrode. We then, define a single band Green function as:

$$G(\boldsymbol{r}_R, \boldsymbol{r}_L, E) = \sum_n \sum_m \psi_m^*(\boldsymbol{\rho}_R) G_{nm}(z_R, z_L, E) \psi_n(\boldsymbol{\rho}_L) \tag{4.18}$$

where the sums are over all the number of channels n at the left and m at right leads, respectively. Then one has:

$$G_{nm}(z_R, z_L, E) = -\frac{i}{\hbar\sqrt{|v_n||v_m|}} t_{nm} e^{i(k_n z_L - k_m z_R)} \tag{4.19}$$

is the Green function associates with channel n^{th} at point z_L in the left electrode, and channel m^{th} at point z_R in the right electrode, $v_{n(m)}$ is the group velocity of an electron in n^{th} (m^{th}) channel. Substituting Eq.4.19 into Eq.4.18. We then obtain:

$$G(\boldsymbol{r}_R, \boldsymbol{r}_L, E) = -\sum_n \sum_m \frac{i}{\hbar\sqrt{|v_n||v_m|}} \psi_m^*(\boldsymbol{\rho}_R) t_{nm} \psi_n(\boldsymbol{\rho}_L) e^{i(k_n z_L - k_m z_R)} \tag{4.20}$$

Following the same procedure for two points $\boldsymbol{r}_L^{'} < \boldsymbol{r}_L$ in the left electrode, a similar expression can be derived that relates the total Green function to the reflection amplitudes:

$$G(\boldsymbol{r}_L, \boldsymbol{r}_L^{'}, E) = -\sum_n \sum_{n'} \frac{i}{\hbar v_n} \psi_{n'}^*(\boldsymbol{\rho}_L^{'}) \left[\delta_{nn'} e^{ik_n\left(z_L^{'} - z_L\right)} + r_{nn'}\sqrt{\frac{v_n}{v_{n'}}} e^{-i\left(k_{n'} z_L^{'} + k_n z_L\right)}\right] \psi_n(\boldsymbol{\rho}_L) \tag{4.21}$$

Equation 4.20 and 4.21 are the expressions relating the Green function to the elements of the scattering matrix. We can now express the total transmission coefficient in terms of the Green function by inverting equation 4.20: multiply it by $\psi_m(\boldsymbol{\rho}_R)\tau_{nm}\psi_n^*(\boldsymbol{\rho}_L)e^{-i(k_n z_L - k_m z_R)}$, integrate over the coordinates $\boldsymbol{r}_L$ and $\boldsymbol{r}_R$ and use the orthonormality condition between the transverse wavefunctions. Then the transmission amplitudes are:

$$t_{nm} = i\hbar\sqrt{v_n v_m} \int d\boldsymbol{\rho}_L \int d\boldsymbol{\rho}_R \psi_m^*(\boldsymbol{\rho}_R)\, G(\boldsymbol{\rho}_R, \boldsymbol{\rho}_L, E)\, \psi_n(\boldsymbol{\rho}_L) \tag{4.22}$$

where we have defined:

$$G(\boldsymbol{\rho}_R, \boldsymbol{\rho}_L, E) = G(\boldsymbol{\rho}_R, z_R = 0, \boldsymbol{\rho}_L, z_L = 0, E) \tag{4.23}$$

The transmission coefficient then reads:

$$\begin{aligned} T_{LR} = \sum_n \sum_m t_{nm} t_{nm}^* = \hbar^2 \sum_n \sum_m v_n v_m \int\int\int\int \psi_m^*(\boldsymbol{\rho}_R) G^+(\boldsymbol{\rho}_R, \boldsymbol{\rho}_L, E) \psi_n(\boldsymbol{\rho}_L) \\ \times \psi_m(\boldsymbol{\rho}_R^{'}) \left[G^+(\boldsymbol{\rho}_R^{'}, \boldsymbol{\rho}_L^{'}, E)\right]^* \psi_n^*(\boldsymbol{\rho}_L^{'}) d\boldsymbol{\rho}_L d\boldsymbol{\rho}_R d\boldsymbol{\rho}_L^{'} d\boldsymbol{\rho}_R^{'} \end{aligned} \tag{4.24}$$

If we define:

$$\Gamma_R(\boldsymbol{\rho}_R^{'}, \boldsymbol{\rho}_R) = \sum_m \psi_m(\boldsymbol{\rho}_R^{'}) \hbar v_m \psi_m^*(\boldsymbol{\rho}_R) \tag{4.25}$$

and:

$$\Gamma_L(\boldsymbol{\rho}_L, \boldsymbol{\rho}_L^{'}) = \sum_n \psi_n(\boldsymbol{\rho}_L) \hbar v_n \psi_n^*(\boldsymbol{\rho}_L^{'}) \tag{4.26}$$

Then Eq. 4.24 becomes:

$$T_{LR} = \int\int\int\int \Gamma_R(\boldsymbol{\rho}_R^{'}, \boldsymbol{\rho}_R) G^+(\boldsymbol{\rho}_R, \boldsymbol{\rho}_L, E) \Gamma_L(\boldsymbol{\rho}_L, \boldsymbol{\rho}_L^{'}) G^-(\boldsymbol{\rho}_L^{'}, \boldsymbol{\rho}_R^{'}, E) d\boldsymbol{\rho}_L d\boldsymbol{\rho}_R d\boldsymbol{\rho}_L^{'} d\boldsymbol{\rho}_R^{'} \tag{4.27}$$

and in the discrete-space representation we can re-write compactly Eq. 4.27 in operator notation as:

$$T_{LR} = Tr\left\{\hat{\Gamma}_R \hat{G}^+ \hat{\Gamma}_L \hat{G}^-\right\} = T_{RL} \tag{4.28}$$

Multilayer structure [263, 264]

We now consider a general case with a multiband scattering process within a multilayers. For simply, we consider a quasi one dimensional problem. Note that each interface within 1D multilayers act as a diffusive (reflected - transmitted) that can be described by a surface potential $\hat{V}_i$. A general (multiband) Green function of the system then satisfy:

$$(\varepsilon - H)\, G = \delta\,(z - z') \tag{4.29}$$

where $H = H_0 + \sum_i \hat{V}_i$, here H_0 is the Hamiltonian of the system without surface potential arising from the interfaces between two layer. Or one has:

$$\left(\varepsilon - H_0 + \sum_i \hat{V}_i\right) G = \delta\,(z - z') \tag{4.30}$$

We define a Green function G_0 as:

$$G_0^{\pm} = \lim_{\epsilon \longrightarrow 0} (\varepsilon - H_0 \pm i\epsilon)^{-1}\,. \tag{4.31}$$

(ϵ is very small) then for one single scattered center, the multiband Green function G reads:

$$G = G_0 + G_0\hat{V}G_0 + G_0\hat{V}G_0\hat{V}G_0 + \ldots \tag{4.32}$$

or equivalently:

$$G = \frac{1}{1 - G_0\hat{V}} G_0 \tag{4.33}$$

giving:

$$G^{-1} = G_0^{-1} - \hat{V} \tag{4.34}$$

We define a T-matrix operator as:

$$\hat{T} = \hat{V} + \hat{V}G_0\hat{V} + \hat{V}G_0\hat{V}G_0\hat{V} + \ldots \tag{4.35}$$

where the right hand side of above equation is a infinite series. If this series converges then $\hat{T}$ will satisfy the well-known Dyson equation:

$$\hat{T} = \hat{V} + \hat{V}G_0\hat{T} \tag{4.36}$$

which possesses the formal solution:

$$\hat{T} = \left(1 - \hat{V}G_0\right)^{-1}\hat{V} = \left(\hat{V}^{-1} - G_0\right)^{-1} \tag{4.37}$$

Note that even in a case the series in Eq 4.35 does not converge, the relation 4.36 between $\hat{T}$ and $\hat{V}$ is still valid, especially for the types of potentials of primary interest here: the surface potential or localized potential. The Green function can be expressed in terms of T-matrix operator [264]:

$$\begin{aligned} G &= G_0 + G_0\hat{V}G_0 + G_0\hat{V}G_0\hat{V}G_0 + \ldots \\ &= G_0 + G_0\hat{V}G \\ &= G_0 + G_0\hat{T}G_0 \end{aligned} \tag{4.38}$$

leading to:

$$\hat{V}G = \hat{T}G_0 \tag{4.39}$$

In general, for multiple scattered center $\hat{V} = \sum_i \hat{V}_i$, the T-matrix operator reads:

$$\hat{T} = \hat{V} + \hat{V}G_0\hat{V} + \hat{V}G_0\hat{V}G_0\hat{V} + ... = \left[\hat{V}^{-1} - G_0\right]^{-1} \tag{4.40}$$

$$= \left[\left(\sum_i \hat{V}_i\right)^{-1} - G_0\right]^{-1} = \sum_i \hat{V}_i + \left[\sum_i \hat{V}_i\right] G_0 \left[\sum_j \hat{V}_j\right] + ... \tag{4.41}$$

One observes that the sum of all repeated, consecutive products with the same potential index i such as $\hat{V}_i + \hat{V}_i G_0 \hat{V}_i + \hat{V}_i G_0 \hat{V}_i G_0 \hat{V}_i + ...$ that can be grouped together. So, if we denote the t-matrix:

$$\hat{t}_i = \hat{V}_i + \hat{V}_i G_0 \hat{V}_i + \hat{V}_i G_0 \hat{V}_i G_0 \hat{V}_i + ... \tag{4.42}$$

Then the T-matrix operator reads:

$$\hat{T} = \sum_i \hat{t}_i + \sum_i \sum_{j \neq i} \hat{t}_i G_0 \hat{t}_j + ... \tag{4.43}$$

Denoting by $\hat{T}_{ij}$ the sum of all terms (scattering sequences) in Eq. 4.43 that start with $\hat{t}_i$ and end with $\hat{t}_j$ then one has:

$$\hat{T} = \sum_{i,j} \hat{T}_{ij} = \left[\left(\sum_i \hat{V}_i\right)^{-1} - G_0\right]^{-1} \tag{4.44}$$

It can be shown through direct iteration that the quantities $\hat{T}_{ij}$ satisfy:

$$\hat{T}_{ij} = \hat{t}_i \delta_{ij} + \hat{t}_i G_0 \sum_{k \neq i} \hat{T}_{kj} \tag{4.45}$$

Now, if we introduce in a unique manner the site off-diagonal element $G_0^{(i,k)}$ of the free particle propagator between i^{th} and $k^t h$ interfaces (that a part of G_0 which connect $\hat{t}_i$ to $\hat{t}_k$ in Eq. 4.43) and write Eq. 4.45 in the form:

$$\hat{T}_{ij} = \hat{t}_i \delta_{ij} + \hat{t}_i \sum_{k \neq i} G_0^{(i,k)} \hat{T}_{kj} \tag{4.46}$$

Then a system of equations like 4.46 for all $\hat{T}_{ij}$ terms can be re-written in a suitable matrix form as following:

$$M = N + N\tilde{G}_0 M \tag{4.47}$$

where M is a matrix that its elements are given by $M_{ij} \equiv \hat{T}_{ij}$:

$$M = \begin{bmatrix} \hat{T}_{11} & ... & \hat{T}_{1i} & ... \\ \vdots & \ddots & \vdots & \vdots \\ \hat{T}_{i1} & ... & \hat{T}_{ii} & ... \\ \vdots & \vdots & \vdots & \ddots \end{bmatrix} \tag{4.48}$$

Matrix N that its elements are given by $N_{ij} \equiv \hat{t}_i \delta_{ij}$ (N is diagonal matrix):

$$N = \begin{bmatrix} \hat{t}_1 & & & \\ & \ddots & & \\ & & \hat{t}_i & \\ & & & \ddots \end{bmatrix} \tag{4.49}$$

and matrix $\tilde{G}_0$ that its elements are given by $\tilde{G}_0^{ij} \equiv G_0^{(i,k)} \left(1 - \delta_{ij}\right)$:

$$\tilde{G}_0 = \begin{bmatrix} 0 & G_0^{(i,j)} \\ G_0^{(i,j)} & 0 \end{bmatrix} \tag{4.50}$$

$\tilde{G}_0$ is a off-diagonal matrix or matrix with the zero-diagonal elements.

Equation 4.47 possesses a solution:

$$M = \left(1 - N\tilde{G}_0\right)^{-1} N = \left[N^{-1}\left(1 - N\tilde{G}_0\right)\right]^{-1} = \left(N^{-1} - \tilde{G}_0\right)^{-1} \tag{4.51}$$

Note that:

$$N^{-1} = \begin{bmatrix} \hat{t}_1^{-1} & & & \\ & \ddots & & \\ & & \hat{t}_i^{-1} & \\ & & & \ddots \end{bmatrix} \tag{4.52}$$

then one could obtain the matrix M as the inverse of a matrix $K = N^{-1} - \tilde{G}_0$ with matrix elements:

$$K_{ij} = \hat{t}_i^{-1} \delta_{ij} - G_0^{(i,j)} \left(1 - \delta_{ij}\right) \tag{4.53}$$

and finally, all the terms $\hat{T}_{ij} = M_{ij}$ can be obtained immediately giving the T-matrix operator $\hat{T}$ afterward.

Besides, the Green function formula in multiple scattered also reads:

$$G = G_0 + G_0 \hat{V} G = G_0 + G_0 \hat{T} G_0 \tag{4.54}$$

where $\hat{V} = \sum_i \hat{V}_i$ and $\hat{T} = \sum_{i,j} \hat{T}_{ij} = \sum_{i,j} M_{ij}$, or in the other words, $\hat{T}$ is a sum over all elements of super matrix M.

Making a comparison to the global scattering matrix formalism developments in Appendix C, one could realize a similarity between M and scattering matrix S_G that their matrix elements describe all possible scattering sequences leading to $\hat{T} \sim S_G$ or simply, one may write:

$$S_G = \hat{j}^{-1} M \tag{4.55}$$

where $\hat{j}$ is the current operator but also the surface potential term. Since we have the important relation (as we will prove it in the next section):

$$G_0 \overleftarrow{j} = P_0 \tag{4.56}$$

and in terms of scattering event at the i^{th} interface, $\hat{t}_i$ plays a role as the interface scattering matrix S_i defined in Appendix C:

$$S_i = \begin{bmatrix} t & r' \\ r & t' \end{bmatrix}_i \tag{4.57}$$

Consequently, that make it possible to write out the matrix M in a compact form as:

$$M = \begin{bmatrix} S_1^{-1} & -G_0^{(2,1)} & 0 & 0 & \dots & 0 & 0 \\ -G_0^{(1,2)} & S_2^{-1} & -G_0^{(3,2)} & 0 & \dots & 0 & 0 \\ 0 & -G_0^{(2,3)} & S_3^{-1} & -G_0^{(4,3)} & \dots & 0 & 0 \\ 0 & 0 & -G_0^{(3,4)} & S_4^{-1} & \dots & 0 & 0 \\ \vdots & \vdots & \vdots & \vdots & \ddots & \vdots & \vdots \\ 0 & 0 & 0 & 0 & \dots & S_{N-1}^{-1} & -G_0^{(N,N-1)} \\ 0 & 0 & 0 & 0 & \dots & -G_0^{(N-1,N)} & S_N^{-1} \end{bmatrix}^{-1} \tag{4.58}$$

Finally, in order to completely finish this description of multiband Green function for multiple scattering, we are going to demonstrate relation 4.56 in framework of **k.p** method in following part.

4.1.3 *k.p theory of Green's function in multilayer*

Considering a multilayer structure, then in a single layer, one has:

$$H = \overleftarrow{\partial}_z \hat{\gamma}_{ij} \overrightarrow{\partial}_z + i\hat{\beta}_{ij} \overrightarrow{\partial}_z + \hat{\Delta}_{ij} \tag{4.59}$$

The schrödinger equation reads:

$$(H - \varepsilon)\,\Psi = 0 \tag{4.60}$$

giving an equation for the wavefunction:

$$\left(\overleftarrow{\partial}_z \hat{\gamma}_{ij} \overrightarrow{\partial}_z + i\hat{\beta}_{ij} \overrightarrow{\partial}_z + \hat{\Delta}_{ij} - \varepsilon\delta_{ij}\right) \Psi = 0 \tag{4.61}$$

and for the Green function:

$$\left(\overleftarrow{\partial}_z \hat{\gamma}_{ij} \overrightarrow{\partial}_z + i\hat{\beta}_{ij} \overrightarrow{\partial}_z + \hat{\Delta}_{ij} - \varepsilon\delta_{ij}\right) G_{ik}^{+}(z, z') = \delta_{jk}\delta(z, z') \tag{4.62}$$

Taking complex conjugate of Eq. 4.62:

$$\left(\overleftarrow{\partial}_z \hat{\gamma}_{ij}^{*} \overrightarrow{\partial}_z + i\hat{\beta}_{ij}^{*} \overrightarrow{\partial}_z + \hat{\Delta}_{ij}^{*} - \varepsilon\delta_{ij}^{*}\right) G_{ki}^{-}(z, z') = \delta_{jk}\delta(z, z') \tag{4.63}$$

or:

$$G_{ki}^{-}(z, z') \left(\overleftarrow{\partial}_z \hat{\gamma}_{ij} \overrightarrow{\partial}_z + i\hat{\beta}_{ij} \overrightarrow{\partial}_z + \hat{\Delta}_{ij} - \varepsilon\delta_{ij}\right) = \delta_{jk}\delta(z, z') \tag{4.64}$$

Left multiplying Eq. 4.61 by $G_{ki}^{-}(z, z')$ and right multiplying Eq. 4.62 by $\Psi_j(z)$ then making summation as well as integration over the z coordinate, one obtains:

$$\Psi_k(z') = \frac{1}{2} G \overleftarrow{j} \Psi_i(z) - \frac{1}{2} G \overrightarrow{j} \Psi_i(z) \tag{4.65}$$

or :

$$\Psi_k(z') = G \overleftarrow{j} \Psi_i(z) \tag{4.66}$$

leading to a fact that $G\overleftarrow{j}$ is the propagation matrix.

So, from which it becomes possible to calculate the wavefunction profile within the whole multilayer involving multiple scattering events.

4.1.4 Link between the Kubo and Landauer's formulas [265]

We are now going to derive the link between the Kubo and Landauer formulas. We will give a generalization of that formulas when we will address the specific multiband $\boldsymbol{k.p}$ theory of spin-current in the next chapter. One has then to consider the general expression of the conductance G in terms of the current-current correlation function as expressed by the Kubo's formula according to:

$$G_{Cond}(\omega) = i\frac{2e^2}{\hbar\omega}\Im\int_{-\infty}^{\infty} dt\,\exp^{i(\omega+i\eta)t}\,\Theta(t)\left\langle[\hat{J}(z,t),\hat{J}(z,0)]\right\rangle_0 \tag{4.67}$$

where Θ is the Heaviside function, ω the frequency with $\epsilon = \hbar\omega$ and $\langle\rangle_0$ means the average of the $[\hat{J}(z,t),\hat{J}(z,0)]$ correlation operator on the ground state and this can be evaluated at any point of the heterostructure due to the current conservation. In terms of the second quantization, one has:

$$\hat{J}_z = \sum_{\alpha\beta} j_{\alpha\beta}(z) c_\alpha^\dagger c_\beta \tag{4.68}$$

where $c_\alpha^\dagger c^\beta$ are the creation and annihilation operators of states α and β. We remind that the matrix element $j_{\alpha\beta}$ writes $j_{\alpha\beta} = (-i)\frac{\hbar}{m^*}\psi_\alpha^* \overleftrightarrow{\hat{J}_z}\, \psi_\beta$ and finally is independent of the space coordinate z. Thus, one obtains:

$$\left\langle[\hat{J}(z,t),\hat{J}(z,0)]\right\rangle_0 = \sum_{\alpha\alpha'} J_{\alpha\alpha'}(z)\sum_{\beta\beta'} J_{\beta\beta'}(z)\exp^{i(\epsilon_\alpha-\epsilon'_\alpha)t/\hbar}\left\langle\left[c_\alpha^\dagger c_{\alpha'}, c_\beta^\dagger c_{\beta'}\right]_0\right\rangle \tag{4.69}$$

$$\left\langle[\hat{J}(z,t),\hat{J}(z,0)]\right\rangle_0 = \sum_{\alpha\alpha'} |J_{\alpha\alpha'}(z)|^2\exp^{i(\epsilon_\alpha-\epsilon'_\alpha)t/\hbar}\left[n_F(\epsilon_\alpha) - n_F(\epsilon_{\alpha'})\right] \tag{4.70}$$

where n_F is the Fermi occupation number. Inserting this equation into Eq. 4.67, we get:

$$G_{Cond}(\omega) = -\frac{2e^2}{\omega}\Im\sum_{\alpha\alpha'}\frac{|J_{\alpha\alpha'}|^2}{\hbar\omega + i\eta + \epsilon_\alpha - \epsilon'_\alpha}\left[n_F(\epsilon_\alpha - \epsilon'_\alpha\right] \tag{4.71}$$

The conductance in the DC limit at zero frequency ($\omega \to 0$) is given by:

$$G_{Cond}(0) = -2\pi\hbar^2\sum_{\alpha\alpha'}|J_{\alpha\alpha'}(z)|^2\left(-\frac{\partial n_F(\epsilon_\alpha)}{\partial\epsilon_\alpha}\right)\delta\left(\epsilon_\alpha - \epsilon_{\alpha'}\right) \tag{4.72}$$

to get:

$$G_{Cond}(0) = -2\pi\hbar^2\sum_{\alpha\alpha'}|J_{\alpha\alpha'}(z)|^2\left(-\frac{\partial n_F(\epsilon_\alpha)}{\partial\epsilon_\alpha}\right)\delta\left(\epsilon_\alpha - \epsilon_{\alpha'}\right) \tag{4.73}$$

The calculation is independent of the z-coordinate thanks to the current conservation property. The calculation can be performed in the right lead for incoming waves from the left. Because of the property that $Re\left(\left\langle m\left|\overrightarrow{\hat{J}}\right|n\right\rangle + \left\langle m\left|\overleftarrow{\hat{J}}\right|n\right\rangle\right) = 0$, one can observe that

$$\sum_{\alpha\alpha'}|J_{\alpha\alpha'}(z)|^2 = \mathrm{Trace}_{(n,m)=k_\parallel}\left|\langle J_m\rangle\right|^2(t_{nm})^\dagger(t_{mn}) \tag{4.74}$$

where n (m) are the ingoing (outgoing) states giving *in fine* the well known Landauer formula:

$$G_{Cond}(0) = \frac{e^2}{h}\text{Trace}_{k_\parallel}\mathcal{T}_{k_\parallel} \tag{4.75}$$

where $\mathcal{T}_{k_\parallel} = \sum_m t^*_{mn}t_{mn}$ is the overall transmission coefficient for incoming channel n. To establish the expression of the latest Landauer formula, we have used the variable change $\sum_{k_\parallel} = \frac{1}{(2\pi J_m \hbar)}\int d\epsilon$. We will give further proofs in the following section dealing with multiband $\boldsymbol{k.p}$ Hamiltonian.

4.2 Green function and spin transport

4.2.1 Interfacial Green's function for spinless particles free of spin and spin-orbit potentials

As an example, we first consider the solution of Eq. 4.15 for a scalar (or spinless) particle in a homogenous potential U_1 for $z < 0$, and U_2 for $z > 0$. *In this part, we have deliberately decided to detail the whole mathematical developments to find the correct description of the GF for a single interface*. The GF satisfies the equation:

$$(\mathcal{E} - H_0)\, G_0(z, z') = \delta(z - z') \tag{4.76}$$

or

$$\left(\mathcal{E} - \frac{\hbar^2}{2}\frac{\partial}{\partial z}\frac{1}{m^*(z)}\frac{\partial}{\partial z} - U(z)\right) G_0(z, z') = \delta(z - z') \tag{4.77}$$

where $H_0 = \left(\frac{\hbar^2}{2}\right)\frac{\partial}{\partial z}\frac{1}{m^*(z)}\frac{\partial}{\partial z} + U(z)$. is the symmetrized Hamiltonian. Equation. 4.77 is an ordinary differential equation, the method to find the GF has been well mentioned in mathematical textbooks, normally it has three main steps. We use this procedure in a particular case, *i.e.*, Eq. 4.77, with the boundary conditions at $z = \pm\infty$.

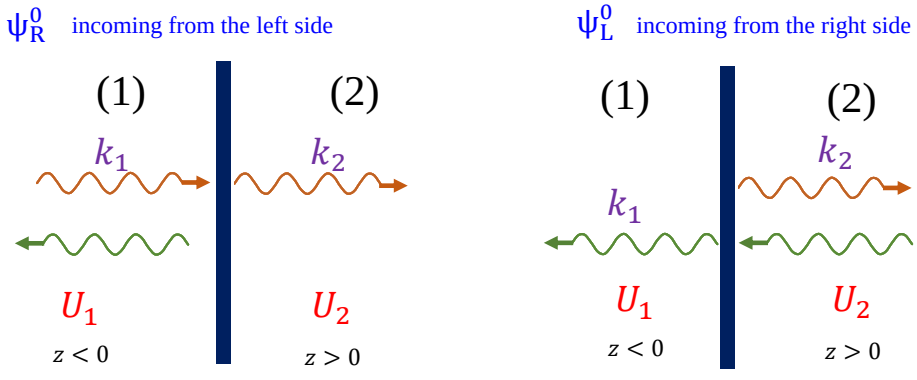

FIGURE 4.2: Schematic fundamental solutions of the Schrödinger equation $(\mathcal{E} - H_0)\Psi = 0$ for a scalar particle in a homogenous potential U_1 for $z < 0$, and U_2 for $z > 0$.

The strategy is:

(i) To find a fundamental system $\{\Psi^0_L, \Psi^0_R\}$ (see fig.5.21) of the homogenous Schrödinger equation $(\mathcal{E} - H_0)\Psi = 0$.

(ii) To find a suitable linear combinations of Ψ_L^0 and Ψ_R^0 and find solutions y_1 and y_2 of the equation $(\mathcal{E} - H_0)\, y = 0$ where $y_1(z)$ is non-infinite at $z = -\infty$, whereas $y_2(z)$ is non-infinite at $z = +\infty$.

(iii) To define the correct GF we make use of the formula

$$G_0(z,z') = \begin{cases} \frac{y_1(z)y_2(z')}{W(y_1,y_2)(z')} \text{if} -\infty < z < z' < +\infty \\ \frac{y_1(z')\,y_2(z)}{W(y_1,y_2)(z')} \text{ if } -\infty < z' < z < +\infty \end{cases}, \tag{4.78}$$

where $W(z') = \frac{\hbar^2}{2m^*(z')}\left[y_1(z')\frac{\partial y_2(z')}{\partial z'} - \frac{\partial y_1(z')}{\partial z'}y_2(z')\right]$ is the Wronskian potential. In the case $\mathcal{E} > U_1 > U_2$, Eq. 4.77 possesses a solution Ψ_L^0 which is finite at $z = -\infty$, and Ψ_R^0 finite at $z = +\infty$,

As well-known, at an energy larger than the potential step, the homogenous Schrödinger equation, $(\mathcal{E} - H_0)\,\Psi = 0$, admits the solutions:

$$\Psi_L^0 = e^{-ik_2 z_>} + r_L e^{ik_2 z_>} + t_L e^{-ik_1 z_<}, \tag{4.79}$$

$$\Psi_R^0 = e^{ik_1 z_<} + r_R e^{-ik_1 z_<} + t_R e^{ik_2 z_>}, \tag{4.80}$$

where we write $z_<$ instead of $z < 0$, and $z_>$ instead of $z > 0$. Concerning their physical meaning: Ψ_R^0 is the wave transmitted from the left to the right and Ψ_L^0 is the wave transmitted from the right to the left at the same energy. They satisfy the matching conditions at the left and right sides respectively.

By using the BDD matching conditions at $z = 0$, one obtains:

$$t_L = \frac{2k_2}{k_2 + k_1}, t_R = \frac{2k_1}{k_2 + k_1}, \tag{4.81}$$

$$r_L = \frac{k_2 - k_1}{k_2 + k_1}, r_R = \frac{k_1 - k_2}{k_2 + k_1}. \tag{4.82}$$

if one chooses $y_1 \equiv \Psi_L^0$, and $y_2 \equiv \Psi_R^0$ satisfying the boundary conditions at $z = \pm\infty$.

Therefore, Eq. 4.77 possesses a solution of the form:

$$G_0(z,z') = \frac{\Psi_L^0(z')\Psi_R^0(z)\Theta(z-z') + \Psi_L^0(z)\Psi_R^0(z')\Theta(z'-z)}{W(z')}, \tag{4.83}$$

with the Wronskian potential:

$$W(z') = \frac{\hbar^2}{2m^*(z')}\left[\Psi_L^0(z')\frac{\partial}{\partial z'}\Psi_R^0(z') - \Psi_R^0(z')\frac{\partial}{\partial z'}\Psi_L^0(z')\right]. \tag{4.84}$$

If one assumes for simplicity and without a big loss of generality that the effective mass remains unchanged in the layers, one obtains $m^*(z') = m^*$. It is easy to derive $\partial W(z')/\partial z' = 0$ to prove that the Wronskian is independent of the coordinate (z and z'). In this case, we obtain:

$$W = \frac{\hbar^2}{2m^*}\frac{4ik_1k_2}{k_2 + k_1}. \tag{4.85}$$

Following Eq. 4.83 we recover the *retarded* GF introduced in Refs. [253, 257]

$$G_0(z,z') = \frac{2m^*}{\hbar^2}\frac{t_R}{2ik_1}e^{-ik_1 z}e^{ik_2 z'};\ z < 0,\ z' > 0, \tag{4.86}$$

$$G_0(z,z') = \frac{2m^*}{\hbar^2}\frac{t_L}{2ik_2}e^{-ik_1 z'}e^{ik_2 z};\quad z > 0,\ z' < 0, \tag{4.87}$$

$$G_0(z,z') = \frac{2m^*}{\hbar^2}\frac{1}{2ik_1}\left[e^{ik_1|z-z'|} + r_R e^{-ik_1(z+z')}\right],\ z < 0,\ z' < 0, \tag{4.88}$$

$$G_0(z,z') = \frac{2m^*}{\hbar^2}\frac{1}{2ik_2}\left[e^{ik_2|z-z'|} + r_L e^{-ik_2(z+z')}\right],\ z>0,\ z'>0. \tag{4.89}$$

Note that the *advanced* GF is generally constructed by inversion of the respective left and right incoming wavefunctions in the expression of the retarded GF.

4.2.2 Interfacial Green's function for a spin-polarized particle without orbital degeneracy: Case of diagonal Green function

In order to demonstrate the efficiency and power of the perturbation methods adapted to the spin-transport case, one first considers the simpler case of the CB, free of any orbital degeneracy, and described by a single $S-$type orbital. Choosing the orthogonal basis functions $|S\rangle \otimes \{|\uparrow\rangle,\ |\downarrow\rangle\}$ allows one to obtain the zeroth-order unperturbed *diagonal* Hamiltonian according to:

$$H_0 = \begin{array}{c} \begin{array}{cc} |S\uparrow\rangle & |S\downarrow\rangle \end{array} \\ \begin{bmatrix} H_0^{\uparrow\uparrow} & 0 \\ 0 & H_0^{\downarrow\downarrow} \end{bmatrix} \end{array}. \tag{4.90}$$

$\Psi_R^0 = \begin{pmatrix} \Psi_R^{0\uparrow} \\ \Psi_R^{0\downarrow} \end{pmatrix}$ and $\Psi_L^0 = \begin{pmatrix} \Psi_L^{0\uparrow} \\ \Psi_L^{0\downarrow} \end{pmatrix}$ are solutions of the homogenous Schrödinger equation satisfying the boundary conditions for the respective left and right incoming waves,

$$\left(\mathcal{E}\hat{\mathbb{I}} - H_0\right)\begin{pmatrix} \Psi_R^{0\uparrow} \\ \Psi_R^{0\downarrow} \end{pmatrix} = 0, \tag{4.91}$$

and

$$\left(\mathcal{E}\hat{\mathbb{I}} - H_0\right)\begin{pmatrix} \Psi_L^{0\uparrow} \\ \Psi_L^{0\downarrow} \end{pmatrix} = 0. \tag{4.92}$$

where $\hat{\mathbb{I}}$ is the 2×2 unitary matrix. Note that $\left(\mathcal{E}\hat{\mathbb{I}} - H_0\right)$ is diagonal.

Now, the spin-polarized GF in the CB is a solution of the following equation

$$\left(\mathcal{E}\hat{\mathbb{I}} - H_0\right)G_0(z,z') = \hat{\mathbb{I}}\delta(z-z'), \tag{4.93}$$

The 2×2 GF admits a diagonal form, due to the orthogonality (no spin mixing) between the basis functions, *i.e.,* $|S\uparrow\rangle$ and $|S\downarrow\rangle$. This makes the treatment rather similar to the spinless case. The diagonal GF then writes:

$$G_0(z,z') = \begin{bmatrix} G_0^{\uparrow\uparrow}(z,z') & 0 \\ 0 & G_0^{\downarrow\downarrow}(z,z') \end{bmatrix}, \tag{4.94}$$

with

$$G_0^{\uparrow\uparrow}(z,z') = \frac{\Psi_R^{0\uparrow}(z)\Psi_L^{0\uparrow}(z')\Theta(z-z') + \Psi_R^{0\uparrow}(z')\Psi_L^{0\uparrow}(z)\Theta(z'-z)}{W^{\uparrow\uparrow}(z')}, \tag{4.95}$$

and

$$G_0^{\downarrow\downarrow}(z,z') = \frac{\Psi_R^{0\downarrow}(z)\Psi_L^{0\downarrow}(z')\Theta(z-z') + \Psi_R^{0\downarrow}(z')\Psi_L^{0\downarrow}(z)\Theta(z'-z)}{W^{\downarrow\downarrow}(z')}. \tag{4.96}$$

The spin-dependent Lippman-Schwinger equation for the Ψ_R state then writes:

$$\begin{pmatrix} \Psi_R^{\uparrow}(z) \\ \Psi_R^{\downarrow}(z) \end{pmatrix} = \begin{pmatrix} \Psi_R^{0\uparrow}(z) \\ \Psi_R^{0\downarrow}(z) \end{pmatrix} + \int \begin{bmatrix} G_0^{\uparrow\uparrow}(z,z') & 0 \\ 0 & G_0^{\downarrow\downarrow}(z,z') \end{bmatrix}\begin{bmatrix} V^{\uparrow\uparrow}(z') & V^{\uparrow\downarrow}(z') \\ V^{\downarrow\uparrow}(z') & V^{\downarrow\downarrow}(z') \end{bmatrix}\begin{pmatrix} \Psi_R^{0\uparrow}(z\prime) \\ \Psi_R^{0\downarrow}(z\prime) \end{pmatrix} dz', \tag{4.97}$$

where $V^{\sigma\sigma'}$ is the matrix element of the perturbed potential in the basis, $|S\uparrow\rangle$ and $|S\downarrow\rangle$.

We then obtain the correction to the overall wave function within the heterostructure according to:

$$\begin{pmatrix} \delta\Psi_R^{\uparrow}(z) \\ \delta\Psi_R^{\downarrow}(z) \end{pmatrix} = \begin{pmatrix} \int G_0^{\uparrow\uparrow}(z,z')V^{\uparrow\uparrow}(z')\Psi_R^{0\uparrow}(z')dz' + \int G_0^{\uparrow\uparrow}(z,z')V^{\uparrow\downarrow}(z')\Psi_R^{0\downarrow}(z')dz' \\ \int G_0^{\downarrow\downarrow}(z,z')V^{\downarrow\uparrow}(z')\Psi_R^{0\uparrow}(z'dz' + \int G_0^{\downarrow\downarrow}(z,z')V^{\downarrow\downarrow}(z')\Psi_R^{0\downarrow}(z')dz' \end{pmatrix} \tag{4.98}$$

4.3 Examples and specificities of spin-transport along the [110] growth directions.

In this chapter we will give some insights in the interest using Green's function technique to explore the specific properties of spin-transport in III-V semiconductors. We will consider in particular the electronic transport through a [110]-oriented tunnel barrier giving rise to *(i)* a new kind of spin-filtering effect at oblique incidence when Rashba SOI interactions is involved at the barrier interfaces [56] and thus associated to the generation of a spin-current (Fig. 4.3) together with *(ii)* a spin-dephasing or spin-rotation effects at normal incidence [55, 183] and that we will illustrate *via* our multiband tunneling code implementation. The spin-orbit interactions are treated here in the volume of the tunneling barrier.

4.3.1 Spin-injection along $[1\bar{1}0]$ and spin-filtering effect [56]

The whole detail of the calculations described in this subsection may be found in Ref. [56].

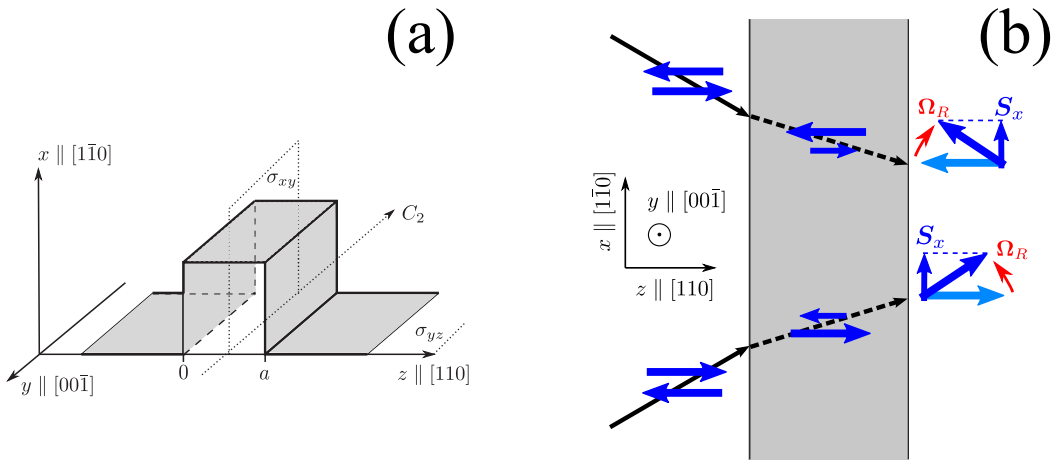

FIGURE 4.3: (a). The sketch of a symmetric tunnel barrier with the [110] crystallographic orientation. The point-group symmetry elements of the structure include the two-fold rotation axis $C_2||y$ and the mirror planes $\sigma_{xy}||(110)$ and $\sigma_{yz}||(1\bar{1}0)$; (b) Model of spin injection via (110)- grown barrier. The spin component $S_x > 0$ of electrons transmitted through the barrier with different in-plane wave vectors emerges due to i) anisotropic spin filtering caused by the Dresselhaus spin-orbit coupling in the barrier interior followed by ii) spin rotation in the interface-induced Rashba effective magnetic field $\mathbf{\Omega}_R$. Taken from Ref.[56].

A particular property of the Dresselhaus interaction lies in its specific dependence of the spin-splitting with the crystallographic direction in the T_d symmetry group. Since the work of Perel' *et al.* [54], it is well-known, that an incident electronic beam crossing a III-V tunnel barrier at oblique incidence leads to a net outgoing spin-polarization of the flux beam according to the following expression:

$$\mathcal{P} = \frac{|t_+|^2 - |t_-|^2}{|t_+|^2 + |t_-|^2} = \tanh\left(2\gamma_D \frac{m_2 k_{\parallel}}{\hbar^2} a q_0\right) \tag{4.99}$$

where $t_\pm$ are the respective transmission coefficients for the respective+ and − spins with the quantification axis set along the direction of the incident parallel wavevector $k_\parallel$, γ_D is the SOI Dresselhaus coefficient, m_2 and q_0 are the effective mass and evanescent wavevector inside the barrier, and a the barrier width. However the overall spin-polarization of the outgoing electronic beam vanishes if one sums over all electronic incidences ($+k_\parallel$ and $-k_\parallel$) for an equal population within the Fermi surface. However, an efficient spin-injection is observed with an [110]-oriented barrier due to the combined action of the Dresselhaus SOI in the barrier and a Rashba SOI at the barrier interfaces as shown by Alekseev [56]. The Rashba coupling may be considered as an effective magnetic field $\mathbf{\Omega}_R$ lying in the interface plane which rotates the spin direction. For that case, the authors consider a zinc-blende semiconductor heterostructure with a symmetric potential barrier grown along the $z \parallel [110]$ axis, and an in-plane wavevector $\mathbf{k}_\parallel = (k_x, k_y)$ where $x \parallel [1\bar{1}0]$ and $y \parallel [00\bar{1}]$. The electron effective Hamiltonian writes in this case:

$$H = H_0 + H_D + H_R, \tag{4.100}$$

where H_0 is the Hamiltonian without SOI, H_R describes the Rashba SOI at the barrier interface:

$$H_R = \alpha \left[\delta(z-a) - \delta(z)\right] \left(\sigma_x k_y - \sigma_y k_x\right), \tag{4.101}$$

where a is the barrier thickness, α is the Rashba coefficient and $\delta(z)$ the Dirac distribution; H_D is the Dresselhaus Hamiltonian projected in the corresponding basis as the sum of four terms

$$\begin{aligned}
H_{D1} &= i\frac{\sigma_x}{2}\left\{\gamma_D(z), \frac{\partial^3}{\partial z^3}\right\} && (4.102)\\
H_{D2} &= \frac{\sigma_z k_x}{2}\frac{\partial}{\partial z}\gamma_D(z)\frac{\partial}{\partial z} && (4.103)\\
H_{D3} &= i\left[\sigma_x\left(\frac{k_x^2}{2} + k_y^2\right) - 2\sigma_y k_x k_y\right]\left\{\gamma_D(z), \frac{\partial}{\partial z}\right\} && (4.104)\\
H_{D4} &= \sigma_z k_x\left(\frac{k_x^2}{2} - k_y^2\right)\gamma_D(z) && (4.105)
\end{aligned}$$

where we recall that $\gamma_D(z)$ is the bulk Dresselhaus coefficient. The kinetic energy of electrons is assumed to be sufficiently smaller than the barrier height to neglect H_{D3} and H_{D4} in comparison with the main contribution H_{D1} and H_{D2}. The calculations demonstrate that the H_{D1} term does not lead to spin-filtering effects at the first order of perturbation [56, 183]. In Ref. [56], the authors focused then on the combined action of the H_{D2} and Rashba terms. The mechanism of spin-injection and spin-filtering effects along the $[1\bar{1}0]$ direction can be schematized on Fig. 4.3. One can assume that the electrons impinging the barrier are unpolarized and that their distribution in the interface plane is isotropic. The incident electrons are transmitted with different in-plane wavevectors k_x. As in the case of the spin-filtering effect, a spin-polarized current is generated. In the case where the Rashba term is absent, an equal population of the k_x and $-k_x$ states makes the net spin polarization to be zero. The Rashba coupling is considered as an effective Hamiltonian with $\mathbf{\Omega}_R$ proportional to k_x, leading to a rotation with opposite axes for electrons with positive and negative k_x. The efficiency of spin-injection is analyzed by using the spin-dependent transfer matrix technique with the assumption that the effective masses inside and outside the barrier are the same (m) and neglecting the spin-orbit coupling outside the barrier.

The conclusion is that the spin distribution of the transmitted electrons is an even function of the in-plane wavevector

$$S_{k,x} = 2\frac{\alpha\gamma_D m^2 k_x^2 k_z a}{\hbar^4 q}, \tag{4.106}$$

where q is the electron wave vector in the barrier when SOI is neglected. It results an effective spin-injection even for an isotropic distribution of the incident electrons in the interface plane.

Besides the spin injection, the authors also consider the reciprocal effect that is the emergence of a direct electric tunneling current j_z through the barrier in the presence of spin polarization along the $[1\bar{1}0]$ direction. Taking into account that the transmission coefficients for the electrons incident upon the barrier from left and from right, the tunneling current density is

$$j_z = e\sum_k Tr\left[T_k(a)\rho_l T_k^+(a)\right] v_z\Theta(v_z) + e\sum_k Tr\left[T_k(-a)\rho_r T_k^+(-a)\right] v_z\Theta(-v_z) \tag{4.107}$$

where ρ_l (ρ_r) is the spin density matrix on the left (right), e is the electron charge, $T_k(a)$ and $T_k(-a)$ are transmission matrices for an electron propagating from the left to the right and from the right to left. The calculation yields the tunnel current

$$j_z = \frac{64ep_s}{105\pi^2}\frac{\alpha\gamma_D mak_F^9}{\hbar^3k^3}\exp(-2\sqrt{2mV/\hbar^2}) \tag{4.108}$$

where k_F is the Fermi wave vector, p_s is the spin polarization along the x axis, V is barrier height.

Main physical issues for the spin-injection mechanism along [110] direction.

Along the [110] direction, the Dresselhaus Hamiltonian contains derivatives of third, second, first, and zeroth order. In a perturbative treatment, we are interested in the third order derivative term like:

$$H_D = \frac{\sigma_x}{2}\left\{\gamma_D(z)k_z^3 + \left(k_z^3\right)^+\gamma_D(z)\right\}. \tag{4.109}$$

Indeed, the presence of the third-order derivative term makes the current discontinuous at the interface [183]. To avoid this problem, the authors considered the k-cubic term as the perturbation term $V(z)$ in the above calculation in order to derive the correction to the transmission coefficient for $\uparrow$ and $\downarrow$ spin channels starting from standard BDD boundary conditions. One chooses here orthogonal basis functions with spin-quantization axis being along the eigenvectors of σ_x according to: $|S\rangle\otimes\{|\uparrow\rangle,\ |\downarrow\rangle\}$ with $|\uparrow\rangle = \frac{1}{\sqrt{2}}\binom{1}{1}$, and $|\downarrow\rangle = \frac{1}{\sqrt{2}}\binom{1}{-1}$.

The unperturbed Hamiltonian possesses then the following block form:

$$H_0 = \begin{bmatrix} H_0^{\uparrow\uparrow} & 0 \\ 0 & H_0^{\downarrow\downarrow} \end{bmatrix}, \tag{4.110}$$

with:

$$H_0^{\uparrow\uparrow} = H_0^{\downarrow\downarrow} = \begin{cases} -\frac{\hbar^2}{2}\frac{\partial}{\partial z}\frac{1}{m^*(z)}\frac{\partial}{\partial z} & \text{for } z<0 \text{ or } z>a \\ -\frac{\hbar^2}{2}\frac{\partial}{\partial z}\frac{1}{m^*(z)}\frac{\partial}{\partial z}+V_0 & \text{for } 0<z<a \end{cases}, \tag{4.111}$$

and where we remind that a is the barrier thickness and V_0 the barrier height. As it is well known, the solutions of the homogenous Schrödinger equation at the same incident energy $\mathcal{E} < V_0$ are respectively:

$$\Psi_R^{0\uparrow} = \Psi_R^{0\downarrow} = \begin{cases} e^{ikz} + r_k e^{-ikz}, & z<0 \\ A_k e^{-qz} + B_k e^{qz}, & 0<z<a \\ t_k e^{ik(z-a)}, & z>a \end{cases}, \tag{4.112}$$

$$\Psi_L^{0\uparrow} = \Psi_L^{0\downarrow} = \begin{cases} t_k e^{-ikz}, & z<0 \\ A_k e^{q(z-a)} + B_k e^{-q(z-a)}, & 0<z<a \\ e^{-ik(z-a)} + r_k e^{ik(z-a)}, & z>a. \end{cases}, \tag{4.113}$$

where $t_k = \left[\cosh qa + \frac{i}{2}\left(\frac{q}{k} - \frac{k}{q}\right)\sinh qa\right]^{-1}$ is the transmission amplitude, $r_k = \left[-\frac{i}{2}\left(\frac{q}{k} + \frac{k}{q}\right)\sinh qa\right] t_k$ the reflection amplitude, A_k and B_k are the amplitudes in the barrier, $A_k = \frac{t_k}{2}\left(1 + i\frac{k}{q}\right)e^{-qa}$, $B_k = \frac{t_k}{2}\left(1 - i\frac{k}{q}\right)e^{qa}$; $k = \sqrt{2m\mathcal{E}/\hbar^2} > 0$ is the initial wavevector, $q = \sqrt{2m\left(V_0 - \mathcal{E}\right)/\hbar^2}$, with the same effective masses inside and outside the barrier. The Wronskian potential is independent of the z' coordinate. We choose $z > a$ to calculate its value.

$$W^{\uparrow\uparrow} = \frac{\hbar^2}{2m^*}\left\{\Psi_L^{\uparrow}(z' > a)\frac{\partial\Psi_R^{\uparrow}(z' > a)}{\partial z} - \frac{\partial\Psi_L^{\uparrow}(z' > a)}{\partial z}\Psi_R^{\uparrow}(z' > a)\right\} = i\frac{\hbar^2 k}{m^*}t_k. \tag{4.114}$$

Note that the Wronskian for the $\downarrow$ spin particle remains unchanged,

$$W^{\downarrow\downarrow} = i\frac{\hbar^2 k}{m^*}t_k. \tag{4.115}$$

Expression for the Dresselhaus SOI potential and perturbation calculation.

We consider now the symmetrized Dresselhaus SOI Hamiltonian within the barrier. Because of:

$$\langle\downarrow|\,\sigma_x\,|\downarrow\rangle = -1, \qquad \langle\uparrow|\,\sigma_x\,|\uparrow\rangle = 1, \tag{4.116}$$

$$\langle\uparrow|\,\sigma_x\,|\downarrow\rangle = \langle\downarrow|\,\sigma_x\,|\uparrow\rangle = 0, \tag{4.117}$$

the perturbed potential can be expressed in a diagonal form according to:

$$V(z) = \begin{bmatrix} V^{\uparrow\uparrow}(z) & 0 \\ 0 & V^{\downarrow\downarrow}(z) \end{bmatrix}, \tag{4.118}$$

where

$$V^{\uparrow\uparrow}(z) = \langle\uparrow|\,H_D\,|\uparrow\rangle = \frac{1}{2}\left\{\gamma_D(z)k_z^3 + \left(k_z^3\right)^+\gamma_D(z)\right\}, \tag{4.119}$$

and

$$V^{\downarrow\downarrow}(z) = \langle\downarrow|\,H_D\,|\downarrow\rangle = -\frac{1}{2}\left\{\gamma_D(z)k_z^3 + \left(k_z^3\right)^+\gamma_D(z)\right\}. \tag{4.120}$$

Following Eq. 4.98, the correction to the zeroth order $\uparrow$-spin wavefunction within the heterostructure is then:

$$\begin{aligned}\delta\Psi_R^{\uparrow}(z) &= \int_0^a G_0^{\uparrow\uparrow}(z,z')V^{\uparrow\uparrow}(z')\Psi_R^{0\uparrow}(z')dz' \text{ for } \uparrow\text{-spin incidence} \\ &= \frac{-im^* e^{ik(z-a)}}{\hbar^2 k}\int_0^a \Psi_L^{0\uparrow}(z')\frac{1}{2}\left\{\gamma_D(z')k_{z'}^3 + \left(k_{z'}^3\right)^+\gamma_D(z')\right\}\Psi_R^{0\uparrow}(z')dz',\end{aligned} \tag{4.121}$$

whereas

$$\begin{aligned}\delta\Psi_R^{\downarrow}(z) &= \int_0^a G_0^{\downarrow\downarrow}(z,z')V^{\downarrow\downarrow}(z')\Psi_R^{0\downarrow}(z')dz' \text{ for } \downarrow\text{-spin incidence} \\ &= \frac{im^* e^{ik(z-a)}}{\hbar^2 k}\int_0^a \Psi_L^{0\downarrow}(z')\frac{1}{2}\left\{\gamma_D(z')k_{z'}^3 + \left(k_{z'}^3\right)^+\gamma_D(z')\right\}\Psi_R^{0\downarrow}(z')dz'.\end{aligned} \tag{4.122}$$

From Eqs. 4.121 and 4.122, we can find the correction to the transmission amplitude for the ↑- and ↓-spin channels respectively, according to:

$$\delta t^{\uparrow\uparrow} = -\delta t^{\downarrow\downarrow} = \frac{-im^*}{\hbar^2 k}\int_0^a \Psi_L^{0\uparrow}(z')\frac{i}{2}\left\{\gamma_D(z')\frac{\overrightarrow{\partial}^3}{\partial z'^3} - \frac{\overleftarrow{\partial}^3}{\partial z'^3}\gamma_D(z')\right\}\Psi_R^{0\uparrow}(z')dz' \tag{4.123}$$

because $\Psi_L^{0\downarrow}$ and $\Psi_L^{0\uparrow}$ possess the same orbital character as $\Psi_R^{0\downarrow}$ and $\Psi_R^{0\uparrow}$, where $\frac{\overrightarrow{\partial}}{\partial z'}$ acts to the right, whereas $\frac{\overleftarrow{\partial}}{\partial z'}$ acts to the left. This is Eq. (A5) in Ref. [56]. The authors finally obtained:

$$\delta t^{\uparrow\uparrow} = -\delta t^{\downarrow\downarrow} = \frac{-im^*}{\hbar^2 k}\int_0^a \Psi_L^{0\uparrow}(z')\frac{i}{2}\left\{\gamma_D(z')\frac{\overrightarrow{\partial}^3}{\partial z'^3} - \frac{\overleftarrow{\partial}^3}{\partial z'^3}\gamma_D(z')\right\}\Psi_R^{0\uparrow}(z')dz' \tag{4.124}$$

$$= \frac{-im^*}{\hbar^2 k}\frac{i}{2}\gamma_D\int_0^a \left\{\Psi_L^{0\uparrow}(z')\frac{\partial^3\Psi_R^{0\uparrow}(z')}{\partial z'^3} - \Psi_R^{0\uparrow}(z')\frac{\partial^3\Psi_L^{0\uparrow}(z')}{\partial z'^3}\right\}dz' \tag{4.125}$$

$$= \frac{\gamma_D m^* q^2 a}{2\hbar^2}t_k. \tag{4.126}$$

The result is that the correction to the transmission coefficient is independent of the incoming spin direction, $\left|\delta t^{\uparrow\uparrow}\right|^2 = \left|\delta t^{\downarrow\downarrow}\right|^2$, in the present situation. It means that there is no particular spin filtering effect with normal electron ingoing but only spin-dephasing or spin-rotation effects around the $[1\bar{1}0]$ direction like demonstrated by Nguyen *et al.* [183].

4.3.2 Spin-dephasing effects occurring under normal incidence along the [110] direction [183]

In this part, we discuss the main results obtained by Nguyen *et al.* on the spin-dephasing or spin-rotation effects for a normal incidence of electrons within the conduction band along a [110]-oriented tunnel barrier of T_d symmetry group. This geometry for electron tunneling is called *paraprocess* [183] in contrast to *orthoprocess* by which an incident particle travels through a [001]-oriented barrier at oblique incidence.

Along the specific [110] direction the Hamiltonian writes:

$$\mathcal{H} = \gamma_C k^2 + \frac{1}{2\sqrt{2}}\gamma_D k_{[110]}^3\left(\hat{\sigma}_x - \hat{\sigma}_y\right) \tag{4.127}$$

where k is the particle wavevector along the [110] direction in the barrier (mainly evanescent) and $\sigma_{x,y}$ the Pauli matrices representing the spin; $\gamma_C = \frac{\hbar^2}{2m^*}$ (in $eV.\text{Å}^2$) and γ_D is the Dresselhaus SOI parameter (in $eV.\text{Å}^3$). Note that the quantized spin axis lies along the $[1\bar{1}0]$ direction that is in the barrier plane perpendicularly to the growth axis. It results in a characteristic electron energy given by:

$$E = \gamma_C k^2 \pm \frac{1}{2}\gamma_D k^3 \tag{4.128}$$

where the wavevector k admits a large imaginary part due to its evanescent character. The evanescent nature of the wavevector $k = k_R + i\kappa$ of the tunneling electron has several important impacts [183]:

A) The requirement of a real energy E, negative from the top of the barrier conduction band, imposes a mixed character to the wavevector $k = Q + iK$ with the necessary addition of a real part $k_r = Q$ in order to satisfy this condition. For $\gamma_D = 0$, $K^2 = \frac{2m^*\Delta_B}{\hbar^2}$.

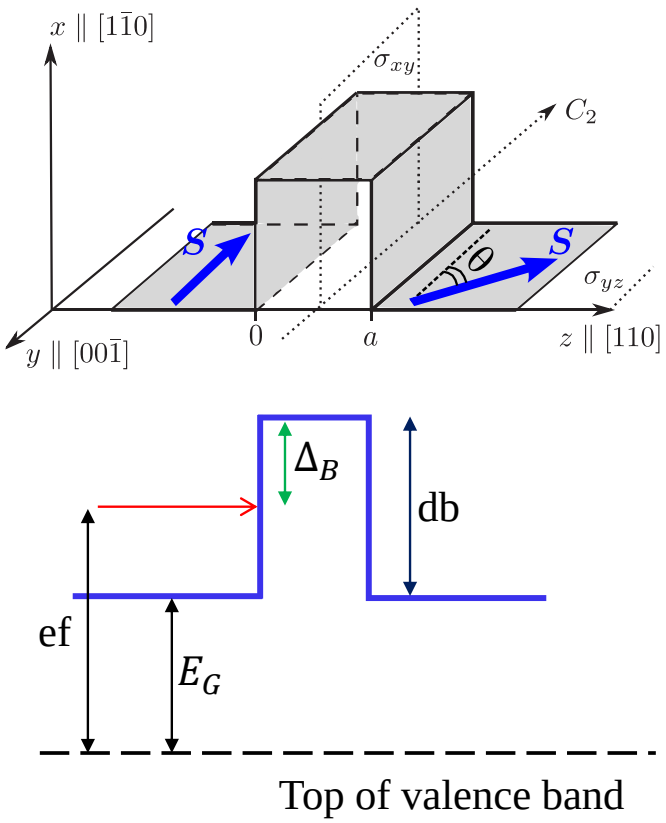

FIGURE 4.4: Schematic of spin rotation through the [110] barrier structure and the potential profile of the structure.

B) The presence of a k^3 term along the [110] current flow needs a re-examination of the current operator definition in a reduced 2×2 spinor form [183]. A larger multiband Hamiltonian involving only linear k and quadratic k^2 terms does not require such a re-examination.

C) In a 2×2 effective model, the current wave admits a discontinuity at both barrier interfaces related to γ_D and such discontinuity is not related to a surface potential term but to the bulk Dresselhaus interaction. In a 14×14, 30×30 and 40×40 multiband model, such discontinuity in the current wave should be materialized by the connection with highly evanescent interfacial states originating from upper conduction band.

D) This tunneling *paraprocess* as well as the *orthoprocess* lead to the formation of specific evanescent textures in the imaginary space of the wave vector in the barriers which may be represented by evanescent loops. Such evanescent loops emerging and absorbed at the top of the barrier conduction band represent the (two) eigenvectors at a given energy characterized by their spin-direction not necessarily orthogonal (the Hamiltonian is not hermitian in the complex k space). However the condition of current continuity is still preserved.

From the statement *A*) and from Eq. 4.130, one can find $\delta k = Q$ in the limit $Q \ll K$ where γ_D is small according to:

$$\delta E = 2\gamma_C k \delta k \pm \frac{1}{2}\gamma_D k^3 = 0 \tag{4.129}$$

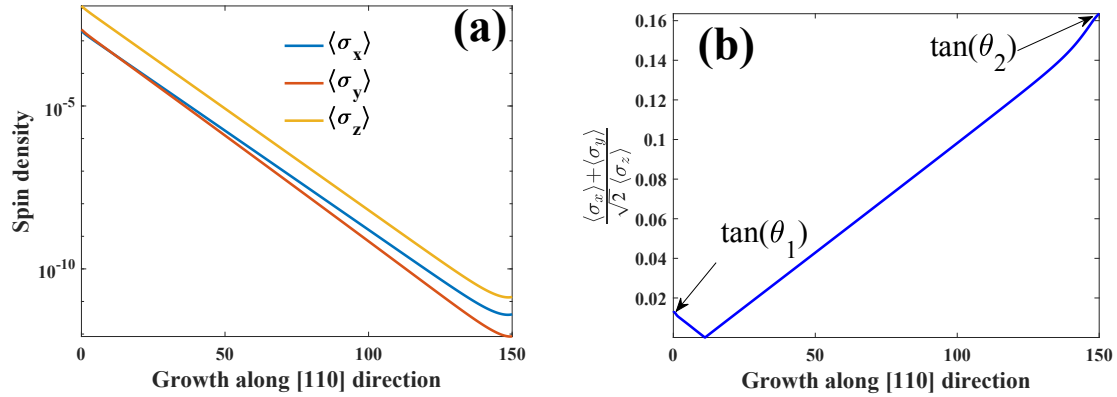

FIGURE 4.5: (a) Spin density profile $\langle\sigma_i\rangle$ along the respective $i = x, y, z$ directions calculated using our 30-band ***k.p*** platform for an incoming electron crossing a [110] GaAs tunnel barrier with incoming spin aligned along the z direction; (b) Same calculations giving the ratio $\frac{\langle\sigma_x\rangle+\langle\sigma_y\rangle}{\sqrt{2}\langle\sigma_z\rangle}$ showing the gradual rotation of the spin component in the {[001],[110]} plan. The rotation is a manifestation of the spin dephasing effect.

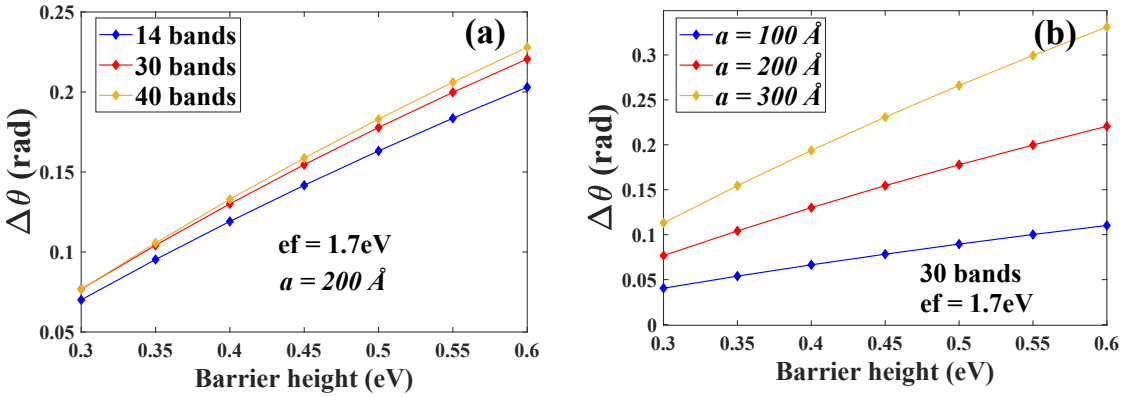

FIGURE 4.6: Spin rotation, experienced by the outgoing electron transmitted through the [110] GaAs barrier, as a function of barrier height up to 0.6 eV. (a) Calculated with different **k.p** platforms for barrier thickness about 200 Å and incident energy $ef = 1.7eV$ above top of valence band. (b) Calculated with 30 bands **k.p** method with different barrier thickness. The rotation of the spin is almost linear proportional to the barrier height.

or

$$Q = \pm\frac{\gamma_D K^2}{4\gamma_C} = \pm\frac{\gamma_D \Delta_B}{4\gamma_C^2} \tag{4.130}$$

where $\Delta_B = \gamma_C K^2$ is the barrier height. A non zero value for $\pm Q$ (+ and − respectively for spin up and spin down along [001] or [110] directions will result in a spin-dephasing from the initial $[1;0]^T$ state towards $[\exp(iQa); \exp(-iQa)]$ after electrons has crossed the barrier of thickness a:

$$\theta = \frac{\gamma_D \Delta_B}{4\gamma_C^2} a \tag{4.131}$$

giving a dephasing of 2π would then correspond to a barrier thickness given by:

$$a_{2\pi} = \frac{8\pi\gamma_C^2}{\gamma_D \Delta_B} \tag{4.132}$$

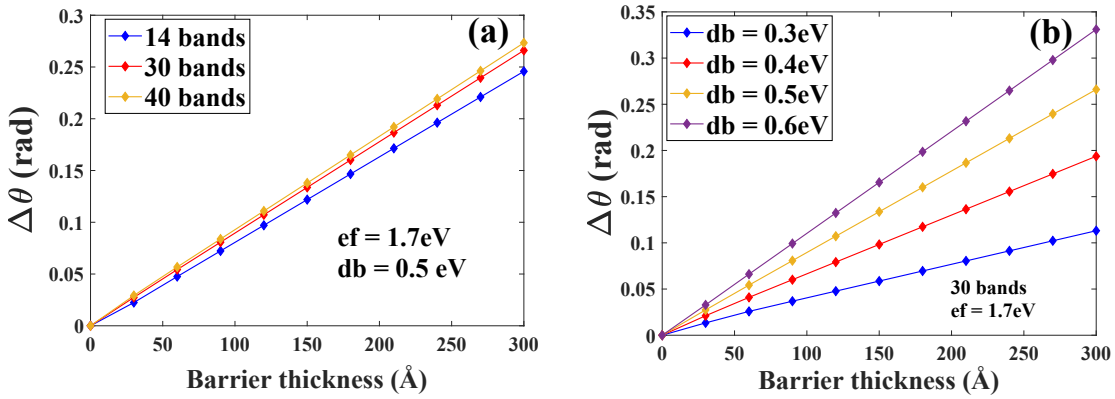

FIGURE 4.7: Spin rotation experienced by the outgoing electron transmitted through the [110] GaAs barrier for different barrier thickness up to 300 Å. (a) Calculated with different **k.p** platforms for $db = 0.5\ eV$ and incident energy $ef = 1.7eV$ above top of valence band. (b) Calculated with 30 bands **k.p** method with different values of db. The rotation of the spin is proportional to the barrier thickness.

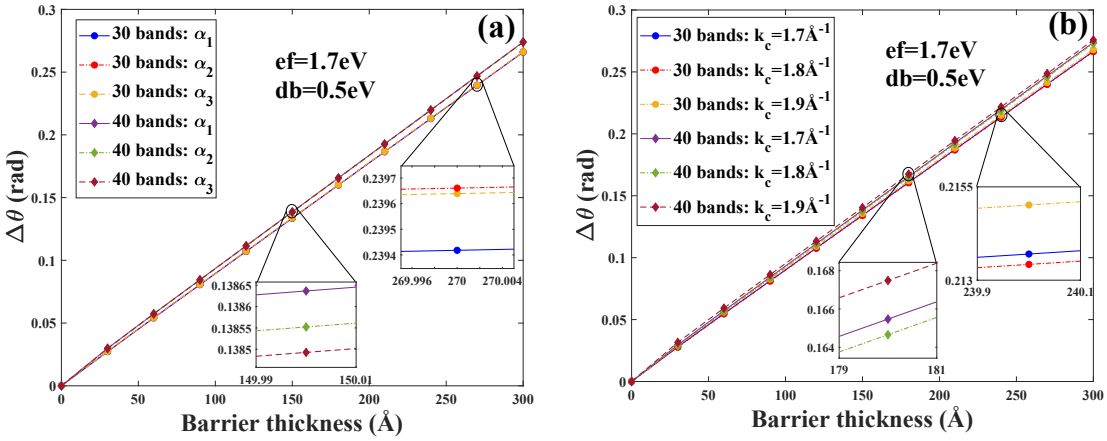

FIGURE 4.8: Spin rotation experienced by the outgoing electron transmitted through the [110] GaAs barrier for different as a function of barrier thickness with fixed barrier height $db = 0.5eV$ and different ghost-band coupling strength $\{\alpha\}$ (a) and at different k_c (b) showing small differences.

Fig. 4.6b and 4.7b display the results of our 30-band ***k.p*** calculations of the spin-rotation observed through a GaAs tunnel barrier ($\gamma_D \simeq 25$ eV.Å^3, $\gamma_C \simeq 50$ eV.Å^2) *vs.* the barrier height Δ_B and the barrier thickness a, respectively. One observes a spin rotation linearly increasing with Δ_B as well as a. In the case of barrier height dependence, a characteristic slope inversely proportional to the barrier thickness while in contrast to barrier height (Δ_B= band discontinuity - Fermi energy) with the barrier thickness dependence. For example, the slope is then found to be equal to 1.25×10^{-2} rad/nm for Δ_B=0.5 eV, 8.75×10^{-3} rad/nm for Δ_B=0.3 eV and 3.5×10^{-3} rad/nm for Δ_B=0.1 eV in Fig 4.7b. This is in pretty good agreement with the formula 4.132 giving a slope of about 8×10^{-3} rad/nm for Δ_B=0.3 eV. Figs. 4.6a and 4.7a shows moreover that the calculations remains robust whatever the multiband code chosen. And finally, Fig 4.8 shows small impact of ghost band on the spin rotation with different ghost band coupling parameters and different coupling point k_c.

To conclude: these good agreements among numerical calculations based on multiband **k.p** method and analytical developments of matching condition with effective Hamiltonian for [110] direction by Nguyen et al. [183] as well as perturbation method by Alekseev et al. [56] give another proof for the effectiveness of the ghost band method developed in this manuscript. Since then, we may use a multiband **k.p** Hamiltonian

that avoids some difficulties with the k^3 or higher terms in effective Hamiltonian to consider spin transport phenomena along [110] direction or in general, along arbitrary directions that are interested.

CHAPTER 5

Anatomy of spin-orbit currents for spin-torque and spin-orbit torque in spintronic semiconductor devices

Contents

In today's spintronics technology, the generation and use of spin-currents, spin-orbit currents and spin-torques are of a particular importance in the aim to switch a small magnetic element or a magnetic memory. This operation is generally possible without the use of any external magnetic field, by the transverse spin-current via the so-called spin-transfer torque (STT). The current is injected from the top to the bottom of the device (in the so-called current perpendicular to plane (CPP) geometry), or via the spin-orbit torque (SOT) in an in-plane current injection geometry. Both STT and SOT mechanisms may provoke, hereafter, a switching of the small magnet from the basic principle conservation of angular momentum. The flux of the spd-hybridized orbital-angular-momentum current (spin but also orbital current) interacts with the local magnetization, typically the local 3d magnetization of a transition metal or the 4p band of the (Ga,Mn)As ferromagnetic semiconductor.

Those switching functionalities require efficient spin current injection at ferromagnet-non magnetic interfaces as well as efficient spin-transfer torques (STT) and possibly efficient spin-Hall effect (SHE) [266]. At present, STT and more particularly SOT switching has been achieved in metallic systems, semiconductors involving (Ga,Mn)As and topological insulators, thus requiring the synthesis of bilayers, one made of heavy material with strong spin-orbit interactions (like Pt, or even In in InGaAs compounds) in contact with the thin magnetic element to flip. The description of magnetic switching is then provoked by the dissipation, close to the interface, of the two components of the spin-current transverse to the local magnetization direction playing the role of spin torque. The two components are respectively called, the *antidamping or Slonczewski* component for the one generating a torque towards the direction of the spin injected, and *field-like* torque for the one generating a torque perpendicularly to the spin injected. In that context, investigations of SOI in solids, interfaces, as well as tunnel junctions are of mandatory [110, 267, 268]. Moreover, SOI at an interface with a broken inversion symmetry can lead to the observation of Bychkov-Rashba-split states [269] for carriers propagating along surface or interface states. Such a splitting, if well controlled, can be used to convert a perpendicular spin current into a lateral charge current by Inverse-Rashba or Inverse Edelstein effect [97, 270, 271]. Alternatively, SOI can lead to inherent spin-memory loss (SML) [239, 272] or spin-current discontinuities [273] when electrons cross interfaces. In that context, investigations of SOI in solids and at interfaces are mandatory for basic physics. No much attention has been paid to the particular anatomy of the electronic spin-polarized transport at SOI-magnetic interfaces where exchange-split interface states may be observed [274–276]. This is the essence of the present chapter and following sections to describe such spin-current local magnetic-moment interactions and subsequent magnetic commutation principles involving both spin and orbital degree of freedom.

Beside metals systems in which one may obtain STT and SOT switching at room temperature, the STT and SOT with ferromagnetic semiconductor also has been tremendous attracted due to low critical switching current density [5]. In the context of GaAs materials concerning semiconductor devices, beyond the demonstration of STT mechanisms in trilayer (Ga,Mn)As/(In,Ga)As/(Ga,Mn)As magnetic tunnel junctions [6, 7], Chernysov [8] was the first to demonstrate the switching functionality in *bulk* GaMnAs using the properties of the SOI. Those results showing up a reduction/increase of the switching field *vs.* sign and amplitude of current injection were explained by the contribution of an effective magnetic field, proportional to the current injected in size and in sign, able to take part to the switching-field process. The inner strain field and related spin-orbit field in the bulk, leading to an inversion asymmetry and k-dependent potential terms in the reciprocal space was invoked to explain this phenomena. More recently, the group of Tanaka at the University of Tokyo [5], demonstrated the switching of a 7 nm thick (Ga,Mn)As single layer by SOT mechanism with the help of the particular Dresselhaus interaction potential characteric of the T_d symmetry group of GaAs and (Ga,Mn)As compound (Fig. 5.1). However, the use of a quite thick (In,Ga)As template buffer layer, in the latter case, cannot totally rule out the spin-Hall effect as partly responsible for the magnetic switching. If the switching mechanism is strongly investigated in terms of interaction between spin-current

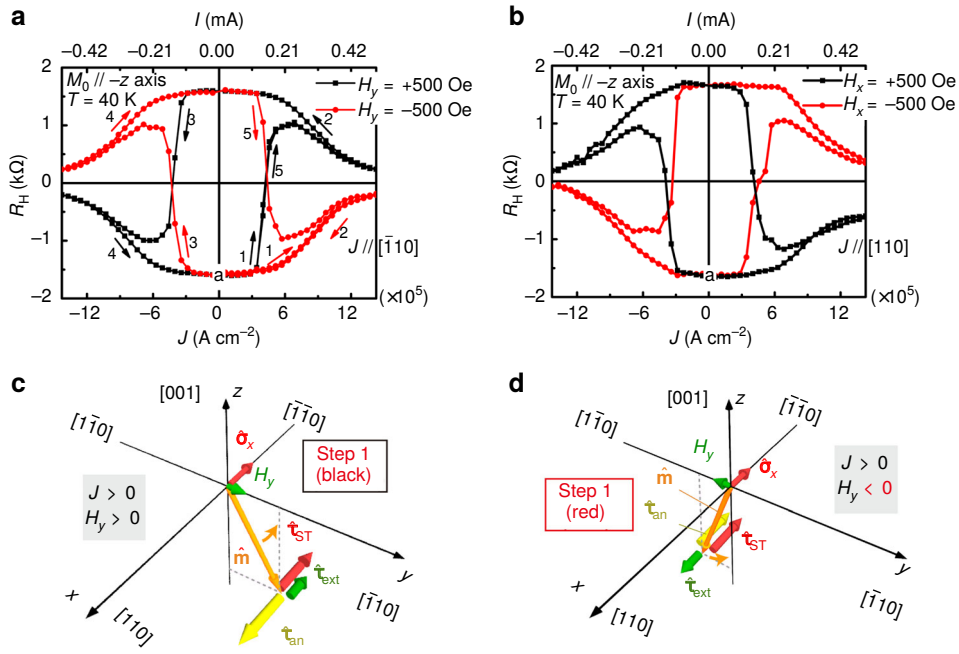

FIGURE 5.1: The SOT switching and the relevant switching mechanism; (a,b) Field-assisted SOT switching with $\boldsymbol{J} \parallel [\bar{1}10]$ and $H_y = \pm 500\ oe$ and with $\boldsymbol{J} \parallel [110]$ and $H_y = \pm 500\ oe$. (c,d) illustrations of the torques exerted by the external field ($\boldsymbol{\tau}_{ext}$), the anisotropy field ($\boldsymbol{\tau}_{an}$) and the spin component along the x direction ($\boldsymbol{\tau}_{ST}$) with $\boldsymbol{J} > 0$ when $H_y > 0$ and $H_y < 0$, here $\boldsymbol{m}$ lies in the y-z plane. Taken from [5].

and local magnetization viewed as a mono-domain (using the so-called Landau-Lifshitz-Gilbert equation describing the magnetization dynamics [277, 278]), the investigation of spin-orbit torques in domain walls has been the matter of recent subject of debates. The latest results [9] emphasized on the particular role of the bulk component of the SOT in (Ga,Mn)As compared to the potential interface contribution.

This work and requirement of a multiband treatment

In the present work and following sections, we focus on the spin-torque components exerted on (Ga,Mn)As by the spin and angular-momentum current generated in a trilayer system by a (Ga,Mn)As polarizer. We calculate the two components of the torques versus angle, versus energy, and versus the thickness of the soft layer to be switched in order to compare with actual prevalent theories excluding the orbital part. Moreover, from the point of view of the spin-transfer and spin-orbit torque anatomy, we show that the interplay of SOI and exchange interactions at interfaces and tunnel junctions may result in a large difference of transmission for carriers, depending on the sign of their incident in-plane wavevector: this leads to interfacial skew-tunneling effects that we refer to as anomalous tunnel Hall effect (ATHE) [12] or tunnel anomalous Hall effect (TAHE) like proposed by other international groups [11]. In a 2×2 exchange-split band model, the transmission asymmetry ($\mathcal{A}$) between incidence angles related to $+k_{\parallel}$ and $-k_{\parallel}$ wavevector components, is shown to be maximal at peculiar points of the Brillouin zone corresponding to a totally quenched transmission ($\mathcal{A} = \frac{T_{+k_{\parallel}} - T_{-k_{\parallel}}}{T_{+k_{\parallel}} - T_{-k_{\parallel}}} = 100\%$) making the transmission difference from the standard tunneling case.

More generally by inclusion of SOI, we demonstrate the universal character of the transmission asymmetry $\mathcal{A}$ *vs.* in-plane wavevector component, for given reduced kinetic energy and exchange parameter, $\mathcal{A}$ being universally scaled by a unique function, independent of the spin-orbit strength and of the material

parameters. Similarly, striking tunneling phenomena arising in topological insulators have just been predicted. While they all are related to the spin-orbit directional anisotropy, ATHE differs from the tunneling planar Hall effect [279], spontaneous anomalous and spin Hall effects [280], or spin-galvanic effect [281], previously reported for electron transport, by its giant forward asymmetry and chiral nature. These features have non-trivial connection with the symmetry properties of the system. All these results show that a new class of tunneling phenomena can now be investigated and experimentally probed.

5.1 General argument on the spin-transfer torque (STT) and spin-orbit torque (SOT) free of orbital-momentum contributions

We consider first, the spin-transfer mechanism in 3d transition metals without involving orbital terms. Those originate from the spin-current/local magnetic moment interactions *via* the *s-d* exchange interactions. We write $\hat{\mathcal{H}}_{sp-d} = -J_{sp-d}\ \boldsymbol{s}.\boldsymbol{M}$ where J_{sp-d} is the exchange constant ($|J_{sp-d}\boldsymbol{M}| \simeq 0.1\ eV/\hbar$) between the *4s-4p* conduction electrons carrying an average spin $\hat{\boldsymbol{\sigma}}$, and the local magnetization $\boldsymbol{M}$ of *3d* orbital character. Here, $\hat{\boldsymbol{\sigma}}$ is written in unit of $\hbar$. It results that:

i) The effective magnetic field $\boldsymbol{B}$ and the subsequent torque $\boldsymbol{T}$ generated by the conduction electrons on the local *3d* magnetization of a unit vector $\boldsymbol{m} = \frac{\boldsymbol{M}}{M_S}$ respectively write:

$$\boldsymbol{B} = J_{sp-d}\ \hat{\boldsymbol{\sigma}} \tag{5.1}$$

$$\boldsymbol{T} = \gamma J_{sp-d}\ \hat{\boldsymbol{\sigma}} \times \boldsymbol{M} \tag{5.2}$$

ii) Conversely, the effective magnetic field $\tilde{\boldsymbol{B}}$ as well as the torque $\tilde{\boldsymbol{T}}$ acting on the conduction spin *4s* write in reaction:

$$\tilde{\boldsymbol{B}} = \frac{J_{sp-d}}{\gamma}\ \boldsymbol{M} \tag{5.3}$$

$$\tilde{\boldsymbol{T}} = \gamma J_{sp-d} \boldsymbol{M} \times \hat{\boldsymbol{\sigma}} \tag{5.4}$$

$\tilde{\boldsymbol{T}} = -\boldsymbol{T}$ should be associated to the conservation of the total spin moment 4*sp*+3*d*. It results that, in a non-collinear magnetic configuration, the dissipation of a given component of the spin-current carried by the 4*sp* conduction electrons by precession or decoherence and transverse to the local magnetization will be associated to a transfer of angular momentum towards the local magnetic moment, at least when the spin-flip mechanisms [1] are neglectable. Without spin-flip term, one obtains:

$$\frac{\partial \boldsymbol{M}}{\partial t} = -\gamma \frac{\partial \boldsymbol{s}}{\partial t} \tag{5.5}$$

iii) On the other hand, we are able to calculate the magnetization dynamics of the conduction electrons according to the principles of quantum mechanics applied to the Bloch electronic wavefunctions. This writes:

$$\gamma \frac{\partial \boldsymbol{s}}{\partial t} = -\boldsymbol{\nabla} \boldsymbol{j}_s + \frac{J_{sp-d}}{\hbar} \boldsymbol{M} \times \boldsymbol{s} - \gamma \frac{\boldsymbol{s}}{\tau_s} \tag{5.6}$$

where $\boldsymbol{j}_s$ is the spin-current due to the polarized carriers and where τ_s is the characteristic time for spin-flip corresponding to the longitudinal component parallel to the local magnetization. This time may be

[1] In this case, the spin-flip terms are the same as spin relaxation.

considered as long compared to the characteristic precession time. In steady-state regime, one has $\frac{\partial \boldsymbol{s}}{\partial t} = 0$, the volume integral of the torque acting on the small ferromagnetic element (5.5) writes:

$$\boldsymbol{\Gamma} = \frac{\partial \int_{\Omega} \boldsymbol{M}}{\partial t} = \int_{\Omega} \frac{\partial \boldsymbol{M}}{\partial t} = -\int_{\Omega} \boldsymbol{\nabla} \boldsymbol{j}_s - \gamma \int_{\Omega} \frac{\boldsymbol{s}}{\tau_s} \tag{5.7}$$

or:

$$\boldsymbol{\Gamma} = \frac{\partial \int_{\Omega} \boldsymbol{M}}{\partial t} = \left(\boldsymbol{I}_s(0) - \boldsymbol{I}_s(t) - \gamma \int_{\Omega} \frac{\boldsymbol{s}}{\tau_s} \right) \tag{5.8}$$

It results that the total torques simply equals the difference between the incoming ($\boldsymbol{I}_s(0)$) and outgoing ($\boldsymbol{I}_s(d)$) flux of spins transverse to the local magnetization that we call $\hat{\boldsymbol{T}}^{\parallel}$ and $\hat{\boldsymbol{T}}^{\perp}$ crossing the ferromagnetic element integrated on the whole surface. The second term to the right is negative, and represents a counter balance due to the spin loss during the spin-transfer mechanism [282]. To conclude, without orbital moment, one can easily describe the two components of the torques according to:

$$\boldsymbol{T}_{spin-torque} = a_j \, \boldsymbol{M} \times (\boldsymbol{M} \times \boldsymbol{s}) - b_j \, \boldsymbol{M} \times \boldsymbol{s} \tag{5.9}$$

- The component $\hat{\boldsymbol{T}}^{\perp} = \frac{b_j}{\hbar} \, \boldsymbol{M} \times \boldsymbol{s}$ is called the 'field-like' component given by the imaginary part of the spin-mixing conductance in the Landauer formula.
- The component $\hat{\boldsymbol{T}}^{\parallel} = \frac{a_j}{\hbar} \, \boldsymbol{M} \times (\boldsymbol{M} \times \boldsymbol{s})$ is called the 'antidamping' component given by the real part of the spin-mixing conductance in the Landauer formula.

where the parameters a_j et b_j depend on the current density and the material parameters as the interface conductance.

5.2 Definition of the spin-current operator and spin-current

The concept of spin-current is crucial for spintronics. However, its definition in a medium where SOI is present remains a subtle point that gives rise to intense discussions and sometimes epistemological controversies [235, 283–286]. Up to now, the standard definition is to write the spin-current tensor as the symmetrized dyadic product $\hat{\sigma} \boldsymbol{v}$ where the velocity $\boldsymbol{v}$ is defined from Hamilton's relation.

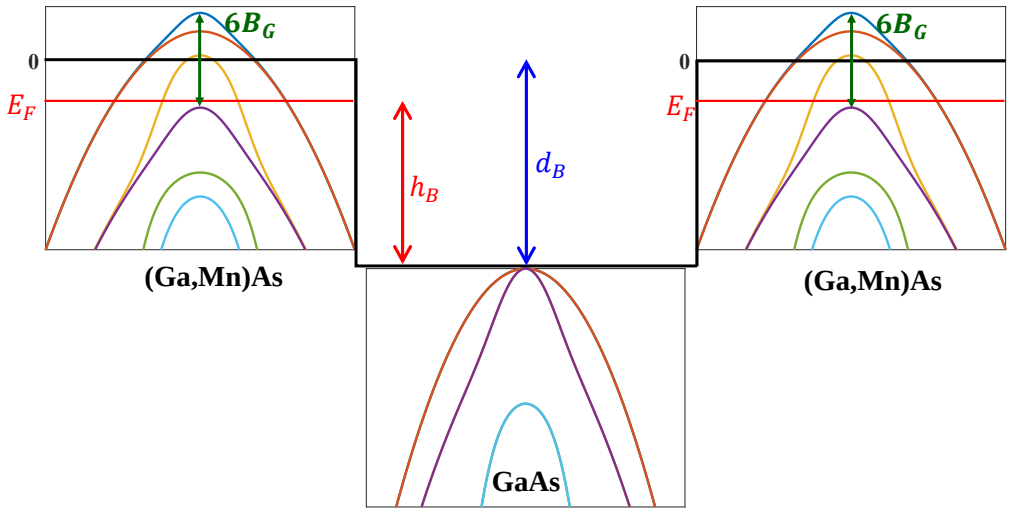

FIGURE 5.2: Band structure's profile of a simple (Ga,Mn)As/GaAs/(Ga,Mn)As based tunnel junction.

$$\hat{\boldsymbol{J}} = \frac{1}{2}\left(\boldsymbol{v}\hat{\sigma} + \hat{\sigma}\boldsymbol{v}\right) \tag{5.10}$$

$$\boldsymbol{v} = \frac{\partial H}{\partial \boldsymbol{p}} \tag{5.11}$$

The conceptual difficulty in current definition is of a general nature and extends to a wide range of physical systems. Because the spin current may be not conserved, there may exist a source term G such that the continuity equation for the density ρ of a physical quantity can be expressed in terms of the current $\boldsymbol{J}$ and G:

$$\frac{\partial \rho}{\partial t} = -\boldsymbol{\nabla}.\boldsymbol{J} + G \tag{5.12}$$

The point is that the source term is not well defined. It can be modified, an arbitrary part of it can be incorporated in the divergence term, accordingly changing the current definition so that only the current/source couple has a physical meaning [235, 285, 287]. This is analogous to a gauge transformation where different vector/scalar-potential couples account for a unique physical reality. In spintronics, the source term is referred to as the 'spin transfer torque'. Then, the problem of defining both current and source terms in a conservation law is an old problem that was discussed in depth by Feynman [288] in his lecture on electromagnetic-field energy current and also by De Groot and Mazure [289] in the context of nonequilibrium thermodynamics, for which, however, the second law of thermodynamics provides additional conditions allowing the currents to be uniquely defined. Even though the argument cannot be used as such in the case of (possibly nondissipative, permanent) quantum currents, there are situations where the equilibrium or steady state regimes impose boundary conditions that lead to unambiguous identification.

Now we are going to consider the spin current corresponding to the two cases of boundary conditions: the standard boundary condition or BDD boundary condition and the boundary condition involving surface potentials.The typical structure under study is composed of a tunnel barrier corresponding to holes with the VB like displayed in Fig. 5.2.

5.2.1 Spin-current and spin-torque with standard matching conditions

Starting with the derivation of spin density $\langle\Psi|\hat{\sigma}_\alpha|\Psi\rangle$ given by:

$$i\hbar\frac{\partial \langle\Psi|\hat{\sigma}_\alpha|\Psi\rangle}{\partial t} = i\hbar\frac{\partial \langle\Psi|\hat{\sigma}_\alpha\Psi\rangle}{\partial t} = i\hbar\left[\left\langle\frac{\partial\Psi}{\partial t}\middle|\hat{\sigma}_\alpha\Psi\right\rangle + \left\langle\Psi\middle|\hat{\sigma}_\alpha\frac{\partial\Psi}{\partial t}\right\rangle\right] \tag{5.13}$$

$$= -\langle H\Psi|\hat{\sigma}_\alpha\Psi\rangle + \langle\Psi|\hat{\sigma}_\alpha H\Psi\rangle = -\left\langle\hat{\sigma}_\alpha^\dagger H\Psi\middle|\Psi\right\rangle + \langle\Psi|\hat{\sigma}_\alpha H\Psi\rangle \tag{5.14}$$

where $\hat{\sigma}_\alpha$ is the Pauli operator, $\hat{\sigma}_\alpha = \{\sigma_x, \sigma_y, \sigma_z\}$.

Since H and $\hat{\sigma}$ are hermitian operators therefore we have:

$$\begin{aligned} H &= H^\dagger \\ \hat{\sigma} &= \hat{\sigma}^\dagger \end{aligned} \tag{5.15}$$

thus

$$(H\hat{\sigma})^\dagger = \hat{\sigma}^\dagger H^\dagger = \hat{\sigma}H = H\hat{\sigma} + [\hat{\sigma}, H] \tag{5.16}$$

Using relations 5.15 then 5.14 can be rewritten as:

$$i\hbar\frac{\partial \langle\Psi|\hat{\sigma}_\alpha|\Psi\rangle}{\partial t} = \langle\Psi|\hat{\sigma}_\alpha H\Psi\rangle - \langle\hat{\sigma}_\alpha H\Psi|\Psi\rangle = 2i\left(Im\left[\langle\Psi|\hat{\sigma}_\alpha H\Psi\rangle\right]\right) \tag{5.17}$$

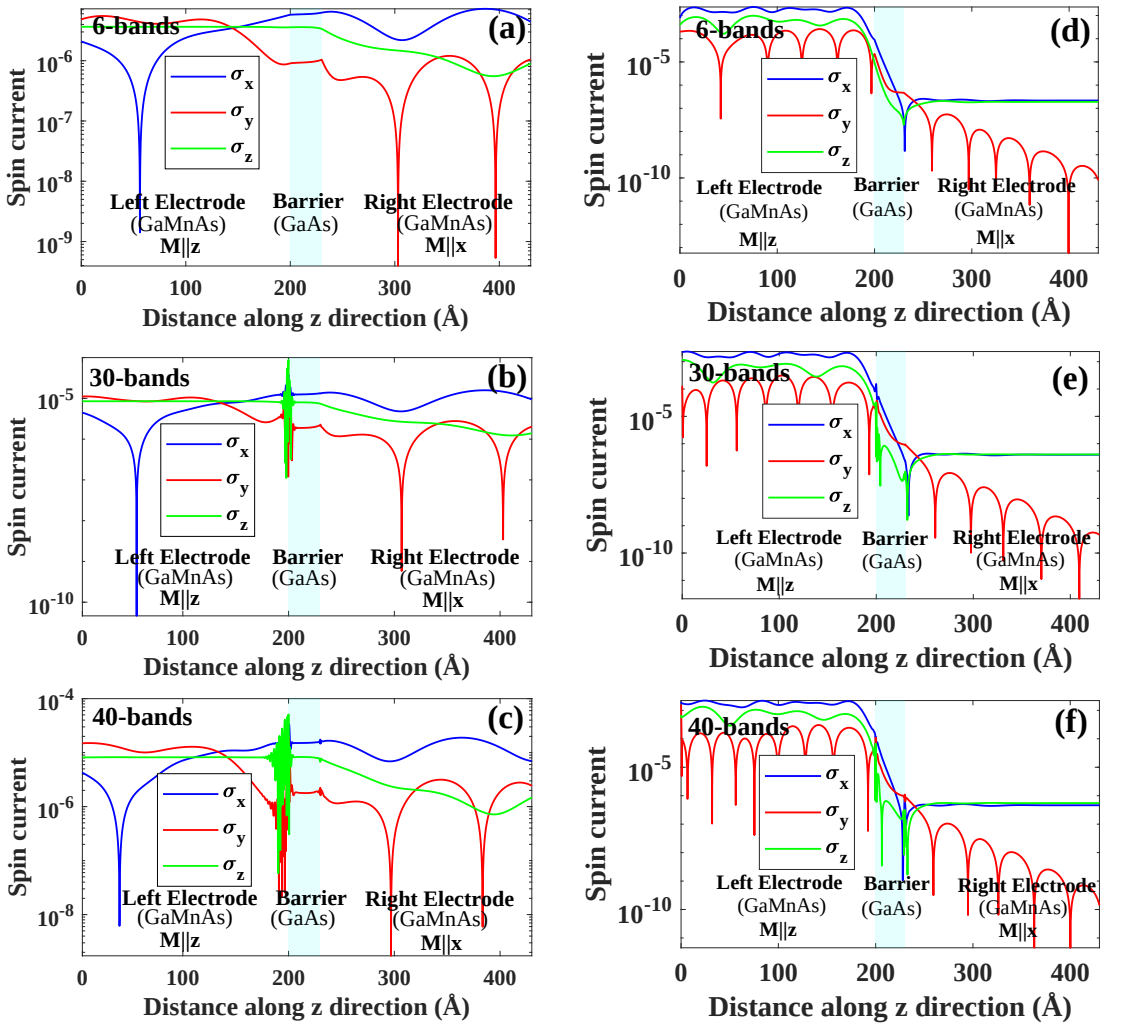

FIGURE 5.3: Profiles of 3-components of the spin current collinear to σ_x, σ_y and σ_z inside (Ga,Mn)As/GaAs/(Ga,Mn)As (fig. 5.2). The magnetization of the thick layer to the left is along z whereas the one to the right is transverse that is along x. Calculations have been performed with respective (a,d) 6-, (b,e) 30- and (c,f) 40-band $\boldsymbol{k.p}$ models showing equivalent results. The energy of hole $E_f = -0.03\ eV$ and corresponding to in-plane wave vector $k_{||}$=[0 0] (a,b,c) and $k_{||}$=[0.05Å 0] (d,e,f).

Since $2\hat{\sigma}H = \hat{\sigma}H + H\hat{\sigma} + [\hat{\sigma}, H]$ (Eq 5.16) together with Eq 5.17 we have:

$$\frac{\partial \langle\Psi|\, \hat{\sigma}_\alpha \,|\Psi\rangle}{\partial t} = Im\left[\frac{1}{\hbar}\langle\Psi|\, (\hat{\sigma}_\alpha H + H\hat{\sigma}_\alpha)\Psi\rangle\right] + Im\left[\frac{1}{\hbar}\langle\Psi|\, [\hat{\sigma}, H]\,\Psi\rangle\right] \tag{5.18}$$

For convenience, we write the Hamiltonian as in Eq.3.8:

$$H = \sum_j a_j \boldsymbol{p_j} + \sum_{j,k} b_{jk} \boldsymbol{p_j p_k} \tag{5.19}$$

Here we have $(a_j)^\dagger = a_j$ and $(b_{jk})^\dagger = b_{jk}$ and thus:

$$\left(a_j\hat{\sigma}_\alpha + \hat{\sigma}_\alpha a_j\right)^\dagger = a_j\hat{\sigma}_\alpha + \hat{\sigma}_\alpha a_j \tag{5.20}$$

$$\left(b_{jk}\hat{\sigma}_\alpha + \hat{\sigma}_\alpha b_{jk}\right)^\dagger = b_{jk}\hat{\sigma}_\alpha + \hat{\sigma}_\alpha b_{jk} \tag{5.21}$$

We now consider the term:

$$\begin{aligned}
&\sum_{j,k} \boldsymbol{p}_i \langle \Psi | b_{jk} \boldsymbol{p}_k \hat{\sigma}_\alpha + \hat{\sigma}_\alpha b_{jk} \boldsymbol{p}_k | \Psi \rangle \\
&= \sum_{j,k} \left[-\langle \boldsymbol{p}_j \Psi | b_{jk} \boldsymbol{p}_k \hat{\sigma}_\alpha + \hat{\sigma}_\alpha b_{jk} \boldsymbol{p}_k | \Psi \rangle + \langle \Psi | \boldsymbol{p}_j b_{jk} \boldsymbol{p}_k \hat{\sigma}_\alpha + \boldsymbol{p}_j \hat{\sigma}_\alpha b_{jk} \boldsymbol{p}_k | \Psi \rangle \right] \\
&= \sum_{j,k} \left[-\langle \boldsymbol{p}_j \Psi | b_{jk} \boldsymbol{p}_k \hat{\sigma}_\alpha + \hat{\sigma}_\alpha b_{jk} \boldsymbol{p}_k | \Psi \rangle + \langle \Psi | b_{jk} \boldsymbol{p}_j \boldsymbol{p}_k \hat{\sigma}_\alpha + \hat{\sigma}_\alpha b_{jk} \boldsymbol{p}_j \boldsymbol{p}_k | \Psi \rangle \right]
\end{aligned} \tag{5.22}$$

where we have used the fact that $\boldsymbol{p}_j b_{jk} \boldsymbol{p}_k = b_{jk} \boldsymbol{p}_j \boldsymbol{p}_k$ and $\boldsymbol{p}_j \hat{\sigma}_\alpha b_{jk} \boldsymbol{p}_k = \hat{\sigma}_\alpha b_{jk} \boldsymbol{p}_j \boldsymbol{p}_k$. Doing the same, one has:

$$\begin{aligned}
&\sum_{j,k} \boldsymbol{p}_j \langle \boldsymbol{p}_k \Psi | b_{jk} \hat{\sigma}_\alpha + \hat{\sigma}_\alpha b_{jk} | \Psi \rangle \\
&= \sum_{j,k} \left[-\langle \boldsymbol{p}_j \boldsymbol{p}_k \Psi | b_{jk} \hat{\sigma}_\alpha + \hat{\sigma}_\alpha b_{jk} | \Psi \rangle + \langle \boldsymbol{p}_k \Psi | \boldsymbol{p}_j b_{jk} \hat{\sigma}_\alpha + \boldsymbol{p}_j \hat{\sigma}_\alpha b_{jk} | \Psi \rangle \right] \\
&= \sum_{j,k} \left[-\langle \boldsymbol{p}_j \boldsymbol{p}_k \Psi | b_{jk} \hat{\sigma}_\alpha + \hat{\sigma}_\alpha b_{jk} | \Psi \rangle + \langle \boldsymbol{p}_k \Psi | b_{jk} \boldsymbol{p}_j \hat{\sigma}_\alpha + \hat{\sigma}_\alpha b_{jk} \boldsymbol{p}_j | \Psi \rangle \right]
\end{aligned} \tag{5.23}$$

Because:

$$\begin{aligned}
&\boldsymbol{p}_j \langle \boldsymbol{p}_k \Psi | b_{jk} \hat{\sigma}_\alpha + \hat{\sigma}_\alpha b_{jk} | \Psi \rangle = \boldsymbol{p}_j \langle \left(b_{jk} \hat{\sigma}_\alpha + \hat{\sigma}_\alpha b_{jk} \right)^\dagger \boldsymbol{p}_k \Psi | \Psi \rangle \\
&= \boldsymbol{p}_j \langle \left(b_{jk} \hat{\sigma}_\alpha + \hat{\sigma}_\alpha b_{jk} \right) \boldsymbol{p}_k \Psi | \Psi \rangle = \boldsymbol{p}_j \langle \left(b_{jk} \boldsymbol{p}_k \hat{\sigma}_\alpha + \hat{\sigma}_\alpha b_{jk} \boldsymbol{p}_k \right) \Psi | \Psi \rangle
\end{aligned} \tag{5.24}$$

and:

$$\begin{aligned}
&\langle \boldsymbol{p}_j \boldsymbol{p}_k \Psi | b_{jk} \hat{\sigma}_\alpha + \hat{\sigma}_\alpha b_{jk} | \Psi \rangle = \langle \left(b_{jk} \hat{\sigma}_\alpha + \hat{\sigma}_\alpha b_{jk} \right)^\dagger \boldsymbol{p}_j \boldsymbol{p}_k \Psi | \Psi \rangle \\
&= \langle \left(b_{jk} \hat{\sigma}_\alpha + \hat{\sigma}_\alpha b_{jk} \right) \boldsymbol{p}_j \boldsymbol{p}_k \Psi | \Psi \rangle = \left\langle \left(b_{jk} \boldsymbol{p}_j \boldsymbol{p}_k \hat{\sigma}_\alpha + \hat{\sigma}_\alpha b_{jk} \boldsymbol{p}_j \boldsymbol{p}_k \right) \Psi \middle| \Psi \right\rangle
\end{aligned} \tag{5.25}$$

and:

$$\sum_{j,k} \langle \boldsymbol{p}_j \Psi | b_{jk} \boldsymbol{p}_k \hat{\sigma}_\alpha + \hat{\sigma}_\alpha b_{jk} \boldsymbol{p}_k | \Psi \rangle = \sum_{j,k} \langle \boldsymbol{p}_k \Psi | b_{jk} \boldsymbol{p}_j \hat{\sigma}_\alpha + \hat{\sigma}_\alpha b_{jk} \boldsymbol{p}_j | \Psi \rangle \tag{5.26}$$

From 5.22, 5.23 , 5.24 , 5.25 and 5.26, one gets:

$$\sum_{j,k} \boldsymbol{p}_j \left(Real \langle \Psi | b_{jk} \boldsymbol{p}_k \hat{\sigma}_\alpha + \hat{\sigma}_\alpha b_{jk} \boldsymbol{p}_k | \Psi \rangle \right) = i \sum_{j,k} Im \left(\langle \Psi | b_{jk} \boldsymbol{p}_j \boldsymbol{p}_k \hat{\sigma}_\alpha + \hat{\sigma}_\alpha b_{jk} \boldsymbol{p}_j \boldsymbol{p}_k | \Psi \rangle \right) \tag{5.27}$$

or

$$\begin{aligned}
&\sum_j \boldsymbol{p}_j \left[Real \left\langle \Psi \middle| \left(\sum_k b_{jk} \boldsymbol{p}_k \right) \hat{\sigma}_\alpha + \hat{\sigma}_\alpha \left(\sum_k b_{jk} \boldsymbol{p}_k \right) \middle| \Psi \right\rangle \right] \\
&= i \sum_j Im \left[\left\langle \Psi \middle| \left(\sum_k b_{jk} \boldsymbol{p}_j \boldsymbol{p}_k \right) \hat{\sigma}_\alpha + \hat{\sigma}_\alpha \left(\sum_j b_{jk} \boldsymbol{p}_j \boldsymbol{p}_k \right) \middle| \Psi \right\rangle \right]
\end{aligned} \tag{5.28}$$

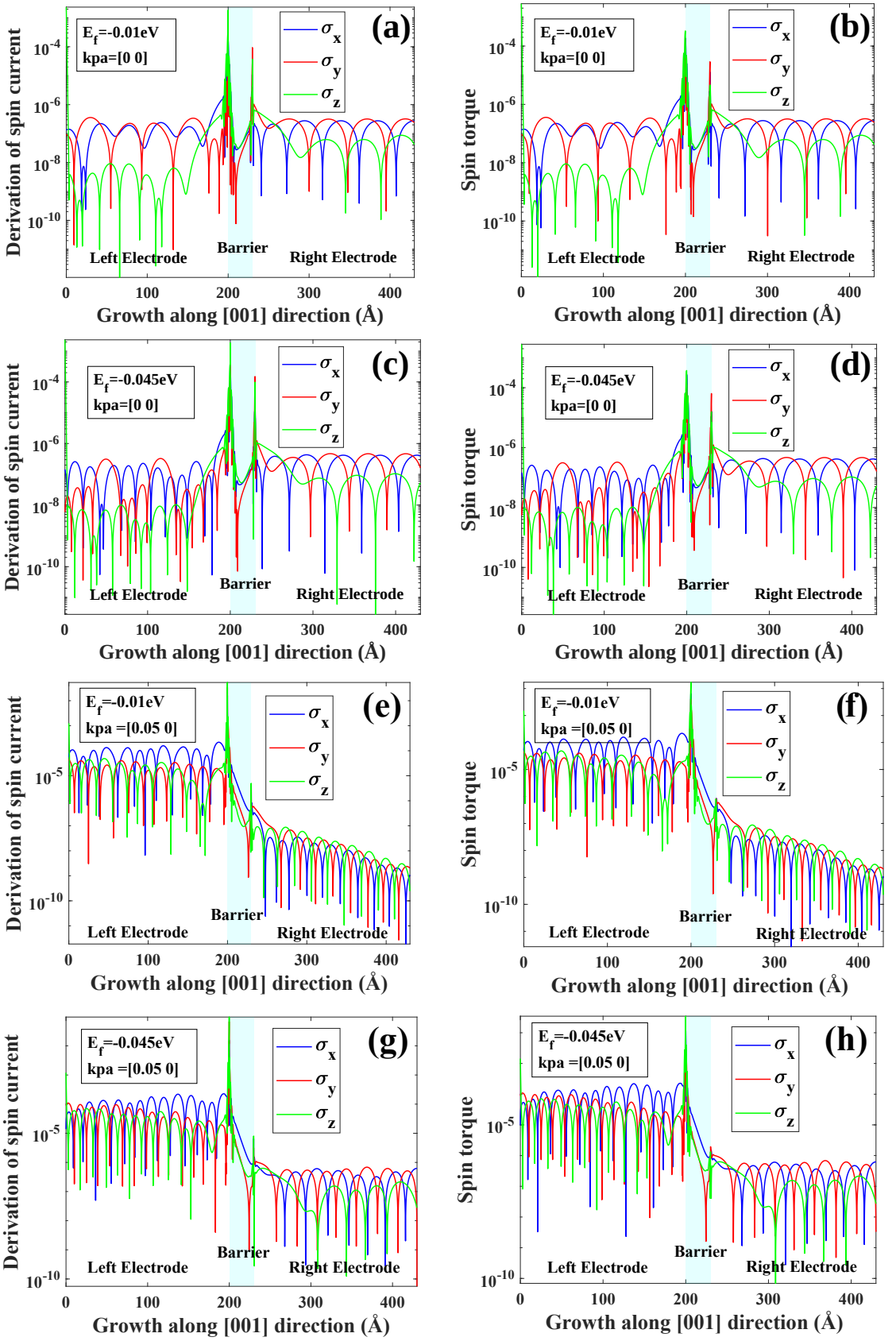

FIGURE 5.4: Derivative of three components of spin-current and three components spin-torque calculated using 30-band $\boldsymbol{k.p}$ model for normal incidence ($k_{||}$ = 0) and oblique incidence ($k_{||}$ = 0.05Å) and different energies of hole: E_f = 0.01eV and E_f = 0.045eV. The exchange energy Δ_{exc} = 0.15eV.

Consider the term:

$$\begin{aligned}\sum_j \boldsymbol{p}_j \langle\Psi|a_j\,\hat{\sigma}_\alpha + \hat{\sigma}_\alpha a_j|\Psi\rangle &= \sum_j \left[-\langle \boldsymbol{p}_j\Psi|a_j\,\hat{\sigma}_\alpha + \hat{\sigma}_\alpha a_j|\Psi\rangle + \langle\Psi|\boldsymbol{p}_j a_j\,\hat{\sigma}_\alpha + \boldsymbol{p}_j\hat{\sigma}_\alpha a_j|\Psi\rangle\right] \\ &= \sum_j \left[-\langle\left(a_j\,\hat{\sigma}_\alpha + \hat{\sigma}_\alpha a_j\right)^\dagger \boldsymbol{p}_j\Psi|\Psi\rangle + \langle\Psi|a_j\boldsymbol{p}_j\,\hat{\sigma}_\alpha + \hat{\sigma}_\alpha a_j\boldsymbol{p}_j|\Psi\rangle\right] \\ &= \sum_j \left[-\left\langle\left(a_j\,\hat{\sigma}_\alpha + \hat{\sigma}_\alpha a_j\right)\boldsymbol{p}_j\Psi\middle|\Psi\right\rangle + \langle\Psi|a_j\boldsymbol{p}_j\,\hat{\sigma}_\alpha + \hat{\sigma}_\alpha a_j\boldsymbol{p}_j|\Psi\rangle\right] \\ &= \sum_j \left[-\left\langle\left(a_j\boldsymbol{p}_j\,\hat{\sigma}_\alpha + \hat{\sigma}_\alpha a_j\boldsymbol{p}_j\right)\Psi\middle|\Psi\right\rangle + \langle\Psi|a_j\boldsymbol{p}_j\,\hat{\sigma}_\alpha + \hat{\sigma}_\alpha a_j\boldsymbol{p}_j|\Psi\rangle\right] \\ &= 2i\sum_j Im\left(\langle\Psi|a_j\boldsymbol{p}_j\,\hat{\sigma}_\alpha + \hat{\sigma}_\alpha a_j\boldsymbol{p}_j|\Psi\rangle\right)\end{aligned} \tag{5.29}$$

to give

$$\sum_j \boldsymbol{p}_j\left\langle\Psi\middle|\frac{a_j}{2}\,\hat{\sigma}_\alpha + \hat{\sigma}_\alpha\frac{a_j}{2}\middle|\Psi\right\rangle = i\sum_j Im\left(\langle\Psi|a_j\boldsymbol{p}_j\,\hat{\sigma}_\alpha + \hat{\sigma}_\alpha a_j\boldsymbol{p}_j|\Psi\rangle\right) \tag{5.30}$$

Doing the same we get also:

$$\sum_j \boldsymbol{p}_j\left\langle\left(\frac{a_j}{2}\,\hat{\sigma}_\alpha + \hat{\sigma}_\alpha\frac{a_j}{2}\right)\Psi\middle|\Psi\right\rangle = i\sum_j Im\left(\langle\Psi|a_j\boldsymbol{p}_j\,\hat{\sigma}_\alpha + \hat{\sigma}_\alpha a_j\boldsymbol{p}_j|\Psi\rangle\right) \tag{5.31}$$

From Eqs 5.30 and 5.31:

$$2\sum_j \boldsymbol{p}_j\left(Re\left\langle\Psi\middle|\frac{a_j}{2}\,\hat{\sigma}_\alpha + \hat{\sigma}_\alpha\frac{a_j}{2}\middle|\Psi\right\rangle\right) = 2i\sum_j Im\left(\langle\Psi|a_j\boldsymbol{p}_j\,\hat{\sigma}_\alpha + \hat{\sigma}_\alpha a_j\boldsymbol{p}_j|\Psi\rangle\right) \tag{5.32}$$

or:

$$\sum_j \boldsymbol{p}_j\left(Re\left\langle\Psi\middle|\frac{a_j}{2}\,\hat{\sigma}_\alpha + \hat{\sigma}_\alpha\frac{a_j}{2}\middle|\Psi\right\rangle\right) = i\sum_j Im\left(\langle\Psi|a_j\boldsymbol{p}_j\,\hat{\sigma}_\alpha + \hat{\sigma}_\alpha a_j\boldsymbol{p}_j|\Psi\rangle\right) \tag{5.33}$$

From Eqs 5.28 and 5.33, one has:

$$\begin{aligned}&\sum_j \boldsymbol{p}_j\left[Real\left\langle\Psi\middle|\left(\frac{a_j}{2} + \sum_k b_{jk}\boldsymbol{p}_k\right)\hat{\sigma}_\alpha + \hat{\sigma}_\alpha\left(\frac{a_j}{2} + \sum_k b_{jk}\boldsymbol{p}_k\right)\middle|\Psi\right\rangle\right] \\ &= i\sum_j Im\left[\left\langle\Psi\middle|\left(a_j\boldsymbol{p}_j + \sum_k b_{jk}\boldsymbol{p}_j\boldsymbol{p}_k\right)\hat{\sigma}_\alpha + \hat{\sigma}_\alpha\left(a_j\boldsymbol{p}_j + \sum_j b_{jk}\boldsymbol{p}_j\boldsymbol{p}_k\right)\middle|\Psi\right\rangle\right]\end{aligned} \tag{5.34}$$

If we introduce $\hat{\mathbf{J}}_j^\alpha$ as the α ($\alpha = \{x,\ y, z\}$) component of spin current operator, along the j direction ($j = \{x,\ y, z\}$) of the charge current,

$$\hat{\mathbf{J}}_j^\alpha = \frac{\hat{\sigma}_\alpha}{2}\frac{\partial H}{\partial \boldsymbol{p}_j} + \frac{\partial H}{\partial \boldsymbol{p}_j}\frac{\hat{\sigma}_\alpha}{2} = \hat{\sigma}_\alpha\left(\frac{a_j}{2} + \sum_k b_{jk}\boldsymbol{p}_k\right) + \left(\frac{a_j}{2} + \sum_k b_{jk}\boldsymbol{p}_k\right)\hat{\sigma}_\alpha \tag{5.35}$$

Using $\boldsymbol{p}_j = -i\hbar\boldsymbol{\nabla}_j$ then Eq 5.34 becomes:

$$-\sum_j \nabla_j\left(Re\,\langle\Psi|\,\hat{\mathbf{J}}_j^\alpha\,\Psi\rangle\right) = \frac{1}{\hbar}Im\,\langle\Psi\,|\,(\hat{\sigma}_\alpha H + H\hat{\sigma}_\alpha)\,\Psi\rangle \tag{5.36}$$

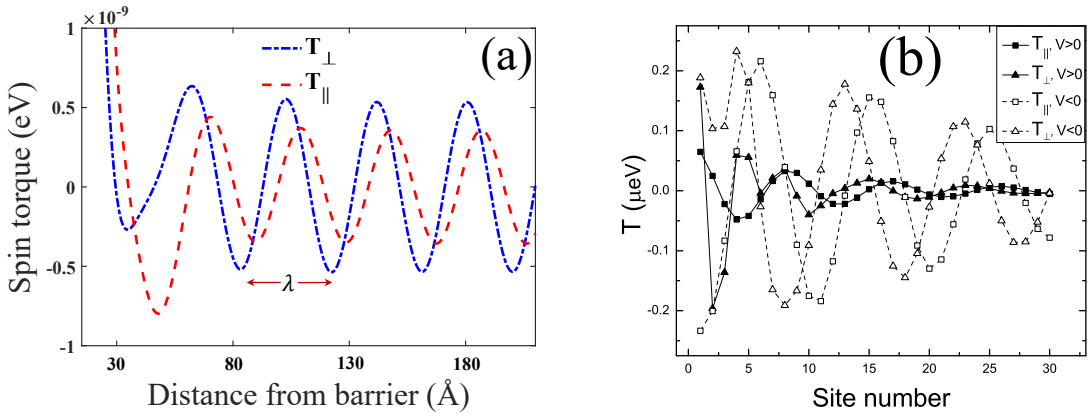

FIGURE 5.5: (a) The parallel and perpendicular components of spin torque act on the right FM as the function of the distance from right interface between barrier and right FM, calculated with zero bias, hole's energy $E_f = -0.05eV$ and exchange energy $\Delta_{exc} = 0.15eV$ in framework of the 30-band $\boldsymbol{k.p}$ tunneling code; (b) Spin torque spatial distribution of the parallel and perpendicular components of the spin torque for positive and negative bias, taken from Ref.[290].

Finally, from 5.18 and 5.36, one has

$$\frac{\partial \langle\Psi|\,\hat{\sigma}_\alpha\,|\Psi\rangle}{\partial t} = -\sum_j \nabla_j \left(Re\,\langle\Psi|\,\hat{\mathbf{J}}_j^\alpha\,\Psi\rangle \right) + Im\left[\frac{1}{\hbar}\,\langle\Psi|\,[\hat{\sigma}_\alpha, H]\,\Psi\rangle\right] \tag{5.37}$$

If we introduce $\tau_s^\alpha = \frac{1}{i\hbar}[\hat{\sigma}_\alpha, H] = -\frac{i}{\hbar}[\hat{\sigma}_\alpha, H]$ then:

$$\frac{\partial \langle\Psi|\,\hat{\sigma}_\alpha\,|\Psi\rangle}{\partial t} = -\sum_j \nabla_j \left(Re\,\langle\Psi|\,\hat{\mathbf{J}}_j^\alpha\,\Psi\rangle \right) + Re\left[\langle\Psi|\,\tau_s^\alpha \Psi\rangle\right] \tag{5.38}$$

where we have used

$$Im\left[\frac{1}{\hbar}\,\langle\Psi|\,[\hat{\sigma}_\alpha, H]\,\Psi\rangle\right] = Re\left[\frac{1}{i\hbar}\,\langle\Psi|\,[\hat{\sigma}_\alpha, H]\,\Psi\rangle\right] \tag{5.39}$$

In the case, when the Hamiltonian is time independent, we obtain the continuity equation for the spin current according to the following form:

$$\sum_j \nabla_j . \left(Re\,\langle\Psi|\,\hat{\mathbf{J}}_j^\alpha\,\Psi\rangle \right) = Re\left[\langle\Psi|\,\tau_s^\alpha \Psi\rangle\right] \tag{5.40}$$

which means that, unlike the charge current which is always conserved, the spin current is conserved on the condition that the Hamiltonian in the bulk and at the interface (see the following section) commutes with the corresponding spinor. On this unique condition, the spin current is conserved within the whole heterostructure. If one considers, for example, the case of a spin-orbit coupling of the form $H_{S.O} = \mathbf{L}.\mathbf{S}$, one can easily observe that its commutator with the spin physical observable $\mathbf{S}$ is not zero but includes the orbital-moment operator $\mathbf{L}$, playing the role of a non-zero external magnetic field acting on the spin. By reciprocity, the orbital current (not defined here, see for instance Ref. [291]) will not be conserved due to the action of the spin $\mathbf{S}$. Note however, that the total angular-momentum ($\mathbf{J} = \mathbf{L} + \mathbf{S}$) is conserved at least in the case of a pure spherical symmetry because it commutes with the spin-orbit Hamiltonian. Another example is the one of an exchange field in a ferromagnet, which is a general problem for the issue of the spin-transfer phenomena. The presence of an exchange field in the ferromagnetic layer to be switched, by STT or by SHE, makes the spin current nonuniform in the layer but modulated by a precession of the local spin-polarized carriers around the local magnetic field. This precession, which is shortly described below,

is responsible for the mixing between the damping-like and field-like torques within the film thickness, as largely emphasized in the case of spin-torques through a tunnel barrier [290, 292, 293].

Figs 5.3 displays the profile of the $j\sigma_{x,y,z}$-components of the spin-current (*absolute value*) calculated within the respective 6, 30 and 40-band approaches. The holes tunnel from the thick layer to the left with magnetization along z to the thin layer to the right with magnetization oriented along the x direction (orthogonal configuration). Those mostly identical profiles obtained with the 6, 30 and 40-band treatment, display an incident spin-current along z parallel to the magnetization of the thick layer, transmitting inside the thin layer in a mainly x-component parallel to the local magnetization and reflected with two z and y components. The reflected y-component is ascribed to a partial precession of the spin-current inside the thin layer. The transverse z-component of the spin-current entering the thin layer to the right is responsible for the dissipative torque (Slonczewski-like) whereas the y component is responsible for the field-like component of the torque (non-dissipative) like discussed above.

Figure 5.4 displays the equivalence between the calculation of derivative of spin current and spin torque (see Eq.5.40) calculated with our 30 bands $\boldsymbol{k.p}$ tunneling code. This shows that our theory and code are robust. Furthermore, one should have:

$$\lambda = \frac{v_F \hbar}{\Delta_{exc}} \tag{5.41}$$

where λ is the period of the spin torque's oscillation within the layer and Δ_{exc} the spin-splitting due to exchange; v_F is Fermi velocity. One observes that with the same incident energy E_F, λ under normal incidence (Fig.5.4a,b,c,d) is greater than the value obtained under oblique incident (Fig. 5.4e,f,g,h) since the Fermi velocity along the tunnel direction (z) decreases as $k_{||}$ increases.

For the parameters corresponding to the calculations shown in Fig.5.5a, one has $v_F \sim 3 \times 10^5 m/s$; $\Delta_{exc} = 0.15eV$ which corresponds to a larger period length, by about a factor of 4 ($\lambda \simeq 40$Å instead of 10 Å for transition metals) extracted from our numerical calculations in Fig. 5.5a compared to the results of Kalitsov et al. in Ref. [290] and plotted in Fig. 5.5b. The difference originates from the different material properties between poor metallic ferromagnetic semiconductors and transition metal systems. In the latest case, the Fermi velocity is larger, approaching 10^6 m/s, which is typically 3 or 4 times larger than the one of light holes, but however characterized by a well smaller characteristic precession time of the order of $\hbar\Delta_{exc} \approx 1$ fs with $\Delta_{exc} \simeq 1$ eV. This leads in the latter case, to a precession period of about 1 nm as shown in the corresponding figure of Kalitsov (Fig. 5.5b). Beside that, the phase relation between parallel and perpendicular component of transfer torque in our numerical calculations is the same with that in Kalitsov et al [290].

The partial conclusion of this section concerning the calculation of spin-torque in multiband $\boldsymbol{k.p}$ theory is that our theory and numerical development compete with the ones led in a Green's function approach or at least give essentially the same results. The strong improvement provided by our technique is that one can involve more easily the surface potential terms (or surface Hamiltonian), like Rashba or Dresselhaus spin-orbit terms. Those are relevant in spin-transport to describe spin-depolarization effects or additional effects like the generation or conversion of charge current into transverse spin-currents (anomalous tunnel Hall effect or inverse Edelstein effect).

We will come back to theoretical calculations of the spin-transfer torque after having described the experimental results dealing with spin-transfer in (Ga,Mn)As/GaAs/(Ga,Mn)As tunnel junctions.

5.2.2 Spin-current and spin-torque involving interface potentials and spin-orbit terms

We are now going to discuss the involvement of the interface potentials on the STT. Let us consider the spin current in heterostructures involving surface potential terms.

$$H_{surface} = \sum_j V_j \delta(x_j - x_0) \tag{5.42}$$

where V_j is a matrix which is independent of the j component of momentum. Then the total Hamiltonian is:

$$H_{total} = H + H_{surface} \tag{5.43}$$

According to Eq. 5.40, we have:

$$\sum_j \nabla_j \left(Re \left\langle \Psi \right| \hat{\mathbf{J}}_j^{\alpha} \left| \Psi \right\rangle \right) = Re \left(\frac{1}{i\hbar} \left\langle \Psi \right| \left[\hat{\sigma}_\alpha, H_{surface} \right] \left| \Psi \right\rangle \right) + Re \left(\frac{1}{i\hbar} \left\langle \Psi \right| \left[\hat{\sigma}_\alpha, H \right] \left| \Psi \right\rangle \right) \tag{5.44}$$

Since:

$$\begin{aligned} &\frac{1}{i\hbar} \left\langle \Psi \right| \left[\hat{\sigma}_\alpha, H_{surface} \right] \left| \Psi \right\rangle = \frac{1}{i\hbar} \left\langle \Psi \right| \hat{\sigma}_\alpha V_j \delta(x_j - x_0) - V_j \delta(x_j - x_0) \hat{\sigma}_\alpha \left| \Psi \right\rangle \\ &= \frac{1}{i\hbar} \nabla_j \left\langle \Psi \right| \hat{\sigma}_\alpha V_j \theta(x_j - x_0) - V_j \theta(x_j - x_0) \hat{\sigma}_\alpha \left| \Psi \right\rangle = \frac{1}{i\hbar} \nabla_j \left[\left\langle \Psi \right| \hat{\sigma}_\alpha V_j - V_j \hat{\sigma}_\alpha \left| \Psi \right\rangle \theta(x_j - x_0) \right] \\ &= \frac{1}{i\hbar} \nabla_j \left[\left\langle \Psi \right| \left[\hat{\sigma}_\alpha, V_j \right] \left| \Psi \right\rangle \theta(x_j - x_0) \right] \end{aligned} \tag{5.45}$$

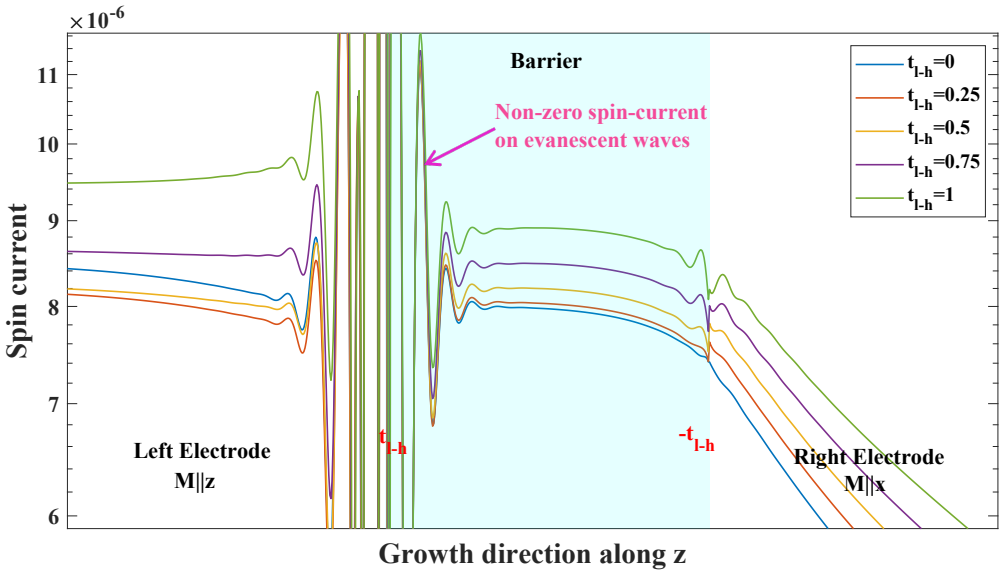

FIGURE 5.6: Profiles of the z-component of the spin current within (Ga,Mn)As/GaAs/(Ga,Mn)As junctions. The magnetization of the thick layer to the left is along z, whereas the one to the right is transverse that is along x for the calculation of the STT. The calculations have been performed with the energy of holes $\epsilon = -0.03eV$ from the middle of the (Ga,Mn)As band. Here, the necessary heavy hole - light hole mixing parameter t_{l-h} varies from 0 to 1. This coefficient is set naturally positive and negative at the respective right and left interface of the barrier due to the specific D_{2d} symmetry of the junction of a symmetric profile.

Equation. 5.44 becomes:

$$\sum_j \nabla_j \left(Re \left\langle \Psi \right| \hat{\mathbf{J}}_j^{\alpha} \left| \Psi \right\rangle \right) - \nabla_j \left(Re \left[\frac{1}{i\hbar} \left\langle \Psi \right| \left[\hat{\sigma}_\alpha, V_j \right] \left| \Psi \right\rangle \theta(x_j - x_0) \right] \right) = Re \left(\frac{1}{i\hbar} \left\langle \Psi \right| \left[\hat{\sigma}_\alpha, H \right] \left| \Psi \right\rangle \right) \quad (5.46)$$

Project Eq. 5.46 onto $j-direction$, one gets:

$$\nabla_j \left(Re \left\langle \Psi \right| \hat{\mathbf{J}}_j^{\alpha} \left| \Psi \right\rangle \right) - \nabla_j \left(Re \left[\frac{1}{i\hbar} \left\langle \Psi \right| \left[\hat{\sigma}_\alpha, V_j \right] \left| \Psi \right\rangle \theta(x_j - x_0) \right] \right)_j = Re \left(\frac{1}{i\hbar} \left\langle \Psi \right| \left[\hat{\sigma}_\alpha, H \right] \left| \Psi \right\rangle \right)_j \quad (5.47)$$

Taking integral of both side of Eq. 5.47 and putting $J_j^{\alpha}(0) = \int Re \left(\frac{1}{i\hbar} \left\langle \Psi \right| \left[\hat{\sigma}_\alpha, H \right] \left| \Psi \right\rangle \right) dx_j$ then we get:

$$Re \left\langle \Psi \right| \hat{\mathbf{J}}_j^{\alpha} \left| \Psi \right\rangle = \begin{cases} J_j^{\alpha}(0) + Re \left(\frac{1}{i\hbar} \left\langle \Psi \right| \left[\hat{\sigma}_\alpha, V_j \right] \left| \Psi \right\rangle \right)_j & \text{if } x_j > x_0 \\ J_j^{\alpha}(0) & \text{if } x_j < x_0 \end{cases} . \quad (5.48)$$

This equation shows the discontinuity of the spin current at the interface induced by the surface potential, which may originate from the Rashba term or reducing from C_{2v} to D_{2d} at the interface of III-V semiconductor heterostructures. Figure 5.6 displays the 30-band **k. p** profile of the z-component of the 'transverse' spin-current injected, and particularly at the interface between the tunnel barrier and the thin (Ga,Mn)As layer. The parameters are the same than those of Fig. 5.3 except that one considers, now, the necessary HH-LH mixing parameter (t_{lh}) varying from 0 to ± 1. This coefficient is set naturally positive and negative at the respective right and left interfaces of the barrier owing to the $\mathcal{D}_{2d}$-symmetry of the junction with a symmetric profile. Surprisingly, it results in a noticeable enhancement of the z-dissipative component of the STT by more than 10% (Fig. 5.6) for $t_{lh} = \pm 1$. Such enhancement in the transverse dissipative part of the spin-current may originate from a transfer of highly spin-polarized heavy holes (pure spin-states) into polarized light holes with a larger transmission (smaller effective mass).

5.3 Spin transfer and spin-orbit torque: Experiments (collaboration UMϕ CNRS-Thales)

We now turn on and discuss the spin-torque experiments involving (Ga,Mn)As-based magnetic tunnel junctions in a perpendicular current geometry (CPP). Since the pioneering experimental work led in Grenoble by M. Tsoi et al. [294] and in Cornell University by J. Katine et al. [295], we know that the magnetic moment of a ferromagnetic body can be reversed or be re-oriented by transfer of the spin angular momentum carried by a spin-polarized current. This concept of spin transfer has been previously introduced by Slonczewski [277] and Berger, [278] before being confirmed by extensive experiments on pillar-shaped magnetic trilayers [296].

The principle of spin-orbit torque process mediated through the spin-Hall effect in semiconductors can be discussed along the same ideas as recently demonstrated by the group of M. Tanaka [5] by the evidence of the magnetization switching of a single magnetic layer of (Ga,Mn)As.

Most current-induced magnetization switching (CIMS) or spin-torque experiments have been performed on purely metallic trilayers [297–302], such as Co/Cu/Co, in lithographically patterned nanopillars with detection of the magnetic switching by giant magnetoresistance effects. Typical critical current density J_C required for magnetization reversal in these systems has been of the order of 10^7 $A.cm^{-2}$ or higher. Since, there have been several reports on current-induced magnetization switching on transition-metal magnetic

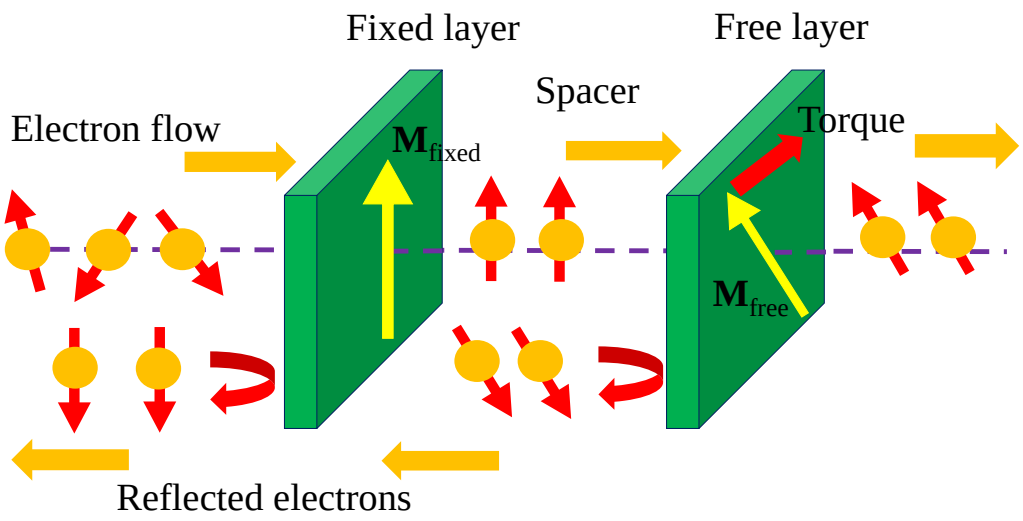

FIGURE 5.7: Scheme of spin transfer torque: the spin polarized currents were prepared by the fixed ferromagnetic layer before entering the free ferromagnetic layer. Because of the conservation of angular momentum, the lost spin part acts like a torque on the magnetization in the free layer and then may switch the direction of magnetization in this layer.

tunnel junctions with low junction resistance at critical current density below 10^6 $A.\text{cm}^{-2}$ [303–305]. Current Induced Magnetization Switching (CIMS) experiments on tunnel junctions bring new physical problems, [306] and are also of particular interest for their promising application to the switching of the MTJ of MRAM (Magnetic Random Access Memory). For a latest review of spin transfer in MgO-based MTJs, the reader can refer to the paper of Katine and Fullerton [307] and references therein. (Ga,Mn)As is known to have a small magnetization of less than 0.05 T and a high spin-polarization of holes which must result in the reduction of critical current according to the Slonczewskis spin-transfer-torque model. It results that a low current density, of the order of 10^5 $A.\text{cm}^{-2}$, is a needed for CIMS with (Ga,Mn)As [6, 7] shows the interest of magnetic semiconductors for spin transfer. Beyond the fundamental point of view and as emphasized by Chiba *et al.* [308], the specificity of the valence-band structure and spin-orbit interactions has to be taken into account and should have the effect to mix the spin states of carriers. In the following, we present results of CIMS experiments obtained on our own (Ga,Mn)As MTJs, they appear to be more or less comparable to those obtained in Ohno's group [6].

On the other hand, considering the spin-orbit torques (SOT), the combination of exchange and SOI in (Ga,Mn)As makes this materials very important. Indeed, more generally, magnetization switching at the interface between ferromagnets and SHE nonmagnetic materials controlled by a current and related current-induced torques are of a particular interest. In that sense, the size and symmetry of the SOI at the interface with relevant materials with surface broken symmetry, like using (Ga,Mn)As (III,V), deserves some clear investigations for potential future applications. With that in mind, SOI current induced torques have been already demonstrated with (Ga,Mn)As [4, 8] and more recently, the specific role of the anti-damping Slonczewski-like torque in the ferromagnetic resonance regime of spin-transfer. This particularly emphasizes the role of the two types, Rashba and Dresselhaus, symmetry-like terms originating from the unidirectional character of the interface, together with the symmetry breaking from T_d to C_{2v} symmetry group.

5.3.1 Experiments on spin transfer torque with (Ga,Mn)As-based tunnel junctions (Ga,Mn)As/GaAs/(Ga,Mn)As heterostructures

Our ferromagnetic semiconductor-based (Ga,Mn)As(50 nm)/GaAs(6 nm)/(Ga,Mn)As(10 nm) structures, depicts in figure 5.8a, were grown by molecular beam epitaxy at 250^{0}C on a *p*-doped GaAs buffer template (doping $p \simeq 2\times10^{19}\ cm^{-3}$) deposited on a GaAs(001) substrate. The two (Ga,Mn)As electrodes were made different according to their thickness and their composition in Mn doping so as to observe a different Curie temperature T_C and coercive field. By SQUID measurements, we find a typical ferromagnetic behavior for the (Ga,Mn)As layers with a Curie temperature of 150 K for the thick 50 nm layer and 55 K for the thinnest 10 nm layer. The magnetization at saturation M_S was measured to be 50 emu/cm^3 and 12 emu/cm^3 for the thick and thin layer respectively.

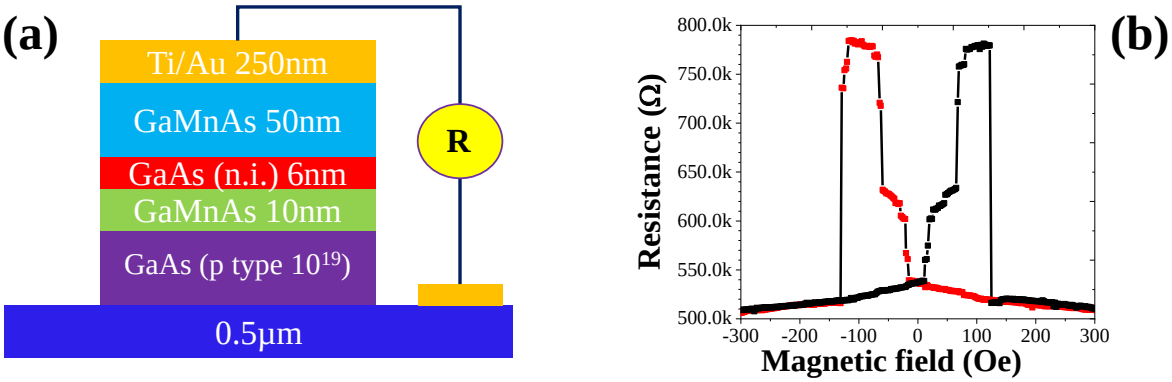

FIGURE 5.8: (a) Structure used for the investigation of the Tunneling Magnetoresistance. (b) Tunneling Magnetoresistance (TMR) obtained on the structure shown in this figure a at temperature of 12 K and at bias of 20 mV. The (Ga,Mn)As layers where made different to promote a different reversal of the two (Ga,Mn)As layers and a clear antiparallel (AP) plateau.

For the tunneling-magnetoresistance (TMR) measurements and spin-torque experiments, 500 nm diameter submicronic pillars were patterned by e-beam lithography methods. The resistance of the junctions were acquired with a standard DC technique between 12 K in magnetic fields up to 6 kOe. The I-V curves (Fig. 5.9b) exhibit a typical nonlinear behavior for tunneling. The resistance-area product (RA) at low bias (20 mV) is about $1.2\times10^{-3}\ \Omega\ cm^2$ at 12 K which appears very similar to junctions with $(In_{0.25},Ga_{0.75})As$ indicating an almost equal barrier height with the two materials. Besides, figure 5.9a displays the dependence of TMR on the bias voltage where the TMR reaches about 115% at zero bias and reduces almost to the zero at bias about 1eV. These results are in the same order of magnitudes that were obtained with $(In_{0.25},Ga_{0.75})As$ (150 at zero bias) as reported previously in ref.[7].

Fig. 5.8b displays an example of a TMR curve acquired at 12 K with a magnetic field H_{ext} = 55 Oe applied along the easy magnetization axis ([100]). The well-defined resistance plateau on the curves is characteristic of an antiparallel (AP) arrangement of the two (Ga,Mn)As layers on the plateau. The MR ratio reaches about 50% at 12 K with a bias voltage of 20 mV. In Fig 5.10a, we show the spin-transfer torque phenomena (STT) obtained on the same (Ga,Mn)As/GaAs(6nm)/(Ga,Mn)As junction. Starting from a saturated parallel (PA) configuration at zero injected current (V=0), the bias is increased step by step up to magnetization switching, and, after each step, brought back to 20 mV for comparison with the results at 20 mV before the current injection process. By this way, one can check whether the magnetic configuration has been irreversibly switched and only irreversible switching can be detected. By comparison with the MR curve at 20 mV, one observes that the magnetic configuration is switched irreversibly from an almost parallel

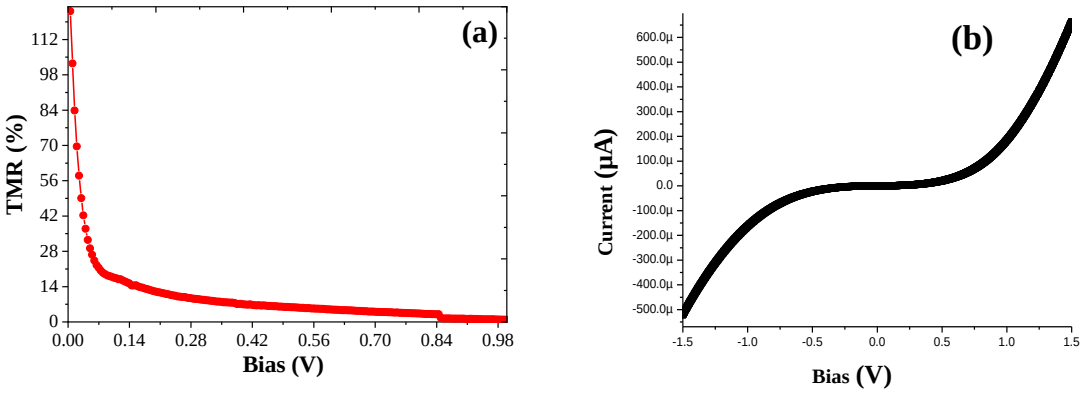

FIGURE 5.9: (a) Tunneling magneto resistance TMR as the function of bias voltage: The TMR reaches very high values at low bias (120 %) and reduces to zero at bias 1V. (b) The I-V curve of our sample.

(P) to an almost antiparallel (AP) configuration by a positive current density (current flowing from the thin magnetic layer to the thick one, $j_{c+} = 2.1 \times 10^5\ A.cm^{-2}$ (V_{c+} = 1.2 V) at 12 K. Then the configuration is switched back to parallel by a negative current above a threshold current density of the same order $j_{c-} = -1.9 \times 10^5 A.cm^{-2}$ at 12 K (V_{c-}=1.4 V). Opposite current directions for the P to AP and AP to P transitions is the characteristic behavior of switching by the STT induced by the current. Reversing the initial orientation of the magnetizations does not reverse the sign of the switching current confirming thus that Oersted field effects can be ruled out and that the transition is due to the magnetic switching of the thin layer.

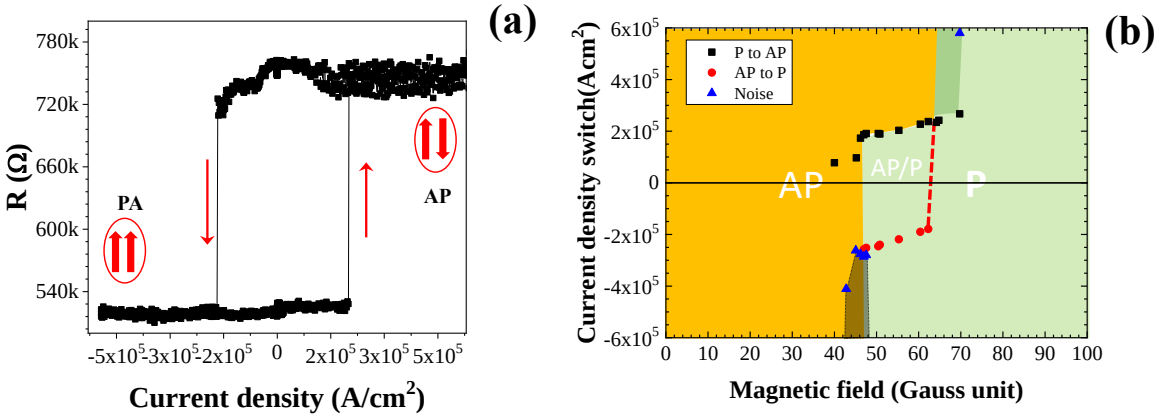

FIGURE 5.10: (a) Spin torque experiment performed on the same nanopillars revealing magnetic reversal for a critical current density of $j_{c+} = 2.1 \times 10^5 A.cm^{-2}$ and $j_{c+} = -1.9 \times 10^5 A.cm^{-2}$ respectively. The applied field is 55 Oe in the in-plane direction; (b) The magnetization diagram switching for this spin torque experiment.

STT experiments similar to those obtained of Fig.5.10a and corresponding switching diagram in Fig.5.10b can be obtained only in a small field window of 4-5 Oe around 50 Oe at 12 K. We found that the dipolar field generated by the thick (Ga,Mn)As layer and acting on the thin layer is close to 55 Oe at 3 K, so that H_{ext}=55 Oe corresponds to about an effective field H_{eff}=0 Oe on the thin layer when the moment of the thick one is in the positive direction (Fig. 5.10a). The behavior of Fig. 5.10a in a field range of a few Oe around H_{eff} = 0 Oe can be explained by the combined effects of the Joule heating and temperature dependence of the magnetic properties [7].

5.3.2 Analytical theory and numerical modeling of the Spin-Transfer torque within the multiband k. p theory frame

General arguments on Spin Transfer phenomena

We now focus to the calculations of the torque within the point of view of the *spin* degree of freedom. One defines $\sigma_{x,y,z}$, the spin of the carriers, generating a local torque on a local magnetization $\boldsymbol{M}$. We call $\boldsymbol{j}$ the charge-current. Concerning the calculation of spin torque in III-V heterojunctions, one can start from an equation giving the time derivative of the angular momenta density operator $\boldsymbol{\mu_i} = \rho \boldsymbol{J}_i$ at a certain position inside the heterostructure where $\boldsymbol{J}_i$ is the angular momentum operator along direction i:

$$\frac{\partial \boldsymbol{\mu}_i}{\partial t} = -\nabla(\boldsymbol{j}\boldsymbol{J}_i) + \rho \frac{\partial \boldsymbol{J}_i}{\partial t}$$
$$\frac{\partial \boldsymbol{\mu}}{\partial t} = -\nabla(\boldsymbol{j}\boldsymbol{J}_i) + \frac{\Delta_{exc}}{\hbar}\boldsymbol{m} \times \boldsymbol{\mu} \tag{5.49}$$

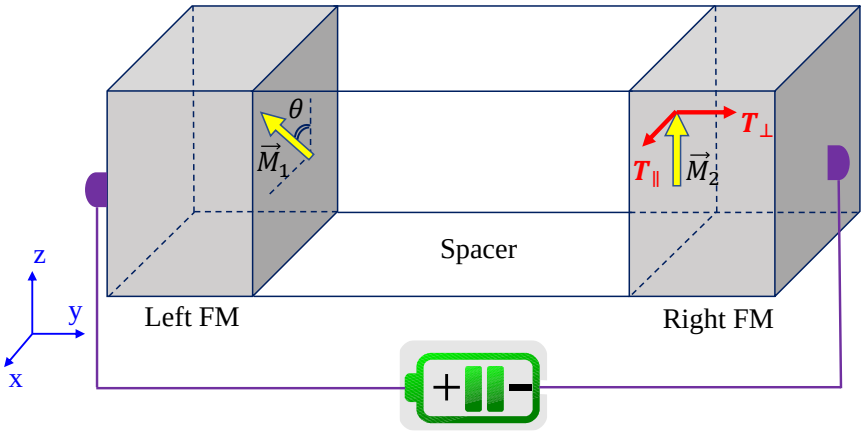

FIGURE 5.11: Shematic structure of the MTJ, consisting of left and right FM leads separated by a nonmagnetic spacer. The magnetization $\boldsymbol{M}_2$ of the right FM lead is along the z axis, whereas the magnetization $\boldsymbol{M}_1$ of the left lead is rotated by an angle θ around the y axis with respect to $\boldsymbol{M}_2$.

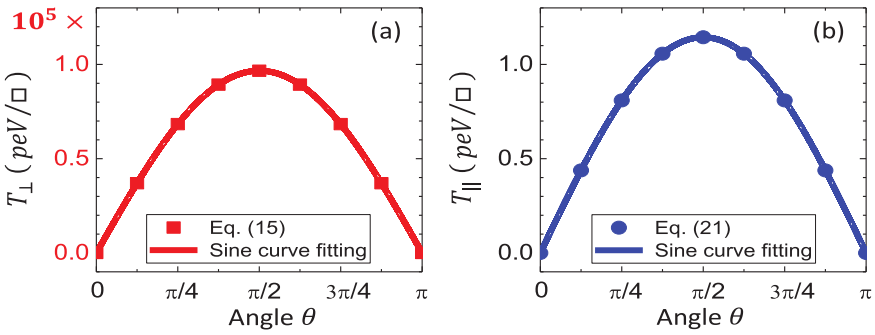

FIGURE 5.12: The angular dependence of (a) $T_\perp$ and (b) $T_{||}$ for SFMJ with bias of 0.2 V. The solid points are analytical calculation and the solid lines are the sine curve fit, taken from Ref.[309].

Summing the latter equation over the different hole states included in the transport gives out (after having considered that the time derivative of the angular moment operator is null in the limit of coherent elastic transport):

$$\langle \nabla (\boldsymbol{j}\boldsymbol{J}_i) \rangle = \frac{\Delta_{exc}}{\hbar} \boldsymbol{m} \times \langle \boldsymbol{\mu} \rangle \tag{5.50}$$

This gives the torque at a given interface (int.) after integration over the semi-infinite structure:

$$\langle \boldsymbol{j}\boldsymbol{J}_i \rangle_{int.} = \int_{\mathcal{V}} H_{exc} \times \langle \boldsymbol{\mu}_J \rangle \tag{5.51}$$

where H_{exc} is the average exchange field experienced by holes and μ_J is the magnetic moment vector (per unit surface) injected in the thin layer subject to the torque by the spin-polarized current. We recover here the general results established by Kalitsov *et al.* [310] in the case of transport in the CB described using the Keldysh framework.

This demonstrates the presence of two intertwined contributions $\langle \boldsymbol{j}\boldsymbol{J}_i \rangle_x$ (parallel to the layer) and $\langle \boldsymbol{j}\boldsymbol{J}_i \rangle_z$ (perpendicular to the layer) for the spin torque ($\hat{y}$ is the magnetization direction) as derived for symmetric [311, 312] and asymmetric barriers [313] and demonstrated experimentally in epitaxial MgO barrier MTJs [314, 315]. These two components of the transverse spin current are also responsible for the particular angular dependence of the tunneling transmission as in the case of the conduction band [316, 317]. These two components of the torque are linked to the average value of the two components of the angular momentum carried by the hole current [310]. Within the general circuit-theory formalism developed by Braatas *et al.* [318] and adapted to metallic trilayers, one can establish that these two contributions to the torque in magnetic tunnel junctions can be linked to the magnetic moment in the barrier (generalization of the spin accumulation) through the real and imaginary part of the tunnel mixing conductance $G_{\uparrow\downarrow}$. These should be calculated in a future work.

Spin Transfer phenomena: Angular variations of spin-torque and spin-orbit torque

The general expression for the magnetic torque acting on the local magnetization $\boldsymbol{M}$ is:

$$\boldsymbol{\Gamma}_{\boldsymbol{M}} = \frac{\partial \int_V \boldsymbol{M}}{\partial t} = \int_V \frac{\Delta_{exc}}{\hbar} \boldsymbol{\mu} \times \boldsymbol{M} \approx - \int_V \frac{\partial \langle \boldsymbol{\mu} \rangle}{\partial t} \tag{5.52}$$

where $\int_V$ means the integral over the volume, V, of the magnetic layer to switch (or thickness). The relationship $\frac{\partial \int \mathbf{M}}{\partial t} \approx - \int \frac{\partial \boldsymbol{\mu}}{\partial t}$ means that the total torque is zero due to the conservation of the angular momentum as it results from general reciprocity argument *via* the exchange term ($\mathcal{H}_{exc}$) acting equally between $\boldsymbol{M}$ and $\boldsymbol{\mu}$ with $H_{exc} = -\Delta_{exc} \boldsymbol{M}\ \boldsymbol{\mu}$. The equality $\frac{\partial \int \mathbf{M}}{\partial t} = - \int \frac{\partial \boldsymbol{\mu}}{\partial t}$ holds exactly for zero spin-orbit coupling. One gets:

$$\frac{\partial \boldsymbol{\mu_i}}{\partial t} = \frac{\partial \rho}{\partial t} \boldsymbol{\sigma}_i + \rho \frac{\partial \boldsymbol{\sigma}_i}{\partial t} \tag{5.53}$$

or equivalently:

$$\frac{\partial \boldsymbol{\mu}_i}{\partial t} = -\nabla (\boldsymbol{j}\boldsymbol{\sigma}_i) + \rho \frac{\partial \boldsymbol{\mu}_i}{\partial t} \tag{5.54}$$

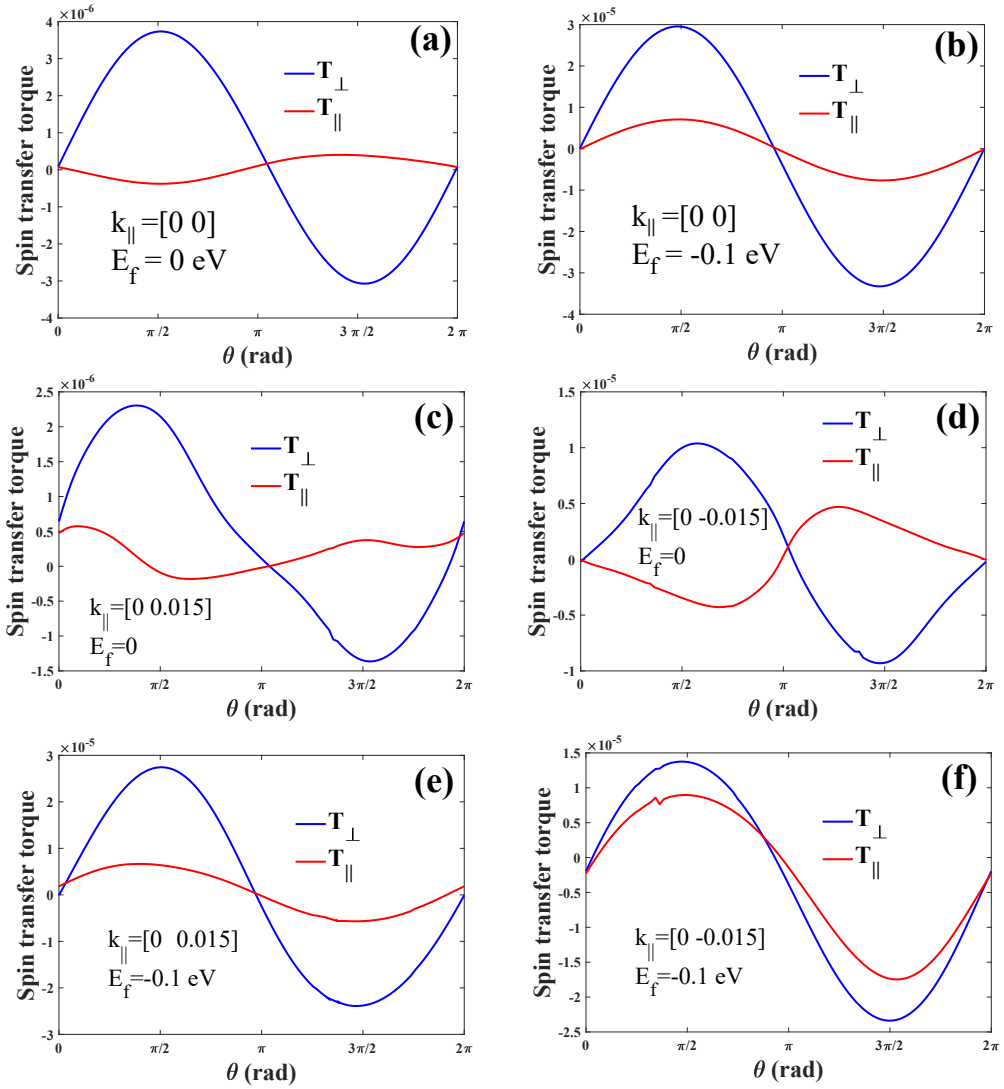

FIGURE 5.13: Angular dependence of spin transfer torque, for nomal incident electron (a,b) and oblique incident electron (c,d,e,f) with different hole's energies, through the (Ga,Mn)As/GaAs/(Ga,Mn)As tunnel junction depicted in Fig. 5.11.

giving:

$$\frac{\partial \boldsymbol{\mu_i}}{\partial t} = -\nabla\left(\boldsymbol{j}\boldsymbol{\sigma}_i\right) + \frac{\Delta_{exc}}{\hbar}\boldsymbol{M}\times\boldsymbol{\mu}_{i,\perp} - \frac{\boldsymbol{\mu}_{i,\perp}}{\tau_\perp} = 0 \tag{5.55}$$

where $\tau_\perp$ is the decoherence time for the two components of the spin-currents transverse to the magnetization. The latter expression holds exactly in the absence of any spin-orbit interactions [4] (core spin-orbit of holes nor spin-orbit at interfaces) whereby the commutator of the spin operator simply involves the exchange field.

Spin-transfer torques involving decoherence and spin-flips

In order to determine the efficiency of spin-transfer and spin-orbit-torque involving decoherence and spin-flips, one needs to compute the dynamics of the spin-polarized carriers with spin σ and local $3d$ transition metal magnetization $\mathbf{M}$ and looking for the different condition limit. From a quantum mechanical picture

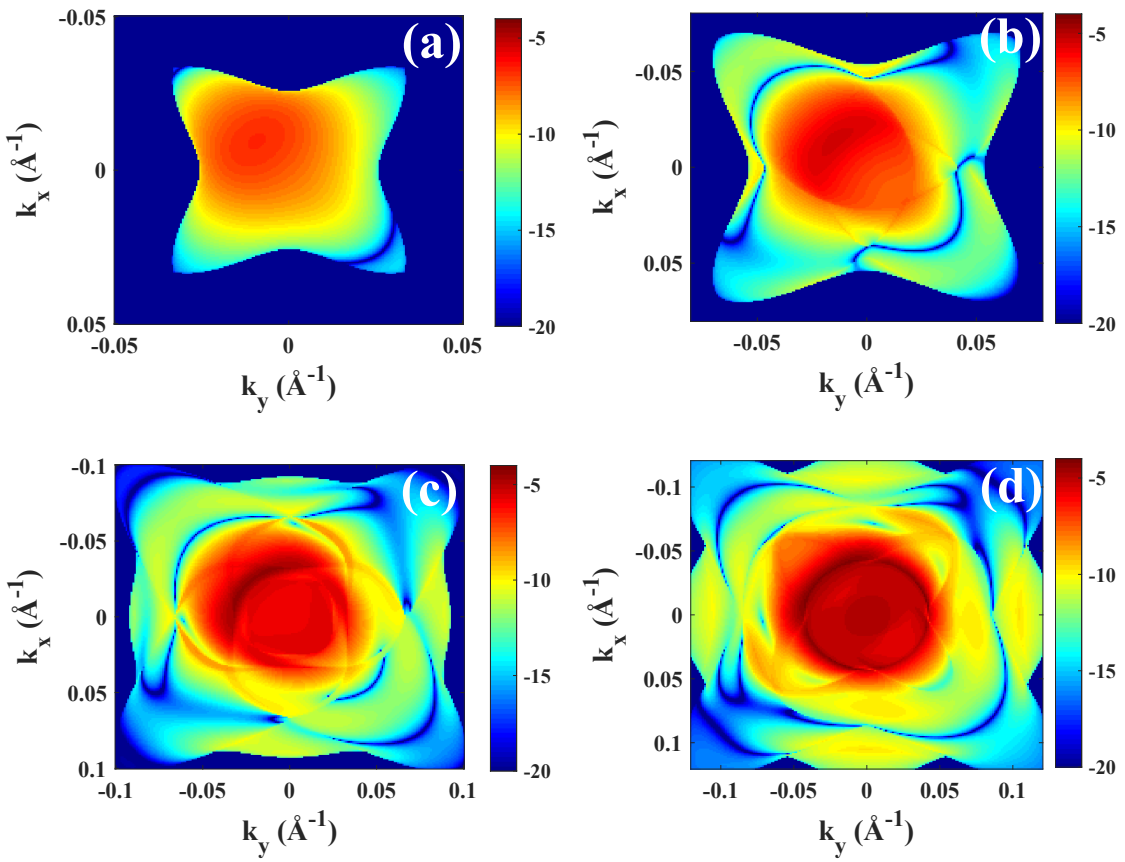

FIGURE 5.14: Transmission coefficient as function of $k_{||}$ wavevector for the maximum spin transfer torque configuration ($\theta = \pi/2$) depicted in Fig. 5.11. The strong asymmetry in the transmission coefficient for the opposite incidence leads to a difference in the angular dependence of the torque upon two opposite incident direction depicted in Fig. 5.13(c-f).

involving supplementary relaxation terms, the dynamics of the magnetic moment $\boldsymbol{\mu}$ inside the ferromagnetic layer to switch writes:

$$\frac{\partial \boldsymbol{\mu}}{\partial t} = \frac{1}{i\hbar}[\boldsymbol{\mu}, H_{exc}]_{coh.\ prec.} - \mathcal{P}_s \mathbf{n} - \frac{\boldsymbol{\mu}}{\tau_\perp}$$

or (5.56)

$$\frac{\partial \boldsymbol{\mu}}{\partial t} = \frac{\Delta_{exc}}{\hbar}\mathbf{M} \times \boldsymbol{\mu} - \mathcal{P}_s \mathbf{n} - \frac{\boldsymbol{\mu}}{\tau_\perp} \quad (5.57)$$

where $\mathbf{n}$ is the unit vector along the divergence of the spin-current $\mathcal{P}_s$ its value (spin-polarization) that is the rate of the spin injected in the small volume one considers. $\mathbf{n}$ is transverse to the magnetization and almost transverse to the spin-current injected from the ferromagnetic source (thick layer) giving rise to the torque. $\tau_\perp$ is a characteristic spin-flip time for the transverse magnetization inside the ferromagnet. If the spin-orbit term, H_{SO} is neglected. The latter equation, derived from general quantum mechanics arguments, gives out the rule for the conservation of the total angular momentum shared between $\boldsymbol{\mu}$ and $\mathbf{M}$. Here, we have used:

$$\frac{\partial \langle \boldsymbol{\mu} \rangle}{\partial t} = \frac{1}{i\hbar} \langle [\boldsymbol{\mu}, H] \rangle \quad (5.58)$$

where $\langle ... \rangle$ represents a certain quantum-mechanical averaging over the non-equilibrium carrier states and $\langle \boldsymbol{\sigma} \rangle = \boldsymbol{\mu}$ and where $\boldsymbol{\mu}$ is the corresponding Pauli matrix. This corresponds to the quantum mechanical precession (*coh. prec.*) giving rise to the torque.

In the case of a long spin-lifetime $\tau_\perp$ compared to the precession time $\tau_{exc} = \frac{\hbar}{\Delta_{exc}}$, one obtains:

$$\boldsymbol{\mu} = \mathcal{P}_s \frac{\hbar}{\Delta_{exc}} (\mathbf{M} \times \mathbf{n}), \tag{5.59}$$

which yields:

$$\frac{\partial \mathbf{M}}{\partial t} = \mathcal{P}_s \mathbf{M} \times (\mathbf{n} \times \mathbf{M}) \tag{5.60}$$

Once integrating over the total thickness t of the ferromagnet, one can express that:

$$\frac{\partial \int_V \mathbf{M}}{\partial t} = \mathbf{M} \times (\mathcal{J}_s \times \mathbf{M}), \tag{5.61}$$

where $\mathcal{J}_s$ is the spin-current injected from the external ferromagnetic source whose magnetization is m_1 involving also the spin-current reflection part. One recovers the standard expression of the Slonczewski-type like torque or antidamping torque (that we denote $T_\parallel$) when $\mathcal{J}_s$ remains strictly parallel to m_1. This part of the spin-current, incident plus reflected, collinear to the ferromagnetic source m_1 should be associated to the antidamping torque proportional to the real part of the spin-mixing conductance $G^R_{\uparrow\downarrow}$. The reflection part of the transverse spin-current, transverse to both m and m_1 gives rise to a field-like torque (that we denote $T_\perp$); this term is proportional to the imaginary part of spin-mixing conductance $G^I_{\uparrow\downarrow}$.

In the case of a very short spin-lifetime $\tau_\perp$ compared to the precession time τ_{exc}, one obtains:

$$\sigma = -\mathcal{P}_s \frac{J_{exc} \tau_\perp}{\hbar} \mathbf{n}, \tag{5.62}$$

giving in the end:

$$\frac{\partial \int_V \mathbf{M}}{\partial t} = \frac{\Delta_{exc} \tau_\perp}{\hbar} (\mathcal{J}_s \times \mathbf{M}), \tag{5.63}$$

which has only a field-like symmetry. This is the so-called field-like torque component transverse to both the magnetization and to the entering spin-current vector. One recovers the general results established by Kalitsov *et al.* for the CB (without any SOI) by the use of the Keldysh formalism [310]. This demonstrates the presence of two intertwined contributions for the STT as derived for symmetric [311, 312] and asymmetric barriers [313] and as evidenced in epitaxial MgO junctions [314, 315]. However, one must be aware that the 'field-like' component maybe non-zero for several other reasons: *i)* an oblique incidence of carrier with a high degree of reflection (case of metals giving rise to a small but non-zero 'field-like' component) or due to *ii)* the SOI or HH-LH mixing terms. Indeed, SOI may introduce an additional precession term in bulk or at interfaces leading to precession and non-conservation of the spin vector. The general effects of SOI requires a reexamination and a generalization of the spin-mixing conductance [319, 320].

Effect of core spin-orbit terms on spin-torque

Moreover, H_{SO} introduces an additional precession term in the bulk or at interfaces (*e. g.* Rashba) which can lead to local spin-memory loss [321] of the longitudinal component (that is parallel to the magnetization)

and to spin-decoherence of its transverse component responsible for spin-transfer. According to this, the *SOI* fields may have the effect, *via* local (interfacial) spin-precession of incoming spin-polarized carriers, to decrease the efficiency of the spin-torque (STT or SOT) reduced from the expected maximum amplitude *e. g.* $\frac{\partial \mathbf{M}t}{\partial t} = \mathcal{J}_s \mathbf{M} \times (\mathbf{n} \times \mathbf{M})$. This total transverse spin-current is generally divided into a spin-torque current in the volume (V) of the ferromagnet and at its interface ($\mathcal{S}$), and expressed like $\int_{V+\mathcal{S}} \frac{J_{exc}}{\hbar} \mathbf{M} \times \langle \sigma \rangle \, dz$, and a spin-current dissipated in the lattice (and then lost) because now $\mathcal{J}_f = \int_{V+\mathcal{S}} \frac{J_{exc}}{\hbar} \mathbf{M} \times \langle \sigma \rangle \, dz$ is no longer fulfilled. The presence of the SOI at surface and in bulk requires a re-examination of the generalized spin-mixing conductance as proposed recently in the case of metallic multilayers [319, 320].

What differs on the core-spin orbit interactions are induced in the Hamiltonian to give:

$$H = H^{(0)} + \lambda_{SO} \boldsymbol{L}.\boldsymbol{S} \tag{5.64}$$

where $H^{(0)}$ is the Hamiltonian free of spin-orbit interaction, but however including the sp-d exchange term; $\lambda_{SO} \boldsymbol{L}.\boldsymbol{S}$ is the core spin-orbit term.

i) Now the precession torque acting on the spin-only can be written as:

$$\frac{\partial \boldsymbol{S}}{\partial t} = \left.\frac{\partial \boldsymbol{S}}{\partial t}\right|_0 + \frac{1}{i\hbar} \lambda_{SO} \left[\boldsymbol{S}, \boldsymbol{L}.\boldsymbol{S}\right] \tag{5.65}$$

$$\frac{\partial \boldsymbol{S}}{\partial t} = \left.\frac{\partial \boldsymbol{S}}{\partial t}\right|_0 + \frac{\lambda_{SO}}{\hbar} \left(\boldsymbol{L} \times \boldsymbol{S}\right) \tag{5.66}$$

where $\left.\frac{\partial \boldsymbol{S}}{\partial t}\right|_0$ means the torque acting on the carriers free of spin-orbit interaction. We can then derive that the torque acting on the local 3d magnetization then writes:

$$\boldsymbol{\Gamma} = \frac{\partial \boldsymbol{M}}{\partial t} = -\frac{\partial \boldsymbol{\mu}}{\partial t} - \frac{\lambda_{SO}}{\hbar} \int_V \langle \boldsymbol{L} \times \boldsymbol{S} \rangle \tag{5.67}$$

$$\boldsymbol{\Gamma} = \boldsymbol{\Gamma}_0 - \frac{\lambda_{SO}}{\hbar} \int_V \langle \boldsymbol{L} \times \boldsymbol{S} \rangle \tag{5.68}$$

where $\boldsymbol{\Gamma}_0$ is the torque previously calculated without spin-orbit and $-\frac{\lambda_{SO}}{\hbar} \int_V \langle \boldsymbol{L} \times \boldsymbol{S} \rangle$ is the torque due to the pure orbital contribution [291].

ii) The alternative would be to calculate the torque acting on the thin ferromagnetic layer from the knowledge of the total angular momentum ($\boldsymbol{J} = \boldsymbol{L} + \boldsymbol{S}$) current given by $\left(\frac{\boldsymbol{jJ}+\boldsymbol{Jj}}{2}\right)$. Writing the exchange term in the form:

$$H_{exc} = -\Delta_{exc} \boldsymbol{S}.\boldsymbol{M} = -\Delta_{exc} \left(\boldsymbol{J} - \boldsymbol{L}\right).\boldsymbol{M} \tag{5.69}$$

this yield in fine (without spin-flip term):

$$\frac{\partial \int_V \boldsymbol{M}}{\partial t} = \boldsymbol{j}_f^{\perp} + \frac{\Delta_{exc}}{\hbar} \int_V \langle \boldsymbol{M} \times \boldsymbol{L} \rangle - \frac{1}{i\hbar} \int_V \left[\boldsymbol{J}, H_{\boldsymbol{k}.\boldsymbol{p}}\right] \tag{5.70}$$

where $\frac{1}{i\hbar} \int_V \left[\boldsymbol{J}, H_{\boldsymbol{k}.\boldsymbol{p}}\right] = \frac{1}{i\hbar} \int_V \left[\boldsymbol{L}, H_{\boldsymbol{k}.\boldsymbol{p}}\right]$ which is non-zero due to the $\boldsymbol{k}.\boldsymbol{p}$ wrapping term represents the torque acting on the lattice and not on the local magnetization.

iii) We come to the important conclusions that the exact determination of the spin-torque acting on a ferromagnetic system involving spin-orbit interactions (spin-orbit, Rashba, Dresselhaus) requires the implementation of a multiband $\boldsymbol{k}.\boldsymbol{p}$ code (14, 30, or 40 bands) allowing to determine the contributions and related angular momentum profiles of :

♣ The spin-current $\boldsymbol{j}_s = \frac{\boldsymbol{j}\sigma + \sigma \boldsymbol{j}}{2}$.

♣ The orbital-current $\boldsymbol{j}_L = \frac{\boldsymbol{jL}+\boldsymbol{Lj}}{2}$.

♣ The angular momentum current $\boldsymbol{j}_J = \frac{\boldsymbol{jJ}+\boldsymbol{Jj}}{2}$.
like made from our multiband $\boldsymbol{k.p}$ platforms.

Calculations of spin torque within 30-band k.p method

In Fig.5.13(a,b), we show the calculation of the angular dependence of the spin transfer torque under normal incidence and under different incident energies performed in a 30 multiband $\boldsymbol{k.p}$ technique. The amplitudes of spin transfer torque are proportional to the tunneling transmissions which are expressed in the figures by the 10^{-6} values in the y-axis. Although developed in a multiband frame generalizing thus the standard $2x2$ spinor approach described by simple Pauli matrix avoiding the orbital moment part, our calculations display an almost sinusoidal shape vs. angle for the two torques in Fig.5.12 omitting however the orbital contribution, as found in Ref.[309]. This simply indicates that the two torques are equal to zero at zero ($\theta = 0$) or π angle which corresponds to the respective parallel and antiparallel configurations of the magnetizations. The calculated component of the spin-current is only nonzero for the z-component corresponding to the direction of the two magnetizations. This is the so-called longitudinal spin-current whose difference between the PA and AP states is associated to the tunneling magnetoresistance effect (TMR).

Note however that, from the respective PA and AP magnetic configurations, the torque increases from zero because associated to a non-collinear magnetic configuration enabling the injection of the transverse spin-current from the local magnetization as discussed in the theory section. The two torques reach a maximum value at $\theta = \pi/2$ where the magnetizations are perpendicular. Besides, the slope at $\theta = 0$ and $\theta = \pi$ have a small difference which means that the critical current switching from PA to AP is different from the critical current switching from AP to PA configuration. This result is a good agreement with the experimental results shown in Fig. 5.10a. Figure 5.13(c,d,e,f) represents the calculations of the angular dependence of the spin-torque profile corresponding to an oblique electronic incidence with $k_y = \pm 0.015$Å and for two different hole energies ($\epsilon = 0$ eV and $\epsilon = -0.1$ eV). The two energies are characteristic of HH and LH bands respectively. The difference in the angular dependence of the torques upon two opposite electronic incidences can be understood as the consequence of the asymmetry in the transmission coefficient displayed in Fig. 5.14. This refers to anomalous Tunnel Hall effect and will be considered in details in the following section.

5.4 Transmission asymmetry and Anomalous Tunnel Hall effect

In this section, we describe the main physical issues of transmission asymmetry (or skew tunneling) and related tunnel anomalous Hall effect (TAHE) [11] in heavy metal/semiconductor heterojunctions or anomalous tunnel Hall effect (ATHE) [12, 57] in ferromagnetic semiconductors/semiconductor interface.

The investigations of anomalous tunnel Hall effect with Ge in Pt/GaAs Schottky barriers has started in 2010 by K. Ando in the group of E. Saitoh [151] demonstrating thus the generation of a sizable transverse spin-current under right or left helicity carrier optical pump. This effect should be associated to a deflection of polarized carriers tunneling through the Schottky barrier into Pt. Since the middle of the 2010, the same kind of experiments are performed in the Polytechnico Milan's group (Prof. F. Ciccacci) using the Pt/Ge group IV semiconductor Schottky barrier [322, 323]. Again, the experimental work consists in pumping spin-polarized carriers in Ge via optically circularly polarized pump, and under oblique incidence, measuring the transverse photovoltage or photocurrent thus generated from their asymmetric tunneling deflection. They recently observed some very large effect, with strong enhancement compared to what is expected from simple Hall effect of Pt, which may be associated to the tunnel asymmetry scattering of carrier (Fig. 5.15).

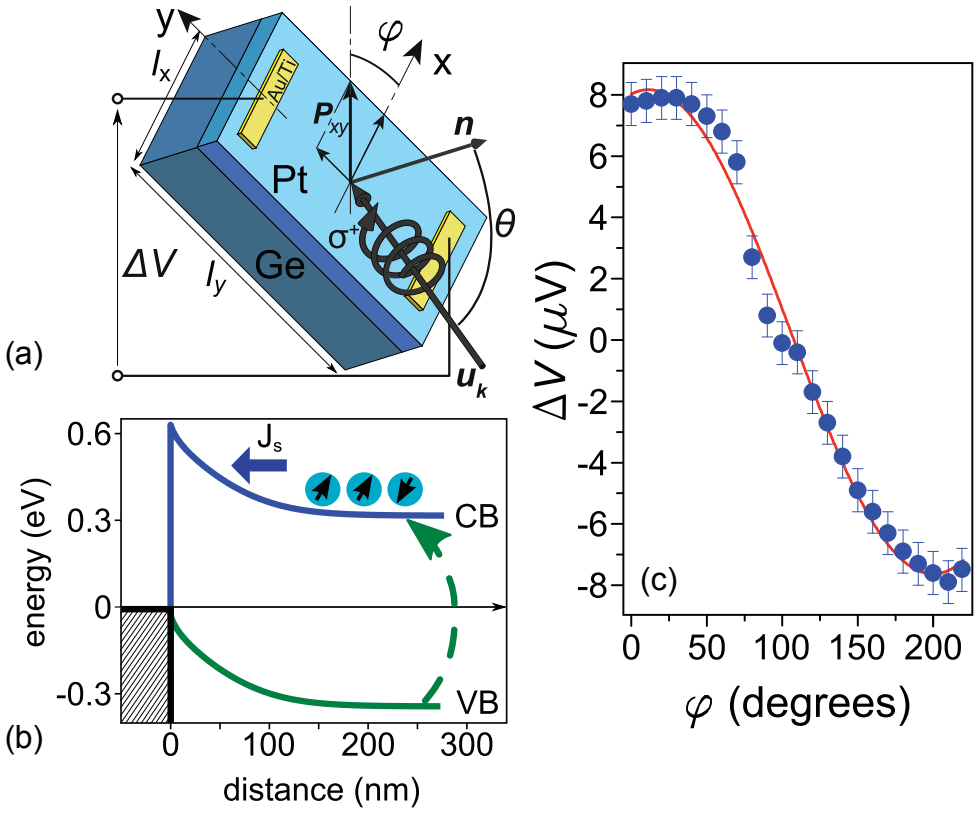

FIGURE 5.15: (a) Sketch of the Pt/Ge junction and experimental geometry: θ is defined as the angle between the direction of the incident photons $\boldsymbol{u_k}$ and the normal to the sample surface $\boldsymbol{n}$, whereas φ is the angle in the xy plane between the projection of $\boldsymbol{u_k}$ in the xy plane and the x axis. (b) Schematic representation of the spin current density J_s, photo induced by optical orientation at the Pt/Ge Schottky junction under illumination. (c) Voltage difference ΔV as a function of φ angle at fixed at $\theta = 65^0$ for the sample with a Pt thickness of $t_{Pt} = 7.2$ nm, taken from Ref. [322].

In order to address the issue in a simple way of the skew tunneling or skew reflection phenomena, we restrict ourselves to the effect of bulk Dresselhaus terms by using the simplest form of the quantum boundary conditions - the standard matching conditions. We will consider the most favorable case of bilayer or tunnel junction which is, a given interface between the two materials, e.g the III-V semiconductor compounds, with the same ferromagnetic contact in the anti parallel (AP) magnetic configuration (Fig.5.17). In such system, the interplay between the spin orbit interaction and exchange interaction results in such giant transport asymmetry of carriers and spin-to-charge conversion at the corresponding interface (Figs. 5.17 and 5.18) corresponding to the anomalous Tunnel Hall effect (ATHE). Presently, the phenomenon of asymmetry scattering of polarized carriers is discussed in systems constituted of ferromagnetic/superconductor junctions in the frame of skew Andreev reflection of Cooper pairs [324].

5.4.1 *Anomalous tunnel Hall effect by matching wavefunctions: Case of the conduction band of semiconductors of T_d symmetry group*

In order to introduce ATHE, we first consider the case of the conduction band of a junction formed by two semiconductors of T_d symmetry group in contact, involving the Dresselhaus and exchange interaction in AP state. The Dresselhaus term is [52, 89], $H_D = (\widehat{\gamma}\chi) \cdot \widehat{\sigma}$,

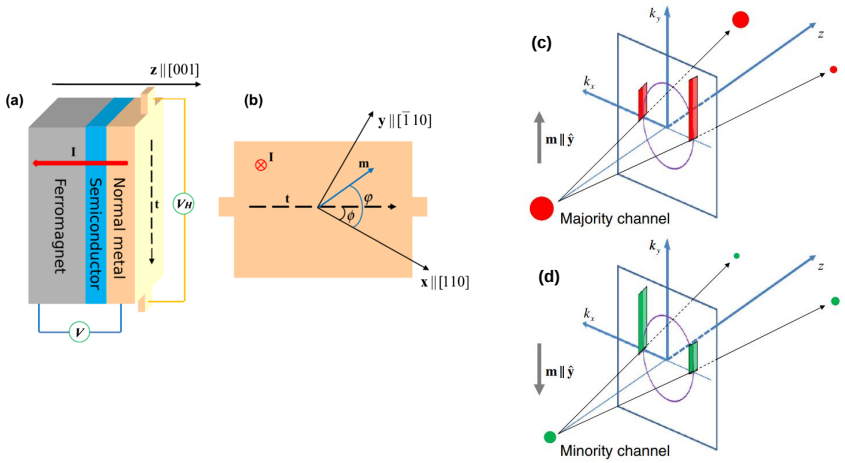

FIGURE 5.16: (a) Schematic of a ferromagnet-semiconductor-normal metal tunnel junction. The tunneling current flowing in the z direction generates the anomalous Hall voltage (V_H) in the nonmagnetic electrode; (b) Side view of (a).Taking the [110] axis as a reference, the magnetization direction ($\boldsymbol{m}$) and the direction along which the Hall voltage is measured ($\boldsymbol{t}$) are determined by the angles ϕ and φ, respectively. Spin-dependent momentum filtering resulting from tunneling through a barrier with Bychkov-Rashba SOC for majority channel (c), and minority channel (d). Taken from Ref. [11].

$$H_D = \begin{pmatrix} -\widetilde{\gamma}\xi^2 k & -i\gamma\xi k^2 \\ i\gamma\xi k^2 & \widetilde{\gamma}\xi^2 k \end{pmatrix} \tag{5.71}$$

We refer the structure to the x, y, z cubic axes (unit vectors $\widehat{x}, \widehat{y}, \widehat{z}$) and assume that electron transport occurs along the z axis, whereas the magnetization lies along x. One then introduces $(0, \xi, k)$ the electron wavevector; $\widehat{\sigma}$ the Pauli operator, and $\chi = \left[0, \xi k^2, -\xi^2 k\right]$ the D'yakonov-Perel' (DP) internal field responsible for the spin splitting [89, 90, 105]. One introduces the tensor $\widehat{\gamma} = \left(\gamma_i \delta_{ij}\right)$ which characterizes the DP-field strength, with $\gamma_x = \gamma_y = \gamma$, $\gamma_z = \widetilde{\gamma}$, and δ_{ij} the Kronecker symbol. We consider the two cases $\widetilde{\gamma} = \gamma$ and $\widetilde{\gamma} = 0$ which switches off the ξ^2 perturbation.

We study the transmission asymmetry when the wavevector component along y is changed from ξ to $-\xi$. Electrons are injected from the first conduction band of material I to the left ($\epsilon = 1$) into the first conduction band of material II to the right ($\epsilon = -1$). Then, the relevant 2×2 Hamiltonians respectively write:

$$\begin{aligned} H_{I,II} &= \gamma_c \left(k^2 + \xi^2\right) \widehat{I} + w\mathbf{m} \cdot \widehat{\sigma} + H_D \\ &= \begin{pmatrix} \gamma_c(k^2 + \xi^2) - \widetilde{\gamma}\xi^2 k & -i\gamma\xi k^2 + \epsilon w \\ i\gamma\xi k^2 + \epsilon w & \gamma_c(k^2 + \xi^2) + \widetilde{\gamma}\xi^2 k \end{pmatrix} \end{aligned} \tag{5.72}$$

where $\widehat{I}$ is the identity matrix, γ_c the conduction effective mass, $\mathbf{m}$ is the unit magnetization, $2w$ the exchange strength.

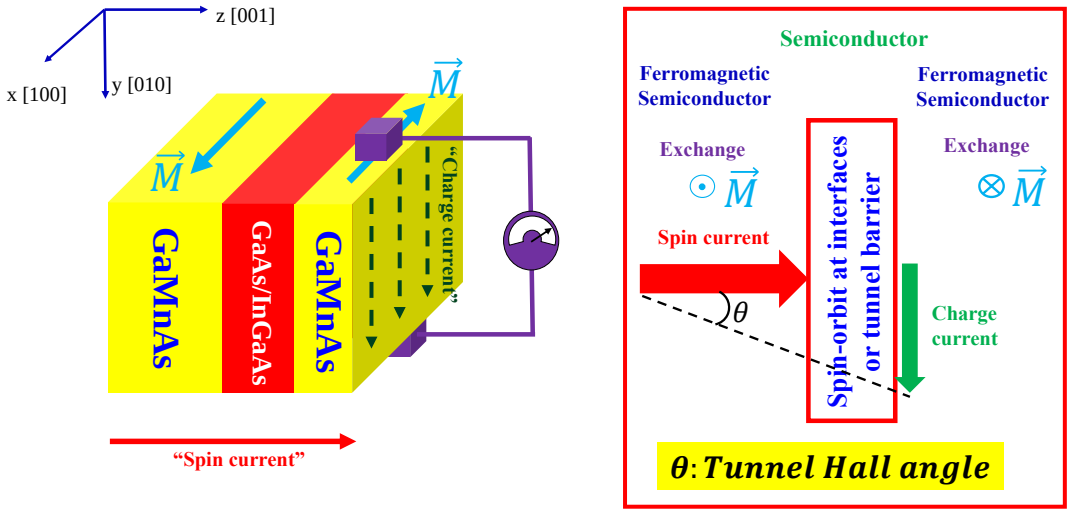

FIGURE 5.17: Scheme of Anomalous Tunnel Hall effect with ferromagnetic semiconductor (Ga,Mn)As junction in anti parallel configuration of magnetization. The spin current is injected along the z direction allowing to obtain the charge current along the y direction if the magnetization direction is along the x axis. The efficiency of ATHE may be described through the tunnel Hall angle θ which is depicted in the right figure.

Transmission from quantum boundary conditions (quantum wavefunction matching)

The two energies in the electrodes are given by $\mathcal{E}_1 = \gamma_c \left(k_1^2 + \xi^2\right) - w$ and $\mathcal{E}_2 = \gamma_c(k_2^2 + \xi^2) + w$, where k_1 (k_2 – pure imaginary–) is the z-component of the wavevector in the lower (upper) subband. The two eigenvectors are:

$$\mathbf{u}_{\epsilon,1}(\xi, k_1) = \left[1 - 2\epsilon i\mu k_1^2, -\epsilon(1 - 2\widetilde{\mu}\xi k_1)\right]/\sqrt{2}, \tag{5.73}$$

$$\mathbf{u}_{\epsilon,2}(\xi, k_2) = \left[1 - 2\epsilon i\mu k_2^2, \epsilon(1 + 2\widetilde{\mu}\xi k_2)\right]/\sqrt{2}, \tag{5.74}$$

where $\mu = \gamma\xi/(2w)$ and $\widetilde{\mu} = \widetilde{\gamma}\xi/(2w)$. Note that the form of the eigenvectors does not foresee any tunneling transmission asymmetry in usual tunneling models [12, 57] based on the density of states [135, 325]. The asymmetry arises from a full-quantum treatment discussed in terms of chirality. Because $k_\parallel$ is conserved, we are dealing with states with the same *longitudinal* kinetic energy E along z and a total kinetic energy $\mathcal{E} = E + \gamma_c\xi^2$. The boundary conditions are the continuity of the wavefunction and of the current wave $\widehat{J}\Psi_{I,II} = (1/\hbar)(\partial\widehat{H}_{I,II}/\partial k)\Psi_{I,II}$ because $\widehat{H}_{I,II}$ contains no more than quadratic k terms [183, 326–329].

The transmission of a pure up-spin incident electron into a pure down-spin state is only possible under oblique incidence *via* SOI which introduces off-diagonal matrix elements. The spin-orbit field is also responsible for a discontinuity of the spin-current between incident (*inc*) and transmitted (*trans.*) waves. Moreover, a non-vanishing diagonal part of SOI is necessary to obtain a non-zero asymmetry although the z component of the DP field along z does not depend on the sign of $k_\parallel$ [12, 57]. Then, from now on, we take $\widetilde{\gamma} = \gamma$. The wavevector k_1 in the lower subband has to be real so that we can define $K = k_1 > 0$. We introduce the parameter $\lambda > 0$ with $k_2 = i\lambda K$, the reduced longitudinal energy $\eta = E/w = \left(1 - \lambda^2\right)/\left(1 + \lambda^2\right)$, and the incidence parameter $t = \xi/K$. One finally obtains the transmission $T(t, \eta)$ and its average $\overline{T}$ upon $\pm\xi$ incidence t and asymmetry $\mathcal{A}$:

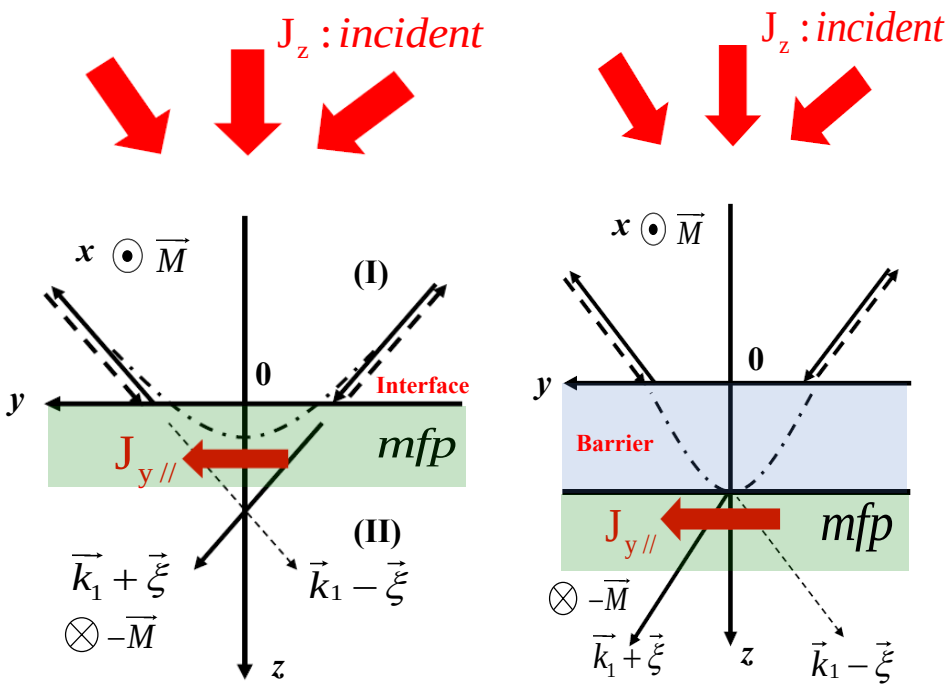

FIGURE 5.18: Scheme of the transmission process at an exchange SOI step (left) and SOI barrier (right) junction with AP magnetization along the x cubic crystal axis. The propagation direction of carriers is along z with propagating wavevector k_I whereas the in-plane incident component $+\xi$ (heavy line) and $-\xi$ (dashed line) is along the y axis; xyz forms a direct frame. The dash-dot curve denotes the evanescent waves, either reflected or transmitted. Carriers with $+\xi$ in-plane wavevector component are more easily transmitted than those with $-\xi$.

$$\overline{T}(|t|,\eta) = \frac{\gamma^2}{\gamma_c^3} w t^2 (1+\eta)^2 \left[4\eta^2(1-\eta) + t^2(1+\eta)(2\eta-1)^2\right], \tag{5.75}$$

$$\mathcal{A}(t,\eta) = \frac{4t\eta\sqrt{1-\eta^2}(2\eta-1)}{4\eta^2(1-\eta) + t^2(1+\eta)(2\eta-1)^2}. \tag{5.76}$$

where $\mathcal{A} = [T(t,\eta) - T(-t,\eta)]/[T(t,\eta) + T(-t,\eta)]$, emphasizing the increase of $T(t,\eta)$ with t and γ. The analytical asymmetry $\mathcal{A}$ is plotted in Fig. 5.19 for several values of t (full lines), where the symbols refer to the 2×2 numerical calculations, showing an excellent agreement. It is a remarkable result that $\mathcal{A}(t,\eta)$ does not depend either on the material parameters or on the sign of γ, thus conferring to $\mathcal{A}$ a universal character. Reversing the magnetization (changing w into $-w$) makes transport occur in the k_2 channel leading to a change of $\mathcal{A}(t,\eta)$ into $-\mathcal{A}(t,\eta)$. Our convention is that $\mathcal{A}$ is positive, at small energy η (or averaged over the energy band) when $(\mathbf{m},\xi,\mathbf{k})$ forms a direct frame and negative otherwise. Another striking feature is that an arbitrarily small perturbation is able to produce a 100% transport asymmetry *i.e.*, a total quenching of the transmission in the CB. Figure 5.20 displays the 2-dimensional map of the electron transmission at a given total energy in the reciprocal space calculated using a 2×2 effective Hamiltonian as well as a full 14×14, 30×30 and 40×40 band $\mathbf{k}\cdot\mathbf{p}$ treatment involving odd-potential coupling terms P' and Δ' [92, 94, 330].

Transverse Surface Currents

The transmitted current summed, $\mathbf{J}[t,\eta] = \mathbf{J}_{\xi}[\Psi_{II}(z)] + \mathbf{J}_{-\xi}[\Psi_{II}(z)]$, originates from incident waves of equal amplitude and opposite $k_{\parallel}$. To the lowest order in γ, we find

$$\mathbf{J}_{y,z}[t,\eta] = \frac{4(\gamma_c w)^{1/2}}{\hbar}(1+\eta)^{1/2} T(t,\eta)[\mathcal{A}(t,\eta)\, t\widehat{y}+\widehat{z}] \tag{5.77}$$

A non-zero $\mathcal{A}$ gives rise to a transverse carrier momentum and then to a tunneling surface current (per unit length) $j_y = J_y.\ell_{mfp}$ (ℓ_{mfp} is the electron mean free path), of the form $\mathbf{J}_C = \mathbf{m}\times\mathbf{J}_{S,z}$ (C for current and S for spin-current), leading to a potentially large $ATHE$. The ratio of the surface transverse to the longitudinal current density, $j_y[t,\eta]/J_z[t,\eta] = t\mathcal{A}(t,\eta)\,\ell_{mfp}$, leads to the $ATHE$ length, or $ATHE$ angles [12, 57], in the spirit of the work dealing with Inverse Edelstein effect (IEE) [331, 332].

5.4.2 Anomalous tunnel Hall effect by Green's function techniques: Case of the CB with perturbation Calculations involving SOI

Using advanced perturbation procedures, one may give a general expression for the change of the transmission amplitude $\delta t^{\sigma\sigma'}$ of a propagating spin-↑ wave from the left transmitted into a propagating spin-↓ wave to the right, after having experienced a SOI potential $V^{\sigma\sigma'}$ (spin-flip) in a confined region of space. The calculation is based on Ref. [56] and we will demonstrate *in fine* that

$$\delta\Psi_{in}^{0\sigma}(z) = \int_0^a G_0^{\sigma\sigma}(z,z')V^{\sigma\sigma'}(z')\Psi_{in}^{0\sigma'}(z')dz', \tag{5.78}$$

and from the expression of G_0, that $t^{\uparrow\downarrow}$ may be written:

$$\delta t^{\sigma\sigma'} = \frac{-im^*}{\hbar^2 k}\int_0^a \Psi_{out}^{0\sigma}(z')V^{\sigma\sigma'}(z')\Psi_{in}^{0\sigma'}(z')dz', \tag{5.79}$$

where (*in*) and (*out*) refer respectively to the unperturbed *incoming* wave at left and *outgoing* wave at right [56]; $G_0^{\sigma\sigma}$ is the (spin-diagonal) Green's function (GF) to consider and that we are searching for. Such perturbative scattering approach has hardly been employed to investigate the role of the evanescent waves in transport like investigated here. The method is particularly suitable for the case of non-degenerate orbital systems but however could be applied, in a future work, to the case of the valence band (VB). We consider the Green's function (GF) G_0 of an Hamiltonian system $H_0 = \left(\frac{\hbar^2}{2}\right)\frac{\partial}{\partial z}\frac{1}{m^*(z)}\frac{\partial}{\partial z} - U(z)$ in a homogeneous potential U_1 for $z<0$, and U_2 for $z>0$ satisfying:

$$(\mathcal{E}-H_0)\,G_0^{\sigma\sigma}(z,z') \quad = \quad \delta(z-z'), \tag{5.80}$$

Green's function without orbital degeneracy

The strategy to find the GF is then *i)* to find two different ground states $\left\{\Psi_L^{0,\uparrow\downarrow},\Psi_R^{0,\uparrow\downarrow}\right\}$ of the homogeneous Schrödinger equation $(\mathcal{E}-H_0)\Psi = 0$ (L for left and R for right whith characteristic wavevector k_I and k_{II}), *ii)* to find the relevant linear combinations of Ψ_L^0 and Ψ_R^0 that make y_1 and y_2 solution of the equation $(\mathcal{E}-H_0)\Psi = 0$ finite at $z=-\infty$ $[y_1(z)]$ and $z=+\infty$ $[y_2(z)]$ depending on the use of the *retarded* or

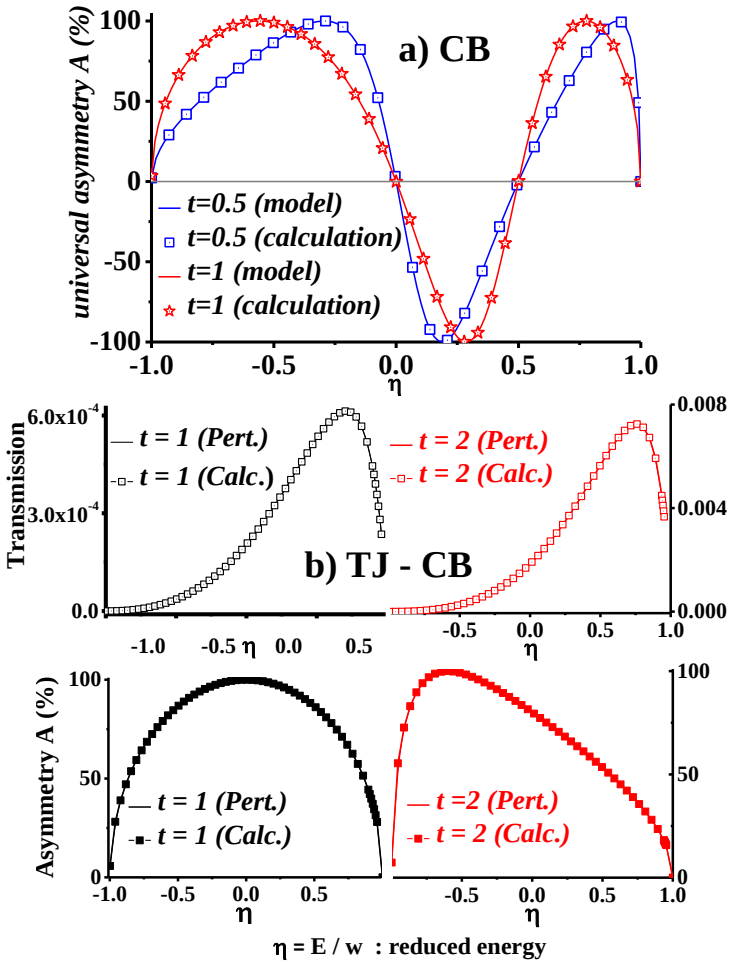

FIGURE 5.19: a) Universal asymmetry coefficient $\mathcal{A} = \frac{T(t,\eta)-T(-t,\eta)}{T(t,\eta)+T(-t,\eta)}$ vs. reduced energy $\eta = E/w$ obtained for an exchange-step with different values of $t = \xi/K$ [t=0.01 (black; circles), t=0.5 (blue; squares), t=1 (red; stars), and t=2 (purple; triangles) by 2-band analytical (full line) and numerical (symbols) calculations. (b) Transmission coefficients and asymmetry coefficient $\mathcal{A}$ vs.reduced energy $\eta = E/w$ obtained for a 3 nm tunnel junction (TJ) with different values of $t = \xi/K$ [t=1 (black),t=2(red), by perturbative scattering (pert.: full lines) method and numerical $\boldsymbol{k.p}$ calculations (Calc.: symbols). Taken from Ref.[57]

advanced quantities, and *iii)* to define the correct GF by making use of:

$$G_0^{\sigma\sigma}(z,z') = \begin{cases} \frac{y_1^\sigma(z)y_2^\sigma(z')}{W(y_1,y_2)} & -\infty < z < z' < +\infty \\ \frac{y_1^\sigma(z')y_2^\sigma(z)}{W(y_1,y_2)} & -\infty < z' < z < +\infty \end{cases}, \tag{5.81}$$

where $W(y_1,y_2) = \frac{\hbar^2}{2m^*}\left[y_1(z')\frac{\partial y_2(z')}{\partial z'} - \frac{\partial y_1(z')}{\partial z'}y_2(z')\right]$ is the Wronskian. The homogeneous Schrödinger equation, $(\mathcal{E} - H_0)\,\Psi = 0$, admits the solutions:

$$\Psi_L^{0,\sigma} = \left(e^{ik_I^\sigma z_<} + r_L^\sigma e^{-ik_I^\sigma z_<} + t_L^\sigma e^{ik_{II}^\sigma z_>}\right)|\sigma\rangle \tag{5.82}$$

$$\Psi_R^{0,\sigma} = \left(e^{-ik_{II}^\sigma z_>} + r_R^\sigma e^{ik_{II}^\sigma z_>} + t_R^\sigma e^{ik_I^\sigma z_<}\right)|\sigma\rangle \tag{5.83}$$

where $z_<$ and $z_>$ stand for $z < 0$ and $z > 0$. If we chose $y_1 = \Psi_R^{0,\sigma}$ and $y_2 = \Psi_L^{0,\sigma}$, Eq. 5.80 admits a particular solution:

$$G_0^{\sigma\sigma}(z,z') = \frac{\Psi_R^{0,\sigma}(z')\Psi_L^{0,\sigma}(z)\Theta(z-z') + \Psi_R^{0,\sigma}(z)\Psi_L^{0,\sigma}(z')\Theta(z'-z)}{W(\Psi_R^0,\Psi_L^0)}, \tag{5.84}$$

On the assumption of a same effective mass, the Wronskian $W = \frac{\hbar^2}{2m^*}\frac{4ik_I^\sigma k_{II}^\sigma}{k_{II}^\sigma + k_I^\sigma}$ is a constant ($\partial W/\partial z' = 0$) and we recover the *retarded* GF introduced in Ref. [253] according to:

$$G_0(z_<,z'_>) = \frac{2m^*}{\hbar^2}\frac{t_L}{2ik_I^\sigma}e^{-ik_I^\sigma z}e^{ik_{II}^\sigma z'}, \tag{5.85}$$

$$G_0(z_>,z'_<) = \frac{2m^*}{\hbar^2}\frac{t_R}{2ik_{II}^\sigma}e^{-ik_I^\sigma z'}e^{ik_{II}^\sigma z}, \tag{5.86}$$

$$G_0(z_<,z'_<) = \frac{2m^*}{\hbar^2}\frac{1}{2ik_1^\sigma}\left[e^{ik_I^\sigma|z-z'|} + r_L^\sigma e^{-ik_I^\sigma(z+z')}\right], \tag{5.87}$$

$$G_0(z_>,z'_>) = \frac{2m^*}{\hbar^2}\frac{1}{2ik_{II}^\sigma}\left[e^{ik_{II}^\sigma|z-z'|} + r_R^\sigma e^{-ik_{II}^\sigma(z+z')}\right] \tag{5.88}$$

that we will use henceforth.

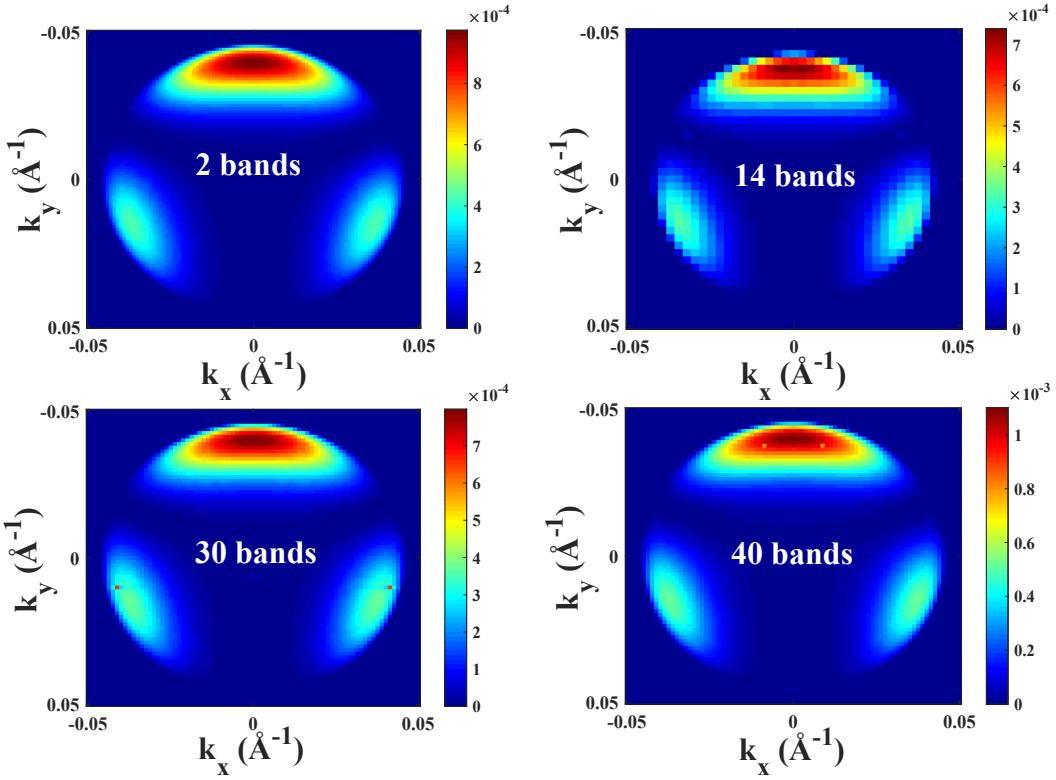

FIGURE 5.20: The transmission coefficient as a function of in-plane wave vector $k_{||} = (k_x, k_y)$ through an exchange-SOI tunnel barrier junction with AP magnetizations. Carriers with plus k_y in-plane wave vector component are more easily transmitted than those carrying minus k_y. These calculations were done for CB within the different $\boldsymbol{k.p}$ framework: 2×2, 14×14, 30×30, and 40×40 band model and a good agreement among them shows that the numerical code is robust. The exchange strength is 0.3 eV and the total kinetic energy $E = 0.23\ eV$, the barrier thickness is 3 nm.

Case of the potential step with exchange interaction in the CB: perturbation treatment

We revisit here the issue and results of section 5.4.1 (exchange-step) with $\hat{H}_0$, eigenvectors and eigenvalues given in section 5.4.1 . We recall that the current is along $\hat{z}$ and magnetizations along $\hat{x}$. The incident wavevector is $\mathbf{k} = (0, \xi, k)$.

Reflection, transmission and perturbative SOI potential

We consider the electron transmission within an energy window in the exchange step, $-w < \mathcal{E} < w$, where the transmission asymmetry takes place, so that $k_I^{\uparrow}$ and $k_{II}^{\downarrow}$ are real whereas $k_I^{\downarrow}$ and and $k_{II}^{\uparrow}$ are pure imaginary quantities. In the right contact, the spin $\uparrow$ state admits a pure propagating character whereas the spin $\downarrow$ state is purely evanescent. It is then quite convenient to define $k_I^{\uparrow} = k_{II}^{\downarrow} = k_1$ and $k_I^{\downarrow} = k_{II}^{\uparrow} = ik_2$. The two solutions of the homogeneous Schrödinger equation, $\Psi_L^{0,\uparrow}$, and $\Psi_R^{0,\downarrow}$ are given by Eq. 5.83 with reflection, $r_{L\uparrow} = r_{R\downarrow} = \frac{k_1 - ik_2}{k_1 + ik_2}$, and transmission, $t_{L\uparrow} = t_{R\downarrow} = \frac{2k_1}{k_1 + ik_2}$ ($t_{R\uparrow} = t_{L\downarrow} = \frac{2k_2}{k_2 - ik_1}$), found via the matching conditions at $z = 0$. This allows possible transmission from propagating to evanescent states ($t_{R\downarrow}$ and $t_{L\uparrow}$) and vice-versa ($t_{L\uparrow}$ and $t_{L\downarrow}$).

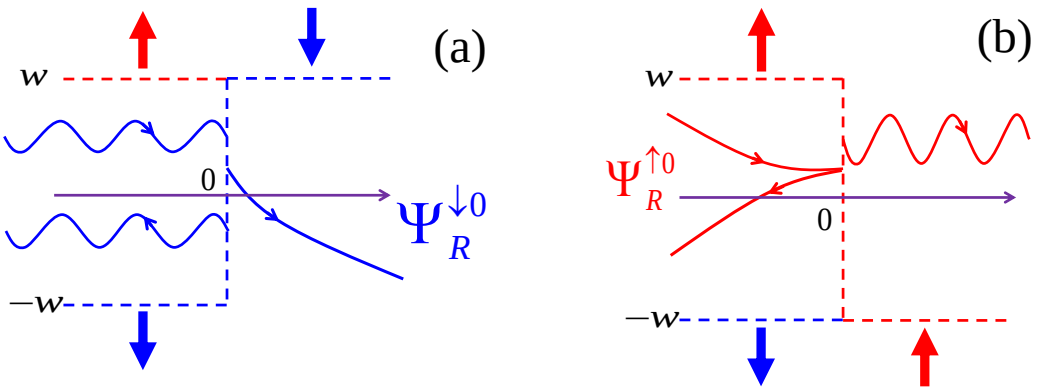

FIGURE 5.21: Scheme of a $\downarrow$-spin electron, $\Psi_R^{\downarrow 0}$ (a) and $\uparrow$-spin electron, $\Psi_R^{\uparrow 0}$ (b), tunneling through an exchange step of height $2w$ from the left to the right side.

The SOI, $H_D^{\sigma\sigma'}$, is then introduced as a perturbation potential according to:

$$\begin{aligned} H_D &= -\left[\frac{\xi^2\sigma_z}{2}\left(\gamma k + k^+\gamma(z)\right) - \frac{\xi\sigma_y}{2}\left(\gamma k^2 + \left(k^+\right)^2\gamma\right)\right] \\ &= \frac{i\xi^2\sigma_z}{2}\left(\gamma\frac{\overrightarrow{\partial}}{\partial z} - \frac{\overleftarrow{\partial}}{\partial z}\gamma\right) - \frac{\xi\sigma_y}{2}\left(\gamma\frac{\overrightarrow{\partial^2}}{\partial z^2} + \frac{\overleftarrow{\partial^2}}{\partial z^2}\gamma\right), \end{aligned} \tag{5.89}$$

with $\gamma = \gamma(z)$. H_D acquires a pure non-diagonal form like:

$$
\begin{aligned}
V^{\uparrow\downarrow} &= \langle\uparrow|H_D|\downarrow\rangle = \left\langle\uparrow\left|\left\{\frac{i\xi^2\sigma_z}{2}\left(\gamma\frac{\overrightarrow{\partial}}{\partial z}-\frac{\overleftarrow{\partial}}{\partial z}\gamma\right)-\frac{\xi\sigma_y}{2}\left(\gamma\frac{\overrightarrow{\partial^2}}{\partial z^2}+\frac{\overleftarrow{\partial^2}}{\partial z^2}\gamma\right)\right\}\right|\downarrow\right\rangle \\
&= \frac{-i\xi^2}{2}\left(\gamma(z)\frac{\overrightarrow{\partial}}{\partial z}-\frac{\overleftarrow{\partial}}{\partial z}\gamma(z)\right)+\frac{i\xi}{2}\left(\gamma(z)\frac{\overrightarrow{\partial^2}}{\partial z^2}+\frac{\overleftarrow{\partial^2}}{\partial z^2}\gamma(z)\right) \\
&= \left(\frac{i\xi^2}{2}\gamma\frac{\overrightarrow{\partial}}{\partial z}-\frac{i\xi}{2}\gamma\frac{\overrightarrow{\partial^2}}{\partial z^2}\right)-\left(\frac{i\xi^2}{2}\frac{\overleftarrow{\partial}}{\partial z}\gamma+\frac{i\xi}{2}\frac{\overleftarrow{\partial^2}}{\partial z^2}\gamma\right),
\end{aligned}
\tag{5.90}
$$

and

$$
V^{\downarrow\uparrow} = \left(\frac{i\xi^2}{2}\gamma\frac{\overrightarrow{\partial}}{\partial z}+\frac{i\xi}{2}\gamma\frac{\overrightarrow{\partial^2}}{\partial z^2}\right)-\left(\frac{i\xi^2}{2}\frac{\overleftarrow{\partial}}{\partial z}\gamma-\frac{i\xi}{2}\frac{\overleftarrow{\partial^2}}{\partial z^2}\gamma\right) \tag{5.91}
$$

From Eq. 5.78 and $W = i\frac{\hbar^2 k_1}{m^*}t_{R\uparrow}$, the correction to the amplitude of transmission is:

$$
\begin{aligned}
\delta t^{\uparrow\downarrow} &= -\frac{m^*}{i\hbar^2 k_1}\int_{-\infty}^{+\infty}\Psi_R^{0\uparrow}(z')\left[-\frac{i\xi^2}{2}\gamma\frac{\partial\Psi_L^{\downarrow 0}(z')}{\partial z}+\frac{i\xi}{2}\gamma\frac{\partial^2\Psi_L^{\downarrow 0}(z')}{\partial z^2}\right] \\
&\quad -\left[\frac{i\xi^2}{2}\gamma\frac{\partial\Psi_R^{0\uparrow}(z')}{\partial z}+\frac{i\xi}{2}\gamma\frac{\partial^2\Psi_R^{0\uparrow}(z')}{\partial z^2}\right]\Psi_L^{\downarrow 0}(z')dz'.
\end{aligned}
\tag{5.92}
$$

We are now going to calculate the properties of the carrier transmission $\mathcal{A}$ for the different SOI configurations: at left, at right, and SOI in both contacts for an incoming left electron.

SOI at left for electrons incoming from left.

We first note that the zeroth-order transmission coefficient, $t_0^{\uparrow\downarrow} = 0$ is zero without spin-mixing interactions. Then, from Eq. 5.92, the transmission amplitude, $t_L^{\uparrow\downarrow}$, with SOI at left is:

$$
\begin{aligned}
\delta t^{\uparrow\downarrow} &= -\frac{m^*}{i\hbar^2 k_1}\int_{-\infty}^{0}\Psi_R^{0\uparrow}(z')\left[-\frac{i\xi^2}{2}\gamma\frac{\partial\Psi_L^{\downarrow 0}(z')}{\partial z}+\frac{i\xi}{2}\gamma\frac{\partial^2\Psi_L^{\downarrow 0}(z')}{\partial z^2}\right] \\
&\quad -\left[\frac{i\xi^2}{2}\gamma\frac{\partial\Psi_R^{0\uparrow}(z')}{\partial z}+\frac{i\xi}{2}\gamma\frac{\partial^2\Psi_R^{0\uparrow}(z')}{\partial z^2}\right]\Psi_L^{\downarrow 0}(z')dz'.
\end{aligned}
\tag{5.93}
$$

By considering $k_1 = K$ (incoming propagating wavevector) and $k_2 = \lambda K$ (imaginary transmitted wavevector), and introducing the respective A_1, and A_2 parameters according to:

$$
A_1 = \int_{-\infty}^{0}\Psi_R^{\uparrow 0}(z')\left[-\frac{i\gamma\xi^2}{2}\frac{\partial\Psi_L^{\downarrow 0}(z')}{\partial z'}+\frac{i\gamma\xi}{2}\frac{\partial^2\Psi_L^{\downarrow 0}(z')}{\partial z'^2}\right]dz', \tag{5.94}
$$

and

$$
A_2 = \int_{-\infty}^{0}\left[\frac{i\gamma\xi^2}{2}\frac{\partial\Psi_R^{0\uparrow}(z')}{\partial z'}+\frac{i\gamma\xi}{2}\frac{\partial^2\Psi_R^{0\uparrow}(z')}{\partial^2 z'}\right]\Psi_L^{\downarrow 0}(z')dz', \tag{5.95}
$$

so that:

$$
\delta t^{\uparrow\downarrow} = \frac{m^*}{i\hbar^2 k_1}(A_1 + A_2). \tag{5.96}
$$

We are now going to calculate A_1, and A_2.

$$
\begin{aligned}
2A_1 &= \int_{-\infty}^{0} \Psi_R^{0\uparrow}(z')\left(-i\xi^2\gamma\frac{\partial}{\partial z}+i\xi\gamma\frac{\partial^2}{\partial z^2}\right)\Psi_L^{\downarrow 0}(z')dz' \qquad (5.97)\\
&= \int_{-\infty}^{0} t_{R\uparrow}e^{k_2 z'}\left\{-i\gamma\xi^2\frac{\partial}{\partial z'}+i\gamma\xi\frac{\partial^2}{\partial z'^2}\right\}\left(e^{ik_1 z'}+r_{L\downarrow}e^{-ik_1 z'}\right)dz'\\
&= \int_{-\infty}^{0} t_{R\uparrow}e^{k_2 z'}\left\{-i\gamma\xi^2\frac{\partial}{\partial z'}\right\}\left(e^{ik_1 z'}+r_{L\downarrow}e^{-ik_1 z'}\right)dz' + \int_{-\infty}^{0} t_{R\uparrow}e^{k_2 z'}\left\{i\gamma\xi\frac{\partial^2}{\partial z'^2}\right\}\left(e^{ik_1 z'}+r_{R\downarrow}e^{-ik_1 z'}\right)dz'\\
&= \int_{-\infty}^{0} t_{R\uparrow}e^{k_2 z'}\left(-i\gamma\xi^2\right)(ik_1)(e^{ik_1 z'}-r_{L\downarrow}e^{-ik_1 z'})dz' + \int_{-\infty}^{0} t_{R\uparrow}e^{k_2 z'}(i\gamma\xi)(-k_1^2)\left(e^{ik_1 z'}+r_{L\downarrow}e^{-ik_1 z'}\right)dz'\\
&= \int_{-\infty}^{0} t_{R\uparrow}\gamma\xi^2 k_1 e^{k_2 z'}(e^{ik_1 z'}-r_{L\downarrow}e^{-ik_1 z'})dz' + \int_{-\infty}^{0} -it_{R\uparrow}\gamma\xi k_1^2 e^{k_2 z'}\left(e^{ik_1 z'}+r_{L\downarrow}e^{-ik_1 z'}\right)dz'
\end{aligned}
$$

If one defines B_1 as:

$$
\begin{aligned}
B_1 &= \int_{-\infty}^{0} t_{R\uparrow}\gamma\xi^2 k_1 e^{k_2 z'}(e^{ik_1 z'}-r_{L\downarrow}e^{-ik_1 z'})dz' = \int_{-\infty}^{0} t_{R\uparrow}\gamma\xi^2 k_1\left(e^{(k_2+ik_1)z'}-r_{L\downarrow}e^{(k_2-ik_1)z'}\right)dz'\\
&= t_{R\uparrow}\gamma\xi^2 k_1\left\{\frac{1}{k_2+ik_1}-\frac{r_{L\downarrow}}{k_2-ik_1}\right\} = \frac{t_{R\uparrow}\gamma\xi^2 k_1}{k_1^2+k_2^2}\left\{(k_2-ik_1)-r_{L\downarrow}(k_2+ik_1)\right\} \qquad (5.98)\\
&= \frac{t_{R\uparrow}\gamma\xi^2 k_1}{k_1^2+k_2^2}\frac{2(k_2^2-k_1^2)}{k_2-ik_1} = \frac{2t_{R\uparrow}\gamma\xi^2 k_1(k_2^2-k_1^2)}{(k_1^2+k_2^2)(k_2-ik_1)}
\end{aligned}
$$

with

$$
\begin{aligned}
&k_2-ik_1-r_{L\downarrow}(k_2+ik_1) = (k_2-ik_1)-\frac{k_1-ik_2}{k_1+ik_2}(k_2+ik_1) = (k_2-ik_1)+\frac{(k_2+ik_1)(k_2+ik_1)}{k_2-ik_1}\\
&= \frac{(k_2-ik_1)^2+(k_2+ik_1)^2}{k_2-ik_1} = \frac{2(k_2^2-k_1^2)}{k_2-ik_1} \qquad (5.99)
\end{aligned}
$$

and

$$
\begin{aligned}
B_2 &= \int_{-\infty}^{0} -it_{R\uparrow}\gamma\xi k_1^2 e^{k_2 z'}\left(e^{ik_1 z'}+r_{L\downarrow}e^{-ik_1 z'}\right)dz' = \int_{-\infty}^{0} -it_{L\uparrow}\gamma\xi k_1^2(e^{(k_2+ik_1)z'}+r_{L\downarrow}e^{(k_2-ik_1)z'})dz'\\
&= -it_{R\uparrow}\gamma\xi k_1^2\left(\frac{1}{k_2+ik_1}+\frac{r_{L\downarrow}}{k_2-ik_1}\right) = \frac{-it_{R\uparrow}\gamma\xi k_1^2}{(k_1^2+k_2^2)}\left\{(k_2-ik_1)+r_{L\downarrow}(k_2+ik_1)\right\} \qquad (5.100)\\
&= \frac{-it_{R\uparrow}\gamma\xi k_1^2}{(k_1^2+k_2^2)}\frac{-4ik_1k_2}{(k_2-ik_1)} = \frac{-4t_{R\uparrow}\gamma\xi k_1^3 k_2}{(k_1^2+k_2^2)(k_2-ik_1)}
\end{aligned}
$$

with

$$
\begin{aligned}
&(k_2-ik_1)+r_{L\downarrow}(k_2+ik_1) = (k_2-ik_1)+\frac{k_1-ik_2}{k_1+ik_2}(k_2+ik_1) = (k_2-ik_1)-\frac{(k_2+ik_1)(k_2+ik_1)}{k_2-ik_1}\\
&= \frac{(k_2-ik_1)^2-(k_2+ik_1)^2}{k_2-ik_1} = \frac{-4ik_1k_2}{k_2-ik_1} \qquad (5.101)
\end{aligned}
$$

$$2A_1 = B_1 + B_2 = \frac{2t_{R\uparrow}\gamma\xi^2 k_1(k_2^2 - k_1^2)}{(k_1^2 + k_2^2)(k_2 - ik_1)} - \frac{4t_{R\uparrow}\gamma\xi k_1^3 k_2}{(k_1^2 + k_2^2)(k_2 - ik_1)} \tag{5.102}$$

Doing the same treatment:

$$\begin{aligned}
2A_2 &= \left\{ \int_{-\infty}^{0} \left(i\xi^2\gamma \frac{\partial \Psi_R^0(z')}{\partial z'} + i\xi\gamma \frac{\partial^2 \Psi_R^0(z')}{\partial z'^2} \right) \Psi_L^0(z') dz' \right\} \\
&= \int_{-\infty}^{0} \left(e^{ik_1 z'} + r_{L\downarrow} e^{-ik_1 z'} \right) \left(i\gamma\xi^2 \frac{\partial}{\partial z'} + i\gamma\xi \frac{\partial^2}{\partial z'^2} \right) t_{R\uparrow} e^{k_2 z'} dz' \\
&= \int_{-\infty}^{0} \left(e^{ik_1 z'} + r_{L\downarrow} e^{-ik_1 z'} \right) \left(i\gamma\xi^2 k_2 + i\gamma\xi k_2^2 \right) t_{R\uparrow} e^{k_2 z'} dz' \\
&= i\gamma\xi k_2 t_{R\uparrow}(\xi + k_2) \int_{-\infty}^{0} (e^{(ik_1 + k_2)z'} + r_{L\downarrow} e^{(k_2 - ik_1)z'}) dz' \\
&= i\gamma\xi k_2 t_{R\uparrow}(\xi + k_2) \left\{ \frac{1}{ik_1 + k_2} + r_{L\downarrow} \frac{1}{k_2 - ik_1} \right\} \\
&= \frac{i\gamma\xi k_2 t_{R\uparrow}}{k_2^2 + k_1^2}(\xi + k_2) \left\{ (k_2 - ik_1) + r_{L\downarrow} ik_1 + k_2 \right\} = \frac{i\gamma\xi k_2 t_{R\uparrow}}{k_2^2 + k_1^2}(\xi + k_2) \frac{-4ik_1 k_2}{k_2 - ik_1} \\
&= \frac{4t_{R\uparrow}\gamma\xi k_1 k_2^2(\xi + k_2)}{\left(k_2^2 + k_1^2\right)(k_2 - ik_1)}
\end{aligned} \tag{5.103}$$

$$\begin{aligned}
\delta t^{\uparrow\downarrow} &= \frac{m^*}{i\hbar^2 k_1}(A_1 + A_2) \\
&= \frac{m^*}{i\hbar^2 k_1} \left[\frac{t_{R\uparrow}\gamma\xi^2 k_1(k_2^2 - k_1^2)}{(k_1^2 + k_2^2)(k_2 - ik_1)} - \frac{2t_{R\uparrow}\gamma\xi k_1^3 k_2}{(k_1^2 + k_2^2)(k_2 - ik_1)} + \frac{2t_{R\uparrow}\gamma\xi k_1 k_2^2(\xi + k_2)}{\left(k_2^2 + k_1^2\right)(k_2 - ik_1)} \right] \\
&= \frac{m^*}{i\hbar^2 k_1} \frac{t_{R\uparrow}\gamma\xi k_1}{(k_1^2 + k_2^2)(k_2 - ik_1)} \left[\xi(k_2^2 - k_1^2) - 2k_1^2 k_2 + 2k_2^2(\xi + k_2) \right] \\
&= \frac{m^*}{i\hbar^2 k_1} \frac{2k_1}{k_1 + ik_2} \frac{\gamma\xi k_1}{(k_1^2 + k_2^2)(k_2 - ik_1)} \left[\xi(3k_2^2 - k_1^2) + 2k_2 \left(k_2^2 - k_1^2 \right) \right] \\
&= \frac{2m^*}{\hbar^2} \frac{\gamma\xi k_1}{(k_1 + ik_2)^2 (k_1^2 + k_2^2)} \left\{ \xi(3k_2^2 - k_1^2) + 2k_2 \left(k_2^2 - k_1^2 \right) \right\}.
\end{aligned} \tag{5.104}$$

With the following notations, $k_1 = K$ (incoming propagating wavevector) and $k_2 = \lambda K$ (imaginary transmitted wavevector), one obtains:

$$\begin{aligned}
\delta t^{\uparrow\downarrow} &= \frac{2m^*}{\hbar^2}\frac{\gamma\xi K}{(K+i\lambda K)^2(K^2+\lambda^2K^2)}\left\{\xi(3\lambda^2K^2-K^2)+2\lambda K\left(\lambda^2K^2-K^2\right)\right\} \\
&= \frac{2m^*}{\hbar^2}\frac{\gamma\xi K}{K^4(1+i\lambda)^2(1+\lambda^2)}K^3\left\{\frac{\xi}{K}(3\lambda^2-1)+2\lambda\left(\lambda^2-1\right)\right\} \\
&= \frac{1}{\gamma_C}\frac{\gamma\xi}{(1+i\lambda)^2(1+\lambda^2)}\left\{\frac{\xi}{K}(3\lambda^2-1)+2\lambda\left(\lambda^2-1\right)\right\} \\
&= \frac{1}{\gamma_C K^2(1+\lambda^2)}\frac{\gamma\xi K^2}{(1+i\lambda)^2}\left\{\frac{\xi}{K}(3\lambda^2-1)+2\lambda\left(\lambda^2-1\right)\right\} \\
&= \frac{1}{2w}\frac{\gamma\xi K^2}{(1+i\lambda)^2}\left\{\frac{\xi}{K}(3\lambda^2-1)+2\lambda\left(\lambda^2-1\right)\right\}. \qquad (5.105)
\end{aligned}$$

One finally obtains:

$$t_L^{\uparrow\downarrow} = -\frac{1}{2w}\frac{\gamma\xi K^2}{(1+i\lambda)^2}\left\{\frac{\xi}{K}(3\lambda^2-1)+2\lambda\left(\lambda^2-1\right)\right\} \qquad (5.106)$$

SOI at right for electrons incoming from left.

The transmission changes from the previous case by changing the integral from $\int_{-\infty}^{0}$ into $\int_{0}^{+\infty}$ giving $t_R^{\uparrow\downarrow} = t_L^{\uparrow\downarrow}$. Indeed, let us introduce the notations A_{R1}, and A_{R2}.

$$\begin{aligned}
A_{R1} &= \int_0^{+\infty}\left(e^{-ik_1z'_>}+r_{R\uparrow}e^{ik_1z'_>}\right)\left\{-i\gamma\xi^2\frac{\partial}{\partial z'}+i\gamma\xi\frac{\partial^2}{\partial z'^2}\right\}t_{L\downarrow}e^{-k_2z'_>}dz' \\
&= \int_0^{+\infty}\left(e^{-ik_1z'_>}+r_{R\uparrow}e^{ik_1z'_>}\right)(i\gamma\xi)(\xi k_2+k_2^2)t_{L\downarrow}e^{-k_2z'_>}dz' \\
&= i\gamma\xi k_2(\xi+k_2)t_{L\downarrow}\int_0^{+\infty}(e^{-(ik_1+k_2)z'}+r_{R\uparrow}e^{(ik_1-k_2)z'})dz' \\
&= -i\gamma\xi k_2(\xi+k_2)t_{L\downarrow}\int_0^{-\infty}(e^{(ik_1+k_2)z'}+r_{R\uparrow}e^{(k_2-ik_1)z'})dz' \\
&= i\gamma\xi k_2(\xi+k_2)t_{L\downarrow}\int_{-\infty}^{0}(e^{(ik_1+k_2)z}+r_{R\uparrow}e^{(k_2-ik_1)z})dz' \\
&= i\gamma\xi k_2(\xi+k_2)t_{L\downarrow}\left\{\frac{1}{(ik_1+k_2)}+r_{R\uparrow}\frac{1}{(k_2-ik_1)}\right\} \\
&= \frac{i\gamma\xi k_2(\xi+k_2)t_{L\downarrow}}{(k_1^2+k_2^2)}\left\{(k_2-ik_1)+r_{R\uparrow}(ik_1+k_2)\right\} = \frac{i\gamma\xi k_2(\xi+k_2)t_{L\downarrow}}{(k_1^2+k_2^2)}\frac{-4ik_1k_2}{k_2-ik_1} \\
&= \frac{4\gamma\xi k_1k_2^2(\xi+k_2)t_{L\downarrow}}{(k_1^2+k_2^2)(k_2-ik_1)} \qquad (5.107)
\end{aligned}$$

where

$$k_2-ik_1)+r_{R\uparrow}(ik_1+k_2) = (k_2-ik_1)+\frac{k_1-ik_2}{k_1+ik_2}(ik_1+k_2) = \frac{-4ik_1k_2}{k_2-ik_1} \qquad (5.108)$$

$$
\begin{aligned}
A_{R2} &= \int_0^{+\infty} \left\{ i\gamma\xi^2 \frac{\partial\left(e^{-ik_1z'} + r_{R\uparrow}e^{ik_1z'}\right)}{\partial z'} + i\gamma\xi \frac{\partial^2\left(e^{-ik_1z'} + r_{R\uparrow}e^{ik_1z'}\right)}{\partial z'^2} \right\} t_{L\downarrow}e^{-k_2z'}dz' \\
&= \int_0^{+\infty} t_{L\downarrow}e^{-k_2z'}(i\gamma\xi^2)\left(-ik_1e^{-ik_1z'} + ik_1r_{R\uparrow}e^{ik_1z'}\right)dz' - \int_0^{+\infty} t_{L\downarrow}e^{-k_2z}(i\gamma\xi k_1^2)\left(e^{-ik_1z_>} + r_{R\uparrow}e^{ik_1z_>}\right)dz' \\
&= \int_0^{+\infty} t_{L\downarrow}\gamma\xi^2k_1(e^{-(ik_1+k_2)z'} - r_{R\uparrow}e^{-(k_2-ik_1)z'})dz' - \int_0^{+\infty} t_{L\downarrow}(i\gamma\xi k_1^2)\left(e^{-(ik_1+k_2)z'} + r_{R\uparrow}e^{-(k_2-ik_1)z'}\right)dz' \\
&= \frac{2t_{L\downarrow}\gamma\xi^2k_1(k_2^2-k_1^2)}{(k_1^2+k_2^2)(k_2-ik_1)} - \frac{4t_{L\downarrow}\gamma\xi k_1^3k_2}{(k_1^2+k_2^2)(k_2-ik_1)}
\end{aligned}
\tag{5.109}
$$

Therefore,

$$
\tau_R^{\uparrow\downarrow} = \frac{m^*}{i\hbar^2k_1}\left[\frac{A_{R1}+A_{R2}}{2}\right] = \frac{m^*}{i\hbar^2k_1}\left[\frac{2\gamma\xi k_1k_2^2(\xi+k_2)t_{L\downarrow}}{(k_1^2+k_2^2)(k_2-ik_1)} + \frac{t_{L\downarrow}\gamma\xi^2k_1(k_2^2-k_1^2)}{(k_1^2+k_2^2)(k_2-ik_1)} - \frac{2t_{L\downarrow}\gamma\xi k_1^3k_2}{(k_1^2+k_2^2)(k_2-ik_1)}\right]. \tag{5.110}
$$

Because $t_{L\downarrow} = t_{R\uparrow}$, one can observe that $\tau_R^{\uparrow\downarrow} = \tau_L^{\uparrow\downarrow}$

SOI at left and right side for electrons incoming from left.

With SOI in the whole space (left and right), we find from Eq. [5.92] the transmission amplitude $t^{\uparrow\downarrow}$:

$$
t^{\uparrow\downarrow} = -\left(\frac{\gamma\xi K^2}{w}\right)\frac{\frac{\xi}{K}(3\lambda^2-1) + 2\lambda\left(\lambda^2-1\right)}{(1+i\lambda)^2} \tag{5.111}
$$

From $T(t,\eta) = |t^{\uparrow\downarrow}|^2$, we recover transmission $T(t,\eta)$ and asymmetry $\mathcal{A}$ derived from the application of the pure matching conditions (Eqs. 5.76). This proves the power of this perturbation methodology involving mixed propagating and evanescent electronic states.

Case of a tunnel junction in the CB: perturbation calculations

We focus now on the case of a tunnel junction, of thickness a, made of two ferromagnetic contacts (in the AP state) and separated by a thin semiconductor belonging to the T_d -symmetry. The contacts are free of SOI. The incident energy in the CB lies in the range of the exchange step, $-w < \mathcal{E} < w$, with a single incident propagating wave of a pure spin $\uparrow$ character. However, the electrons may scatter, now, at the two different interfaces of the junction and this makes the problem generally different from the previous treatment. One then considers a particular value for the barrier height equal to the exchange potential, $V_0 = |w|$, so as to prevent any back and forth scattering. The calculation of the most general shape of the GF is given in Ref. [257]. To the first order of perturbation, the transmission, $\delta t^{\downarrow\uparrow}$, now equals:

$$
\begin{aligned}
\delta t^{\uparrow\downarrow} &= \frac{m^*}{i\hbar^2k_1}\int_0^a \Psi_L^{0\uparrow}(z')\left[-\frac{i\gamma\xi^2}{2}\frac{\partial\Psi_R^{\downarrow 0}(z')}{\partial z} + \frac{i\gamma\xi}{2}\frac{\partial^2\Psi_R^{\downarrow 0}(z')}{\partial z^2}\right]dz' \\
&\quad - \frac{m^*}{i\hbar^2k_1}\int_0^a \left[\frac{i\gamma\xi^2}{2}\frac{\partial\Psi_L^{0\uparrow}(z')}{\partial z} + \frac{i\gamma\xi}{2}\frac{\partial^2\Psi_L^{0\uparrow}(z')}{\partial z^2}\right]\Psi_R^{\downarrow 0}(z')dz',
\end{aligned}
\tag{5.112}
$$

The coefficient of the wave functions $\Psi_R^{0\downarrow}$, and $\Psi_L^{0\uparrow}$, without SOI, are found from the relevant matching condition in a similar way to the case of the exchange step to give:

$$\Psi_L^{0\uparrow} = t_{L\uparrow} e^{-k_2 z} = \frac{2k_1}{k_1 + ik_2} e^{-k_2 z}, \text{ for } z > 0$$
$$\Psi_R^{0\downarrow} = t_{L\uparrow} e^{k_2(z-a)} = \frac{2k_1}{k_1 + ik_2} e^{k_2(z-a)}, \text{ for } z < a \tag{5.113}$$

Considering the first term in Eq. 5.112

$$\begin{aligned} 2A_1 &= \int_0^a \Psi_L^{\uparrow 0}(z') \left(-i\xi^2\gamma \frac{\partial}{\partial z'} + i\xi\gamma \frac{\partial^2}{\partial z'^2} \right) \Psi_R^{\downarrow 0}(z') dz' = \int_0^a t_{L\uparrow} e^{k_2(z'-a)} \left\{ -i\gamma\xi^2 \frac{\partial}{\partial z'} + i\gamma\xi \frac{\partial^2}{\partial z'^2} \right\} t_{R\downarrow} e^{-k_2 z} dz' \\ &= \int_0^a t_{L\uparrow} e^{k_2(z'-a)} \left\{ i\gamma\xi^2 k_2 + i\gamma\xi k_2^2 \right\} t_{R\downarrow} e^{-k_2 z} dz' = \int_0^a e^{-k_2 a} t_{L\uparrow} t_{R\downarrow} i\gamma\xi k_2 (\xi + k_2) dz' \\ &= e^{-k_2 a} t_{L\uparrow} t_{R\downarrow} i\gamma\xi k_2 (\xi + k_2) a \end{aligned} \tag{5.114}$$

and the second term

$$\begin{aligned} 2A_2 &= \int_0^a \left(i\xi^2\gamma \frac{\partial \Psi_L^{\uparrow 0}(z')}{\partial z'} + i\xi\gamma \frac{\partial^2 \Psi_L^{\downarrow 0}(z')}{\partial z'^2} \right) \Psi_R^{\downarrow 0}(z') dz' = \int_0^a t_{R\downarrow} e^{-k_2 z'} \left\{ i\gamma\xi^2 \frac{\partial}{\partial z'} + i\gamma\xi \frac{\partial^2}{\partial z'^2} \right\} t_{L\uparrow} e^{k_2(z'-a)} dz' \\ &= \int_0^a t_{R\downarrow} e^{-k_2(z'+a)} \left\{ i\gamma\xi^2 k_2 + i\gamma\xi k_2^2 \right\} t_{L\uparrow} e^{k_2 z} dz' = e^{-k_2 a} t_{L\uparrow} t_{R\downarrow} i\gamma\xi k_2 (\xi + k_2) a \end{aligned} \tag{5.115}$$

One obtains:

$$\begin{aligned} \delta t^{\uparrow\downarrow} &= \frac{m^*}{i\hbar^2 k_1} (A_1 + A_2) = e^{-k_2 a} \frac{m^*}{i\hbar^2 k_1} \left(t_{L\uparrow} t_{R\downarrow} \right) i\gamma\xi k_2 (\xi + k_2) a \\ &= e^{-k_2 a} \frac{m^*}{i\hbar^2 k_1} \left[\frac{2k_1}{k_1 + ik_2} \frac{2k_1}{k_1 + ik_2} \right] i\gamma\xi k_2 (\xi + k_2) a = e^{-k_2 a} \frac{2m^*}{\hbar^2} \frac{2k_1 \gamma\xi k_2 (\xi + k_2) a}{(k_1 + ik_2)^2} \\ &= \frac{e^{-k_2 a}}{\gamma_c} \frac{2\gamma\xi k_2 k_1 a}{(k_1 + ik_2)^2} (\xi + k_2) \end{aligned} \tag{5.116}$$

giving out the transmission coefficient we are searching for:

$$\delta t^{\uparrow\downarrow} = \frac{e^{-k_2 a}}{\gamma_c} \frac{2\gamma\xi k_2 k_1 a}{(k_1 + ik_2)^2} (\xi + k_2). \tag{5.117}$$

where we remind that a is the barrier thickness.

Without SOI perturbation, the transmission coefficient is also zero in the situation of pure spin states, and consequently, $T^{\uparrow\downarrow} = \left| \delta t^{\uparrow\downarrow} \right|^2$. If one defines again the incidence parameter $t = \tan\theta = \xi/K$ for and $\eta = \frac{1-\lambda^2}{1+\lambda^2} = \frac{\mathcal{E}}{w}$ the reduced incident kinetic energy, we find the asymmetry of transmission for the tunnel barrier to be like:

$$\mathcal{A} = \frac{|\xi + k_2|^2 - |-\xi + k_2|^2}{|\xi - k_2|^2 + |-\xi - k_2|^2} = 2\frac{\sqrt{(1-\eta)(1+\eta)}t}{t^2(1+\eta) + (1-\eta)}. \tag{5.118}$$

One obtains a perfect agreement between the perturbative scattering method and our multiband calculations for $|t^{\uparrow\downarrow}|^2$ and $\mathcal{A}$ (Fig. 5.19b). The transmission coefficient for an incoming propagating spin-$\uparrow$ electron into an outgoing propagating spin-$\downarrow$ electron is non-zero after SOI is branched on. The transmission *vs.* incident kinetic energy and incident angle is different from the case of a simple exchange-step. The maximum

of transmission depends also on the incidence angle or t parameter. The $\mathbf{k}\cdot\mathbf{p}$ theory gives a maximum of asymmetry when the evanescent wavevector equals in magnitude the parallel incoming wavevectors in the CB.

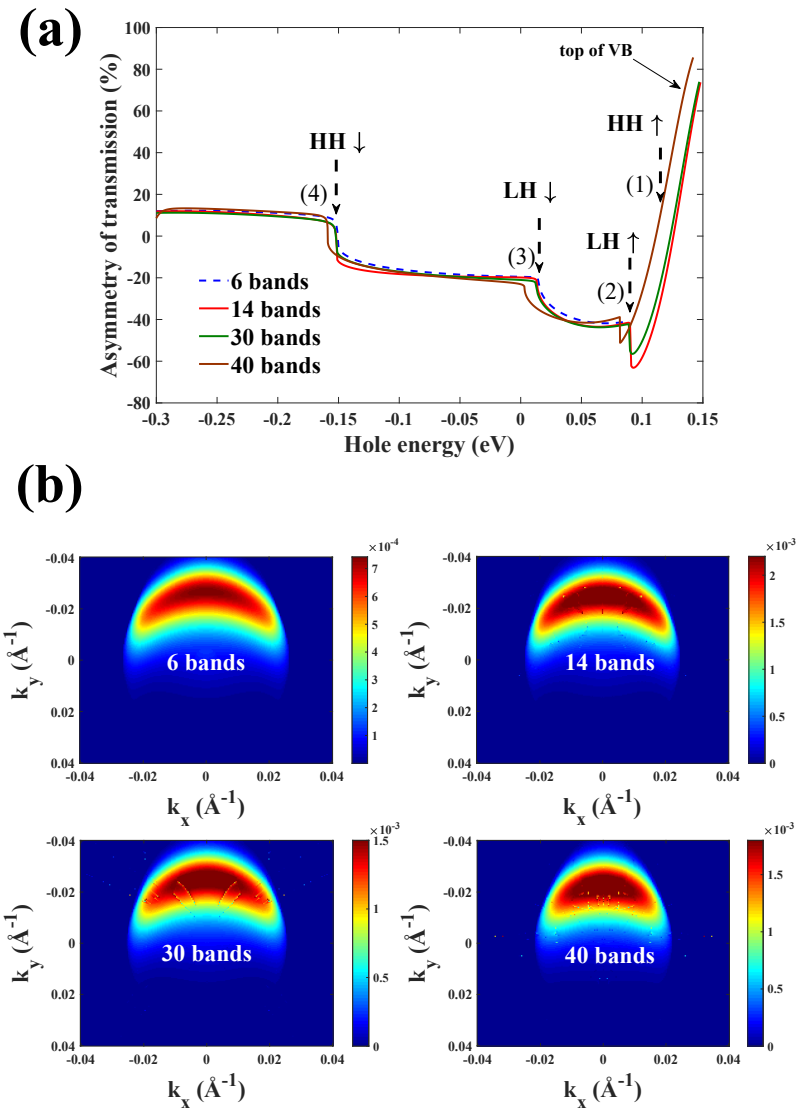

FIGURE 5.22: (a) Asymmetry coefficient $\mathcal{A}$ vs. reduced energy calculated in the VB of (Ga,Mn)As/GaAs/(Ga,Mn)As 3 nm thick tunnel junction with AP magnetizations for $k = 0.05\ nm^{-1}$ and (b) the transmission coefficient as function of in-plane wave vector $k_{||} = (k_x, k_y)$. Carriers with plus k_y in-plane wavevector component are more easily transmitted than those carrying minus k_y. These calculations were done for VB within the different ***k.p*** framework: 6–, 14–, 30–, and 40– band model and a good agreement among them showing that the numerical code is robust. The exchange strength is 0.3 eV and the total kinetic energy $E = 0.23eV$, the barrier thickness being 3 nm.

5.4.3 *Anomalous tunnel Hall effect with valence bands: Case of intrinsic Core SOI in the VB and spin-chirality*

We now turn to the case of the VB of a tunnel junction composed of two p-type ferromagnets separated by a thin tunnel barrier (3 nm in the present case). The barrier height have been chosen so as to match with the exchange strength (0.3 eV). The structure is free of any odd-potential k-terms ($\widehat{H}_D = 0$) and only includes

core SOI (p-orbitals). Results are displayed in Fig. 5.22b for the transmission maps and Fig. 5.22a for the corresponding asymmetry resulting from a multiband $\boldsymbol{k.p}$ treatment.

In the 2D-map calculation procedures obtained for a hole kinetic energy of $\epsilon = 0.23$ eV, we have checked (Fig. 5.22b) that the whole numerical approaches (6, 14, 30 and 40-bands models) provide about exactly similar data. The transmission scales within the range $7-25\times10^{-4}$ with $P^{'}=0$ and $\Delta^{'}=0$. Those results demonstrate that the absence of inversion symmetry (T_d) is not mandatory to observe an asymmetry $\mathcal{A}$ in valence band (we have checked the existence of asymmetry with the silicon barrier structure which is a structure with inversion symmetry). Figure 5.22a displays the asymmetry $\mathcal{A}$ *vs.* hole energy $\mathcal{E}$ for $k_{\|}=0.05$ nm^{-1}. The energy range covers the spin-$\uparrow,\downarrow$ heavy (HH) and light (LH)-hole subbands whereas the respective spin $\uparrow$ and $\downarrow$ split-off bands are not represented here. We refer to points (1) to (4) marked by vertical arrows in the following discussion. Here, the energy of the $HH\uparrow$ ($HH\downarrow$) corresponds to 0.15 eV [−0.15 eV] as indicated by point (1) [(4)], the energy zero being taken at the top of the VB of the non-magnetic material. Correspondingly, one observes a large negative transmission asymmetry (−60%) in this energy range for predominant majority spin $\uparrow$ injection as far as $HH\downarrow$ does not contribute to the current. At more negative energy [$\mathcal{E}<-0.15$ eV: point (4)], a sign change of $\mathcal{A}$ occurs at the onset of $HH\downarrow$ to reach about +20%. From Ref. [12, 57] $\mathcal{A}$ changes sign two times at characteristic energy points corresponding to a sign change of the injected particle spin. Also, we have performed similar calculations for a simple contact [12, 57]. Remarkably, $\mathcal{A}$, although smaller, keeps the same trends as for the tunnel junction, except for a change of sign. Without tunnel junctions, $\mathcal{A}$ abruptly disappears as soon as $SO\downarrow$ contributes to tunneling *i.e.*, when evanescent states disappear. In the case of tunnel junction, $\mathcal{A}$, although small, subsists in this energy range and this should be related to the evanescent character of the wavefunction in the barrier.

5.4.4 *A short report about ATHE for electron in CB: A multiband k.p treatments.*

In the previous sections, we have used the effective Hamiltonian involving the bulk inversion asymmetry, or Dresselhaus term, to study the transmission asymmetry of an electron in conduction band tunnels through exchange step junction with antiparallel configuration. We then got a result that if we discard the out of plane term in the 2x2 Dresselhaus Hamiltonian, there is no asymmetry in CB.

On the other word, the odd-potential k-terms are needed to obtain the transmission asymmetry for CB (within 2x2 effective Hamiltonian), in contrast to the effect in VB. This result surprised us a lot at the beginning since from the physical point of view, the point group symmetry of the studied structure is D_{2d} where the irreducible representations relevant for the conduction and valence band states are the same. Therefore, it is reasonable to expect the similar form of the spin-orbit interaction and, hence, spin-orbit interaction induced anomalous tunnel Hall effect. Recently, the difference between the effect in the conduction and valence bands has been elucidated completely and will be published soon by our group in the collaboration with Ioffe Institute, Politekhnicheskaya 26 194021 St.Petersburg. We now present here our short conclusions about it.

First of all, one has to emphasize that all analytical calculations we have done with effective Hamiltonian for CB are mathematically correct, but however, in framework of effective Hamiltonian for CB, there is no contribution of s-p hybridization in CB that make it different from effective Hamiltonian for VB. This means that if one takes into account the s-p hybridization in CB (by using multiband like 30 bands Hamiltonian) then the transmission asymmetry effect for electron in CB would have the same features as in VB, on the other word, the transmission asymmetry should exist in CB even when the Dresselhaus terms are discarded. Figure 5.23 displays the numerical calculations of transmission coefficient for plus and minus in-plane wave vector $k_{||}$ and transmission asymmetry for an electron in CB tunnels through exchange step junction with antiparallel configuration of magnetization. Figs 5.23b is the calculation using effective Hamiltonian (without s-p hybridization) and without Dresselhaus term ($\gamma_D=0$) showing a zero asymmetry

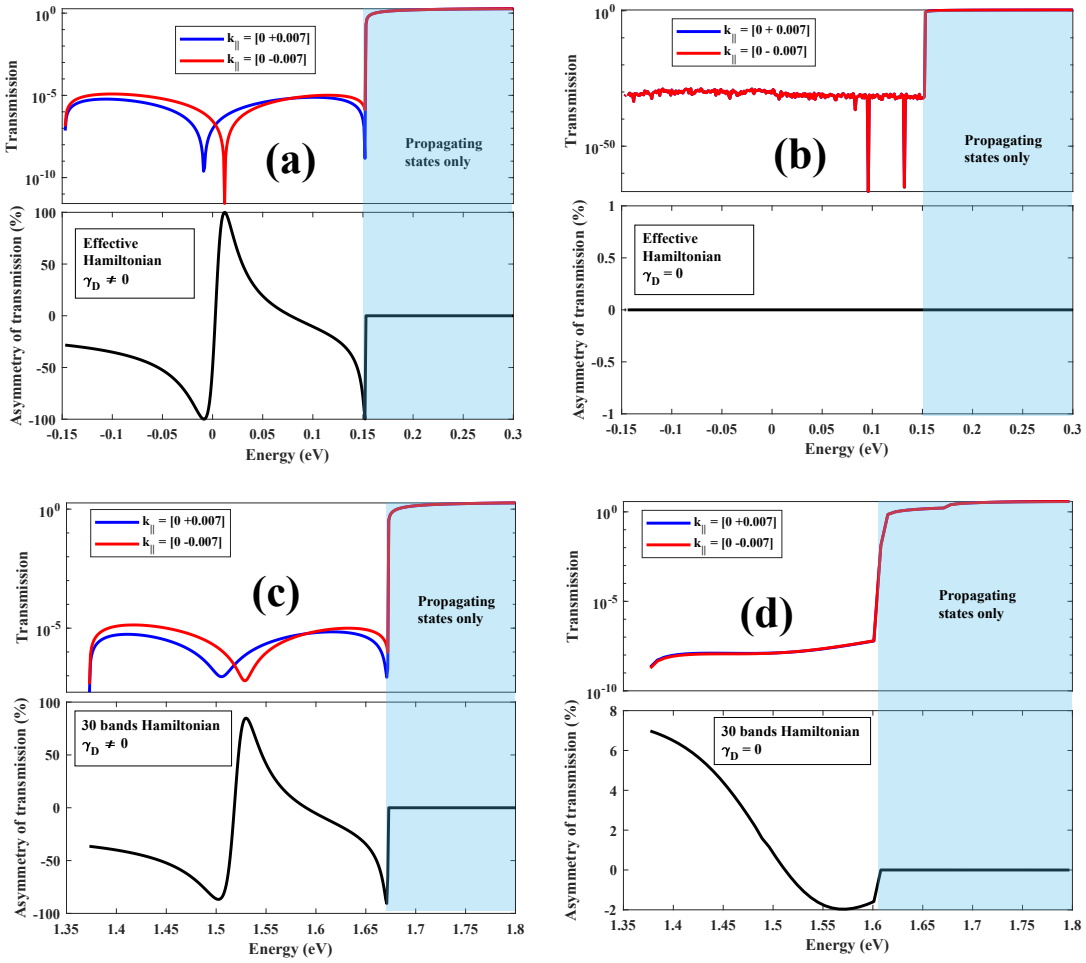

FIGURE 5.23: The transmission coefficient for plus and minus inplane wave vector $k_{||}$ and transmission asymmetry for an electron in CB tunnels through exchange step junction with antiparallel configuration of magnetization. Figs (a, b) are calculations using effective Hamiltonian (without s-p hybridization) with and without Dresselhaus term $\gamma_D \neq 0$ ($\gamma_D = 0$). (c, d) are calculations using 30 bands Hamiltonian (taking into account s-p hybridization) with and without Dresselhaus term $\gamma_D \neq 0$ ($\gamma_D = 0$).

in transmission that is the same treatment as presented in previous sections with analytical calculations. But, however, in contrast with effective Hamiltonian, the 30 bands Hamiltonian shows a non-zero asymmetry even when we discarded Dresselhaus term responsible for the absence of inversion symmetry in the bulk III-V semiconductor. When the absence of inversion symmetry in III-V semiconductor is taken into account, the asymmetry calculations of both effective Hamiltonian and 30 bands Hamiltonian return a same feature of very large asymmetry as discussed previously.

Finally, a short conclusion for this section is that one has to take into account both Dresselhaus terms and s-p hybridization in CB in order to recover the similar form of the spin-orbit interaction and, hence, spin-orbit interaction induced anomalous tunnel Hall effect between CB and VB. That makes the multiband **k.p** method developed in this manuscript become more important to consider the real ATHE effect in both CB and VB of III-V semiconductor based heterostructure.

5.4.5 *Device application of ATHE: Resonant structures*

One observed from previous calculations that in the both two cases of the exchange step or the barrier structure, the universal asymmetry $\mathcal{A}$ is large but, however, the transmission is rather small. Therefore,

in order to obtain both large universal asymmetry and transmission coefficient, one may construct more complicated structures involving resonant tunneling to increase the transmission up to a fraction of unity while keeping extremely high asymmetries. Such structures would be suitable for device application of ATHE in the future.

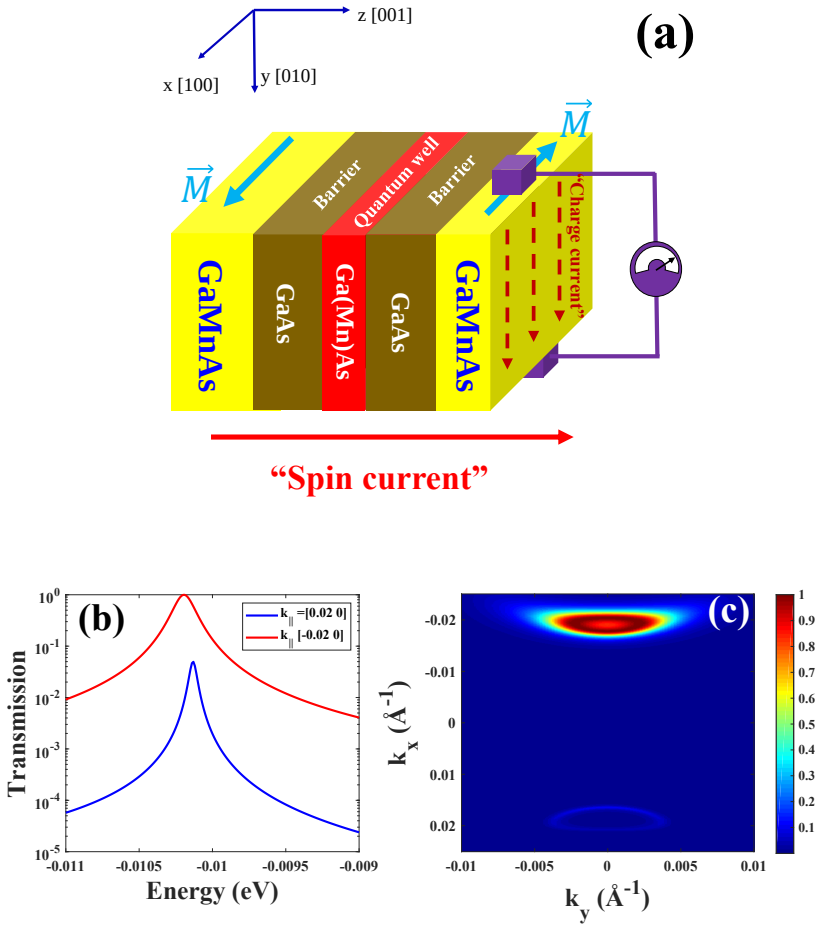

FIGURE 5.24: (a) Schematic of Anomalous Tunnel Hall effect in a GaAs quantum well with 2 nm barrier thickness and 10nm quantum well width, 0.5 eV barrier height and ↑↑↓ magnetization configuration; (b): transmission as function of energy for anti-parallel configuration with opposite incident wave vectors $k_{||}$ around the second peak of quantum well dispersion, and (c) two dimensional map of transmission vs. $k_{||}$ calculated for hole's energy which corresponds to the energy position of the peak in (b).

As an example, in Fig. 5.24, we depict the structure consisting of a magnetic quantum well sandwiched between two magnetic electrodes and separated by non-magnetic barriers of different thicknesses. The magnetization of each layer can be reversed independently. There are 4 possible different magnetization configurations: ↑↑↑, ↑↓↑, ↑↑↓ and ↑↓↓. This constitutes a paradigm for a 4-state memory. In Fig. 5.24b the transmissions as the function of energy for opposite parallel wavevector components $k_{||} = \pm 0.02$ are plotted around the second peak for ↑↑↓ magnetization configuration. One observes that the peak transmission reaches a values close to unity for the $k_{||} = -0.02$Å whereas for the $k_{||} = 0.02$Å the peak transmission is very small. It makes the asymmetry to become very high, almost 100% which is evidenced by the strong difference between plus k_x and minus k_x in 2D map of transmission as function of $k_{||}$ in Fig. 5.24c. Eventually, an experimental confirmation of these predictions would yield a fingerprint of ATHE.

CHAPTER 6

Spin VCSELs and optical anisotropy in (001) InGaAs/GaAs QWs revisited by multiband k.p methods

Contents

For several decades, continuous research efforts have been devoted to the physics and development of spin lasers made of *e. g.* spin-polarized vertical-cavity surface-emitting lasers (spin VCSELs) as a source of coherent circular polarized light with novel and enhanced performances. As a source of coherent circular-polarized light, spin-lasers introduce strong non-linearities at their emission threshold possibly enabling an amplification of the spin-information encoded with light helicity from a spin-controlled carrier optical or electrical injection. On the other hand, spin lasers would provide a number of advantages over conventional vertical-cavity surface-emitting lasers for the future optical communication systems such as spin-driven reconfigurable optical interconnects [23], fast modulation dynamics [333, 334], polarization control [24, 25] as well as higher performances such as laser threshold reduction [335, 336], improved laser intensity, and polarization stability. Laser threshold reduction was observed [335, 337, 338] and explained theoretically from the argument of the removal of the degeneration of the carrier densities [26, 339, 340]. Additionally, they have been shown to exhibit a polarization emission much more directional than conventional side-emitting laser diodes. Moreover, optical [24, 341–343] and electrical [25, 27] spin-injection were already achieved in monolithic VCSEL structures. A clear control of the laser polarization via optical spin injection was also demonstrated [24, 341, 344]. In particular, experimental investigations showed that the output circular polarization degree can exceed the input polarization via strong non-linear gain effects [341]. Even more recently, it was demonstrated, by the Thales TRT group in Palaiseau, France, a clear controllable elliptically-polarized laser emission in 1/2-VCSELs via circular optical pumps once the intrinsic linear birefringence of the device were compensated to zero [345]. It exists nowadays two kinds of surface emitting semiconductor lasers: monolithic micro-cavity-type VCSELs that allows for highly integrated low current threshold devices and on the other hand vertical-external-cavity surface-emitting lasers (VECSEL). In that goal, quantum-well VECSELs are very promising solutions for spin-lasers as they are inherently compact, wavelength flexible, widely tunable, powerful and highly coherent [346, 347] (spectrally, spatially and in terms of polarization) along with a class-A dynamics low noise regime [348, 349]. For spin-lasers functionality, optically-pumped III-V semiconductor VECSEL technology is a candidate of choice due to its inherent easier control of in-plane isotropy of the material. Typically, the resonant optical cavity of a VECSEL is made of a semiconductor chip, also called 1/2-VCSEL, and an external output coupler. The 1/2-VCSEL nanostructure integrates a Bragg reflector and a semiconductor quantum well (QW) [350] or a quantum dot (QD) gain medium. For a recent review, the reader can refer *e.g.* to Refs. [13, 14, 346, 347, 351–354]).

However, the properties of vector dipole sources in active regions of VECSELs do not necessarily force the polarization of the emitted light to be in the same direction because of the result of the residual optical anisotropies as linear birefringences and linear gain anisotropy within the semiconductor multilayers. These anisotropic properties of the dielectric function strongly impact the performance and properties of laser operation [355] leading to preferential linearly-polarized laser emission (Fig.6.1a-b) (see also *e. g.* the results presented in Ref. [345]) and to an additional favorable coupling between modes and complex polarization dynamics and polarization switching. These also impact the polarization dynamics of electrically pumped VCSEL [356–359] by pinning the polarization mode to a certain linearly polarized state [338, 360–365]. On the other hand, the dynamics of the circular polarization experiences very fast oscillations in the GHz range, much faster than the relaxation oscillation in the device for the same pump conditions [366]. This results in mode beating [334] whose frequency splitting is tuned by the birefringence. Previous theoretical as well as experimental investigations have allowed to distinguish between two different contributions that we will discuss hereafter in much details: a linear birefringence originating from interfaces between ternary quantum wells and barriers (GaAsP/(In,Ga)As/GaAsP) and local surface strain of III-V materials after surface crystalline reconstruction [367–369]. An in-plane optical anisotropy of III-V quantum well structures was

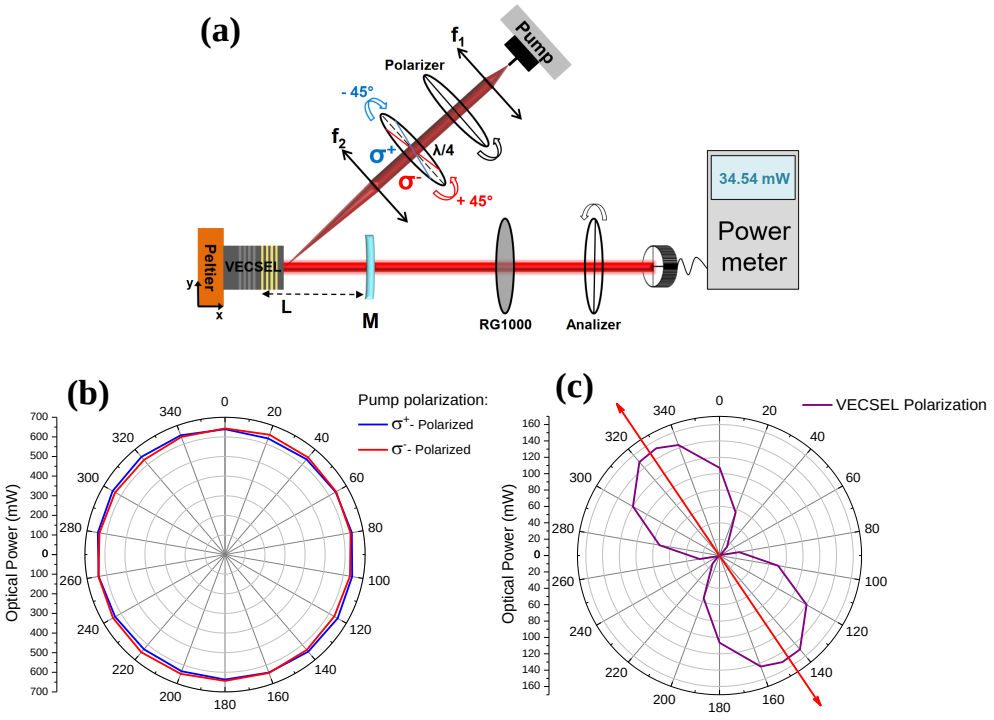

FIGURE 6.1: a) Figure of optically-pumped spin-VECSELs experiments, b) Angular-dependence of the spin-VECSELs output optical power showing a classical $\cos^2\theta$ dependence associated to a pinning of a linear polarization due to optical anisotropies and c) Angular-dependence of the spin-VECSELs output optical power almost constant associated to a pure output optical circular polarization when a strong circular birefringent media is introduced in the optical cavity.

found due to the breakdown of the rotational inversion symmetry at a semiconductor interface (by the reduction from T_d to C_{2v} symmetry group when the host materials do not share any common atoms) [368, 369] and evaluated numerically from a pseudo-potential microscopic model as well as by **k. p** theory approached by correct electronic boundary conditions [369–372], as well as chemical segregation [368] and strain effect in QWs. Such effect of linear birefringence in the QWs is generally measured by optical reflectance anisotropy [373], by transmission anisotropy [374] or by absorption anisotropy [375] like previously evidenced. The second contribution originating from surface may have two different causes: a surface-bulk electro-optical effect due to the appearance of a significant electric field developing from the top surface by pinning of the Fermi level [376, 377] and an effect related to strain by surface reconstruction [378].

6.1 Principles of Spin VECSELs

We are now giving some details about the working principles of spin VECSELS with optical pumping method based on optical selection rules and the dynamical descriptions from the optical Maxwell-Bloch equations.

6.1.1 Optical pumping and optical gain: optical selection rules

Generally one can distinguish between devices optically-pumped like spin-VCSELS and devices electrically pumped like spin light-emitting diodes (spin-LEDs) and electrically-pumped spin-VCSELS. In those devices, the emission of circularly polarized coherent light originates from radiative recombinations of spin polarized electrons with unpolarized holes in active media such as quantum wells (QWs). The output spin

TABLE 6.1: Optical selection rule obtained from the characteristic dipole matrix element at Γ point.

	CB ↑ $\langle 1/2,+1/2\vert$	CB ↓ $\langle 1/2,-1/2\vert$
HH ↑ $\langle 3/2,+3/2\vert$	$-\sqrt{1/2}(\hat{x}+i\hat{y})$	0
HH ↓ $\langle 3/2,-3/2\vert$	0	$\sqrt{1/2}(\hat{x}-i\hat{y})$
LH ↑ $\langle 1/2,+1/2\vert$	$\sqrt{2/3}\hat{z}$	$-\sqrt{1/6}(\hat{x}+i\hat{y})$
LH ↓ $\langle 1/2,-1/2\vert$	$\sqrt{1/6}(\hat{x}-i\hat{y})$	$\sqrt{2/3}\hat{z}$

polarization is directly related, although in a non-linear way, to the polarization injected (optical or electrical) via the optical quantum selection rules governing the radiative recombination. There is a proportionality relation between the spin polarization of the injected current P_s and the degree of circular polarization of the emitted light P_{circ}, in particular along the quantization axis parallel to the growth direction in the case of a quantum well (any direction can play this role for bulk optically active materials). The annihilation of an electron-hole pair during the inter-band recombination process triggers a transfer of the total electron-hole angular momentum to the emitted photon. In $\hbar$ units, polarized photons have an angular momentum projection on the wave vector direction equal to +1 or -1 respectively. Thus the radiation resulting from the recombination of the spin-polarized carriers will be partially circular if the spin orientation has not entirely relaxed within the time of recombination. Thereupon, the degree of circular polarization of the radiation serves as a useful and direct measure of the carrier density spin state as well as its change under the influence of external factors and relaxation process. The efficiency of the conversion of the spin-polarization between pump and output coherent light can be quantified from optical polarization measurements (*e. g.* spin-resolved electroluminescence or spin-resolved photoluminescence) through the examination of the optical quantum selection rules [14]. In a direct gap III-V semiconductor, the interband transitions rates are given by the Fermi golden rule 1.52 where the transition matrix element $D = |\langle f|V_{fi}|o\rangle|$, proportional to the overlap integral, quantifies the coupling strength between the initial state and the final state via the dipolar Hamiltonian perturbation V_{fi}. For electronic states close to the Γ point, the electron wavefunction in the CB and VB can be described by the quantized states or standing waves formed with the Bloch wavefunctions (sum of forward and backward traveling waves) with associated Bloch states $|j,m_j\rangle$ denoted according to the total angular momentum j and its projection onto the quantization axis m_j. In this notation, the wavefunctions describing the CB and VB states near the Γ point can be expressed in terms of wavefunctions with s, p_x, p_y and p_z orbital character.

The V_{fi} , perturbation operator, is the operator describing the physical interaction coupling between the initial and final states. The dipolar Hamiltonian interactions $\mathbf{H}_d = -\mathbf{E}.\mathbf{d}$, where $\mathbf{d} = \frac{1}{V}\sum_{(m)} e.\mathbf{r}_{(\mathbf{m})}$ is the host vector dipole moment of electrons with charge e, position vectors $\mathbf{r}_{(\mathbf{m})}$ in the volume V and space coordinate m ($m = x = [100]$, $y = [010]$, $z = [001]$), leading to both spontaneous and stimulated emission [355]. In the case of the $i-$polarized electric field E_i it takes the form $\mathbf{H}_d = -\sum_i E_i \hat{d}_i$ with the off-diagonal matrix elements between two levels $|1\rangle$ and $|2\rangle$, $d_{21,i} = \langle 1|\hat{d}_i|2\rangle$, which is also called the dipolar coupling coefficient. In the present case, the interaction arises between an electrical dipole and an external field such that the interaction operator is given by:

$$V_{fi} = \vec{d}.\vec{E} = d_x E_x + d_y E_y + d_z E_z \tag{6.1}$$

where $\vec{d}$ is the dipole moment and $\vec{E}$ is the electric field of the light wave. The components of the electric field E_x, E_y and E_z are considered constant as the electric field variations are small compared to the periodical variation of the lattice potential. When the vector $\vec{d}$ is expressed as a spherical tensor $d_\pm$ for $\sigma^\pm$ optical transition, the Wigner-Eckart theorem states that the non-zero dipolar matrix element $D = |\langle f|V_{fi}|o\rangle|$ are

the terms verifying the relation $\Delta m_j = \pm 1$ [379]. The transition probabilities for allowed transitions are given in table 6.1.

The orientation convention is to consider that a photon has a right circular polarization σ^+ (respectively left circular polarization σ^-) when emitted from a $\Delta m_j = -1$ transition and propagating toward the surface (respectively toward the backside). The optical selection rules are only strictly valid at the Γ point. By moving away from the Γ point, the HH and LH band mixture results in a non-ideal optical polarization.

$$P_{circ} \approx \frac{3n_\downarrow - 3n_\uparrow}{3n_\downarrow + 3n_\uparrow} = -P_s \tag{6.2}$$

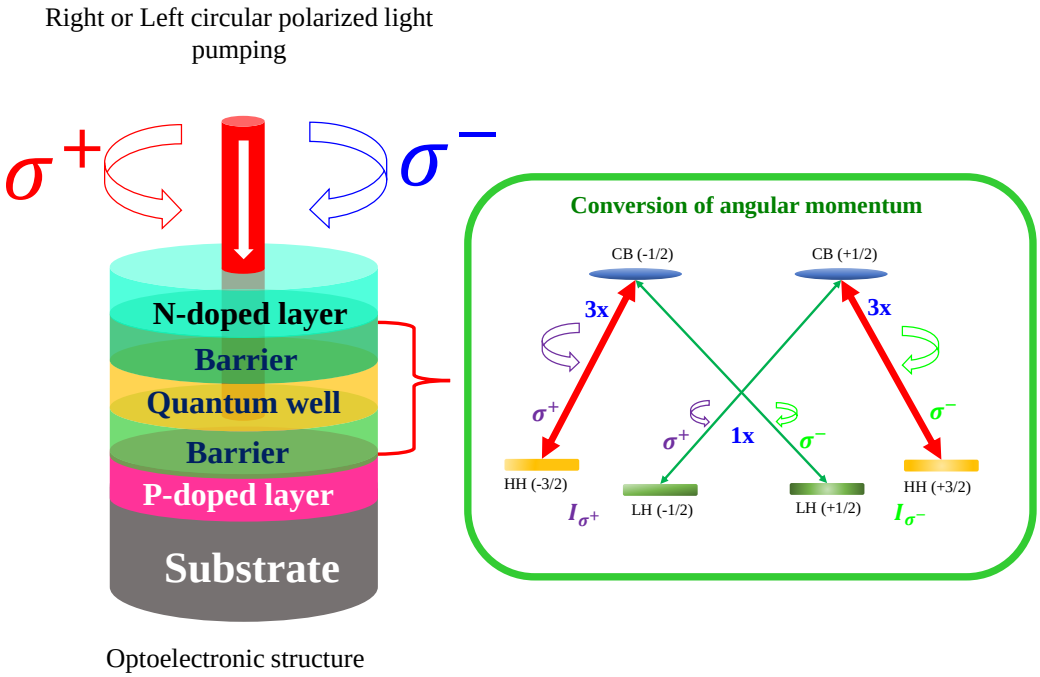

FIGURE 6.2: Scheme of the circularly polarized optical pumping mechanism: Spin generation happens through preferential transitions driven by the optical quantum selection rules in the active medium of the optoelectronic device.

At the Γ point, the $CB \rightarrow HH$ transitions are three times more probable than the $CB \rightarrow LH$ transitions regardless to the active medium nature. In a bulk semiconductor, the HH-band and the LH-band are degenerate at the Γ point, which intrinsically limits the degree of circular polarization degree injected in the device. Thus, the maximum value theoretically reachable for P_{circ} with a bulk active medium will be limited to 50% for a carrier spin polarization of 100%

$$P_{circ} = \frac{I(\sigma^+) - I(\sigma^-)}{I(\sigma^+) + I(\sigma^-)} = \frac{(3n_\downarrow + n_\uparrow) - (3n_\uparrow + n_\downarrow)}{(3n_\downarrow + n_\uparrow) + (3n_\uparrow + n_\downarrow)} = \frac{n_\downarrow - n_\uparrow}{2(n_\downarrow + n_\uparrow)} = -\frac{P_s}{2} \tag{6.3}$$

where $I(\sigma^+)$ and $I(\sigma^-)$ are the intensities for σ^+ and σ^- polarizations respectively; $n_\uparrow$ and $n_\downarrow$ stands for the density of states of spin up and spin down electrons respectively.

The case of QWs is much more appealing as the quantum confinement and potential epitaxial strain lift the degeneracy between the HH-band and LH-band at the Γ point. For example, in $Al_xGa_{1-x}As$ and $In_xGa_{1-x}As$ which we extensively used in the active medium of spin-LEDs and spin-VCSELs, the HH-band is energetically higher than the LH-band. Consequently, the LH states can be ignored, especially since the $CB \rightarrow HH$ transitions are three times more probable than the $CB \rightarrow LH$ transitions. It is then

theoretically possible to reach 100% degree of circular polarization for an injected spin polarization of 100%.

6.1.2 Dynamics of the system: the optical Maxwell-Bloch equations.

We now give more details on the optical transitions and related transition matrices. From a pure quantum-mechanical approach, physical processes responsible for the optical gain involve optically active recombination regions, typically multiple quantum wells (MQWs) wherein the electronic-to-photonic information transfer occurs *via* the optical quantum selection rules for dipole radiation. This is associated with the conservation of angular momentum in active media or QWs [17]. From a material point of view, binary (GaAs, InP, GaN) and ternary (InGaAs, GaAsP) III-V semiconductor compounds are widely used in opto-electronics as reference materials for light sources and detectors with the advantage of a direct gap. The amplification effects induced by the combination of a gain medium and a resonant optical cavity gives a unique opportunity to maximize the conversion efficiency of the carrier spin-information into light helicity. A particular example of the derivation of the dynamics of VCSELs and spin-VCSELs is Bloch equations refined in terms of the so-called spin-flip model established in the mid-nineties [360, 380]. This describes the dynamics of spin-polarized pumped carriers and correlated polarized electric field in the optical cavities and thus generating elliptical optical eigenmodes. However, what is missing in the latter approach is a correct evaluation of the optical gain properties and its different anisotropic contributions from a pure quantum mechanical approach. The optical gain property has to take into account the anisotropic contributions according to circularly or elliptically polarized electronic injection in QW (via optical, electrical or hybrid pumping). This includes possible linear gain anisotropy between different in-plane [110] and [1$\bar{1}$0] crystallographic axes, originating from the interfacial symmetry breaking between III-V quantum wells and barriers, which is reduced from the bulk T_d or structural D_{2d} to the interface C_{2v} symmetry group as demonstrated recently [368].

The carrier-photon dynamics of spin lasers may then be modeled, starting from the Maxwell-Bloch equations [381–384], using a spin-dependent rate equation analysis. The rate equations can provide a direct relation between material characteristics and device parameters [26, 333, 385]. A set of equations which relates the polarization behavior of V(E)CSEL to the quantum structure of the active medium and to the anisotropies of the cavity may then be derived. The first anisotropy to consider is the unavoidable linear phase anisotropy induced by a possible local strain-field in the material host *via* electro-optical effects and originating *e.g.* from lattice mismatch [356, 357] or from crystal relaxation at the interface. As a consequence of this anisotropy [110] and [1$\bar{1}$0] axes, the directional degeneracy of the electric field will be removed and the frequencies of orthogonally linearly polarized light fields will be split. One possible description is a generalization of the equations within a full transfer-matrix method developed recently in our group [386].

The dynamical Maxwell-Bloch dynamical equations link the electromagnetic electric field $\mathbf{E}$ and the medium polarization $\mathbf{P}$ in a vectorial form as well as the spin-dependent carrier density which may be different via the electrical or optical circularly-polarized pumps. These equations generally derive from the density matrix dynamics [381–384] of carriers coupled to photons via the dipolar interactions Hamiltonian $\mathbf{H}_d = -\mathbf{E}.\mathbf{d}$. If one considers slowly varying amplitudes of the electric field, conveniently written in the relevant reference basis (circularly or linearly polarized eigenmodes), rate equations for $\mathbf{E}$, and for carrier density can be derived as $\mathbf{P} = \hat{\chi}\mathbf{E}$, where χ is the susceptibility tensor. Indeed, one admits here that the transverse relaxation time of the optical polarizability is very short which is generally true for class A and class B lasers as in Ref. [387].

Nonetheless, crystallographic and electro-optical anisotropies in the QWs can make that the vectorial orientations of $\mathbf{E}$ and $\mathbf{P}$ slightly differ in the active regions where the carrier recombination and optical gain

take place. This can be explained *via* the property of the optical activity. Even if the resulting optical gain would only represent a small fraction of the electromagnetic wave intensity in the cavity, this property of non-collinearity between **E** and **P** in QWs is crucial to analyze and understand the eigenmode polarization and the mode coupling. This is what we will demonstrate below. Note that, although outside of the scope of the present thesis, such possible non-collinearity between **E** and **P** also appears to be of the first importance to understand optical eigenmodes obtained with pumps competing with intrinsic linear gain anisotropy like observed in recent experiments [345, 388].

Generally, in order to take into account realistic physical situations dealing with III-V (spin-)VCSELS involving anisotropic interfaces (C_{2v} symmetry), a possible way consists in considering differential optical losses for the two different crystallographic axes. However, if this method correctly mimics the difference in the optical activities (losses and corresponding threshold [360, 380]), it cannot account for additional mode coupling as far as the dipolar-transitions remain, here, unaffected by the surface properties. An alternate and novel method that we propose here, would be to determine the correct properties of the dipolar interband transitions from a pure quantum-mechanical picture taking into account the orbital bonding anisotropy imposed by interfaces. By this way, we will be able to determine the true dipolar amplification properties as well as the optical eigenmodes that can be then made different, and in this specific case, the optical coupling between modes imposed by electro-optical properties originating from interfaces. It may also lead to a generation of mode splitting like observed recently [389–391].

6.2 Impact of the optical anisotropies in the semiconductor cavity.

6.2.1 Linear birefringence and circular gain dichroism

Those additional linear in-plane anisotropies in the multilayer semiconductor cavity strongly impact the performance and properties of spin-laser operation, leading to complex polarization dynamics. Previous theoretical as well as experiment investigations have allowed to distinguish between several different contributions:

♣ A linear birefringence originating from interfaces between ternary quantum wells and barriers like (In,Ga)As/GaAs quantum well structure.

♣ Possible local surface strain of III-V material after surface crystalline reconstruction.

♣ A magneto-optical anisotropy.

The first contribution, an in-plane optical anisotropy of III-V quantum well structures, was found due to the reduction from D_{2d} to C_{2v} symmetry group when the host materials do not share any common atoms, as well as chemical segregation and strain effect in quantum well. The second contribution originating from the surface may have two different causes: a surface-bulk electro-optical effect due to the appearance of a significant electric field developing from the top surface and an effect related to strain by surface reconstruction. The last contribution is given by magneto-optical effects which cause the circular dischroism and birefringence in a magnetized ferromagnetic layer used as a spin-injector.

6.2.2 Natural interface anisotropy in quantum wells and optical active regions.

The natural interface anisotropy is a form of an inversion asymmetry resulting from the structure of chemical bonding at the interfaces. An example of such an interface with symmetry reduction from D_{2d} to C_{2v} is shown in Fig. 6.3 which depicts the atomic structure of zinc-blend type quantum wells along the [110] axis grown on [001]-oriented substrates. Figure 6.3a shows the case of a quantum well/barrier system with a common atom. While within each layer, the anions (black circles) are surrounded by equivalent cations (white circles), the interfacial anion is bonded to different cations from the upper and lower layers.

An example of such system is GaAs/AlAs structure depicted in Fig 6.3e. The planes of the As-Al and As-Ga bonds involving a common anion are rotated by $\pi/2$ with respect to each other at each side of the interface. It results from this particular C_{2v} symmetry leading to a possible heavy to light hole mixing in the component of the wavefunction at interface [30, 31] yielding the optical anisotropy. Consequently, different optical properties are expected along the [110] and [1$\bar{1}$0] directions. However, even if the top interface exhibits any anisotropy due to the symmetry reason, such anisotropy would be compensated at the bottom interface because the chemical bonds themselves are the same. The quantum well/barrier system thus remain symmetric. On the other hand, the different situation is in the case when quantum well/barrier system does not share any common atoms as depicted in Fig 6.3 (b,c,d). The anisotropy of the top interface is not compensated at the bottom interface because the chemical bonds are different and thus the system is no longer symmetric.

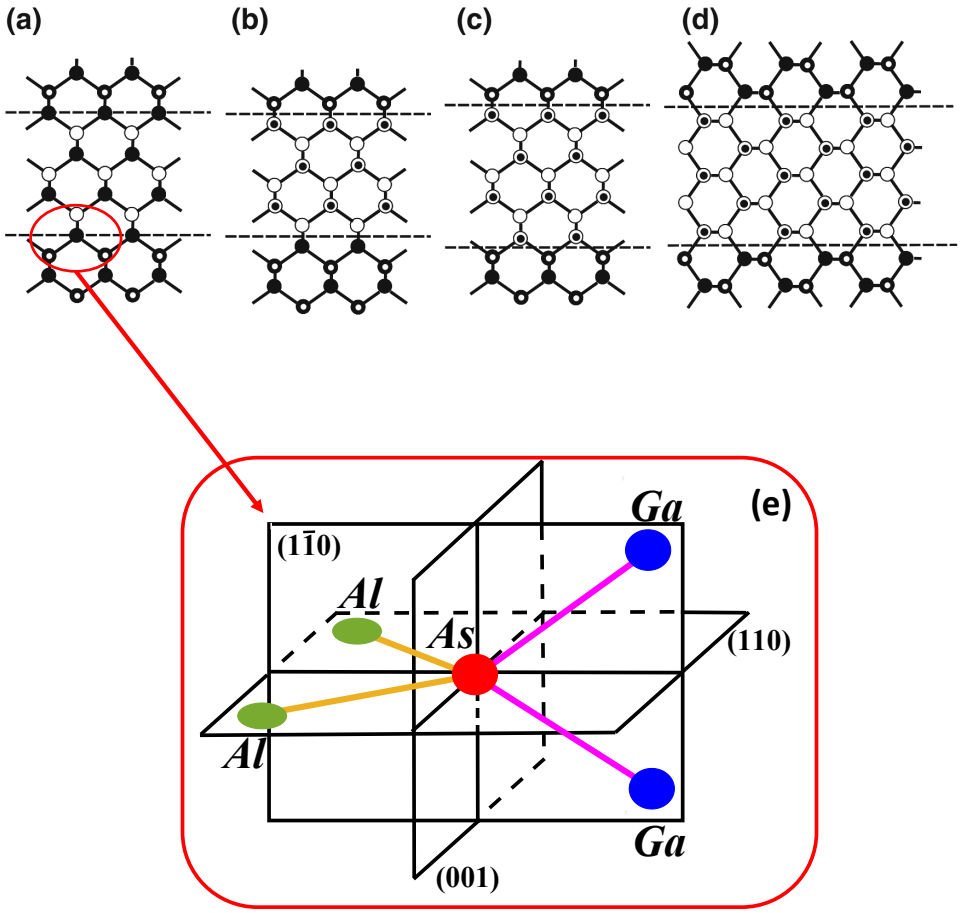

FIGURE 6.3: Illustrating the origin of the natural interface asymmetry in quantum wells grown on (001) substrates (a-c) and on a (011) substrate (d). Taken from [392]

In this work, we mainly focus on $In_{0.25}Ga_{0.75}As/GaAs_{0.95}P_{0.05}$ quantum well structure where quantum wells and barriers share the common atoms Ga and As. However, the average cation type and anion type atoms (InGa) and (As) in quantum wells are different from the average atoms (Ga) and (AsP) in the barriers. Therefore the symmetry breaking leading to the optical linear birefringence and dichroism is expected. Moreover, the local surface strain of III-V materials due to even a small lattice mismatch after surface crystalline reconstruction as well as due to the chemical segregation can be present.

6.2.3 Anisotropy at the surface

The linear birefringence and dichroism originating from the surface may have two different origins: the effect related to the strain by surface reconstruction and the surface bulk electro-optic effect due to the appearance of a significant electric field at a surface.

One contribution to the overall anisotropy predicted and observed at clean (001) surfaces of binary III-V semiconductors is caused by the surface reconstruction with its characteristic dimer-configuration and back-bonds as depicted in fig.6.3. This anisotropy could be understood on the basis of trigonally bonded overlayers leading to the strain and thus different optical properties along the [110] and $[1\bar{1}0]$ directions. Typical examples are the As or Ga dimers found on the different reconstruction of the GaAs surface. Since the dimers have a preferential orientation, electronic transitions involving these states are expected to be highly anisotropic. Moreover, reconstruction induces small changes in atomic positions in the atomic layers close to the surface and thus producing a strain field.

Another contribution to the surface linear anisotropy is due to the linear electro-optic, bulk-related effect induced by the sample surface electric field. Such effect originates from an electric charge exchange between the bulk and the surface states of the semiconductor, in order for the material to attain thermodynamical equilibrium. As a result of this process, the Fermi level becomes pinned at the semiconductor surface at an energy located in the forbidden gap. The presence of the surface electric field results in the breaking of the symmetry of GaAs near the surface and in the loss of the optical isotropy in this region. A systematic studies of this effect on n-type GaAs has been done by Acosta-Ortiz by using reflectance different technique [393].

Besides, the electro-optic effects can appear also in the presence of an applied external electric field (electrically injected VCSELs) or the electric field from high-power pumping laser (optical pumped VECSELs). When an electric field is present along the [001] direction, the refractive indices along the [110] and $[1\bar{1}0]$ directions are given by [394]

$$n_{[110]} = n_0 - \frac{n^3}{2}\tilde{r}E \tag{6.4}$$

$$n_{[1\bar{1}0]} = n_0 + \frac{n^3}{2}\tilde{r}E \tag{6.5}$$

where n_0 is the refractive index in the absence of an electric field and $\tilde{r}$ is the electro-optical coefficient. Such electro-optical birefringence can be used to control the cavity resonance of the polarized light along the [110] and $[1\bar{1}0]$ directions, which are shifted to shorter and longer wavelengths depending on the direction of the applied electric field.

6.2.4 Electronic susceptibility, optical anisotropy, and optical gain: The Maxwell-Bloch equations revisited.

Generalities

The objectives of the general scientific program is to investigate both by analytical and numerical procedures the static and time-dependent properties of output laser eigenmodes emitted from VECSEL and 1/2 VECSEL cavity *vs.* the known dielectric optical constants of each constituting material. Those investigations include the effects and properties of light-sources in each active layers (or quantum wells) with possible related linear birefringence (uniaxial in-plane strain field), anisotropy of linear gain due to stress, circular gain due to spin injection and possibly dichroism due to the presence of a ferromagnetic film. For the Spin-VECSEL applications, it has been proposed in the frame of Tibor Fordös's thesis to develop computation and modeling of the coherent light-emitted from VECSEL or 1/2 VECSEL cavities based on

the scattering-matrix approach. A number of properties have been derived, namely the properties of laser threshold, output-light polarization in terms of output Jones vector including possible linear-birefringence and strain-induced field effect at surfaces and interfaces (quantum wells, Bragg reflectors, surface with air).

The electric field and polarization-field vectors, are respectively $\mathbf{E}$ and $\mathbf{P}$. We refer now to the sketch and notations given by Fördos *et al.* [395]. Let us define the electromagnetic field of the two-mode laser $\mathbf{E}_{(1,2)}$ as a sum of two orthogonal coupled lasing eigenmodes $A_{(1,2)}\boldsymbol{\eta}_{(1,2)}$ in the following way

$$\mathbf{E} = \sum_{i=1,2} \mathbf{E}_{(i)} \exp\left(\omega_{(i)}t - k_{(i)}z\right) + c.\,c. = \sum_{i=1,2} A_{(i)}\boldsymbol{\eta}_{(i)} \exp\left(\omega_{(i)}t - k_{(i)}z\right) + c.\,c. \tag{6.6}$$

$$\mathbf{P} = \sum_{i=1,2} \mathbf{P}_{(i)} \exp\left(\omega_{(i)}t - k_{(i)}z\right) + c.\,c. \tag{6.7}$$

where the $\boldsymbol{\eta}_{(1,2)}$ are the polarization of the eigenmodes, either (1) or (2) to be calculated and that we yet consider to be known at this stage, $A_{(i)}(\mathbf{r},t)$ is the time slowly varying envelope and transverse spatial amplitude, and $\mathbf{P}_{(i)}$ the polarization $\mathbf{P}_{(i)} = \hat{\chi}\mathbf{E}_{(i)}$ of the mode i ($i = 1,2$), respectively. The derivation is made by projecting the incoming electric field vector of the propagating wave crossing the active region in the reference basis corresponding to the two optically active circular recombination channels (+ and −). This will thus generate a certain 2×2 non-diagonal amplification-matrix (gain-tensor) in the active region for the vectorial electric fields to find.

Role of the susceptibility tensor in the light-matter coupling

The interaction between light and matter is generally described by the susceptibility tensor $\chi = \chi_R + i\chi_I$ that links the electronic polarization and electric field according to $P = \chi\epsilon_0 E$ and where $P = tr\{e\rho\hat{r}\}$ stands for the electronic polarization P. From the Maxwell equations, the susceptibility tensor $\chi_{\alpha\beta}$ is linked to the dielectrical tensor $\epsilon_{\alpha\beta}$ and conductivity tensor $\sigma_{\alpha\beta}$ by the following relationship (Gaussian units):

$$\hat{\epsilon} = \epsilon_0\left(\hat{1} + 4\pi\hat{\chi}\right) = \hat{\epsilon}_0 + 4\pi i\frac{\hat{\sigma}}{\omega} \tag{6.8}$$

where ω is the optical fequency. One may distinguish between intraband and interband virtual or effective transitions and several models have been proposed to describe such interactions. The intraband transitions are responsible for optical absorption, *e. g.* dealing with free carriers in metals or in electron gas systems in semiconductor, whereas the interband transitions are responsible for the dynamical host conductivity, host optical index and optical gain. On may also distinguish between longitudinal (Coulomb problem) and transverse (electromagnetic wave) optical response. We shortly review, here, the main models:

• The Lorentz-model describes the response of an electron bounds to a given center excited by an electromagnetic wave excitation or AC-electric field. The steady-state dynamical response gives an ac-susceptibility:

$$\chi = \frac{ne^2}{m\epsilon_0}\frac{1}{(\omega^2 - \omega_0^2) - i\frac{\omega}{\tau}} \tag{6.9}$$

where ω_0 is the resonance frequency of the bound system and τ its characteristic relaxation time. We note $\omega_p = \sqrt{\frac{4\pi ne^2}{m\epsilon_0}}$ the characteristic plasma frequency. It results that the real part of the conductivity (absorption) that reads $\sigma_R = \frac{\chi_R\omega\epsilon_0}{4i\pi}$ satisfies the well-known sum rule:

$$\int_{\omega=0}^{\omega=\infty} \sigma_R d\omega = \frac{\epsilon_0\omega_p^2}{8} \tag{6.10}$$

• From pure quantum-mechanical point of view, for the calculation of both intraband and interband transitions, we have for the longitudinal optical response:

$$\chi_{\parallel}(\mathbf{q},\omega) = \frac{e^2}{V\epsilon_0\mathbf{q}^2}\sum_{k}\sum_{l,l'}\frac{f^0(\mathcal{E}_{\mathbf{k}+\mathbf{q},l'}) - f^0(\mathcal{E}_{\mathbf{k},l})}{\mathcal{E}_{\mathbf{k}+\mathbf{q},l'} - \mathcal{E}_{\mathbf{k},l} - \hbar\omega - i\hbar\eta}\left|\langle \mathbf{k}+\mathbf{q}l'|\exp\{i\mathbf{k}.\mathbf{r}\}|\mathbf{k}l\rangle\right|^2 \tag{6.11}$$

where V the volume, l, l' are the initial ($|l\rangle$) and final ($|l'\rangle$) electronic states and $|\langle \mathbf{k}+\mathbf{q}l'|\exp\{i\mathbf{k}.\mathbf{r}\}|\mathbf{k}l\rangle|^2 = \delta_{ll'} + (1-\delta_{ll'})\left(\frac{\mathbf{q}}{m\omega_{ll'}}\right)^2|P_{ll'}|^2$ represents the transition matrix element within the $\mathbf{k}.\mathbf{p}$ theory frame. On the other hand, the transverse response reads:

$$\chi_{\perp}(\mathbf{q},\omega) = \frac{ne^2}{m\epsilon_0\omega^2\mathbf{q}^2} + \frac{ne^2}{V\epsilon_0 m^2\omega^2}\sum_{k}\sum_{l,l'}\frac{f^0(\mathcal{E}_{\mathbf{k}+\mathbf{q},l'}) - f^0(\mathcal{E}_{\mathbf{k},l})}{\mathcal{E}_{\mathbf{k}+\mathbf{q},l'} - \mathcal{E}_{\mathbf{k},l} - \hbar\omega - i\hbar\eta}\left|\langle \mathbf{k}+\mathbf{q}l'|P^2|\mathbf{k}l\rangle\right|^2 \tag{6.12}$$

• It results that for semiconductors, if one notes $|0\rangle$ the top of the valence band state, the susceptibility writes *in fine*:

$$\chi(\mathbf{q},\omega) = \frac{ne^2}{m\epsilon_0}\sum_{l'}\frac{f_{l'0}}{\left(\omega_{l'0^2} - \omega^2\right) - i\frac{\omega}{\tau}} \tag{6.13}$$

where $f_{l'0} = \frac{2|P_{0l'}|^2}{m\hbar\omega_{0l'}}$ is the optical oscillator strength between the initial state $|0\rangle$ and the final state $|l'\rangle$ and where $\omega_{0l'} = \mathcal{E}_{l'} - \mathcal{E}_0$ is the energy gap. We can note that $\sum_{l'} f_{l'0} = \frac{m}{m^*}$ with m^* the effective mass of the semiconductor near state $|0\rangle$. It results that the sum rule for the optical conductivity is retrieved according to:

$$\int_{\omega=0}^{\omega=\infty}\sigma_R d\omega = \frac{\epsilon_0\omega_p^2}{8} \tag{6.14}$$

Kramers-Kronig relationships

The Kramers-Kronig relies the real and imaginary part of the susceptibility tensor according to the following Cauchy integration:

$$\chi(\omega_0) = \int_{-\infty}^{+\infty}\frac{\chi(\omega)}{\omega - \omega_0 + i\eta}d\omega \tag{6.15}$$

which allows one to derive the real part of χ once its imaginary part (optical absorption) is known. This relationship allows us to introduce the Henry factor in optically active region by $\frac{\chi_R}{\chi_I} \approx 3.5$ for standard III-V semiconductor compound.

For that purpose, the dipolar amplitude responsible for the optical gain and corresponding to each of the two spin-populations, $(+)$ for spin $\uparrow$ and $(-)$ for spin $\downarrow$, must be derived depending on possible linear anisotropies. We define $\mathbf{A}_{\pm}^{d}$ as these dipolar amplitude in a Jones-vectorial form in a Cartesian optical reference basis associated to the two optically active circular recombination channels, $(+)$ and $(-)$ respectively. For a 2-level model, we note $N_{\pm}$ the respective spin-up $(+)$ and spin-down $(-)$ carrier densities in quantum wells above transparency (tr) ($N_{\pm} = N_{\uparrow\downarrow} - N_{tr}$) associated to the respective pumping rates $N_{0\pm}$, Γ the off-diagonal damping factor for the off-diagonal density-matrix elements (media polarization), the damping rate of the carrier densities γ, γ_s the spin-flip rate, and the spectral detuning δ'. One then gets the dynamical

behavior of each of the physical constituents that are **E**, **P** in a vectorial form according to [381, 383]:

$$\frac{\partial \mathbf{P}_{(1,2)}}{\partial t} = -(\Gamma + i\delta')\mathbf{P}_{(1,2)} - i\frac{\mu^2}{\hbar}\left[\left(\mathbf{E}_{(1,2)}\mathbf{A}_{+}^{d*}\right)\mathbf{A}_{+}^{d}N_{+} + \left(\mathbf{E}_{(1,2)}\mathbf{A}_{-}^{d*}\right)\mathbf{A}_{-}^{d}N_{-}\right] \tag{6.16}$$

$$\frac{\partial N_{\pm}}{\partial t} = -\gamma\left(N_{\pm} - N_{0\pm}\right) \mp \gamma_s\left(N_{+} - N_{-}\right)) - \frac{i}{\hbar}\sum_{i=1,2}\left\{\left(\mathbf{E}_{(i)}^{*}\mathbf{A}_{\pm}^{d}\right)\left(\mathbf{P}_{(i)}\mathbf{A}_{\pm}^{d*}\right) - c.c\right\} \tag{6.17}$$

$$\frac{\partial^2}{\partial t^2}\mathbf{P}_{(1,2)}\exp\left(\omega t - k_{(1,2)}z\right) = \left[c^2\,\nabla^2 - \epsilon\frac{\partial^2}{\partial t^2} - \kappa\frac{\partial}{\partial t}\right]\mathbf{E}_{(1,2)}\exp\left(\omega t - k_{(1,2)}z\right). \tag{6.18}$$

Those three equations represent a generalization of the Maxwell-Bloch equations, and of the spin-flip model, to the case of anisotropic active regions.

Application to optical anisotropy in spin-VCSELs

In active media or laser devices, the optical response to an electromagnetic wave excitation can be described by the equation governing the two-level ($i = 1,2$) density matrix ρ_{ij} *via* the time-dependent Schrödinger equation. From that equation that we do not detail here, one obtains the expression of χ. At low light intensity, close to threshold, it is given by:

$$\chi_R = \frac{n\mu^2}{\epsilon\hbar}(\rho_{22}^{(0)} - \rho_{11}^{(0)})\frac{\delta}{\delta^2 + \Gamma^2} \tag{6.19}$$

$$\chi_I = \frac{n\mu^2}{\epsilon\hbar}(\rho_{22}^{(0)} - \rho_{11}^{(0)})\frac{\Gamma}{\delta^2 + \Gamma^2} \tag{6.20}$$

where n is the density of atoms, ϵ the host dielectric constant, and where $\rho_{22}^{(0)} - \rho_{11}^{(0)}$ represents the population inversion at the laser threshold. The optical gain α_g then follows from the imaginary part of the susceptibility tensor χ_I as:

$$\alpha = -\frac{n_0\omega}{2c}\chi_I \tag{6.21}$$

The absorption coefficient is shown to be linked to the imaginagy part of the susceptibility tensor!

6.3 *Thesis objectives: from past, present to beyond.*

6.3.1 *What has been performed:*

These analytical and numerical modelings already focused in particular on:

(*1*) The representation of (circular) optical gain in active layers (quantum wells) with dipole sources and derived from the very general optical-selection rules applied to III-V semiconductor compounds and including possible local Hamiltonian terms in III-V materials (Rashba, Dresselhauss) derived from the electronic structure. The possible study of the effect of residual stress-induced linear birefringence on output optical properties.

(*2*) The integration the Spin-Flip model [396] for the gain of the electromagnetic-field inside the cavity into the propagative S-matrix formalism.

(*3*) The analytical and computational modeling of light emission in resonant multilayer structures was performed by using an appropriate 4×4 matrix approach fulfilling Maxwell equations in each layer together with relevant boundary conditions for the electromagnetic field.

(*4*) The determination of the laser threshold and resonance where both amplitudes and phases of the waves in the cavity was reproduced and compared to experiments. Losses in the magneto-optically active

ferromagnetic injector and strain-induced optical anisotropy at the interfaces of III-V QWs have crucial impact on laser threshold and was included in the model using experimentally obtained optical parameters. Experimental study of resonance conditions and emitted polarization of the half spin-VECSELs was performed at Thales TRT and UMϕ CNRS/Thales. Optimization of the structure geometry, film thicknesses, number of QWs, etc. in order to enhance spin-lasers overall performance and to design electrically-injected full spin-VCSELs.

(*5*) The development of analytical method and numerical codes including several sources of active layers (quantum wells) in Spin-VECSELs was performed and achieved by S-matrix recursive method. This particular worktask aimed at generalizing the previous work of Fördos et al. [28] to the case of multi-wells VECSELs structures.

6.3.2 *This thesis project:*

We propose in this thesis to tackle the problem of the properties of the dipolar optical transitions (band-to-band) near the center of the Brillouin zone of quantum wells in a 14×14, 30×30 and 40×40 multiband $\boldsymbol{k.p}$ framework. This theory will use the specific matching conditions for wavefunctions derived in the previous chapters taking into account local non-symmetric potential (Dresselhauss, heavy to light hole mixing) in bulk and active layer interfaces. These dipolar optical transitions determine the selection rules during transitions and are needed to study either the properties of the optical gain as well as the properties of the optical pump in Spin-VECSELs operations in both steady-state and dynamical regime of spin injection. These optical transitions may involve the effect of stress-induced linear birefringence at the surface of III-V QWs interfaces.

Moreover, when dealing with electrical spin-injection or electrically-pumped devices, on needs to inject the spin-polarized carriers from a ferromagnetic injector or magnetic tunnel barrier, magnetic injectors which constitute the optical device by itself. One thus have to consider the modeling of a real hybrid devices, inhomogeneous by essence, constituted by magnetic injector and an optically active region from a monolithic point-of-view. This deserves the development of our multiband **k. p** tunneling platform to model spin-injection processes and spin-currents.

6.4 *Experimental study of surface and interfacial optical anisotropy by ellipsometry methods (collaboration University of Ostrava) [397].*

This section refers to the recent experimental results obtained by ellipsometry methods on GaAsP/InGaAs/GaAsP quantum well based spin-VCSELs. Those experiments as well as data analysis have been performed in the framework of Tibor Fördos thesis [28] within a joint degree program between University d'Ostrava and LSI Ecole Polytechnique. We recall the main results and connect to our recent $\boldsymbol{k.p}$ calculations realized during the present thesis.

6.4.1 *Design of the VECSEL structure*

Generally, the VECSEL device is based on a laser resonator and the active gain medium: quantum wells or quantum dots.

Figure.6.4 shows schematically the general VECSEL laser structure and the particular structure to be investigated in this work consists of an epitaxial high reflectivity (99.9%) bottom AlAs/GaAs Bragg mirror (26

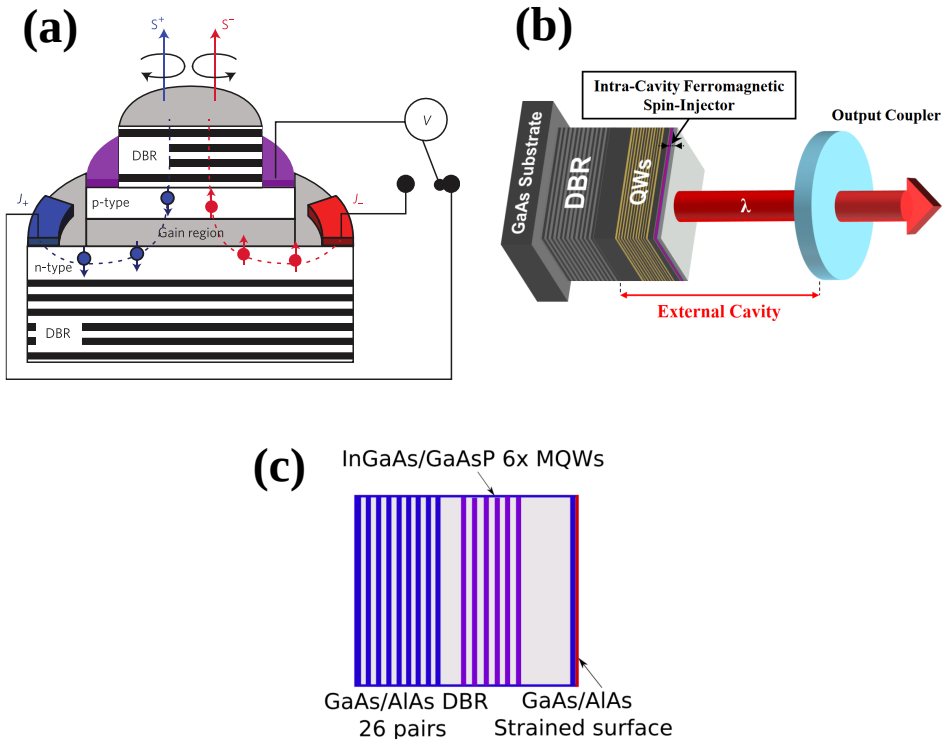

FIGURE 6.4: (a) Schematic of a VECSEL (not to scale) with a semiconductor gain chip and an external laser resonator. Reprinted from [398]. (b,c) VECSEL with the quantum well structure is to be investigated in this work.

pairs) of nominal thickness $t_{AlAs} = 85.37\ nm$ and $t_{GaAs} = 71.8\ nm$. The $\frac{13}{2}\lambda$-thick active region is constituted of 6 strain-balanced 8 nm thick InGaAs/GaAsP QWs with emitting laser frequency at $\lambda \approx 1\mu m$. Each pairs of QWs is separated by GaAs spacer which size decreases when getting closer to the surface. A 30 nm thick insulating AlAs layer in-between the surface and the active medium used as a carrier confinement layer in optical pumping experiments. The nominal thickness of GaAs capping layer is 10 nm.

6.4.2 *Methodology: Optical function of semiconductors in a layer-by-layer approach*

The critical step involved in fitting Mueller matrix ellipsometric data to a given structural model is the proper parametrization of the unknown energy-dependent complex optical functions $\epsilon_r(E) = \epsilon_1 - i\epsilon_2$. We have used a Kramers-Kronig (KK) consistent Tauc-Lorentz (TL) model function, which was developed by Jellisson using the Tauc joint density of states and the Lorentz oscillator. This approach is combined by subset of more general Herzinger-Johs (HJ) parametrized function shapes with KK properties to model the shape of an M_0 critical point seen in direct gap semiconductors such as GaAs around the gap energy E_g.

Tauc-Lorentz model [399]

In the approximation of parabolic bands, Tauc's dielectric function describing inter-band mechanisms above the band edge is in the form [400]

$$\epsilon_2^T(E) = \begin{cases} A_T \left(\frac{E-E_g}{E}\right)^2 & E \geq E_g \\ 0 & E < E_g \end{cases} \tag{6.22}$$

where A_T is the Tauc coefficient, E is the phonon energy and E_g is the energy of optical bandgap.

On the other hand, the derivation of the Lorentz oscillator is based on the classical theory of interaction between light and matter and is used to describe frequency dependent polarization due to bound charge, which are supposed to be analogy to a spring-mass system. Bounded electrons react to an electromagnetic field by vibrating like damped harmonic oscillators leading to the imaginary part of the relative permitivity

$$\epsilon_2^L = \frac{A_L \Gamma E_0 E}{(E^2 - E_0^2)^2 + \Gamma^2 E^2} \tag{6.23}$$

where Γ is the broadening parameter and E_0 is the energy of the central peak with amplitude A_L. Multiplying Eq. 6.22 and Eq.6.23 leads to the Tauc-Lorentz dispersion formula:

$$\epsilon_2(E) = \begin{cases} \frac{1}{E}\frac{AE_0\Gamma(E-E_g)^2}{(E^2-E_0^2)^2+\Gamma^2E^2} & E \geq E_g \\ 0 & E < E_g \end{cases} \tag{6.24}$$

with the overall amplitude $A = A_T A_L$. The real part of the dielectric function is derived using Kramers-Kronig integration:

$$\epsilon_1(E) = \epsilon_{1\infty} + \frac{2}{\pi} P_C \int_{E_g}^{\infty} \frac{E'\epsilon_2(E')}{E'-E} dE' \tag{6.25}$$

where P_C is the Cauchy principal value and $\epsilon_{1\infty}$ is the constant term originating from high-energy absorbtions [399].

Herzinger-Johs model [401]

The model developed by Johs which combines functional shape with Kramers-Kronig consistent properties is convenient when reproducing complicated dielectric function shape without the need of additional oscillators between critical points. Analytically, a single oscillator is formed by four-order Gaussian broadened polynomials, which are grouped into four polynomial ensembles connected end-to-end and centered on critical point E_C. Each spline connects smoothly with the advanced spline, forming a single, continuous function as depicted in Fig. 6.5. Generally, each critical point is described by 9 parameters. E_C is the CP energy with amplitude A_C, while E_L and E_U are the end points. Energies E_{LM} and E_{UM} with respective amplitudes A_{LM} and A_{UM} describe two control points for establishing the asymmetry of the line-shape. The center, the bounding energies and center amplitude are specified absolutely. The position of the control points, which corresponds to the joining points of four polynomials, are defined relatively to these absolutes.

The general expression of the dielectric function is then given as a summation of the Herzinger-Johs dielectric function [401]:

$$\epsilon^{HJ}(\omega) = \epsilon_1^{HJ} - i\epsilon_2^{HJ} \tag{6.26}$$

and P_0 poles representing contribution from outside region of studied spectra:

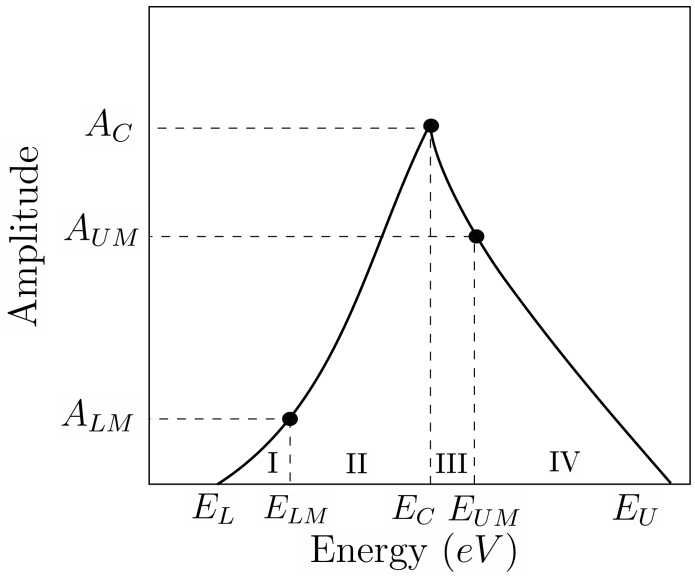

FIGURE 6.5: Schematic of a single unbroadened CP structure in the Herzinger-Johs model. Taken from [28].

$$\epsilon(\omega) = 1 + \epsilon^{HJ}(\omega) + \sum_{j=1}^{P_0} \frac{A_j}{(\hbar\omega)^2 - E_j^2} \tag{6.27}$$

The imaginary part of the Herzinger-Johs dielectric function ϵ_2^{HJ} is described using m energy-bounded polynomials given by:

$$\epsilon_2^{HJ}(\omega) = \sum_{j=1}^{m} \int_{E_{min}}^{E_{max}} W_j(E)\Phi(\hbar\omega, E, \sigma_j)dE \tag{6.28}$$

where $\Phi(\hbar\omega, E, \sigma_j)$ is the Gaussian broadening factor and $W_j(E)$ is the fourth-order (N = 4) polynomial function:

$$W_j(E) = \sum_{k=0}^{N} P_{jmk} E^k u(E - a_j)u(b_j - E) \tag{6.29}$$

with coefficient $P_{j,k}$ and unit step functions $u(x)$/ The corresponding real part of the dielectric function ϵ_1^{HJ} is obtained by Kramers-Kronig transformation. In this work, we use HJ function to model the sahpe of M_0 CP of the zinc-blende semiconductor such as GaAs.

6.4.3 Main experimental results [397]

We present the main experimental results consisting of Muller ellipsometry measurement that we performed in the full energy range from 0.73 to 6.4 eV. Those are afterwards compared to the fit alter data analysis using tabulated optical constants of GaAs, AlAs, InGaAs, GaAsP and involving a thin GaAs oxide layer on the top.

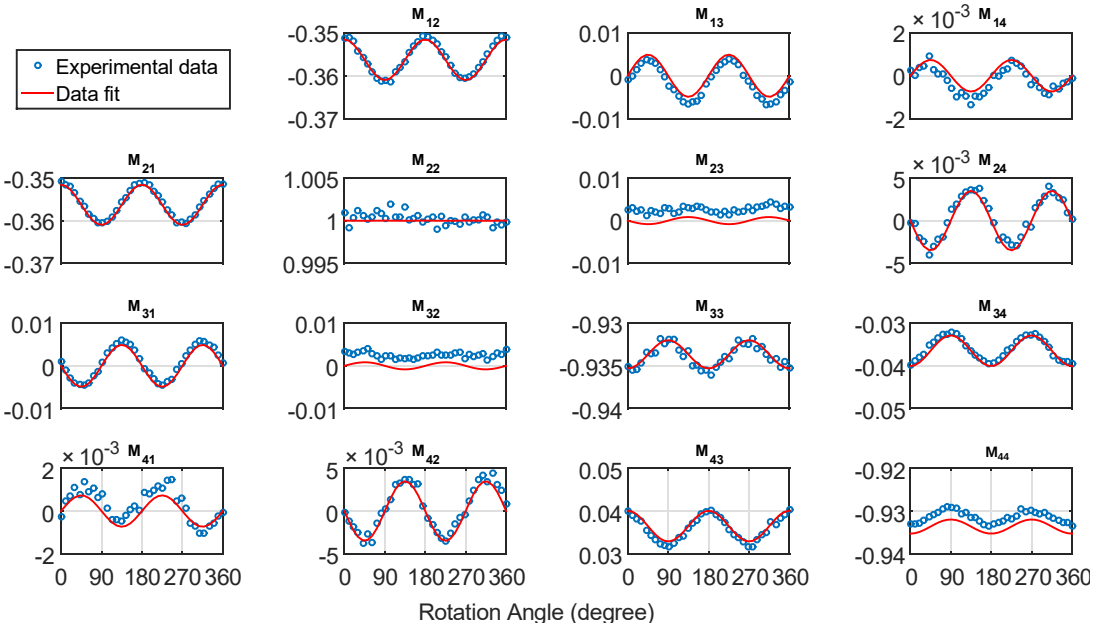

FIGURE 6.6: The measured Mueller matrix elements as a function of the in-plane azimuth rotation angle ranging from 0 to 360 degree for E = 2.2 eV and for the angle of incidence $\theta = 40^0$. Taken from [397].

Using ellipsometry techniques, the output results are given by the Mueller matrix elements where $M_{12} = M_{21}$, $M_{43} = -M_{34}$ and $M_{33} = M_{44}$ are the main ones in the present case and reveal a particular optical anisotropy. Considering the general form of the reflection coefficient r_{ss} and r_{pp} where 's' and 'p' stands respectively for 's' and 'p' polarization, one can show that [28] $M_{21} \propto |r_{ss}|^2 - |r_{pp}|^2$ and $M_{44} \propto \Re\left\{r_{ss} r_{pp}^*\right\}$ leading to the sensitivity on linear dichroism, while $M_{34} \propto \Im\left\{r_{ss} r_{pp}^*\right\}$ is the most sensitive element to the linear birefringence. The analysis procedure of VECSEL structure then consists of the following steps: i) the analysis of the full measured spectra from 0.73 to 6.4 eV, variable angle of incidence, and ii) using tabulated optical constants in order to fit and extract the precise thicknesses of all semiconductor layers.

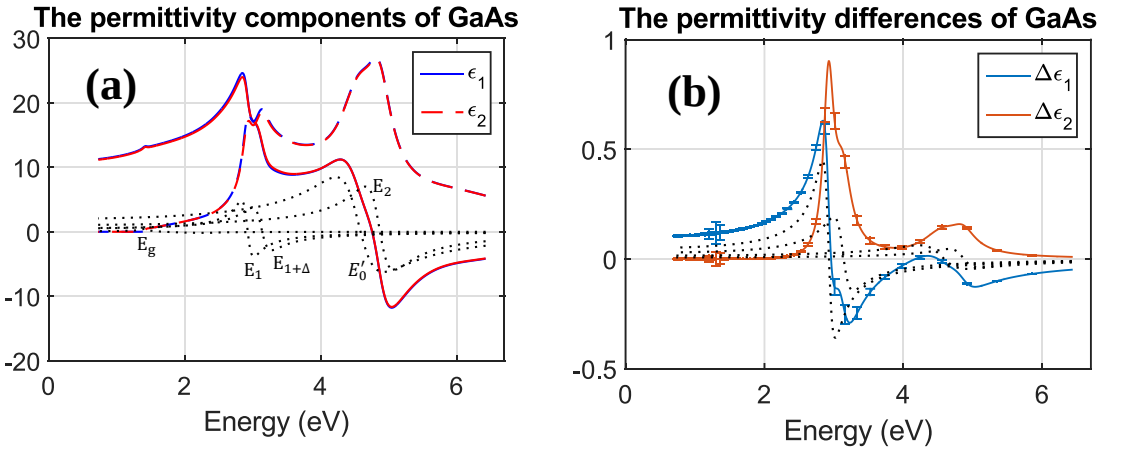

FIGURE 6.7: a) The ordinary (blue curve) and extraordinary (red curve) optical constants and b) the permittivity differences of real $\Delta\varepsilon_1$ and imaginary $\Delta\varepsilon_2$ parts of GaAs. Taken from [397].

As mentioned above, the critical step involved in fitting Mueller matrix ellipsometric data to a given

structural model is the proper parametrization of the energy dependent complex material optical functions described by the complex permitivity $\epsilon(E) = \epsilon_1 - i\epsilon_2$. The Ostravas's group have used the Kramers-Kronig (KK) consistent Tauc-Lorentz (TL) model function described in previous section. This approach is combined by subset of more general HJ parametrized function shapes with KK properties to model the shape of an M_0 critical point seen in direct gap semiconductors such as GaAs around the energy gap E_g. In combination with 4×4 matrix formalism describing the light propagation in anisotropic stratified media, the Levenberg-Marquardt least square algorithm is used to obtain Mueller matrix data fit.

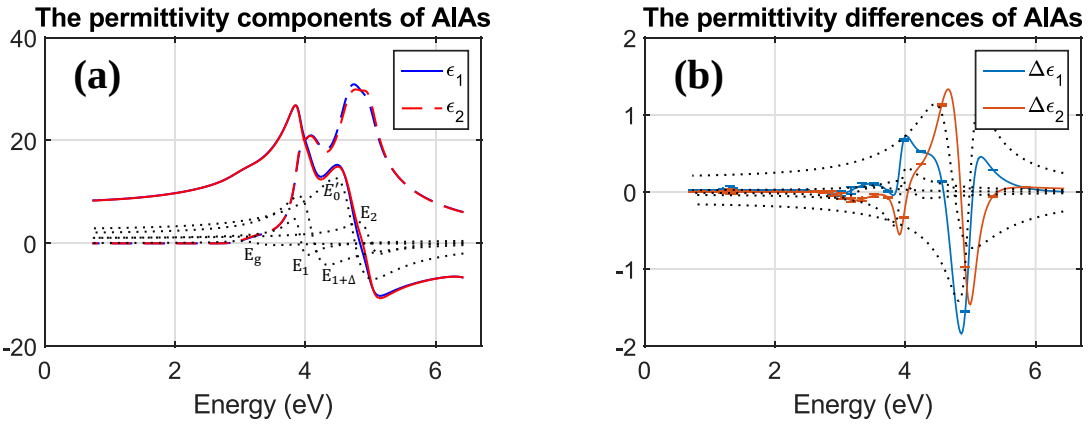

FIGURE 6.8: a) The ordinary (blue curve) and extraordinary (red curve) optical constants and b) the permittivity differences of real $\Delta\varepsilon_1$ and imaginary $\Delta\varepsilon_2$ parts of AlAs. Taken from [397].

Figure 6.6 displays the measured Mueller matrix elements as a function of the in-plane azimuth rotation angle ranging from 0 to 360 degrees for the photon energy of $E = 2.2\ eV$. Clear evidence of the broken in-plane symmetry at the surface GaAs/AlAs layers is observed due to the 180 degree symmetry of the measured MM dependence on the rotation angle. Note that effects of the sample tilt and misalignment would exhibit 360 degree symmetry. The present model is based on the optical-function parametrization of the GaAs/AlAs top layers by TL model with the amplitudes as a fitting parameter in the absorbing range from 1.7 to 6.4 eV, while all other structure parameters (thickness, optical constants of quantum wells and barriers, etc.) are fixed. The resulting optical constants are shown in Fig. 6.7 and Fig. 6.8. For the lasing energy of $E = 1.24\ eV$, the difference between ordinary and extraordinary optical constants $\Delta\epsilon_1 = \epsilon_{1,0} - \epsilon_{1,e0}$ gives $\Delta\epsilon_1 = 0.115 \pm 0.005$ for 10 nm thick GaAs and $\Delta\epsilon_1 = 0.021 \pm 0.005$ for 30 nm thick AlAs, giving the average value about $\Delta\tilde{\epsilon_1} = 0.04$ for a 40 nm thick layer composed of GaAs/AlAs at surface in agreement with the recent analysis using active lasing configuration described in [28].

We will discuss now the connection between particular interband transitions of zinc-blende type semiconductors with the obtained permitivity functions. The fundamental absorption edge of zinc-blende type GaAs and AlAs corresponds to direct transitions from the highest valence band to the lowest conduction band at the Γ point (Brillouin zone center) with the energy $E_g = 1.42\ eV$ for GaAs and $E_g = 2.89\ eV$ for AlAs as depicted in Figs 6.7 and 6.8. Above the E_g critical point, we observe E_1 and $E_1 + \Delta$ (spin-orbit split) transitions, which occur at the L point of the Brillouin zone or along the Λ line. The $E_0^{'}$ describes the transitions between the valence bands and higher conduction bands at the Γ point. The imaginary part of the permittivity ϵ_2 reaches a strong absolute maximum known as the E_2 peak, which contains contribution over a large region close to the edges in the [100] (X point) and [110] (K point) directions of the Brillouin zone.

In Figs 6.7 and 6.8, one can observe each of the resonant peak absorption s corresponding to each critical points of the Brillouin zone. The main contribution of the anisotropy of the GaAs originates from the E_1

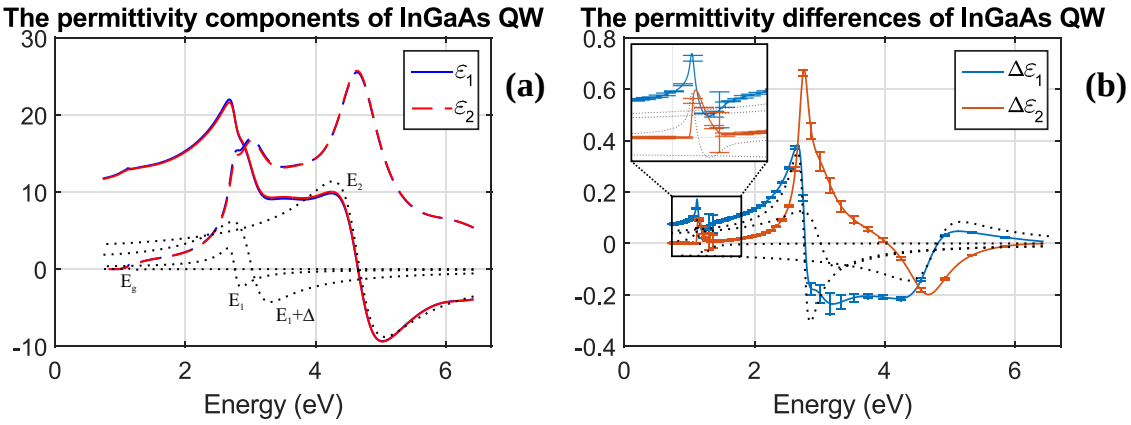

FIGURE 6.9: a) The ordinary (blue curve) and extraordinary (red curve) optical constants and b) the permittivity differences of real $\Delta\varepsilon_1$ and imaginary $\Delta\varepsilon_2$ parts of an InGaAs quantum well. Taken from [397].

TABLE 6.2: Table of the optical constants and their extracted difference.

	$\epsilon_1 = \epsilon_{1,o}$	$\epsilon_2 = \epsilon_{2,o}$	$\Delta\epsilon_1 = \epsilon_{1,o} - \epsilon_{1,eo}$	$\Delta\epsilon_2 = \epsilon_{2,o} - \epsilon_{2,eo}$
GaAs	12.30	0	0.115	0
AlAs	8.69	0	0.021	0
InGaAs	13.10	0.76	0.047	0.026

and $E_1 + \Delta$ transitions giving a positive anisotropy between ordinary and extraordinary axes $\Delta\epsilon_1 > 0$ and $\Delta\epsilon_2 > 0$ up to the energy of $E = 2.9\ eV$ and opposite $\Delta\epsilon_1 < 0$ for higher energy. The contribution of AlAs to the surface anisotropy for energy below band gap E_g is much smaller due to the compensation between E_1 and E_0' oscillators.

In the following step, the extracted optical constants of the surface layers have been considered fixed, while the optical constants of the InGaAs QW are parametrized and fitted to the experimental data in the full range from 0.73 to 6.4eV. The optical constants in all QWs are considered identical (coupled) in order to obtain reduced number of fitting parameters. Results are depicted in Fig. 6.9. We note that the highest accuracy is obtained in the region below 1.8 eV, while the features above are determined only qualitatively. The contribution of the QW to the overall birefringence admits two main parts: i) a positive one originating from the region of E_1 and E_1' spin-orbit-split transitions and ii) a negative one from the region of higher energies around E_2 transition. For the lasing energy $E = 1.24\ eV$ this gives $\Delta\epsilon_1 = 0.047 \pm 0.005$ for a 8 nm thick InGaAs QW (48 nm total). We first note a positive sign of $\Delta\epsilon_1 > 0$, identical to the surface birefringence, which should be correlated to a corresponding negative sign in the regime of laser operation due to population inversion. The larger value of $\Delta\epsilon_1$, although not yet understood, may originate on the non-saturated population inversion in laser operation, where the average birefringence has been extracted close to 6×10^{-3}.

6.5 *k.p modeling: optical anisotropy from dipolar transition matrix transitions revisited in a 30-band model.*

We are now going to focus on the fundamentals of optical transitions in quantum wells from a quantum mechanical point of view and its anisotropy vs. the emitted electric field polarization. We describe here the

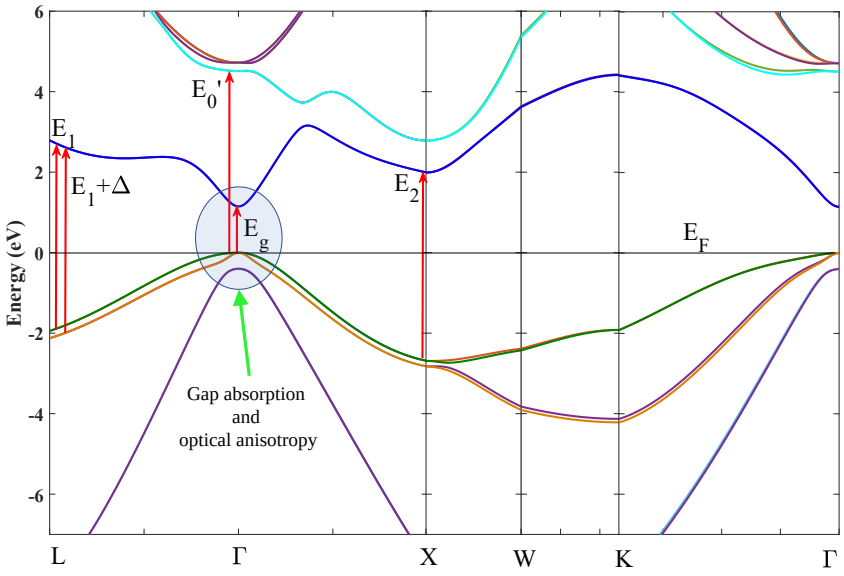

FIGURE 6.10: Electronic energy-band structure of $In_{0.25}Ga_{0.75}As$ calculated by 30 band k.p method. The main interband transitions are indicated by the vertical arrows.

main physical issues corresponding to the dipolar interaction and oscillator strength of interband transitions between the valance band and conduction band close to the gap energy.

6.5.1 Electron in Electromagnetic Field: The dipolar interactions

For that concern, we recall here the interaction Hamiltonian describing the interactions between an electron and an electromagnetic field according to Ref. [220, 402, 403] and adapt it to the $\boldsymbol{k.p}$ framework:

$$H = \frac{1}{2m_0}(\boldsymbol{p} - e\boldsymbol{A})^2 + e\phi + V(\boldsymbol{r}) = \frac{p^2}{2m_0} - \frac{e}{2m_0}(\boldsymbol{p.A} + \boldsymbol{A.p}) + \frac{e^2}{2m_0}A^2 + e\phi + V(\boldsymbol{r}) \tag{6.30}$$

where $V(\boldsymbol{r})$ is the crystal potential and $\boldsymbol{A}$ is the potential vector which is expressed by the plane wave:

$$\boldsymbol{A} = \frac{1}{2}A_0\hat{\boldsymbol{E}}\left[e^{i(\boldsymbol{k}_p\boldsymbol{r}-\omega t)} + e^{-i(\boldsymbol{k}_p\boldsymbol{r}-\omega t)}\right] \tag{6.31}$$

where $\boldsymbol{k}_p$ and $\hat{\boldsymbol{E}}$ are the wave vector of the electromagnetic field and its unit vector (polarization vector), respectively. In a quantum mechanical point of view, since the momentum $\boldsymbol{p}$ is a differential operator, then one has:

$$\frac{e}{2m_0}\boldsymbol{p.A} = \frac{e}{2m_0}\boldsymbol{A.p} - \frac{ie\hbar}{2m_0}(\nabla.\boldsymbol{A}) \tag{6.32}$$

Thus, the Hamiltonian in Eq.6.30 may be rewritten as:

$$H = \frac{p^2}{2m_0} - \frac{e}{m_0}\boldsymbol{A.p} + \frac{ie\hbar}{2m_0}(\nabla.\boldsymbol{A}) + \frac{e^2}{2m_0}A^2 + e\phi + V(\boldsymbol{r}) \tag{6.33}$$

Here, we only work with the radiation gauge and weak optical power. Consequently, $(\nabla.\boldsymbol{A}) = \phi = 0$ and $\boldsymbol{A}$ is small, thus one can neglect the second order term in A. The Hamiltonian finally reads:

$$H = \frac{p^2}{2m_0} + V(\boldsymbol{r}) - \frac{e}{m_0}\boldsymbol{A.p} = -\frac{\hbar}{2m_0}\nabla^2 + V(\boldsymbol{r}) + \frac{e}{m_0}\boldsymbol{A.p} \tag{6.34}$$

6.5.2 Dipole moment of transition and selection rules

Because the term $\frac{e}{m_0}\boldsymbol{A}.\boldsymbol{p}$ is the perturbation of H since A is small, the transition probability per unit time w_{cv} for the electron from the initial state $|v\boldsymbol{k}\rangle$ to the final state $|c\boldsymbol{k'}\rangle$ is calculated from [220]:

$$w_{cv} = \frac{2\pi}{\hbar}\left|\left\langle c\boldsymbol{k'}\left|\frac{e}{m}\boldsymbol{A}.\boldsymbol{p}\right|v\boldsymbol{k}\right\rangle\right|^2 \delta\left[\varepsilon_c(\boldsymbol{k'}) - \varepsilon_v(\boldsymbol{k}) - \hbar\omega\right] \tag{6.35}$$

$$= \frac{e^2\pi}{2m^2\hbar}A_0^2\left|\left\langle c\boldsymbol{k'}\left|exp(i\boldsymbol{k}_p.\boldsymbol{r})\hat{\boldsymbol{E}}.\boldsymbol{p}\right|v\boldsymbol{k}\right\rangle\right|^2 \delta\left[\varepsilon_c(\boldsymbol{k'}) - \varepsilon_v(\boldsymbol{k}) - \hbar\omega\right] \tag{6.36}$$

The matrix element of the term which includes the momentum operator $\left|\left\langle c\boldsymbol{k'}\left|exp(i\boldsymbol{k}_p.\boldsymbol{r})\hat{\boldsymbol{E}}.\boldsymbol{p}\right|v\boldsymbol{k}\right\rangle\right|$ is called the matrix element of the transition and gives the selection rule and the strength of the transition. Therefore, in order to study optical anisotropy, we have to determine this term. Using the Bloch function 2.35 as a basis set, then the dipolar matrix element D_{nm} is given by:

$$D_{nm} = \frac{1}{V}\int_V e^{-i\boldsymbol{k'}.\boldsymbol{r}}\psi^*_{n\boldsymbol{k'}}(\boldsymbol{r})e^{i\boldsymbol{k}_p\boldsymbol{r}}\hat{\boldsymbol{E}}.\boldsymbol{p}\,e^{i\boldsymbol{k}\boldsymbol{r}}\psi_{m\boldsymbol{k}}(\boldsymbol{r})d^3\boldsymbol{r} \tag{6.37}$$

$$= \frac{1}{V}\int_V e^{i(\boldsymbol{k}_p+\boldsymbol{k}-\boldsymbol{k'}).\boldsymbol{r}}\psi^*_{n\boldsymbol{k'}}(\boldsymbol{r})\hat{\boldsymbol{E}}.(\boldsymbol{p}+\hbar\boldsymbol{k})\psi_{m\boldsymbol{k}}(\boldsymbol{r})d^3\boldsymbol{r} \tag{6.38}$$

One has $\psi(\boldsymbol{r}) = \psi(\boldsymbol{r}+\boldsymbol{R_l})$ where $\boldsymbol{R_l}$ is the translation vector (properties of Bloch functions), then the matrix element is rewritten as:

$$D_{nm} = \frac{1}{V}\sum_l exp\left[i(\boldsymbol{k}_p+\boldsymbol{k}-\boldsymbol{k'}).\boldsymbol{R_l}\right]\int_\Omega e^{i(\boldsymbol{k}_p+\boldsymbol{k}-\boldsymbol{k'}).\boldsymbol{r}}\psi^*_{n\boldsymbol{k'}}(\boldsymbol{r})\hat{\boldsymbol{E}}.(\boldsymbol{p}+\hbar\boldsymbol{k})\psi_{m\boldsymbol{k}}(\boldsymbol{r})d^3\boldsymbol{r} \tag{6.39}$$

where Ω is the volume of the unit cell. The summation with respect to $\boldsymbol{R_l}$ becomes zero except for:

$$\boldsymbol{k}_p + \boldsymbol{k} - \boldsymbol{k'} = n\boldsymbol{G} \tag{6.40}$$

where $\boldsymbol{G}$ is the smallest reciprocal lattice vector and n is an integer. Note that, commonly the inequality $\boldsymbol{k}_p \ll \boldsymbol{G}$ is fulfilled in general [220]. Therefore, the largest contribution to the integral in Eq.6.39 is due to the term for $n\boldsymbol{G} = 0$ (n = 0) [220]. This condition may be understood to be equivalent to the conservation of momentum. From these considerations, Eq.6.40 leads to the important relation:

$$\boldsymbol{k} = \boldsymbol{k'} \tag{6.41}$$

for the optical transition. That is, electron transitions are allowed between states with the same wave vector $\boldsymbol{k}$ in $\boldsymbol{k}-space$. In other words, when a photon of energy greater than the band gap is incident on a semiconductor, an electron with wave vector $\boldsymbol{k}$ in the valence band is excited into a state with the same wave vector in the conduction band . From this fact the transition is referred to as a direct transition.

Since the integral with respect to $\hbar\boldsymbol{k}$ in Eq.6.39 vanishes because of the orthogonality of the Bloch functions, one obtains:

$$D_{nm} = \frac{1}{\Omega}\int_\Omega \psi^*_{n\boldsymbol{k'}}(\boldsymbol{r})\hat{\boldsymbol{E}}.\boldsymbol{p}\psi_{m\boldsymbol{k}}(\boldsymbol{r})d^3\boldsymbol{r}\,\delta_{\boldsymbol{k},\boldsymbol{k'}} = \frac{1}{\Omega}\int_\Omega \psi^*_{n\boldsymbol{k}}(\boldsymbol{r})\hat{\boldsymbol{E}}.\boldsymbol{p}\psi_{m\boldsymbol{k}}(\boldsymbol{r})d^3\boldsymbol{r} \tag{6.42}$$

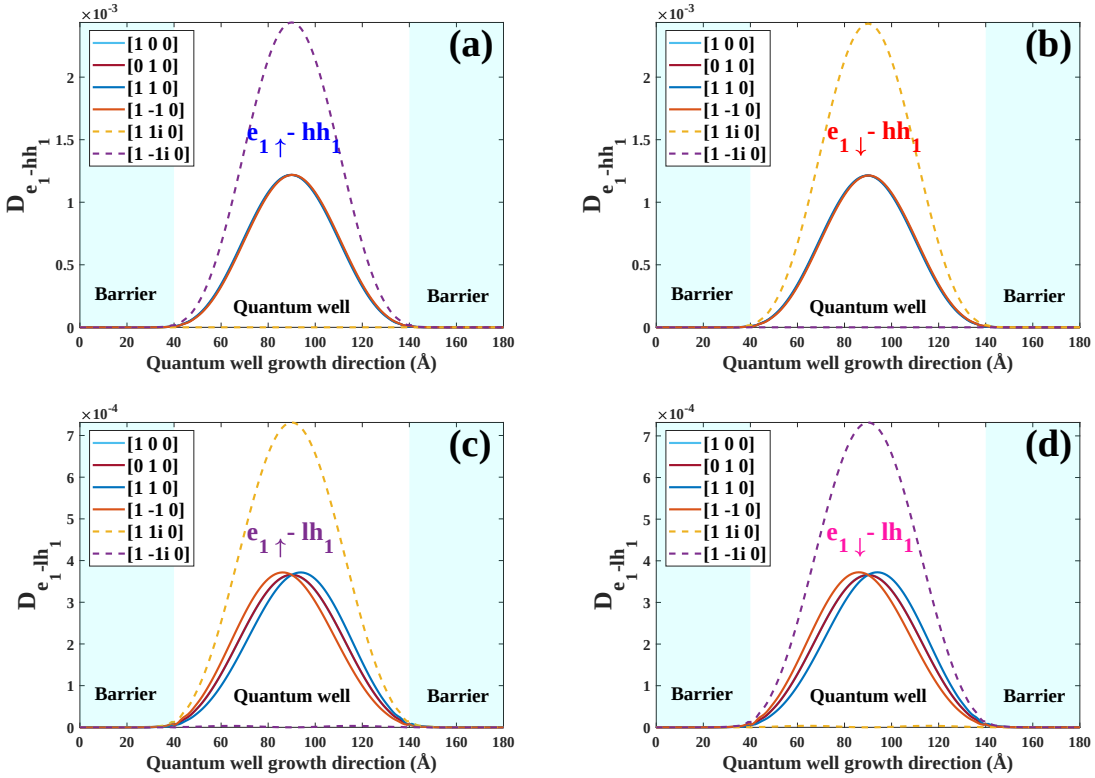

FIGURE 6.11: Dipolar matrix elements in Eq. 6.44 for the electron-heavy hole transition (figure a) and electron-light hole transition (figure b)in InGaAs/GaAs 10nm thick QW with different polarization directions [100], [010], [110], and [1$\bar{1}$0].

Looking back at Eq.2.47, one may observe that if we define a term $H_{\frac{\hbar^2}{m_0}\boldsymbol{k}.\boldsymbol{p}}$ which is extracted from $\boldsymbol{k}.\boldsymbol{p}$ Hamiltonian as following:

$$H_{\frac{\hbar^2}{m_0}\boldsymbol{k}.\boldsymbol{p}} = H_{\boldsymbol{k}.\boldsymbol{p}} - H_{(\boldsymbol{k}=0).\boldsymbol{p}} - Diag\left(H_{\boldsymbol{k}.\boldsymbol{p}} - H_{(\boldsymbol{k}=0).\boldsymbol{p}}\right) \tag{6.43}$$

then the optical selection rules are found by evaluating the dipole moment of transitions between the conduction band state $\langle c|$ and valence band state $|v\rangle$ at the Γ point [14]

$$D_{cv} = \left\langle c\left|\hat{\boldsymbol{E}}.\boldsymbol{p}\right|v\right\rangle = \left\langle c\left|H_{\hat{\boldsymbol{E}}.\boldsymbol{p}}\right|v\right\rangle \tag{6.44}$$

where $H_{\hat{\boldsymbol{E}}.\boldsymbol{p}}$ is obtained from $H_{\frac{\hbar^2}{m_0}\boldsymbol{k}.\boldsymbol{p}}$ in Eq.6.43 by replacing $\boldsymbol{k}$ by $\frac{m_0}{\hbar^2}\hat{\boldsymbol{E}}$.

Figure. 6.11 displays the calculations of dipole moment of transition between the conduction band states and heavy-light hole band states in $In_{0.25}Ga_{0.75}As$/GaAs 10nm QW structure. One observes that the dipole moment between the CB and HH is almost 3 times greater than between CB and LH, as expected from the optical selection rules for quantum wells depicted in fig.6.12. One can easily check that the relation among different polarization direction calculations in Fig.6.11 also satisfies the Table.6.1. Furthermore, as pointed out in a work of Kajikawa in Ref.[221], when one considers the optical transition in a quantum well involving materials with strong spin-orbit coupling, then SO band may contribute in the CB and LH transition. Particularly, Kajikawa considered the optical matrix elements at the zone center in framework of 6− band $\boldsymbol{k}.\boldsymbol{p}$ model involving the SO subband and found that the dipolar matrix elements for x, y, z polarizations respectively can be written as:

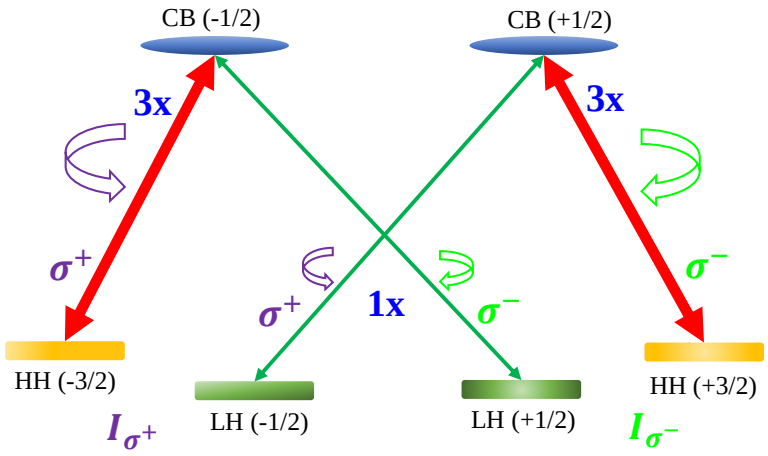

FIGURE 6.12: Schematic of optical selection rules in quantum well structures.

$$D_{cv}^{x} = \left| \frac{1}{\sqrt{2}} I_{c-HH} - \frac{1}{\sqrt{6}} I_{c-LH} + \frac{1}{\sqrt{3}} I_{c-SO} \right|^2 P^2 \tag{6.45}$$

$$D_{cv}^{y} = \left| \frac{1}{\sqrt{2}} I_{c-HH} + \frac{1}{\sqrt{6}} I_{c-LH} - \frac{1}{\sqrt{3}} I_{c-SO} \right|^2 P^2 \tag{6.46}$$

$$D_{cv}^{z} = \left| \frac{2}{\sqrt{6}} I_{c-LH} + \frac{1}{\sqrt{3}} I_{c-SO} \right|^2 P^2 \tag{6.47}$$

where $P = |\langle s|p_x|x\rangle| = |\langle s|p_y|y\rangle| = |\langle s|p_z|z\rangle|$; I_{c-HH}, I_{c-LH} and I_{c-SO} are respectively the overlap integrals between CB and HH, CB and LH, CB and SO. Note that for heavy-hole transition, both overlap integrals I_{c-LH} and I_{c-SO} are equal to zeros and the optical matrix elements are derived only from I_{c-HH} transition [221] while, on the other hand, the optical-matrix elements for light-hole transition are calculated from:

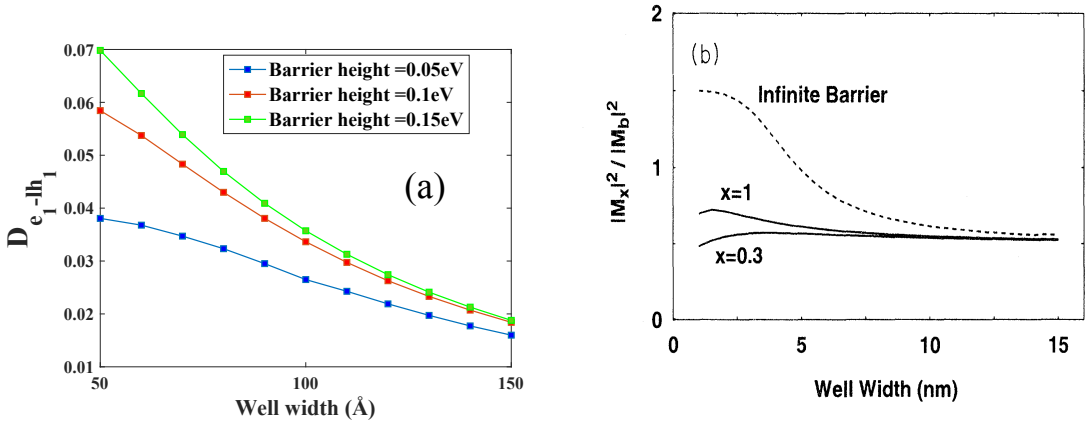

FIGURE 6.13: Dipolar matrix elements as function of quantum well width electron-light hole transitions with polarization along [100] direction calculated by our 30×30 band ***k.p*** code (a) compares with result of Kajikawa (b) taken from ref.[221].

$$D_{cv}^{x} = \left| -\frac{1}{\sqrt{6}} I_{c-LH} + \frac{1}{\sqrt{3}} I_{c-SO} \right|^2 P^2 \tag{6.48}$$

$$D_{cv}^{y} = \left| \frac{1}{\sqrt{6}} I_{c-LH} - \frac{1}{\sqrt{3}} I_{c-SO} \right|^2 P^2 \tag{6.49}$$

$$D_{cv}^{z} = \left| \frac{2}{\sqrt{6}} I_{c-LH} + \frac{1}{\sqrt{3}} I_{c-SO} \right|^2 P^2 \tag{6.50}$$

It is observed that in the case of [001] quantum well $D_{cv}^{x} = D_{cv}^{y}$ becomes smaller while D_{cv}^{z} becomes larger than those calculated within the model neglecting the SO band if we assume that the overlap integral I_{c-SO} has same sign with I_{c-LH}. Besides, the factor between the CB1-HH1 and CB1-LH1 transitions may be smaller than 3.

Finally, taking into account the impact of the SO band, one may expect also that the strength of dipolar matrix element for CB1-LH1 transition with poralization along [100] direction decreases as the quantum well width increases [221] as shows in Fig.6.13. Figure 6.13a displays the calculations of dipolar matrix element for CB1-LH1 transitions as a function of quantum well width with different barrier height using our 30 band $\boldsymbol{k.p}$ model, in comparison with the Kajikawa's result for CB1-LH1 transition in Fig.6.13b.

6.6 Optical anisotropy revisited in the framework of 14-, 30-, and 40-bands k.p method

Now we are going to consider the linear birefringence originating from interfaces between ternary quantum wells and barriers in a $In_{25}Ga_{75}As$/GaAs structure, depicted in figure 6.14, using advanced **k.p** and scattering matrix methods. In this case, the reduced symmetry from D_{2d} to C_{2v} at the interfaces of ternary quantum wells and barriers is described by modifying the boundary conditions of tunneling problem.

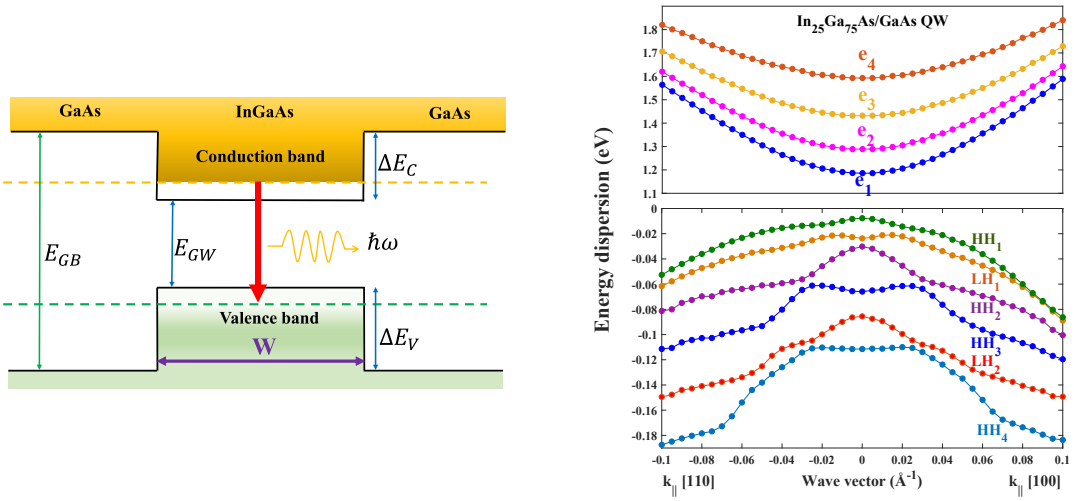

FIGURE 6.14: Scheme of InGaAs/GaAs quantum well(left figure) and the dispersion of electron in CB and hole in VB of InGaAs/GaAs 6 nm thick quantum well (right figure) calculated by 30-band **k.p** model.

6.6.1 Optical properties of $In_{25}Ga_{75}As/GaAs$ quantum well

The theory and experiment have shown that the anisotropic transition in InGaAs/GaAs quantum well mainly originates from the mixing between the heavy holes and light holes that can be attributed, by part, to indium segregation effect [404]. Both mixing between heavy holes and light holes and the segregation effect are described by an additional term in the $\boldsymbol{k.p}$ theory namely [404–408]:

$$H' = \left[\frac{P_1}{l_1} exp\left(-\frac{z - w/2}{l_1}\right)\Theta(z - w/2) - \frac{P_2}{l_2} exp\left(-\frac{z + w/2}{l_2}\right)\Theta(z + w/2)\right]\{J_x.J_y\} \tag{6.51}$$

for the basis $|\frac{3}{2},\frac{3}{2}\rangle$, $|\frac{3}{2},\frac{1}{2}\rangle$, $|\frac{3}{2},-\frac{1}{2}\rangle$ and $|\frac{3}{2},-\frac{3}{2}\rangle$ where,

$$\{J_x J_y\} = \begin{pmatrix} 0 & i & 0 & 0 \\ -i & 0 & 0 & 0 \\ 0 & 0 & 0 & i \\ 0 & 0 & -i & 0 \end{pmatrix} \tag{6.52}$$

P_1 and P_2 are the lower and upper interface potential parameters describing the effect of C_{2v} interface symmetry, respectively. The parameters l_1 and l_2 are the segregation length in the left and right interface and $z = \pm w/2$ is the location of the QW's interfaces. In the limit where $l_1, l_2 \to 0$, one has:

$$\frac{1}{l_1} exp\left(-\frac{z - w/2}{l_1}\right)\Theta(z - w/2) \to \delta(z - w/2) \tag{6.53}$$

and

$$\frac{1}{l_2} exp\left(-\frac{z + w/2}{l_2}\right)\Theta(z + w/2) \to \delta(z + w/2) \tag{6.54}$$

The additional term 6.51 then becomes:

$$H' = [P_1\delta(z - w/2) - P_2\delta(z + w/2)]\{J_x.J_y\} \tag{6.55}$$

One may observe that the term on the right of Eq. 6.55 is the surface potential term which describes the heavy hole-light hole mixing proposed by Ivchenko et al. [30]. The influence of segregation effect is described through the two interface parameters P_1 and P_2 which are different from each other ($P_1 \neq P_2$). If there is no segregation effect then $P_1 = P_2$, we get back to the results of Ivchenko et al [30].

The heavy hole - light hole mixing and the segregation effect allows to expect anisotropy in optical transitions between the [110] and $[1\bar{1}0]$ directions. Furthermore, it is reasonable to expect that the optical anisotropy transition from the first CB to HH1 is three time smaller than from that one to LH1. Figure 6.15 displays the calculations of dipolar matrix elements in a quantum well as the function of z along the quantum well growth direction, for the CB1-HH1 and CB1-LH1 optical transitions with two polarizations, [110] and $[1\bar{1}0]$ directions respectively. The anisotropy then is defined as:

$$AOT = \frac{OT_{[110]} - OT_{[1\bar{1}0]}}{OT_{[110]} + OT_{[1\bar{1}0]}} \tag{6.56}$$

where AOT is the optical anisotropy; $OT_{[110]}$, $OT_{[1\bar{1}0]}$ are respectively the optical transition strength described by the dipolar matrix elements with polarization along [110] and $[1\bar{1}0]$. The values of AOT are depicted in Fig. 6.15 for each case correspondingly. These calculations were done with fixed mixing parameter at left interface of quantum well, $P_1 = 0.5$, while the mixing parameter at right interface P_2 is varying

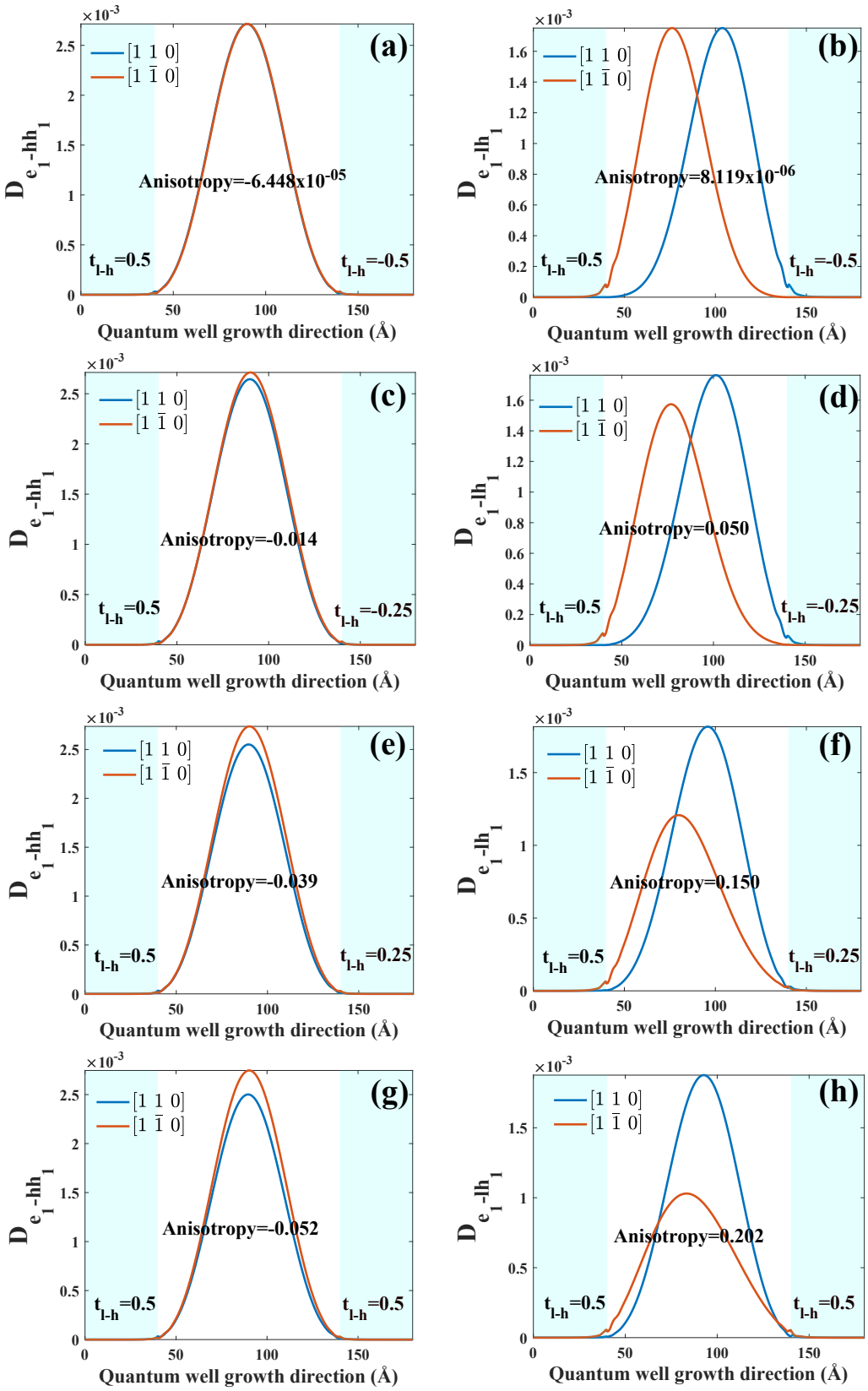

FIGURE 6.15: Calculated z-dependence of the dipolar matrix element in a single quantum well along the growth direction. Those correspond to optical transitions between the respective envelope functions of fundamentals CB1, HH1, and LH1 levels in CB1-HH1 and CB1-LH1 optical transitions. The calculations have been performed for different heavy-to-light-hole mixing coefficients at interfaces leading to optical anisotropic transition.

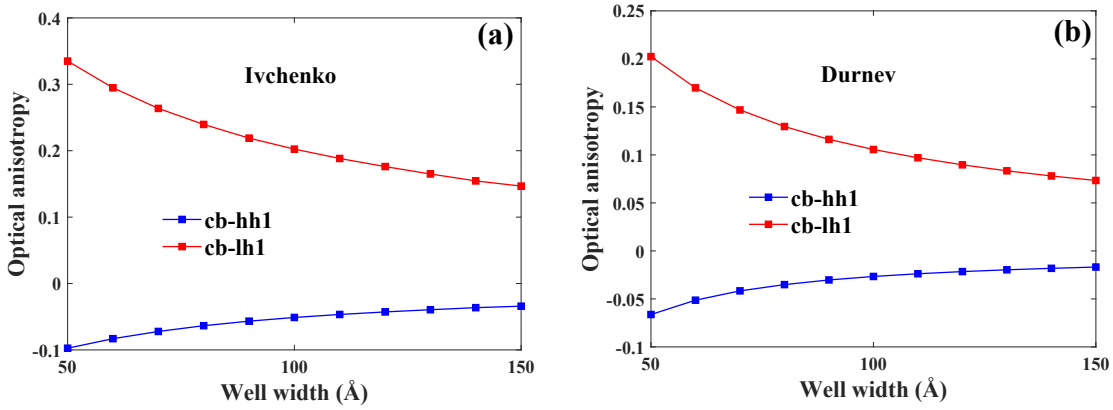

FIGURE 6.16: The anisotropy of optical matrix transition elements vs. well width indicates a pure interfacial effect like originating from HH to LH mixing. See Ivchenko P.127 in Ref.[409].

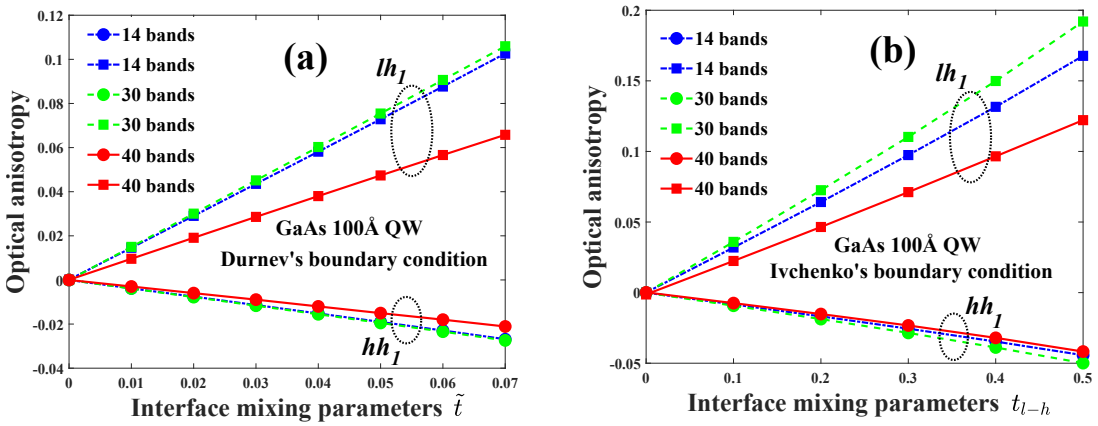

FIGURE 6.17: The annisotropy of optical matrix transitions elements vs. mixing term parameters originating from HH and LH calculated within different ***k.p*** platforms (14-30-40 bands) and with two types of matching conditions: (a) the matching conditions proposed by Durnev et al. [31, 249] and (b) the matching conditions proposed by Ivchenko et al. [30, 409].

from -0.5 to 0.5. In the case of $P_1 = -P2 = 0.5$ since if the left interface exhibits any anisotropy due to the symmetry reduction, such anisotropy however would be compensated at the right interface because of the chemical bonds themselves are the same. Then, as expected, the optical anisotropy for this case, calculated by our numerical method, is almost zero $\sim 6\times10^{-5}$ for $CB1-HH1$ transition and $\sim 8\times10^{-6}$ for $CB1-LH1$ transition. In the other case when $P_1 \neq -P_2$, those anisotropies are different from zero.

Figure6.17 displays the optical anisotropy calculated from the oscillator strength by our 14-, 30- and 40-band ***k.p*** platforms for respective heavy-hole and light-hole quantized states vs. interface mixing parameters. Here the mixing parameters are set as $P_1 = -P_2 = t_{l-h}$ for Ivchenko's matching conditions or $P_1 = -P_2 = \tilde{t}$ for Durnev's matching conditions. For the HH1 state, one recovers the result given by Ivchenko et al in Ref.[409] (see Fig. 6.18) giving an optical anisotropy of about 25 % for $t^R_{l-h} = 0.5$ and $t^L_{l-h} = 0$. One can infer from our calculation that the calculation with $\left(t^R_{l-h} = t^L_{l-h} = 0.5\right)$, like we calculate, give twice the effect compared to the result given by Ivchenko with $\left(t^R_{l-h} = 1, t^L_{l-h} = 0\right)$. Moreover, one recovers the relationship anisotropy (LH1) $\equiv -3$ (HH1) for the 40-band ***k.p*** calculation. The 14- and 30-band calculations give a factor close to -4 between LH1 and HH1 that we do not understand completely

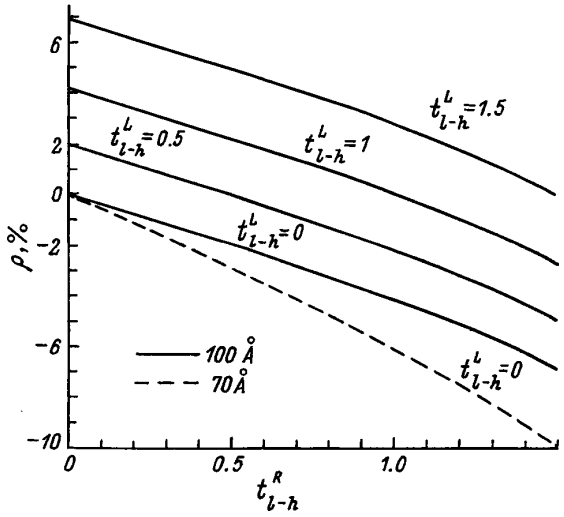

FIGURE 6.18: The annisotropy of optical matrix transitions elements as a function of the mixing term parameter at right interface of quantum well originating from HH and LH with different values of mixing term parameter at left interface, taken from Ref.[409].

up to now. We may explain the difference by the fact that one has considered the scattering wavefunction and not the bound state in the present situation. In addition, as mentioned in the previous part, the effect of SO band may contribute to the anisotropy of LH1 and then result in the difference of 14- and 30-band calculation as well.

6.6.2 *Analyses and conclusions*

We are now going to give a detailed analysis of our ellipsometry results and compare the results to our multi-band **k.p** optical anisotropy calculations given above. The method generally employed here is the derivation of the optical gain and refraction index using its characteristic spectrum extracted from the electronic band structure of the semiconductor or related heterostructure (quantum well) like explained in the paper of Balle [410]. This derivation involves single particle spectrum and neglects thus the many-body effects and band gap renormalization due to Coulomb interactions. On can quite straightforwardly calculate the optical gain from the susceptibility tensor and shows that it is linearly related to the imaginary part of the dielectric constant (and susceptibility tensor) according to the following relationship!

Note that we have the light propagation through active medium (quantum well) $\sim exp(ikz) = exp(i\frac{n\omega}{c}z)$ where z is the growth direction, ω is the frequency of light; c is the velocity of the light; n is the optical index. One has:

$$n = n_r + in_I = \sqrt{\epsilon_1 + i\epsilon_2} \tag{6.57}$$

where $\epsilon_1 \gg \epsilon_2$, then one obtains:

$$n \simeq \sqrt{\epsilon_1} + \frac{1}{2}\frac{i\epsilon_2}{\sqrt{\epsilon_1}} \tag{6.58}$$

Thus,

$$\boldsymbol{E} \sim exp\left(i\frac{\sqrt{\epsilon_1}\omega}{c}z\right).exp\left(-\frac{\epsilon_2\omega}{2\sqrt{\epsilon_1}c}z\right) \tag{6.59}$$

The intensity of light is then:

$$I \sim exp\left(-\frac{\epsilon_2\omega}{2\sqrt{\epsilon_1}c}W\right) \tag{6.60}$$

where W is the quantum well width. Since $\epsilon_1 \gg \epsilon_2$ then $n \simeq \sqrt{\epsilon_1}$, therefore the absorption $= \frac{\epsilon_2 \omega}{2nc} W$. So that:

$$\frac{\Delta\epsilon_2}{\epsilon_2} \equiv \textit{anisotropy of absorption} \tag{6.61}$$

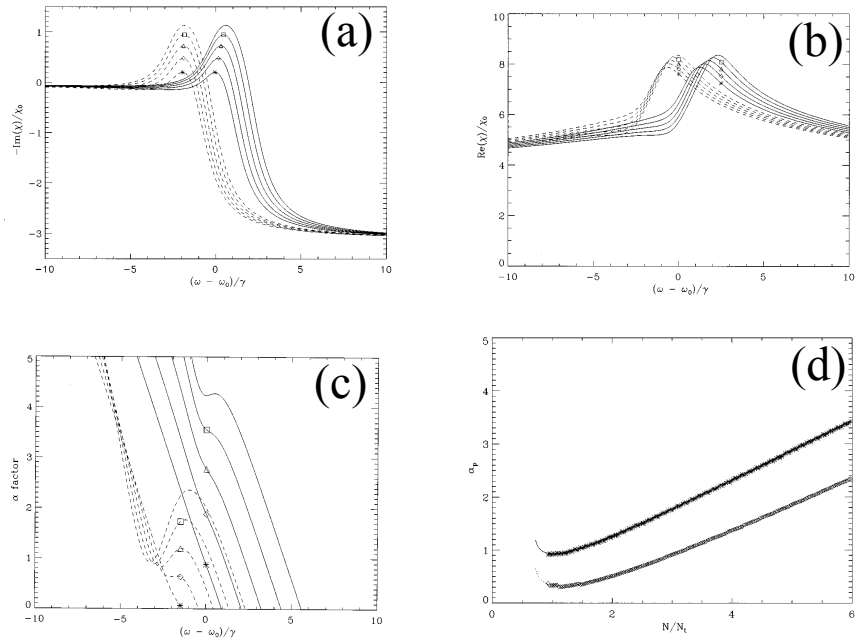

FIGURE 6.19: (a) Normalized imaginary part of the susceptibility as a function of the mormalized frequency deviation from the nominal band-gap frequency $(\omega - \omega_0)/\gamma$, for increasing carrier densities N/N_t = 1.2 (star), 1.5 (diamond), 1.8 (triangle), 2.1 (square), and 2.4 (no symbol). Solid lines correspond to σ = 0.2, while dashed lines correspond to σ = 2; (b) Normalized real part of the susceptibility as a function of the normalized frequency deviation from the nominal band-gap frequency $(\omega - \omega_0)/\gamma$ for the same carrier densities and σ values as in figure a; (c) Line width enhancement factor α as a function of the normalized frequency deviation from the nominal band-gap frequency,$(\omega - \omega_0)/\gamma$ for carrier densities n/N_t = 1.17 (star), 2.37 (diamond), 3.57 (triangle), 4.77 (square), and 5.97 (no symbol). Solid lines correspond to σ = 0.2, while dashed lines correspond to σ = 2; (d) Line width enhancement factor at the gain peak, α_p, as a function of the normalized carrier density N/N_t. The symbols denote value obtained numerically from the electrical susceptibility, while the solid line corresponds to equation (18) in Ref. [410]. Taken from Ref. [410]

The ellipsometry measurements give $\Delta\epsilon_2/\epsilon_2 = 0.04$ (4%) which has to be directly related to the anisotropy of the optical gain just under the laser threshold we are searching for. A direct comparison to our calculations presented in Fig. 6.17, in agreement with the 6 band calculations of Ivchenko, allows to extract a heavy-to-light hole mixing of about 0.45. This should be associated, as explained above, to an inhomogeneous In segregation at the two different interfaces of the (In,Ga)As quantum well.

However, a particular care should be taken about the ellipsometry measurements and subsequent analyses. The ellipsometry measurements are performed in the configuration of optical absorption whereby photons are absorbed and generate electron-hole pairs in the respective conduction and valence bands, at any singular points of the Brillouin zone. In the lasing regime behavior, a population inversion took place under electrical and optical pumping near the Γ point, with the result that the contribution of that particular point (zone center) on the optical anisotropy, and at that point only, should be of opposite sign compared

to ellipsometry measurements. The overall optical anisotropy being the sum of all the singular point contribution within the BZ, the resulting amplitude of the optical anisotropy in the hot cavity (laser behavior) should slightly differ and should be calculated precisely summing all the contribution of the Brillouin zone separately:

$$\Delta\epsilon_2 = \Delta\epsilon_2^{E_G} + \Delta\epsilon_2^{E_1} + \Delta\epsilon_2^{E_{1+\Delta}} + \Delta\epsilon_2^{E_2} + \Delta\epsilon_2^{E_0'} \tag{6.62}$$

leading to the fact that the 30-band (or 40-band) $\boldsymbol{k.p}$ model is mandatory to describe the optical anisotropy since it may give the full Brillouin zone description.

Note that the Henry's factor, that is the α parameter, which represents the amplitude-phase coupling of the laser mode [14] can be extracted from the optical index anisotropy (real part and imaginary part) according to the well-know Kramers-Kronig relationship. The detail calculation is given in the paper of Balle [410]. Whereas the Fig. 6.19 a (Fig.1 of the present reference) displays the imaginary part of the optical susceptibility vs. photon energy, showing a positive peak near the gap, the real aprt is given in Fig. 6.19 b (Fig. 3 of the present reference) on the same energy window. The Henry's factor α is plotted in Fig.6.19 c (Fig.4 of the present reference) varying from 0.1 to 5 depending on the pumping strength and emission wavelength.

Conclusion and perspective

Summary

This thesis is devoted to the theoretical, analytical and computational study of III-V semiconductors based spintronic devices structure and related phenomena from fundamentals to experiments, understanding and analyses. In particular, we focus on developing some theoretical basis, analytical and computational codes and studying of the electronic and photonic spin-current profiles, within multilayers in an multiband effective Hamiltonian approach (2-14-30-40 bands effective mass model, III-V semiconductors based spintronic devices structures). Mostly, we focused on the theoretical study of the electronic and photonic spin-current as well as spin-orbit profiles, in a multiscale approach, in devices and hybrid heterostructures possibly operated under either selected optical polarization or electrical spin-pumps, taking into account all possible interactions, in particular the Rashba and Dresselhaus structure and bulk inversion asymmetry in III-V semiconductors.

We have, first, provided a "novel ghost-band" method. This method allows one to get rid of the unphysical 'spurious' states which are a natural consequence of the truncation of the remote bands necessary to recover the Bloch periodicity in multiband **k.p** methods from 8 bands to 40 bands and so on. The 'novel ghost-band' method was then, applied to very wide cases in this work, from 14- up to 30- and 40-band **k.p** Hamiltonians. We have systematically checked the validity of this method in different situations and showed that the error with the effective mass, spin current or dispersion of holes in quantum well structures induced by this method are very small making our method to become extremely robust. Besides, throughout this thesis, the numerical calculations, which were done with multiband **k.p** Hamiltonians using the novel ghost-band method, are always compared with the analytical calculations or numerical calculations based on an effective Hamiltonian for CB or VB (without spurious states) to show a good agreement among those results. Together with the matching conditions, the novel ghost band method provides one of the most advanced implementation of numerical **k.p** tunneling transport code to investigate the spin-orbit field effects in carrier transport in a new class of spintronic and spinorbitronic structures.

On the basis of STT experiments on (Ga,Mn)As/GaAs/(Ga,Mn)As magnetic tunnel junctions, we have studied, by advanced 30- and 40-band **k.p** calculations, the anatomy of the spin currents in the tunnel devices. Beyond the TMR, they reveal the strong peculiarity of the spin currents in the AP state with the evidence of a TAHE. With the boundary conditions corresponding to HH-to-LH mixing of the relevant C_{2v} and D_{2d} symmetry at III–V interfaces, we demonstrate that the efficiency of the spin current necessary for STT is surprisingly enhanced by the hole mixing terms. We have also presented theoretical evidence for large interfacial tunneling asymmetry of carriers (scattering), electrons or holes, vs. their incidence in exchange-split semiconductor structures. This transmission asymmetry have been revealed by taking into account boundary wavefunctions matching, advanced multiband calculations as well as scattering perturbation theory. After averaging over incoming states, a large surface current may exist parallel to the barrier results in an Anomalous Tunnel Hall effect. A short discussion about the equivalence of ATHE in CB and VB as expected from symmetry point of view, were also given and proven using multiband **k.p** treatments.

For the device's application of ATHE, the quantum well structure seems to be very good candidate since it gives rise to a transmission up to a fraction of unity while keeping extremely high asymmetries.

Finally, even in the context of information processing, spin lasers (spin VECSELs) are truly promising, but however, the additional in-plane linear anisotropies in the multilayered semiconductor cavity strongly impact the performance and properties of spin VECSELs operation. Therefore, we have given the evidence for the optical anisotropy of dipolar optical transitions near the center of the zone of quantum wells which is induced by the symmetry breaking at the interfaces of semiconductor heterostructures as well as the segregation effect based on 14-, 30- and 40-band **k.p** technique together with the matching conditions. These dipolar optical transitions drive the selection rules during transitions and are needed to study either the properties of the optical gain as well as the properties of the optical pump in spin VECSELs operations in both steady-state and dynamical regime of spin injection. These optical transitions may involve the effect of stress-induced linear birefringence at the surface of III-V QWs interfaces.

Perspective

Even though the thesis is closed here, there are still many aspects that are implementing and will be further performed:

Issues are under implementations

First of all, technically the numerical calculations of STT for (Ga,Mn)As tunnel junction within the entire wave vector k-space and energy domains to give a full treatment for experimental data of STT with (Ga,Mn)As tunnel junction presented in chapter 5, is still left open because of a question of time calculation. In addition, the numerical developments of multiband Green function based on **k.p** technique for multilayer structures were not implemented completely with the same reason. These calculations can be easily finished with the help of a super computing and will be implemented in our group in short future.

Secondly, the spin-to-charge interconversion with ATHE that theoretically developed in this work seems to be very intriguing and interesting for their contributions in terms of spintronics and spinorbitronics devices applications. However, it still needs to be verified by empirical results (that is under consideration by optical detection at LSI Ecole Polytechnique).

Further works

The analytical and numerical approaches derived in this thesis can be further extended and developed to study the timely issues today in spintronics like spin photodiode effect, spin laser dynamics or spintronic THz emission and beyond.

In particular, the optical anisotropy arising from broken symmetry and chemical segregation at the interfaces considered in this work with **k.p** method can be used for description of dynamical behavior of spin-VCSEL with multiple active quantum well region (being under the study in the collaboration among LSI Ecole Polytechnique, CNRS Thales and University of Ostrava), including modeling of time dependent electric field in the cavity described by the Maxwell-Bloch equations. This will lead to a comprehensive model of spin-VCSEL structure enabling calculation of its properties like threshold, polarization state of the emitted light, mode splitting and possibly adapted to perspective quantum dot as well as quantum wire spin-lasers.

Beyond that one of the future works will be also focused on a THz radiation since in this thesis we have focused on the theoretical study of the electronic spin-current and spin-orbit profiles, in a multiscale approach, in devices and hybrid heterostructures possibly operated under either selected optical polarization

or electrical spin-pumps. This takes into account possible interactions, in particular the Rashba and Dresselhaus structure and bulk inversion asymmetry which is possibly involved in the physics of spintronic THz emission. One possibility is to extend such modelling to transition metals/LAO/STO (Fe/LAO/STO see e.g. "Tunable spin and orbital polarization in SrTiO3-based heterostructures", C. S. Ho et al. New J. Phys. 21 (2019) 103016) . We also plan to participate and work with the experimental study and investigations of spin-to-charge conversion in Rashba systems (and Topological insulators) by Spin-transfer-torque FMR experiments on relevant systems. This would be very appropriated to characterized the spintronic interfaces for the THz study.

And finally, it could be also interesting in using strain to control spin-polarized current as well as impact of strain on the performance and properties of spin-laser device.

APPENDIX A

Matrix representation of Hamiltonian

In this appendix, we present the details of 14, 30 and 40 bands $\boldsymbol{k.p}$ method in order to describe the electronic band structure and spin-polarized transport in the semiconductor heterostructures considering as main focus of this work. Note that in term of semiconductor physics, $\boldsymbol{k.p}$ approach is known to be very efficient to describe the properties of the electronic structure in the vicinity of the extreme point, commonly the Γ point or the Brillouin zone center where one can use 2 bands model and 6 bands model to describe the conduction and valence bands respectively. However, a 8 bands $\boldsymbol{k.p}$ Hamiltonian is necessary to describe the coupling between the CB and VB, whereas 14 bands $\boldsymbol{k.p}$ Hamiltonian is mandatory to deal properly with the absence of inversion symmetry in a semiconductor belongs to T_D group. The 14 bands $\boldsymbol{k.p}$ Hamiltonian describe approximately 20 % of the first Brillouin zone [29]. Beyond that, an extended 30 or 40 bands $\boldsymbol{k.p}$ Hamiltonian is needed to describe the spin-injection properties in a full-BZ description as required for indirect band gap semiconductor like Si or Ge.

A.1 14-band k.p model [29]

We are now emphasizing on building the 14×14 $\boldsymbol{k.p}$ Hamiltonian matrix because it is the smallest Hamiltonian that can describe the SOI. As mentioned before, we need an Hamiltonian which describes the properties of the CB and of the VB when the SOI is taken into account, the smallest possible Hamiltonian being the 14×14 matrix. This Hamiltonian is built in the $\{\Gamma_{8C},\Gamma_{7C},\Gamma_6,\Gamma_7,\Gamma_8\}$ irreducible representations like described in Ref. [29]. Its elements will be introduced hereafter. The basis which is chosen to construct the 14×14 $\mathbf{k}.\mathbf{p}$ matrix according to Ref. [29] was presented in Table. 2.3. This basis of functions consist of pairs of Kramers' conjugates

$$\hat{K}\left|\frac{3}{2},\pm\frac{3}{2}\right\rangle = \pm\left|\frac{3}{2},\mp\frac{3}{2}\right\rangle, \tag{A.1}$$

$$\hat{K}\left|\frac{3}{2},\pm\frac{1}{2}\right\rangle = \mp\left|\frac{3}{2},\mp\frac{1}{2}\right\rangle, \tag{A.2}$$

$$\hat{K}\left|\frac{1}{2},\pm\frac{1}{2}\right\rangle = \pm\left|\frac{1}{2},\mp\frac{1}{2}\right\rangle. \tag{A.3}$$

or

$$\hat{K}\,|j,m\rangle = (-1)^{j-m}\,|j,-m\rangle\,. \tag{A.4}$$

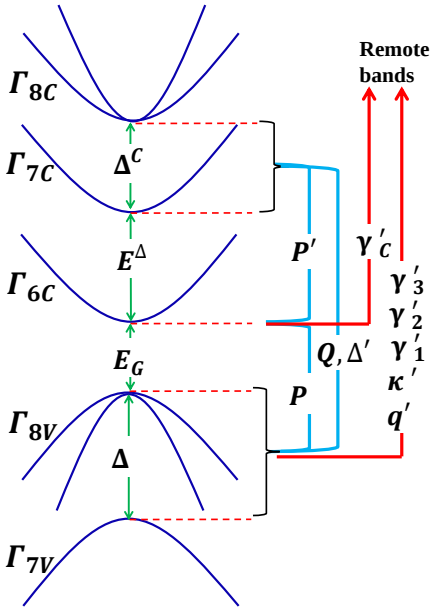

FIGURE A.1: Schematic of band structure using in 14×14 band $\boldsymbol{k.p}$ Hamiltonian model.

k.p coupling term

Note that $\hat{H}_{SC} = \hat{H}_{\mathfrak{U}} + \hat{H}_{SO}$ and $\langle \varphi_n | \hat{H}_{\mathfrak{U}} | \varphi_m \rangle = E_n \delta_{nm}$, particularly in this case

$$\left\langle \frac{3}{2}, M \middle| \hat{H}_{\mathfrak{U}} \middle| \frac{3}{2}, M \right\rangle_{\Gamma_{8C}} = \left\langle \frac{1}{2}, M \middle| \hat{H}_{\mathfrak{U}} \middle| \frac{1}{2}, M \right\rangle_{\Gamma_{7C}} = E_{5C}, \tag{A.5}$$

$$\langle \pm | \hat{H}_{\mathfrak{U}} | \pm \rangle = E_1, \tag{A.6}$$

$$\left\langle \frac{3}{2}, M \middle| \hat{H}_{\mathfrak{U}} \middle| \frac{3}{2}, M \right\rangle_{\Gamma_8} = \left\langle \frac{1}{2}, M \middle| \hat{H}_{\mathfrak{U}} \middle| \frac{1}{2}, M \right\rangle_{\Gamma_7} = E_5, \tag{A.7}$$

with $M = \left\{\pm\frac{3}{2}, \pm\frac{1}{2}\right\}$ for Γ_{8C} and Γ_8, $M = \left\{\pm\frac{1}{2}\right\}$ for Γ_{7C} and Γ_7, so that we need to describe two terms $\langle \varphi_m | (\hbar/m_0)\, \mathbf{k}.\mathbf{p} | \varphi_n \rangle$, called $\mathbf{k}.\mathbf{p}$ terms, and $\langle \varphi_m | \hat{H}_{SO} | \varphi_n \rangle$ called spin-orbit term to find all the matrix elements in Eq. 2.47.

Let $U_{n\sigma}$ be the set of functions $\{X_C, Y_C, Z_C, S, X, Y, Z\} \otimes \{\uparrow, \downarrow\}$; the basis functions in Table. 2.3 are linear combinations of $U_{n\sigma}$. This allows us to calculate $\langle U_{n\sigma} | (\hbar/m_0)\, \mathbf{k}.\mathbf{p} | U_{n'\sigma'} \rangle$.

$$\langle U_{n\sigma} | \frac{\hbar}{m_0} \mathbf{k}.\mathbf{p} | U_{n'\sigma'} \rangle = \langle U_n | \frac{\hbar}{m_0} \mathbf{k}.\mathbf{p} | U_{n'} \rangle \delta_{\sigma\sigma'} \tag{A.8}$$

This term is possibly non-zero only when the spin remains unchanged ($\sigma = \sigma'$). In summary, the non-zero $\mathbf{k}.\mathbf{p}$ terms are:

(i) the coupling terms between Γ_6 and $\{\Gamma_7, \Gamma_8\}$ representations

$$\langle S | p_x | iX \rangle = \langle S | p_y | iY \rangle = \langle S | p_z | iZ \rangle = \varpi; \tag{A.9}$$

(ii) the coupling terms between Γ_6 and the second CBs $\{\Gamma_{7C}, \Gamma_{8C}\}$ in the case of lack of inversion center

$$\langle S | p_x | iX_C \rangle = \langle S | p_y | iY_C \rangle = \langle S | p_z | iZ_C \rangle = \varpi', \tag{A.10}$$

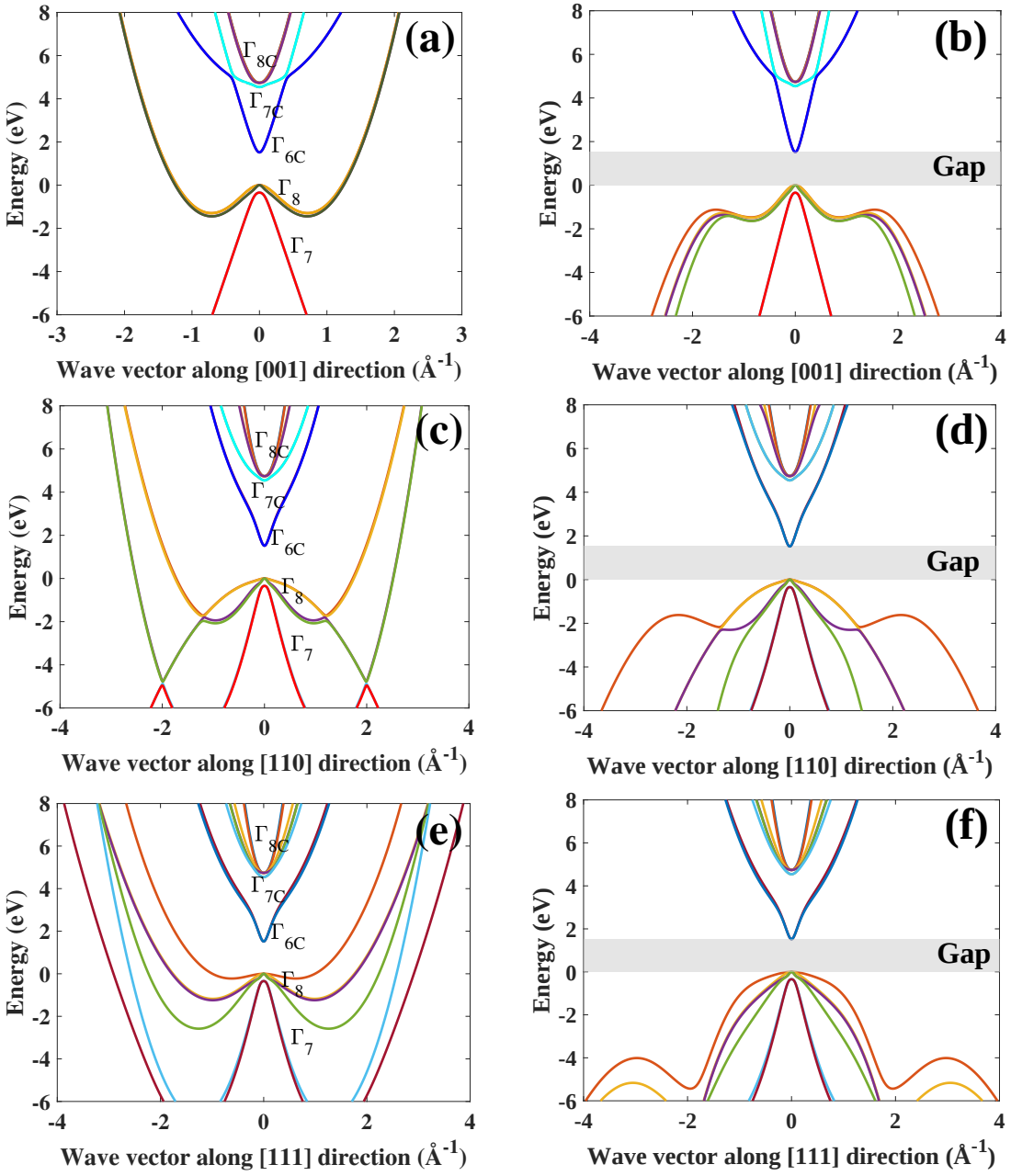

FIGURE A.2: The real band structure along three characteristic directions of GaAs calculated in 14 band $\boldsymbol{k.p}$ model before (a,c,e) and after (b,d,f) using our novel ghost-band method to remove spurious states. The parameters for 14-band $\boldsymbol{k.p}$ Hamiltonian is taken from Ref.[92]

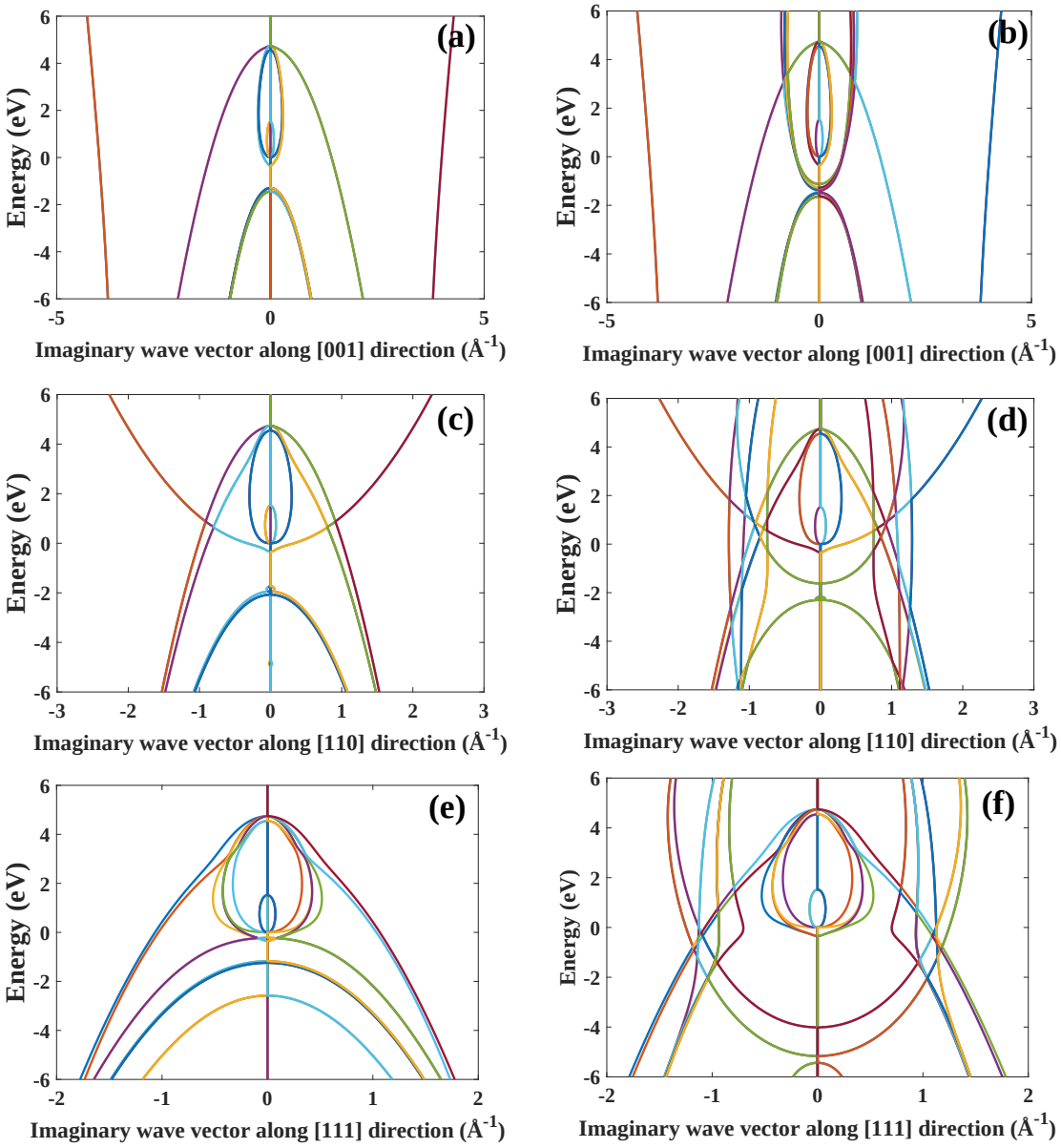

FIGURE A.3: The complex band structure along three characteristic directions of GaAs calculated by 14-band $\boldsymbol{k.p}$ model before (a,c,e) and after (b,d,f) using our novel ghost-band method to remove spurious states.

(iii) and the coupling terms between $\{\Gamma_7, \Gamma_8\}$ and $\{\Gamma_{7C}, \Gamma_{8C}\}$

$$\langle X| p_y |iZ_C\rangle = \langle X| p_z |iY_C\rangle = \langle Y| p_x |iZ_C\rangle \tag{A.11}$$

$$= \langle Y| p_z |iX_C\rangle = \langle Z| p_x |iY_C\rangle = \langle Z| p_y |iX_C\rangle = -\varpi_X \tag{A.12}$$

where ϖ, ϖ', and ϖ_X are real with a notice in the O_h group, $\varpi' = 0$. The natural $\mathbf{k}.\mathbf{p}$ parameters are introduced according to:

$$P = \frac{\hbar}{m_0}\varpi, \qquad P' = \frac{\hbar}{m_0}\varpi', \qquad P_X = \frac{\hbar}{m_0}\varpi_X; \tag{A.13}$$

with the characteristic energy

$$E_P = \frac{2m_0}{\hbar^2}P^2, \qquad E_P^{'} = \frac{2m_0}{\hbar^2}P'^2, \qquad E_{PX} = \frac{2m_0}{\hbar^2}P_X^2. \tag{A.14}$$

A.1.1 Spin-orbit coupling

The SOC terms were evaluated using the book of Koster *et al.* [411]. We resume here the couplings which may differ from zero:

(i) The core spin-orbit in the second CB

$$\Delta^C = \left(\frac{3\hbar^2}{4m_0^2c^2}\right)\langle X_C| \frac{\partial \mathfrak{U}}{\partial x}p_y - \frac{\partial \mathfrak{U}}{\partial y}p_x |iY_C\rangle . \tag{A.15}$$

(ii) The core spin-orbit in the VB

$$\Delta = \left(\frac{3\hbar^2}{4m_0^2c^2}\right)\langle X| \frac{\partial \mathfrak{U}}{\partial x}p_y - \frac{\partial \mathfrak{U}}{\partial y}p_x |iY\rangle . \tag{A.16}$$

(iii) And the spin-orbit caused by the lack of inversion center in the T_d group

$$\Delta' = \left(\frac{3\hbar^2}{4m_0^2c^2}\right)\langle X| \frac{\partial \mathfrak{U}}{\partial x}p_y - \frac{\partial \mathfrak{U}}{\partial y}p_x |iY_C\rangle . \tag{A.17}$$

In the O_h group, $\Delta' = 0$.

A.1.2 The 14×14 k.p matrix

The supplementary perturbations originate from remote bands, out of the 14-band subset, *i.e.*, the bands lower than $\{\Gamma_7, \Gamma_8\}$ or upper than $\{\Gamma_6, \Gamma_{7C}, \Gamma_{8C}\}$. They are introduced through the terms:

$$K' = \frac{2}{m_0}\sum_{n\neq 5C,1,5}\frac{\langle S| p_x |n\rangle\langle n| p_x |S\rangle}{E_1 - E_n}, \tag{A.18}$$

$$L' = \frac{2}{m_0}\sum_{n\neq 5C,1,5}\frac{\langle X| p_x |n\rangle\langle n| p_x |X\rangle}{E_5 - E_n}, \tag{A.19}$$

$$M' = \frac{2}{m_0}\sum_{n\neq 5C,1,5}\frac{\langle X| p_y |n\rangle\langle n| p_y |X\rangle}{E_5 - E_n}, \tag{A.20}$$

$$N' = \frac{2}{m_0}\sum_{n\neq 5C,1,5}\frac{\langle X| p_x |n\rangle\langle n| p_y |X\rangle + \langle X| p_y |n\rangle\langle n| p_x |X\rangle}{E_5 - E_n}. \tag{A.21}$$

The full 14×14 **k**.**p** matrix, including perturbations of all remote bands, can be expressed through the measurable effective Luttinger–Kohn parameters γ_C, γ_j, $\gamma_{\Delta j}$ ($j = 1,2,3$) in both the CB and VB:

$$\gamma_C = 1 - \frac{E'_P}{3}\left(\frac{2}{E_{8C-6}} + \frac{1}{E_{7C-6}}\right) + \frac{E_P}{3}\left(\frac{2}{E_{6-8}} + \frac{1}{E_{6-7}}\right) + K', \tag{A.22}$$

$$\gamma_1 = -1 + \frac{E_{PX}}{3}\left(\frac{1}{E_{8C-8}} + \frac{1}{E_{7C-8}}\right) - \frac{L' + 2M'}{3} + \frac{E_P}{3E_{6-8}}, \tag{A.23}$$

$$\gamma_2 = -\frac{1}{6}\frac{E_{PX}}{E_{7C-8}} - \frac{L' - M'}{6} + \frac{E_P}{6E_{6-8}}, \tag{A.24}$$

$$\gamma_3 = \frac{1}{6}\frac{E_{PX}}{E_{7C-8}} - \frac{N'}{6} + \frac{E_P}{6E_{6-8}}, \tag{A.25}$$

$$\gamma_{\Delta 1} = -1 + \frac{2}{3}\frac{E_{PX}}{E_{8C-7}} - \frac{L' + 2M'}{3} + \frac{E_P}{3E_{6-7}}, \tag{A.26}$$

$$\gamma_{\Delta 2} = -\frac{E_{PX}}{12}\left(\frac{1}{E_{8C-8}} + \frac{1}{E_{8C-7}}\right) - \frac{L' - M'}{6} + \frac{E_P}{12}\left(\frac{1}{E_{6-8}} + \frac{1}{E_{6-7}}\right), \tag{A.27}$$

$$\gamma_{\Delta 3} = \frac{E_{PX}}{12}\left(\frac{1}{E_{8C-8}} + \frac{1}{E_{8C-7}}\right) - \frac{N'}{6} + \frac{E_P}{12}\left(\frac{1}{E_{6-8}} + \frac{1}{E_{6-7}}\right); \tag{A.28}$$

together with the notations in table A.1 where $\check{k}_\pm = \check{k}_x \pm i\check{k}_y$, $\check{k}^2_\rho = \check{k}^2_x + \check{k}^2_y$. E'_{8C}, E'_{7C}, E_8 , and E_7 would, respectively, be the energies $E(\Gamma_{8C})$, $E(\Gamma_{7C})$, $E(\Gamma_8)$, and $E(\Gamma_7)$ at $\mathbf{k} = 0$ if the interband spin-orbit coupling Δ' were equal to zero.

TABLE A.1: Notations for 14×14 $\boldsymbol{k.p}$ Hamiltonian.

$E^H_{8C} = E'_{8C} - \gamma'_{C1}\check{k}^2 + \mathfrak{U}'_C$	$E^L_{8C} = E'_{8C} - \gamma'_{C1}\check{k}^2 - \mathfrak{U}'_C$
$E^k_{7C} = E'_{7C} - \gamma'_{C\Delta 1}\check{k}^2$	$E^k_6 = E_6 + \gamma'_C\check{k}^2$
$E^H_8 = E'_8 - \gamma'_1\check{k}^2 + \mathfrak{U}'$	$E^L_8 = E'_8 - \gamma'_1\check{k}^2 - \mathfrak{U}'$
$E^k_7 = E'_7 - \gamma'_{\Delta 1}\check{k}^2$	$\mathfrak{U}'_C = \gamma'_{C2}\left(2\check{k}^2_z - \check{k}^2_\rho\right)$
$\mathfrak{U}'_{C\Delta} = \gamma'_{C\Delta 2}\left(2\check{k}^2_z - \check{k}^2_\rho\right)$	$\mathfrak{B}'_C = 2\sqrt{3}\gamma'_{C3}\check{k}_z\check{k}_-$
$\mathfrak{B}'_{C\Delta} = 2\sqrt{3}\gamma'_{C\Delta 3}\check{k}_z\check{k}_-$	$\mathfrak{C}'_C = \sqrt{3}\left[\gamma'_{C2}\left(\check{k}^2_x - \check{k}^2_y\right) - 2i\gamma'_{C3}\check{k}_x\check{k}_y\right]$
$\mathfrak{C}'_{\Delta C} = \sqrt{3}\left[\gamma'_{\Delta C2}\left(\check{k}^2_x - \check{k}^2_y\right) - 2i\gamma'_{\Delta C3}\check{k}_x\check{k}_y\right]$	$\mathfrak{U}' = \gamma'_2\left(2\check{k}^2_z - \check{k}^2_\rho\right)$
$\mathfrak{U}'_\Delta = \gamma'_{\Delta 2}\left(2\check{k}^2_z - \check{k}^2_\rho\right)$	$\mathfrak{B}' = 2\sqrt{3}\gamma'_3\check{k}_z\check{k}_-$
$\mathfrak{B}'_\Delta = 2\sqrt{3}\gamma'_{\Delta 3}\check{k}_z\check{k}_-$	$\mathfrak{C}' = \sqrt{3}\left[\gamma'_2\left(\check{k}^2_x - \check{k}^2_y\right) - 2i\gamma'_3\check{k}_x\check{k}_y\right]$
$\mathfrak{C}'_\Delta = \sqrt{3}\left[\gamma'_{\Delta 2}\left(\check{k}^2_x - \check{k}^2_y\right) - 2i\gamma'_{\Delta 3}\check{k}_x\check{k}_y\right]$	

Furthermore, one has:

$$\gamma'_C = \gamma_C - \frac{E_P}{3}\left(\frac{2}{E_{6-8}} + \frac{1}{E_{6-7}}\right) + \frac{E'_P}{2}\left(\frac{2}{E_{8C-6}} + \frac{1}{E_{7C-6}}\right), \tag{A.29}$$

$$\gamma'_1 = \gamma_1 - \frac{E_P}{3E_{6-8}} - \frac{E_{PX}}{3}\left(\frac{1}{E_{7C-8}} + \frac{1}{E_{8C-8}}\right), \tag{A.30}$$

$$\gamma'_2 = \gamma_2 - \frac{E_P}{6E_{6-8}} + \frac{E_{PX}}{6E_{7C-8}}, \tag{A.31}$$

$$\gamma'_3 = \gamma_3 - \frac{E_P}{6E_{6-8}} - \frac{E_{PX}}{6E_{7C-8}}, \tag{A.32}$$

TABLE A.2: $k = 0$ Parameters used in 14-band $\mathbf{k} \cdot \mathbf{p}$ model.

	AlP	GaP	InP	AlAs	GaAs	InAs	AlSb	GaSb	InSb
E_0 (eV)	3.63	2.2895	1.423	3.130	1.519	0.418	2.38	0.81	0.235
$E_0^{'}$ (eV)	4.78	4.38	4.78	4.55	4.54	4.48	3.53	3.11	3.18
Δ_0 (eV)	0.06	0.08	0.107	0.3	0.341	0.38	0.67	0.76	0.81
$\Delta_0^{'}$ (eV)	0.04	0.09	0.19	0.15	0.2	0.31	0.24	0.33	0.46
Δ_0^{-} (eV)	-0.03	0.04	0.11	-0.19	-0.17	-0.05	-0.41	-0.4	-0.26
P (eV,A^0)	9.51	9.53	8.45	8.88	9.88	9.01	8.57	9.69	9.63
$P^{'}$ (eV,A^0)	0.19	0.36	0.34	0.34	0.41	0.66	0.51	1.34	1.2
Q (eV,A^0)	8.10	8.49	7.88	8.07	8.68	7.72	7.8	8.25	7.83

$$\gamma'_{C1} = \gamma_{C1} + \frac{E'_P}{3E_{8C-6}} + \frac{E_{PX}}{3}\left(\frac{1}{E_{8C-8}} + \frac{1}{E_{8C-7}}\right), \tag{A.33}$$

$$\gamma'_{C2} = \gamma_{C2} + \frac{E'_P}{6E_{8C-6}} - \frac{E_{PX}}{6E_{8C-7}}, \tag{A.34}$$

$$\gamma'_{C3} = \gamma_{C3} + \frac{E'_P}{6E_{8C-6}} + \frac{E_{PX}}{6E_{8C-7}}, \tag{A.35}$$

$$\gamma'_{\Delta j} \simeq \gamma'_j; \;\; \gamma'_{C\Delta j} \simeq \gamma'_{Cj}, \tag{A.36}$$

It is necessary to stress the particular point that the lack of inversion center does not contribute to the parameters in the VB. We take here the Hamiltonian in a 14×14 **k**.**p** model and plot in Fig. A.2 the band structure along three characteristic directions with parameters close to the values introduced in Ref. [92]. One needs to note also that we consider here the overall 14×14 **k**.**p** Hamiltonian with the perturbation of all remote bands which includes linear or quadratic k_i terms but no cubic terms. Finally, the 14×14 Hamiltonian has the form:

$$
H_{14\times14} = \begin{array}{c}
\begin{matrix} |c\tfrac{3}{2}\rangle & |c\tfrac{1}{2}\rangle & |c\tfrac{-1}{2}\rangle & |c\tfrac{-3}{2}\rangle & |c\tfrac{7}{2}\rangle & |c\tfrac{-7}{2}\rangle & |+\rangle & |-\rangle & |\tfrac{3}{2}\rangle & |\tfrac{1}{2}\rangle & |\tfrac{-1}{2}\rangle & |\tfrac{-3}{2}\rangle & |\tfrac{7}{2}\rangle & |\tfrac{-7}{2}\rangle \end{matrix} \\
\begin{pmatrix}
E_{8C}^{H} & \mathfrak{B}_{C}^{\prime} & \mathfrak{C}_{C}^{\prime} & 0 & \frac{1}{\sqrt{2}}\mathfrak{B}_{C\Delta}^{\prime} & \sqrt{2}\mathfrak{C}_{C\Delta}^{\prime} & \frac{-1}{\sqrt{2}}P^{\prime-} & 0 & \frac{1}{3}\Delta^{\prime} & \frac{1}{\sqrt{3}}P_{X}^{+} & \frac{1}{\sqrt{3}}P_{X}^{z} & 0 & \frac{1}{\sqrt{6}}P_{X}^{+} & \sqrt{\frac{2}{3}}P_{X}^{z} \\
\mathfrak{B}_{C}^{\prime *} & E_{8C}^{L} & 0 & \mathfrak{C}_{C}^{\prime} & -\sqrt{2}\mathfrak{U}_{C\Delta}^{\prime} & -\sqrt{\frac{3}{2}}\mathfrak{B}_{C\Delta}^{\prime} & \sqrt{\frac{2}{3}}P^{\prime z} & \frac{-1}{\sqrt{6}}P^{\prime-} & \frac{-1}{\sqrt{3}}P_{X}^{-} & \frac{1}{3}\Delta^{\prime} & 0 & \frac{1}{\sqrt{3}}P_{X}^{z} & 0 & \frac{-1}{\sqrt{2}}P_{X}^{+} \\
\mathfrak{C}_{C}^{\prime *} & 0 & E_{8C}^{L} & -\mathfrak{B}_{C}^{\prime} & -\sqrt{\frac{3}{2}}\mathfrak{B}_{C\Delta}^{\prime *} & \sqrt{2}\mathfrak{U}_{C\Delta}^{\prime} & \frac{1}{\sqrt{6}}P^{\prime+} & \sqrt{\frac{2}{3}}P^{\prime z} & \frac{-1}{\sqrt{3}}P_{X}^{z} & 0 & \frac{1}{3}\Delta^{\prime} & \frac{1}{\sqrt{3}}P_{X}^{+} & \frac{1}{\sqrt{2}}P_{X}^{-} & 0 \\
0 & \mathfrak{C}_{C}^{\prime *} & -\mathfrak{B}_{C}^{\prime *} & E_{8C}^{H} & -\sqrt{2}\mathfrak{C}_{C\Delta}^{\prime *} & \frac{1}{\sqrt{2}}\mathfrak{B}_{C\Delta}^{\prime *} & 0 & \frac{1}{\sqrt{2}}P^{\prime+} & 0 & \frac{-1}{\sqrt{3}}P_{X}^{z} & \frac{1}{\sqrt{3}}P_{X}^{-} & \frac{1}{3}\Delta^{\prime} & \sqrt{\frac{2}{3}}P_{X}^{z} & \frac{-1}{\sqrt{6}}P_{X}^{-} \\
\frac{1}{\sqrt{2}}\mathfrak{B}_{C\Delta}^{\prime *} & -\sqrt{2}\mathfrak{U}_{C\Delta}^{\prime} & -\sqrt{\frac{3}{2}}\mathfrak{B}_{C\Delta}^{\prime} & -\sqrt{2}\mathfrak{C}_{C\Delta}^{\prime} & E_{7C}^{k} & 0 & \frac{1}{\sqrt{3}}P^{\prime z} & \frac{1}{\sqrt{3}}P^{\prime-} & \frac{-1}{\sqrt{6}}P_{X}^{-} & 0 & \frac{-1}{\sqrt{2}}P_{X}^{+} & -\sqrt{\frac{2}{3}}P_{X}^{z} & 0 & \frac{-2}{3}\Delta^{\prime} \\
\sqrt{2}\mathfrak{C}_{C\Delta}^{\prime *} & -\sqrt{\frac{3}{2}}\mathfrak{B}_{C\Delta}^{\prime *} & \sqrt{2}\mathfrak{U}_{C\Delta}^{\prime} & \frac{1}{\sqrt{2}}\mathfrak{B}_{C\Delta}^{\prime} & 0 & E_{7C}^{k} & \frac{1}{\sqrt{3}}P^{\prime+} & \frac{-1}{\sqrt{3}}P^{\prime z} & \frac{-1}{\sqrt{2}}P^{+} & \sqrt{\frac{2}{3}}P^{z} & 0 & \frac{1}{\sqrt{3}}P^{z} & \frac{1}{\sqrt{3}}P^{-} \\
\frac{-1}{\sqrt{2}}P^{\prime+} & \sqrt{\frac{2}{3}}P^{\prime z} & \frac{1}{\sqrt{6}}P^{\prime-} & 0 & \frac{1}{\sqrt{3}}P^{\prime+} & \frac{1}{\sqrt{3}}P^{\prime-} & E_{6}^{k} & 0 & \frac{-1}{\sqrt{2}}P^{+} & \frac{-1}{\sqrt{6}}P^{+} & \mathfrak{B}^{\prime} & \frac{1}{\sqrt{3}}P^{-} & \frac{1}{\sqrt{3}}P^{+} & \frac{-1}{\sqrt{3}}P^{z} \\
0 & \frac{-1}{\sqrt{6}}P^{\prime+} & \sqrt{\frac{2}{3}}P^{\prime z} & \frac{1}{\sqrt{2}}P^{\prime-} & \frac{1}{\sqrt{3}}P^{\prime+} & \frac{-1}{\sqrt{3}}P^{\prime z} & 0 & E_{6}^{k} & 0 & E_{8}^{H} & \mathfrak{B}^{\prime} & \mathfrak{C}^{\prime} & 0 & \sqrt{2}\mathfrak{C}_{\Delta}^{\prime} \\
\frac{1}{3}\Delta^{\prime} & \frac{-1}{\sqrt{3}}P_{X}^{+} & \frac{-1}{\sqrt{3}}P_{X}^{z} & 0 & \frac{-1}{\sqrt{6}}P_{X}^{+} & -\sqrt{\frac{2}{3}}P_{X}^{z} & \frac{-1}{\sqrt{2}}P_{-} & 0 & E_{8}^{H} & \mathfrak{B}^{\prime *} & E_{8}^{L} & \mathfrak{C}^{\prime} & 0 & -\sqrt{2}\mathfrak{U}^{\prime} \\
\frac{1}{3}\Delta^{\prime} & \frac{1}{3}\Delta^{\prime} & 0 & \frac{-1}{\sqrt{3}}P_{X}^{z} & 0 & \frac{1}{\sqrt{2}}P_{X}^{+} & \sqrt{\frac{2}{3}}P^{z} & \frac{-1}{\sqrt{6}}P_{-} & \mathfrak{C}^{\prime *} & 0 & E_{8}^{L} & -\mathfrak{B}^{\prime} & -\sqrt{\frac{3}{2}}\mathfrak{B}_{\Delta}^{\prime *} & \sqrt{2}\mathfrak{U}_{\Delta}^{\prime} \\
\frac{1}{\sqrt{3}}P_{X}^{-} & \frac{1}{3}\Delta^{\prime} & \frac{-1}{\sqrt{3}}P_{X}^{-} & \frac{1}{3}\Delta^{\prime} & -\sqrt{\frac{2}{3}}P_{X}^{z} & \frac{1}{\sqrt{6}}P_{X}^{-} & 0 & \frac{1}{\sqrt{2}}P^{+} & 0 & \mathfrak{C}^{\prime *} & -\mathfrak{B}^{\prime *} & E_{8}^{H} & -\sqrt{2}\mathfrak{C}_{\Delta}^{\prime *} & \frac{1}{\sqrt{2}}\mathfrak{B}_{\Delta}^{\prime *} \\
\frac{1}{\sqrt{3}}P_{X}^{z} & 0 & \frac{1}{\sqrt{2}}P_{X}^{+} & \sqrt{\frac{2}{3}}P_{X}^{z} & \frac{-1}{\sqrt{2}}P_{X}^{-} & 0 & \frac{1}{\sqrt{3}}P^{z} & \frac{1}{\sqrt{3}}P^{-} & \frac{1}{\sqrt{2}}\mathfrak{B}_{\Delta}^{\prime *} & -\sqrt{2}\mathfrak{U}^{\prime} & -\sqrt{\frac{3}{2}}\mathfrak{B}_{\Delta}^{\prime} & -\sqrt{2}\mathfrak{C}_{\Delta}^{\prime} & E_{7}^{k} & 0 \\
0 & \frac{1}{\sqrt{3}}P_{X}^{z} & \frac{-1}{\sqrt{3}}P_{X}^{-} & \frac{1}{3}\Delta^{\prime} & -\sqrt{\frac{2}{3}}P_{X}^{z} & \frac{1}{\sqrt{6}}P_{X}^{-} & 0 & \frac{1}{\sqrt{2}}P^{+} & 0 & \mathfrak{C}^{\prime *} & -\mathfrak{B}^{\prime *} & E_{8}^{H} & -\sqrt{2}\mathfrak{C}_{\Delta}^{\prime *} & \frac{1}{\sqrt{2}}\mathfrak{B}_{\Delta}^{\prime *} \\
\frac{1}{\sqrt{6}}P_{X}^{-} & 0 & \frac{1}{\sqrt{2}}P_{X}^{+} & \sqrt{\frac{2}{3}}P_{X}^{z} & \frac{-2}{3}\Delta^{\prime} & 0 & \frac{1}{\sqrt{3}}P^{z} & \frac{1}{\sqrt{3}}P^{-} & \frac{1}{\sqrt{2}}\mathfrak{B}_{\Delta}^{\prime *} & -\sqrt{2}\mathfrak{U}^{\prime} & -\sqrt{\frac{3}{2}}\mathfrak{B}_{\Delta}^{\prime} & -\sqrt{2}\mathfrak{C}_{\Delta}^{\prime} & E_{7}^{k} & 0 \\
\sqrt{\frac{2}{3}}P_{X}^{z} & \frac{-1}{\sqrt{2}}P_{X}^{-} & 0 & \frac{-1}{\sqrt{6}}P_{X}^{+} & 0 & \frac{-2}{3}\Delta^{\prime} & \frac{1}{\sqrt{3}}P^{+} & \frac{-1}{\sqrt{3}}P^{z} & -\sqrt{\frac{3}{2}}\mathfrak{B}_{\Delta}^{\prime *} & \sqrt{2}\mathfrak{C}_{\Delta}^{\prime *} & \frac{1}{\sqrt{2}}\mathfrak{B}_{\Delta}^{\prime} & 0 & E_{7}^{k} & 0
\end{pmatrix}
\end{array}
\tag{A.37}
$$

A.2 30-band k.p model [29, 412, 413]

We recall here the 30 × 30 band $\boldsymbol{k.p}$ Hamiltonian taken from Ref. [29] which takes into account the Γ_6^V,Γ_7^V;Γ_8^V; Γ_6^C; Γ_7^C; Γ_8^C; Γ_6^U; Γ_3^C; Γ_{7d}^C; Γ_{8d}^C; and Γ_{6q}^C. The basis functions are the same Bloch functions as those used by Cardona and Pollak to describe Si and Ge band structures without spin-orbit coupling. The set of Luttinger–Kohn periodic amplitudes used in our calculations is specified in TableA.3. Note that Γ_{6u} and Γ_{6q} are due to the $(n+1)$ s levels whereas the ns levels induce Γ_{6V} VB and Γ_{6C} CB. Our 30 × 30 band $\boldsymbol{k.p}$ model is schematically represented at $\boldsymbol{k}=0$ in Fig. A.8. In this figure, both the wavefunctions corresponding to the bands and the matrix elements are indicated. The Hamiltonian H_{30} is given explicitly for $\boldsymbol{k}=(k_x,k_y,k_z)$. For the T_d group, the $\boldsymbol{k.p}$ elements of interest are: $P=\frac{\hbar}{m_0}\langle S|P_x|iX\rangle$, $P_X=\frac{\hbar}{m_0}\langle X_C|P_y|iZ\rangle$, $P_2=\frac{\hbar}{m_0}\langle S_2|P_x|iX\rangle$, $P_3=\frac{\hbar}{m_0}\langle D_z|P_x|iX\rangle$, $P_S=\frac{\hbar}{m_0}\langle S_V|P_x|iX_C\rangle$, $P_d=\frac{\hbar}{m_0}\langle S|P_x|iX_d\rangle$, $P_{Xd}=\frac{\hbar}{m_0}\langle X_C|P_y|iZ_d\rangle$, $P_{2d}=\frac{\hbar}{m_0}\langle S_2|P_x|iX_d\rangle$, $P_{3d}=\frac{\hbar}{m_0}\langle D_z|P_x|iX_d\rangle$, $P_U=\frac{\hbar}{m_0}\langle S_U|P_x|iX_C\rangle$, $P'=\frac{\hbar}{m_0}\langle S|P_x|iX_C\rangle$, $P'_2=\frac{\hbar}{m_0}\langle S_2|P_x|iX_C\rangle$, $P'_3=\frac{\hbar}{m_0}\langle D_z|P_x|iX_C\rangle$, $P'_S=\frac{\hbar}{m_0}\langle S_V|P_x|iX\rangle$, $P'_U=\frac{\hbar}{m_0}\langle S_U|P_x|iX\rangle$, $P'_d=\frac{\hbar}{m_0}\langle X_d|P_y|iZ\rangle$, $P'_{Sd}=\frac{\hbar}{m_0}\langle S_V|P_x|iX_d\rangle$ and $P'_{ud}=\frac{\hbar}{m_0}\langle S_U|P_x|iX_d\rangle$.

TABLE A.3: Luttinger–Kohn periodic amplitudes used in the 30-band **k.p** model. The phases are chosen to give real matrix elements to the **k.p** Hamiltonian.

$\lvert q+\rangle = \lvert S_q\uparrow\rangle$	$\lvert q-\rangle = \lvert S_q\downarrow\rangle$
$\left\lvert d\frac{3}{2}\right\rangle = \left\lvert i\left[\frac{1}{\sqrt{2}}(X_d-iY_d)\downarrow\right]\right\rangle$	$\left\lvert d-\frac{3}{2}\right\rangle = \left\lvert i\left[-\frac{1}{\sqrt{2}}(X_d+iY_d)\uparrow\right]\right\rangle$
$\left\lvert d\frac{1}{2}\right\rangle = \left\lvert i\left[\sqrt{\frac{2}{3}}Z_d\uparrow-\frac{1}{\sqrt{6}}(X_d+iY_d)\downarrow\right]\right\rangle$	$\left\lvert d-\frac{1}{2}\right\rangle = \left\lvert i\left[\frac{1}{\sqrt{6}}(X_d-iY_d)\uparrow+\sqrt{\frac{2}{3}}Z_d\downarrow\right]\right\rangle$
$\left\lvert d\frac{7}{2}\right\rangle = \left\lvert i\left[\frac{1}{\sqrt{3}}Z_d\uparrow+\frac{1}{\sqrt{3}}(X_d+iY_d)\downarrow\right]\right\rangle$	$\left\lvert d-\frac{1}{2}\right\rangle = \left\lvert i\left[\frac{1}{\sqrt{3}}(X_d-iY_d)\uparrow-\frac{1}{\sqrt{3}}Z_d\downarrow\right]\right\rangle$
$\lvert D_z+\rangle = \lvert D_z\uparrow\rangle$	$\lvert D_z-\rangle = \lvert D_z\downarrow\rangle$
$\lvert D_x+\rangle = \lvert D_x\uparrow\rangle$	$\lvert D_x-\rangle = \lvert D_x\downarrow\rangle$
$\lvert U+\rangle = \lvert S_u\uparrow\rangle$	$\lvert U-\rangle = \lvert S_u\downarrow\rangle$
$\left\lvert C\frac{3}{2}\right\rangle = \left\lvert i\left[\frac{1}{\sqrt{2}}(X_C-iY_C)\downarrow\right]\right\rangle$	$\left\lvert C-\frac{3}{2}\right\rangle = \left\lvert i\left[-\frac{1}{\sqrt{2}}(X_C+iY_C)\uparrow\right]\right\rangle$
$\left\lvert C\frac{1}{2}\right\rangle = \left\lvert i\left[\sqrt{\frac{2}{3}}Z_C\uparrow-\frac{1}{\sqrt{6}}(X_C+iY_C)\downarrow\right]\right\rangle$	$\left\lvert C-\frac{1}{2}\right\rangle = \left\lvert i\left[\frac{1}{\sqrt{6}}(X_C-iY_C)\uparrow+\sqrt{\frac{2}{3}}Z_C\downarrow\right]\right\rangle$
$\left\lvert C\frac{7}{2}\right\rangle = \left\lvert i\left[\frac{1}{\sqrt{3}}Z_C\uparrow+\frac{1}{\sqrt{3}}(X_C+iY_C)\downarrow\right]\right\rangle$	$\left\lvert C-\frac{1}{2}\right\rangle = \left\lvert i\left[\frac{1}{\sqrt{3}}(X_C-iY_C)\uparrow-\frac{1}{\sqrt{3}}Z_C\downarrow\right]\right\rangle$
$\lvert +\rangle = \lvert S\uparrow\rangle$	$\lvert -\rangle = \lvert S\downarrow\rangle$
$\left\lvert \frac{3}{2}\right\rangle = \left\lvert i\left[\frac{1}{\sqrt{2}}(X-iY)\downarrow\right]\right\rangle$	$\left\lvert -\frac{3}{2}\right\rangle = \left\lvert i\left[-\frac{1}{\sqrt{2}}(X+iY)\uparrow\right]\right\rangle$
$\left\lvert \frac{1}{2}\right\rangle = \left\lvert i\left[\sqrt{\frac{2}{3}}Z\uparrow-\frac{1}{\sqrt{6}}(X+iY)\downarrow\right]\right\rangle$	$\left\lvert -\frac{1}{2}\right\rangle = \left\lvert i\left[\frac{1}{\sqrt{6}}(X-iY)\uparrow+\sqrt{\frac{2}{3}}Z\downarrow\right]\right\rangle$
$\left\lvert \frac{7}{2}\right\rangle = \left\lvert i\left[\frac{1}{\sqrt{3}}Z\uparrow+\frac{1}{\sqrt{3}}(X+iY)\downarrow\right]\right\rangle$	$\left\lvert -\frac{1}{2}\right\rangle = \left\lvert i\left[\frac{1}{\sqrt{3}}(X-iY)\uparrow-\frac{1}{\sqrt{3}}Z\downarrow\right]\right\rangle$
$\lvert V+\rangle = \lvert S_V\uparrow\rangle$	$\lvert V-\rangle = \lvert S_V\downarrow\rangle$

And the spin-orbit energies are defined as:

(i) The core SOI

$$\begin{aligned}\Delta &= \frac{3\hbar}{4m_0^2c^2}\left\langle X\left|\frac{\partial V}{\partial x}p_y-\frac{\partial V}{\partial y}p_x\right|iY\right\rangle\\ \Delta_C &= \frac{3\hbar}{4m_0^2c^2}\left\langle X_C\left|\frac{\partial V}{\partial x}p_y-\frac{\partial V}{\partial y}p_x\right|iY_C\right\rangle\\ \Delta_d &= \frac{3\hbar}{4m_0^2c^2}\left\langle X_d\left|\frac{\partial V}{\partial x}p_y-\frac{\partial V}{\partial y}p_x\right|iY_d\right\rangle\end{aligned} \tag{A.38}$$

(ii) The coupling between the two different multiplets (Γ_8,Γ_7) and $(\Gamma_{8d},\Gamma_{7d})$.

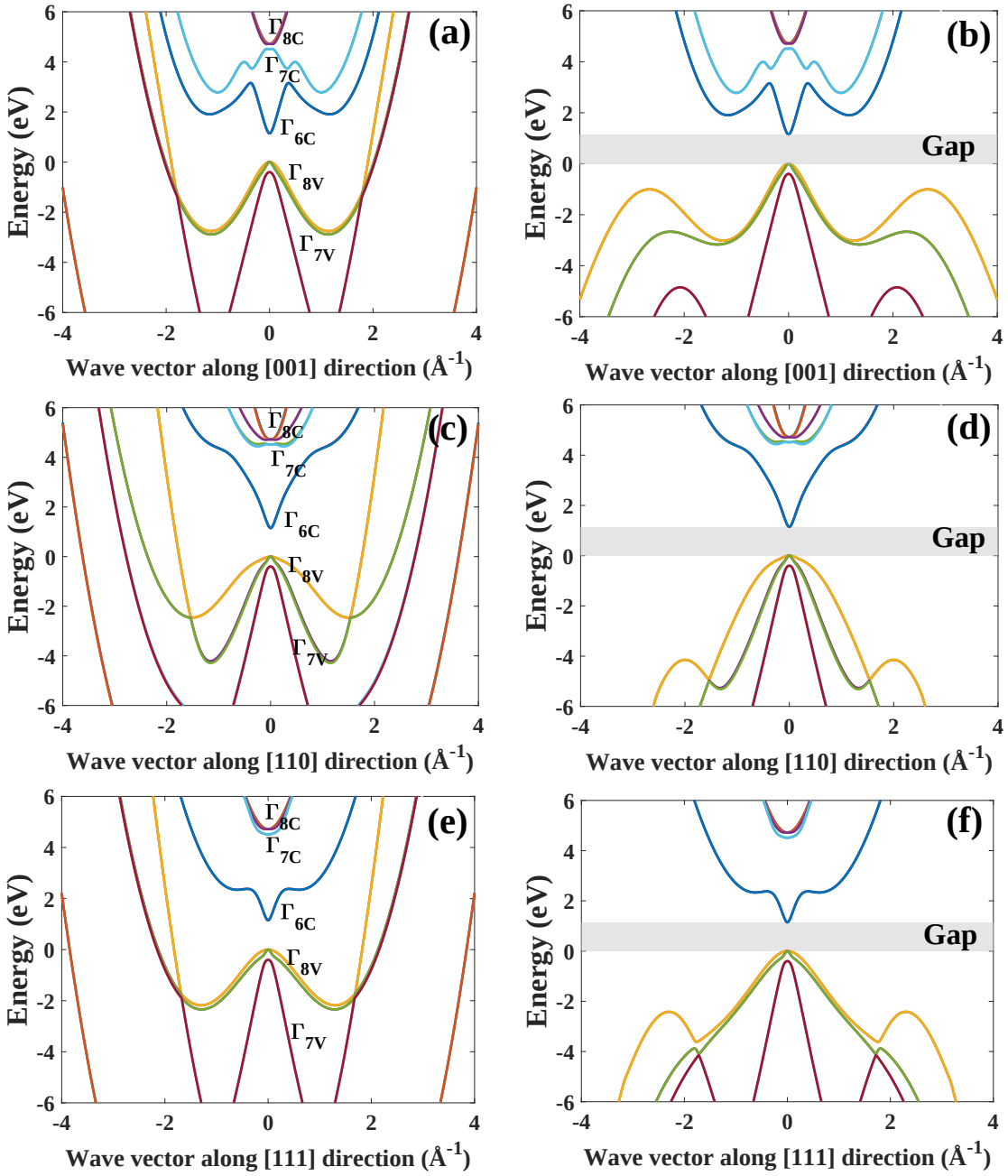

FIGURE A.4: Real band structure of InGaAs via 30-band $\boldsymbol{k.p}$ model before (a,c,e) and after (b,d,f) using our novel ghost-band method to remove spurious states.

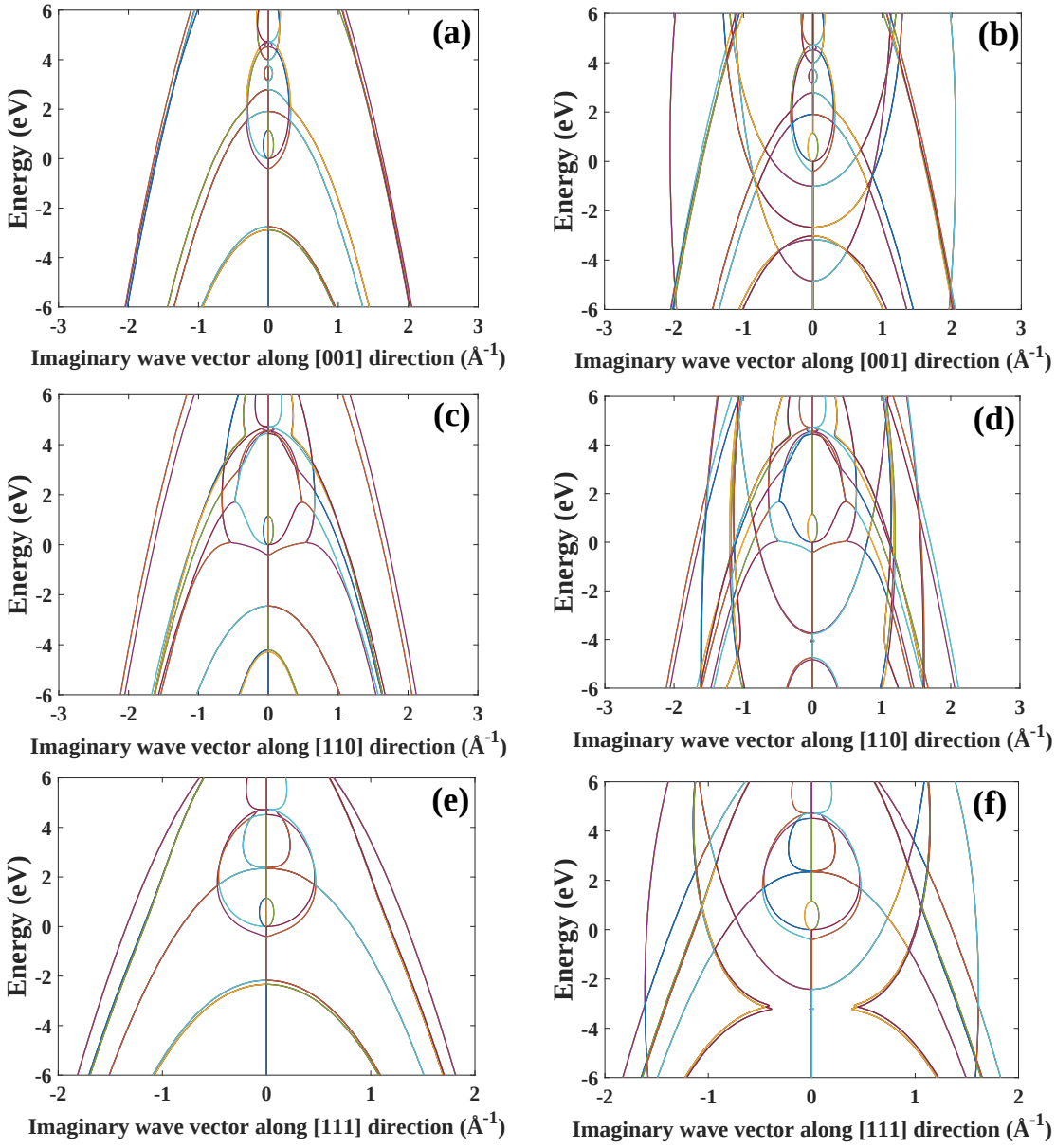

FIGURE A.5: Complex band structure of InGaAs via 30-band $\boldsymbol{k.p}$ model before (a,c,e) and after (b,d,f) using our novel ghost-band method to remove spurious states.

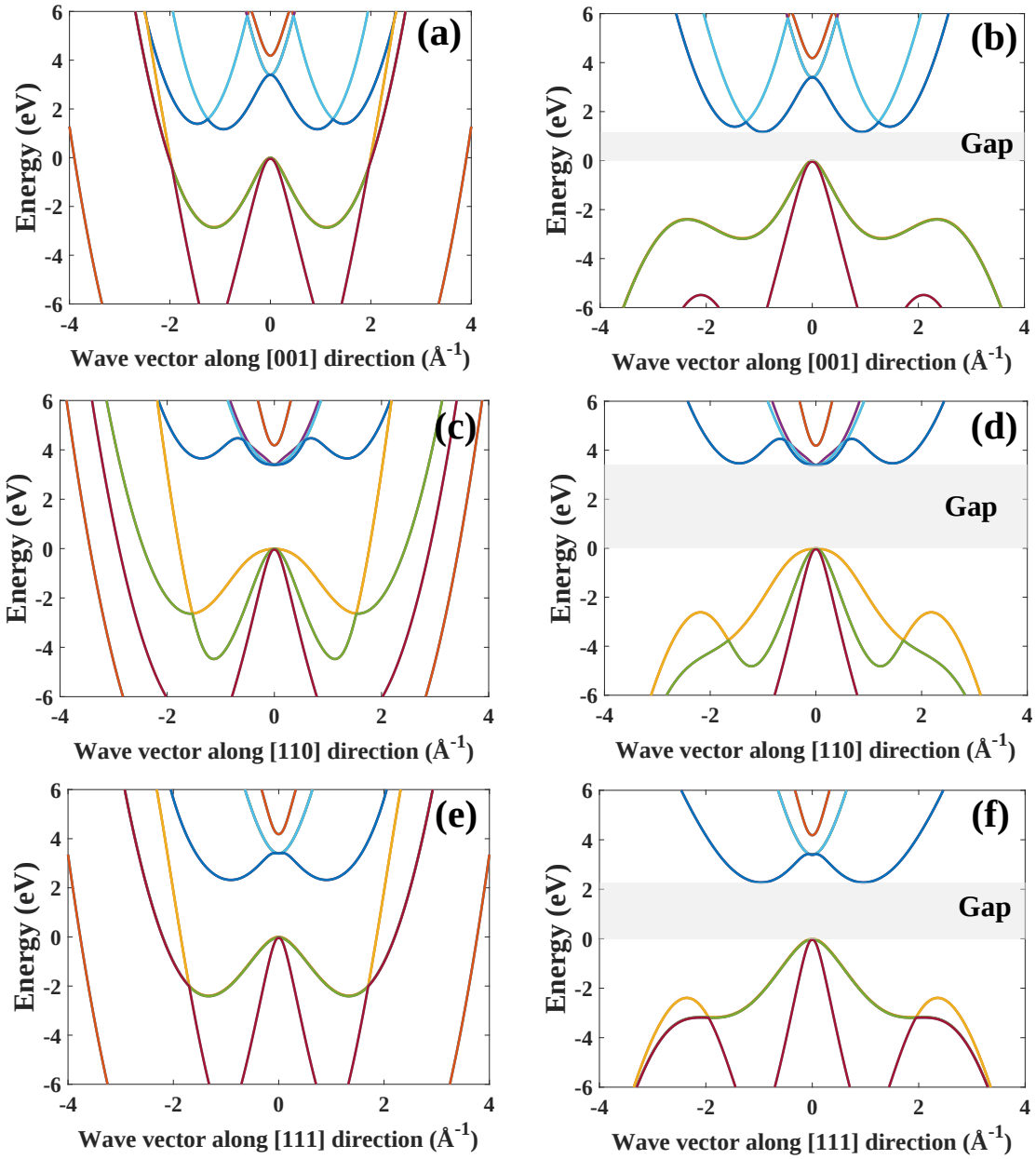

FIGURE A.6: Real band structure of Silicon via 30-band $\boldsymbol{k.p}$ model before (a,c,e) and after (b,d,f) using our novel ghost-band method to remove spurious states.

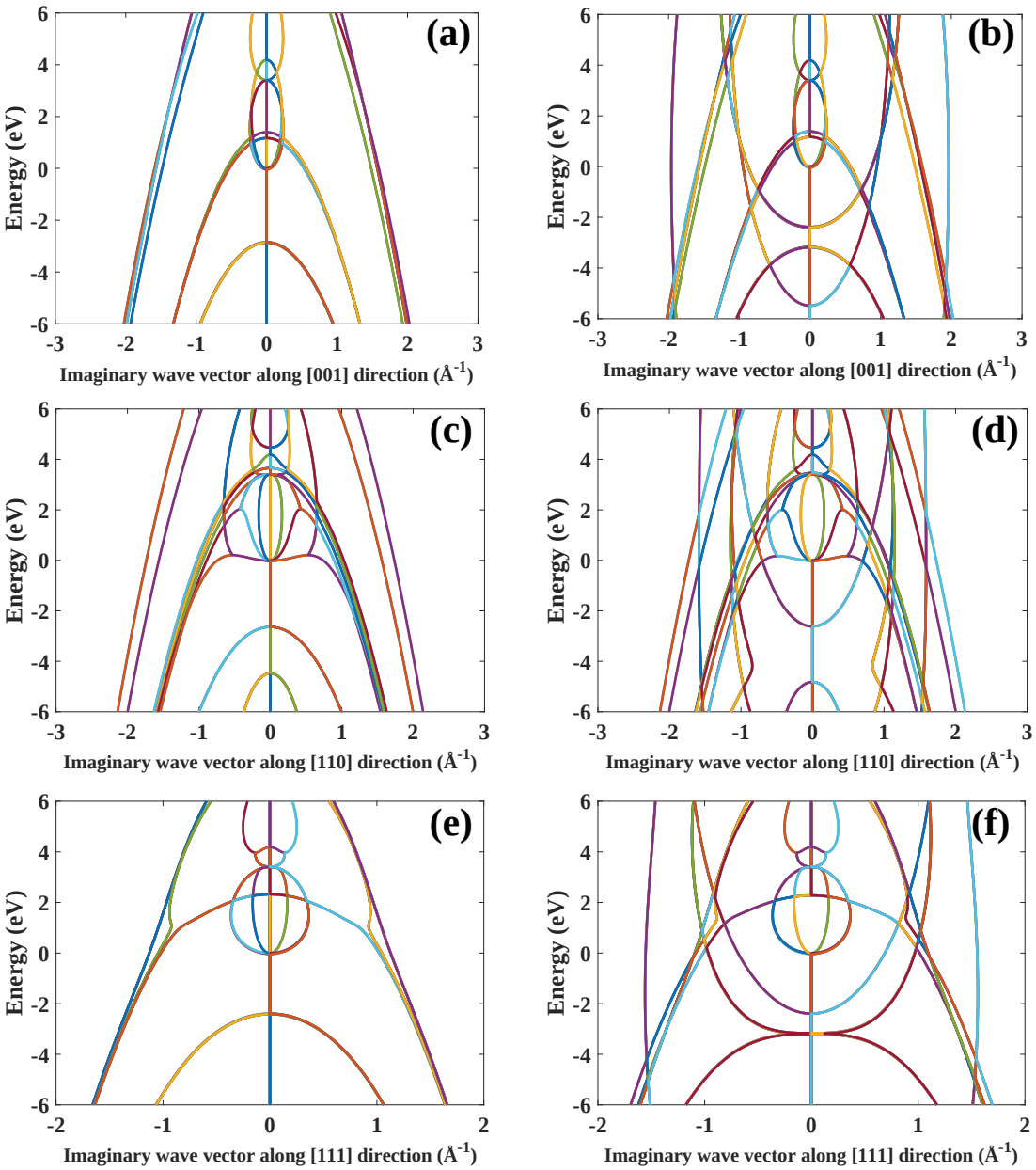

FIGURE A.7: Complex band structure of Silicon via 30-band $\boldsymbol{k.p}$ model before (a,c,e) and after (b,d,f) using our novel ghost-band method to remove spurious states.

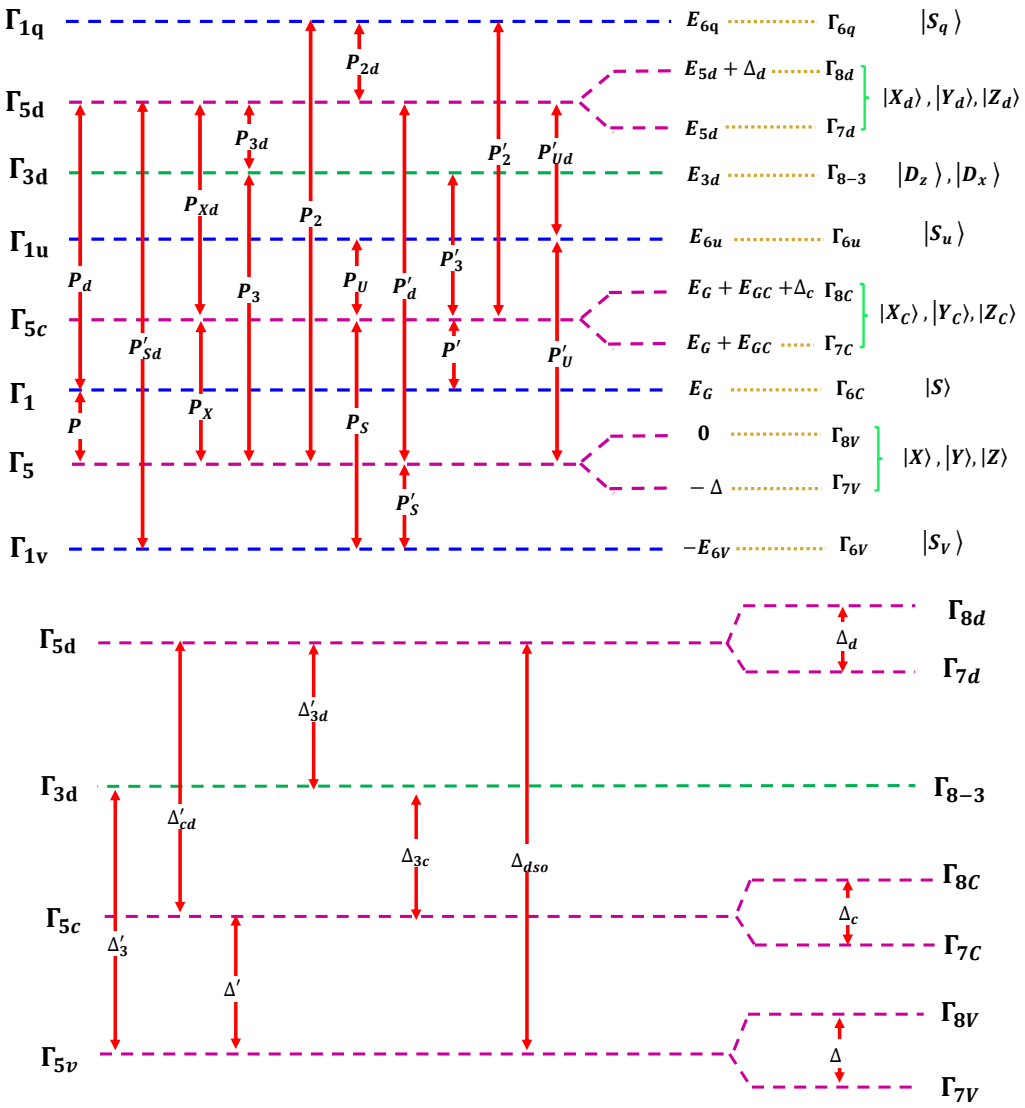

FIGURE A.8: Schematic representation of the 30-band **k.p** model representing involved bands, relevant parameters, momentum matrix elements and spin-orbit couplings.

$$\Delta_{dso} = \frac{3\hbar}{4m_0^2c^2}\left\langle X_d \left| \frac{\partial V}{\partial x}p_y - \frac{\partial V}{\partial y}p_x \right| iY \right\rangle \tag{A.39}$$

(iii) The coupling between $(\Gamma_{8C}, \Gamma_{7C})$ multiplet and $(\Gamma_{8d}, \Gamma_{7d})$ multiplet

$$\Delta_{3C} = \frac{3\hbar}{4m_0^2c^2}\left\langle D_1 \left| \frac{\partial V}{\partial x}p_z - \frac{\partial V}{\partial y}p_y \right| iX_C \right\rangle \tag{A.40}$$

For the T_d group, there are some additional SOCs:
(1) The coupling inside (Γ_8, Γ_7) multiplets:

$$\begin{aligned} \Delta^{'} &= \frac{3\hbar}{4m_0^2c^2}\left\langle X_C \left| \frac{\partial V}{\partial x}p_y - \frac{\partial V}{\partial y}p_x \right| iY \right\rangle \\ \Delta^{'}_{Cd} &= \frac{3\hbar}{4m_0^2c^2}\left\langle X_d \left| \frac{\partial V}{\partial x}p_y - \frac{\partial V}{\partial y}p_x \right| iY_C \right\rangle \end{aligned} \tag{A.41}$$

(2) The coupling inside (Γ_8, Γ_7)

$$\begin{aligned} \Delta^{'}_{3} &= \frac{3\hbar}{4m_0^2c^2}\left\langle D_1 \left| \frac{\partial V}{\partial x}p_y - \frac{\partial V}{\partial y}p_x \right| iX \right\rangle \\ \Delta^{'}_{3d} &= \frac{3\hbar}{4m_0^2c^2}\left\langle D_1 \left| \frac{\partial V}{\partial x}p_z - \frac{\partial V}{\partial y}p_y \right| iX_d \right\rangle \end{aligned} \tag{A.42}$$

Because of inversion symmetry, all the matrix elements that are indexed by "′" are equal to zero in the diamond group (O_h). Furthermore, we define the related energies as usual, namely the energies $E^{(')}_{Pj}$ by $E^{(')}_{Pj} = \left(\frac{2m_0}{\hbar^2}\right)\left[P^{(')}_j\right]^2$. All the matrix elements are real adjustable parameters. The 30-band $\boldsymbol{k.p}$ theory in the above form contains three kinds of parameters: the energy gaps, the matrix elements of the momentum and the spin-orbit interaction as well as the combinations of both. All these parameters are given explicitly in the Table. A.5. One may note that all the spin-orbit coupling terms appear between the different Γ_5 levels namely Γ_{5V} VBs, Γ_{5C} and Γ_{5d} CBs, or between Γ_5 and Γ_{3d} levels. Figure A.8 represents schematically the effect of spin-orbit interaction in the 30-band $\boldsymbol{k.p}$ model. One of the interests of this model is the calculation of Luttinger–Kohn parameters and Γ effective mass of CB. Using second order *Löwdin* perturbation theory, the Luttinger–Kohn parameters γ_j are given by:

$$\begin{aligned} \gamma_1 = -1 + \frac{E_P}{3E_G} + \frac{E_{PX}}{3}\left(\frac{1}{E_G + E_{GC}} + \frac{1}{E_G + E_{GC} + \Delta_C}\right) \\ + \frac{E^{'}_{PU}}{3E_{6U}} + \frac{4}{3}\frac{E_{P3}}{E_{3d}} + \frac{E^{'}_{Pd}}{3}\left(\frac{1}{E_{5d}} + \frac{1}{E_{5d} + \Delta_d}\right) \\ + \frac{E_{P2}}{3E_{6q}} - \frac{E^{'}_{PS}}{3E_{6V}} \end{aligned} \tag{A.43}$$

$$\gamma_2 = \frac{1}{6}\left(\frac{E_P}{E_G} + \frac{E^{'}_{PU}}{E_{6U}} + \frac{E_{P2}}{E_{6q}}\right) + \frac{2}{3}\frac{E_{P3}}{E_{3d}} - \frac{1}{6}\left(\frac{E_{PX}}{E_G + E_{GC}} + \frac{E^{'}_{Pd}}{E_{5d}} + \frac{E^{'}_{PS}}{E_{6V}}\right) \tag{A.44}$$

$$\gamma_3 = \frac{1}{6}\left(\frac{E_P}{E_G} + \frac{E_{PU}^{'}}{E_{6U}} + \frac{E_{P2}}{E_{6q}} + \frac{E_{Pd}^{'}}{E_{5d}} + \frac{E_{PX}}{E_F + E_{GC}}\right) - \frac{1}{3}\frac{E_{P3}}{E_{3d}} - \frac{1}{6}\frac{E_{PS}^{'}}{E_{6V}} \tag{A.45}$$

TABLE A.4: $k = 0$ energy levels (eV) used in the 30-band $\mathbf{k}\cdot\mathbf{p}$ model.

eV	Ge	Si	GaAs	AlAs	GaP	InAs	InP	InSb
Γ_{8C}	3.22	3.40	4.569	4.69	4.87	4.63	4.794	3.59
Γ_{7C}	3.01	3.40	4.488	4.54	4.87	4.39	4.72	3.16
Γ_6	0.90	4.185	1.519	3.13	2.895	0.37	1.424	0.25
Γ_8	0	0	0	0	0	0	0	0
Γ_7	-0.290	-0.044	-0.341	-0.30	-0.08	-0.43	-0.108	-0.82
Γ_{6v}	-13.14	-12.92	-12.55	-11.95	-12.30	-12.69	-11.078	-11.71
Γ_{6q}	18.36	13.46	13.64	13.64	13.3	12.64	12.99	12.64
Γ_{8d}	17.0	12.78	11.89	12.50	11.80	11.89	11.50	9.89
Γ_{7d}	17.0	12.78	11.89	12.50	11.80	11.89	11.50	9.89
Γ_{8-3}	10.47	9.66	10.17	10.50	9.80	9.88	9.50	8.88
Γ_{6u}	7.77	7.07	8.56	9.89	8.80	8.55	8.50	8.56

TABLE A.5: Dipole Matrix elements of GaAs and AlAs in a 30-band $\mathbf{k}\cdot\mathbf{p}$ model given in unit of energy with definition of Ref. [200]. Energies E and matrix elements P are linked by $E = 2m_0/\hbar^2 P^2$.

eV	Ge	Si	GaAs	AlAs	GaP	InAs	InP	InSb
E_P	24.60	19.96	22.37	21.10	21.0	19.04	18.012	24.5
E_{PX}	17.65	14.81	16.79	16.80	17.01	15.64	14.01	14.5
E_{P3}	5.212	4.475	4.916	2.99	3.41	3.89	4.01	3.77
E_{P2}	2.510	3.993	6.280	0.00	6.20	1.00	6.20	0.17
E_{PS}	1.071	1.092	2.434	0.10	3.43	5.00	3.43	0.40
$E_P^{'}$	0	0	0.0656	0.16	0.50	0.01	0.15	0.03
E_{Pd}	0.0051	1.193	0.010	0.1	0.10	0.1	0.1	0.03
E_{PXd}	12.23	7.491	4.344	4.12	7.00	5.00	7.50	2.34
E_{P3d}	15.76	9.856	8.888	13.06	12.50	11.66	11.15	8.60
E_{P2d}	27.59	20.76	23.15	3.50	2.51	2.50	2.51	7.99
E_{PU}	17.84	16.36	19.63	18.00	20.05	19.00	20.05	16.00
$E_{PS}^{'}$	0	0	0	0	0.012	0	0	0
$E_{Pd}^{'}$	0	0	0	0	0.20	0	0	0
$E_{Pud}^{'}$	0	0	0	0	0.10	0	0	0

The 30-band $\boldsymbol{k.p}$ Hamiltonian is given in the form:

$$H_{30\times30} = \begin{pmatrix} A & B \\ C & D \end{pmatrix} \tag{A.46}$$

where

$$
A = \begin{array}{c}
\begin{array}{cccccccccccccc}
|q+\rangle & |q-\rangle & \left|d\tfrac{3}{2}\right\rangle & \left|d\tfrac{1}{2}\right\rangle & \left|d-\tfrac{1}{2}\right\rangle & \left|d-\tfrac{3}{2}\right\rangle & \left|d\tfrac{7}{2}\right\rangle & \left|d-\tfrac{7}{2}\right\rangle & |D_z\uparrow\rangle & |D_z\downarrow\rangle & |D_x\uparrow\rangle & |D_x\downarrow\rangle & |U+\rangle & |U-\rangle
\end{array} \\
\left(\begin{array}{cccccccccccccc}
E^k_{6q} & 0 & \frac{-1}{\sqrt{2}}P^+_{2d} & \sqrt{\frac{2}{3}}P^z_{2d} & \frac{1}{\sqrt{6}}P^-_{2d} & 0 & \frac{1}{\sqrt{3}}P^z_{2d} & \frac{1}{\sqrt{3}}P^-_{2d} & 0 & 0 & 0 & 0 & 0 & 0 \\
0 & E^k_{6q} & 0 & \frac{-1}{\sqrt{6}}P^+_{2d} & \sqrt{\frac{2}{3}}P^z_{2d} & \frac{1}{\sqrt{2}}P^-_{2d} & \frac{1}{\sqrt{3}}P^+_{2d} & \frac{-1}{\sqrt{3}}P^z_{2d} & 0 & 0 & 0 & 0 & 0 & 0 \\
\frac{-1}{\sqrt{2}}P^-_{2d} & 0 & E^k_{8d} & \mathcal{B}_d & C_d & 0 & \frac{1}{\sqrt{2}}\mathcal{B}_d & \sqrt{2}C_d & \frac{-1}{\sqrt{2}}P^-_{3d} & \frac{-1}{2}\Delta'_{3d} & \sqrt{\frac{3}{2}}P^+_{3d} & 0 & \frac{-1}{\sqrt{2}}P'^-_{ud} & 0 \\
\sqrt{\frac{2}{3}}P^z_{2d} & \frac{-1}{\sqrt{6}}P^-_{2d} & \mathcal{B}^*_d & E^k_{8d} & 0 & C_d & -\sqrt{2}\mathcal{A}_d & -\sqrt{\frac{3}{2}}\mathcal{B}_d & -2\sqrt{\frac{2}{3}}P^z_{3d} & \frac{-1}{\sqrt{6}}P^-_{3d} & \frac{-1}{2}\Delta'_{3d} & \frac{1}{\sqrt{2}}P^+_{3d} & \sqrt{\frac{2}{3}}P'^z_{ud} & \frac{-1}{\sqrt{6}}P'^-_{ud} \\
\frac{1}{\sqrt{6}}P^+_{2d} & \sqrt{\frac{2}{3}}P^z_{2d} & C^*_d & 0 & E^k_{8d} & -\mathcal{B}_d & -\sqrt{\frac{3}{2}}\mathcal{B}^*_d & \sqrt{2}\mathcal{A}_d & \frac{1}{\sqrt{6}}P^+_{3d} & -2\sqrt{\frac{2}{3}}P^-_{3d} & \frac{-1}{\sqrt{2}}P^-_{3d} & \frac{1}{\sqrt{6}}P'^+_{ud} & \frac{1}{\sqrt{6}}P'^+_{ud} & \sqrt{\frac{2}{3}}P'^-_{ud} \\
0 & \frac{1}{\sqrt{2}}P^+_{2d} & 0 & C^*_d & -\mathcal{B}^*_d & E^k_{8d} & -\sqrt{2}C^*_d & \frac{1}{\sqrt{2}}\mathcal{B}^*_d & \frac{1}{2}\Delta'_{3d} & \frac{1}{\sqrt{2}}P^+_{3d} & 0 & -\sqrt{\frac{3}{2}}P^-_{3d} & 0 & \frac{1}{\sqrt{2}}P'^+_{ud} \\
\frac{1}{\sqrt{3}}P^z_{2d} & \frac{1}{\sqrt{3}}P^-_{2d} & \frac{1}{\sqrt{2}}\mathcal{B}^*_d & -\sqrt{2}\mathcal{A}_d & -\sqrt{\frac{3}{2}}\mathcal{B}_d & -\sqrt{2}C_d & E^k_{7d} & 0 & \frac{-2}{\sqrt{3}}P^z_{3d} & \frac{1}{\sqrt{3}}P^-_{3d} & 0 & -P^+_{3d} & \frac{1}{\sqrt{3}}P'^z_{ud} & \frac{1}{\sqrt{3}}P'^-_{ud} \\
\frac{1}{\sqrt{3}}P^+_{2d} & \frac{-1}{\sqrt{3}}P^z_{2d} & \sqrt{2}C^*_d & -\sqrt{\frac{3}{2}}\mathcal{B}^*_d & \sqrt{2}\mathcal{A}_d & \frac{1}{\sqrt{2}}\mathcal{B}_d & 0 & E^k_{7d} & \frac{1}{\sqrt{3}}P^+_{3d} & \frac{2}{\sqrt{3}}P^z_{3d} & -P^-_{3d} & 0 & \frac{1}{\sqrt{3}}P'^+_{ud} & \frac{-1}{\sqrt{3}}P'^z_{ud} \\
0 & 0 & \frac{-1}{\sqrt{2}}P^+_{3d} & -2\sqrt{\frac{2}{3}}P^z_{3d} & \frac{1}{\sqrt{6}}P^-_{3d} & \frac{1}{2}\Delta'_{3d} & \frac{-2}{\sqrt{3}}P^z_{3d} & \frac{1}{\sqrt{3}}P^-_{3d} & E^k_{3d} & 0 & 0 & 0 & 0 & 0 \\
0 & 0 & -\frac{1}{2}\Delta'_{3d} & \frac{-1}{\sqrt{6}}P^+_{3d} & -2\sqrt{\frac{2}{3}}P^z_{3d} & \frac{1}{\sqrt{2}}P^-_{3d} & \frac{1}{\sqrt{3}}P^+_{3d} & \frac{2}{\sqrt{3}}P^z_{3d} & 0 & E^k_{3d} & 0 & 0 & 0 & 0 \\
0 & 0 & \sqrt{\frac{3}{2}}P^-_{3d} & -\frac{1}{2}\Delta'_{3d} & \frac{-1}{\sqrt{2}}P^+_{3d} & 0 & 0 & -P^+_{3d} & 0 & 0 & E^k_{3d} & 0 & 0 & 0 \\
0 & 0 & 0 & \frac{1}{\sqrt{2}}P^-_{3d} & \frac{1}{2}\Delta'_{3d} & -\sqrt{\frac{3}{2}}P^+_{3d} & -P^-_{3d} & 0 & 0 & 0 & 0 & E^k_{3d} & 0 & 0 \\
0 & 0 & \frac{-1}{\sqrt{2}}P'^+_{ud} & \sqrt{\frac{2}{3}}P'^z_{ud} & \frac{1}{\sqrt{6}}P'^-_{ud} & 0 & \frac{1}{\sqrt{3}}P'^z_{ud} & \frac{1}{\sqrt{3}}P'^-_{ud} & 0 & 0 & 0 & 0 & E^k_{6u} & 0 \\
0 & 0 & 0 & \frac{-1}{\sqrt{6}}P'^+_{ud} & \sqrt{\frac{2}{3}}P'^z_{ud} & \frac{1}{\sqrt{6}}P'^-_{ud} & \frac{1}{\sqrt{3}}P'^+_{ud} & \frac{-1}{\sqrt{3}}P'^z_{ud} & 0 & 0 & 0 & 0 & 0 & E^k_{6u}
\end{array}\right)
\end{array}
\tag{A.47}
$$

$$
B = \begin{array}{c}
\begin{array}{cccccccccccccccc}
\left|c\frac{3}{2}\right\rangle & \left|c\frac{1}{2}\right\rangle & \left|c-\frac{1}{2}\right\rangle & \left|c-\frac{3}{2}\right\rangle & \left|c\frac{7}{2}\right\rangle & \left|c-\frac{7}{2}\right\rangle & |+\rangle & |-\rangle & \left|\frac{3}{2}\right\rangle & \left|\frac{1}{2}\right\rangle & \left|-\frac{1}{2}\right\rangle & \left|-\frac{3}{2}\right\rangle & \left|\frac{7}{2}\right\rangle & \left|-\frac{7}{2}\right\rangle & |V+\rangle & |V-\rangle
\end{array} \\
\left(\begin{array}{cccccccccccccccc}
\frac{-1}{\sqrt{2}}P_2'^{+} & \sqrt{\frac{2}{3}}P_2'^{z} & \frac{1}{\sqrt{6}}P_2'^{-} & 0 & \frac{1}{\sqrt{3}}P_2'^{z} & \frac{1}{\sqrt{3}}P_2'^{-} & 0 & 0 & \frac{-1}{\sqrt{2}}P_2^{+} & \sqrt{\frac{2}{3}}P_2^{z} & \frac{1}{\sqrt{6}}P_2^{-} & 0 & \frac{1}{\sqrt{3}}P_2^{z} & \frac{1}{\sqrt{3}}P_2^{-} & 0 & 0 \\
0 & \frac{-1}{\sqrt{6}}P_2'^{+} & \sqrt{\frac{2}{3}}P_2'^{z} & \frac{1}{\sqrt{2}}P_2'^{-} & \frac{1}{\sqrt{3}}P_2'^{+} & \frac{-1}{\sqrt{3}}P_2'^{z} & 0 & 0 & 0 & \frac{-1}{\sqrt{6}}P_2^{+} & \sqrt{\frac{2}{3}}P_2^{z} & \frac{1}{\sqrt{2}}P_2^{-} & \frac{1}{\sqrt{3}}P_2^{+} & \frac{-1}{\sqrt{3}}P_2^{z} & 0 & 0 \\
\frac{1}{3}\Delta_{Cd}' & \frac{1}{\sqrt{3}}P_{Xd}^{+} & 0 & 0 & \frac{1}{\sqrt{6}}P_{Xd}^{+} & \sqrt{\frac{2}{3}}P_{Xd}^{z} & \frac{1}{3}\Delta_{dso} & 0 & \frac{-1}{\sqrt{3}}P_d'^{+} & \frac{1}{\sqrt{3}}P_d'^{+} & \frac{1}{\sqrt{3}}P_d'^{z} & 0 & \frac{1}{\sqrt{6}}P_d'^{+} & \sqrt{\frac{2}{3}}P_d'^{z} & \frac{-1}{\sqrt{2}}P_{sd}'^{-} & 0 \\
\frac{-1}{\sqrt{3}}P_{Xd}^{-} & \frac{1}{3}\Delta_{Cd}' & 0 & \frac{1}{\sqrt{3}}P_{Xd}^{z} & \frac{-1}{\sqrt{2}}P_{Xd}^{+} & \frac{-1}{\sqrt{6}}P_{Xd}^{-} & \frac{-1}{\sqrt{6}}P_d^{-} & \frac{1}{\sqrt{2}}P_d^{+} & \frac{1}{3}\Delta_{dso} & 0 & \frac{1}{\sqrt{3}}P_d'^{-} & \frac{1}{\sqrt{2}}P_d'^{-} & \frac{-1}{\sqrt{6}}P_d'^{-} & 0 & \frac{-1}{\sqrt{6}}P_{Sd}'^{-} & \frac{1}{\sqrt{2}}P_{Sd}'^{+} \\
\frac{-1}{\sqrt{3}}P_{Xd}^{z} & 0 & \frac{1}{3}\Delta_{Cd}' & \frac{-1}{\sqrt{3}}P_{Xd}^{+} & \frac{1}{\sqrt{2}}P_{Xd}^{-} & 0 & \frac{1}{\sqrt{6}}P_d^{+} & \frac{1}{\sqrt{3}}P_d^{z} & 0 & \frac{1}{3}\Delta_{dso} & \frac{1}{\sqrt{3}}P_d'^{z} & \frac{-1}{\sqrt{3}}P_d'^{z} & \frac{1}{\sqrt{3}}P_d'^{z} & \frac{-1}{\sqrt{3}}P_{sd}'^{z} & \frac{1}{\sqrt{3}}P_{Sd}'^{z} & \frac{1}{\sqrt{3}}P_{Sd}'^{-} \\
0 & \frac{-1}{\sqrt{3}}P_{Xd}^{z} & \frac{1}{\sqrt{3}}P_{Xd}^{-} & \frac{1}{3}\Delta_{Cd}' & \frac{-1}{\sqrt{6}}P_{Xd}^{-} & \frac{-1}{\sqrt{6}}P_{Xd}^{-} & 0 & \frac{1}{\sqrt{2}}P_d^{+} & 0 & \frac{-1}{\sqrt{6}}P_d'^{-} & \frac{1}{\sqrt{2}}P_d'^{+} & \frac{1}{3}\Delta_{dso} & \frac{-1}{\sqrt{3}}P_d'^{z} & \frac{1}{\sqrt{6}}P_{sd}'^{+} & 0 & \frac{1}{\sqrt{2}}P_{Sd}'^{+} \\
\frac{-1}{\sqrt{6}}P_{Xd}^{-} & \frac{-1}{\sqrt{2}}P_{Xd}^{+} & \frac{-1}{\sqrt{2}}P_{Xd}^{+} & \frac{-1}{\sqrt{3}}P_{Xd}^{z} & \frac{1}{\sqrt{3}}P_d^{z} & \frac{-1}{\sqrt{6}}P_d^{-} & \frac{1}{\sqrt{3}}P_d^{-} & \frac{-1}{\sqrt{3}}P_d^{z} & \frac{-1}{\sqrt{6}}P_d'^{-} & 0 & \frac{1}{\sqrt{2}}P_d'^{-} & \frac{-1}{\sqrt{3}}P_d'^{z} & 0 & \frac{1}{\sqrt{3}}P_{sd}'^{z} & \frac{1}{\sqrt{3}}P_{Sd}'^{-} & \frac{-1}{\sqrt{3}}P_{Sd}'^{z} \\
-\sqrt{\frac{2}{3}}P_{Xd}^{z} & 0 & 0 & \frac{1}{\sqrt{6}}P_{Xd}^{+} & 0 & \frac{-2}{3}\Delta_{Cd}' & \frac{1}{\sqrt{3}}P_d^{+} & 0 & -\sqrt{\frac{2}{3}}P_d'^{z} & 0 & 0 & \frac{-2}{3}\Delta_{dso} & 0 & \frac{-2}{3}\Delta_{dso} & 0 & 0 \\
\frac{-1}{\sqrt{2}}P_3'^{+} & \frac{1}{\sqrt{6}}P_3'^{-} & \frac{1}{\sqrt{6}}P_3'^{-} & \frac{1}{2}\Delta_{3C} & \frac{-2}{\sqrt{3}}P_3'^{z} & \frac{1}{\sqrt{3}}P_3'^{-} & 0 & 0 & \frac{-1}{\sqrt{2}}P_S^{+} & -2\sqrt{\frac{2}{3}}P_S^{z} & \frac{1}{\sqrt{6}}P_S^{-} & \frac{1}{2}\Delta_3' & \frac{-2}{\sqrt{3}}P_S^{z} & \frac{1}{\sqrt{3}}P_S^{-} & 0 & 0 \\
\frac{-1}{2}\Delta_{3C} & -2\sqrt{\frac{2}{3}}P_3'^{z} & \frac{1}{2}P_3'^{-} & \frac{1}{2}P_3'^{-} & \frac{1}{\sqrt{3}}P_3'^{+} & \frac{2}{\sqrt{3}}P_3'^{z} & 0 & 0 & \frac{-1}{2}\Delta_3' & -2\sqrt{\frac{2}{3}}P_S^{z} & \frac{-1}{\sqrt{6}}P_S^{+} & \frac{1}{2}P_S^{-} & \frac{1}{\sqrt{3}}P_S^{+} & \frac{2}{\sqrt{3}}P_S^{z} & 0 & 0 \\
\sqrt{\frac{3}{2}}P_3'^{-} & \frac{-1}{\sqrt{2}}\Delta_{3C} & \frac{-1}{\sqrt{2}}P_3'^{+} & 0 & 0 & -P_3'^{+} & 0 & 0 & \sqrt{\frac{3}{2}}P_S^{-} & \frac{-1}{2}\Delta_3' & \frac{-1}{\sqrt{2}}P_S^{+} & 0 & 0 & -P_S^{+} & 0 & 0 \\
0 & \frac{1}{\sqrt{2}}P_3'^{-} & \frac{1}{2}\Delta_{3C} & -\sqrt{\frac{3}{2}} & -P_3'^{+} & 0 & 0 & 0 & 0 & \frac{1}{\sqrt{2}}P_S^{-} & \frac{1}{2}\Delta_3' & -\sqrt{\frac{3}{2}}P_S^{+} & -P_S^{-} & 0 & 0 & 0 \\
\frac{-1}{\sqrt{2}}P_u^{+} & \sqrt{\frac{2}{3}}P_u^{z} & \frac{1}{\sqrt{6}}P_u^{-} & 0 & \frac{1}{\sqrt{3}}P_u^{z} & \frac{1}{3}P_u^{-} & 0 & 0 & \frac{-1}{\sqrt{2}}P_u'^{+} & \sqrt{\frac{2}{3}}P_u'^{z} & \frac{1}{\sqrt{6}}P_u'^{-} & 0 & \frac{1}{\sqrt{3}}P_u'^{z} & \frac{1}{\sqrt{3}}P_u'^{-} & 0 & 0 \\
0 & \frac{-1}{\sqrt{6}}P_u^{+} & \sqrt{\frac{2}{3}}P_u^{z} & \frac{1}{\sqrt{2}}P_u^{-} & \frac{1}{\sqrt{3}}P_u^{+} & \frac{-1}{\sqrt{3}}P_u^{z} & 0 & 0 & 0 & \frac{-1}{\sqrt{6}}P_u'^{+} & \sqrt{\frac{2}{3}}P_u'^{z} & \frac{1}{\sqrt{2}}P_u'^{-} & \frac{1}{\sqrt{3}}P_u'^{+} & \frac{-1}{\sqrt{3}}P_u'^{z} & 0 & 0
\end{array}\right)
\end{array} \tag{A.48}
$$

$$
C = \begin{pmatrix}
 & |q-\rangle & \left|d\tfrac{3}{2}\right\rangle & \left|d\tfrac{1}{2}\right\rangle & \left|d-\tfrac{1}{2}\right\rangle & \left|d-\tfrac{3}{2}\right\rangle & \left|d\tfrac{7}{2}\right\rangle & \left|d-\tfrac{7}{2}\right\rangle & |D_z\uparrow\rangle & |D_z\downarrow\rangle & |D_x\uparrow\rangle & |D_x\downarrow\rangle & |U+\rangle & |U-\rangle \\
\langle q+| & 0 & \frac{1}{3}\Delta'_{Cd} & \frac{-1}{\sqrt{3}}P^+_{Xd} & \frac{-1}{\sqrt{3}}P^z_{Xd} & 0 & \frac{-1}{\sqrt{6}}P^+_{Xd} & -\frac{\sqrt{2}}{3}P^z_{Xd} & \frac{-1}{\sqrt{2}}P'^-_3 & \frac{-1}{2}\Delta_{3C} & \frac{\sqrt{3}}{2}P'^+_3 & 0 & \frac{-1}{\sqrt{2}}P^-_u & 0 \\
\langle q-| & 0 & \frac{1}{3}\Delta'_{Cd} & \frac{-1}{\sqrt{3}}P^-_{Xd} & 0 & \frac{1}{3}\Delta'_{Cd} & 0 & \frac{1}{\sqrt{2}}P^+_{Xd} & -2\frac{\sqrt{2}}{3}P'^z_3 & \frac{-1}{\sqrt{6}}P'^-_3 & \frac{-1}{\sqrt{2}}P'^-_3 & \frac{1}{2}\Delta_{3C} & \frac{1}{\sqrt{6}}P^+_u & \frac{-1}{\sqrt{6}}P^-_u \\
\left|d\tfrac{3}{2}\right\rangle & \frac{1}{3}\Delta'_{Cd} & \frac{1}{\sqrt{3}}P^-_{Xd} & \frac{-1}{\sqrt{3}}P^z_{Xd} & \frac{1}{\sqrt{2}}P^+_{Xd} & \frac{-1}{\sqrt{3}}P^-_{Xd} & \frac{-1}{\sqrt{2}}P^z_{Xd} & \frac{1}{\sqrt{2}}P^-_{Xd} & \frac{1}{\sqrt{6}}P^+_3 & \frac{1}{2}\Delta_{3C} & \frac{1}{\sqrt{2}}P'^+_3 & -\frac{\sqrt{3}}{2}P'^-_3 & \frac{1}{\sqrt{2}}P^+_u & \frac{1}{\sqrt{3}}P^-_u \\
\left|d\tfrac{1}{2}\right\rangle & \frac{1}{3}\Delta'_{Cd} & \frac{1}{\sqrt{3}}P^z_{Xd} & \frac{1}{\sqrt{2}}P^-_{Xd} & \frac{-1}{\sqrt{3}}P^+_{Xd} & \frac{1}{\sqrt{3}}P^z_{Xd} & \frac{-1}{\sqrt{3}}P^-_{Xd} & \frac{1}{\sqrt{2}}P^z_{Xd} & \frac{-1}{\sqrt{3}}P'^-_3 & \frac{2}{\sqrt{3}}P'^z_3 & 0 & -P'^+_3 & \frac{1}{\sqrt{3}}P^z_u & \frac{-1}{\sqrt{3}}P^z_u \\
\left|d-\tfrac{1}{2}\right\rangle & 0 & \frac{-1}{\sqrt{3}}P^+_{Xd} & \frac{-1}{\sqrt{3}}P^z_{Xd} & 0 & \frac{-1}{\sqrt{6}}P^+_{Xd} & 0 & \frac{1}{\sqrt{6}}P^-_{Xd} & \frac{1}{\sqrt{6}}P^+_3 & \frac{1}{2}\Delta_{3C} & 0 & -\frac{\sqrt{3}}{2}P'^-_3 & 0 & \frac{1}{\sqrt{2}}P^+_u \\
\left|d-\tfrac{3}{2}\right\rangle & 0 & \frac{1}{\sqrt{3}}P^z_{Xd} & \frac{1}{\sqrt{3}}P^+_{Xd} & \frac{1}{3}\Delta'_{Cd} & \frac{\sqrt{2}}{3}P^z_{Xd} & \frac{-1}{\sqrt{6}}P^+_{Xd} & 0 & \frac{-2}{3}\Delta'_{Cd} & \frac{-2}{3}P'^z_3 & \frac{1}{\sqrt{3}}P'^+_3 & 0 & \frac{1}{\sqrt{3}}P^+_u & \frac{1}{\sqrt{3}}P^-_u \\
\left|d\tfrac{7}{2}\right\rangle & 0 & 0 & \frac{-1}{\sqrt{6}}P^+_{Xd} & \frac{-1}{\sqrt{3}}P^-_{Xd} & 0 & \frac{1}{\sqrt{3}}P^z_d & \frac{1}{\sqrt{3}}P^-_d & 0 & 0 & 0 & 0 & 0 & 0 \\
\left|d-\tfrac{7}{2}\right\rangle & 0 & 0 & \frac{1}{\sqrt{6}}P^-_d & 0 & \frac{1}{\sqrt{2}}P^-_d & \frac{1}{\sqrt{3}}P^+_d & \frac{-1}{\sqrt{3}}P^z_d & 0 & 0 & 0 & 0 & 0 & 0 \\
|D_z\uparrow\rangle & \frac{-1}{\sqrt{2}}P'^-_3 & \frac{-1}{\sqrt{6}}P'^-_3 & \frac{-1}{\sqrt{3}}P^z_{Xd} & \frac{1}{\sqrt{3}}P^+_{Xd} & \frac{-1}{\sqrt{3}}P^z_{Xd} & \frac{-1}{\sqrt{6}}P^+_d & \frac{-1}{\sqrt{2}}P^-_d & \frac{1}{\sqrt{6}}P^+_3 & \frac{-1}{\sqrt{2}}P^-_3 & \frac{\sqrt{3}}{2}P^+_3 & 0 & \frac{-1}{\sqrt{2}}P'^-_u & 0 \\
|D_z\downarrow\rangle & \frac{-1}{2}\Delta_{3C} & \frac{-1}{\sqrt{6}}P'^-_3 & -2\frac{\sqrt{2}}{3}P'^z_3 & \frac{-1}{\sqrt{2}}P'^+_3 & \frac{1}{\sqrt{3}}P'^-_3 & \frac{2}{\sqrt{3}}P'^z_3 & 0 & 0 & 0 & 0 & 0 & 0 & 0 \\
|D_x\uparrow\rangle & \sqrt{\frac{3}{2}}P'^+_3 & \frac{-1}{2}\Delta_{3C} & \frac{-1}{\sqrt{2}}P'^-_3 & 0 & -\sqrt{\frac{3}{2}}P'^-_3 & -P'^-_3 & 0 & 0 & 0 & 0 & 0 & 0 & 0 \\
|D_x\downarrow\rangle & 0 & \frac{1}{\sqrt{2}}P'^+_3 & \frac{1}{2}\Delta_{3C} & -\sqrt{\frac{3}{2}}P'^-_3 & -P'^+_3 & 0 & -\frac{\sqrt{3}}{2}P'^-_3 & 0 & 0 & 0 & 0 & 0 & 0 \\
|U+\rangle & \frac{-1}{\sqrt{2}}P^-_u & \frac{1}{\sqrt{3}}P^z_u & \frac{1}{\sqrt{6}}P^+_u & 0 & \frac{1}{\sqrt{3}}P^z_u & \frac{1}{\sqrt{3}}P^+_u & 0 & 0 & 0 & 0 & 0 & 0 & 0 \\
|U-\rangle & 0 & \frac{-1}{\sqrt{6}}P^-_u & \sqrt{\frac{2}{3}}P^z_u & \frac{1}{\sqrt{2}}P^+_u & \frac{1}{\sqrt{3}}P^-_u & \frac{-1}{\sqrt{3}}P^z_u & 0 & 0 & 0 & 0 & 0 & 0 & 0
\end{pmatrix}
\tag{A.49}
$$

$$
D = \begin{array}{c}
\begin{array}{cccccccccccccccc}
\left|c\,\frac{3}{2}\right\rangle & \left|c\,\frac{1}{2}\right\rangle & \left|c-\frac{1}{2}\right\rangle & \left|c-\frac{3}{2}\right\rangle & \left|c\,\frac{7}{2}\right\rangle & \left|c-\frac{7}{2}\right\rangle & |+\rangle & |-\rangle & \left|\frac{3}{2}\right\rangle & \left|\frac{1}{2}\right\rangle & \left|-\frac{1}{2}\right\rangle & \left|-\frac{3}{2}\right\rangle & \left|\frac{7}{2}\right\rangle & \left|-\frac{7}{2}\right\rangle & |V+\rangle & |V-\rangle
\end{array} \\
\left(\begin{array}{cccccccccccccccc}
E_{8C}^{k} & \mathcal{B}_C & C_C & 0 & \frac{1}{\sqrt{2}}\mathcal{B}_C & \sqrt{2}C_C & \frac{-1}{\sqrt{2}}P'^{-} & 0 & \frac{1}{3}\Delta' & \frac{1}{\sqrt{3}}P_X^{+} & \frac{1}{\sqrt{3}}P_X^{z} & 0 & \frac{1}{\sqrt{6}}P_X^{+} & \sqrt{\frac{2}{3}}P_X^{z} & \frac{-1}{\sqrt{2}}P_S^{-} & 0 \\
\mathcal{B}_C^{*} & E_{8C}^{k} & 0 & C_C & -\sqrt{2}\mathcal{A}_C & -\sqrt{\frac{3}{2}}\mathcal{B}_C & \sqrt{\frac{2}{3}}P'^{z} & \frac{-1}{\sqrt{6}}P'^{-} & \frac{-1}{\sqrt{3}}P_X^{-} & \frac{1}{3}\Delta' & 0 & \frac{1}{\sqrt{3}}P_X^{z} & 0 & \frac{-1}{\sqrt{2}}P_X^{+} & \sqrt{\frac{2}{3}}P_S^{z} & \frac{-1}{\sqrt{6}}P_S^{-} \\
C_C^{*} & 0 & E_{8C}^{k} & -\mathcal{B}_C & -\sqrt{\frac{3}{2}}\mathcal{B}_C^{*} & \sqrt{2}\mathcal{A}_C & \frac{1}{\sqrt{6}}P'^{+} & \sqrt{\frac{2}{3}}P'^{z} & \frac{-1}{\sqrt{3}}P_X^{z} & 0 & \frac{1}{3}\Delta' & \frac{1}{\sqrt{2}}P_X^{-} & 0 & \frac{1}{\sqrt{2}}P_X^{-} & \frac{1}{\sqrt{6}}P_S^{+} & \sqrt{\frac{2}{3}}P_S^{z} \\
0 & C_C^{*} & -\mathcal{B}_C^{*} & E_{8C}^{k} & -\sqrt{2}C_C^{*} & \frac{1}{\sqrt{2}}\mathcal{B}_C^{*} & 0 & \frac{1}{\sqrt{2}}P'^{+} & 0 & \frac{-1}{\sqrt{3}}P_X^{z} & \frac{1}{3}\Delta' & \frac{1}{\sqrt{3}}P_x^{-} & \frac{-1}{\sqrt{6}}P_X^{-} & 0 & \frac{1}{\sqrt{2}}P_S^{+} & \frac{1}{\sqrt{2}}P_S^{-} \\
\frac{1}{\sqrt{2}}\mathcal{B}_C^{*} & -\sqrt{2}\mathcal{A}_C & -\sqrt{\frac{3}{2}}\mathcal{B}_C & -\sqrt{2}C_C & E_{7C}^{k} & 0 & \frac{1}{\sqrt{3}}P'^{z} & \frac{-1}{\sqrt{3}}P'^{-} & \frac{-1}{\sqrt{6}}P_X^{-} & 0 & \frac{-1}{\sqrt{2}}P_X^{+} & -\sqrt{\frac{2}{3}}P_X^{z} & 0 & \frac{1}{\sqrt{3}}P_S^{z} & \frac{1}{\sqrt{3}}P_S^{-} & \frac{-1}{\sqrt{3}}P_S^{z} \\
\sqrt{2}C_C^{*} & -\sqrt{\frac{3}{2}}\mathcal{B}_C^{*} & \sqrt{2}\mathcal{A}_C & \frac{1}{\sqrt{2}}\mathcal{B}_C & 0 & E_{7C}^{k} & \frac{1}{\sqrt{3}}P'^{+} & \frac{-1}{\sqrt{3}}P'^{z} & -\sqrt{\frac{2}{3}}P_X^{z} & \frac{1}{\sqrt{2}}P_X^{-} & \frac{1}{\sqrt{3}}P_z^{z} & \frac{1}{\sqrt{6}}P_X^{-} & \frac{1}{\sqrt{3}}P_X^{+} & \frac{-1}{\sqrt{3}}P_S^{z} & \frac{1}{\sqrt{3}}P_S^{+} & \frac{1}{\sqrt{3}}P_S^{-} \\
\frac{-1}{\sqrt{2}}P'^{+} & \sqrt{\frac{2}{3}}P'^{z} & \frac{1}{\sqrt{6}}P'^{-} & 0 & \frac{1}{\sqrt{3}}P'^{z} & \frac{1}{\sqrt{3}}P'^{-} & E_{6C}^{k} & 0 & \frac{-1}{\sqrt{2}}P^{+} & \sqrt{\frac{2}{3}}P_X^{z} & \frac{1}{\sqrt{6}}P_X^{-} & \frac{1}{\sqrt{2}}P_X^{-} & 0 & 0 & 0 & 0 \\
0 & \frac{-1}{\sqrt{6}}P'^{+} & \sqrt{\frac{2}{3}}P'^{z} & \frac{1}{\sqrt{2}}P'^{-} & \frac{1}{\sqrt{3}}P'^{+} & \frac{-1}{\sqrt{3}}P'^{z} & 0 & E_{6C}^{k} & 0 & \frac{-1}{\sqrt{6}}P^{+} & \sqrt{\frac{2}{3}}P^{z} & \frac{1}{\sqrt{3}}P^{+} & \frac{1}{\sqrt{3}}P^{-} & \frac{-1}{\sqrt{3}}P^{z} & 0 & 0 \\
\frac{1}{3}\Delta' & \frac{-1}{\sqrt{3}}P_X^{+} & \frac{-1}{\sqrt{3}}P_X^{z} & 0 & \frac{-1}{\sqrt{6}}P_X^{+} & \frac{-1}{\sqrt{2}}P_X^{-} & 0 & \frac{-1}{\sqrt{6}}P^{-} & E_{8V}^{k} & \mathcal{B}^{*} & \mathcal{B} & C & 0 & \frac{1}{\sqrt{2}}\mathcal{B} & \sqrt{2}C & 0 \\
\frac{1}{\sqrt{3}}P_X^{-} & \frac{1}{3}\Delta' & 0 & \frac{-1}{\sqrt{3}}P_X^{z} & \frac{1}{\sqrt{2}}P_X^{+} & \frac{1}{\sqrt{2}}P^{z} & \frac{1}{\sqrt{6}}P^{+} & \frac{-1}{\sqrt{6}}P^{-} & E_{8V}^{k} & E_{8V}^{k} & 0 & C & -\sqrt{2}\mathcal{A} & -\sqrt{\frac{3}{2}}\mathcal{B} & \sqrt{2}\mathcal{A} & \frac{-1}{\sqrt{6}}P_S'^{-} \\
\frac{1}{\sqrt{3}}P_X^{z} & 0 & \frac{1}{3}\Delta' & \frac{1}{\sqrt{3}}P_X^{+} & \frac{-1}{\sqrt{2}}P_X^{-} & 0 & \frac{1}{\sqrt{6}}P^{+} & \sqrt{\frac{2}{3}}P^{z} & C^{*} & 0 & E_{8V}^{k} & -\mathcal{B} & -\sqrt{\frac{2}{3}}\mathcal{B}^{*} & \sqrt{2}\mathcal{A} & \frac{1}{\sqrt{6}}P_S'^{+} & \sqrt{\frac{2}{3}}P_S'^{z} \\
0 & \frac{1}{\sqrt{3}}P_X^{z} & \frac{-1}{\sqrt{3}}P_X^{-} & \frac{1}{3}\Delta' & \frac{-1}{\sqrt{6}}P_X^{-} & \frac{1}{\sqrt{6}}P_X^{-} & \frac{1}{\sqrt{2}}P^{+} & \frac{1}{\sqrt{2}}P^{-} & C^{*} & -\mathcal{B}^{*} & E_{8V}^{k} & -\sqrt{2}C^{*} & \frac{1}{\sqrt{2}}\mathcal{B}^{*} & 0 & \frac{1}{\sqrt{2}}P_S'^{+} & \\
\frac{1}{\sqrt{6}}P_X^{-} & 0 & \frac{1}{\sqrt{2}}P_X^{+} & \sqrt{\frac{2}{3}}P_X^{z} & \frac{-2}{3}\Delta' & 0 & \frac{1}{\sqrt{3}}P^{z} & \frac{1}{\sqrt{3}}P^{-} & \frac{1}{\sqrt{2}}\mathcal{B}^{*} & -\sqrt{2}\mathcal{A} & -\sqrt{\frac{3}{2}}\mathcal{B} & E_{7V}^{k} & 0 & \frac{1}{\sqrt{3}}P_S'^{z} & \frac{1}{\sqrt{3}}P_S'^{-} & \\
\sqrt{\frac{2}{3}}P_X^{z} & \frac{-1}{\sqrt{2}}P_X^{-} & 0 & \frac{-1}{\sqrt{6}}P_X^{+} & 0 & \frac{-2}{3}\Delta' & \frac{1}{\sqrt{3}}P^{+} & \frac{-1}{\sqrt{3}}P^{z} & \sqrt{2}C^{*} & -\sqrt{\frac{3}{2}}\mathcal{B}^{*} & \sqrt{2}\mathcal{A} & \frac{1}{\sqrt{2}}\mathcal{B} & 0 & E_{7V}^{k} & \frac{1}{\sqrt{3}}P_S'^{+} & \frac{1}{\sqrt{3}}P_S'^{-} \\
\frac{-1}{\sqrt{2}}P_S^{+} & \sqrt{\frac{2}{3}}P_S^{z} & \frac{1}{\sqrt{6}}P_S^{-} & 0 & \frac{1}{\sqrt{3}}P_S^{z} & \frac{1}{\sqrt{3}}P_S^{-} & 0 & 0 & \frac{-1}{\sqrt{2}}P'^{+} & \sqrt{\frac{2}{3}}P_S'^{z} & \frac{1}{\sqrt{6}}P_S'^{-} & 0 & \frac{1}{\sqrt{3}}P_S'^{z} & \frac{1}{\sqrt{3}}P_S'^{-} & E_{6V}^{k} & 0 \\
0 & \frac{-1}{\sqrt{6}}P_S^{+} & \sqrt{\frac{2}{3}}P_S^{z} & \frac{1}{\sqrt{2}}P_S^{-} & \frac{-1}{\sqrt{3}}P_S^{+} & \frac{-1}{\sqrt{3}}P_S^{z} & 0 & 0 & 0 & \frac{-1}{\sqrt{6}}P_S^{+} & \sqrt{\frac{2}{3}}P_S^{z} & \frac{1}{\sqrt{2}}P_S^{-} & \frac{-1}{\sqrt{3}}P_S^{+} & \frac{-1}{\sqrt{3}}P_S^{z} & 0 & E_{6V}^{k}
\end{array}\right)
\end{array}
\tag{A.50}
$$

A.2.1 Band parameters of semiconductors in 30-band k.p model

In Tables A.4 and A.5 we displays the parameters of several semiconductors using in 30-band $\boldsymbol{k.p}$ method, taken from Ref [412]. Furthermore, for the InGaAs alloys, the Vitual Crystal Approximation (VCA) has been used to compute $In_xGa_{1-x}As$ band structure for any In mole fraction x in a work of Mugny et al. [413]. In this approximation, a virtual binary crystal is constructed, with atomic parameters interpolated between the two initial elements (In and Ga atoms in our case). Linear interpolation is made for all parameters, except for the energies E_g and Δ_{SO} for which bowing coefficients B are used:

$$P_{InGaAs} = P_{InAs}x + P_{GaAs}(1-x) - Bx(1-x) \tag{A.51}$$

where $B = 0.477$ for E_g and $B = 0.15$ for Δ_{SO}.

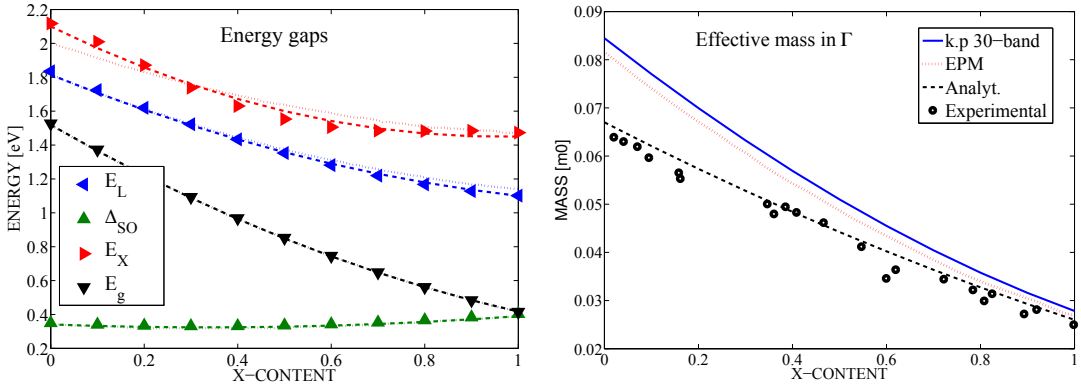

FIGURE A.9: Variation of the lowest band gap at $T = 300k$ and electron effective mass at Γ conduction bands of $In_{1-x}Ga_xAs$(taken from [50])

Figure 2.10 displays the band structure along the three characteristic directions: [001]; [110] and [111] direction of InGaAs before (Fig (a), (b), (c)) and after (Fig (d), (e), (f)) the spurious states treatment using the ghost-band method.

A.3 40 band k.p model [414, 415]

We are now going to present the Hamiltonian which is enlarged to include ten further levels (compare to the 30-band $\boldsymbol{k.p}$ model), namely, the $d-valence$ levels can be divided into two types associated with the symmetry of the wave function: the Γ^V_{3d} are associated to $d-like$ atomic levels which have the symmetry of $D_1 = 3z^2 - r^2$ and $D_2 = \sqrt{3}(x^2 - y^2)$, and Γ_{5d} levels which are associated to $p-like$ functions which are split into two levels Γ^V_{7d} and Γ^V_{8d}. The dimension of the Hamiltonian including $d-valence$ levels is 40 which is the $\boldsymbol{k.p}$ Hamiltonian, denoted by H_{40}, in a sp^3d^5 model framework.

This model is schematically represented at $\boldsymbol{k} = 0$ in Fig A.10. In this figure, both the wave functions corresponding to the bands and the matrix elements are indicated. Here, $\left(|X^V_d\rangle, |Y^V_d\rangle, |Z^V_d\rangle\right)$ are $\left(\Gamma^V_{7d}, \Gamma^V_{8d}\right)$ orbital functions, and D^V_z and D^V_x are Γ^V_{8-3} orbital functions. Moreover, $|S\rangle$; $|X\rangle$; $|Y\rangle$ and $|Z\rangle$ are respectively, Γ^C_1 (Γ^C_6) and Γ^V_5 (Γ^V_8, Γ^V_7) orbital function as usual. $|S_V\rangle$; $|X_C\rangle$; $|Y_C\rangle$ and $|Z_C\rangle$ are respectively, Γ^V_1 (Γ^V_6) and Γ^C_5 (Γ^C_8, Γ^C_7) orbital functions. These eight functions correspond to the sp^3 Tight-Binding functions. $|S_U\rangle$ and $|S_q\rangle$ are, respectively, Γ^C_{6U} and Γ^C_{6q} orbital functions. $|D_z\rangle$ and $|D_x\rangle$ are Γ^C_{8-3} orbital functions. $|X_d\rangle$; $|Y_d\rangle$ and $|Z_d\rangle$ are (Γ^C_{8d}, Γ^C_{7d}) orbital functions. In comparison to the $30-band$ $\boldsymbol{k.p}$ model, we have twelve additional matrix elements namely:

TABLE A.6: Luttinger-Kohn periodic amplitudes used in the 40-band **k.p** model. The phases are chosen to give real matrix elements to the **k.p** Hamiltonian.

$\|q+\rangle = \|S_q \uparrow\rangle$	$\|q-\rangle = \|S_q \downarrow\rangle$
$\left\|d\frac{3}{2}\right\rangle = \left\|i\left[\frac{1}{\sqrt{2}}(X_d - iY_d)\downarrow\right]\right\rangle$	$\left\|d-\frac{3}{2}\right\rangle = \left\|i\left[-\frac{1}{\sqrt{2}}(X_d + iY_d)\uparrow\right]\right\rangle$
$\left\|d\frac{1}{2}\right\rangle = \left\|i\left[\sqrt{\frac{2}{3}}Z_d\uparrow - \frac{1}{\sqrt{6}}(X_d + iY_d)\downarrow\right]\right\rangle$	$\left\|d-\frac{1}{2}\right\rangle = \left\|i\left[\frac{1}{\sqrt{6}}(X_d - iY_d)\uparrow + \sqrt{\frac{2}{3}}Z_d\downarrow\right]\right\rangle$
$\left\|d\frac{7}{2}\right\rangle = \left\|i\left[\frac{1}{\sqrt{3}}Z_d\uparrow + \frac{1}{\sqrt{3}}(X_d + iY_d)\downarrow\right]\right\rangle$	$\left\|d-\frac{1}{2}\right\rangle = \left\|i\left[\frac{1}{\sqrt{3}}(X_d - iY_d)\uparrow - \frac{1}{\sqrt{3}}Z_d\downarrow\right]\right\rangle$
$\|D_z+\rangle = \|D_z\uparrow\rangle$	$\|D_z-\rangle = \|D_z\downarrow\rangle$
$\|D_x+\rangle = \|D_x\uparrow\rangle$	$\|D_x-\rangle = \|D_x\downarrow\rangle$
$\|U+\rangle = \|S_u\uparrow\rangle$	$\|U-\rangle = \|S_u\downarrow\rangle$
$\left\|C\frac{3}{2}\right\rangle = \left\|i\left[\frac{1}{\sqrt{2}}(X_C - iY_C)\downarrow\right]\right\rangle$	$\left\|C-\frac{3}{2}\right\rangle = \left\|i\left[-\frac{1}{\sqrt{2}}(X_C + iY_C)\uparrow\right]\right\rangle$
$\left\|C\frac{1}{2}\right\rangle = \left\|i\left[\sqrt{\frac{2}{3}}Z_C\uparrow - \frac{1}{\sqrt{6}}(X_C + iY_C)\downarrow\right]\right\rangle$	$\left\|C-\frac{1}{2}\right\rangle = \left\|i\left[\frac{1}{\sqrt{6}}(X_C - iY_C)\uparrow + \sqrt{\frac{2}{3}}Z_C\downarrow\right]\right\rangle$
$\left\|C\frac{7}{2}\right\rangle = \left\|i\left[\frac{1}{\sqrt{3}}Z_C\uparrow + \frac{1}{\sqrt{3}}(X_C + iY_C)\downarrow\right]\right\rangle$	$\left\|C-\frac{1}{2}\right\rangle = \left\|i\left[\frac{1}{\sqrt{3}}(X_C - iY_C)\uparrow - \frac{1}{\sqrt{3}}Z_C\downarrow\right]\right\rangle$
$\|+\rangle = \|S\uparrow\rangle$	$\|-\rangle = \|S\downarrow\rangle$
$\left\|\frac{3}{2}\right\rangle = \left\|i\left[\frac{1}{\sqrt{2}}(X - iY)\downarrow\right]\right\rangle$	$\left\|-\frac{3}{2}\right\rangle = \left\|i\left[-\frac{1}{\sqrt{2}}(X + iY)\uparrow\right]\right\rangle$
$\left\|\frac{1}{2}\right\rangle = \left\|i\left[\sqrt{\frac{2}{3}}Z\uparrow - \frac{1}{\sqrt{6}}(X + iY)\downarrow\right]\right\rangle$	$\left\|-\frac{1}{2}\right\rangle = \left\|i\left[\frac{1}{\sqrt{6}}(X - iY)\uparrow + \sqrt{\frac{2}{3}}Z\downarrow\right]\right\rangle$
$\left\|\frac{7}{2}\right\rangle = \left\|i\left[\frac{1}{\sqrt{3}}Z\uparrow + \frac{1}{\sqrt{3}}(X + iY)\downarrow\right]\right\rangle$	$\left\|-\frac{1}{2}\right\rangle = \left\|i\left[\frac{1}{\sqrt{3}}(X - iY)\uparrow - \frac{1}{\sqrt{3}}Z\downarrow\right]\right\rangle$
$\|V+\rangle = \|S_V\uparrow\rangle$	$\|V-\rangle = \|S_V\downarrow\rangle$
$\left\|d^V\frac{3}{2}\right\rangle = \left\|i\left[\frac{1}{\sqrt{2}}(X_d^V - iY_d^V)\downarrow\right]\right\rangle$	$\left\|d^V-\frac{3}{2}\right\rangle = \left\|i\left[-\frac{1}{\sqrt{2}}(X_d^V + iY_d^V)\uparrow\right]\right\rangle$
$\left\|d^V\frac{1}{2}\right\rangle = \left\|i\left[\sqrt{\frac{2}{3}}Z_d^V\uparrow - \frac{1}{\sqrt{6}}(X_d^V + iY_d^V)\downarrow\right]\right\rangle$	$\left\|d^V-\frac{1}{2}\right\rangle = \left\|i\left[\frac{1}{\sqrt{6}}(X_d^V - iY_d^V)\uparrow + \sqrt{\frac{2}{3}}Z_d^V\downarrow\right]\right\rangle$
$\left\|d^V\frac{7}{2}\right\rangle = \left\|i\left[\frac{1}{\sqrt{3}}Z_d^V\uparrow + \frac{1}{\sqrt{3}}(X_d^V + iY_d^V)\downarrow\right]\right\rangle$	$\left\|d^V-\frac{1}{2}\right\rangle = \left\|i\left[\frac{1}{\sqrt{3}}(X_d^V - iY_d^V)\uparrow - \frac{1}{\sqrt{3}}Z_d^V\downarrow\right]\right\rangle$
$\|D_z^V+\rangle = \|D_z^V\uparrow\rangle$	$\|D_z^V-\rangle = \|D_z^V\downarrow\rangle$
$\|D_x^V+\rangle = \|D_x^V\uparrow\rangle$	$\|D_x^V-\rangle = \|D_x^V\downarrow\rangle$

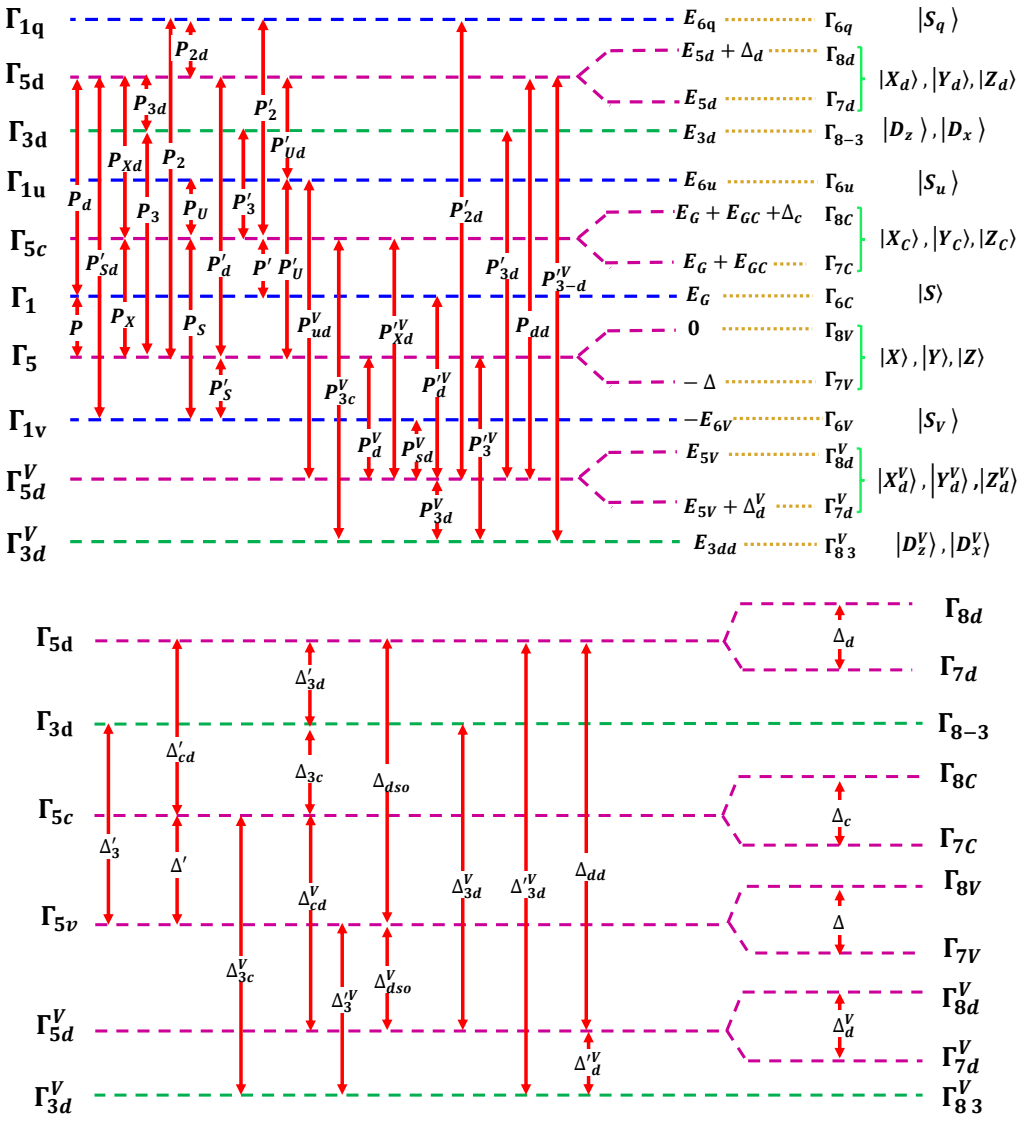

FIGURE A.10: Schematic representation of the 40-band **k.p** model representing involved bands, relevant parameters, momentum matrix elements and spin-orbit couplings.

TABLE A.7: $k = 0$ energy level (eV) used in the 40-band $\mathbf{k}\cdot\mathbf{p}$ model.

eV	GaAs	InAs	InP	Insb
Γ_6^V	-12.50	-12.69	-11.08	-11.71
Γ_7^V	-0.34	-0.43	-0.10	-0.82
Γ_8^V	0	0	0	0
Γ_6^C	1.51	0.37	1.42	0.25
Γ_7^C	4.52	4.35	4.59	3.16
Γ_8^C	4.70	4.62	4.78	3.59
Γ_{6U}^C	9.02	7.82	9.81	9.37
Γ_3^C	9.65	8.65	10.23	9.85
Γ_{7d}^C	12.25	13.62	11.08	10.28
Γ_{8d}^C	12.25	13.62	11.08	10.28
Γ_{6q}^C	15.34	14.47	13.00	11.38
Γ_{5d}^V	-20.57	-15.27	-16.07	-15.30
Γ_{3d}^V	-22.54	-15.74	-19.54	-15.94

TABLE A.8: Dipole Matrix elements of GaAs and AlAs in a 40-band $\mathbf{k}\cdot\mathbf{p}$ model given in unit of energy in definition of Ref. [200]. Energies E and matrix components P are linked by $E = 2m_0/\hbar^2 P^2$.

eV	GaAs	InAs	InP	InSb	eV	GaAs	InAs	InP	InSb
E_P	23.81	19.33	18.81	24.08	E_{3cV}	0.23	0.63	0.03	0.73
E_{PX}	15.79	17.97	16.03	12.55	E'_{PdV}	12.87	11.07	8.87	14.97
E_{P3}	6.22	4.32	4.66	4.72	E'_{P3V}	4.72	0.92	0.22	0.91
E_{P2}	0.11	10.51	14.37	0.08	E_{dV}	2.27	2.13	0.07	0.43
E_{PS}	6.14	4.29	4.88	3.92	E_{SdV}	0.03	0.01	0.11	0.01
E'_P	0.11	0.11	0.15	0.03	E_{udV}	1.867	1.970	1.871	1.869
E_{Pd}	1.59	0.38	0.10	0.01	E'_{P3d}	0.096	0.095	0.093	0.096
E_{PXd}	5.64	5.04	6.97	8.84	E'_{P3dV}	0.27	0.42	0.10	0.42
E_{P3d}	13.38	13.11	8.42	11.32	E'_{PxdV}	2.47	0.77	7.07	1.17
E_{P2d}	19.93	26.51	16.72	8.99	E_{dd}	10.87	1.98	3.17	1.98
E_{PU}	26.64	23.04	24.78	23.85	E'_{P2d}	0.060	0.058	0.060	0.16
E'_{3dV}	8.04	0.012	0.082	0.322	Δ	0.341	0.43	0.108	0.82
Δ_c	0.180	0.24	0.19	0.43	Δ_{3C}	0.26	0.140	-0.067	0.29
Δ_d	0.217	0.02	0.013	0.04	Δ'_{cd}	0.26	0.08	0.06	0.20
Δ'	-0.17	0.140	-0.067	0.29	Δ_{dso}	-0.95	0.67	0.38	0.07
Δ_d^V	0.01	0.09	0.03	0.082	Δ_{dso}^V	0.37	-0.38	0.20	-0.08

$P_{3C}^V = \frac{\hbar}{m_0}\langle D_Z^V|P_x|iX_C\rangle$, $P_d^V = \frac{\hbar}{m_0}\langle X_d^V|P_y|iZ\rangle$, $P_{Sd}^V = \frac{\hbar}{m_0}\langle S_V|P_x|iX_d^V\rangle$, $P_{ud}^V = \frac{\hbar}{m_0}\langle S_u|P_x|iX_d^V\rangle$, $P_{dd} = \frac{\hbar}{m_0}\langle X_d|P_y|iZ_d^V\rangle$, $P_{3d}^V = \frac{\hbar}{m_0}\langle D_z^V|P_x|iX_d^V\rangle$, $P_{Xd}^{\prime V} = \frac{\hbar}{m_0}\langle X_C|P_y|iZ_d^V\rangle$, $P_d^{\prime V} = \frac{\hbar}{m_0}\langle S|P_x|iX_d^V\rangle$, $P_3^{\prime V} = \frac{\hbar}{m_0}\langle D_Z^V|P_x|iX\rangle$, $P'_{3d} = \frac{\hbar}{m_0}\langle D_Z|P_x|iX_d^V\rangle$, $P_{3d}^{\prime V} = \frac{\hbar}{m_0}\langle D_z^V|P_x|iX_d\rangle$, and $P'_{2d} = \frac{\hbar}{m_0}\langle S_q|P_x|iX_d^V\rangle$

The 40-band ***k.p*** theory in the above form contains three kinds of parameters: The energy gaps, the matrix elements of momentum, the spin-orbit interaction, and the combinations of both. We can notice that all the spin-orbit coupling appear between the different Γ_5 levels, namely, Γ_{5v} and Γ_{5d}^V VBs, Γ_{5c} and Γ_{5d} CBs, or between Γ_5 and Γ_{3d} or Γ_{3d}^V levels. In Fig. A.10 we present schematically the effect of spin-orbit interaction in the 40 – *band* ***k.p*** model. In comparison with the 30 – *band* ***k.p*** model, we have eight additional spin-orbit coupling terms which appear between the different Γ_5 levels, or between Γ_5 and Γ_3 levels.

And finally, the Luttinger-Kohn parameters in the 40 – *band* ***k.p*** model are modified from 30 – *band* ***k.p*** model as:

$$\gamma_1 = \gamma_1^{30} - \frac{1}{3}\left(\frac{E_{dV}}{E_{5dV} + \Delta_d^V} + \frac{E_{dV}}{E_{5dV}} + 4\frac{E_{P3V}^{'}}{E_{3dd}}\right) \tag{A.52}$$

$$\gamma_2 = \gamma_2^{30} - \frac{1}{6}\left(\frac{E_{dV}}{E_{5dV}} - \frac{E_{P3V}^{'}}{E_{3dd}}\right) \tag{A.53}$$

$$\gamma_3 = \gamma_3^{30} - \frac{1}{6}\left(\frac{E_{dV}}{E_{5dV}} + 2\frac{E_{P3V}^{'}}{E_{3dd}}\right) \tag{A.54}$$

Where γ_j^{30} $(j = 1, 2, 3)$ are the Luttinger-Kohn parameter defined in $30 - band\ \boldsymbol{k.p}$ model: Eqs: A.43 ; A.44 and A.45 respectively. Besides, the $40 - band\ \boldsymbol{k.p}$ Hamiltonian can be built from $30 - band\ \boldsymbol{k.p}$ Hamiltonian by adding following block:

$$H_{10\times 40} = \begin{pmatrix} \mathbb{E} \\ \mathbb{F} \end{pmatrix} \tag{A.55}$$

where

(A.56)

$$
\mathbb{E} = \begin{pmatrix}
\frac{-1}{\sqrt{2}}P^{V-}_{3C} & \frac{-1}{2}\Delta^{V}_{3C} & \sqrt{\frac{3}{2}}P^{V+}_{3C} & 0 & \frac{1}{3}\Delta^{V}_{Cd} & \frac{1}{\sqrt{3}}P'^{V+}_{Xd} & \frac{1}{\sqrt{3}}P'^{Vz}_{Xd} & 0 & \frac{1}{\sqrt{6}}P'^{V+}_{Xd} & \sqrt{\frac{2}{3}}P'^{Vz}_{Xd} \\
-2\sqrt{\frac{2}{3}}P^{Vz}_{3C} & \frac{-1}{\sqrt{6}}P^{V-}_{3C} & -2\sqrt{\frac{2}{3}}P^{Vz}_{3C} & \frac{1}{\sqrt{2}}P^{V+}_{3C} & \frac{-1}{\sqrt{3}}P'^{V-}_{Xd} & \frac{1}{3}\Delta^{V}_{Cd} & \frac{-1}{\sqrt{3}}P'^{V+}_{Xd} & 0 & \frac{-1}{\sqrt{2}}P'^{V-}_{Xd} & \frac{-1}{\sqrt{2}}P'^{V+}_{Xd} \\
\frac{1}{\sqrt{6}}P^{V+}_{3C} & -2\sqrt{\frac{2}{3}}P^{Vz}_{3C} & \frac{1}{2}\Delta^{V}_{3C} & \frac{-1}{\sqrt{3}}P^{V-}_{3C} & \frac{-1}{\sqrt{3}}P'^{Vz}_{Xd} & 0 & \frac{1}{3}\Delta^{V}_{Cd} & \frac{-1}{\sqrt{3}}P'^{V+}_{Xd} & \frac{1}{\sqrt{2}}P'^{V-}_{Xd} & 0 \\
\frac{1}{2}\Delta^{V}_{3C} & \frac{1}{\sqrt{2}}P^{V+}_{3C} & -\sqrt{\frac{3}{2}}P^{V-}_{3C} & 0 & 0 & \frac{-1}{\sqrt{3}}P'^{Vz}_{Xd} & \frac{1}{\sqrt{3}}P'^{V-}_{Xd} & \frac{1}{3}\Delta^{V}_{Cd} & \sqrt{\frac{2}{3}}P'^{Vz}_{Xd} & \frac{-1}{\sqrt{6}}P'^{V-}_{Xd} \\
\frac{-2}{\sqrt{3}}P^{Vz}_{3C} & \frac{1}{\sqrt{3}}P^{V-}_{3C} & -P^{V+}_{3C} & 0 & \frac{-1}{\sqrt{6}}P'^{V-}_{Xd} & \frac{-1}{\sqrt{2}}P'^{V+}_{Xd} & \frac{-1}{\sqrt{2}}P'^{V+}_{Xd} & -\sqrt{\frac{2}{3}}P'^{Vz}_{Xd} & 0 & 0 \\
\frac{1}{\sqrt{3}}P^{V+}_{3C} & \frac{2}{\sqrt{3}}P^{Vz}_{3C} & -P^{V-}_{3C} & 0 & -\sqrt{\frac{2}{3}}P'^{Vz}_{Xd} & \frac{1}{\sqrt{2}}P'^{V-}_{Xd} & \frac{1}{\sqrt{3}}P'^{V+}_{Xd} & 0 & \frac{1}{\sqrt{3}}P'^{Vz}_{d} & \frac{-2}{3}\Delta^{V}_{Cd} \\
0 & 0 & 0 & 0 & \frac{-1}{\sqrt{2}}P'^{Vz}_{d} & \frac{1}{\sqrt{6}}P'^{V-}_{d} & 0 & \frac{1}{\sqrt{3}}P'^{Vz}_{d} & \frac{1}{\sqrt{3}}P'^{V-}_{d} & \frac{1}{\sqrt{3}}P'^{V-}_{d} \\
0 & 0 & 0 & 0 & 0 & \sqrt{\frac{2}{3}}P'^{Vz}_{d} & \frac{1}{\sqrt{2}}P'^{V-}_{d} & \frac{1}{\sqrt{3}}P'^{V+}_{d} & \frac{-1}{\sqrt{3}}P'^{Vz}_{d} & \frac{-1}{\sqrt{3}}P'^{Vz}_{d} \\
\frac{-1}{\sqrt{2}}P'^{V-}_{3} & \frac{-1}{2}\Delta'^{V}_{3} & \sqrt{\frac{3}{2}}P'^{V+}_{3} & 0 & \frac{1}{3}\Delta^{V}_{dso} & \frac{-1}{\sqrt{3}}P'^{Vz}_{d} & \frac{-1}{\sqrt{3}}P'^{V+}_{d} & 0 & \frac{-1}{\sqrt{6}}P'^{V+}_{d} & -\sqrt{\frac{2}{3}}P'^{Vz}_{d} \\
-2\sqrt{\frac{2}{3}}P'^{Vz}_{3} & \frac{-1}{\sqrt{6}}P'^{V-}_{3} & -2\sqrt{\frac{2}{3}}P'^{Vz}_{3} & \frac{1}{\sqrt{2}}P'^{V+}_{3} & \frac{1}{3}\Delta^{V}_{dso} & 0 & \frac{1}{3}\Delta^{V}_{dso} & \frac{-1}{\sqrt{3}}P'^{V-}_{d} & \frac{1}{\sqrt{3}}P'^{V+}_{d} & 0 \\
\frac{1}{\sqrt{6}}P'^{V+}_{3} & \frac{1}{2}\Delta'^{V}_{3} & \frac{1}{2}\Delta'^{V}_{3} & \frac{-1}{\sqrt{2}}P'^{V-}_{3} & 0 & \frac{1}{\sqrt{3}}P'^{Vz}_{d} & \frac{1}{3}\Delta^{V}_{dso} & \frac{-1}{\sqrt{2}}P'^{V-}_{d} & \frac{-1}{\sqrt{2}}P'^{V-}_{d} & \frac{1}{\sqrt{6}}P'^{V-}_{d} \\
\frac{1}{2}\Delta'^{V}_{3} & \frac{1}{\sqrt{2}}P'^{V+}_{3} & \frac{-1}{2}\Delta'^{V}_{3} & -\sqrt{\frac{3}{2}}P'^{V-}_{3} & 0 & \frac{1}{\sqrt{3}}P'^{V-}_{d} & \frac{1}{3}\Delta^{V}_{dso} & \frac{1}{\sqrt{3}}P'^{Vz}_{d} & -\frac{2}{3}\Delta^{V}_{dso} & 0 \\
\frac{-2}{\sqrt{3}}P'^{Vz}_{3} & \frac{1}{\sqrt{3}}P'^{V-}_{3} & -P'^{V+}_{3} & \frac{1}{\sqrt{6}}P'^{V-}_{d} & 0 & \frac{1}{\sqrt{2}}P'^{V+}_{d} & \frac{1}{\sqrt{3}}P'^{Vz}_{d} & \frac{-1}{\sqrt{6}}P'^{V+}_{d} & 0 & \frac{-2}{3}\Delta^{V}_{dso} \\
\frac{1}{\sqrt{3}}P'^{V+}_{3} & \frac{-2}{\sqrt{3}}P'^{Vz}_{3} & -P'^{V-}_{3} & \frac{-1}{\sqrt{2}}P'^{V-}_{d} & \frac{1}{\sqrt{3}}P'^{Vz}_{d} & 0 & \frac{1}{\sqrt{6}}P'^{V-}_{Sd} & \frac{1}{\sqrt{3}}P'^{Vz}_{Sd} & \frac{1}{\sqrt{3}}P'^{V-}_{Sd} & \frac{1}{\sqrt{3}}P'^{V-}_{Sd} \\
0 & 0 & 0 & 0 & \frac{-1}{\sqrt{2}}P'^{V+}_{Sd} & 0 & \frac{1}{\sqrt{6}}P'^{V-}_{Sd} & \frac{1}{\sqrt{3}}P'^{V+}_{Sd} & \frac{1}{\sqrt{3}}P'^{Vz}_{Sd} & \frac{-1}{\sqrt{3}}P'^{Vz}_{Sd} \\
0 & 0 & 0 & 0 & 0 & \frac{-1}{\sqrt{6}}P'^{V+}_{Sd} & \sqrt{\frac{2}{3}}P'^{Vz}_{Sd} & \frac{1}{\sqrt{2}}P'^{V-}_{Sd} & 0 & \frac{1}{\sqrt{3}}P'^{V-}_{ud} \\
0 & 0 & 0 & 0 & \frac{-1}{\sqrt{2}}P'^{V+}_{ud} & \sqrt{\frac{2}{3}}P'^{Vz}_{ud} & \frac{1}{\sqrt{6}}P'^{V-}_{ud} & 0 & \frac{1}{\sqrt{3}}P'^{Vz}_{ud} & \frac{-1}{\sqrt{3}}P'^{Vz}_{ud} \\
0 & 0 & 0 & 0 & 0 & \frac{-1}{\sqrt{6}}P'^{V+}_{ud} & \sqrt{\frac{2}{3}}P'^{Vz}_{ud} & \frac{1}{\sqrt{3}}P'^{V+}_{ud} & \frac{-2}{\sqrt{3}}P'^{z}_{3d} & \frac{1}{\sqrt{3}}P'^{-}_{3d} \\
0 & 0 & 0 & 0 & \frac{-1}{\sqrt{2}}P'^{+}_{3d} & -2\sqrt{\frac{2}{3}}P'^{z}_{3d} & \frac{1}{\sqrt{6}}P'^{-}_{3d} & \frac{1}{2}\Delta^{V}_{3d} & \frac{1}{\sqrt{3}}P'^{-}_{3d} & \frac{2}{\sqrt{3}}P'^{z}_{3d} \\
0 & 0 & 0 & 0 & \frac{-1}{2}\Delta^{V}_{3d} & \frac{-1}{\sqrt{6}}P'^{+}_{3d} & -2\sqrt{\frac{2}{3}}P'^{z}_{3d} & \frac{1}{\sqrt{2}}P'^{-}_{3d} & \frac{1}{\sqrt{3}}P'^{+}_{3d} & \frac{1}{\sqrt{3}}P'^{-}_{3d}
\end{pmatrix}
$$

$$
\mathbb{F} = \begin{pmatrix}
0 & 0 & 0 & 0 & \sqrt{\frac{3}{2}}P^{\prime -}_{3d} & \frac{-1}{2}\Delta^{V}_{3d} & \frac{-1}{\sqrt{2}}P^{\prime +}_{3d} & 0 & 0 & -P^{\prime +}_{3d} \\
0 & 0 & 0 & 0 & 0 & \frac{1}{\sqrt{2}}P^{\prime -}_{3d} & \frac{1}{2}\Delta^{V}_{3d} & -\sqrt{\frac{3}{2}}P^{\prime +}_{3d} & -P^{\prime -}_{3d} & 0 \\
\frac{-1}{\sqrt{2}}P^{\prime V-}_{3d} & \frac{-1}{2}\Delta^{V}_{3d} & \sqrt{\frac{3}{2}}P^{\prime V+}_{3d} & 0 & \frac{1}{2}\Delta_{dd} & \frac{1}{\sqrt{3}}P^{+}_{dd} & \frac{1}{\sqrt{3}}P^{z}_{dd} & 0 & \frac{1}{\sqrt{6}}P^{+}_{dd} & \sqrt{\frac{2}{3}}P^{z}_{dd} \\
-2\sqrt{\frac{2}{3}}P^{\prime Vz}_{3d} & \frac{-1}{\sqrt{6}}P^{\prime V-}_{3d} & \frac{-1}{2}\Delta^{V}_{3d} & \frac{1}{\sqrt{2}}P^{\prime V+}_{3d} & \frac{-1}{\sqrt{3}}P^{-}_{dd} & \frac{1}{3}\Delta_{dd} & 0 & \frac{1}{\sqrt{3}}P^{z}_{dd} & 0 & \frac{-1}{\sqrt{2}}P^{+}_{dd} \\
\frac{1}{\sqrt{6}}P^{\prime V+}_{3d} & -2\sqrt{\frac{2}{3}}P^{\prime Vz}_{3d} & \frac{-1}{\sqrt{2}}P^{\prime V-}_{3d} & \frac{1}{2}\Delta^{V}_{3d} & \frac{-1}{\sqrt{3}}P^{z}_{dd} & 0 & \frac{-1}{\sqrt{3}}P^{+}_{dd} & \frac{\Delta_{dd}}{3} & \sqrt{\frac{2}{3}}P^{z}_{dd} & \frac{-1}{\sqrt{6}}P^{-}_{dd} \\
\frac{1}{2}\Delta^{V}_{3d} & \frac{1}{\sqrt{2}}P^{\prime V+}_{3d} & 0 & -\sqrt{\frac{3}{2}}P^{\prime V-}_{3d} & 0 & \frac{-1}{\sqrt{3}}P^{z}_{dd} & \frac{-1}{\sqrt{3}}P^{-}_{dd} & -\sqrt{\frac{2}{3}}P^{z}_{dd} & \frac{-2}{3}\Delta_{dd} & 0 \\
\frac{-2}{\sqrt{3}}P^{\prime Vz}_{3d} & \frac{1}{\sqrt{3}}P^{\prime V-}_{3d} & 0 & -P^{V+}_{3d} & \frac{-1}{\sqrt{6}}P^{-}_{dd} & 0 & \frac{-1}{\sqrt{2}}P^{+}_{dd} & \frac{1}{\sqrt{6}}P^{+}_{dd} & 0 & \frac{-2}{3}\Delta_{dd} \\
\frac{1}{\sqrt{3}}P^{\prime V+}_{3d} & \frac{2}{\sqrt{3}}P^{\prime Vz}_{3d} & -P^{\prime V-}_{3d} & 0 & -\sqrt{\frac{2}{3}}P^{z}_{dd} & \frac{1}{\sqrt{2}}P^{-}_{dd} & 0 & \frac{1}{\sqrt{2}}P^{\prime -}_{2d} & \frac{1}{\sqrt{3}}P^{\prime z}_{2d} & \frac{1}{\sqrt{3}}P^{\prime -}_{2d} \\
0 & 0 & 0 & 0 & 0 & \frac{1}{\sqrt{2}}P^{\prime -}_{2d} & \frac{1}{\sqrt{2}}P^{\prime z}_{2d} & \frac{1}{\sqrt{2}}P^{\prime -}_{2d} & \frac{1}{\sqrt{3}}P^{\prime +}_{2d} & \frac{-1}{\sqrt{3}}P^{\prime z}_{2d} \\
0 & 0 & 0 & 0 & 0 & \frac{-1}{\sqrt{6}}P^{\prime +}_{2d} & \sqrt{\frac{2}{3}}P^{\prime z}_{2d} & \frac{-1}{\sqrt{2}}P^{\prime +}_{2d} & \frac{-2}{\sqrt{3}}P^{Vz}_{3d} & \frac{1}{\sqrt{3}}P^{V-}_{3d} \\
E^{kV}_{dd} & 0 & 0 & 0 & \frac{-1}{\sqrt{2}}P^{V+}_{3d} & -2\sqrt{\frac{2}{3}}P^{Vz}_{3d} & \frac{1}{\sqrt{6}}P^{V-}_{3d} & \frac{1}{2}\Delta^{V}_{d} & \frac{1}{\sqrt{3}}P^{V+}_{3d} & -P^{V+}_{3d} \\
cc & E^{kV}_{dd} & 0 & 0 & \frac{-1}{2}\Delta^{V}_{d} & \frac{-1}{\sqrt{6}}P^{V+}_{3d} & -2\sqrt{\frac{2}{3}}P^{Vz}_{3d} & \frac{1}{\sqrt{2}}P^{V-}_{3d} & \frac{1}{\sqrt{3}}P^{V+}_{3d} & \frac{2}{\sqrt{3}}P^{Vz}_{3d} \\
cc & cc & E^{kV}_{dd} & 0 & \sqrt{\frac{3}{2}}P^{V-}_{3d} & \frac{-1}{2}\Delta^{V}_{d} & \frac{-1}{\sqrt{2}}P^{V+}_{3d} & 0 & 0 & -P^{V+}_{3d} \\
cc & cc & cc & E^{kV}_{dd} & 0 & \frac{1}{2}\Delta^{V}_{d} & \frac{1}{\sqrt{2}}P^{V-}_{3d} & -\sqrt{\frac{3}{2}}P^{V+}_{3d} & -P^{V-}_{3d} & 0 \\
cc & cc & cc & cc & E^{kV}_{8d} & \mathcal{B}^{V}_{d} & C^{V}_{d} & 0 & \frac{1}{\sqrt{2}}\mathcal{B}^{V}_{d} & \sqrt{2}C^{V}_{d} \\
cc & cc & cc & cc & cc & E^{kV}_{8d} & 0 & C^{V}_{d} & -\sqrt{2}\mathcal{U}^{V}_{d} & -\sqrt{\frac{3}{2}}\mathcal{B}^{V}_{d} \\
cc & cc & cc & cc & cc & cc & E^{kV}_{8d} & -\mathcal{B}^{V}_{d} & -\sqrt{\frac{3}{2}}\left(\mathcal{B}^{V}_{d}\right)^{*} & \sqrt{2}\mathcal{U}^{V}_{d} \\
cc & cc & cc & cc & cc & cc & cc & E^{kV}_{8d} & -\sqrt{2}\left(C^{V}_{d}\right)^{*} & \frac{1}{\sqrt{2}}\left(\mathcal{B}^{V}_{d}\right)^{*} \\
cc & cc & cc & cc & cc & cc & cc & cc & E^{kV}_{7d} & 0 \\
cc & cc & cc & cc & cc & cc & cc & cc & cc & E^{kV}_{7d}
\end{pmatrix}
\tag{A.57}
$$

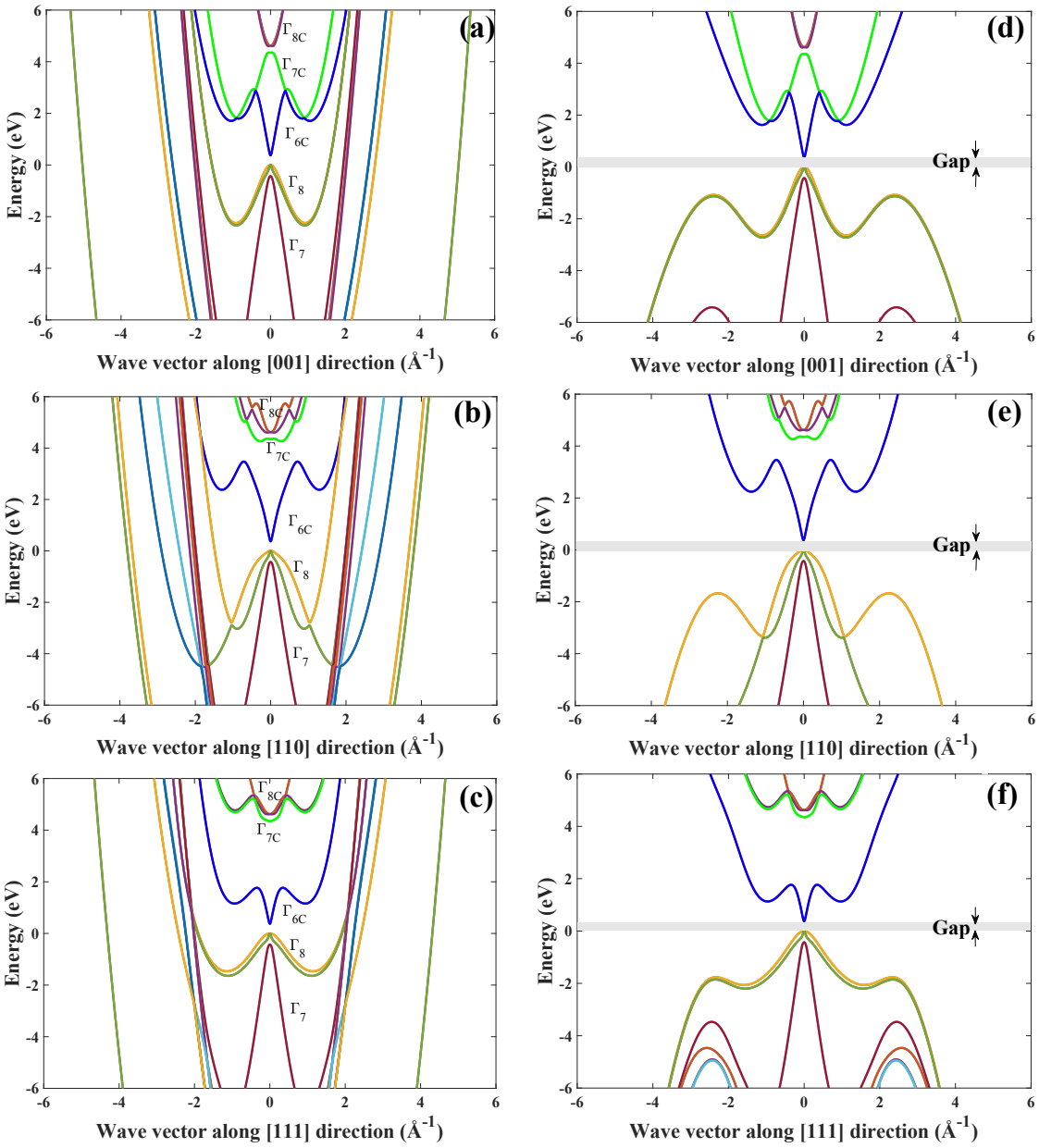

FIGURE A.11: Real band structure of InAs calculated via 40 bands $\boldsymbol{k.p}$ model before (a,b,c) and after (d,e,f) using our novel ghost-band method to remove spurious states.

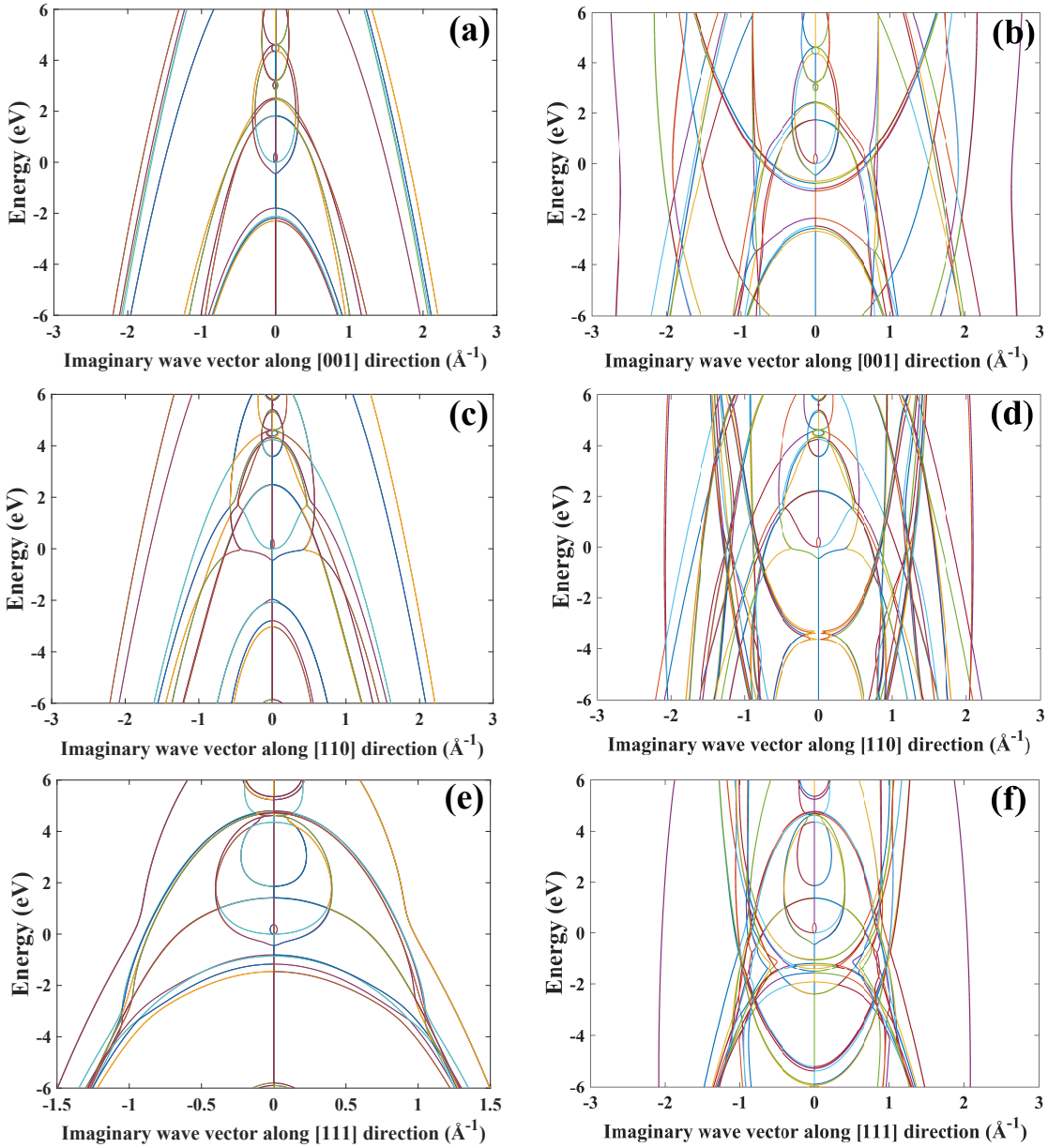

FIGURE A.12: Complex band structure of InAs calculated via 40 bands $\boldsymbol{k.p}$ model before (a,b,c) and after (d,e,f) using our novel ghost-band method to remove spurious states.

APPENDIX B

Error estimation of ghost-band method

This appendix is devoted to the validation of ghost band method with tunneling problem as well as with band structure. By considering the tunneling of an electron or a hole through simple barrier structure and plotting the transmission coefficient as a function of barrier thickness in logarithm scale with different ghost-band coupling strengths, one may extract the effective mass for electron and holes as well as the errors induced by ghost band method. Typically, we will show that the relative error of effective mass will be very small in order of 10^{-5}. Besides, using Löwdin partitioning method to obtain an effective Hamiltonian for the Γ_1 conduction band and Γ_5^v valence band from 14 band $\boldsymbol{k.p}$ Hamiltonian involving the ghost bands, we show that the contribution of ghost band on dispersion of CB and VB are in the order of k^5 where k is the wave vector. The same treatment can be done with 30 and 40 band method with the same argument prove that our ghost band method is extremely robust to get rid of spurious states.

B.1 Error on effective mass extracted from a tunneling problem

In order to extract the effective mass and its error induced by ghost-band method, we now consider a tunneling problem where an electron with wavefunction $\psi(x) = e^{ikx}$ of energy $E = \hbar^2 k^2/2m$ from $-\infty$, tunnels through a square potential $V(x) = V_0([0, a])$.

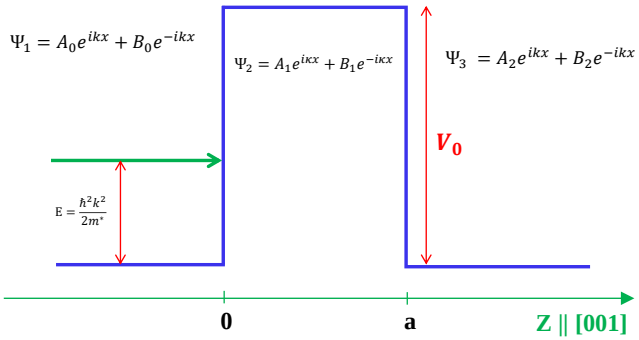

FIGURE B.1: Scheme of the tunneling process of an electron through a barrier structure.

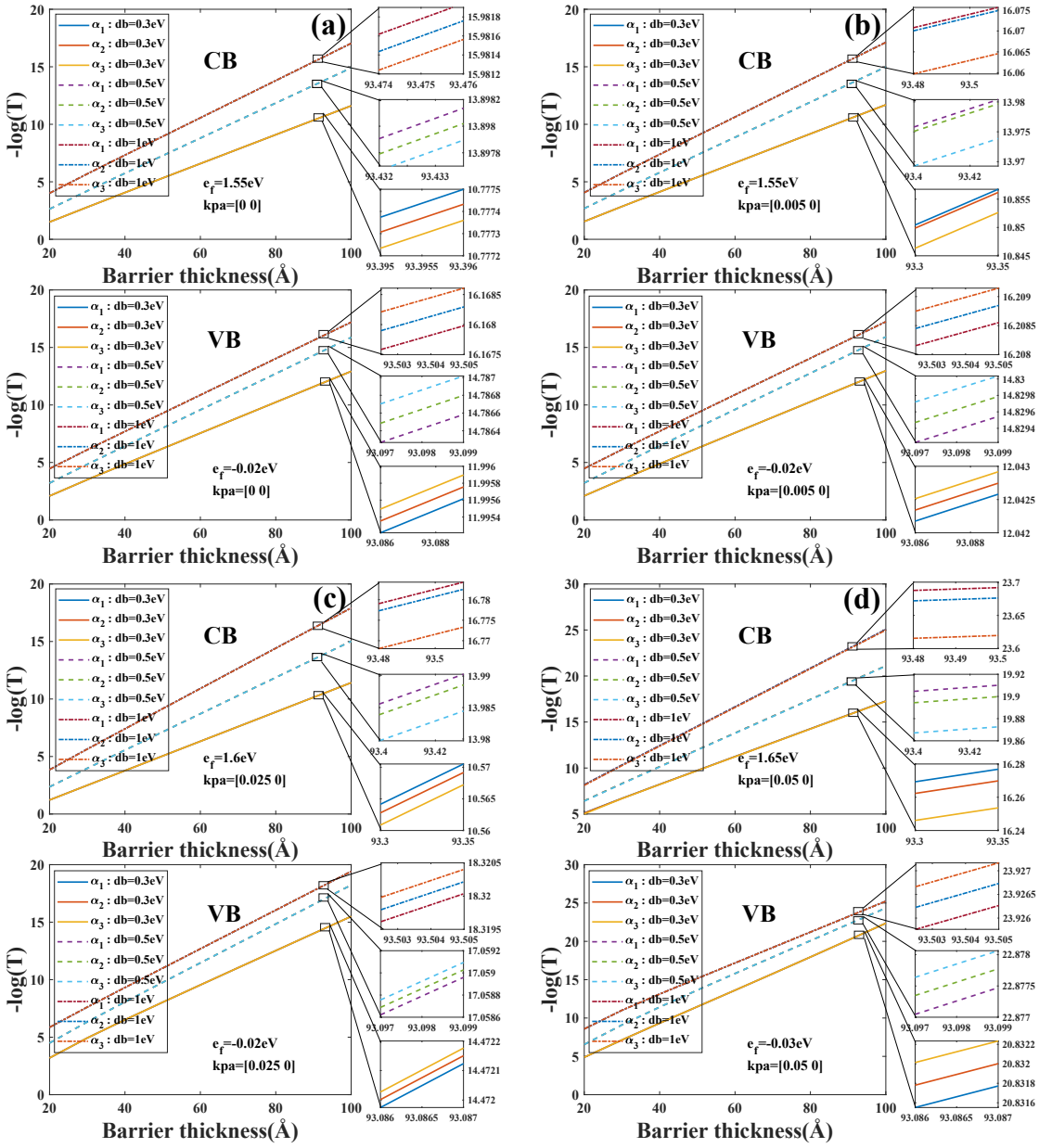

FIGURE B.2: Transmission of carriers (in log. scale) vs. the barrier thickness d in fictitious GaAs/GaAs/GaAs trilayer barrier with different barrier's height and different incident electron wave vectors. The slope of the transmission in log. scale vs d is related to the tunneling effective mass which remains robust under ghost-spurious coupling strength α: $\{\alpha_1 = 1eV.A^{-2}; \alpha_2 = 1.5eV.A^{-2}; \alpha_3 = 2eV.A^{-2}\}$ in framework of 30-band model.

The solutions of Schrödinger equation $(p^2/2m + V)\psi = E\psi$ in each of the domains can be written as:

$$\psi(x) = A_0 e^{ikx} + B_0 e^{-ikx}, \quad \text{for } x \in [-\infty, 0] \tag{B.1}$$

$$\psi(x) = A_1 e^{\kappa x} + B_1 e^{-\kappa x}, \quad \text{for } x \in [0, a] \tag{B.2}$$

$$\psi(x) = A_2 e^{ikx} + B_2 e^{-ikx}, \quad \text{for } x \in [a, +\infty] \tag{B.3}$$

where $k = \sqrt{2m^* E}/\hbar$ and $\kappa = \sqrt{2m^*(V_0 - E)}/\hbar$.

Applying the standard matching conditions at each interface, one obtains:

$$1 + B_0 = A_1 + B_1 \tag{B.4}$$

$$ik - ikB_0 = \kappa A_1 - \kappa A_2 \tag{B.5}$$

$$A_1 e^{\kappa a} + B_1 e^{-\kappa a} = A_2 e^{ika} \tag{B.6}$$

$$\kappa A_1 e^{\kappa a} - \kappa B_1 e^{-\kappa a} = ikA_2 e^{ika} \tag{B.7}$$

The transmission coefficient is given by:

$$T = \frac{|\psi_{out}|^2}{|\psi_{in}|^2} = |A_2|^2 = 16\left(\frac{k\kappa}{k^2 + \kappa^2}\right)^2 e^{-2\kappa a} \tag{B.8}$$

we thus have a relation between the logarithm of the transmission coefficient T and the barrier thickness a

$$\ln T = C(k, \kappa) - 2\kappa a = \tilde{C}(E, \phi) - \frac{2\sqrt{2m^*\phi}}{\hbar} a \tag{B.9}$$

where $\phi = V_0 - E$. The effective mass m^* can be extracted from the slope of $\ln T$ as a function of barrier thickness a. Figure B.2 displays the calculations of transmission coefficient as a function of the barrier thickness. Those show that the slopes remain robust under three different values of ghost-spurious coupling strength. On the other word, the effective mass is weakly affected by the ghost-band method.

B.2 Errors induced by ghost-band method: The effective Hamiltonian

B.2.1 Luttinger–Kohn perturbation theory

Theory and demonstration The Luttinger-Kohn perturbation theory or Löwdin partitioning is a generalization of perturbations theory in quantum mechanics. This method is very powerful and general because it no longer distinguishes between degenerate and non-degenerate cases leading to a possibility to deal this perturbation with subspaces of any dimension of the Hilbert space. However, this method is not so well-known in quantum mechanics, we therefore present here the description of this method and will then apply it to calculate the errors induced by our novel ghost band method with effective Hamiltonian.

The key point of this method is that one may assume that the Hamiltonian $\mathcal{H}$ of interested systems can be expressed as the sum of two part: $\mathcal{H}_0$ with known eigenvalues and eigengunctions; and $\mathcal{H}'$ which can be treated as a perturbation:

$$\mathcal{H} = \mathcal{H}_0 + \mathcal{H}' \tag{B.10}$$

Assuming that the Hilbert space corresponding to $\mathcal{H}$ can be divided into two sets A and B leading to the fact that one can write this Hamiltonian in the block form. If we are only interested in the eigenvalues

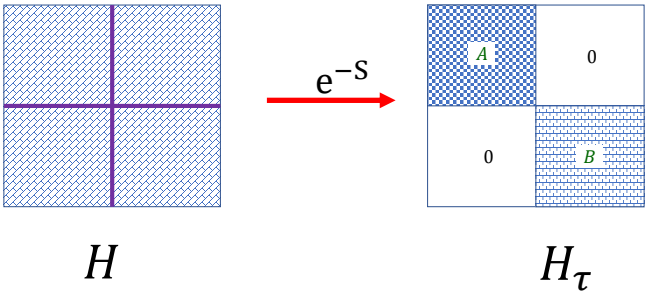

FIGURE B.3: Removal of off-diagonal elements of H.

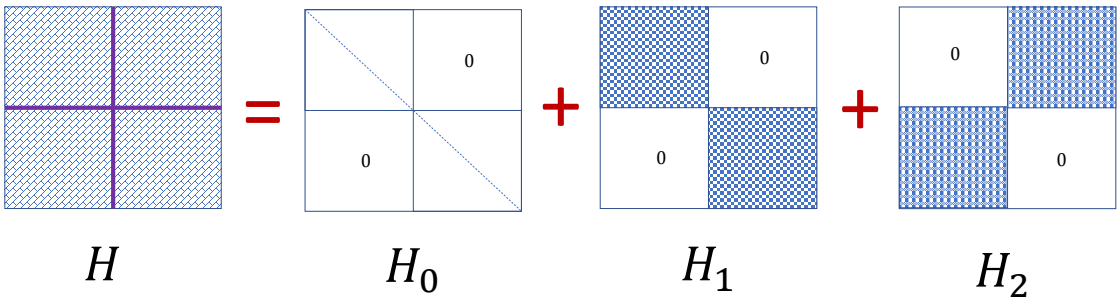

FIGURE B.4: Representation of H as the sum of H_0, H_1, and H_2 where H_0 is a truly diagonal matrix, H_1 is diagonal block matrix and H_2 is off-diagonal block matrix

of the block generated by the set A, the Luttinger-Kohn's perturbation theory makes it possible to deal with the effect of the couplings between A and B due to $\mathcal{H}'$, as well as the effect of projection of set B into set A, as perturbations.

The basic idea of this theory is to find (construct) a representation via a unitary operator $e^{\mathcal{S}}$ such that for the transformed Hamiltonian

$$\mathcal{H}_{\mathcal{T}} = e^{-\mathcal{S}}\mathcal{H}e^{\mathcal{S}} \tag{B.11}$$

this Hamiltonian $\mathcal{H}_{\mathcal{T}}$ does not have any couplings between the two spaces. In order to do that, we first start with the perturbative Hamiltonian $\mathcal{H}'$ and assume that this Hamiltonian $\mathcal{H}'$ can be divided in two part:

- $\mathcal{H}_1$: which has nonzero matrix elements only between the eigenfunctions within the sets A and B.
- $\mathcal{H}_2$: which has nonzero matrix elements only between the sets A and B

This procedure is depicted in the Fig. B.4. One observes that, we must construct $\mathcal{S}$ such that the transformation B.11 converts $\mathcal{H}_2$ into a block-diagonal Hamiltonian as same as H_1 while keeping the desired block-diagonal form of $\mathcal{H}_0 + \mathcal{H}_1$. Moreover, since $e^{\mathcal{S}}$ is unitary, therefore $\mathcal{S}$ must be anti-hermitian, i.e. $\mathcal{S}^{\dagger} = -\mathcal{S}$. In order to determine $\mathcal{S}$, we expand $e^{\pm\mathcal{S}}$ in a series:

$$e^{\pm\mathcal{S}} = \sum_{n=0}^{\infty} \frac{(\pm 1)^n}{n!}\mathcal{S}^n \tag{B.12}$$

writing $\mathcal{H}_\mathcal{T}$ as a polynomial function of $\mathcal{S}$, one has:

$$\mathcal{H}_\mathcal{T} = \left(\sum_{n=0}^{\infty} \frac{(-1)^n}{n!}\mathcal{S}^n\right)\mathcal{H}\left(\sum_{k=0}^{\infty}\frac{1}{k!}\mathcal{S}^k\right) = \sum_{n=0}^{\infty}\sum_{k=0}^{\infty}\frac{(-1)^n}{n!k!}\mathcal{S}^n\mathcal{H}\mathcal{S}^k \tag{B.13}$$

If we define commutators between two operators $\mathcal{A}$ and $\mathcal{B}$ as following:

$$[\mathcal{A},\mathcal{B}]^{(0)} = \mathcal{A} \tag{B.14}$$

$$[\mathcal{A},\mathcal{B}]^{(1)} = [\mathcal{A},\mathcal{B}] = \mathcal{A}\mathcal{B} - \mathcal{B}\mathcal{A} \tag{B.15}$$

$$[\mathcal{A},\mathcal{B}]^{(n+1)} = \left[[\mathcal{A},\mathcal{B}]^{(n)},\mathcal{B}\right] \tag{B.16}$$

then one may easily prove that:

$$[\mathcal{A},\mathcal{B}]^{(n)} = \sum_{k=0}^{n}(-1)^k\binom{n}{k}\mathcal{B}^k\mathcal{A}\mathcal{B}^{n-k} \tag{B.17}$$

or in the case of $\mathcal{H}$ and $\mathcal{S}$:

$$[\mathcal{H},\mathcal{S}]^{(n)} = \sum_{k=0}^{n}(-1)^k\binom{n}{k}\mathcal{S}^k\mathcal{H}\mathcal{S}^{n-k} \tag{B.18}$$

by inductive approach. Indeed, one observes that for $n = 0$, the equality is correct. If we assume that the equality is correct up to the rank n, the:

$$[\mathcal{H},\mathcal{S}]^{(n+1)} = [\mathcal{H},\mathcal{S}]^{(n)}\mathcal{S} - \mathcal{S}\,[\mathcal{H},\mathcal{S}]^{(n)} \tag{B.19}$$

$$= \sum_{k=0}^{n}(-1)^k\binom{n}{k}\mathcal{S}^k\mathcal{H}\mathcal{S}^{(n+1-k)} - \sum_{k=1}^{n+1}(-1)^{k-1}\binom{n}{k-1}\mathcal{S}^k\mathcal{H}\mathcal{S}^{(n+1-k)} \tag{B.20}$$

$$= \mathcal{H}\mathcal{S}^{n+1} + (-1)^{n+1}\mathcal{S}^{n+1}\mathcal{H} + \sum_{k=1}^{n}(-1)^k\left(\binom{n}{k} + \binom{n}{k-1}\right)\mathcal{S}^k\mathcal{H}\mathcal{S}^{(n+1-k)} \tag{B.21}$$

$$= \sum_{k=0}^{n+1}(-1)^k\binom{n+1}{k}\mathcal{S}^k\mathcal{H}\mathcal{S}^{(n+1-k)} \tag{B.22}$$

Or one may state that the equality B.18 is fulfilled for all n. Besides, one has :

$$\sum_{n=0}^{\infty}\frac{1}{n!}[\mathcal{H},\mathcal{S}]^{(n)} = \sum_{n=0}^{\infty}\sum_{k=0}^{\infty}\mathbb{1}(k\le n)\frac{(-1)^k n!}{n!k!(n-k)!}\mathcal{S}^k\mathcal{H}\mathcal{S}^{n-k} \tag{B.23}$$

$$= \sum_{k=0}^{\infty}\sum_{n'=-k}^{\infty}\frac{\mathbb{1}(k\le n'+k)(-1)^k}{k!n'!}\mathcal{S}^k\mathcal{H}\mathcal{S}^{n'} \tag{B.24}$$

$$= \sum_{n=0}^{\infty}\sum_{k=0}^{\infty}\frac{(-1)^k}{k!n!}\mathcal{S}^k\mathcal{H}\mathcal{S}^n \tag{B.25}$$

$$= \mathcal{H}_\mathcal{T} \tag{B.26}$$

We are now trying to divide $\mathcal{H}_\mathcal{T}$ into a purely block-diagonal part and purely non-block-diagonal part. For this, we notice that a product of p (number of) block-diagonal matrices and q (number of) non-block-diagonal matrices is block-diagonal matrix if q is even and non-block-diagonal matrix if q is odd. We then have the division of $\mathcal{H}_\mathcal{T}$ in its diagonal part $\mathcal{H}_\mathcal{T}^d$ and off-diagonal part $\mathcal{H}_\mathcal{T}^{hd}$ read:

$$\mathcal{H}_\mathcal{T} = \mathcal{H}_\mathcal{T}^d + \mathcal{H}_\mathcal{T}^{hd} \tag{B.27}$$

where

$$\mathcal{H}_{\mathcal{T}}^{d} = \sum_{j=0}^{\infty} \frac{1}{(2j)!} [\mathcal{H}_0 + \mathcal{H}_1, \mathcal{S}]^{(2j)} + \sum_{j=0}^{\infty} \frac{1}{(2j+1)!} [\mathcal{H}_2, \mathcal{S}]^{(2j+1)} \tag{B.28}$$

$$\mathcal{H}_{\mathcal{T}}^{hd} = \sum_{j=0}^{\infty} \frac{1}{(2j+1)!} [\mathcal{H}_0 + \mathcal{H}_1, \mathcal{S}]^{(2j+1)} + \sum_{j=0}^{\infty} \frac{1}{(2j)!} [\mathcal{H}_2, \mathcal{S}]^{(2j)} \tag{B.29}$$

Note that our initial goal was to transform $\mathcal{H}$ into diagonal block. It can be done if the condition $\mathcal{H}_{\mathcal{T}}^{hd} = 0$ is satisfied. We recall that the Hamiltonian $\mathcal{H} = \mathcal{H}_0 + \mathcal{H}_1 + \mathcal{H}_2$ where $\mathcal{H}_0$ is of the order 0 and $\mathcal{H}_1$ as well as $\mathcal{H}_2$ are of the order 1. We then expand the matrix $\mathcal{S} = \mathcal{S}^{(1)} + \mathcal{S}^{(2)} + \mathcal{S}^{(3)} + ...$, with $\mathcal{S}^{(p)}$ is order p.

Since each order in $\mathcal{S}$ and $\mathcal{H}$ satisfies the equation $\mathcal{H}_{\mathcal{T}}^{hd} = 0$, we obtain:

$$\left[\mathcal{H}_0, \mathcal{S}^{(1)}\right] = -\mathcal{H}_2 \tag{B.30}$$

$$\left[\mathcal{H}_0, \mathcal{S}^{(2)}\right] = -\left[\mathcal{H}_0, \mathcal{S}^{(1)}\right] \tag{B.31}$$

$$\left[\mathcal{H}_0, \mathcal{S}^{(3)}\right] = -\left[\mathcal{H}_1, \mathcal{S}^{(2)}\right] - \frac{1}{3}\left[\mathcal{H}_2, \mathcal{S}^{(1)}\right]^{(2)} \tag{B.32}$$

These relations can be reversed to find the $\mathcal{S}_{ml}^{(p)}$. If we assume that m, m', m'', etc. correspond to the set A, and l, l', l'' are those of set B, then one has:

$$\mathcal{S}_{ml}^{(1)} = -\frac{\mathcal{H}_{ml}}{E_m - E_l} \tag{B.33}$$

$$\mathcal{S}_{ml}^{(2)} = \frac{1}{E_m - E_l}\left(\sum_{m'} \frac{\mathcal{H}_{mm'}\mathcal{H}_{m'l}}{E_{m'} - E_l} - \sum_{l'} \frac{\mathcal{H}_{ml'}\mathcal{H}_{l'l}}{E_m - E_{l'}}\right) \tag{B.34}$$

$$\mathcal{S}_{ml}^{(3)} = \frac{1}{E_m - E_l}\Bigg(- \sum_{m'm''} \frac{\mathcal{H}_{mm''}\mathcal{H}_{m''m'}\mathcal{H}_{m'l}}{(E_{m''} - E_l)(E_{m'} - E_l)} - \sum_{l'l''} \frac{\mathcal{H}_{ml'}\mathcal{H}_{l'l''}\mathcal{H}_{l''l}}{(E_m - E_{l''})(E_m - E_{l'})} \tag{B.35}$$

$$+ \sum_{l'm'} \frac{\mathcal{H}_{mm'}\mathcal{H}_{m'l'}\mathcal{H}_{l'l}}{(E_{m'} - E_l)(E_{m'} - E_{l'})} + \sum_{l'm'} \frac{\mathcal{H}_{mm'}\mathcal{H}_{m'l'}\mathcal{H}_{l'l}}{(E_m - E_{l'})(E_{m'} - E_{l'})} \tag{B.36}$$

$$+ \frac{1}{3}\sum_{l'm'} \frac{\mathcal{H}_{ml'}\mathcal{H}_{l'm'}\mathcal{H}_{m'l}}{(E_{m'} - E_{l'})(E_{m'} - E_l)} + \frac{1}{3}\sum_{l'm'} \frac{\mathcal{H}_{ml'}\mathcal{H}_{l'm'}\mathcal{H}_{m'l}}{(E_m - E_{l'})(E_{m'} - E_{l'})} \tag{B.37}$$

$$+ \frac{2}{3}\sum_{l'm'} \frac{\mathcal{H}_{ml'}\mathcal{H}_{l'm'}\mathcal{H}_{m'l}}{(E_m - E_{l'})(E_{m'} - E_l)}\Bigg) \tag{B.38}$$

$$... = ... \tag{B.39}$$

where $H_{ml} = \langle\psi_m|H|\psi_l\rangle$. Inserting this expression of $\mathcal{S}$ into the expression of $\mathcal{H}_{\mathcal{T}} = \mathcal{H}_{\mathcal{T}}^{d}$ to obtain the series expression of $\mathcal{H}_{\mathcal{T}} = \mathcal{H}_{\mathcal{T}}^{(0)} + \mathcal{H}_{\mathcal{T}}^{(1)} + \mathcal{H}_{\mathcal{T}}^{(2)} + ...$ where:

$$H^{(0)}_{mm'} = H^{0}_{mm'} \tag{B.40}$$

$$H^{(1)}_{mm'} = H^{'}_{mm'} \tag{B.41}$$

$$H^{(2)}_{mm'} = \frac{1}{2}\sum_{l} H^{'}_{ml}H^{'}_{lm'}\left[\frac{1}{E_m - E_l} + \frac{1}{E_{m'} - E_l}\right] \tag{B.42}$$

$$H^{(3)}_{mm'} = -\frac{1}{2}\sum_{l,m''}\left[\frac{H^{'}_{ml}H^{'}_{lm''}H^{'}_{m''m'}}{(E_{m'} - E_l)(E_{m''} - E_l)} + \frac{H^{'}_{mm''}H^{'}_{m''l}H^{'}_{lm'}}{(E_m - E_l)(E_{m''} - E_l)}\right] + \frac{1}{2}\sum_{l,l'} H^{'}_{ml}H^{'}_{ll'}H^{'}_{l'm'}\left[\frac{1}{(E_m - E_l)(E_m - E_{l'})} + \frac{1}{(E_{m'} - E_l)(E_{m'} - E_{l'})}\right] \tag{B.43}$$

$$\begin{aligned} H^{(4)}_{mm'} = {} & \frac{1}{2}\sum_{l,m'',m'''} \frac{1}{(E_{m''} - E_l)(E_{m''} - E_l)}\left[\frac{H^{'}_{mm''}H^{'}_{m''m'''}H^{'}_{m'''l}H^{'}_{lm'}}{E_m - E_l} + \frac{H^{'}_{ml}H^{'}_{lm''}H^{'}_{m''m'''}H^{'}_{m'''m'}}{E_{m'} - E_l}\right] \\ & - \frac{1}{2}\sum_{l,l',m''}\left[\frac{H^{'}_{ml}H^{'}_{ll'}H^{'}_{l'm''}H^{'}_{m''m'}}{(E_{m'} - E_l)(E_{m''} - E_{l'})}\left(\frac{1}{E_{m''} - E_l} + \frac{1}{E_{m'} - E_{l'}}\right) + \frac{H^{'}_{mm''}H^{'}_{m''l}H^{'}_{ll'}H^{'}_{l'm'}}{(E_m - E_{l'})(E_{m''} - E_l)}\left(\frac{1}{E_{m''} - E_{l'}} + \frac{1}{E_m - E_l}\right)\right] \\ & - \frac{1}{24}\sum_{l,l',m''} H^{'}_{ml}H^{'}_{lm''}H^{'}_{m''l'}H^{'}_{l'm'}\left[\frac{8}{(E_m - E_l)(E_m - E_{l'})(E_{m''} - E_{l'})} + \frac{8}{(E_{m'} - E_l)(E_{m'} - E_{l'})(E_{m''} - E_l)}\right. \\ & \quad + \frac{4}{(E_m - E_{l'})(E_{m''} - E_l)}\left(\frac{1}{E_m - E_l} + \frac{1}{E_{m''} - E_{l'}}\right) + \frac{4}{(E_{m'} - E_l)(E_{m''} - E_{l'})}\left(\frac{1}{E_{m'} - E_{l'}} + \frac{1}{E_{m''} - E_l}\right) \\ & \quad \left. - \frac{1}{(E_{m''} - E_l)(E_{m''} - E_{l'})}\left(\frac{1}{E_m - E_l} + \frac{1}{E_{m'} - E_{l'}}\right) - \frac{3}{(E_m - E_l)(E_{m'} - E_{l'})}\left(\frac{1}{E_{m''} - E_l} + \frac{1}{E_{m''} - E_{l'}}\right)\right] \\ & + \frac{1}{2}\sum_{l,l',l''} H^{'}_{ml}H^{'}_{ll'}H^{'}_{l'l''}H^{'}_{l''m'}\left[\frac{1}{(E_m - E_l)(E_m - E_{l'})(E_m - E_{l''})} + \frac{1}{(E_{m'} - E_l)(E_{m'} - E_{l'})(E_{m'} - E_{l''})}\right] \end{aligned} \tag{B.44}$$

$$\ldots = \ldots\ldots\ldots\ldots\ldots\ldots \tag{B.45}$$

These endless expressions do not lend themselves at first sight to a simple interpretation. However, they obey a certain structure that allows one to understand it as pathways of disruption. We can therefore represent it by a diagram proposed by Cardona et al. in Ref. [416] which will be described in following example.

Application of Luttinger-Kohn perturbation: The k^3 Dresselhaus term via Cardona's diagram
In order to illustrate the Luttinger-Kohn perturbation, let us now consider an example on the effect of Dresselhaus interactions. A Luttinger-Kohn perturbation up to order n is generally written in the following manner:

$$H_{mm'} = \sum_{i_1,\dots i_{n-1}} H'_{mi_1} H_{i_1 i_2} \dots H_{i_{n-2} i_{n-1}} H'_{i_{n-1} m'} \left(\sum \prod \frac{\gamma}{E_\alpha - E_\beta} \right) \tag{B.46}$$

where i_p indicates the inner index m'' as well as the outer index l'', and $\left(\sum \prod \frac{\gamma}{E_\alpha - E_\beta} \right)$ is a symbolic notation which corresponds to a sum of products of inverses of differences of energies between the bands; γ is weighting which changes from term to term and that we do not try to determine. The only imperative on the indices is that the path starts from the inner index m and stop at the inner index m' by traversing n paths or edges through mute interior or exterior index:

$$(m, i_1),\ (i_1, i_2),\ \dots\ (i_n - 1, m') \tag{B.47}$$

A diagram representing the perturbation paths was introduced by Cardona et al. in Ref. [416] make it easy to represent the various possible perturbation. The numbers which indicate the order of perturbation are displayed in Fig. B.5

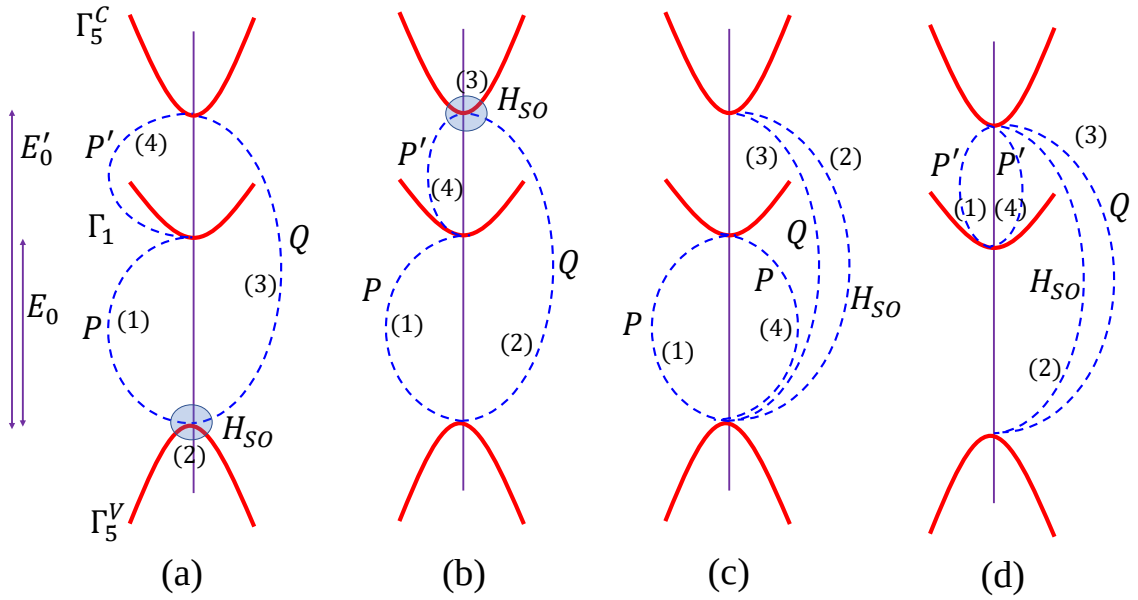

FIGURE B.5: Cardona diagram [416] of the four terms which contribute to the Dresselhaus coefficient γ of valence band.

Let us apply this method to find the k^3 Dresselhaus term by considering the extended Kane Hamiltonian

$$H_k = \begin{bmatrix} \Gamma_5^c & 0 & Qk \\ 0 & \Gamma_1^c & Pk \\ (Qk)^\dagger & (Pk)^\dagger & \Gamma_5^v \end{bmatrix} \tag{B.48}$$

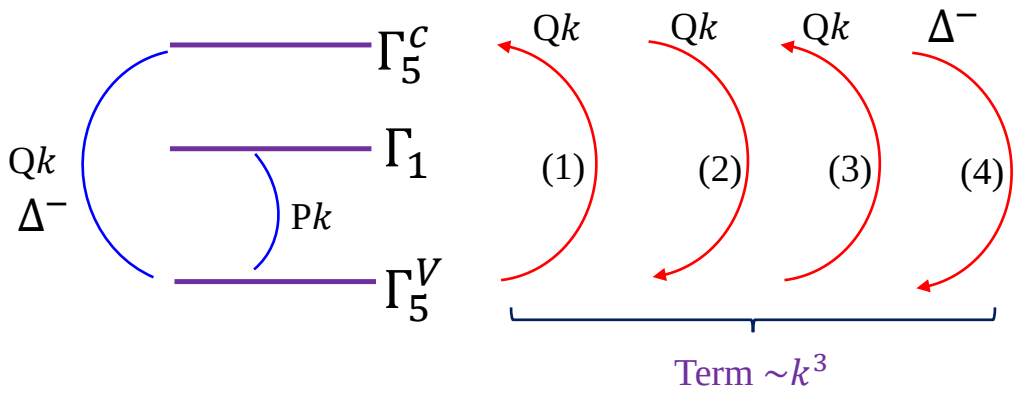

FIGURE B.6: Diagram of the contribution of spin-orbit coupling on the Dresselhaus coefficient in valence band.

In order to introduce spin-orbit coupling, we add to the Qk blocks a Δ^- spin-orbit coupling of zeroth order in k. Here, for the sake of simplicity, we neglect the effect of P' term.

$$H_k^{SO} = \begin{bmatrix} \Gamma_5^c & 0 & Qk + \Delta^- \\ 0 & \Gamma_1^c & Pk \\ (Qk)^\dagger + (\Delta^-)^\dagger & (Pk)^\dagger & \Gamma_5^v \end{bmatrix} \tag{B.49}$$

We then try to project this Hamiltonian into the valence band Γ_5^v by the Luttinger-Kohn perturbation method. When calculating the perturbation terms, the presence of Δ^- allows to adding a Δ^- disruption path which is independent of Qk between Γ_5^c and Γ_5^v . Therefore one observes that the Dresselhaus term is proportional to $(Qk)^3\Delta^-$. Note that Δ^- is non-zero only in symmetry T_d (without inversion center). If $\Delta^- = 0$, as is the case in symmetry O_h (with inversion center), any path involving exactly three times a term of the first order in k can not leave from Γ_5^v and back to Γ_5^v. Since the coupling Δ^- does not involve k, we can make as many round trips as we want on the edge of the Cardona's diagram corresponding to the coupling Δ^-. However, we have $\Delta^- \ll E_0$ (E_0 is the energy gap) which is the characteristic magnitude of the problem. The contribution of the terms of high order in Δ^- is therefore negligible and it is sufficient to consider only the smallest orders.

Explicitly, one may obtain the following term of first order in Δ^-:

$$H'^{\text{Dresselhaus}}_{vv'} = -\frac{1}{24} \sum_{\kappa,\kappa',v''} \left([Qk]_{v\kappa}[Qk]_{\kappa v''}[Qk]_{v''\kappa'}\Delta^-_{\kappa' v'} + p.c. \right) \left(\sum \prod \frac{\gamma}{E_\alpha - E_\beta} \right) \tag{B.50}$$

where $p.c.$ denotes the circular permutation of the indices.

Note that the hypothesis $P' = 0$ was taken into account to simplify the problem but is not necessarily true, since the term in P' is often greater than the term in Δ^-. This problem is discussed in a work of Durnev et al. in Ref. [31], but we will only note that the hypothesis $P' \neq 0$ implies the appearance of terms in k^3 proportional to $QPP'k^3$ which exist even in symmetry O_h when Δ^- is null.

B.2.2 Validation of the ghost-band approach

Ghost-bands method in framework of the 14×14 Hamiltonian

Let us now explain the principle of the elimination of spurious states by inserting ghost bands. For convenience, we consider the extended Kane 14×14 Hamiltonian:

$$H_k^{14\times14} = \begin{bmatrix} \Gamma_5^c & P'k & Qk \\ (P'k)^\dagger & \Gamma_1^c & Pk \\ (Qk)^\dagger & (Pk)^\dagger & \Gamma_5^v \end{bmatrix} \tag{B.51}$$

where the diagonal blocks Γ_5^c, Γ_1 are diagonal matrices.

In order to eliminate spurious states at larger wave vector k, we increase the size of this Hamiltonian by adding to it fictitious energy levels via a diagonal block Φ, which, for the moment, totally decouple in the new Hamiltonian. Therefore, there is no physical change at the moment.

$$H_k = \begin{bmatrix} \Phi & 0 & 0 & 0 \\ 0 & \Gamma_5^c & P'k & Qk \\ 0 & (P'k)^\dagger & \Gamma_1^c & Pk \\ 0 & (Qk)^\dagger & (Pk)^\dagger & \Gamma_5^v \end{bmatrix} \tag{B.52}$$

This Hamiltonian can be diagonalized for any k by the unitary matrix C which is the matrix of eigenvectors of the Hamiltonian:

$$H_k^{rot} = C_k H_k C_k^\dagger \tag{B.53}$$

The shape of the Hamiltonian B.52 with the ghost-bands makes it possible to write C_k in blocks as follows:

$$C_k = \begin{bmatrix} I & 0 & 0 & 0 \\ 0 & & & \\ 0 & & \hat{\omega}_k & \\ 0 & & & \end{bmatrix} \tag{B.54}$$

where $\hat{\omega}_k$ is also a unitary matrix. Now, in order to make the supplementary terms to be operated at specific k_c point, we then impose a rotation to the H_k Hamiltonian via C_{k_c}:

$$H_k^{rot} = C_{k_c} H_k C_{k_c}^\dagger \tag{B.55}$$

After the rotation of the Hamiltonian, we can add a weak pure imaginary coupling in k^2:

$$V_k^{off} = \left[\begin{array}{c|ccc} 0 & i\hat{\alpha}k^2 & & \\ \hline -i\hat{\alpha}^\dagger k^2 & 0 & 0 & 0 \\ & 0 & 0 & 0 \\ & 0 & 0 & 0 \end{array}\right] \tag{B.56}$$

between the ghost-bands and the initial Hamiltonian to give the new Hamiltonian

$$\tilde{H}_k^{rot} = C_{k_c} H_k C_{k_c}^\dagger + V_k^{off} \tag{B.57}$$

This will allow, as we will see, to eliminate the spurious without much altering the energy levels or the effective mass at the small k. Note that one has:

$$C_{k_c}^{\dagger} V_k^{off} C_{k_c} = \left[\begin{array}{cccc} I & 0 & 0 & 0 \\ 0 & & & \\ 0 & & \hat{\omega}_{k_c}^{\dagger} & \\ 0 & & & \end{array}\right] \left[\begin{array}{c|ccc} 0 & & i\hat{\alpha}k^2 & \\ \hline -i\hat{\alpha}^{\dagger}k^2 & & 0\ 0\ 0 & \\ & & 0\ 0\ 0 & \\ & & 0\ 0\ 0 & \end{array}\right] \left[\begin{array}{cccc} I & 0 & 0 & 0 \\ 0 & & & \\ 0 & & \hat{\omega}_{k_c} & \\ 0 & & & \end{array}\right] = \left[\begin{array}{c|ccc} 0 & & i\hat{\alpha}\omega_{k_c}k^2 & \\ \hline \left(i\hat{\alpha}\omega_{k_c}k^2\right)^{\dagger} & & 0\ 0\ 0 & \\ & & 0\ 0\ 0 & \\ & & 0\ 0\ 0 & \end{array}\right] \tag{B.58}$$

Then one can apply the inverse rotation to the new Hamiltonian B.57 to obtain $\boldsymbol{k.p}$ Hamiltonian as:

$$\tilde{H}_k = C_{k_c}^{\dagger} \tilde{H}_k^{rot} C_{k_c} = H_k + C_{k_c}^{\dagger} V_k^{off} C_{k_c} = \left[\begin{array}{c|ccc} \Phi & & i\hat{\alpha}k^2\hat{\omega}_{k_c} & \\ \hline \left(i\hat{\alpha}k^2\hat{\omega}_{k_c}\right)^{\dagger} & & \Gamma_5^c & P'k\ \ Qk \\ & & (P'k)^{\dagger} & \Gamma_1^c\ \ Pk \\ & & (Qk)^{\dagger} & (Pk)^{\dagger}\ \ \Gamma_5^v \end{array}\right] \tag{B.59}$$

Since the diagonal blocks (Φ, Γ_5^c, Γ_1^c, and Γ_5^v) are still diagonal matrices, then we have the matrix without the diagonal blocks, which is useful for Luttinger-Kohn perturbation in the following section:

$$\tilde{H}'_k = \left[\begin{array}{c|ccc} 0 & & i\hat{\alpha}k^2\omega_{k_c} & \\ \hline \left(i\hat{\alpha}k^2\omega_{k_c}\right)^{\dagger} & & 0 & P'k\ \ Qk \\ & & (P'k)^{\dagger} & 0\ \ Pk \\ & & (Qk)^{\dagger} & (Pk)^{\dagger}\ \ 0 \end{array}\right] \tag{B.60}$$

Note that the analytic calculation with this matrix seems to be very difficult even impossible. Therefore, we have checked numerically that in order to remove the spurious in the right way, one may choose a matrix parameters α to couple the ghost-bands only with the valence bands because the valence bands are growing with k and will cross the band-gap as they should not. A coefficient $\alpha = 1\ \text{eV}\,\text{Å}^2$ is then the minimum value of the coefficient of couplings which allows one to remove the spurious states in 14×14 $\boldsymbol{k.p}$ Hamiltonian.

Luttinger-Kohn perturbations and ghost-band method

Now we are going to obtain an effective Hamiltonian for the Γ_1 conduction band (respectively for the conduction band Γ_5^c) taking into account the influences of the ghost-bands and the other physical bands which are considered as perturbations. Using the Luttinger-Kohn perturbations for Hamiltonian B.60 at the orders from 0 to 3, one has:

$$H^{(0)}_{cc'} = E_c \delta_{cc'} \tag{B.61}$$

$$H^{(1)}_{cc'} = 0 \tag{B.62}$$

$$H^{(2)}_{cc'} = \sum_{v} \frac{[Pk]_{cv} \left[(Pk)^\dagger\right]_{vc'}}{E_c - E_v} + \sum_{\kappa} \frac{[P'k]_{c\kappa} \left[(P'k)^\dagger\right]_{\kappa c'}}{E_c - E_\kappa} + \sum_{\phi} \frac{\left[i\alpha k^2 \omega_{k_c}\right]_{c\phi} \left[(i\alpha k^2 \omega_{k_c})^\dagger\right]_{\phi c'}}{E_c - E_\phi} \tag{B.63}$$

$$H^{(3)}_{cc'} = \sum_{v,\kappa} \frac{[Pk]_{cv} \left[(Qk)^\dagger\right]_{v\kappa} [P'k]_{\kappa c'} + \left[(P'k)^\dagger\right]_{c\kappa} [Qk]_{\kappa v} \left[(Pk)^\dagger\right]_{vc'}}{(E_c - E_v)(E_c - E_\kappa)} \tag{B.64}$$

$$+ \sum_{v,\phi} \frac{[Pk]_{cv} \left[(i\alpha k^2 \omega_{k_c})^\dagger\right]_{v\phi} \left[i\alpha k^2 \omega_{k_c}\right]_{\phi c'} + \left[(i\alpha k^2 \omega_{k_c})^\dagger\right]_{c\phi} \left[i\alpha k^2 \omega_{k_c}\right]_{\phi v} \left[(Pk)^\dagger\right]_{vc'}}{(E_c - E_v)(E_c - E_\phi)} \tag{B.65}$$

$$+ \sum_{\kappa,\phi} \frac{\left[(P'k)^\dagger\right]_{c\kappa} \left[(i\alpha k^2 \omega_{k_c})^\dagger\right]_{\kappa\phi} \left[i\alpha k^2 \omega_{k_c}\right]_{\phi c'} + \left[(i\alpha k^2 \omega_{k_c})^\dagger\right]_{c\phi} \left[i\alpha k^2 \omega_{k_c}\right]_{\phi\kappa} [P'k]_{\kappa c'}}{(E_c - E_\kappa)(E_c - E_\phi)} \tag{B.66}$$

Where ϕ is the block of ghost-band; κ is the block of Γ_5^c; c is the block of Γ_1^c; and v is the block of Γ_5^v. Doing the same treatment for VB, one has:

$$H^{(0)}_{vv'} = E_c \delta_{vv'} \tag{B.67}$$

$$H^{(1)}_{vv'} = 0 \tag{B.68}$$

$$H^{(2)}_{vv'} = \sum_{c} \frac{[Pk]_{vc} \left[(Pk)^\dagger\right]_{cv'}}{E_v - E_c} + \sum_{\kappa} \frac{[Qk]_{v\kappa} \left[(Qk)^\dagger\right]_{\kappa v'}}{E_v - E_\kappa} + \sum_{\phi} \frac{\left[i\alpha k^2 \omega_{k_c}\right]_{v\phi} \left[(i\alpha k^2 \omega_{k_c})^\dagger\right]_{\phi v'}}{E_v - E_\phi} \tag{B.69}$$

$$H^{(3)}_{vv'} = \sum_{c,\kappa} \frac{[Pk]_{vc} \left[(P'k)^\dagger\right]_{c\kappa} [Qk]_{\kappa v'} + \left[(Qk)^\dagger\right]_{v\kappa} [P'k]_{\kappa c} \left[(Pk)^\dagger\right]_{cv'}}{(E_v - E_c)(E_v - E_\kappa)} \tag{B.70}$$

$$+ \sum_{c,\phi} \frac{[Pk]_{vc} \left[(i\alpha k^2 \omega_{k_c})^\dagger\right]_{c\phi} \left[i\alpha k^2 \omega_{k_c}\right]_{\phi v'} + \left[(i\alpha k^2 \omega_{k_c})^\dagger\right]_{v\phi} \left[i\alpha k^2 \omega_{k_c}\right]_{\phi c} \left[(Pk)^\dagger\right]_{cv'}}{(E_v - E_c)(E_v - E_\phi)} \tag{B.71}$$

$$+ \sum_{\kappa,\phi} \frac{\left[(Qk)^\dagger\right]_{v\kappa} \left[(i\alpha k^2 \omega_{k_c})^\dagger\right]_{\kappa\phi} \left[i\alpha k^2 \omega_{k_c}\right]_{\phi v'} + \left[(i\alpha k^2 \omega_{k_c})^\dagger\right]_{v\phi} \left[i\alpha k^2 \omega_{k_c}\right]_{\phi\kappa} [Qk]_{\kappa v'}}{(E_v - E_\kappa)(E_v - E_\phi)} \tag{B.72}$$

Here, we neglected any zeros order of k couplings of the Δ^- type. In this case, an analysis of the perturbation make it possible to state that the ghost-band coupling does not induce any perturbation at orders less than k^3 and that any perturbation of order of k^4 (respectively k^5) involving ghost-band couplings must be in the term $H^{(2)}_{cc'}$ (respectively $H^{(3)}_{cc'}$). Therefore, the ghost-band contributes no change in effective mass (related to the term k^2) at the Γ point. Let us now estimate the perturbation on the effective mass at fixed k wave vector. One has the relation between the wave vector k and the kinetic energy of the electron:

$$E_{cin} = \frac{\hbar^2 k^2}{2m_0} \Rightarrow |k| = \frac{\sqrt{2m_0 E_{cin}}}{\hbar} \tag{B.73}$$

We denote E_k the energy before including ghost-band, $\tilde{E}_k$ the energy after including ghost-band, then $\tilde{E}_k - E_k = \sum_i \mathcal{P}^{(i)} k^i$ where $\mathcal{P}^{(i)}$ is the perturbation term which relates to ghost-band coupling; m_0 the effective mass before including ghost-band and m^* after including ghost-band, we have:

$$\frac{1}{m^*} = \frac{1}{\hbar^2} \frac{\partial^2 \tilde{E}_k}{\partial k^2} = \frac{1}{m_0} + \frac{12\mathcal{P}^{(4)} k^2}{\hbar^2} + O(k^3) \tag{B.74}$$

thus

$$\frac{|m_0 - m^*|}{m_0} \approx \frac{12 m_0 \mathcal{P}^{(4)} k^2}{\hbar^2} = \frac{24 m_0^2 \mathcal{P}^{(4)} E_{cin}}{\hbar^4} \tag{B.75}$$

Analyses of the errors induced by ghost-band approach

Ghost-band contributions are up to order k^5 In order to evaluate the orders of magnitude of the perturbations, We use parameters which are given in the book of Winkler [44] for GaAs as following:

$\hbar = 4 \cdot 10^{-15}$ eV s

$P \approx 10$ eV Å,

$Q \approx 8$ eV Å ,

$P' \approx 5i$ eV Å,

$E_c - E_\kappa = E_0 - E_0' \approx -3$eV

$E_c - E_v = E_0 \approx 2$eV

$E_c - E_\phi \approx -15$eV

$N_\phi = 4$, $N_\kappa = 6$, $N_c = 2$, $N_v = 6$ where N_ϕ is the number of ghost-band; N_κ is the number of Γ_5^C conduction band; N_c is the number of Γ_1 conduction band; and N_v is the number of Γ_5^V valence band.

$m_0 \approx 0,0665 \cdot m_e$

Here the ghost-band coupling, we use in this work, varies between $\alpha_{\min}$ and $\alpha_{\max}$ according to:

$\alpha_{\min} \approx 1$ eV Å^2

$\alpha_{\max} \approx 10$ eV Å^2

Since the matrix ω_{k_c} is unitary then one may assume that $\left|\left[\omega_{k_c}\right]_{ij}\right| \leq 1$

The highest kinetic energy (and corresponding wave vector) used in effective mass calculations B.1 via the tunneling through barrier structure, is of the order of half of the gap:

$$E_{cin} \approx E_0 \approx 0.7\text{eV} \tag{B.76}$$

$$|k| = \frac{\sqrt{2 m_0 E_{cin}}}{\hbar} \approx 0.11 \text{ Å}^{-1} \tag{B.77}$$

We recall the notation:

$$\tilde{E}_k - E_k = \sum_i \mathcal{P}^{(i)} k^i \tag{B.78}$$

First, let us neglect the zero order contribution in k related to the term Δ^-. We can therefore estimate the perturbations at k^4 for $\alpha \approx 1$ eV Å^2, which corresponds to the minimal correction to make the spurious disappear:

$$\mathcal{P}_c^{(4)} |k|^4 = \left| \sum_\phi \frac{\left[i\alpha k^2 \omega_{k_c}^\dagger \right]_{c\phi} \left[(i\alpha k^2 \omega_{k_c}^\dagger)^\dagger \right]_{\phi c'}}{E_c - E_\phi} \right| \approx \frac{N_\phi |\alpha|^2}{|E_c - E_\phi|} |k|^4 \approx 4,0 \cdot 10^{-5} \text{ eV} \tag{B.79}$$

$$\mathcal{P}_c^{(4)} \approx 0,27 \text{ eV Å}^4 \tag{B.80}$$

or the perturbation at k^4 for $\alpha \approx 1$ eV Å^2

$$\frac{\mathcal{P}_c^{(4)} |k|^4}{E_0} \approx 1 \cdot 10^{-4} \tag{B.81}$$

Let us now estimate the perturbations at k^5 taking into account that P is the largest of the couplings.

$$\mathcal{P}_c^{(5)}|k|^5 \approx \left|\sum_{\kappa,\phi} ...\right| + \left|\sum_{v,\phi} ...\right| \approx \frac{2N_\phi(N_v+N_\kappa)|P||\alpha|^2}{|E_c-E_v|\cdot|E_c-E_\phi|}|k|^5 \tag{B.82}$$

$$\approx 5,1\cdot 10^{-4}\text{eV} \tag{B.83}$$

$$\tag{B.84}$$

$$\mathcal{P}_c^{(5)} \approx 32\ \text{eV}\,\text{Å}^5 \tag{B.85}$$

or

$$\frac{\mathcal{P}_c^{(5)}|k|^5}{E_0} \approx 3\cdot 10^{-4} \tag{B.86}$$

The error in the effective mass:

$$\frac{|m_0-m^*|}{m_0} = \frac{24m_0\mathcal{P}_c^{(4)}E_{cin}}{\hbar^4} \approx \frac{24m_0^2N_\phi|\alpha|^2E_{cin}}{(E_c-E_\phi)\hbar^4} \tag{B.87}$$

one finds:

- for $\alpha \approx 1\ \text{eV}\,\text{Å}^2$, $\frac{|m_0-m^*|}{m_0} \approx 3\cdot 10^{-4}$
- for $\alpha \approx 10\ \text{eV}\,\text{Å}^2$, $\frac{|m_0-m^*|}{m_0} \approx 3\cdot 10^{-2}$

The calculation is similar for the valence band, except that the perturbation terms that mix the ghost-band couplings and the physical couplings will no longer be P' and P but P and Q. Since P remains the largest coupling, the sum which is found for the conduction band is also valid for the valence band. We then find for $\alpha \approx 1\ \text{eV}\,\text{Å}^2$:

$$\mathcal{P}_v^{(4)} \approx 0,23\ \text{eV}\,\text{Å}^4 \tag{B.88}$$

$$\mathcal{P}_v^{(4)}|k|^4 \approx \frac{N_\phi\,|\alpha|^2}{|E_v-E_\phi|}|k|^4 \approx 3,4\cdot 10^{-5}\ \text{eV} \tag{B.89}$$

$$\mathcal{P}_v^{(5)} \approx 19\ \text{eV}\,\text{Å}^5 \tag{B.90}$$

$$\mathcal{P}_v^{(5)}|k|^5 \approx \frac{2N_\phi(N_c+N_\kappa)|P||\alpha|^2}{|E_c-E_v|\cdot|E_v-E_\phi|}|k|^5 \approx 3,1\cdot 10^{-4}\ \text{eV} \tag{B.91}$$

The effects of Δ^- term We have so far neglected the terms $\Delta^- \approx 5\cdot 10^{-2}$ in our calculations above. We will now justify it. According to Cardona's perturbation diagram in Ref. [416], in order to consider the effect of Δ^- in the perturbation calculation, one has to replace the coupling Qk between the bands Γ_5^c and Γ_5^v by two independent couplings, Qk and Δ^-. This is explained by the terms obtained in k^4 when one expands a polynomial of the form $\prod_{a,b}(Qk)^a(\Delta^-)^{n-a}$.

In the conduction band, the Δ^- terms do not strictly induce any perturbation in the order of k^4 because the coupling Δ^- does not act directly on the conduction band. In the valence band, the terms of order of k^4 involving Δ^- may be written in the form:

$$\frac{(\Delta^-)^n(i\alpha k^2)^2}{(\delta E)^{n+1}} \tag{B.92}$$

where $n \in \mathbb{N}^*$ and δE is the smallest difference in energy between bands involving Δ^-. This formula can be rewritten as following:

$$\frac{\alpha^2k^4}{\delta E}\cdot\left(\frac{\Delta^-}{\delta E}\right)^n \tag{B.93}$$

One may write the term $\left(\frac{\Delta^-}{\delta E}\right)^n$, in the form:

$$\left(\frac{\Delta^-}{\delta E}\right)^n = \exp\left(n \ln\left(\frac{\Delta^-}{\delta E}\right)\right) = \exp\left(-\frac{n}{\nu}\right) \tag{B.94}$$

where $\nu = -\left(\ln\left(\frac{\Delta^-}{\delta E}\right)\right)^{-1} \approx 0.3$ for GaAs. It is therefore clear that one may consider only the term $n = 1$ in calculation of $\left(\frac{\Delta^-}{\delta E}\right)^n$.

Besides, one has the first term:

$$\frac{i\alpha^2 k^4}{\delta E} \approx 7{,}3 \cdot 10^{-5} \text{ eV} \tag{B.95}$$

and

$$\frac{1}{P^{(4)}k^4} \cdot \frac{i\alpha^2 k^4}{\delta E} \approx 2 \tag{B.96}$$

The first term is thus 20 times smaller than the term of order k^4, and we have for all n:

$$\frac{\frac{\alpha^2 k^4}{\delta E} \cdot \left(\frac{\Delta^-}{\delta E}\right)^n}{P^{(4)}k^4} \approx 2 \cdot (0.025)^n \tag{B.97}$$

We can therefore conclude that the perturbations induced by Δ^- at the order k^4 are negligible compared to the other perturbations.

For the order terms of k^5, the perturbations for both the conduction band and the valence band can be written in the form:

$$\frac{\tilde{P}k(\Delta^-)^n(\alpha k^2)^2}{(\delta E)^{n+2}} = \frac{\tilde{P}\alpha^2 k^5}{(\delta E)^2} \cdot \left(\frac{\Delta^-}{\delta E}\right)^n \tag{B.98}$$

where $\tilde{P} = P$, P' and Q. The second term is treated the same as for k^4, the first term is:

$$\frac{\tilde{P}\alpha^2 k^5}{(\delta E)^2} \approx 4 \cdot 10^{-5}\text{eV} \tag{B.99}$$

and

$$\frac{1}{P^{(5)}k^5} \cdot \frac{\tilde{P}\alpha^2 k^5}{(\delta E)^2} \approx 0.1 \tag{B.100}$$

For the order k^5, the terms induced by Δ^- are therefore also negligible.

Generalization to 30×30 and 40×40 Hamiltonian model The procedures for a 30-band or 40-band Hamiltonian are similar to those for the 14 bands, with the following corrections:

- There is a larger number of coupling coefficients, but one only has to consider the larger calculations
- There are more possible procedure paths, so the results must be corrected by a multiplicative factor related to the number of procedure paths

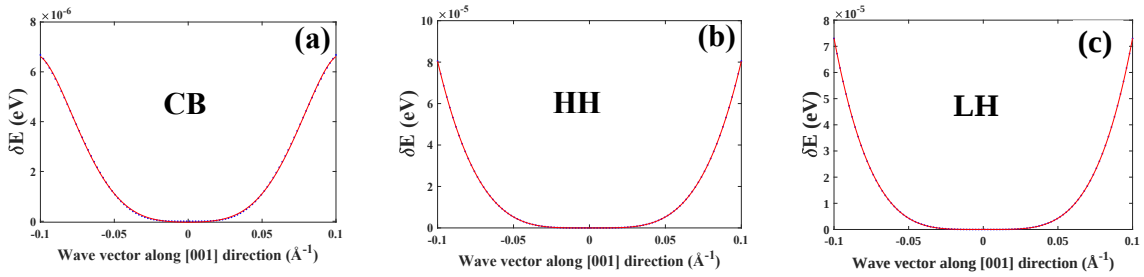

FIGURE B.7: Numerical calculations of errors for CB, HH and LH subband, calculated via 30-band $\boldsymbol{k.p}$ model.

Comparison between analytical and numerical calculations

We found that:

Band	Analytical calculations of the error (eV)	Numerical calculations of the error (eV)
CB ($k = 0.1\text{Å}^{-1}$)	$8.8 \cdot 10^{-6}$	$7 \cdot 10^{-6}$
VB HH ($k = 0.1\text{Å}^{-1}$)	$3.3 \cdot 10^{-4}$	$8 \cdot 10^{-5}$
VB LH ($k = 0.1\text{Å}^{-1}$)	$3.3 \cdot 10^{-4}$	$7.5 \cdot 10^{-5}$

(B.101)

Our analytical predictions are therefore in a perfect agreement with our numerical results illustrated in figure B.7. Note also that for the conduction band at $k = 0.1\text{Å}^{-1}$, the term in k^5 actually contributes the most weight to the analytical error. One observes that the analytical errors are barely larger than the numerical error, which shows that the analytical expression in k^5 is a good estimation!

Note that the 14 bands **k.p** model describes approximately 20 % of Brillouin zone. Thus, we have only compared the analytical predictions of error induced by ghost-band method (in framework of 14 bands **k.p** Hamiltonian) to the numerical calculations (with 30 bands **k.p** Hamiltonian) at the wave vector k is small ($\simeq 0.1\text{Å}^{-1}$) in order to make sure an accuracy of the comparisons. Beyond that, we have also check numerically with 30 bands **k.p** Hamiltonian, the error induced by ghost-band at the edge of the first Brillouin zone for CB and confirmed that the error is very small. So, in conclusion, we can state that the ghost-band method is good enough to give full Brillouin zone descriptions.

APPENDIX C

Transfer and scattering matrices in framework of multi-band k.p method

We present here in this appendix, firstly, the details of scattering and transfer matrix approach with recursion method in order to consider transport properties through an heterostructure. Besides, an alternative approach for recursion method is to use a global scattering or transfer matrix which seems to be very interesting since it gives us a appropriate connection to Green's function technique presented in Chapter 4.

C.1 *Transfer and Scattering matrix approach in framework of multiband k.p theory*

In this section, we introduce and discuss the mathematical formulas describing the transfer and scattering scattering matrix allowing a description of the electron or hole propagation through the heterostructure. One notes that there are two different definitions of the transfer matrix used in the literature [245]. One of them uses the linear relationship between the wavefunctions denoted by $\boldsymbol{M}$ and the other one uses of the linear relationship between coefficients denoted by $\boldsymbol{T}$. The transmission and reflection coefficients T and R extracted from these two definitions are the same since the transfer matrices $\boldsymbol{M}$ and $\boldsymbol{T}$ differ from each other only in the phase [245]. In this work, we focus on the transfer matrix $\boldsymbol{T}$ since it is convenient to describe both the standard matching conditions and extended matching conditions for possible symmetry reduction from T_d to C_{2v} at the interfaces.

C.1.1 *Scattering and Transfer matrix for standard matching conditions*

In the frame work of the $\boldsymbol{k.p}$ theory, wavefunctions are linear combinations of Bloch functions shown in Eq.2.35. One assumes that the electron/holes tunnel through a heterostructure grown along the z axis, each medium being described by its own Hamiltonian. Suppose that the incident energy ε and the in-plane wavevector $\boldsymbol{k}_{||} = (k_x, k_y)$ are conserved during the transport (case of elastic tunneling), then we have to find the relevant out of plane wave vector k_z and eigenvectors of the Hamiltonian in each medium, it means that the term $e^{i(\boldsymbol{k}.\boldsymbol{r})}$ and $\psi_{j,\boldsymbol{k}}(\boldsymbol{r})$ in 2.35 can be re-written in the form: $e^{i(\boldsymbol{k}.\boldsymbol{r})} \rightarrow e^{i(\boldsymbol{k}_{||}.\boldsymbol{\rho})} e^{i(k_z.z)}$ and $\psi_{j,\boldsymbol{k}}(\boldsymbol{r}) = \psi_{j,\boldsymbol{k}_{||},k_z}(\boldsymbol{r})$, where $\boldsymbol{\rho} = (x, y)$ is the in-plane vector. Let us assume that the medium within the n^{th} layer is homogeneous then the $\psi^n_{j,\boldsymbol{k}_{||},k_z}(\boldsymbol{r})$, which is an eigenvector in j^{th} band of n^{th} layer's own Hamiltonian, does not depend on the proper coordinate z of n^{th} layer. Therefore, for convenience, one may

replace $\psi^n_{j,\boldsymbol{k}_{||},k_z}(\boldsymbol{r})$ by $\psi_n(\boldsymbol{k}_{||},k_z^j)$ or simply by $\psi_n(k_z^j)$ with keeping in mind that $\psi_n(k_z^j)$ depends also on $k_{||}$ which is conserved within the whole considered structure. The total wavefunction in the n^{th} layer at the point defined by $(\boldsymbol{\rho},z_n)$, then, may be expressed as :

$$\Psi_n = e^{i(\boldsymbol{k}_{||}\cdot\boldsymbol{\rho})}\sum_{j=1}^{m}\left[a_n^j\psi_n(k_n^j)e^{ik_n^jz_n} + b_n^j\psi_n(-k_n^j)e^{-ik_n^jz_n}\right] \tag{C.1}$$

where m is the band index in the **k**.**p** model, *i.e.*, $m = 6$ in 6-band **k**.**p** model, $m = 40$ in 40-band **k**. **p** model ; k_n^j (respective value of k_z) is the eigenvalue of Hamiltonian in n^{th} layer with incident energy ε in the j^{th} band; $\psi_n(k_n^j)$ is the eigenvector of the Hamiltonian in the n^{th} layer corresponding to a solution k_n^j with incident energy ε and z_n is the proper coordinate of nth layer:

$$\psi_n(k_n^j) = \left[\psi_n^1(k_n^j),.....,\psi_n^m(k_n^j)\right]^T \tag{C.2}$$

It is convenient to write $-k_n^j = k_n^{j+m}$ and without loss of generality, one considers the normal incident $\boldsymbol{k}_{||} = 0$ (one can easily see that we get the same result for $\boldsymbol{k}_{||} \neq 0$) then we can write the Eq.C.1 in a matrix form:

$$\Psi_n = \begin{bmatrix} \psi_n^1(k_n^1) & ... & \psi_n^1(k_n^{2m}) \\ . & . & . \\ . & . & . \\ . & . & . \\ . & . & . \\ . & . & . \\ . & . & . \\ \psi_n^m(k_n^1) & ... & \psi_n^m(k_n^{2m}) \end{bmatrix}\begin{bmatrix} e^{ik_n^1z_n} & ... & 0 \\ . & . & . \\ . & . & . \\ . & . & . \\ . & . & . \\ . & . & . \\ . & . & . \\ 0 & ... & e^{ik_n^{2m}z_n} \end{bmatrix}\begin{bmatrix} a_n^1 \\ . \\ . \\ a_n^m \\ b_n^1 \\ . \\ . \\ b_n^m \end{bmatrix} \tag{C.3}$$

Similarly, one may write the matrix form for the current wave in the n^{th} layer as:

$$J_z\Psi_n = \begin{bmatrix} J_z\psi_n^1(k_n^1) & ... & J_z\psi_n^1(k_n^{2m}) \\ . & . & . \\ . & . & . \\ . & . & . \\ . & . & . \\ . & . & . \\ . & . & . \\ J_z\psi_n^m(k_n^1) & ... & J_z\psi_n^m(k_n^{2m}) \end{bmatrix}\begin{bmatrix} e^{ik_n^1z} & ... & 0 \\ . & . & . \\ . & . & . \\ . & . & . \\ . & . & . \\ . & . & . \\ . & . & . \\ 0 & ... & e^{ik_n^{2m}z} \end{bmatrix}\begin{bmatrix} a_n^1 \\ . \\ . \\ a_n^m \\ b_n^1 \\ . \\ . \\ b_n^m \end{bmatrix} \tag{C.4}$$

We consider the nth and $(n+1)th$ layer with proper coordinate chosen as depicted in Fig C.1. Then, the wavefunction inside n^{th} layer at $z_n = 0$ is $\Psi_n^{(0)}$ and its expansion coefficients are a_n^j and b_n^j. The same for the $(n+1)^{th}$ layer: the wavefunction inside the $(n+1)^{th}$ layer at $z_{n+1} = 0$ is $\Psi_{n+1}^{(0)}$ and its coefficients expansion are a_{n+1}^j and b_{n+1}^j. In order to find the relation which links the a_n^j and b_n^j to a_{n+1}^j and b_{n+1}^j, one must apply the standard matching conditions at the interface I_{n+1} between the n^{th} layer and $(n+1)^{th}$ layer where the wavefunction and the current wave are continuous at the interface. If we denote the wavefunction inside the n^{th} layer close to the I_{n+1} interface is $\Psi_n^{(d_n)}$ with $z_n = d_n$: the thickness of n^{th} layer. Then, the matching conditions generally given by:

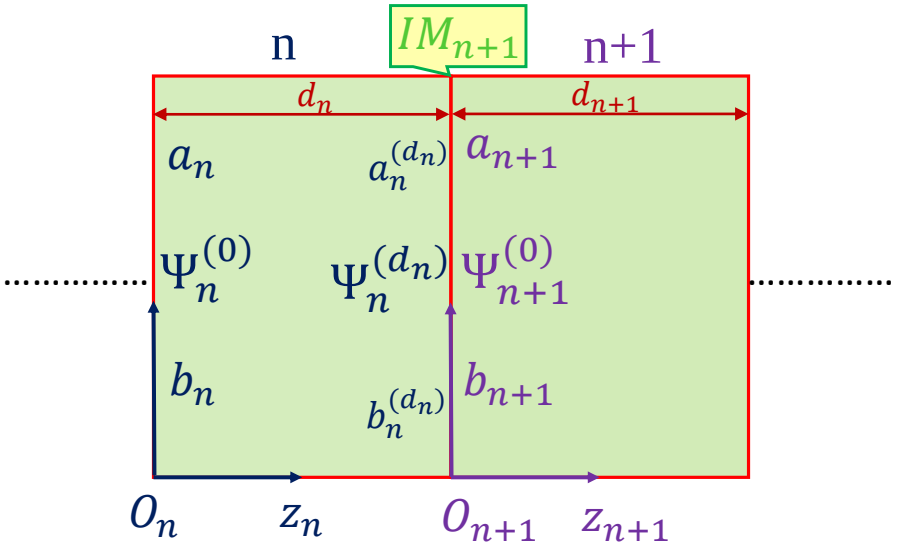

FIGURE C.1: The wave function in nth layer and (n+1)th layer. $\Psi_n^{(0)}$ is the wavefunction at O_n point in nth layer, a_n and b_n are coefficients corresponding to $\Psi_n^{(0)}$; $\Psi_n^{(d_n)}$ is the wavefunction at d_n point in nth layer, ($a_n^{d_n)}$ and $b_n^{(d_n)}$ are coefficients corresponding to $\Psi_n(d_n)$; $\Psi_{n+1}^{(0)}$ is the wavefunction at O_{n+1} point in nth layer, a_{n+1} and b_{n+1} are coefficients corresponding to $\Psi_{n+1}^{(0)}$. Here $O_i z_i$ is the proper coordinate in ith layer where O_i was chosen as the point at the interface between (i-1)th and ith layer.

$$\Psi_n^{(d_n)} = \Psi_{n+1}^{(0)} \tag{C.5}$$

$$J_z \Psi_n^{(d_n)} = J_z \Psi_{n+1}^{(0)} \tag{C.6}$$

where

$$\Psi_n^{(d_n)} = \begin{bmatrix} \psi_n^1(k_n^1) & \dots & \psi_n^1(k_n^{2m}) \\ . & . & . \\ . & . & . \\ . & . & . \\ . & . & . \\ . & . & . \\ . & . & . \\ \psi_n^m(k_n^1) & \dots & \psi_n^m(k_n^{2m}) \end{bmatrix} \begin{bmatrix} a_n^{1(d_n)} \\ . \\ . \\ a_n^{m(d_n)} \\ b_n^{1(d_n)} \\ . \\ . \\ b_n^{m(d_n)} \end{bmatrix} = \begin{bmatrix} \psi_n^1(k_n^1) & .... & \psi_n^1(k_n^{2m}) \\ . & . & . \\ . & . & . \\ . & . & . \\ . & . & . \\ . & . & . \\ . & . & . \\ \psi_n^m(k_n^1) & \dots & \psi_n^m(k_n^{2m}) \end{bmatrix} \begin{bmatrix} e^{ik_n^1 d_n} & \dots & 0 \\ . & . & . \\ . & . & . \\ . & . & . \\ . & . & . \\ . & . & . \\ . & . & . \\ 0 & \dots & e^{ik_n^{2m} d_n} \end{bmatrix} \begin{bmatrix} a_n^1 \\ . \\ . \\ a_n^m \\ b_n^1 \\ . \\ . \\ b_n^m \end{bmatrix} \tag{C.7}$$

and

$$\Psi^{(0)}_{n+1} = \begin{bmatrix} \psi^1_{n+1}(k^1_{n+1}) & \dots & \psi^1_{n+1}(k^{2m}_{n+1}) \\ . & . & . \\ . & . & . \\ . & . & . \\ . & . & . \\ . & . & . \\ . & . & . \\ \psi^m_{n+1}(k^1_{n+1}) & \dots & \psi^m_{n+1}(k^{2m}_{n+1}) \end{bmatrix} \begin{bmatrix} a^1_{n+1} \\ . \\ . \\ a^m_{n+1} \\ b^1_{n+1} \\ . \\ . \\ b^m_{n+1} \end{bmatrix} \tag{C.8}$$

and

$$\Psi^{(0)}_{n} = \begin{bmatrix} \psi^1_{n}(k^1_{n}) & \dots & \psi^1_{n}(k^{2m}_{n}) \\ . & . & . \\ . & . & . \\ . & . & . \\ . & . & . \\ . & . & . \\ . & . & . \\ \psi^m_{n}(k^1_{n}) & \dots & \psi^m_{n}(k^{2m}_{n}) \end{bmatrix} \begin{bmatrix} a^1_{n} \\ . \\ . \\ a^m_{n} \\ b^1_{n} \\ . \\ . \\ b^m_{n} \end{bmatrix} \tag{C.9}$$

Applying the standard matching conditions for multiband transport, Ψ and $\hat{J}_z\Psi$ are continuous at the interface between n^{th} and $(n+1)^{th}$ layer:

$$\begin{bmatrix} \psi^1_n(k^1_n) & \dots & \psi^1_n(k^{2m}_n) \\ . & . & . \\ . & . & . \\ \psi^m_n(k^1_n) & \dots & \psi^m_n(k^{2m}_n) \\ J_z\psi^1_n(k^1_n) & \dots & J_z\psi^1_n(k^{2m}_n) \\ . & . & . \\ . & . & . \\ J_z\psi^m_n(k^1_n) & \dots & J_z\psi^m_n(k^{2m}_n) \end{bmatrix} \begin{bmatrix} e^{ik^1_n d_n} & \dots & 0 \\ . & . & . \\ . & . & . \\ . & . & . \\ . & . & . \\ . & . & . \\ . & . & . \\ 0 & \dots & e^{ik^{2m}_n d_n} \end{bmatrix} \begin{bmatrix} a^1_n \\ . \\ . \\ a^m_n \\ b^1_n \\ . \\ . \\ b^m_n \end{bmatrix} = \begin{bmatrix} \psi^1_{n+1}(k^1_{n+1}) & \dots & \psi^1_{n+1}(k^{2m}_{n+1}) \\ . & . & . \\ . & . & . \\ \psi^m_{n+1}(k^1_{n+1}) & \dots & \psi^m_{n+1}(k^{2m}_{n+1}) \\ J_z\psi^1_{n+1}(k^1_{n+1}) & \dots & J_z\psi^1_{n+1}(k^{2m}_{n+1}) \\ . & . & . \\ . & . & . \\ J_z\psi^m_{n+1}(k^1_{n+1}) & \dots & J_z\psi^m_{n+1}(k^{2m}_{n+1}) \end{bmatrix} \begin{bmatrix} a^1_{n+1} \\ . \\ . \\ a^m_{n+1} \\ b^1_{n+1} \\ . \\ . \\ b^m_{n+1} \end{bmatrix} \tag{C.10}$$

For simplicity, we define the vectors

$$\boldsymbol{a}_n = \left[a^1_n, ..., a^m_n\right]^T \tag{C.11}$$

and

$$\boldsymbol{b}_n = \left[b^1_n, ..., b^m_n\right]^T \tag{C.12}$$

as the coefficients describing the wavefucntion and current wave in the n^{th} layer. Then one may re-write Eq. C.10 in the form:

$$\begin{bmatrix} \boldsymbol{a}_n \\ \boldsymbol{b}_n \end{bmatrix} = \boldsymbol{I}(n+1) \begin{bmatrix} \boldsymbol{a}_{n+1} \\ \boldsymbol{b}_{n+1} \end{bmatrix}, \tag{C.13}$$

where $\boldsymbol{I}(n+1) = Q^{-1} * IM(n+1)$; here $IM(n+1)$ is well known as the interfacial matrix at the $(n+1)^{th}$ interface:

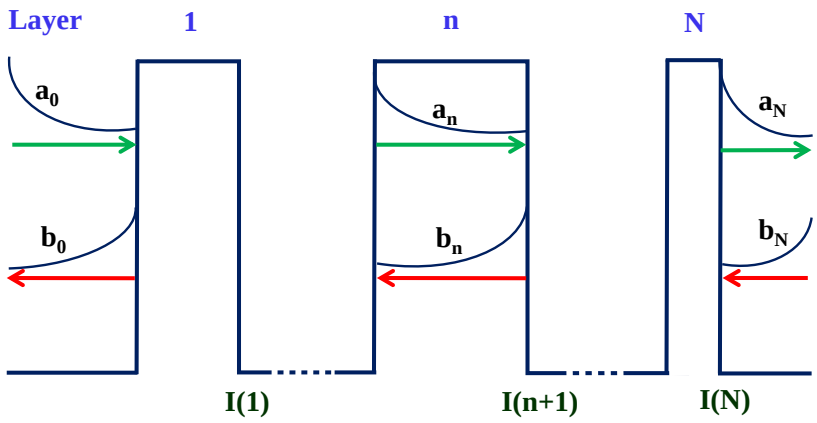

FIGURE C.2: Schematic diagram of electron tunneling through heterostrucutre.

$$\boldsymbol{IM}(n+1) = \begin{bmatrix} \psi_n^1(k_n^1) & \dots & \psi_n^1(k_n^{2m}) \\ . & . & . \\ . & . & . \\ \psi_n^m(k_n^1) & \dots & \psi_n^m(k_n^{2m}) \\ J_z\psi_n^1(k_n^1) & \dots & J_z\psi_n^1(k_n^{2m}) \\ . & . & . \\ . & . & . \\ J_z\psi_n^m(k_n^1) & \dots & J_z\psi_n^m(k_n^{2m}) \end{bmatrix}^{-1} \begin{bmatrix} \psi_{n+1}^1(k_{n+1}^1) & \dots & \psi_{n+1}^1(k_{n+1}^{2m}) \\ . & . & . \\ . & . & . \\ \psi_{n+1}^m(k_{n+1}^1) & \dots & \psi_{n+1}^m(k_{n+1}^{2m}) \\ J_z\psi_{n+1}^1(k_{n+1}^1) & \dots & J_z\psi_{n+1}^1(k_{n+1}^{2m}) \\ . & . & . \\ . & . & . \\ J_z\psi_{n+1}^m(k_{n+1}^1) & \dots & J_z\psi_{n+1}^m(k_{n+1}^{2m}) \end{bmatrix} \tag{C.14}$$

and :

$$Q = \begin{bmatrix} e^{ik_n^1 d_n} & \dots & 0 \\ . & . & . \\ . & . & . \\ . & . & . \\ 0 & \dots & e^{ik_n^{2m} d_n} \end{bmatrix} \tag{C.15}$$

More generally, when the heterostructure is composed of N different layers, in the framework of the transfer matrix theory, the relation between the coefficients is given by:

$$\begin{bmatrix} \boldsymbol{a}_0 \\ \boldsymbol{b}_0 \end{bmatrix} = \boldsymbol{T}(0,N) \begin{bmatrix} \boldsymbol{a}_N \\ \boldsymbol{b}_N \end{bmatrix}, \tag{C.16}$$

linking the wavefunction amplitude to the right $\begin{bmatrix} \boldsymbol{a}_0 \\ \boldsymbol{b}_0 \end{bmatrix}$ to the one at the left $\begin{bmatrix} \boldsymbol{a}_N \\ \boldsymbol{b}_N \end{bmatrix}$.

The equivalent scattering matrix relationship linking outgoing to ingoing waves scattered from one interface would be [417]

$$\begin{bmatrix} \boldsymbol{a}_N \\ \boldsymbol{b}_0 \end{bmatrix} = \boldsymbol{S}(0,N) \begin{bmatrix} \boldsymbol{a}_0 \\ \boldsymbol{b}_N \end{bmatrix}, \tag{C.17}$$

The $T(0,N)$ and $S(0,N)$ are known as Transfer matrix and Scattering matrix, respectively. For the subsystem up to the n^{th} layer, we have:

$$\begin{bmatrix} \boldsymbol{a}_0 \\ \boldsymbol{b}_0 \end{bmatrix} = \boldsymbol{T}(0,n) \begin{bmatrix} \boldsymbol{a}_n \\ \boldsymbol{b}_n \end{bmatrix}, \tag{C.18}$$

$$\begin{bmatrix} \boldsymbol{a}_n \\ \boldsymbol{b}_0 \end{bmatrix} = \boldsymbol{S}(0,n) \begin{bmatrix} \boldsymbol{a}_0 \\ \boldsymbol{b}_n \end{bmatrix}, \tag{C.19}$$

Note that sometime, for convenience, one may work with the Scattering and Transfer matrices $\boldsymbol{S}(n,0)$ and $\boldsymbol{T}(n,0)$ which are defined by:

$$\begin{bmatrix} \boldsymbol{a}_n \\ \boldsymbol{b}_n \end{bmatrix} = \boldsymbol{T}(n,0) \begin{bmatrix} \boldsymbol{a}_0 \\ \boldsymbol{b}_0 \end{bmatrix} \tag{C.20}$$

$$\begin{bmatrix} \boldsymbol{a}_0 \\ \boldsymbol{b}_n \end{bmatrix} = \boldsymbol{S}(n,0) \begin{bmatrix} \boldsymbol{a}_n \\ \boldsymbol{b}_0 \end{bmatrix} \tag{C.21}$$

Obviously, one has

$$\boldsymbol{T}(0,n) = \boldsymbol{T}^{-1}(n,0) \tag{C.22}$$

$$\boldsymbol{S}(0,n) = \boldsymbol{S}^{-1}(n,0) \tag{C.23}$$

The T and S matrices are linked together via a certain relationship according to which:

$$\begin{aligned} \boldsymbol{T}(0,n) &= \begin{bmatrix} T_{11} & T_{12} \\ T_{21} & T_{22} \end{bmatrix} = \begin{bmatrix} S_{11}^{-1} & -S_{11}^{-1}S_{12} \\ S_{21}S_{11}^{-1} & S_{22} - S_{21}S_{11}^{-1}S_{12} \end{bmatrix} \\ \boldsymbol{S}(0,n) &= \begin{bmatrix} S_{11} & S_{12} \\ S_{21} & S_{22} \end{bmatrix} = \begin{bmatrix} T_{11}^{-1} & -T_{11}^{-1}T_{12} \\ T_{21}T_{11}^{-1} & T_{22} - T_{21}T_{11}^{-1}T_{12} \end{bmatrix} \end{aligned} \tag{C.24}$$

$$\begin{aligned} \boldsymbol{T}(n,0) &= \begin{bmatrix} \overline{T}_{11} & \overline{T}_{12} \\ \overline{T}_{21} & \overline{T}_{22} \end{bmatrix} = \begin{bmatrix} \overline{S}_{11}^{-1} & -\overline{S}_{11}^{-1}\overline{S}_{12} \\ \overline{S}_{21}\overline{S}_{11}^{-1} & \overline{S}_{22} - \overline{S}_{21}\overline{S}_{11}^{-1}\overline{S}_{12} \end{bmatrix} \\ \boldsymbol{S}(n,0) &= \begin{bmatrix} \overline{S}_{11} & \overline{S}_{12} \\ \overline{S}_{21} & \overline{S}_{22} \end{bmatrix} = \begin{bmatrix} \overline{T}_{11}^{-1} & -\overline{T}_{11}^{-1}\overline{T}_{12} \\ \overline{T}_{21}\overline{T}_{11}^{-1} & \overline{T}_{22} - \overline{T}_{21}\overline{T}_{11}^{-1}\overline{T}_{12} \end{bmatrix} \end{aligned} \tag{C.25}$$

where the relationship between submatrices of $\boldsymbol{T}(0,n)$ and $\boldsymbol{S}(n,0)$ is given by:

$$\boldsymbol{T}(0,n) = \begin{bmatrix} T_{11} & T_{12} \\ T_{21} & T_{22} \end{bmatrix} = \begin{bmatrix} \overline{S}_{11} - \overline{S}_{12}\overline{S}_{22}^{-1}\overline{S}_{21} & \overline{S}_{12}\overline{S}_{22}^{-1} \\ -\overline{S}_{22}^{-1}\overline{S}_{21} & \overline{S}_{22}^{-1} \end{bmatrix} \tag{C.26}$$

C.1.2 *Recursive approach for the respective transfer and scattering matrices.*

Substituting Eq.C.18 into Eq.C.13 to get:

$$\begin{aligned} \begin{bmatrix} \boldsymbol{a}_0 \\ \boldsymbol{b}_0 \end{bmatrix} &= \boldsymbol{T}(0,n)\boldsymbol{I}(n+1) \begin{bmatrix} \boldsymbol{a}_{n+1} \\ \boldsymbol{b}_{n+1} \end{bmatrix} \\ &= \boldsymbol{T}(0,n+1) \begin{bmatrix} \boldsymbol{a}_{n+1} \\ \boldsymbol{b}_{n+1} \end{bmatrix} \end{aligned} \tag{C.27}$$

Then the new transfer matrix $\boldsymbol{T}(0,n+1)$ can easily be obtained by multiplication:

$$\boldsymbol{T}(0,n+1) = \boldsymbol{T}(0,n)\boldsymbol{I}(n+1) \tag{C.28}$$

Moreover, from Eq.C.19; Eq.C.21 and Eq.C.13 we have:

$$\begin{bmatrix} \boldsymbol{a}_n \\ \boldsymbol{b}_0 \end{bmatrix} = \begin{bmatrix} S_{11} & S_{12} \\ S_{21} & S_{22} \end{bmatrix} \begin{bmatrix} \boldsymbol{a}_0 \\ \boldsymbol{b}_n \end{bmatrix} \tag{C.29}$$

$$\begin{bmatrix} \boldsymbol{a}_0 \\ \boldsymbol{b}_n \end{bmatrix} = \begin{bmatrix} \overline{S}_{11} & \overline{S}_{12} \\ \overline{S}_{21} & \overline{S}_{22} \end{bmatrix} \begin{bmatrix} \boldsymbol{a}_n \\ \boldsymbol{b}_0 \end{bmatrix} \tag{C.30}$$

and:

$$\begin{bmatrix} \boldsymbol{a}_n \\ \boldsymbol{b}_n \end{bmatrix} = \begin{bmatrix} I_{11} & I_{12} \\ I_{21} & I_{22} \end{bmatrix} \begin{bmatrix} \boldsymbol{a}_{n+1} \\ \boldsymbol{b}_{n+1} \end{bmatrix} \tag{C.31}$$

then the coefficients a_n and b_n may be eliminated from the above equation to give:

$$\boldsymbol{a}_n = I_{11}\boldsymbol{a}_{n+1} + I_{12}\boldsymbol{b}_{n+1} \tag{C.32}$$

$$\boldsymbol{b}_n = I_{21}\boldsymbol{a}_{n+1} + I_{22}\boldsymbol{b}_{n+1} \tag{C.33}$$

Replacing $\boldsymbol{a}_n$ and $\boldsymbol{b}_n$ in Eq.C.29 to obtain:

$$\begin{bmatrix} I_{11}\boldsymbol{a}_{n+1} + I_{12}\boldsymbol{b}_{n+1} \\ \boldsymbol{b}_0 \end{bmatrix} = \begin{bmatrix} S_{11} & S_{12} \\ S_{21} & S_{22} \end{bmatrix} \begin{bmatrix} \boldsymbol{a}_0 \\ I_{21}\boldsymbol{a}_{n+1} + I_{22}\boldsymbol{b}_{n+1} \end{bmatrix} \tag{C.34}$$

equivalently:

$$\begin{bmatrix} I_{11}\boldsymbol{a}_{n+1} \\ \boldsymbol{b}_0 \end{bmatrix} + \begin{bmatrix} I_{12}\boldsymbol{b}_{n+1} \\ 0 \end{bmatrix} = \begin{bmatrix} S_{11} & S_{12} \\ S_{21} & S_{22} \end{bmatrix} \begin{bmatrix} \boldsymbol{a}_0 \\ I_{22}\boldsymbol{b}_{n+1} \end{bmatrix} + \begin{bmatrix} S_{11} & S_{12} \\ S_{21} & S_{22} \end{bmatrix} \begin{bmatrix} 0 \\ I_{21}\boldsymbol{a}_{n+1} \end{bmatrix} \tag{C.35}$$

or:

$$\begin{bmatrix} I_{11}\boldsymbol{a}_{n+1} \\ \boldsymbol{b}_0 \end{bmatrix} - \begin{bmatrix} S_{11} & S_{12} \\ S_{21} & S_{22} \end{bmatrix} \begin{bmatrix} 0 \\ I_{21}\boldsymbol{a}_{n+1} \end{bmatrix} = \begin{bmatrix} S_{11} & S_{12} \\ S_{21} & S_{22} \end{bmatrix} \begin{bmatrix} \boldsymbol{a}_0 \\ I_{22}\boldsymbol{b}_{n+1} \end{bmatrix} - \begin{bmatrix} I_{12}\boldsymbol{b}_{n+1} \\ 0 \end{bmatrix} \tag{C.36}$$

or:

$$\begin{bmatrix} (I_{11} - S_{12}I_{21})\boldsymbol{a}_{n+1} \\ \boldsymbol{b}_0 - S_{22}I_{21}\boldsymbol{a}_{n+1} \end{bmatrix} = \begin{bmatrix} S_{11}\boldsymbol{a}_0 + (S_{12}I_{22} - I_{12})\boldsymbol{b}_{n+1} \\ S_{21}\boldsymbol{a}_0 + S_{22}I_{22}\boldsymbol{b}_{n+1} \end{bmatrix} \tag{C.37}$$

Finally, one gets:

$$\begin{bmatrix} -S_{22}I_{21} & \mathbb{I} \\ I_{11} - S_{12}I_{21} & 0 \end{bmatrix} \begin{bmatrix} \boldsymbol{a}_{n+1} \\ \boldsymbol{b}_0 \end{bmatrix} = \begin{bmatrix} S_{21} & S_{22}I_{22} \\ S_{11} & S_{12}I_{22} - I_{12} \end{bmatrix} \begin{bmatrix} \boldsymbol{a}_0 \\ \boldsymbol{b}_{n+1} \end{bmatrix} \tag{C.38}$$

where $\mathbb{I}$ is $m \times m$ identity matrix. From C.38, the new scattering matrix $\boldsymbol{S}(0,n+1)$ may be generated according to the recursive formula:

$$\begin{bmatrix} \boldsymbol{a}_{n+1} \\ \boldsymbol{b}_0 \end{bmatrix} = \begin{bmatrix} 0 & (I_{11} - S_{12}I_{21})^{-1} \\ \mathbb{I} & S_{22}I_{21}\,(I_{11} - S_{12}I_{21})^{-1} \end{bmatrix} \begin{bmatrix} S_{21} & S_{22}I_{22} \\ S_{11} & S_{12}I_{22} - I_{12} \end{bmatrix} \begin{bmatrix} \boldsymbol{a}_0 \\ \boldsymbol{b}_{n+1} \end{bmatrix} = \boldsymbol{S}(0,n+1) \begin{bmatrix} \boldsymbol{a}_0 \\ \boldsymbol{b}_{n+1} \end{bmatrix} \tag{C.39}$$

Replacing $\boldsymbol{a}_n$ and $\boldsymbol{b}_n$ in Eq.C.30 and doing the same treatment, one has:

$$\begin{bmatrix} \mathbb{I} & -\overline{S}_{11}I_{12} \\ 0 & I_{22} - \overline{S}_{21}I_{12} \end{bmatrix} \begin{bmatrix} \boldsymbol{a}_0 \\ \boldsymbol{b}_{n+1} \end{bmatrix} = \begin{bmatrix} \overline{S}_{11}I_{11} & \overline{S}_{12} \\ \overline{S}_{21}I_{11} - I_{21} & \overline{S}_{22} \end{bmatrix} \begin{bmatrix} \boldsymbol{a}_{n+1} \\ \boldsymbol{b}_0 \end{bmatrix} \tag{C.40}$$

to obtain:

$$\begin{bmatrix} \boldsymbol{a}_0 \\ \boldsymbol{b}_{n+1} \end{bmatrix} = \begin{bmatrix} \mathbb{I} & \overline{S}_{11}I_{12}(I_{22} - \overline{S}_{21}I_{12})^{-1} \\ 0 & (I_{22} - \overline{S}_{21}I_{12})^{-1} \end{bmatrix} \begin{bmatrix} \overline{S}_{11}I_{11} & \overline{S}_{12} \\ \overline{S}_{21}I_{11} - I_{21} & \overline{S}_{22} \end{bmatrix} \begin{bmatrix} \boldsymbol{a}_{n+1} \\ \boldsymbol{b}_0 \end{bmatrix} = \boldsymbol{S}(n+1,0) \begin{bmatrix} \boldsymbol{a}_{n+1} \\ \boldsymbol{b}_0 \end{bmatrix} \tag{C.41}$$

Eventually, the submatrices of the new scattering matrix $\boldsymbol{S}(0,n+1)$ are, explicitly given from the different components of the $S(0,n)$ matrix according to:

$$\begin{aligned} S_{11}(0,n+1) &= \left(\mathbb{I} - I_{11}^{-1}S_{12}I_{21}\right)^{-1} I_{11}^{-1}S_{11} \\ S_{12}(0,n+1) &= \left(\mathbb{I} - I_{11}^{-1}S_{12}I_{21}\right)^{-1} I_{11}^{-1}\left(S_{12}I_{22} - I_{12}\right) \\ S_{21}(0,n+1) &= S_{22}I_{21}S_{11}(0,n+1) + S_{21} \\ S_{22}(0,n+1) &= S_{22}I_{21}S_{12}(0,n+1) + S_{22}I_{22} \end{aligned} \tag{C.42}$$

and the submatrices of the new scattering matrix $\boldsymbol{S}(n+1,0)$ are given by:

$$\begin{aligned} \overline{S}_{21}(n+1,0) &= (\mathbb{I} - I_{22}^{-1}\overline{S}_{21}I_{12})^{-1} I_{22}^{-1}(\overline{S}_{21}I_{11} - I_{21}) \\ \overline{S}_{22}(n+1,0) &= (\mathbb{I} - I_{22}^{-1}\overline{S}_{21}I_{12})^{-1} I_{22}^{-1}\overline{S}_{22} \\ \overline{S}_{11}(n+1,0) &= \overline{S}_{11}I_{12}\overline{S}_{21}(n+1,0) + \overline{S}_{11}I_{11} \\ \overline{S}_{12}(n+1,0) &= \overline{S}_{11}I_{12}\overline{S}_{22}(n+1,0) + \overline{S}_{12} \end{aligned} \tag{C.43}$$

These equations C.38; C.39 and C.42 express the propagation of the wave function through the layers. Starting with the unit matrix for $\boldsymbol{S}(0,0)$ the successive scattering matrices $\boldsymbol{S}(0,1),\boldsymbol{S}(0,2),...,\boldsymbol{S}(0,n)$ may be calculated from which the transmission and reflection coefficients can then be obtained using Eq.C.64. This iterative procedure is not as easy to use as the transfer-matrix method, which simply reverts to a product of matrices, but the gain in stability more than compensates. The stability and accuracy of the scattering matrix method is derived from the separation of the forward and backward states and by doing so, the less localized and the propagating states dominate numerically, the physics of the tunneling process is more faithfully described [417].

In multiple-barrier systems, the wavefunction in the intermediate layers is often of interest, since one may extract the information on properties such as inelastic-scattering matrix elements, real-space transfers, and oscillator strengths from a wavefunction. For large systems the transfer matrix fails again because the coefficients in a given layer are evaluated from those in the previous layers, hence the numerical errors increase with the growing exponential [417]. To avoid this, the scattering matrix formalism may be used again. For the n^{th} layer of an N layer system, we have:

$$\begin{aligned} \begin{bmatrix} \boldsymbol{a}_n \\ \boldsymbol{b}_0 \end{bmatrix} &= \boldsymbol{S}(0,n) \begin{bmatrix} \boldsymbol{a}_0 \\ \boldsymbol{b}_n \end{bmatrix} \\ \begin{bmatrix} \boldsymbol{a}_N \\ \boldsymbol{b}_n \end{bmatrix} &= \boldsymbol{S}(n,N) \begin{bmatrix} \boldsymbol{a}_n \\ \boldsymbol{b}_N \end{bmatrix} \end{aligned} \tag{C.44}$$

$$\begin{aligned}\begin{bmatrix} \boldsymbol{a}_0 \\ \boldsymbol{b}_n \end{bmatrix} &= \boldsymbol{S}(n,0)\begin{bmatrix} \boldsymbol{a}_n \\ \boldsymbol{b}_0 \end{bmatrix} \\ \begin{bmatrix} \boldsymbol{a}_n \\ \boldsymbol{b}_N \end{bmatrix} &= \boldsymbol{S}(N,n)\begin{bmatrix} \boldsymbol{a}_N \\ \boldsymbol{b}_n \end{bmatrix}\end{aligned} \tag{C.45}$$

The second equation expresses the coupling with the final layer of the system. The a_N and b_0 may be eliminated from C.44 giving the required intermediate coefficients:

$$\begin{aligned}\boldsymbol{a}_n &= [\mathbb{I} - S_{12}(0,n)S_{21}(n,N)]^{-1} \times [S_{11}(0,n)\boldsymbol{a}_0 + S_{12}(0,n)S_{22}(n,N)\boldsymbol{b}_N] \\ \boldsymbol{b}_n &= [\mathbb{I} - S_{21}(n,N)S_{12}(0,n)]^{-1} \times [S_{21}(n,N)S_{11}(0,n)\boldsymbol{a}_0 + S_{22}(n,N)\boldsymbol{b}_N]\end{aligned} \tag{C.46}$$

This particular form has the advantage that only the initial boundary conditions a_0 and b_N are required, hence the errors in the coefficients do not propagate from one layer to the next. Doing the same treatment for relations C.45 to obtain:

$$\begin{aligned}\boldsymbol{a}_n &= \left[\mathbb{I} - \overline{S}_{12}(N,n)\overline{S}_{21}(n,0)\right]^{-1} \times \left[\overline{S}_{11}(N,n)\boldsymbol{a}_N + \overline{S}_{12}(N,n)\overline{S}_{22}(n,0)\boldsymbol{b}_0\right] \\ \boldsymbol{b}_n &= \left[\mathbb{I} - \overline{S}_{21}(n,0)\overline{S}_{12}(N,n)\right]^{-1} \times \left[\overline{S}_{21}(n,0)\overline{S}_{11}(N,n)\boldsymbol{a}_N + \overline{S}_{22}(n,0)\boldsymbol{b}_0\right]\end{aligned} \tag{C.47}$$

One must be noted that the scattering matrix and its submatrices become singular in the limit of a large system. There is merely a reflection of the physical insignificance of the more localized states. Numerically, this makes the rank of the matrices smaller than their actual order and so direct inversions of the submatrices should be avoided.

More generally, if the initial coefficients are a_i, b_i at i^{th} layer and a_j, b_j at j^{th} layer (j>i), then the coefficients a_n and b_n in whole heterostructure can be calculated by considering three cases:

Case $n < i$:

$$\begin{aligned}\begin{bmatrix} \boldsymbol{a}_i \\ \boldsymbol{b}_n \end{bmatrix} &= \boldsymbol{S}(n,i)\begin{bmatrix} \boldsymbol{a}_n \\ \boldsymbol{b}_i \end{bmatrix} \\ \begin{bmatrix} \boldsymbol{a}_j \\ \boldsymbol{b}_n \end{bmatrix} &= \boldsymbol{S}(n,j)\begin{bmatrix} \boldsymbol{a}_n \\ \boldsymbol{b}_j \end{bmatrix}\end{aligned} \tag{C.48}$$

$$\begin{aligned}\begin{bmatrix} \boldsymbol{a}_n \\ \boldsymbol{b}_i \end{bmatrix} &= \boldsymbol{S}(i,n)\begin{bmatrix} \boldsymbol{a}_i \\ \boldsymbol{b}_n \end{bmatrix} \\ \begin{bmatrix} \boldsymbol{a}_n \\ \boldsymbol{b}_j \end{bmatrix} &= \boldsymbol{S}(j,n)\begin{bmatrix} \boldsymbol{a}_j \\ \boldsymbol{b}_n \end{bmatrix}\end{aligned} \tag{C.49}$$

The coefficients are then

$$\begin{aligned}\boldsymbol{a}_n &= A^{-1}\left[S_{22}(n,i)S_{12}^{-1}(n,i)\boldsymbol{a}_i - S_{22}(n,j)\boldsymbol{b}_j\right] \\ \boldsymbol{a}_n &= S_{21}(n,j)A^{-1}\left[S_{22}(n,i)S_{12}^{-1}(n,i)\boldsymbol{a}_i - S_{22}(n,j)\boldsymbol{b}_j\right] + S_{22}(n,j)\boldsymbol{b}_j\end{aligned} \tag{C.50}$$

or

$$\begin{aligned}\boldsymbol{a}_n &= \overline{S}_{12}(j,n)\overline{A}^{-1}\left[\overline{S}_{11}(i,n)\overline{S}_{21}^{-1}(i,n)\boldsymbol{b}_i - \overline{S}_{11}(j,n)\boldsymbol{a}_j\right] + \overline{S}_{11}(j,n)\boldsymbol{a}_j \\ \boldsymbol{b}_n &= \overline{A}^{-1}\left[\overline{S}_{11}(i,n)\overline{S}_{21}^{-1}(i,n)\boldsymbol{b}_i - \overline{S}_{11}(j,n)\boldsymbol{a}_j\right]\end{aligned} \tag{C.51}$$

where

$$A = S_{21}(n,j) - S_{21}(n,i) + S_{22}(n,i)S_{12}^{-1}(n,i)S_{11}(n,i) \tag{C.52}$$

$$\overline{A} = \overline{S}_{12}(j,n) - \overline{S}_{12}(i,n) + \overline{S}_{11}(i,n)\overline{S}_{21}^{-1}(i,n)\overline{S}_{22}(i,n) \tag{C.53}$$

Case $i \leq n \leq j$:

$$\begin{aligned} \begin{bmatrix} \boldsymbol{a}_n \\ \boldsymbol{b}_i \end{bmatrix} &= \boldsymbol{S}(i,n) \begin{bmatrix} \boldsymbol{a}_i \\ \boldsymbol{b}_n \end{bmatrix} \\ \begin{bmatrix} \boldsymbol{a}_j \\ \boldsymbol{b}_n \end{bmatrix} &= \boldsymbol{S}(n,j) \begin{bmatrix} \boldsymbol{a}_n \\ \boldsymbol{b}_j \end{bmatrix} \end{aligned} \tag{C.54}$$

$$\begin{aligned} \begin{bmatrix} \boldsymbol{a}_i \\ \boldsymbol{b}_n \end{bmatrix} &= \boldsymbol{S}(n,i) \begin{bmatrix} \boldsymbol{a}_n \\ \boldsymbol{b}_i \end{bmatrix} \\ \begin{bmatrix} \boldsymbol{a}_n \\ \boldsymbol{b}_j \end{bmatrix} &= \boldsymbol{S}(j,n) \begin{bmatrix} \boldsymbol{a}_j \\ \boldsymbol{b}_n \end{bmatrix} \end{aligned} \tag{C.55}$$

The coefficients are then:

$$\begin{aligned} \boldsymbol{a}_n &= [\mathbb{I} - S_{12}(i,n)S_{21}(n,j)]^{-1} \times \left[S_{11}(i,n)\boldsymbol{a}_i + S_{12}(i,n)S_{22}(n,j)\boldsymbol{b}_j\right] \\ \boldsymbol{b}_n &= [\mathbb{I} - S_{21}(n,j)S_{12}(i,n)]^{-1} \times \left[S_{21}(n,j)S_{11}(i,n)\boldsymbol{a}_i + S_{22}(n,j)\boldsymbol{b}_j\right] \end{aligned} \tag{C.56}$$

or:

$$\begin{aligned} \boldsymbol{a}_n &= \left[\mathbb{I} - \overline{S}_{12}(j,n)\overline{S}_{21}(n,i)\right]^{-1} \times \left[\overline{S}_{11}(j,n)\boldsymbol{a}_j + \overline{S}_{12}(j,n)\overline{S}_{22}(n,i)\boldsymbol{b}_i\right] \\ \boldsymbol{b}_n &= \left[\mathbb{I} - \overline{S}_{21}(n,i)\overline{S}_{12}(j,n)\right]^{-1} \times \left[\overline{S}_{21}(n,i)\overline{S}_{11}(j,n)\boldsymbol{a}_j + \overline{S}_{22}(n,i)\boldsymbol{b}_i\right] \end{aligned} \tag{C.57}$$

Case $n > j$:

$$\begin{aligned} \begin{bmatrix} \boldsymbol{a}_n \\ \boldsymbol{b}_i \end{bmatrix} &= \boldsymbol{S}(i,n) \begin{bmatrix} \boldsymbol{a}_i \\ \boldsymbol{b}_n \end{bmatrix} \\ \begin{bmatrix} \boldsymbol{a}_n \\ \boldsymbol{b}_j \end{bmatrix} &= \boldsymbol{S}(j,n) \begin{bmatrix} \boldsymbol{a}_j \\ \boldsymbol{b}_n \end{bmatrix} \end{aligned} \tag{C.58}$$

$$\begin{aligned} \begin{bmatrix} \boldsymbol{a}_i \\ \boldsymbol{b}_n \end{bmatrix} &= \boldsymbol{S}(n,i) \begin{bmatrix} \boldsymbol{a}_n \\ \boldsymbol{b}_i \end{bmatrix} \\ \begin{bmatrix} \boldsymbol{a}_j \\ \boldsymbol{b}_n \end{bmatrix} &= \boldsymbol{S}(n,j) \begin{bmatrix} \boldsymbol{a}_n \\ \boldsymbol{b}_j \end{bmatrix} \end{aligned} \tag{C.59}$$

The coefficients are then:

$$\begin{aligned} \boldsymbol{a}_n &= S_{12}(i,n)B^{-1}\left[S_{11}(j,n)S_{21}(j,n)\boldsymbol{b}_j - S_{11}(i,n)\boldsymbol{a}_i\right] + S_{11}(i,n)\boldsymbol{a}_i \\ \boldsymbol{b}_n &= B^{-1}\left[S_{11}(j,n)S_{21}(j,n)\boldsymbol{b}_j - S_{11}(i,n)\boldsymbol{a}_i\right] \end{aligned} \tag{C.60}$$

or

$$\begin{aligned} \boldsymbol{a}_n &= \overline{B}^{-1}\left[\overline{S}_{22}(n,j)\overline{S}_{12}^{-1}(n,j)\boldsymbol{a}_j - \overline{S}_{22}(n,i)\boldsymbol{b}_i\right] \\ \boldsymbol{b}_n &= \overline{S}_{21}(n,i)\overline{B}^{-1}\left[\overline{S}_{22}(n,j)\overline{S}_{12}^{-1}(n,j)\boldsymbol{a}_j - \overline{S}_{22}(n,i)\boldsymbol{b}_i\right] + \overline{S}_{22}(n,i)\boldsymbol{b}_i \end{aligned} \tag{C.61}$$

where

$$B = S_{12}(i,n) - S_{12}(j,n) + S_{11}(j,n)S_{21}^{-1}(j,n)S_{22}(j,n) \tag{C.62}$$

$$\overline{B} = \overline{S}_{21}(n,i) - \overline{S}_{21}(n,j) + \overline{S}_{22}(n,j)\overline{S}_{12}^{-1}(n,j)\overline{S}_{11}(n,j) \tag{C.63}$$

C.1.3 Transmission and Reflection amplitudes

According to the definition of the scattering matrix in the previous part, the scattering and trnsfer matrix entries are denoted respectively as [418]

$$S(0,N) = \begin{bmatrix} t & r' \\ r & t' \end{bmatrix}; \qquad T(0,N) = \begin{bmatrix} t^{-1} & -t^{-1}r' \\ rt^{-1} & t' - rt^{-1}r' \end{bmatrix} \tag{C.64}$$

We have to note that the reference to incoming and outgoing amplitudes does not necessarily mean that the above analysis is restricted to a basis of propagating states only. As is well-known by appropriate analytical continuation, wavevectors change from real to complex, *i.e.*, change from waves propagating to the right/ left into waves decaying to the right left and the same formal analysis holds for bound states, if there are any.

We discuss now the general relationship linking the scattering waves treated in the S-matrix theory to the Landauer formula for the conductivity. This is an important challenge to make the connections between both quantities S-matrix and conductivity *via* the transmission coefficients. This connection allows one to calculate the different properties of multilayers structures like tunneling transport, spin-Hall effects, tunneling Hall effects and optical responses and related optical anisotropies.

We consider a diffusive region involving interfaces and we start with the general expressions giving the scattering waves incident from the left reservoir (designed by +) or from the right reservoir (designed by −); + and − sign means waves propagating from left to right and from right to left respectively. The scattered waves ψ that obeys the Schrödinger equation in each part of the system and in the two reservoirs. They are expressed like:

$$\begin{aligned} \psi_n^+ &= \phi_{Ln}^+ + \Sigma_n' r_{n,n'}\phi_{Ln}^- \text{ in the left part} \\ \psi_n^+ &= \Sigma_n' t_{n,n'}\phi_{Rn}^+ \text{ in the right part} \end{aligned} \tag{C.65}$$

for the left incoming wave, where $r_{n,n'}\phi_{Ln}^-$ and $t_{n,n'}\phi_{Rn}^+$ are the respective reflected waves to the left and transmitted waves to the right part; n and n' are the respective incoming and outgoing channels. In the same way, for the right incoming waves, one has:

$$\begin{aligned} \psi_n^- &= \phi_{Rn}^- + \Sigma_n' r_{n,n'}\phi_{Rn}^+ \text{ in the right part} \\ \psi_n^- &= \Sigma_n' t_{n,n'}\phi_{Ln}^- \text{ in the left part} \end{aligned} \tag{C.66}$$

In order to put forward the importance of the unitarity of the S-matrix, one may express the average current density along the propagation direction z according to:

$$J(z) = \psi^*(z) \overleftrightarrow{\hat{J}}_z \psi(z) = \psi^*(z)\hat{J}_z\psi(z) - \psi(z)\hat{J}_z\psi^*(z) \tag{C.67}$$

where $\overleftrightarrow{\hat{J}} = \overleftarrow{\hat{J}} + \overrightarrow{\hat{J}}$, with $\overleftarrow{\hat{J}}$ acts on the left and $\overrightarrow{\hat{J}}$ acts on the right, giving thus the current density calculated to the left according to:

$$J_L(z) = \left(a_n^+\phi_{Ln}^+ + a_n^-\phi_{Ln}^-\right)^* \overleftrightarrow{\hat{J}}_z \left(a_n^+\phi_{Ln}^+ + a_n^-\phi_{Ln}^-\right) = \sum_n J_n \left(|a_n^+|^2 - |ra_n^- + t'b_n^-|^2\right) \tag{C.68}$$

where $a_n^\pm$ and $b_n^\pm$ are the amplitude of the channel wavefunction to the left (a) and to the right (b) normalized by their unit of flux J_n. We have identically for the right part:

$$J_R(z) = \left(b_n^-\phi_{Rn}^- + b_n^+\phi_{Rn}^+\right)^* \overleftrightarrow{\hat{J}}_z \left(b_n^-\phi_{Rn}^- + b_n^+\phi_{Rn}^+\right) = \sum_n \frac{\hbar}{m^*} \left(-|b_n^-|^2 + |r'b_n^+ + ta_n^+|^2\right) \tag{C.69}$$

where we have used the major property that $Re\left(\left\langle m\left|\overrightarrow{\hat{J}}_z\right|n\right\rangle + \left\langle m\left|\overleftarrow{\hat{J}}_z\right|n\right\rangle\right) = 0$ for $|n\rangle \neq |m\rangle$ like established in the previous chapter (see section 3.2.1). Developing both equalities on r, r', t and t' finally gives:

$$J_L(z) = \frac{\hbar}{m^*}\left[\left(a^+\right)^\dagger\left(\hat{1} - r^\dagger r\right)a^+ - \left(b^-\right)^\dagger\left(t'^\dagger t'\right)b^- - 2Re\left[\left(a^+\right)^\dagger r^\dagger t' b^-\right]\right] \tag{C.70}$$

$$J_R(z) = \frac{\hbar}{m^*}\left[\left(b^-\right)^\dagger\left(-\hat{1} + r'^\dagger r'\right)b^- + \left(a^+\right)^\dagger\left(t^\dagger t\right)a^+ - 2Re\left[\left(a^+\right)^\dagger t^\dagger r' b^-\right]\right] \tag{C.71}$$

Making J_L and J_R equal for every channel contribution, whatever their weight a_n^+ and b_n^- gives the necessary conditions for the unitary matrix:

$$[\mathbf{r}]^\dagger[\mathbf{r}] + [\mathbf{t}]^\dagger[\mathbf{t}] = [\hat{\mathbf{1}}] \tag{C.72}$$

$$[\mathbf{r'}]^\dagger[\mathbf{r}] + [\mathbf{t'}]^\dagger[\mathbf{t}] = \left[\hat{\mathbf{1}}\right] \tag{C.73}$$

$$[\mathbf{r}]^\dagger[\mathbf{t'}] + [\mathbf{t}]^\dagger[\mathbf{r'}] = \left[\hat{\mathbf{0}}\right] \tag{C.74}$$

demonstrating thus the unitarity of the S-matrix. Here $\left[\hat{\mathbf{1}}\right]$ and $\left[\hat{\mathbf{0}}\right]$ indicate the unit matrix and zeros matrix respectively. Therefore, in terms of the elements of the S-matrix, we obtain

$$\sum_{k=1}^{2m} |S_{kn}|^2 = \sum_{k=1}^{2m} |S_{nk}|^2, \tag{C.75}$$

or equivalenty,

$$\begin{aligned} \sum_{k=1}^{m} |r_{kn}|^2 + \sum_{k=1}^{m} |t'_{kn}|^2 &= \sum_{k=1}^{m} |r_{nk}|^2 + \sum_{k=1}^{m} |t_{nk}|^2, \\ \text{and } \sum_{k=1}^{m} |t_{kn}|^2 + \sum_{k=1}^{m} |r'_{kn}|^2 &= \sum_{k=1}^{m} |t'_{nk}|^2 + \sum_{k=1}^{m} |r'_{nk}|^2. \end{aligned} \tag{C.76}$$

As a consequence of Eq. C.76, we obtain

$$\sum_{k=1,n=1}^{k=m,n=m} |t_{kn}|^2 = \sum_{k=1,n=1}^{k=m,n=m} |t'_{kn}|^2 . \tag{C.77}$$

Equation C.77 shows that the total transmission coefficients of the left and right incoming waves are equal.

C.2 Global transfer and scattering matrices

The concept of global transfer matrix was introduced as early in Ref. [419] and recently, was developed for a semiconductor heterostructure in Ref [420]. The ideal of the global transfer matrix is to replace the recursion method of conventional transfer matrix for a heterostructure by increasing the site of matrix. Then even though, one has to deal with large site matrix however, with one step, it is possible to extract all the needed information of tunneling through heterostructure from the calculation. In this section, we review the details of global transfer matrix and then introduce the same treatment with global scattering matrix for a heterostructure.

C.2.1 Global transfer matrix

We now are considering a heterostructure described in Fig. C.2. Using the notation of transfer matrix $\boldsymbol{T}(N,0)$ in the transfer matrix formalism's section and writing out matching equations for the wavefunction at each interface of the heterostructure, it is possible to obtain a set of equations as following :

$$\begin{aligned}
\boldsymbol{T}(1,0)\begin{bmatrix} \boldsymbol{a}_0 \\ \boldsymbol{b}_0 \end{bmatrix} - \begin{bmatrix} \boldsymbol{a}_1 \\ \boldsymbol{b}_1 \end{bmatrix} &= 0 \\
\boldsymbol{T}(2,1)\begin{bmatrix} \boldsymbol{a}_1 \\ \boldsymbol{b}_1 \end{bmatrix} - \begin{bmatrix} \boldsymbol{a}_2 \\ \boldsymbol{b}_2 \end{bmatrix} &= 0 \\
\ldots\ldots\ldots\ldots\ldots &= \ldots \\
\boldsymbol{T}(N,N-1)\begin{bmatrix} \boldsymbol{a}_{N-1} \\ \boldsymbol{b}_{N-1} \end{bmatrix} - \begin{bmatrix} \boldsymbol{a}_N \\ \boldsymbol{b}_N \end{bmatrix} &= 0
\end{aligned} \tag{C.78}$$

Since we are interested in the tunneling problems through heterostructure with an incoming electron from the left, then one may assume that $\boldsymbol{a}_0$ are input parameters describing the incoming wavefunction of the electron, $\boldsymbol{b}_0$ are output parameters describing the reflected wavefunction of the electron at the first interface, $\boldsymbol{a}_N$ are also output parameters describing the outgoing wavefunction of the electron tunnels through the structure and $\boldsymbol{b}_N = 0$. Then conveniently, one rewrites the system of equations C.79 as:

Then one can re-write the system of equations as:

$$
\begin{aligned}
\boldsymbol{T}(1,0)\begin{bmatrix}\mathbf{0}\\ \boldsymbol{b}_0\end{bmatrix} - \begin{bmatrix}\boldsymbol{a}_1\\ \boldsymbol{b}_1\end{bmatrix} &= -\boldsymbol{T}(1,0)\begin{bmatrix}\boldsymbol{a}_0\\ \mathbf{0}\end{bmatrix}\\
\boldsymbol{T}(2,1)\begin{bmatrix}\boldsymbol{a}_1\\ \boldsymbol{b}_1\end{bmatrix} - \begin{bmatrix}\boldsymbol{a}_2\\ \boldsymbol{b}_2\end{bmatrix} &= 0\\
\ldots\ldots\ldots\ldots\ldots &= \ldots\\
\boldsymbol{T}(N,N-1)\begin{bmatrix}\boldsymbol{a}_{N-1}\\ \boldsymbol{b}_{N-1}\end{bmatrix} - \begin{bmatrix}\boldsymbol{a}_N\\ \mathbf{0}\end{bmatrix} &= 0
\end{aligned}
\tag{C.79}
$$

Or in the compact from, one has:

$$K_G[\boldsymbol{v}] = [\boldsymbol{u}] \tag{C.80}$$

or:

$$[\boldsymbol{v}] = K_G^{-1}[\boldsymbol{u}] \tag{C.81}$$

where:

$$
[\boldsymbol{v}] = \begin{bmatrix}\boldsymbol{b}_0\\ \boldsymbol{a}_N\\ \boldsymbol{a}_1\\ \boldsymbol{b}_1\\ \vdots\\ \boldsymbol{a}_{N-1}\\ \boldsymbol{b}_{N-1}\end{bmatrix};\ [\boldsymbol{u}] = \begin{bmatrix}-\boldsymbol{T}(1,0)\begin{bmatrix}\boldsymbol{a}_0\\ \mathbf{0}\end{bmatrix}\\ 0\\ 0\\ \vdots\\ 0\\ 0\end{bmatrix} = \begin{bmatrix}-\boldsymbol{T}(1,0)\begin{bmatrix}\mathbb{I}\\ \mathbf{0}\end{bmatrix}\\ 0\\ 0\\ \vdots\\ 0\\ 0\end{bmatrix}\boldsymbol{a}_0
\tag{C.82}
$$

and

$$
K_G = \begin{bmatrix}
\boldsymbol{T}(1,0)\boldsymbol{M}_1 & -\mathbb{I} & 0 & \ldots & 0 & 0\\
0 & \boldsymbol{T}(2,1) & -\mathbb{I} & \ldots & 0 & 0\\
0 & 0 & \boldsymbol{T}(3,2) & \ldots & 0 & 0\\
\vdots & \vdots & \vdots & \ddots & \vdots & \vdots\\
0 & 0 & 0 & \ldots & \boldsymbol{T}(N-1,N-2) & -\mathbb{I}\\
-\boldsymbol{M}_2 & 0 & 0 & \ldots & 0 & \boldsymbol{T}(N,N-1)
\end{bmatrix}
\tag{C.83}
$$

with

$$\boldsymbol{M}_1 = \begin{bmatrix}0 & 0\\ \mathbb{I} & 0\end{bmatrix};\quad \boldsymbol{M}_2 = \begin{bmatrix}0 & \mathbb{I}\\ 0 & 0\end{bmatrix} \tag{C.84}$$

So, if we define:

$$
T_G = K_G^{-1}\begin{bmatrix}-\boldsymbol{T}(1,0)\begin{bmatrix}\mathbb{I}\\ \mathbf{0}\end{bmatrix}\\ 0\\ 0\\ \vdots\\ 0\\ 0\end{bmatrix}
\tag{C.85}
$$

then the Eq. C.81 can be re-written as:

$$[\boldsymbol{v}] = T_G\boldsymbol{a}_0 \tag{C.86}$$

and in this sense, T_G, a global transfer matrix, is a rectangular matrix with 2N super-rows numbered by 1, 2, 3, ... 2N and one super-column.

Note that since the global transfer matrix is not unique, then one may define the other global transfer matrix by using the following system of equations:

$$\begin{aligned} \boldsymbol{T}(0,1)\begin{bmatrix} \boldsymbol{a}_1 \\ \boldsymbol{b}_1 \end{bmatrix} - \begin{bmatrix} 0 \\ \boldsymbol{b}_0 \end{bmatrix} &= \begin{bmatrix} \boldsymbol{a}_0 \\ \boldsymbol{0} \end{bmatrix} \\ \boldsymbol{T}(1,2)\begin{bmatrix} \boldsymbol{a}_2 \\ \boldsymbol{b}_2 \end{bmatrix} - \begin{bmatrix} \boldsymbol{a}_1 \\ \boldsymbol{b}_1 \end{bmatrix} &= 0 \\ \ldots\ldots\ldots\ldots\ldots &= \ldots \\ \boldsymbol{T}(N-1,N)\begin{bmatrix} \boldsymbol{a}_N \\ 0 \end{bmatrix} - \begin{bmatrix} \boldsymbol{a}_{N-1} \\ \boldsymbol{b}_{N-1} \end{bmatrix} &= 0 \end{aligned} \tag{C.87}$$

giving:

$$\tilde{K}_G\,[v] = [\tilde{u}] \tag{C.88}$$

or

$$\tilde{T}_G\,[\tilde{u}] = [v] \tag{C.89}$$

where:

$$\tilde{T}_G = \tilde{K}_G^{-1} = \begin{bmatrix} -\boldsymbol{M}_1 & \boldsymbol{T}(0,1) & 0 & \ldots & 0 & 0 \\ 0 & -\mathbb{I} & \boldsymbol{T}(1,2) & \ldots & 0 & 0 \\ 0 & 0 & -\mathbb{I} & \ldots & 0 & 0 \\ \vdots & \vdots & \vdots & \ddots & \vdots & \vdots \\ 0 & 0 & 0 & \ldots & -\mathbb{I} & \boldsymbol{T}(N-2,N-1) \\ \boldsymbol{T}(N-1,N)\boldsymbol{M}_2 & 0 & 0 & \ldots & 0 & -\mathbb{I} \end{bmatrix}^{-1} \tag{C.90}$$

and

$$[\tilde{u}] = \begin{bmatrix} \begin{bmatrix} \boldsymbol{a}_0 \\ \boldsymbol{0} \end{bmatrix} \\ 0 \\ 0 \\ \vdots \\ 0 \\ 0 \end{bmatrix} \tag{C.91}$$

$\tilde{T}_G$ is also a global transfer matrix which is equivalent to T_G for the same heterostructure.

Transmission and reflection coefficients from global transfer matrix

Looking at Eq. C.86, one observes that if we write the global matrix T_G as following:

$$T_G = \begin{bmatrix} T_{G1} \\ T_{G2} \\ \vdots \\ T_{GN} \end{bmatrix} \tag{C.92}$$

where

$$T_{Gj} = \begin{bmatrix} T^1_{Gj} \\ T^2_{Gj} \end{bmatrix} \tag{C.93}$$

then T^1_{G1} will be a reflection matrix $\boldsymbol{r}$ and T^2_{G1} will be a transmission matrix $\boldsymbol{t}$. The other super-elements of T_G will yield the coefficients in the intermediate domains in the form:

$$\begin{bmatrix} \boldsymbol{a}_n \\ \boldsymbol{b}_n \end{bmatrix} = \begin{bmatrix} T^1_{Gn}\boldsymbol{a}_0 \\ T^2_{Gn}\boldsymbol{a}_0 \end{bmatrix} \tag{C.94}$$

Note that if we write the global transfer matrix $\tilde{T}_G$ as:

$$\tilde{T}_G = \begin{bmatrix} \tilde{T}_{G11} & \tilde{T}_{G12} & \dots & \tilde{T}_{G1N} \\ \tilde{T}_{G21} & \tilde{T}_{G22} & \dots & \tilde{T}_{G2N} \\ \vdots & \vdots & \ddots & \vdots \\ \tilde{T}_{GN1} & \tilde{T}_{GN2} & \dots & \tilde{T}_{GNN} \end{bmatrix} \tag{C.95}$$

and:

$$\tilde{T}_{G11} = \begin{bmatrix} \tilde{T}^{11}_{G11} & \tilde{T}^{12}_{G11} \\ \tilde{T}^{21}_{G11} & \tilde{T}^{22}_{G11} \end{bmatrix} \tag{C.96}$$

then $\tilde{T}^{11}_{G11}$ will be a reflection matrix $\boldsymbol{r}$ and $\tilde{T}^{21}_{G11}$ will be a transmission matrix $\boldsymbol{t}$.

C.2.2 Global scattering matrix

Now, we will present the same treatments with an introduction of a global scattering matrix. In addition to the recursive method to construct scattering matrices for a heterostructure presenting in the previous sections, one has alternative way to describe this scattering problem by using the global scattering matrix.

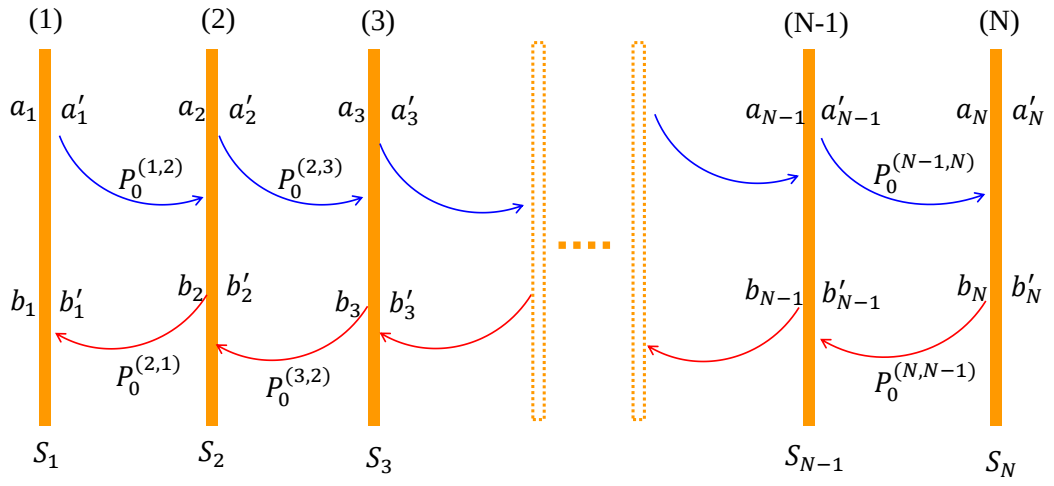

FIGURE C.3: Schematic of scattering process within a heterostructure.

In order to introduce the global scattering matrix in a convenient way, let us describe the scattering process within a heterostructure as depicted in Fig. C.3. We define:

$$S_i = \begin{bmatrix} t_i & r'_i \\ r_i & t'_i \end{bmatrix} \tag{C.97}$$

is an interfacial scattering matrix at the i^{th} interface and $P_0^{(i,i+1)}$ is the propagation from i^{th} interface to $(i+1)^{th}$ interface:

$$P_0^{(i,i+1)} = \begin{bmatrix} P_0^{(i,i+1)} & 0 \\ 0 & 0 \end{bmatrix} \tag{C.98}$$

and

$$P_0^{(i+1,i)} = \begin{bmatrix} 0 & 0 \\ 0 & \tilde{P}_0^{(i,i+1)} \end{bmatrix} \tag{C.99}$$

are the propagation from i^{th} to $(i+1)^{th}$ interface and from $(i+1)^{th}$ back to i^{th} interface (Thank to the time inversion symmetry, one has: $P_0^{ij} \equiv \tilde{P}_0^{ij}$).

One has:

$$\begin{bmatrix} \boldsymbol{a}_1 \\ \boldsymbol{b}_1^{'} \end{bmatrix} = S_1^{-1} \begin{bmatrix} \boldsymbol{a}_1^{'} \\ \boldsymbol{b}_1 \end{bmatrix} \tag{C.100}$$

$$\begin{bmatrix} 0 \\ \boldsymbol{b}_1^{'} \end{bmatrix} = \begin{bmatrix} 0 & 0 \\ 0 & \tilde{P}_0^{(1,2)} \end{bmatrix} \begin{bmatrix} \boldsymbol{a}_2^{'} \\ \boldsymbol{b}_2 \end{bmatrix} = P_0^{(2,1)} \begin{bmatrix} \boldsymbol{a}_2^{'} \\ \boldsymbol{b}_2 \end{bmatrix} \tag{C.101}$$

giving:

$$S_1^{-1} \begin{bmatrix} \boldsymbol{a}_1^{'} \\ \boldsymbol{b}_1 \end{bmatrix} - P_0^{(2,1)} \begin{bmatrix} \boldsymbol{a}_2^{'} \\ \boldsymbol{b}_2 \end{bmatrix} = \begin{bmatrix} \boldsymbol{a}_1 \\ 0 \end{bmatrix} \tag{C.102}$$

Furthermore:

$$\begin{bmatrix} \boldsymbol{a}_2 \\ 0 \end{bmatrix} = \begin{bmatrix} P_0^{(1,2)} & 0 \\ 0 & 0 \end{bmatrix} \begin{bmatrix} \boldsymbol{a}_1^{'} \\ \boldsymbol{b}_1 \end{bmatrix} = P_0^{(1,2)} \begin{bmatrix} \boldsymbol{a}_1^{'} \\ \boldsymbol{b}_1 \end{bmatrix} \tag{C.103}$$

$$\begin{bmatrix} \boldsymbol{a}_2 \\ \boldsymbol{b}_2^{'} \end{bmatrix} = S_2^{-1} \begin{bmatrix} \boldsymbol{a}_2^{'} \\ \boldsymbol{b}_2 \end{bmatrix} \tag{C.104}$$

$$\begin{bmatrix} 0 \\ \boldsymbol{b}_2^{'} \end{bmatrix} = \begin{bmatrix} 0 & 0 \\ 0 & \tilde{P}_0^{(2,3)} \end{bmatrix} \begin{bmatrix} \boldsymbol{a}_3^{'} \\ \boldsymbol{b}_3 \end{bmatrix} = P_0^{(3,2)} \begin{bmatrix} \boldsymbol{a}_3^{'} \\ \boldsymbol{b}_3 \end{bmatrix} \tag{C.105}$$

giving:

$$-P_0^{(1,2)} \begin{bmatrix} \boldsymbol{a}_1^{'} \\ \boldsymbol{b}_1 \end{bmatrix} + S_2^{-1} \begin{bmatrix} \boldsymbol{a}_2^{'} \\ \boldsymbol{b}_2 \end{bmatrix} - P_0^{(3,2)} \begin{bmatrix} \boldsymbol{a}_3^{'} \\ \boldsymbol{b}_3 \end{bmatrix} = 0 \tag{C.106}$$

Doing the same treatments, one finally obtain a system of equations as:

$$S_1^{-1}\begin{bmatrix} \boldsymbol{a}_1' \\ \boldsymbol{b}_1 \end{bmatrix} - P_0^{(2,1)}\begin{bmatrix} \boldsymbol{a}_2' \\ \boldsymbol{b}_2 \end{bmatrix} = \begin{bmatrix} \boldsymbol{a}_1 \\ 0 \end{bmatrix} \tag{C.107}$$

$$-P_0^{(1,2)}\begin{bmatrix} \boldsymbol{a}_1' \\ \boldsymbol{b}_1 \end{bmatrix} + S_2^{-1}\begin{bmatrix} \boldsymbol{a}_2' \\ \boldsymbol{b}_2 \end{bmatrix} - P_0^{(3,2)}\begin{bmatrix} \boldsymbol{a}_3' \\ \boldsymbol{b}_3 \end{bmatrix} = 0 \tag{C.108}$$

$$\ldots\ldots\ldots\ldots\ldots = \ldots$$

$$-P_0^{(i-1,i)}\begin{bmatrix} \boldsymbol{a}_{i-1}' \\ \boldsymbol{b}_{i-1} \end{bmatrix} + S_i^{-1}\begin{bmatrix} \boldsymbol{a}_i' \\ \boldsymbol{b}_i \end{bmatrix} - P_0^{(i+1,i)}\begin{bmatrix} \boldsymbol{a}_{i+1}' \\ \boldsymbol{b}_{i+1} \end{bmatrix} = 0 \tag{C.109}$$

$$\ldots\ldots\ldots\ldots\ldots = \ldots$$

$$-P_0^{(N-2,N-1)}\begin{bmatrix} \boldsymbol{a}_{N-2}' \\ \boldsymbol{b}_{N-2} \end{bmatrix} + S_{N-1}^{-1}\begin{bmatrix} \boldsymbol{a}_{N-1}' \\ \boldsymbol{b}_{N-1} \end{bmatrix} - P_0^{(N,N-1)}\begin{bmatrix} \boldsymbol{a}_N' \\ \boldsymbol{b}_N \end{bmatrix} = 0 \tag{C.110}$$

$$-P_0^{(N-1,N)}\begin{bmatrix} \boldsymbol{a}_{N-1}' \\ \boldsymbol{b}_{N-1} \end{bmatrix} + S_N^{-1}\begin{bmatrix} \boldsymbol{a}_N' \\ \boldsymbol{b}_N \end{bmatrix} = \begin{bmatrix} 0 \\ \boldsymbol{b}_N' \end{bmatrix} \tag{C.111}$$

This system of equations can be re-written in the compact form:

$$S_T\boldsymbol{\nu} = \boldsymbol{u} \tag{C.112}$$

or:

$$S_G\boldsymbol{u} = \boldsymbol{\nu} \tag{C.113}$$

where

$$S_T = \begin{bmatrix} S_1^{-1} & -P_0^{(2,1)} & 0 & 0 & \ldots & 0 & 0 \\ -P_0^{(1,2)} & S_2^{-1} & -P_0^{(3,2)} & 0 & \ldots & 0 & 0 \\ 0 & -P_0^{(2,3)} & S_3^{-1} & -P_0^{(4,3)} & \ldots & 0 & 0 \\ 0 & 0 & -P_0^{(3,4)} & S_4^{-1} & \ldots & 0 & 0 \\ \vdots & \vdots & \vdots & \vdots & \ddots & \vdots & \vdots \\ 0 & 0 & 0 & 0 & \ldots & S_{N-1}^{-1} & -P_0^{(N,N-1)} \\ 0 & 0 & 0 & 0 & \ldots & -P_0^{(N-1,N)} & S_N^{-1} \end{bmatrix} \tag{C.114}$$

and

$$S_G = \begin{bmatrix} S_1^{-1} & -P_0^{(2,1)} & 0 & 0 & \ldots & 0 & 0 \\ -P_0^{(1,2)} & S_2^{-1} & -P_0^{(3,2)} & 0 & \ldots & 0 & 0 \\ 0 & -P_0^{(2,3)} & S_3^{-1} & -P_0^{(4,3)} & \ldots & 0 & 0 \\ 0 & 0 & -P_0^{(3,4)} & S_4^{-1} & \ldots & 0 & 0 \\ \vdots & \vdots & \vdots & \vdots & \ddots & \vdots & \vdots \\ 0 & 0 & 0 & 0 & \ldots & S_{N-1}^{-1} & -P_0^{(N,N-1)} \\ 0 & 0 & 0 & 0 & \ldots & -P_0^{(N-1,N)} & S_N^{-1} \end{bmatrix}^{-1} \tag{C.115}$$

here S_G is called the Global scattering matrix, and

$$\boldsymbol{v} = \begin{bmatrix} \begin{bmatrix} \boldsymbol{a}_1' \\ \boldsymbol{b}_1 \end{bmatrix} \\ \vdots \\ \begin{bmatrix} \boldsymbol{a}_i' \\ \boldsymbol{b}_i \end{bmatrix} \\ \vdots \\ \begin{bmatrix} \boldsymbol{a}_N' \\ \boldsymbol{b}_N \end{bmatrix} \end{bmatrix}; \quad \boldsymbol{u} = \begin{bmatrix} \begin{bmatrix} \boldsymbol{a}_1 \\ \boldsymbol{0} \end{bmatrix} \\ 0 \\ \vdots \\ 0 \\ \begin{bmatrix} \boldsymbol{0} \\ \boldsymbol{b}_N' \end{bmatrix} \end{bmatrix} \tag{C.116}$$

Transmission and reflection coefficients from global scattering matrix

Assuming that after doing an inversion calculation of the right hand side of Eq.C.115, one may write the global scattering matrix S_G in the following form:

$$S_G = \begin{bmatrix} S_{G11} & S_{G12} & \dots & S_{G1N} \\ S_{G21} & S_{G22} & \dots & S_{G2N} \\ \vdots & \vdots & \ddots & \vdots \\ S_{GN1} & S_{GN2} & \dots & S_{GNN} \end{bmatrix} \tag{C.117}$$

then the element S_{Gij} of global scattering matrix S_G will describe a scattering process from initial state at j^{th} layer to the ending state at i^{th} layer. In particular, two scattering processes giving rise the transmission and reflection of an electron through the heterostructure are interesting to be considered. For the reflected process of an electron through the heterostructure, the electron starts at the first layer and then after a number of transmitted as well as reflected within the heterostructure, the electron is ending up with going back to the first layer. Therefore, this process can be described by the element S_{G11}, and if we write:

$$S_{G11} = \begin{bmatrix} S_{G11}^{11} & S_{G11}^{12} \\ S_{G11}^{21} & S_{G11}^{22} \end{bmatrix} \tag{C.118}$$

then S_{G11}^{21} is the matrix of reflection coefficient.

With the same argument, one has S_{GN1} describe the transmitted process from first layer to Nth layer or on the other hand, the transmitted process of an electron through whole heterostructure. So, if we write:

$$S_{GN1} = \begin{bmatrix} S_{GN1}^{11} & S_{GN1}^{12} \\ S_{GN1}^{21} & S_{GN1}^{22} \end{bmatrix} \tag{C.119}$$

then the element S_{GN1}^{11} will giving rise the matrix of transmission coefficient.

C.2.3 *Bound and quasi bound state in framework of global transfer and scattering matrices*

In order to consider bound state in quantum heterostructure, we use Eq. C.80 with global transfer matrix and C.112 with global scattering matrix, with the same treatment as in conventional scattering matrix formalism: the wavefunction decays in the both left and right sides of the structure. This leads to a fact that $\boldsymbol{a}_0 = \boldsymbol{b}_N = 0$ in the case of global transfer matrix and $\boldsymbol{a}_1 = \boldsymbol{b}_N' = 0$ in the case of global scattering matrix. The Eqs. C.80

and C.112 for bound state can be read:

$$K_G[v] = 0 \tag{C.120}$$

and

$$S_T v = 0 \tag{C.121}$$

respectively, leading to a condition for bound state as following:

$$det[K_G] = 0 \tag{C.122}$$

and

$$det[S_T] = 0 \tag{C.123}$$

Again, one may solve these equations numerically by varying the energy and find the local minimum of $det[K_G]$ and $det[S_T]$ then extract the corresponding bound energies and eigenvectors. The wavefunctions of bound state are then the linear combinations of the eigenvectors extracted above. Besides, for quasi-bound state considerations, one may use the same argument with the ideal of imaginary energy as presented in section 3.3.2.

C.2.4 An example of global scattering matrix with single barrier structure

Let us now consider a simple example of global scattering matrix with a single barrier structure with two interfaces. The global scattering matrix in this case is given by:

$$S_G = \begin{bmatrix} S_{G11} & S_{G12} \\ S_{G21} & S_{G22} \end{bmatrix} = \begin{bmatrix} S_1^{-1} & -P_0^{(2,1)} \\ -P_0^{(1,2)} & S_2^{-1} \end{bmatrix}^{-1} \tag{C.124}$$

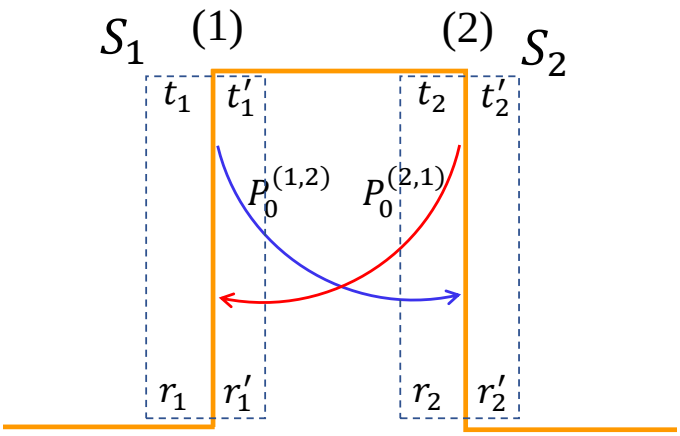

FIGURE C.4: Schematic of scattering process within a simple barrier structure.

Not that if

$$M = \begin{bmatrix} A & B \\ C & D \end{bmatrix} \tag{C.125}$$

and

$$M^{-1} \begin{pmatrix} \alpha & \beta \\ \gamma & \eta \end{pmatrix} \tag{C.126}$$

where $M * M^{-1} = \mathbb{I}$: identity matrix, then one has:

$$\alpha = \left[A - BD^{-1}C\right]^{-1} \tag{C.127}$$

$$\beta = \left[C - DB^{-1}A\right]^{-1} \tag{C.128}$$

$$\gamma = \left[B - AC^{-1}D\right]^{-1} \tag{C.129}$$

$$\eta = \left[D - CA^{-1}B\right]^{-1} \tag{C.130}$$

So, the matrix components of global matrix S_G are then:

$$S_{G11} = \left[S_1^{-1} - P_0^{(2,1)} S_2 P_0^{(1,2)}\right]^{-1} = \left[\mathbb{I} - S_1 P_0^{(2,1)} S_2 P_0^{(1,2)}\right]^{-1} S_1 \tag{C.131}$$

$$\begin{aligned} S_{G12} &= \left[-P_0^{(1,2)} + S_2^{-1}\left(P_0^{(2,1)}\right)^{-1} S_1^{-1}\right]^{-1} = \left\{\left[-P_0^{(1,2)} S_1 P_0^{(2,1)} S_2 + \mathbb{I}\right]\left[S_2^{-1}\left(P_0^{(2,1)}\right)^{-1} S_1^{-1}\right]\right\}^{-1} \\ &= S_1 P_0^{(2,1)} S_2 \left[\mathbb{I} - P_0^{(1,2)} S_1 P_0^{(2,1)} S_2\right]^{-1} \end{aligned} \tag{C.132}$$

$$\begin{aligned} S_{G21} &= \left[-P_0^{(2,1)} - S_1^{-1}\left(P_0^{(1,2)}\right)^{-1} S_2^{-1}\right]^{-1} = \left\{\left[-P_0^{(2,1)} S_2 P_0^{(1,2)} S_1 + \mathbb{I}\right]\left[S_1^{-1}\left(P_0^{(1,2)}\right)^{-1} S_2^{-1}\right]\right\}^{-1} \\ &= S_2 P_0^{(1,2)} S_1 \left[\mathbb{I} - P_0^{(2,1)} S_2 P_0^{(1,2)} S_1\right]^{-1} \end{aligned} \tag{C.133}$$

$$S_{G22} = \left[S_2^{-1} - P_0^{(1,2)} S_1 P_0^{(2,1)}\right]^{-1} = \left[\mathbb{I} - S_2 P_0^{(1,2)} S_1 P_0^{(2,1)}\right]^{-1} S_2 \tag{C.134}$$

Transmission and reflection coefficient from global scattering matrix

Now we are going to extract the transmission and reflection coefficient from global scattering matrix defined for single barrier structure above.

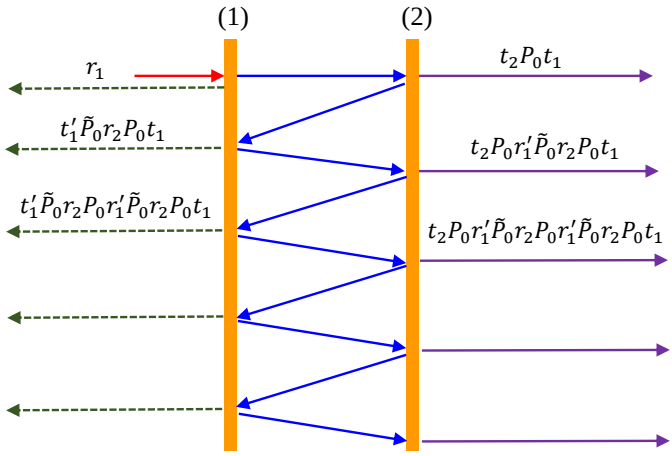

FIGURE C.5: Schematic of scattering process within a simple barrier structure.

Let us now consider the term S_{G11} and S_{G21}, using the Taylor's expansion, one has:

$$\begin{aligned} S_{G11} &= \left[\mathbb{I} - S_1 P_0^{(2,1)} S_2 P_0^{(1,2)}\right]^{-1} S_1 \\ &= \left[\mathbb{I} + S_1 P_0^{(2,1)} S_2 P_0^{(1,2)} + S_1 P_0^{(2,1)} S_2 P_0^{(1,2)} S_1 P_0^{(2,1)} S_2 P_0^{(1,2)} + \ldots\right] S_1 \\ &= S_1 + S_1 P_0^{(2,1)} S_2 P_0^{(1,2)} S_1 + S_1 P_0^{(2,1)} S_2 P_0^{(1,2)} S_1 P_0^{(2,1)} S_2 P_0^{(1,2)} S_1 + \ldots \end{aligned} \tag{C.135}$$

$$\begin{aligned} S_{G21} &= S_2 P_0^{(1,2)} S_1 \left[\mathbb{I} - P_0^{(2,1)} S_2 P_0^{(1,2)} S_1\right]^{-1} \\ &= S_2 P_0^{(1,2)} S_1 \left[\mathbb{I} + P_0^{(2,1)} S_2 P_0^{(1,2)} S_1 + P_0^{(2,1)} S_2 P_0^{(1,2)} S_1 P_0^{(2,1)} S_2 P_0^{(1,2)} S_1 + \ldots\right] \\ &= S_2 P_0^{(1,2)} S_1 + S_2 P_0^{(1,2)} S_1 P_0^{(2,1)} S_2 P_0^{(1,2)} S_1 + S_2 P_0^{(1,2)} S_1 P_0^{(2,1)} S_2 P_0^{(1,2)} S_1 P_0^{(2,1)} S_2 P_0^{(1,2)} S_1 + \ldots \end{aligned} \tag{C.136}$$

If we put:

$$\begin{aligned} S_{G11} &= \begin{bmatrix} S_{G11}^{11} & S_{G11}^{12} \\ S_{G11}^{21} & S_{G11}^{22} \end{bmatrix} \\ &= S_1 + S_1 P_0^{(2,1)} S_2 P_0^{(1,2)} S_1 + S_1 P_0^{(2,1)} S_2 P_0^{(1,2)} S_1 P_0^{(2,1)} S_2 P_0^{(1,2)} S_1 + \ldots \end{aligned} \tag{C.137}$$

$$\begin{aligned} S_{G21} &= \begin{bmatrix} S_{G21}^{11} & S_{G21}^{12} \\ S_{G21}^{21} & S_{G21}^{22} \end{bmatrix} \\ &= S_2 P_0^{(1,2)} S_1 + S_2 P_0^{(1,2)} S_1 P_0^{(2,1)} S_2 P_0^{(1,2)} S_1 + S_2 P_0^{(1,2)} S_1 P_0^{(2,1)} S_2 P_0^{(1,2)} S_1 P_0^{(2,1)} S_2 P_0^{(1,2)} S_1 + \ldots \end{aligned} \tag{C.138}$$

then we are going to prove that :

♣ S_{G21}^{11} is the transmission coefficient of an electron moving through this simple barrier structure.

♣ S_{G11}^{21} is the reflection coefficient of an electron moving through this simple barrier structure.

Note that:

$$S_1 = \begin{bmatrix} t_1 & r_1^{'} \\ r_1 & t_1^{'} \end{bmatrix};\ S_2 = \begin{bmatrix} t_2 & r_2^{'} \\ r_2 & t_2^{'} \end{bmatrix};\ P_0^{(1,2)} = \begin{bmatrix} P_0 & 0 \\ 0 & 0 \end{bmatrix};\ P_0^{(2,1)} = \begin{bmatrix} 0 & 0 \\ 0 & \tilde{P}_0 \end{bmatrix} \tag{C.139}$$

where $P_0 \equiv \tilde{P}_0$.

In order to show that S_{G21}^{11} is the transmission coefficient of an electron moving through this simple barrier structure, let us now consider, for example, the first term in Eq. C.142:

$$S_2 P_0^{(1,2)} S_1 = \begin{bmatrix} t_2 & r_2^{'} \\ r_2 & t_2^{'} \end{bmatrix} \begin{bmatrix} P_0 & 0 \\ 0 & 0 \end{bmatrix} \begin{bmatrix} t_1 & r_1^{'} \\ r_1 & t_1^{'} \end{bmatrix} = \begin{bmatrix} t_2 P_0 t_1 & t_2 P_0 r_1^{'} \\ r_2 P_0 t_1 & r_2 P_0 r_1^{'} \end{bmatrix} \tag{C.140}$$

and the second term in Eq. C.142:

$$
\begin{aligned}
S_2 P_0^{(1,2)} S_1 P_0^{(2,1)} S_2 P_0^{(1,2)} S_1 &= \left(S_2 P_0^{(1,2)} S_1\right) P_0^{(2,1)} \left(S_2 P_0^{(1,2)} S_1\right) \\
&= \begin{bmatrix} t_2 P_0 t_1 & t_2 P_0 r_1^{'} \\ r_2 P_0 t_1 & r_2 P_0 r_1^{'} \end{bmatrix} \begin{bmatrix} 0 & 0 \\ 0 & \tilde{P}_0 \end{bmatrix} \begin{bmatrix} t_2 P_0 t_1 & t_2 P_0 r_1^{'} \\ r_2 P_0 t_1 & r_2 P_0 r_1^{'} \end{bmatrix} \\
&= \begin{bmatrix} t_2 P_0 r_1^{'} \tilde{P}_0 r_2 P_0 t_1 & t_2 P_0 r_1^{'} \tilde{P}_0 r_2 P_0 r_1^{'} \\ r_2 P_0 r_1^{'} \tilde{P}_0 r_2 P_0 t_1 & r_2 P_0 r_1^{'} \tilde{P}_0 r_2 P_0 r_1^{'} \end{bmatrix}
\end{aligned}
\tag{C.141}
$$

doing the same for the other terms in Eq. C.142 then one may get a result that:

$$
S_{G21}^{11} = t_2 P_0 t_1 + t_2 P_0 r_1^{'} \tilde{P}_0 r_2 P_0 t_1 + t_2 P_0 r_1^{'} \tilde{P}_0 r_2 P_0 r_1^{'} \tilde{P}_0 r_2 P_0 t_1 + \ldots \tag{C.142}
$$

Considering, for example, the second term in Eq. C.137:

$$
S_1 P_0^{(2,1)} S_2 P_0^{(1,2)} S_1 = \begin{bmatrix} t_1 & r_1^{'} \\ r_1 & t_1^{'} \end{bmatrix} \begin{bmatrix} 0 & 0 \\ 0 & \tilde{P}_0 \end{bmatrix} \begin{bmatrix} t_2 & r_2^{'} \\ r_2 & t_2^{'} \end{bmatrix} \begin{bmatrix} P_0 & 0 \\ 0 & 0 \end{bmatrix} \begin{bmatrix} t_1 & r_1^{'} \\ r_1 & t_1^{'} \end{bmatrix} = \begin{bmatrix} r_1^{'} \tilde{P}_0 r_2 P_0 t_1 & r_1^{'} \tilde{P}_0 r_2 P_0 r_1^{'} \\ t_1^{'} \tilde{P}_0 r_2 P_0 t_1 & t_1^{'} \tilde{P}_0 r_2 P_0 r_1^{'} \end{bmatrix} \tag{C.143}
$$

doing the same treatment for the other terms in Eq. C.137, finally, it is possible to obtain:

$$
S_{G11}^{21} = r_1 + t_1^{'} \tilde{P}_0 r_2 P_0 t_1 + t_1^{'} \tilde{P}_0 r_2 P_0 r_1^{'} \tilde{P}_0 r_2 P_0 t_1 + \ldots \tag{C.144}
$$

The equations C.142 and C.144 give exactly the expressions of transmission and reflection coefficients for considering case as describe in the Fig C.5 for schematic of scattering process within a simple barrier structure. So that, in conclusion, beside the conventional scattering and transfer matrices, one may use the global scattering or global transfer matrix in order to describe the tunneling problem through heterostructure. Note that, the size of global scattering or global transfer matrix are larger than the conventional ones, but however with one step of calculation, one may obtain all characterized information of an electron tunneling through the heterostructure.

APPENDIX D

Calculations of the oscillator strength and optical anisotropy for heavy and light holes [250]

This section is devoted to the mathematical demonstration of the general relationship linking the anisotropic part of the optical response (absorption, gain) involving the respective HH and LH VB states near the Γ point.

Considering the wave function in CB and VB and taking in to account the mixing between heavy holes and light holes in valence band, then we have [250]:

$$\left|\pm\frac{3}{2}\right\rangle = C(z)\left|\pm\frac{3}{2}\right\rangle^{(0)} \pm i\alpha S(z)\left|\mp\frac{1}{2}\right\rangle^{(0)} \tag{D.1}$$

$$\left|\pm\frac{1}{2}\right\rangle = C(z)\left|\pm\frac{1}{2}\right\rangle^{(0)} \mp i\alpha S(z)\left|\mp\frac{3}{2}\right\rangle^{(0)} \tag{D.2}$$

$$|s\rangle = |\pm 0\rangle \tag{D.3}$$

where α is the heavy-light hole mixing component, $C(z)$ is mostly cosinus (even function) and $S(z)$ is mostly sinus (odd function) [250].

$$\left|\frac{3}{2}\right\rangle = C(z)\left|\frac{\mathcal{X}+i\mathcal{Y}}{\sqrt{2}}\uparrow\right\rangle^{(0)} + i\alpha S(z)\left[\left|\frac{\mathcal{X}-i\mathcal{Y}}{\sqrt{6}}\uparrow\right\rangle^{(0)} + \sqrt{\frac{2}{3}}|\mathcal{Z}\downarrow\rangle^{(0)}\right] \tag{D.4}$$

$$\left|-\frac{3}{2}\right\rangle = C(z)\left|\frac{\mathcal{X}-i\mathcal{Y}}{\sqrt{2}}\downarrow\right\rangle^{(0)} - i\alpha S(z)\left[\left|\frac{\mathcal{X}+i\mathcal{Y}}{\sqrt{6}}\downarrow\right\rangle^{(0)} + \sqrt{\frac{2}{3}}|\mathcal{Z}\uparrow\rangle^{(0)}\right] \tag{D.5}$$

$$\left|\frac{1}{2}\right\rangle = C(z)\left[\left|\frac{\mathcal{X}+i\mathcal{Y}}{\sqrt{6}}\downarrow\right\rangle^{(0)} + \sqrt{\frac{2}{3}}|\mathcal{Z}\uparrow\rangle^{(0)}\right] - i\alpha S(z)\left|\frac{\mathcal{X}-i\mathcal{Y}}{\sqrt{2}}\downarrow\right\rangle^{(0)} \tag{D.6}$$

$$\left|-\frac{1}{2}\right\rangle = C(z)\left[\left|\frac{\mathcal{X}-i\mathcal{Y}}{\sqrt{6}}\uparrow\right\rangle^{(0)} + \sqrt{\frac{2}{3}}|\mathcal{Z}\downarrow\rangle^{(0)}\right] + i\alpha S(z)\left|\frac{\mathcal{X}+i\mathcal{Y}}{\sqrt{2}}\uparrow\right\rangle^{(0)} \tag{D.7}$$

Then the optical transition term between the $HH\uparrow$ and e_1 is proportional to:

$$\left\langle s\left|\hat{r}\right|\pm\frac{3}{2}\right\rangle = \left\langle s\left|\hat{r}\left\{C(z)\left|\pm\frac{3}{2}\right\rangle^{(0)} \pm i\alpha S(z)\right|\mp\frac{1}{2}\right\rangle^{(0)}\right\} \tag{D.8}$$

The transition along [110] direction is:

$$\left|\left\langle s\left|\left(\frac{x+y}{\sqrt{2}}\right)\right|\frac{3}{2}\right\rangle\right|^2_{[110]} = \frac{1}{2}\left|\left(\frac{C(z)}{\sqrt{2}}+\frac{\alpha S(z)}{\sqrt{6}}\right)+i\left(\frac{C(z)}{\sqrt{2}}+\frac{\alpha S(z)}{\sqrt{6}}\right)\right|^2+\frac{1}{3}\left|\alpha S(z)\right|^2 \tag{D.9}$$

or we have:

$$OT_{[110]} = \left|\left\langle s\left|\left(\frac{x+y}{\sqrt{2}}\right)\right|\frac{3}{2}\right\rangle\right|^2_{[110]} = \frac{1}{2}|C(z)|^2+\frac{1}{2}|\alpha S(z)|^2+\frac{1}{12}|\Re(\alpha)C(z)S(z)| \tag{D.10}$$

In the same way for transitions along $1\bar{1}0$ direction, we have:

$$\left|\left\langle s\left|\left(\frac{x-y}{\sqrt{2}}\right)\right|\frac{3}{2}\right\rangle\right|^2_{[1\bar{1}0]} = \frac{1}{2}\left|\left(\frac{C(z)}{\sqrt{2}}-\frac{\alpha S(z)}{\sqrt{6}}\right)-i\left(\frac{C(z)}{\sqrt{2}}-\frac{\alpha S(z)}{\sqrt{6}}\right)\right|^2+\frac{1}{3}\left|\alpha S(z)\right|^2 \tag{D.11}$$

and

$$OT_{[1\bar{1}0]} = \left|\left\langle s\left|\left(\frac{x-y}{\sqrt{2}}\right)\right|\frac{3}{2}\right\rangle\right|^2_{[1\bar{1}0]} = \frac{1}{2}|C(z)|^2+\frac{1}{2}|\alpha S(z)|^2-\frac{1}{12}|\Re(\alpha)C(z)S(z)| \tag{D.12}$$

Optical transitions: $HH\downarrow$ along [110] direction corresponds to:

$$\left|\left\langle s\left|\left(\frac{x+y}{\sqrt{2}}\right)\right|-\frac{3}{2}\right\rangle\right|^2_{[110]} = \frac{1}{2}\left|\left(\frac{C(z)}{\sqrt{2}}+\frac{\alpha S(z)}{\sqrt{6}}\right)-i\left(\frac{C(z)}{\sqrt{2}}+\frac{\alpha S(z)}{\sqrt{6}}\right)\right|^2+\frac{1}{3}\left|\alpha S(z)\right|^2 \tag{D.13}$$

or we have:

$$OT_{[110]} = \left|\left\langle s\left|\left(\frac{x+y}{\sqrt{2}}\right)\right|-\frac{3}{2}\right\rangle\right|^2_{[110]} = \frac{1}{2}|C(z)|^2+\frac{1}{2}|\alpha S(z)|^2+\frac{1}{12}|\Re(\alpha)C(z)S(z)| \tag{D.14}$$

Similarly for transitions along $1\bar{1}0$ direction, we have:

$$\left|\left\langle s\left|\left(\frac{x-y}{\sqrt{2}}\right)\right|-\frac{3}{2}\right\rangle\right|^2_{[1\bar{1}0]} = \frac{1}{2}\left|\left(\frac{C(z)}{\sqrt{2}}-\frac{\alpha S(z)}{\sqrt{6}}\right)-i\left(\frac{C(z)}{\sqrt{2}}+\frac{\alpha S(z)}{\sqrt{6}}\right)\right|^2+\frac{1}{3}\left|\alpha S(z)\right|^2 \tag{D.15}$$

and

$$OT_{[1\bar{1}0]} = \left|\left\langle s\left|\left(\frac{x-y}{\sqrt{2}}\right)\right|-\frac{3}{2}\right\rangle\right|^2_{[1\bar{1}0]} = \frac{1}{2}|C(z)|^2+\frac{1}{2}|\alpha S(z)|^2-\frac{1}{12}|\Re(\alpha)C(z)S(z)| \tag{D.16}$$

Optical transitions : $LH\uparrow$

$$\left|\left\langle s\left|\left(\frac{x+y}{\sqrt{2}}\right)\right|\frac{1}{2}\right\rangle\right|^2_{[110]}=\frac{1}{2}\left|\left(\frac{C(z)}{\sqrt{6}}-\frac{\alpha S(z)}{\sqrt{2}}\right)+i\left(\frac{C(z)}{\sqrt{6}}-\frac{\alpha S(z)}{\sqrt{2}}\right)\right|^2+\frac{1}{2}|\alpha S(z)|^2 \tag{D.17}$$

$$OT_{[110]}=\left|\left\langle s\left|\left(\frac{x+y}{\sqrt{2}}\right)\right|\frac{1}{2}\right\rangle\right|^2_{[110]}=\frac{1}{6}|C(z)|^2+|\alpha S(z)|^2-\frac{1}{12}|\Re(\alpha)C(z)S(z)| \tag{D.18}$$

$$\left|\left\langle s\left|\left(\frac{x-y}{\sqrt{2}}\right)\right|\frac{1}{2}\right\rangle\right|^2_{[110]}=\frac{1}{2}\left|\left(\frac{C(z)}{\sqrt{6}}+\frac{\alpha S(z)}{\sqrt{2}}\right)+i\left(\frac{C(z)}{\sqrt{6}}+\frac{\alpha S(z)}{\sqrt{2}}\right)\right|^2+\frac{1}{2}|\alpha S(z)|^2 \tag{D.19}$$

$$OT_{[1\bar{1}0]}=\left|\left\langle s\left|\left(\frac{x-y}{\sqrt{2}}\right)\right|\frac{1}{2}\right\rangle\right|^2_{[1\bar{1}0]}=\frac{1}{6}|C(z)|^2+|\alpha S(z)|^2-\frac{1}{12}|\Re(\alpha)C(z)S(z)| \tag{D.20}$$

Optical transitions : $LH\downarrow$

$$\left|\left\langle s\left|\left(\frac{x+y}{\sqrt{2}}\right)\right|-\frac{1}{2}\right\rangle\right|^2_{[110]}=\frac{1}{2}\left|\left(\frac{C(z)}{\sqrt{6}}-\frac{\alpha S(z)}{\sqrt{2}}\right)-i\left(\frac{C(z)}{\sqrt{6}}-\frac{\alpha S(z)}{\sqrt{2}}\right)\right|^2+\frac{1}{2}|\alpha S(z)|^2 \tag{D.21}$$

$$OT_{[110]}=\left|\left\langle s\left|\left(\frac{x+y}{\sqrt{2}}\right)\right|-\frac{1}{2}\right\rangle\right|^2_{[110]}=\frac{1}{6}|C(z)|^2+|\alpha S(z)|^2-\frac{1}{12}|\Re(\alpha)C(z)S(z)| \tag{D.22}$$

$$\left|\left\langle s\left|\left(\frac{x-y}{\sqrt{2}}\right)\right|-\frac{1}{2}\right\rangle\right|^2_{[1\bar{1}0]}=\frac{1}{2}\left|\left(\frac{C(z)}{\sqrt{6}}+\frac{\alpha S(z)}{\sqrt{2}}\right)+i\left(\frac{C(z)}{\sqrt{6}}+\frac{\alpha S(z)}{\sqrt{2}}\right)\right|^2+\frac{1}{2}|\alpha S(z)|^2 \tag{D.23}$$

$$OT_{[1\bar{1}0]}=\left|\left\langle s\left|\left(\frac{x-y}{\sqrt{2}}\right)\right|\frac{1}{2}\right\rangle\right|^2_{[1\bar{1}0]}=\frac{1}{2}|C(z)|^2+\frac{1}{2}|\alpha S(z)|^2-\frac{1}{12}|\Re(\alpha)C(z)S(z)| \tag{D.24}$$

Optical transition : $HH\uparrow + HH\downarrow$

$$OT_{[110]}=|C(z)|^2+|\alpha S(z)|^2+\frac{1}{\sqrt{3}}|\Re(\alpha)C(z)S(z)| \tag{D.25}$$

$$OT_{[1\bar{1}0]}=|C(z)|^2+|\alpha S(z)|^2-\frac{1}{\sqrt{3}}|\Re(\alpha)C(z)S(z)| \tag{D.26}$$

Then the optical transition anisotopy is:

$$AOT_{HH}=\frac{OT_{[110]}-OT_{[1\bar{1}0]}}{OT_{[110]}+OT_{[1\bar{1}0]}}=\frac{1}{\sqrt{3}}\frac{|\Re(\alpha)C(z)S(z)|}{|C(z)|^2+|\alpha S(z)|^2} \tag{D.27}$$

The optical transitions for light holes ($LH\uparrow + LH\downarrow$) are

$$OT_{[110]} = \frac{1}{3}|C(z)|^2 + 2|\alpha S(z)|^2 - \frac{1}{\sqrt{3}}|\Re(\alpha)C(z)S(z)| \tag{D.28}$$

$$OT_{[1\bar{1}0]} = \frac{1}{3}|C(z)|^2 + 2|\alpha S(z)|^2 + \frac{1}{\sqrt{3}}|\Re(\alpha)C(z)S(z)| \tag{D.29}$$

Then one deduces the optical transition anisotropy according to the following formula:

$$AOT_{LH} = \frac{OT_{[110]} - OT_{[1\bar{1}0]}}{OT_{[110]} + OT_{[1\bar{1}0]}} = \sqrt{3}\frac{|\Re(\alpha)C(z)S(z)|}{|C(z)|^2 + |\alpha S(z)|^2} = -3AOT_{HH} \tag{D.30}$$

showing that the anisotropy of CB1-LH1 is three time larger than CB1-HH1.

Bibliography

[1] M. N. Baibich et al. “Giant Magnetoresistance of (001)Fe/(001)Cr Magnetic Superlattices”. In: *Physical review letters* 61 (1988), pp. 2472–2475. DOI: /10.1103/PhysRevLett.61.2472 (cit. on p. 1).

[2] G. Binasch et al. “Enhanced magnetoresistance in layered magnetic structures with antiferromagnetic interlayer exchange”. In: *Phys. Rev. B* 39 (1989), pp. 4828–4830. DOI: 10.1103/PhysRevB.39.4828. URL: https://link.aps.org/doi/10.1103/PhysRevB.39.4828 (cit. on p. 1).

[3] R. Jansen et al. “Silicon spintronics with ferromagnetic tunnel devices”. In: *Semiconductor Science and Technology* 27 (2012). DOI: /10.1088/0268-1242/27/8/083001 (cit. on p. 1).

[4] T. Jungwirth et al. “Spin-dependent phenomena and device concepts explored in (Ga,Mn)As”. In: *Rev. Mod. Phys.* 86 (3 2014), pp. 855–896. DOI: 10.1103/RevModPhys.86.855. URL: https://link.aps.org/doi/10.1103/RevModPhys.86.855 (cit. on pp. 2, 176, 181).

[5] M. Jiang et al. “Efficient full spin–orbit torque switching in a single layer of a perpendicularly magnetized single-crystalline ferromagnet”. In: *Nature communications* 10.1 (2019), p. 2590 (cit. on pp. 2, 163, 164, 175).

[6] D. Chiba et al. “Current-Driven Magnetization Reversal in a Ferromagnetic Semiconductor (Ga, Mn)As/GaAs/(Ga, Mn)As Tunnel Junction”. In: *Phys. Rev. Lett.* 93 (21 2004), p. 216602. DOI: 10.1103/PhysRevLett.93.216602. URL: https://link.aps.org/doi/10.1103/PhysRevLett.93.216602 (cit. on pp. 2, 163, 176).

[7] M . Elsen et al. “Spin transfer experiments on (Ga, Mn) As/(In, Ga) As/(Ga, Mn) As tunnel junctions”. In: *Physical Review B* 73.3 (2006), p. 035303 (cit. on pp. 2, 22, 163, 176–178).

[8] A. Chernyshov et al. “Evidence for reversible control of magnetization in a ferromagnetic material by means of spin–orbit magnetic field”. In: *Nature Physics* 5.9 (2009), p. 656 (cit. on pp. 2, 163, 176).

[9] L. Thevenard et al. “Spin transfer and spin-orbit torques in in-plane magnetized (Ga,Mn)As tracks”. In: *Phys. Rev. B* 95 (5 2017), p. 054422. DOI: 10.1103/PhysRevB.95.054422. URL: https://link.aps.org/doi/10.1103/PhysRevB.95.054422 (cit. on pp. 2, 164).

[10] A. Manchon et al. “New perspectives for Rashba spin–orbit coupling”. In: *Nature materials* 14 (2015). DOI: /10.1038/nmat4360 (cit. on p. 2).

[11] A. Matos-Abiague and J. Fabian. “Tunneling Anomalous and Spin Hall Effects”. In: *Physical Review Letters* 115 (2015). DOI: /10.1103/PhysRevLett.115.056602 (cit. on pp. 2, 17, 28, 72, 164, 185, 187).

[12] T. H. Dang et al. “Giant forward-scattering asymmetry and anomalous tunnel Hall effect at spin-orbit-split and exchange-split interfaces”. In: *Physical Review B, Rapid communication* 92 (2015). DOI: /10.1103/PhysRevB.92.060403 (cit. on pp. 2, 17, 28, 72, 164, 185, 188, 190, 201).

[13] I. Zutic and P. E Faria. “Semiconductor lasers: Taken for a spin”. In: *Nature Nanotechnology* 9 (2014), pp. 750–752 (cit. on pp. 3, 4, 207).

[14] P. E. Faria Junior et al. “Toward high-frequency operation of spin lasers”. In: *Phys. Rev. B* 92 (7 2015), p. 075311. DOI: 10.1103/PhysRevB.92.075311. URL: https://link.aps.org/doi/10.1103/PhysRevB.92.075311 (cit. on pp. 4, 207, 209, 227, 235).

[15] C. H. Li et al. “Electrical spin injection into the In As/ Ga As wetting layer”. In: *Applied Physics Letters* 91.26 (2007), p. 262504 (cit. on p. 4).

[16] A. Fert and H. Jaffrès. “Conditions for efficient spin injection from a ferromagnetic metal into a semiconductor”. In: *Phys. Rev. B* 64 (18 2001), p. 184420. DOI: 10.1103/PhysRevB.64.184420. URL: https://link.aps.org/doi/10.1103/PhysRevB.64.184420 (cit. on p. 4).

[17] S. A. Crooker et al. “Optical spin resonance and transverse spin relaxation in magnetic semiconductor quantum wells”. In: *Phys. Rev. B* 56 (12 1997), pp. 7574–7588. DOI: 10.1103/PhysRevB.56.7574. URL: https://link.aps.org/doi/10.1103/PhysRevB.56.7574 (cit. on pp. 4, 211).

[18] R. Fiederling et al. “Injection and detection of a spin-polarized current in a light-emitting diode”. In: *Nature* 402.6763 (1999), p. 787 (cit. on p. 4).

[19] B. T. Jonker et al. “Electrical spin-injection into silicon from a ferromagnetic metal/tunnel barrier contact”. In: *Nature Physics* 3.8 (2007), p. 542 (cit. on p. 4).

[20] L. Lombez et al. “Electrical spin injection into p-doped quantum dots through a tunnel barrier”. In: *Applied physics letters* 90.8 (2007), p. 081111 (cit. on p. 4).

[21] J. Zarpellon et al. “Spin injection at remanence into III-V spin light-emitting diodes using (Co/Pt) ferromagnetic injectors”. In: *Phys. Rev. B* 86 (20 2012), p. 205314. DOI: 10.1103/PhysRevB.86.205314. URL: https://link.aps.org/doi/10.1103/PhysRevB.86.205314 (cit. on p. 4).

[22] S. H. Liang et al. “Large and robust electrical spin injection into GaAs at zero magnetic field using an ultrathin CoFeB/MgO injector”. In: *Phys. Rev. B* 90 (8 2014), p. 085310. DOI: 10.1103/PhysRevB.90.085310. URL: https://link.aps.org/doi/10.1103/PhysRevB.90.085310 (cit. on p. 4).

[23] H. Dery et al. “Silicon spin communication”. In: *Applied Physics Letters* 99.8 (2011), p. 082502 (cit. on pp. 4, 207).

[24] H. Ando, T. Sogawa, and H. Gotoh. “Photon-spin controlled lasing oscillation in surface-emitting lasers”. In: 73.5 (1998), pp. 566–568. DOI: 10.1063/1.121857. URL: http://link.aip.org/link/?APL/73/566/1 (cit. on pp. 4, 207).

[25] M. Holub et al. “Electrical Spin Injection and Threshold Reduction in a Semiconductor Laser”. In: *Phys. Rev. Lett.* 98 (14 2007), p. 146603. DOI: 10.1103/PhysRevLett.98.146603. URL: http://link.aps.org/doi/10.1103/PhysRevLett.98.146603 (cit. on pp. 4, 207).

[26] C. Gothgen et al. “Analytical model of spin-polarized semiconductor lasers”. In: *Applied Physics Letters* 93.4 (2008), p. 042513. DOI: 10.1063/1.2967739. URL: http://aip.scitation.org/doi/abs/10.1063/1.2967739 (cit. on pp. 4, 207, 211).

[27] D. Basu, D. Saha, and P. Bhattacharya. "Optical Polarization Modulation and Gain Anisotropy in an Electrically Injected Spin Laser". In: *Phys. Rev. Lett.* 102 (9 2009), p. 093904. DOI: 10.1103/PhysRevLett.102.093904. URL: http://link.aps.org/doi/10.1103/PhysRevLett.102.093904 (cit. on pp. 4, 207).

[28] T. Fordos. *Coherent light sources with spin-polarized current*. PhD Thesis. Ecole Polytechique, Universite Paris-Saclay France, 2018 (cit. on pp. 4, 218, 221–223).

[29] G. Fishman. *Semi-conducteurs : les bases de la théorie k.p*. Les Éditions de l'École Polytechnique, 2010. ISBN: 9782730214971 (cit. on pp. 5, 17, 22, 44, 51, 52, 70, 75, 78, 79, 82, 84, 241, 249).

[30] E. L. Ivchenko, A. Yu. Kaminski, and U. Rössler. "Heavy-light hole mixing at zinc-blende (001) interfaces under normal incidence". In: *Physical review B* 54 (1996). DOI: /10.1103/PhysRevB.54.5852 (cit. on pp. 6, 51, 89, 94, 119–124, 131, 132, 135, 213, 230, 232).

[31] M. V. Durnev, M. M. Glazov, and E. L. Ivchenko. "Spin-orbit splitting of valence subbands in semiconductor nanostructures". In: *Physical review B* 89 (Feb. 2014). DOI: /10.1103/PhysRevB.89.075430 (cit. on pp. 6, 17, 51, 71, 89, 94, 98, 122–124, 127, 130–133, 135, 213, 232, 279).

[32] T. Jungwirth et al. "Theory of ferromagnetic (III,Mn)V semiconductors". In: *Reviews of Modern Physics* 78 (2006). DOI: /10.1103/RevModPhys.78.809 (cit. on pp. 9, 18, 19).

[33] M. Tanaka, S. Ohya, and N. H. Pham. "Recent progress in III-V based ferromagnetic semiconductors: Band structure, Fermi level, and tunneling transport". In: *Applied Physics Reviews* 1.1 (2014), p. 011102 (cit. on p. 9).

[34] T. Dietl and H. Ohno. "Dilute ferromagnetic semiconductors: Physics and spintronic structures". In: *Rev. Mod. Phys.* 86 (1 2014), pp. 187–251. DOI: 10.1103/RevModPhys.86.187. URL: https://link.aps.org/doi/10.1103/RevModPhys.86.187 (cit. on p. 9).

[35] T. Jungwirth et al. "Spin-dependent phenomena and device concepts explored in (Ga,Mn)As". In: *Rev. Mod. Phys.* 86 (3 2014), pp. 855–896. DOI: 10.1103/RevModPhys.86.855. URL: https://link.aps.org/doi/10.1103/RevModPhys.86.855 (cit. on p. 9).

[36] D. A. Le, N. H. Pham, and M. Tanaka. "Observation of spontaneous spin-splitting in the band structure of an n-type zinc-blende ferromagnetic semiconductor". In: *Nature communications* 7 (2016), p. 13810 (cit. on p. 9).

[37] I. Žutić, J. Fabian, and S. Das Sarma. "Spintronics: Fundamentals and applications". In: *Review of Modern Physics* 76 (2004). DOI: /10.1103/RevModPhys.76.323 (cit. on pp. 9, 18, 22, 24, 25, 33–36, 94).

[38] S. Souma et al. "Fermi level position, Coulomb gap, and Dresselhaus splitting in (Ga, Mn) As". In: *Scientific reports* 6 (2016), p. 27266 (cit. on p. 9).

[39] S. Ohya et al. "Valence-band structure of ferromagnetic semiconductor (In,Ga,Mn)As". In: *Phys. Rev. B* 86 (9 2012), p. 094418. DOI: 10.1103/PhysRevB.86.094418. URL: https://link.aps.org/doi/10.1103/PhysRevB.86.094418 (cit. on p. 9).

[40] T. Ishii et al. "Electronic structure near the Fermi level in the ferromagnetic semiconductor GaMnAs studied by ultrafast time-resolved light-induced reflectivity measurements". In: *Phys. Rev. B* 93 (24 2016), p. 241303. DOI: 10.1103/PhysRevB.93.241303. URL: https://link.aps.org/doi/10.1103/PhysRevB.93.241303 (cit. on p. 9).

[41] M. Tanaka and Y. Higo. "Large Tunneling Magnetoresistance in GaMnAs /AlAs /GaMnAs Ferromagnetic Semiconductor Tunnel Junctions". In: *Phys. Rev. Lett.* 87 (2 2001), p. 026602. DOI: 10.1103/PhysRevLett.87.026602. URL: https://link.aps.org/doi/10.1103/PhysRevLett.87.026602 (cit. on p. 9).

[42] S. Datta and B. Das. "Electronic analog of the electro-optic modulator". In: *Applied Physiscs Letters* 56 (1990). DOI: /10.1063/1.102730 (cit. on p. 9).

[43] J. J. Sakurai and J. Napolitano. *Modern Quantum Mechanics*. Cambridge University Press, 2017. ISBN: 9781108499996. DOI: /10.1017/9781108499996 (cit. on pp. 10, 13, 14, 18, 30, 49, 106, 117, 118).

[44] R. Winkler. *Spin-orbit Coupling Effects in Two-Dimensional Electron and Hole Systems*. Springer Tracts in Modern Physics. Springer, 2003. ISBN: 978-3-540-01187-3. DOI: 10.1007/b13586 (cit. on pp. 10, 13, 15, 24, 26, 70, 89, 121, 283).

[45] Internet. "What is the magnetic moment, and what does it have to do with the spin of the electron". In: (). URL: https://physics.stackexchange.com/questions/285098/what-is-the-magnetic-moment-and-what-does-it-have-to-do-with-the-spin-of-the-el (cit. on p. 11).

[46] T. Ihn. *Semiconductor Nanostructures: Quantum states and electronic transport*. Oxford Scholarship, 2009. ISBN: 9780199534425. DOI: 10.1093/acprof:oso/9780199534425.001.0001 (cit. on pp. 11, 39, 43, 85).

[47] H. Kroemer. "The Thomas precession factor in spin-orbit interaction". In: *American Journal of Physics* 72 (2003). DOI: /10.1119/1.1615526 (cit. on pp. 12, 13).

[48] M. D Schwartz. *Quantum field theory and the standard model*. Cambridge University Press, 2014 (cit. on p. 13).

[49] Leslie L. Foldy and Siegfried A. Wouthuysen. "On the Dirac Theory of Spin 1/2 Particles and Its Non-Relativistic Limit". In: *Phys. Rev.* 78 (1 1950), pp. 29–36. DOI: 10.1103/PhysRev.78.29. URL: https://link.aps.org/doi/10.1103/PhysRev.78.29 (cit. on p. 15).

[50] Kasap et al. *Springer Handbook of Electronic and Photonic Materials, 2nd edition*. Springer Handbooks. Springer, 2017. ISBN: 978-3-319-48931-5. DOI: 10.1007/978-3-319-48933-9 (cit. on pp. 16, 261).

[51] A. G. Baca and C. I.H. Ashby. *Fabrication of GaAs devices*. 6. IET, 2005 (cit. on pp. 16, 17).

[52] G. Dresselhaus. "Spin-Orbit Coupling Effects in Zinc Blende Structures". In: *Physical review journal achive* 100 (1955). DOI: /10.1103/PhysRev.100.580 (cit. on pp. 17, 186).

[53] P. Y. Yu and M. Cardona. *Fundamentals of Semiconductors: Physics and Materials Properties*. Graduate Texts in Physics. Springer, 2010. ISBN: 9783642007095. DOI: 10.1007/978-3-642-00710-1 (cit. on pp. 17, 39, 49, 51, 62, 75, 76, 78, 79).

[54] V. I. Perel' et al. "Spin-dependent tunneling through a symmetric semiconductor barrier". In: *Physical Review B, Rapid Communication* 67 (2003). DOI: /10.1103/PhysRevB.67.201304 (cit. on pp. 17, 24, 72, 73, 75, 152).

[55] T. L. H. Nguyen et al. "Spin-orbit engineering of semiconductor heterostructures: A spin-sensitive quantum-phase shifter". In: *Applied Physics Letters* 95 (2009). DOI: /10.1063/1.3211118 (cit. on pp. 17, 64, 65, 152).

[56] P. S. Alekseev, M. M. Glazov, and S. A. Tarasenko. “Spin injection via (110)-grown semiconductor barriers”. In: *Physical review B* 89 (2014). DOI: /10.1103/PhysRevB.89.155306 (cit. on pp. 17, 72, 98, 152, 153, 156, 159, 190).

[57] T. H. Dang et al. “Theory of the anomalous tunnel hall effect at ferromagnet-semiconductor junctions”. In: *Journal of Magnetism and Magnetic Materials* 459 (2018). DOI: /10.1016/j.jmmm.2017.12.065 (cit. on pp. 17, 28, 72, 185, 188, 190, 191, 201).

[58] S. Tiwari and D. J. Frank. “Empirical fit to band discontinuities and barrier heights in III–V alloy systems”. In: *Applied Physics Letters* 60 (1992). DOI: /10.1063/1.106575 (cit. on p. 17).

[59] V. I. Zubkov et al. “Determination of band offsets in strained InGaAs/GaAs quantum wells by capacitance-voltage profiling and Schrödinger-Poisson self-consistent simulation”. In: *Physical Review B* 70 (2004). DOI: /10.1103/PhysRevB.70.075312 (cit. on p. 17).

[60] I. Vurgaftman, J. R. Meyer, and L. R. Ram-Mohan. “Band parameters for III-V compound semiconductors and their alloys”. In: *Applied Physics Review* 89 (2001). DOI: /10.1063/1.1368156 (cit. on pp. 17, 18, 24).

[61] H. Ohno et al. “Magnetotransport properties of p-type (In,Mn)As diluted magnetic III-V semiconductors”. In: *Physical Review Letters* 68 (1992). DOI: /10.1103/PhysRevLett.68.2664 (cit. on pp. 18, 19).

[62] H. Ohno et al. “(Ga,Mn)As: A new diluted magnetic semiconductor based on GaAs”. In: *Applied Physics Letters* 69 (1996). DOI: /10.1063/1.118061 (cit. on pp. 18, 19).

[63] A. Haury et al. “Observation of a Ferromagnetic Transition Induced by Two-Dimensional Hole Gas in Modulation-Doped CdMnTe Quantum Wells”. In: *Physical Review Letters* 79 (1997). DOI: /10.1103/PhysRevLett.79.511 (cit. on p. 18).

[64] D. Ferrand et al. “Indication of ferromagnetic ordering in P-Zn1-xMnxTe”. In: *Physica B: Condensed Matter* 284-288 (2000). DOI: /10.1016/S0921-4526(99)02603-4 (cit. on p. 18).

[65] J. K. Furdyna. “Diluted magnetic semiconductors”. In: *Journal of Applied Physics* 64 (1988). DOI: /10.1063/1.341700 (cit. on p. 18).

[66] Tohoku University. “Spintronics development gets boost with new findings into ferromagnetism in Mn-doped GaAs”. In: (2016). URL: https://phys.org/news/2016-06-spintronics-boost-ferromagnetism-mn-doped-gaas.html (cit. on p. 18).

[67] H. Ohno. “Making nonmagnetic semiconductors ferromagnetic”. In: *science* 281.5379 (1998), pp. 951–956 (cit. on pp. 18, 30).

[68] S. Bandyopadhyay and M. Cahay. *Introduction to Spintronics*. CRC Press, 2015. ISBN: 9781482255560 (cit. on pp. 19, 29).

[69] N. O. Lipari and A. Baldereschi. “Angular Momentum Theory and Localized States in Solids. Investigation of Shallow Acceptor States in Semiconductors”. In: *Phys. Rev. Lett.* 25 (1970), pp. 1660–1664. DOI: doi.org/10.1103/PhysRevLett.25.1660. URL: https://journals.aps.org/prl/abstract/10.1103/PhysRevLett.25.1660 (cit. on p. 19).

[70] A. Baldereschi and Nunzio O. Lipari. “Spherical Model of Shallow Acceptor States in Semiconductors”. In: *Phys. Rev. B* 8 (6 1973), pp. 2697–2709. DOI: 10.1103/PhysRevB.8.2697. URL: https://link.aps.org/doi/10.1103/PhysRevB.8.2697 (cit. on p. 19).

[71] A. Baldereschi and N. O. Lipari. "Cubic contributions to the spherical model of shallow acceptor states". In: *Phys. Rev. B* 9 (1973), pp. 1525–1539. DOI: doi.org/10.1103/PhysRevB.9.1525. URL: https://journals.aps.org/prb/abstract/10.1103/PhysRevB.9.1525 (cit. on p. 19).

[72] M. Linnarsson et al. "Electronic structure of the GaAs:Mn_{Ga}scenter". In: *Phys. Rev. B* 55 (11 1997), pp. 6938–6944. DOI: 10.1103/PhysRevB.55.6938. URL: https://link.aps.org/doi/10.1103/PhysRevB.55.6938 (cit. on p. 19).

[73] M. E. Tang J.-M.and Flatté. "Spin-orientation-dependent spatial structure of a magnetic acceptor state in a zinc-blende semiconductor". In: *Phys. Rev. B* 72 (16 2005), p. 161315. DOI: 10.1103/PhysRevB.72.161315. URL: https://link.aps.org/doi/10.1103/PhysRevB.72.161315 (cit. on p. 20).

[74] T. Jungwirth et al. "Low-temperature magnetization of (Ga,Mn)As semiconductors". In: *Phys. Rev. B* 73 (16 2006), p. 165205. DOI: 10.1103/PhysRevB.73.165205. URL: https://link.aps.org/doi/10.1103/PhysRevB.73.165205 (cit. on p. 20).

[75] B. E. Larsson et al. "Theory of exchange interactions and chemical trends in diluted magnetic semiconductors". In: *Phys. Rev. B* 37 (1988), pp. 4137–4154. DOI: doi.org/10.1103/PhysRevB.37.4137. URL: https://journals.aps.org/prb/abstract/10.1103/PhysRevB.37.4137 (cit. on p. 20).

[76] J. C. Slater and G. F. Koster. "Simplified LCAO Method for the Periodic Potential Problem". In: *Phys. Rev.* 94 (6 1954), pp. 1498–1524. DOI: 10.1103/PhysRev.94.1498. URL: https://link.aps.org/doi/10.1103/PhysRev.94.1498 (cit. on pp. 20, 43).

[77] J. Okabayashi et al. "Core-level photoemission study of $Ga_{1-x}Mn_xAs$". In: *Phys. Rev. B* 58 (8 1998), R4211–R4214. DOI: 10.1103/PhysRevB.58.R4211. URL: https://link.aps.org/doi/10.1103/PhysRevB.58.R4211 (cit. on p. 20).

[78] Y. Ohno et al. "Valence band barrier at (Ga, Mn) As/GaAs interfaces". In: *Physica E: Low-dimensional Systems and Nanostructures* 13.2-4 (2002), pp. 521–524 (cit. on p. 22).

[79] O. Thomas et al. "Measuring the hole chemical potential in ferromagnetic $Ga_{1-x}Mn_xAs$/GaAs heterostructures by photoexcited resonant tunneling". In: *Appl. Phys. Lett.* 90 (2007), p. 082106 (cit. on p. 22).

[80] T. Tsuruoka et al. "Local electronic structures of GaMnAs observed by cross-sectional scanning tunneling microscopy". In: *Applied physics letters* 81.15 (2002), pp. 2800–2802 (cit. on p. 22).

[81] J. Jungwirth et al. "Character of states near the Fermi level in (Ga,Mn)As: Impurity to valence band crossover". In: *Phys. Rev. B* 76 (2007), p. 125206 (cit. on p. 22).

[82] K. S. Burch et al. "Impurity Band Conduction in a High Temperature Ferromagnetic Semiconductor". In: *Phys. Rev. Lett.* 97 (2006), p. 087208 (cit. on p. 22).

[83] K. Ando et al. "Origin of the Anomalous Magnetic Circular Dichroism Spectral Shape in Ferromagnetic $Ga_{1-x}Mn_xAs$: Impurity Bands inside the Band Gap". In: *Phys. Rev. Lett.* 100 (2008), p. 067204 (cit. on p. 22).

[84] J. M. Tang and M. E. Flatté. "Magnetic Circular Dichroism from the Impurity Band in III-V Diluted Magnetic Semiconductors". In: *Phys. Rev. Lett.* 101 () (cit. on p. 22).

[85] D. Neumaier et al. "All-Electrical Measurement of the Density of States in (Ga,Mn)As". In: *Phys. Rev. Lett.* 103 (8 2009), p. 087203. DOI: 10.1103/PhysRevLett.103.087203. URL: https://link.aps.org/doi/10.1103/PhysRevLett.103.087203 (cit. on p. 22).

[86] T. Dietl et al. “Zener Model Description of Ferromagnetism in Zinc-Blende Magnetic Semiconductors”. In: *Science* 287 (2000). DOI: 10.1126/science.287.5455.1019 (cit. on p. 22).

[87] T. Dietl, H. Ohno, and F. Matsukura. “Hole-mediated ferromagnetism in tetrahedrally coordinated semiconductors”. In: *Physical Review B* 63 (2001). DOI: /10.1103/PhysRevB.63.195205 (cit. on pp. 22, 80).

[88] S. D. Ganichev and L. E. Golub. “Interplay of Rashba/Dresselhaus spin splittings probed by photogalvanic spectroscopy–A review”. In: *physica status solidi (b)* 251.9 (2014), pp. 1801–1823 (cit. on p. 23).

[89] G. Dresselhaus, A. F. Kip, and C. Kittel. “Cyclotron Resonance of Electrons and Holes in Silicon and Germanium Crystals”. In: *Physical review journal achive* 98 (1955). DOI: /10.1103/PhysRev.98.368 (cit. on pp. 23, 44, 78, 186, 187).

[90] M. I. Dyakonov and V. I. Perel’. “Spin Orientation of electrons associated with the interband absorption of light in semiconductors”. In: *JETP Lett.* 33 (1971) (cit. on pp. 24, 71, 187).

[91] M. I. Dyakonov and V. Y. Kachorovskii. “Spin relaxation of two dimensional electrons in noncentrosymmetric semiconductors”. In: *Sov. Phys. Semicond.* 20 (1986) (cit. on pp. 24, 25).

[92] J.-M. Jancu et al. “Atomistic spin-orbit coupling and k.p parameters in III-V semiconductors”. In: *Physical Review B* 72 (2005). DOI: /10.1103/PhysRevB.72.193201 (cit. on pp. 24, 71, 189, 243, 247).

[93] T. H. Dang. *Interfacial skew tunneling in group III-V and group IV semiconductors driven by exchange and spin-orbit interactions: Study in the frame of an extended k.p theory*. PhD Thesis. Ecole Polytechique, Universite Paris-Saclay France, 2016 (cit. on pp. 24, 54, 55, 75).

[94] M. Cardona, N. E. Christensen, and G. Fasol. “Relativistic band structure and spin-orbit splitting of zinc-blende-type semiconductors”. In: *Physical Review B* 38 (1988). DOI: /10.1103/PhysRevB.38.1806 (cit. on pp. 25, 40, 72, 189).

[95] X. Cartoixà, D. Z.-Y. Ting, and Y.-C. Chang. “Suppression of the D’yakonov-Perel’ spin-relaxation mechanism for all spin components in [111] zincblende quantum wells”. In: *Physical Review B* 71 (2005). DOI: /10.1103/PhysRevB.71.045313 (cit. on p. 25).

[96] I. A. Nechaev et al. “Hole dynamics in a two-dimensional spin-orbit coupled electron system: Theoretical and experimental study of the Au(111) surface state”. In: *Phys. Rev. B* 80 (11 2009), p. 113402. DOI: 10.1103/PhysRevB.80.113402. URL: https://link.aps.org/doi/10.1103/PhysRevB.80.113402 (cit. on p. 25).

[97] J. C. R. Sánchez et al. “Spin-to-charge conversion using Rashba coupling at the interface between non-magnetic materials”. In: *Nature communications* 4 (2013), p. 2944. DOI: 10.1038/nature07321 (cit. on pp. 25, 163).

[98] A. G. Aronov and Yu B. Lyanda-Geller. “Nuclear electric resonance and orientation of carrier spins by an electric field”. In: *Soviet Journal of Experimental and Theoretical Physics Letters* 50 (1989), p. 431 (cit. on p. 25).

[99] A. G. Aronov, Yu B. Lyanda-Geller, and G. E. Pikus. “Spin polarization of electrons by an electric current”. In: *Sov. Phys. JETP* 73 (1991), pp. 537–541 (cit. on p. 25).

[100] E. L. Ivchenko, Yu B. Lyanda-Geller, and G. E. Pikus. “Photocurrent in structures with quantum wells with an optical orientation of free carriers”. In: *JETP Lett* 50.3 (1989), pp. 175–177 (cit. on p. 25).

[101] Y. A. Bychkov and E. I. Rashba. "Properties of a 2D electron gas with lifted spectral degeneracy". In: *JETP Lett.* 39 (1984) (cit. on p. 26).

[102] Y. A. Bychkov and E. I. Rashba. "Oscillatory effects and the magnetic sus- ceptibility of carriers in inversion layers". In: *J. Phys. C: Solid State Phys.* 17 (1984) (cit. on p. 26).

[103] M. W. Wu, J. H. Jiang, and M. Q. Weng. "Spin dynamics in semiconductors". In: *Physics Reports* 493 (2010). DOI: /10.1016/j.physrep.2010.04.002 (cit. on pp. 26, 35).

[104] R. Winkler. "Rashba spin splitting in two-dimensional electron and hole systems". In: *Physical Review B* 62 (Aug. 2000). DOI: /10.1103/PhysRevB.62.4245 (cit. on p. 26).

[105] M. I. Dyakonov and V. I. Perel'. "Possibility of Orienting Electron Spins with Current". In: *JETP Lett.* 13 (1971) (cit. on pp. 26, 71, 187).

[106] J. Wunderlich et al. "Experimental Observation of the Spin-Hall Effect in a Two-Dimensional Spin-Orbit Coupled Semiconductor System". In: *Phys. Rev. Lett.* 94 (4 2005), p. 047204. DOI: 10.1103/PhysRevLett.94.047204. URL: https://link.aps.org/doi/10.1103/PhysRevLett.94.047204 (cit. on p. 26).

[107] Y. Kato et al. "Coherent spin manipulation without magnetic fields in strained semiconductors". In: *Nature* 427.6969 (2004), p. 50 (cit. on pp. 26, 81).

[108] C.-Z. Chang and M. Li. "Quantum anomalous Hall effect in time-reversal-symmetry breaking topological insulators". In: *Journal of Physics: Condensed Matter* 28 (2016). DOI: 10.1088/0953-8984/28/12/123002 (cit. on p. 27).

[109] M. I. Dyakonov and V. I. Perel'. "Current-induced spin orientation of electrons in semiconductors". In: *Physics Letters A* 35 (1971). DOI: /10.1016/0375-9601(71)90196-4 (cit. on pp. 26, 28, 71).

[110] L. Liu et al. "Spin-Torque Switching with the Giant Spin Hall Effect of Tantalum". In: *Science* 336 (2012). DOI: /10.1126/science.1218197 (cit. on pp. 27, 163).

[111] L. Liu et al. "Spin-Torque Ferromagnetic Resonance Induced by the Spin Hall Effect". In: *Physical Review Letters* 106 (2011). DOI: /10.1103/PhysRevLett.106.036601 (cit. on p. 27).

[112] J. Wunderlich et al. "Spin Hall Effect Transistor". In: *Science* 330 (2010). DOI: /10.1126/science.1195816 (cit. on p. 27).

[113] S. Takahashi and S. Maekawa. "Spin current, spin accumulation and spin Hall effect". In: *Science and Technology of Advanced Materials* 9.1 (2008), p. 014105. DOI: 10.1088/1468-6996/9/1/014105. URL: https://doi.org/10.1088%2F1468-6996%2F9%2F1%2F014105 (cit. on p. 27).

[114] E. Saitoha, M. Ueda, and H. Miyajima. "Conversion of spin current into charge current at room temperature: Inverse spin-Hall effect". In: *Applied Physics Letters* 88 (2006). DOI: /10.1063/1.2199473 (cit. on p. 28).

[115] T. Kimura et al. "Room-Temperature Reversible Spin Hall Effect". In: *Physical Review Letters* 98 (2007). DOI: /10.1103/PhysRevLett.98.156601 (cit. on p. 28).

[116] H. Atsufumi and T. Koki. "Future perspectives for spintronic devices". In: *Journal of Physics D: Applied Physics* 47.19 (2014), p. 193001. DOI: 10.1088/0022-3727/47/19/193001. URL: https://doi.org/10.1088%2F0022-3727%2F47%2F19%2F193001 (cit. on p. 28).

[117] K. Uchida et al. "Observation of the spin Seebeck effect". In: *Nature* 455.7214 (2008), p. 778. DOI: /10.1038/nature07321 (cit. on p. 28).

[118] W. G. Clark and G. Feher. "Nuclear Polarization in InSb by a dc Current". In: *Phys. Rev. Lett.* 10 (4 1963), pp. 134–138. DOI: 10.1103/PhysRevLett.10.134. URL: https://link.aps.org/doi/10.1103/PhysRevLett.10.134 (cit. on p. 29).

[119] A. G. Aronov. "Spin injection and polarization of excitations and nuclei in superconductors". In: *Zh. Eksp. Teor. Fiz* 71 (1976), pp. 370–376 (cit. on p. 29).

[120] A. G. Aronov. "Spin injection in metals and polarization of nuclei". In: *Jetp Lett* 24.1 (1976), pp. 32–34 (cit. on p. 29).

[121] A. G. Aronov and G. E. Pikus. "Spin injection into semiconductors". In: *Soviet Physics Semiconductors-Ussr* 10.6 (1976), pp. 698–700 (cit. on p. 29).

[122] A. Fert and I. A. Campbell. "A. Fert and I. A. Campbell". In: *Physical review letters* 21 (1968). DOI: /10.1103/PhysRevLett.21.1190 (cit. on p. 29).

[123] N. F. Mott. "Electrons in transition metals". In: *Advances in Physics* 13 (1964). DOI: /10.1080/00018736400101041 (cit. on p. 29).

[124] Z. G. Yu and M. E. Flatté. "Spin diffusion and injection in semiconductor structures: Electric field effects". In: *Physical Review B* 66 (2002). DOI: /10.1103/PhysRevB.66.235302 (cit. on p. 29).

[125] T. Valet and A. Fert. "Theory of the perpendicular magnetoresistance in magnetic multilayers". In: *Physical Review B* 48 (1993). DOI: /10.1103/PhysRevB.48.7099 (cit. on p. 29).

[126] C. Chappert, A. Fert, and F. Nguyen Van Dau. "The emergence of spin electronics in data storage". In: *Nature materials* 6 (2007). DOI: /10.1038/nmat2024 (cit. on p. 29).

[127] A. Fert and H. Jaffrès. "Conditions for efficient spin injection from a ferromagnetic metal into a semiconductor". In: *Physical Review B* 64 (2001). DOI: /10.1103/PhysRevB.64.184420 (cit. on p. 29).

[128] H. Jaffrès and A. Fert. "Spin injection from a ferromagnetic metal into a semiconductor". In: *Journal of Applied Physics* 91 (2002). DOI: /10.1063/1.1451887 (cit. on p. 29).

[129] Y. Ohno et al. "Electrical spin injection in a ferromagnetic semiconductor heterostructure". In: *Nature* 402.6763 (1999), p. 790 (cit. on p. 29).

[130] G. Schmidt et al. "Fundamental obstacle for electrical spin injection from a ferromagnetic metal into a diffusive semiconductor". In: *Physical Review B* 62 (2000). DOI: /10.1103/PhysRevB.62.R4790 (cit. on p. 29).

[131] P. R. Hammar et al. "Observation of Spin Injection at a Ferromagnet-Semiconductor Interface". In: *Physical Review Letters* 83 (1999). DOI: /10.1103/PhysRevLett.83.203 (cit. on p. 29).

[132] W. Y. Lee et al. "Magnetization reversal and magnetoresistance in a lateral spin-injection device". In: *Journal of Applied Physics* 85 (1999). DOI: /10.1063/1.370504 (cit. on p. 29).

[133] A. T. Filip et al. "Experimental search for the electrical spin injection in a semiconductor". In: *Physical Review B* 62 (2000). DOI: /10.1103/PhysRevB.62.9996 (cit. on p. 29).

[134] J. Fabian et al. "Semiconductor Spintronics". In: *Acta Physica Slovaca* 57 (2007). URL: http://www.physics.sk/aps/pub.php?y=2007&pub=aps-07-04 (cit. on p. 29).

[135] M. Julliere. "Tunneling between ferromagnetic films". In: *Physics Letters A* 54 (1975). DOI: /10.1016/0375-9601(75)90174-7 (cit. on pp. 29, 188).

[136] S. F. Alvarado and P. Renaud. "Observation of spin-polarized-electron tunneling from a ferromagnet into GaAs". In: *Physiccal Review Letters* 68 (1992). DOI: /10.1103/PhysRevLett.68.1387 (cit. on p. 29).

[137] H. J. Zhu et al. "Room-Temperature Spin Injection from Fe into GaAs". In: *Physiccal Review Letters* 87 (2001). DOI: /10.1103/PhysRevLett.87.016601 (cit. on p. 29).

[138] A. T. Hanbicki et al. "Analysis of the transport process providing spin injection through an Fe/AlGaAs Schottky barrier". In: *Applied Physics Letters* 82 (2003). DOI: /10.1063/1.1580631 (cit. on p. 29).

[139] C. Adelmann et al. "Spin injection and relaxation in ferromagnet-semiconductor heterostructures". In: *Physical Review B* 71 (2005). DOI: /10.1103/PhysRevB.71.121301 (cit. on p. 29).

[140] V. F. Motsnyi et al. "Electrical spin injection in a ferromagnet/tunnel barrier/semiconductor heterostructure". In: *Applied Physics Letters* 81.2 (2002), pp. 265–267. DOI: /10.1063/1.1491010 (cit. on p. 29).

[141] X. Jiang et al. "Highly Spin-Polarized Room-Temperature Tunnel Injector for Semiconductor Spintronics using MgO(100)". In: *Phys. Rev. Lett.* 94 (5 2005), p. 056601. DOI: 10.1103/PhysRevLett.94.056601. URL: http://link.aps.org/doi/10.1103/PhysRevLett.94.056601 (cit. on p. 29).

[142] L. Esaki. "New phenomenon in narrow germanium p- n junctions". In: *Physical review* 109.2 (1958), p. 603 (cit. on p. 30).

[143] M. Kohda et al. "A spin Esaki diode". In: *Japanese Journal of Applied Physics* 40.12A (2001), p. L1274 (cit. on p. 30).

[144] M. Ciorga et al. "Electrical spin injection and detection in lateral all-semiconductor devices". In: *Physical Review B* 79.16 (2009), p. 165321. DOI: /10.1103/PhysRevB.79.165321 (cit. on p. 30).

[145] M. Ciorga et al. "Local spin valve effect in lateral (Ga, Mn) As/GaAs spin Esaki diode devices". In: *AIP Advances* 1.2 (2011), p. 022113 (cit. on p. 30).

[146] M. Ciorga et al. "Effect of contact geometry on spin-transport signals in nonlocal (Ga, Mn) As/GaAs devices". In: *Physical Review B* 88.15 (2013), p. 155308. DOI: /10.1103/PhysRevB.88.155308 (cit. on p. 30).

[147] Y. Ohno et al. "Electrical spin injection in a ferromagnetic semiconductor heterostructure". In: *Nature* 402.6763 (1999), p. 790. DOI: /10.1038/45509 (cit. on p. 30).

[148] E. Johnston-Halperin et al. "Spin-polarized Zener tunneling in (Ga, Mn) As". In: *Physical Review B* 65.4 (2002), p. 041306. DOI: /10.1103/PhysRevB.65.041306 (cit. on p. 30).

[149] P. Van Dorpe et al. "Very high spin polarization in GaAs by injection from a (Ga, Mn) As Zener diode". In: *Applied physics letters* 84.18 (2004), pp. 3495–3497. DOI: /10.1063/1.1738515 (cit. on p. 30).

[150] P. Sankowski et al. "Spin-dependent tunneling in modulated structures of (Ga, Mn) As". In: *Physical Review B* 75.4 (2007), p. 045306. DOI: /10.1103/PhysRevB.75.045306 (cit. on p. 30).

[151] K. Ando et al. "Photoinduced inverse spin-Hall effect: Conversion of light-polarization information into electric voltage". In: *Applied Physics Letters* 96.8 (2010), p. 082502 (cit. on pp. 30, 185).

[152] B. Endres et al. “Demonstration of the spin solar cell and spin photodiode effect”. In: *Nature communications* 4 (2013), p. 2068. DOI: 10.1038/ncomms3068. URL: https://doi.org/10.1038/ncomms3068 (cit. on pp. 31, 32).

[153] I. Zutic, J. Fabian, and S. Das Sarma. “Spin injection through the depletion layer: A theory of spin-polarized p-n junctions and solar cells”. In: *Phys. Rev. B* 64 (12 2001), p. 121201. DOI: 10.1103/PhysRevB.64.121201. URL: https://link.aps.org/doi/10.1103/PhysRevB.64.121201 (cit. on p. 32).

[154] I. Zutic, J. Fabian, and S. Das Sarma. “Spin-Polarized Transport in Inhomogeneous Magnetic Semiconductors: Theory of Magnetic/Nonmagnetic $p-n$ Junctions”. In: *Phys. Rev. Lett.* 88 (6 2002), p. 066603. DOI: 10.1103/PhysRevLett.88.066603. URL: https://link.aps.org/doi/10.1103/PhysRevLett.88.066603 (cit. on p. 32).

[155] G. L. Bir, A. G. Aronov, and G. E. Pikus. “Spin relaxation of electrons due to scattering by holes”. In: *JETP Lett.* 42 (1975) (cit. on p. 34).

[156] A. G. Aronov, G. E. Pikus, and A. N. Titkov. “Spin relaxation of conduction electrons in p-type Ill-V compounds”. In: *JETP Lett.* 57 (1983) (cit. on pp. 34, 35).

[157] S. Döhrmann et al. “Anomalous Spin Dephasing in (110) GaAs Quantum Wells: Anisotropy and Intersubband Effects”. In: *Phys. Rev. Lett.* 93 (14 2004), p. 147405. DOI: 10.1103/PhysRevLett.93.147405. URL: https://link.aps.org/doi/10.1103/PhysRevLett.93.147405 (cit. on p. 35).

[158] G. M. Müller et al. “Spin Noise Spectroscopy in GaAs (110) Quantum Wells: Access to Intrinsic Spin Lifetimes and Equilibrium Electron Dynamics”. In: *Phys. Rev. Lett.* 101 (20 2008), p. 206601. DOI: 10.1103/PhysRevLett.101.206601. URL: https://link.aps.org/doi/10.1103/PhysRevLett.101.206601 (cit. on p. 35).

[159] A. N. Andriotis, R. M. Sheetz, and M. Menon. “LSDA + U method: A calculation of the U values at the Hartree-Fock level of approximation”. In: *Phys. Rev. B* 81 (24 2010), p. 245103. DOI: 10.1103/PhysRevB.81.245103. URL: https://link.aps.org/doi/10.1103/PhysRevB.81.245103 (cit. on p. 39).

[160] Y. M. Niquet et al. “Onsite matrix elements of the tight-binding Hamiltonian of a strained crystal: Application to silicon, germanium, and their alloys”. In: *Phys. Rev. B* 79 (24 2009), p. 245201. DOI: 10.1103/PhysRevB.79.245201. URL: https://link.aps.org/doi/10.1103/PhysRevB.79.245201 (cit. on p. 39).

[161] D. Rideau, F. Triozon, and P. Dollfus. “Electronic Band Structure: Empirical Pseudopotentials, k· p and Tight-Binding Methods”. In: *Simulation of Transport in Nanodevices* (2016), pp. 97–130 (cit. on p. 39).

[162] J. M. Luttinger. “Quantum Theory of Cyclotron Resonance in Semiconductors: General Theory”. In: *Physical review journal achive* 102 (1956). DOI: /10.1103/PhysRev.102.1030 (cit. on pp. 39, 44).

[163] D. L. Smith and C. Mailhiot. “Theory of semiconductor superlattice electronic structure”. In: *Reviews of modern physics* 62 (1990). DOI: /10.1103/RevModPhys.62.173 (cit. on pp. 40, 44–46, 48, 101).

[164] K. I. Kolokolov, J. Li, and C. Z. Ning. “k.p Hamiltonian without spurious-state solutions”. In: *PHYSICAL REVIEW B* 68 (2003). DOI: /10.1103/PhysRevB.68.161308 (cit. on pp. 40, 53–56, 66).

[165] A. H. MacDonald and S. H. Vosko. “A relativistic density functional formalism”. In: *Journal of Physics C: Solid State Physics* 12.15 (1979), p. 2977 (cit. on p. 40).

[166] U. von Barth and L. Hedin. “A local exchange-correlation potential for the spin polarized case. i”. In: *Journal of Physics C: Solid State Physics* 5.13 (1972), p. 1629 (cit. on pp. 40, 42).

[167] P. Hohenberg and W. Kohn. “Inhomogeneous Electron Gas”. In: *Phys. Rev.* 136 (3B 1964), B864–B871. DOI: 10.1103/PhysRev.136.B864. URL: https://link.aps.org/doi/10.1103/PhysRev.136.B864 (cit. on p. 40).

[168] M. Levy. “Electron densities in search of Hamiltonians”. In: *Phys. Rev. A* 26 (3 1982), pp. 1200–1208. DOI: 10.1103/PhysRevA.26.1200. URL: https://link.aps.org/doi/10.1103/PhysRevA.26.1200 (cit. on p. 40).

[169] W. Kohn and L. J. Sham. “Self-Consistent Equations Including Exchange and Correlation Effects”. In: *Phys. Rev.* 140 (4A 1965), A1133–A1138. DOI: 10.1103/PhysRev.140.A1133. URL: https://link.aps.org/doi/10.1103/PhysRev.140.A1133 (cit. on pp. 41, 42).

[170] R. O. Jones and O. Gunnarsson. “The density functional formalism, its applications and prospects”. In: *Rev. Mod. Phys.* 61 (3 1989), pp. 689–746. DOI: 10.1103/RevModPhys.61.689. URL: https://link.aps.org/doi/10.1103/RevModPhys.61.689 (cit. on p. 41).

[171] M. M. Pant and A. K. Rajagopal. “Theory of inhomogeneous magnetic electron gas”. In: *Solid State Communications* 10.12 (1972), pp. 1157–1160 (cit. on p. 42).

[172] K. Capelle. “A bird’s-eye view of density-functional theory”. In: *Brazilian Journal of Physics* 36.4A (2006), pp. 1318–1343 (cit. on p. 42).

[173] J. P. Perdew, K. Burke, and M. Ernzerhof. “Generalized Gradient Approximation Made Simple”. In: *Phys. Rev. Lett.* 77 (18 1996), pp. 3865–3868. DOI: 10.1103/PhysRevLett.77.3865. URL: https://link.aps.org/doi/10.1103/PhysRevLett.77.3865 (cit. on p. 43).

[174] V. I. Anisimov et al. “First-principles calculations of the electronic structure and spectra of strongly correlated systems: dynamical mean-field theory”. In: 9.35 (1997), pp. 7359–7367. DOI: 10.1088/0953-8984/9/35/010. URL: https://doi.org/10.1088%2F0953-8984%2F9%2F35%2F010 (cit. on p. 43).

[175] J.-M. Jancu et al. “Empirical spds* tight-binding calculation for cubic semiconductors: General method and material parameters”. In: *Phys. Rev. B* 57 (11 1998), pp. 6493–6507. DOI: 10.1103/PhysRevB.57.6493. URL: https://link.aps.org/doi/10.1103/PhysRevB.57.6493 (cit. on p. 43).

[176] Y. Sun, S. E. Thompson, and T. Nishida. *Strain effect in semiconductors: theory and device applications*. Springer Science & Business Media, 2009 (cit. on pp. 43, 44, 82, 84, 94).

[177] P.-O. Löwdin. “A note on the quantum-mechanical perturbation theory”. In: *The Journal of Chemical Physics* 19.11 (1951), pp. 1396–1401 (cit. on p. 44).

[178] G. L. Bir and G. E. Pikus. *Symmetry and Strain-induced Effects in Semiconductors*. Wiley, 1974 (cit. on p. 44).

[179] Y. V. Lew et al. *The k p Method: Electronic Properties of Semiconductors*. Springer, 2009. ISBN: 9783540928713. DOI: 10.1007/978-3-540-92872-0 (cit. on pp. 44, 51, 66, 68, 82, 84).

[180] E. O. Kane. “Energy band structure in p-type germanium and silicon”. In: *Journal of Physics and Chemistry of Solids* 1 (1956). DOI: /10.1016/0022-3697(56)90014-2 (cit. on p. 44).

[181] M. Cardona and F. H. Pollak. “Energy-Band Structure of Germanium and Silicon: The k·p Method”. In: *Physical review journal achive* 142 (1966). DOI: /10.1103/PhysRev.142.530 (cit. on p. 44).

[182] E. O. Kane. “Band structure of indium antimonide”. In: *Journal of Physics and Chemistry of Solids* 1.4 (1957), pp. 249–261 (cit. on p. 47).

[183] T. L. H. Nguyen et al. “Spin rotation, spin filtering, and spin transfer in directional tunneling through barriers in noncentrosymmetric semiconductors”. In: *Physical review B* 79 (2009). DOI: /10.1103/PhysRevB.79.165204 (cit. on pp. 48, 64, 65, 72, 75, 89, 91, 96, 152–154, 156, 157, 159, 188).

[184] H. Ishida. “Bulk versus surface contributions to the Rashba spin splitting of Shockley surface states”. In: *Phys. Rev. B* 98 (20 2018), p. 205412. DOI: 10.1103/PhysRevB.98.205412. URL: https://link.aps.org/doi/10.1103/PhysRevB.98.205412 (cit. on pp. 48, 64).

[185] T. L. H. Nguyen. *Spin properties of evanescent states and tunneling in semiconductors*. PhD Thesis. Ecole Polytechique, France, 2010 (cit. on pp. 51, 64, 65, 72, 75, 96).

[186] B. A. Foreman. “Elimination of spurious solutions from eight-band k.p theory”. In: *PHYSICAL REVIEW B* 56 (1997). DOI: /10.1103/PhysRevB.56.R12748 (cit. on pp. 53, 54).

[187] L.-W. Wang. “Real and spurious solutions of the 8x8 k.p model for nanostructures”. In: *PHYSICAL REVIEW B* 61 (2000). DOI: /10.1103/PhysRevB.61.7241 (cit. on p. 53).

[188] B. A. Foreman. “Choosing a basis that eliminates spurious solutions in k.p theory”. In: *PHYSICAL REVIEW B* 75 (2007). DOI: /10.1103/PhysRevB.75.235331 (cit. on p. 53).

[189] F. Szmulowicz. “Solution to spurious bands and spurious real solutions in the envelope-function approximation”. In: *PHYSICAL REVIEW B* 71 (2005). DOI: /10.1103/PhysRevB.71.245117 (cit. on p. 53).

[190] R. G. Veprek, S. Steiger, and B. Witzigmann. “Ellipticity and the spurious solution problem of k.p envelope equations”. In: *PHYSICAL REVIEW B* 76 (2007). DOI: /10.1103/PhysRevB.76.165320 (cit. on p. 53).

[191] S. R. White and L. J. Sham. “Electronic Properties of Flat-Band Semiconductor Heterostructures”. In: *PHYSICAL REVIEW LETTERS* 47 (1981). DOI: /10.1103/PhysRevLett.47.879 (cit. on p. 53).

[192] D. L. Smith and C. Mailhiot. “k.ptheory of semiconductor superlattice electronic structure. I.Formal results”. In: *PHYSICAL REVIEW B* 33 (1986). DOI: /10.1103/PhysRevB.33.8345 (cit. on p. 53).

[193] W. Yang and K. Chang. “Origin and elimination of spurious solutions of the eight-band k.p theory”. In: *PHYSICAL REVIEW B* 72 (2005). DOI: /10.1103/PhysRevB.72.233309 (cit. on pp. 53, 54).

[194] D. Sytnyk and R. Melnik. “The Luttinger-Kohn theory for multiband Hamiltonians: A revision of ellipticity requirements”. In: (2018). URL: https://arxiv.org/abs/1808.06988 (cit. on p. 53).

[195] W. Trzeciakowski. “Effective-mass approximation in semiconductor heterostructures: One-dimensional analysis”. In: *PHYSICAL REVIEW B* 38 (1988). DOI: /10.1103/PhysRevB.38.12493 (cit. on p. 54).

[196] R. Winkler and U. Rössler. “General approach to the envelope-function approximation based on a quadrature method”. In: *PHYSICAL REVIEW B* 48 (1993). DOI: /10.1103/PhysRevB.48.8918 (cit. on p. 54).

[197] C. Aversa and J. E. Sipe. “Nonlinear optical susceptibilities of semiconductors: Results with a length-gauge analysis”. In: *PHYSICAL REVIEW B* 52 (1995). DOI: /10.1103/PhysRevB.52.14636 (cit. on p. 54).

[198] A. T. Meney, B. Gonul, and E. P. O’Reilly. “Evaluation of various approximations used in the envelope-function method”. In: *PHYSICAL REVIEW B* 50 (1994). DOI: /10.1103/PhysRevB.50.10893 (cit. on p. 54).

[199] F. Szmulowicz. “Numerically stable Hermitian secular equation for the envelope-function approximation for superlattices”. In: *PHYSICAL REVIEW B* 54 (1997). DOI: /10.1103/PhysRevB.54.11539 (cit. on p. 54).

[200] S. Richard, F. Aniel, and G. Fishman. “Energy-band structure of Ge, Si, and GaAs: A thirty-band k.p method”. In: *Phys. Rev. B* 70 (23 2004), p. 235204. DOI: 10.1103/PhysRevB.70.235204. URL: https://link.aps.org/doi/10.1103/PhysRevB.70.235204 (cit. on pp. 60, 256, 264).

[201] S. Richard. “Modélisation physique de la structure électronique, du transport et de l’ionisation par choc dans les matériaux IV-IV massifs, contraints et dans les puits quantiques”. Theses. Université Paris Sud - Paris XI, 2004. URL: https://tel.archives-ouvertes.fr/tel-00008310 (cit. on pp. 60, 64, 65).

[202] R. Eppenga, M. F. H. Schuurmans, and S. Colak. “New k·p theory for GaAs/$Ga_{1-x}A1_xAs$-type quantum wells”. In: *Phys. Rev. B* 36 (3 1987), pp. 1554–1564. DOI: 10.1103/PhysRevB.36.1554. URL: https://link.aps.org/doi/10.1103/PhysRevB.36.1554 (cit. on pp. 60, 61).

[203] R. Winkler and A. I. Nesvizhskii. “Anisotropic hole subband states and interband optical absorption in [mmn]-oriented quantum wells”. In: *Phys. Rev. B* 53 (15 1996), pp. 9984–9992. DOI: 10.1103/PhysRevB.53.9984. URL: https://link.aps.org/doi/10.1103/PhysRevB.53.9984 (cit. on pp. 60, 61).

[204] S. Richard et al. “Structure of spin-split evanescent states in the fundamental gap of zinc-blende-type semiconductors”. In: *Journal of applied physics* 97.8 (2005), p. 083706 (cit. on pp. 64, 65).

[205] V. Heine. “On the General Theory of Surface States and Scattering of Electrons in Solids”. In: *Proceedings of the Physical Society* 81.2 (1963), pp. 300–310. DOI: 10.1088/0370-1328/81/2/311. URL: https://doi.org/10.1088%2F0370-1328%2F81%2F2%2F311 (cit. on pp. 64, 65).

[206] R. O. Jones. “Surface representations and complex band structure of a diamond-type semiconductor”. In: *Proceedings of the Physical Society* 89.2 (1966), pp. 443–451. DOI: 10.1088/0370-1328/89/2/327. URL: https://doi.org/10.1088%2F0370-1328%2F89%2F2%2F327 (cit. on p. 64).

[207] Y.-C. Chang. “Complex band structures of zinc-blende materials”. In: *Physical Review B* 25 (1982). DOI: /10.1103/PhysRevB.25.605 (cit. on p. 64).

[208] M. F. H. Schuurmans and G. W.’t Hooft. “Simple calculations of confinement states in a quantum well”. In: *Physical Review B* 31 (1985). DOI: /10.1103/PhysRevB.31.8041 (cit. on p. 64).

[209] N. Rougemaille et al. “Spin-Induced Forbidden Evanescent States in III-V Semiconductors”. In: *Phys. Rev. Lett.* 95 (18 2005), p. 186406. DOI: 10.1103/PhysRevLett.95.186406. URL: https://link.aps.org/doi/10.1103/PhysRevLett.95.186406 (cit. on p. 64).

[210] G. Bastard. “Superlattice band structure in the envelope-function approximation”. In: *Phys. Rev. B* 24 (10 1981), pp. 5693–5697. DOI: 10.1103/PhysRevB.24.5693. URL: https://link.aps.org/doi/10.1103/PhysRevB.24.5693 (cit. on p. 67).

[211] G. Bastard. “Theoretical investigations of superlattice band structure in the envelope-function approximation”. In: *Phys. Rev. B* 25 (12 1982), pp. 7584–7597. DOI: 10.1103/PhysRevB.25.7584. URL: https://link.aps.org/doi/10.1103/PhysRevB.25.7584 (cit. on p. 67).

[212] G. Bastard. “Wave mechanics applied to semiconductor heterostructures”. In: (1990) (cit. on p. 67).

[213] B. A. Foreman. “Effective-mass Hamiltonian and boundary conditions for the valence bands of semiconductor microstructures”. In: *Phys. Rev. B* 48 (7 1993), pp. 4964–4967. DOI: 10.1103/PhysRevB.48.4964. URL: https://link.aps.org/doi/10.1103/PhysRevB.48.4964 (cit. on p. 67).

[214] M. G. Burt. “A new effective-mass equation for microstructures”. In: *Semiconductor science and technology* 3.12 (1988), p. 1224 (cit. on p. 67).

[215] M. G. Burt. “An exact formulation of the envelope function method for the determination of electronic states in semiconductor microstructures”. In: *Semiconductor science and technology* 2.7 (1987), p. 460 (cit. on p. 67).

[216] M. M. Glazov et al. “Spin-dependent resonant tunneling in symmetrical double-barrier structures”. In: *Phys. Rev. B* 71 (15 2005), p. 155313. DOI: 10.1103/PhysRevB.71.155313. URL: https://link.aps.org/doi/10.1103/PhysRevB.71.155313 (cit. on p. 72).

[217] S. A. Tarasenko, V. I. Perel’, and I. N. Yassievich. “In-Plane Electric Current Is Induced by Tunneling of Spin-Polarized Carriers”. In: *Phys. Rev. Lett.* 93 (5 2004), p. 056601. DOI: 10.1103/PhysRevLett.93.056601. URL: https://link.aps.org/doi/10.1103/PhysRevLett.93.056601 (cit. on p. 72).

[218] D. J. BenDaniel and C. B. Duke. “Space-Charge Effects on Electron Tunneling”. In: *Phys. Rev.* 152 (2 1966), pp. 683–692. DOI: 10.1103/PhysRev.152.683. URL: https://link.aps.org/doi/10.1103/PhysRev.152.683 (cit. on pp. 74, 90, 97, 120).

[219] J. M. Luttinger and W. Kohn. “Motion of Electrons and Holes in Perturbed Periodic Fields”. In: *Phys. Rev.* 97 (4 1955), pp. 869–883. DOI: 10.1103/PhysRev.97.869. URL: https://link.aps.org/doi/10.1103/PhysRev.97.869 (cit. on p. 75).

[220] C. Hamaguchi. *Basic Semiconductor Physics*. Springer, 2017. ISBN: 978-3-319-66860-4. DOI: /10.1007/978-3-319-66860-4 (cit. on pp. 76, 225, 226).

[221] Y. Kajikawa. “Well-width dependence of the optical anisotropies in (001) and (110) semiconductor quantum wells: The effect of spin-orbit split-off bands”. In: *Phys. Rev. B* 51 (23 1995), pp. 16790–16800. DOI: 10.1103/PhysRevB.51.16790. URL: https://link.aps.org/doi/10.1103/PhysRevB.51.16790 (cit. on pp. 79, 227–229).

[222] M. Abolfath et al. “Theory of magnetic anisotropy in $III_{1-x}Mn_xV$ ferromagnets”. In: *Phys. Rev. B* 63 (5 2001), p. 054418. DOI: 10.1103/PhysRevB.63.054418. URL: https://link.aps.org/doi/10.1103/PhysRevB.63.054418 (cit. on p. 80).

[223] M. Elsen. "Magnetoresistances and spin transfer in (Ga,Mn)As based heterostructures". Theses. Université Pierre et Marie Curie - Paris VI, 2007. URL: https://tel.archives-ouvertes.fr/tel-00151311 (cit. on p. 81).

[224] D. Rideau et al. In: *Phys. Rev. B* 74 (19 2006), p. 195208. DOI: 10.1103/PhysRevB.74.195208. URL: https://link.aps.org/doi/10.1103/PhysRevB.74.195208 (cit. on pp. 81, 82).

[225] Harry H. Hall, J. Bardeen, and G. L. Pearson. "The Effects of Pressure and Temperature on the Resistance of $p-n$ Junctions in Germanium". In: *Phys. Rev.* 84 (1 1951), pp. 129–132. DOI: 10.1103/PhysRev.84.129. URL: https://link.aps.org/doi/10.1103/PhysRev.84.129 (cit. on p. 81).

[226] J. Welser, J. L. Hoyt, and J. F. Gibbons. "Electron mobility enhancement in strained-Si n-type metal-oxide-semiconductor field-effect transistors". In: *IEEE Electron Device Letters* 15.3 (1994), pp. 100–102 (cit. on p. 81).

[227] Y. K. Kato et al. "Current-Induced Spin Polarization in Strained Semiconductors". In: *Phys. Rev. Lett.* 93 (17 2004), p. 176601. DOI: 10.1103/PhysRevLett.93.176601. URL: https://link.aps.org/doi/10.1103/PhysRevLett.93.176601 (cit. on p. 81).

[228] S. A. Crooker and D. L. Smith. "Imaging Spin Flows in Semiconductors Subject to Electric, Magnetic, and Strain Fields". In: *Phys. Rev. Lett.* 94 (23 2005), p. 236601. DOI: 10.1103/PhysRevLett.94.236601. URL: https://link.aps.org/doi/10.1103/PhysRevLett.94.236601 (cit. on p. 81).

[229] M. Hruska et al. "Effects of strain, electric, and magnetic fields on lateral electron-spin transport in semiconductor epilayers". In: *Phys. Rev. B* 73 (7 2006), p. 075306. DOI: 10.1103/PhysRevB.73.075306. URL: https://link.aps.org/doi/10.1103/PhysRevB.73.075306 (cit. on p. 81).

[230] B. M. Norman et al. "Mapping spin-orbit splitting in strained (In,Ga)As epilayers". In: *Phys. Rev. B* 82 (8 2010), p. 081304. DOI: 10.1103/PhysRevB.82.081304. URL: https://link.aps.org/doi/10.1103/PhysRevB.82.081304 (cit. on p. 81).

[231] K. Olejník et al. "Electrical detection of magnetization reversal without auxiliary magnets". In: *Phys. Rev. B* 91 (18 2015), p. 180402. DOI: 10.1103/PhysRevB.91.180402. URL: https://link.aps.org/doi/10.1103/PhysRevB.91.180402 (cit. on p. 89).

[232] C. O. Avci et al. "Unidirectional spin Hall magnetoresistance in ferromagnet/normal metal bilayers". In: *Nature Physics* 11.7 (2015), p. 570 (cit. on p. 89).

[233] C. O. Avci et al. "Magnetoresistance of heavy and light metal/ferromagnet bilayers". In: *Applied Physics Letters* 107.19 (2015), p. 192405 (cit. on p. 89).

[234] J. Kim et al. "Spin Hall Magnetoresistance in Metallic Bilayers". In: *Phys. Rev. Lett.* 116 (9 2016), p. 097201. DOI: 10.1103/PhysRevLett.116.097201. URL: https://link.aps.org/doi/10.1103/PhysRevLett.116.097201 (cit. on p. 89).

[235] H.-J. Drouhin et al. *Spin-Orbit Engineering of Semiconductor Heterostructures*. 2013, pp. 551–594. DOI: 10.1117/3.1002245.Ch22 (cit. on pp. 91, 92, 166, 167).

[236] F. Bottegoni et al. "Probability-current definition in presence of spin-orbit interaction". In: *Journal of Applied Physics* 111.7 (2012). cited By 9. DOI: 10.1063/1.3672399. URL: https://aip.scitation.org/doi/abs/10.1063/1.3672399 (cit. on p. 91).

[237] F. Bottegoni et al. “Probability- and spin-current operators for effective Hamiltonians”. In: *Phys. Rev. B* 85 (23 2012), p. 235313. DOI: 10.1103/PhysRevB.85.235313. URL: https://link.aps.org/doi/10.1103/PhysRevB.85.235313 (cit. on p. 91).

[238] F. Bottegoni et al. “Spin-Orbit Engineering of Semiconductor Heterostructures”. In: *arXiv preprint arXiv:1109.5097* (2011) (cit. on p. 92).

[239] V. P. Amin and M. D. Stiles. “Spin transport at interfaces with spin-orbit coupling: Formalism”. In: *Phys. Rev. B* 94 (10 2016), p. 104419. DOI: 10.1103/PhysRevB.94.104419. URL: https://link.aps.org/doi/10.1103/PhysRevB.94.104419 (cit. on pp. 99, 163).

[240] J. E. Inglesfield, S. Crampin, and H. Ishida. “Embedding potential definition of channel functions”. In: *Phys. Rev. B* 71 (15 2005), p. 155120. DOI: 10.1103/PhysRevB.71.155120. URL: https://link.aps.org/doi/10.1103/PhysRevB.71.155120 (cit. on p. 102).

[241] S. Datta. *Electronic transport in mesoscopic systems*. Cambridge university press, 1997 (cit. on p. 105).

[242] A. Perot and C. Fabry. “On the application of interference phenomena to the solution of various problems of spectroscopy and metrology”. In: *The Astrophysical Journal* 9 (1899), p. 87 (cit. on p. 112).

[243] C. Fabry. “Theorie et applications d’une nouvelle methods de spectroscopie intereferentielle”. In: *Ann. Chim. Ser. 7* 16 (1899), pp. 115–144 (cit. on p. 112).

[244] J. H. Davies. *The physics of low-dimensional semiconductors: an introduction*. Cambridge university press, 1998 (cit. on pp. 113, 117, 118).

[245] P. Markoš and C. M. Soukoulis. *Wave Propagation: From Electrons to Photonic Crystals and Left-Handed Materials*. Princeton University Press, 2008. ISBN: 978-0-691-13003-3 (cit. on pp. 113, 114, 287).

[246] Nguyen H.-C. *Quasi-bound states induced by one-dimensional potentials in graphene*. Bachelor Thesis. VNU University of Science., 2008 (cit. on pp. 117, 118).

[247] H. C. Nguyen, M. T. Hoang, and V. L. Nguyen. “Quasi-bound states induced by one-dimensional potentials in graphene”. In: *Phys. Rev. B* 79 (3 2009), p. 035411. DOI: 10.1103/PhysRevB.79.035411. URL: https://link.aps.org/doi/10.1103/PhysRevB.79.035411 (cit. on pp. 117, 118).

[248] L. D. Landau and E. M. Lifshitz. *Quantum mechanics: non-relativistic theory*. Vol. 3. Elsevier, 2013 (cit. on p. 118).

[249] M. V. Durnev. *Spin splitting of valence sub-bands in semiconductor quantum wells and quantum dots*. URL: http://www.ioffe.ru/get_file.php?dir=theses/content&file=Thes_0396content.pdf (cit. on pp. 127, 128, 232).

[250] M. V. Durnev. “Zeeman splitting of light hole in quantum wells: Comparison of theory and experiments”. In: *Physics of the Solid State* 56.7 (2014), pp. 1416–1423. ISSN: 1090-6460. DOI: 10.1134/S1063783414070117. URL: https://doi.org/10.1134/S1063783414070117 (cit. on pp. 132, 134, 135, 311–314).

[251] E. I. Rashba and E. Ya. Sherman. “Spin-orbital band splitting in symmetric quantum wells”. In: *Physics Letters A* 129.3 (1988), pp. 175–179 (cit. on p. 134).

[252] J. W Negele. *Quantum many-particle systems*. CRC Press, 2018 (cit. on p. 139).

[253] D. A. Stewart et al. “Interfacial scattering in magnetic multilayers and spin valves”. In: *Phys. Rev. B* 68 (1 2003), p. 014433. DOI: 10.1103/PhysRevB.68.014433. URL: https://link.aps.org/doi/10.1103/PhysRevB.68.014433 (cit. on pp. 139, 142, 150, 192).

[254] R. Kubo. “Statistical-Mechanical Theory of Irreversible Processes. I. General Theory and Simple Applications to Magnetic and Conduction Problems”. In: *Journal of the Physical Society of Japan* 12.6 (1957), pp. 570–586. DOI: 10.1143/JPSJ.12.570. URL: https://doi.org/10.1143/JPSJ.12.570 (cit. on p. 139).

[255] W. H. Butler et al. “First-principles calculations of electrical conductivity and giant magnetoresistance of Co||Cu||Co spin valves”. In: *Phys. Rev. B* 52 (18 1995), pp. 13399–13410. DOI: 10.1103/PhysRevB.52.13399. URL: https://link.aps.org/doi/10.1103/PhysRevB.52.13399 (cit. on p. 139).

[256] A. A. Lucas et al. “Scattering-theoretic approach to elastic one-electron tunneling through localized barriers: Application to scanning tunneling microscopy”. In: *Phys. Rev. B* 37 (18 1988), pp. 10708–10720. DOI: 10.1103/PhysRevB.37.10708. URL: https://link.aps.org/doi/10.1103/PhysRevB.37.10708 (cit. on pp. 139, 142).

[257] M. A. M. de Aguiar. “Exact Green’s function for the step and square-barrier potentials”. In: *Phys. Rev. A* 48 (4 1993), pp. 2567–2573. DOI: 10.1103/PhysRevA.48.2567. URL: https://link.aps.org/doi/10.1103/PhysRevA.48.2567 (cit. on pp. 139, 142, 150, 198).

[258] V. F. Los and A. V. Los. “Theory of interlayer magnetic coupling in nanostructures with disordered interfaces”. In: *Phys. Rev. B* 77 (2 2008), p. 024410. DOI: 10.1103/PhysRevB.77.024410. URL: https://link.aps.org/doi/10.1103/PhysRevB.77.024410 (cit. on pp. 139, 142).

[259] E. Y. Tsymbal, O. N. Mryasov, and P. R. LeClair. “Spin-dependent tunnelling in magnetic tunnel junctions”. In: *Journal of Physics: Condensed Matter* 15.4 (2003), R109 (cit. on p. 139).

[260] S. Lowitzer et al. “Extrinsic and Intrinsic Contributions to the Spin Hall Effect of Alloys”. In: *Phys. Rev. Lett.* 106 (5 2011), p. 056601. DOI: 10.1103/PhysRevLett.106.056601. URL: https://link.aps.org/doi/10.1103/PhysRevLett.106.056601 (cit. on p. 139).

[261] J. E. Inglesfield. *The Embedding Method for Electronic Structure*. 2053-2563. IOP Publishing, 2015. ISBN: 978-0-7503-1042-0. DOI: 10.1088/978-0-7503-1042-0. URL: http://dx.doi.org/10.1088/978-0-7503-1042-0 (cit. on p. 141).

[262] M. Di Ventra. *Electrical Transport in Nanoscale Systems*. Cambridge University Press, 2008. DOI: 10.1017/CBO9780511755606 (cit. on p. 142).

[263] D. Sébilleau, K. Hatada, and H. Ebert. *Multiple Scattering Theory for Spectroscopies*. Springer, 2018 (cit. on p. 144).

[264] A. Gonis and W. H. Butler. *Multiple scattering in solids*. Springer Science & Business Media, 2012 (cit. on p. 144).

[265] H. Bruus and K. Flensberg. *Many-body quantum theory in condensed matter physics: an introduction*. Oxford university press, 2004 (cit. on p. 148).

[266] A. Hoffmann. “Spin Hall Effects in Metals”. In: *IEEE Transactions on Magnetics* 49.10 (2013), pp. 5172–5193. ISSN: 0018-9464. DOI: 10.1109/TMAG.2013.2262947 (cit. on p. 163).

[267] I. M. Miron et al. “Current-driven spin torque induced by the Rashba effect in a ferromagnetic metal layer”. In: *Nature materials* 9.3 (2010), p. 230 (cit. on p. 163).

[268] K. Garello et al. “Symmetry and magnitude of spin–orbit torques in ferromagnetic heterostructures”. In: *Nature nanotechnology* 8.8 (2013), p. 587 (cit. on p. 163).

[269] Y. A Bychkov and É I Rashba. “Properties of a 2D electron gas with lifted spectral degeneracy”. In: *JETP lett* 39.2 (1984), p. 78 (cit. on p. 163).

[270] K. Shen, G. Vignale, and R. Raimondi. “Microscopic Theory of the Inverse Edelstein Effect”. In: *Phys. Rev. Lett.* 112 (9 2014), p. 096601. DOI: 10.1103/PhysRevLett.112.096601. URL: https://link.aps.org/doi/10.1103/PhysRevLett.112.096601 (cit. on p. 163).

[271] E. Lesne et al. “Highly efficient and tunable spin-to-charge conversion through Rashba coupling at oxide interfaces”. In: *Nature Materials* 15.12 (2016), pp. 1261–1266. DOI: 10.1038/nmat4726 (cit. on p. 163).

[272] J.-C. Rojas-Sánchez et al. “Spin Pumping and Inverse Spin Hall Effect in Platinum: The Essential Role of Spin-Memory Loss at Metallic Interfaces”. In: *Phys. Rev. Lett.* 112 (10 2014), p. 106602. DOI: 10.1103/PhysRevLett.112.106602. URL: https://link.aps.org/doi/10.1103/PhysRevLett.112.106602 (cit. on p. 163).

[273] Y. Liu et al. “Interface Enhancement of Gilbert Damping from First Principles”. In: *Phys. Rev. Lett.* 113 (20 2014), p. 207202. DOI: 10.1103/PhysRevLett.113.207202. URL: https://link.aps.org/doi/10.1103/PhysRevLett.113.207202 (cit. on p. 163).

[274] O. Krupin et al. “Rashba effect at magnetic metal surfaces”. In: *Phys. Rev. B* 71 (20 2005), p. 201403. DOI: 10.1103/PhysRevB.71.201403. URL: https://link.aps.org/doi/10.1103/PhysRevB.71.201403 (cit. on p. 163).

[275] G. Bihlmayer et al. “The Rashba-effect at metallic surfaces”. In: *surface science* 600.18 (2006), pp. 3888–3891 (cit. on p. 163).

[276] O. Krupin et al. “Rashba effect at the surfaces of rare-earth metals and their monoxides”. In: *New Journal of Physics* 11.1 (2009), p. 013035. DOI: 10.1088/1367-2630/11/1/013035. URL: https://doi.org/10.1088%2F1367-2630%2F11%2F1%2F013035 (cit. on p. 163).

[277] J. C. Slonczewski. “Current-driven excitation of magnetic multilayers”. In: *Journal of Magnetism and Magnetic Materials* 159.1 (1996), pp. L1 –L7. ISSN: 0304-8853. DOI: https://doi.org/10.1016/0304-8853(96)00062-5. URL: http://www.sciencedirect.com/science/article/pii/0304885396000625 (cit. on pp. 164, 175).

[278] L. Berger. “Emission of spin waves by a magnetic multilayer traversed by a current”. In: *Phys. Rev. B* 54 (13 1996), pp. 9353–9358. DOI: 10.1103/PhysRevB.54.9353. URL: https://link.aps.org/doi/10.1103/PhysRevB.54.9353 (cit. on pp. 164, 175).

[279] B. Scharf et al. “Tunneling Planar Hall Effect in Topological Insulators: Spin Valves and Amplifiers”. In: *Phys. Rev. Lett.* 117 (16 2016), p. 166806. DOI: 10.1103/PhysRevLett.117.166806. URL: https://link.aps.org/doi/10.1103/PhysRevLett.117.166806 (cit. on p. 165).

[280] A. Vedyayev et al. “Spontaneous Anomalous and Spin Hall Effects Due to Spin-Orbit Scattering of Evanescent Wave Functions in Magnetic Tunnel Junctions”. In: *Phys. Rev. Lett.* 110 (24 2013), p. 247204. DOI: 10.1103/PhysRevLett.110.247204. URL: https://link.aps.org/doi/10.1103/PhysRevLett.110.247204 (cit. on p. 165).

[281] P. S. Alekseev. “Tunneling hall effect”. In: *JETP Letters* 92.12 (2010), pp. 788–792. ISSN: 1090-6487. DOI: 10.1134/S0021364010240021. URL: https://doi.org/10.1134/S0021364010240021 (cit. on p. 165).

[282] F. Hellman et al. “Interface-induced phenomena in magnetism”. In: *Rev. Mod. Phys.* 89 (2 2017), p. 025006. DOI: 10.1103/RevModPhys.89.025006. URL: https://link.aps.org/doi/10.1103/RevModPhys.89.025006 (cit. on p. 166).

[283] V. A. Sablikov, A. A. Sukhanov, and Y. Ya. Tkach. “Equilibrium edge spin currents in two-dimensional electron systems with spin-orbit interaction”. In: *Phys. Rev. B* 78 (15 2008), p. 153302. DOI: 10.1103/PhysRevB.78.153302. URL: https://link.aps.org/doi/10.1103/PhysRevB.78.153302 (cit. on p. 166).

[284] Q.-f. Sun, X. C. Xie, and J. Wang. “Persistent spin current in nanodevices and definition of the spin current”. In: *Phys. Rev. B* 77 (3 2008), p. 035327. DOI: 10.1103/PhysRevB.77.035327. URL: https://link.aps.org/doi/10.1103/PhysRevB.77.035327 (cit. on p. 166).

[285] E. B. Sonin. “Equilibrium spin currents in the Rashba medium”. In: *Phys. Rev. B* 76 (3 2007), p. 033306. DOI: 10.1103/PhysRevB.76.033306. URL: https://link.aps.org/doi/10.1103/PhysRevB.76.033306 (cit. on pp. 166, 167).

[286] E. I. Rashba. “Spin currents in thermodynamic equilibrium: The challenge of discerning transport currents”. In: *Phys. Rev. B* 68 (24 2003), p. 241315. DOI: 10.1103/PhysRevB.68.241315. URL: https://link.aps.org/doi/10.1103/PhysRevB.68.241315 (cit. on p. 166).

[287] J. Shi et al. “Proper Definition of Spin Current in Spin-Orbit Coupled Systems”. In: *Phys. Rev. Lett.* 96 (7 2006), p. 076604. DOI: 10.1103/PhysRevLett.96.076604. URL: https://link.aps.org/doi/10.1103/PhysRevLett.96.076604 (cit. on p. 167).

[288] M. Sands, R. P. Feynman, and R. Leighton. *The Feynman Lectures on Physics: Mainly Electromagnetism and Matter, Volume 2*. 2017 (cit. on p. 167).

[289] S. R. De Groot and P. Mazur. *Non-equilibrium thermodynamics*. Courier Corporation, 2013 (cit. on p. 167).

[290] A. Kalitsov et al. “Spin-polarized current-induced torque in magnetic tunnel junctions”. In: *Journal of applied physics* 99.8 (2006), 08G501 (cit. on pp. 172, 173).

[291] P. M. Haney and M. D. Stiles. “Current-Induced Torques in the Presence of Spin-Orbit Coupling”. In: *Phys. Rev. Lett.* 105 (12 2010), p. 126602. DOI: 10.1103/PhysRevLett.105.126602. URL: https://link.aps.org/doi/10.1103/PhysRevLett.105.126602 (cit. on pp. 172, 184).

[292] A. Kalitsov et al. “Spin-transfer torque in magnetic tunnel junctions”. In: *Phys. Rev. B* 79 (17 2009), p. 174416. DOI: 10.1103/PhysRevB.79.174416. URL: https://link.aps.org/doi/10.1103/PhysRevB.79.174416 (cit. on p. 173).

[293] W. H. Butler. “Tunneling magnetoresistance from a symmetry filtering effect”. In: *Science and Technology of Advanced Materials* 9.1 (2008), p. 014106. DOI: 10.1088/1468-6996/9/1/014106. URL: https://doi.org/10.1088%2F1468-6996%2F9%2F1%2F014106 (cit. on p. 173).

[294] M. Tsoi et al. “Excitation of a Magnetic Multilayer by an Electric Current”. In: *Phys. Rev. Lett.* 80 (19 1998), pp. 4281–4284. DOI: 10.1103/PhysRevLett.80.4281. URL: https://link.aps.org/doi/10.1103/PhysRevLett.80.4281 (cit. on p. 175).

[295] J. A. Katine and E. E. Fullerton. “Device implications of spin-transfer torques”. In: *Journal of Magnetism and Magnetic Materials* 320.7 (2008), pp. 1217–1226 (cit. on p. 175).

[296] M. D. Stiles and J. Miltat. "Spin-Transfer Torque and Dynamics". In: *Spin Dynamics in Confined Magnetic Structures III*. Ed. by Burkard Hillebrands and André Thiaville. Berlin, Heidelberg: Springer Berlin Heidelberg, 2006, pp. 225–308. ISBN: 978-3-540-39842-4. DOI: 10.1007/10938171_7. URL: https://doi.org/10.1007/10938171_7 (cit. on p. 175).

[297] J. A. Katine et al. "Current-Driven Magnetization Reversal and Spin-Wave Excitations in Co /Cu /Co Pillars". In: *Phys. Rev. Lett.* 84 (14 2000), pp. 3149–3152. DOI: 10.1103/PhysRevLett.84.3149. URL: https://link.aps.org/doi/10.1103/PhysRevLett.84.3149 (cit. on p. 175).

[298] S. Il. Kiselev et al. "Microwave oscillations of a nanomagnet driven by a spin-polarized current". In: *nature* 425.6956 (2003), p. 380 (cit. on p. 175).

[299] J. Grollier et al. "Spin-polarized current induced switching in Co/Cu/Co pillars". In: *Applied Physics Letters* 78.23 (2001), pp. 3663–3665 (cit. on p. 175).

[300] J. Grollier et al. "Field dependence of magnetization reversal by spin transfer". In: *Phys. Rev. B* 67 (17 2003), p. 174402. DOI: 10.1103/PhysRevB.67.174402. URL: https://link.aps.org/doi/10.1103/PhysRevB.67.174402 (cit. on p. 175).

[301] J. Z. Sun et al. "Batch-fabricated spin-injection magnetic switches". In: *Applied Physics Letters* 81.12 (2002), pp. 2202–2204 (cit. on p. 175).

[302] S. Urazhdin et al. "Switching current versus magnetoresistance in magnetic multilayer nanopillars". In: *Applied physics letters* 84.9 (2004), pp. 1516–1518 (cit. on p. 175).

[303] Y. Huai et al. "Observation of spin-transfer switching in deep submicron-sized and low-resistance magnetic tunnel junctions". In: *Applied Physics Letters* 84.16 (2004), pp. 3118–3120 (cit. on p. 176).

[304] Y. Liu et al. "Current-induced magnetization switching in magnetic tunnel junctions". In: *Applied physics letters* 82.17 (2003), pp. 2871–2873 (cit. on p. 176).

[305] G. D. Fuchs et al. "Spin-transfer effects in nanoscale magnetic tunnel junctions". In: *Applied Physics Letters* 85.7 (2004), pp. 1205–1207 (cit. on p. 176).

[306] J. C. Slonczewski. "Currents, torques, and polarization factors in magnetic tunnel junctions". In: *Phys. Rev. B* 71 (2 2005), p. 024411. DOI: 10.1103/PhysRevB.71.024411. URL: https://link.aps.org/doi/10.1103/PhysRevB.71.024411 (cit. on p. 176).

[307] J. A. Katine and Eric E. Fullerton. "Device implications of spin-transfer torques". In: *Journal of Magnetism and Magnetic Materials* 320.7 (2008), pp. 1217–1226 (cit. on p. 176).

[308] D. Chiba, F. Matsukura, and H. Ohno. "Electrical magnetization reversal in ferromagnetic III–V semiconductors". In: *Journal of Physics D: Applied Physics* 39.13 (2006), R215–R225. DOI: 10.1088/0022-3727/39/13/r01. URL: https://doi.org/10.1088%2F0022-3727%2F39%2F13%2Fr01 (cit. on p. 176).

[309] Y.-H. Tang, Z.-W. Huang, and B.-H. Huang. "Analytic expression for the giant fieldlike spin torque in spin-filter magnetic tunnel junctions". In: *Phys. Rev. B* 96 (6 2017), p. 064429. DOI: 10.1103/PhysRevB.96.064429. URL: https://link.aps.org/doi/10.1103/PhysRevB.96.064429 (cit. on pp. 179, 185).

[310] A. Kalitsov et al. "Spin-polarized current-induced torque in magnetic tunnel junctions". In: *Journal of applied physics* 99.8 (2006), 08G501 (cit. on pp. 180, 183).

[311] A. Kalitsov et al. “Spin-transfer torque in magnetic tunnel junctions”. In: *Phys. Rev. B* 79 (17 2009), p. 174416. DOI: 10.1103/PhysRevB.79.174416. URL: https://link.aps.org/doi/10.1103/PhysRevB.79.174416 (cit. on pp. 180, 183).

[312] I. Theodonis et al. “Anomalous Bias Dependence of Spin Torque in Magnetic Tunnel Junctions”. In: *Phys. Rev. Lett.* 97 (23 2006), p. 237205. DOI: 10.1103/PhysRevLett.97.237205. URL: https://link.aps.org/doi/10.1103/PhysRevLett.97.237205 (cit. on pp. 180, 183).

[313] Y.-H. Tang et al. “Controlling the Nonequilibrium Interlayer Exchange Coupling in Asymmetric Magnetic Tunnel Junctions”. In: *Phys. Rev. Lett.* 103 (5 2009), p. 057206. DOI: 10.1103/PhysRevLett.103.057206. URL: https://link.aps.org/doi/10.1103/PhysRevLett.103.057206 (cit. on pp. 180, 183).

[314] H. Kubota et al. “Quantitative measurement of voltage dependence of spin-transfer torque in MgO-based magnetic tunnel junctions”. In: *Nature Physics* 4.1 (2008), p. 37 (cit. on pp. 180, 183).

[315] J. C. Sankey et al. “Measurement of the spin-transfer-torque vector in magnetic tunnel junctions”. In: *Nature Physics* 4.1 (2008), p. 67 (cit. on pp. 180, 183).

[316] J. C. Slonczewski. “Conductance and exchange coupling of two ferromagnets separated by a tunneling barrier”. In: *Phys. Rev. B* 39 (10 1989), pp. 6995–7002. DOI: 10.1103/PhysRevB.39.6995. URL: https://link.aps.org/doi/10.1103/PhysRevB.39.6995 (cit. on p. 180).

[317] H. Jaffrès et al. “Angular dependence of the tunnel magnetoresistance in transition-metal-based junctions”. In: *Phys. Rev. B* 64 (6 2001), p. 064427. DOI: 10.1103/PhysRevB.64.064427. URL: https://link.aps.org/doi/10.1103/PhysRevB.64.064427 (cit. on p. 180).

[318] A. Brataas, G. E.W. Bauer, and P. J. Kelly. “Non-collinear magnetoelectronics”. In: *Physics Reports* 427.4 (2006), pp. 157–255 (cit. on p. 180).

[319] V. P. Amin and M. D. Stiles. “Spin transport at interfaces with spin-orbit coupling: Formalism”. In: *Phys. Rev. B* 94 (10 2016), p. 104419. DOI: 10.1103/PhysRevB.94.104419. URL: https://link.aps.org/doi/10.1103/PhysRevB.94.104419 (cit. on pp. 183, 184).

[320] V. P. Amin and M. D. Stiles. “Spin transport at interfaces with spin-orbit coupling: Phenomenology”. In: *Phys. Rev. B* 94 (10 2016), p. 104420. DOI: 10.1103/PhysRevB.94.104420. URL: https://link.aps.org/doi/10.1103/PhysRevB.94.104420 (cit. on pp. 183, 184).

[321] J.-C. Rojas-Sánchez et al. “Spin Pumping and Inverse Spin Hall Effect in Platinum: The Essential Role of Spin-Memory Loss at Metallic Interfaces”. In: *Phys. Rev. Lett.* 112 (10 2014), p. 106602. DOI: 10.1103/PhysRevLett.112.106602. URL: https://link.aps.org/doi/10.1103/PhysRevLett.112.106602 (cit. on p. 183).

[322] F. Bottegoni et al. “Spin diffusion in Pt as probed by optically generated spin currents”. In: *Phys. Rev. B* 92 (21 2015), p. 214403. DOI: 10.1103/PhysRevB.92.214403. URL: https://link.aps.org/doi/10.1103/PhysRevB.92.214403 (cit. on pp. 185, 186).

[323] F. Bottegoni et al. “Modeling the photo-induced inverse spin-Hall effect in Pt/semiconductor junctions”. In: *Journal of Applied Physics* 124.3 (2018), p. 033902 (cit. on p. 185).

[324] A. Costa, A. Matos-Abiague, and J. Fabian. “Skew Andreev reflection in ferromagnet/superconductor junctions”. In: *arXiv preprint arXiv:1905.12525* (2019) (cit. on p. 186).

[325] J. C. Slonczewski. “Conductance and exchange coupling of two ferromagnets separated by a tunneling barrier”. In: *Phys. Rev. B* 39 (10 1989), pp. 6995–7002. DOI: 10.1103/PhysRevB.39.6995. URL: https://link.aps.org/doi/10.1103/PhysRevB.39.6995 (cit. on p. 188).

[326] A. G. Petukhov, A. N. Chantis, and D. O. Demchenko. “Resonant Enhancement of Tunneling Magnetoresistance in Double-Barrier Magnetic Heterostructures”. In: *Phys. Rev. Lett.* 89 (10 2002), p. 107205. DOI: 10.1103/PhysRevLett.89.107205. URL: https://link.aps.org/doi/10.1103/PhysRevLett.89.107205 (cit. on p. 188).

[327] M. Elsen et al. “Exchange-Mediated Anisotropy of (Ga,Mn)As Valence-Band Probed by Resonant Tunneling Spectroscopy”. In: *Phys. Rev. Lett.* 99 (12 2007), p. 127203. DOI: 10.1103/PhysRevLett.99.127203. URL: https://link.aps.org/doi/10.1103/PhysRevLett.99.127203 (cit. on p. 188).

[328] H.-J. Drouhin, G. Fishman, and J.-E. Wegrowe. “Spin currents in semiconductors: Redefinition and counterexample”. In: *Phys. Rev. B* 83 (11 2011), p. 113307. DOI: 10.1103/PhysRevB.83.113307. URL: https://link.aps.org/doi/10.1103/PhysRevB.83.113307 (cit. on p. 188).

[329] F. Bottegoni et al. “Probability- and spin-current operators for effective Hamiltonians”. In: *Phys. Rev. B* 85 (23 2012), p. 235313. DOI: 10.1103/PhysRevB.85.235313. URL: https://link.aps.org/doi/10.1103/PhysRevB.85.235313 (cit. on p. 188).

[330] P. Pfeffer and W. Zawadzki. “Conduction electrons in GaAs: Five-level k·p theory and polaron effects”. In: *Phys. Rev. B* 41 (3 1990), pp. 1561–1576. DOI: 10.1103/PhysRevB.41.1561. URL: https://link.aps.org/doi/10.1103/PhysRevB.41.1561 (cit. on p. 189).

[331] J. C. R. Sánchez et al. “Spin-to-charge conversion using Rashba coupling at the interface between non-magnetic materials”. In: *Nature communications* 4 (2013), p. 2944 (cit. on p. 190).

[332] E. Lesne et al. “Highly efficient and tunable spin-to-charge conversion through Rashba coupling at oxide interfaces”. In: *Nature materials* 15.12 (2016), p. 1261 (cit. on p. 190).

[333] J. Lee et al. “Spin modulation in semiconductor lasers”. In: *Applied Physics Letters* 97.4 (2010), p. 041116 (cit. on pp. 207, 211).

[334] N. C. Gerhardt et al. “Ultrafast spin-induced polarization oscillations with tunable lifetime in vertical-cavity surface-emitting lasers”. In: *Applied Physics Letters* 99.15 (2011), p. 151107. DOI: 10.1063/1.3651339. URL: http://aip.scitation.org/doi/abs/10.1063/1.3651339 (cit. on p. 207).

[335] J. Rudolph et al. “Room-temperature threshold reduction in vertical-cavity surface-emitting lasers by injection of spin-polarized electrons”. In: *Applied Physics Letters* 87.24 (2005), p. 241117. DOI: 10.1063/1.2146064. URL: http://aip.scitation.org/doi/abs/10.1063/1.2146064 (cit. on p. 207).

[336] M. Holub and B. T. Jonker. “Threshold current reduction in spin-polarized lasers: Role of strain and valence-band mixing”. In: 83 (12 2011), p. 125309. DOI: 10.1103/PhysRevB.83.125309. URL: http://link.aps.org/doi/10.1103/PhysRevB.83.125309 (cit. on p. 207).

[337] J. Rudolph et al. “Laser threshold reduction in a spintronic device”. In: *Applied Physics Letters* 82.25 (2003), pp. 4516–4518. DOI: 10.1063/1.1583145. URL: http://aip.scitation.org/doi/abs/10.1063/1.1583145 (cit. on p. 207).

[338] D. Basu et al. “Electrically injected InAs/GaAs quantum dot spin laser operating at 200K”. In: *Applied Physics Letters* 92.9 (2008), p. 091119. DOI: 10.1063/1.2883953. URL: http://aip.scitation.org/doi/abs/10.1063/1.2883953 (cit. on p. 207).

[339] I. Vurgaftman et al. “Estimating threshold reduction for spin-injected semiconductor lasers”. In: *Applied Physics Letters* 93.3 (2008), p. 031102. DOI: 10.1063/1.2957656. URL: http://aip.scitation.org/doi/abs/10.1063/1.2957656 (cit. on p. 207).

[340] M. Holub and B. T. Jonker. “Threshold current reduction in spin-polarized lasers: Role of strain and valence-band mixing”. In: *Phys. Rev. B* 83 (12 2011), p. 125309. DOI: 10.1103/PhysRevB.83.125309. URL: http://link.aps.org/doi/10.1103/PhysRevB.83.125309 (cit. on p. 207).

[341] N. Gerhardt et al. “Enhancement of spin information with vertical cavity surface emitting lasers”. In: *Electronics Letters* 42.2 (2006), pp. 88–89. ISSN: 0013-5194. DOI: 10.1049/el:20062890 (cit. on p. 207).

[342] S. Iba et al. “Room temperature circularly polarized lasing in an optically spin injected vertical-cavity surface-emitting laser with (110) GaAs quantum wells”. In: *Applied Physics Letters* 98.8 (2011), p. 081113. DOI: 10.1063/1.3554760. URL: http://aip.scitation.org/doi/abs/10.1063/1.3554760 (cit. on p. 207).

[343] K. Schires et al. “Optically-pumped dilute nitride spin-VCSEL”. In: *Opt. Express* 20.4 (2012), pp. 3550–3555. DOI: 10.1364/OE.20.003550. URL: http://www.opticsexpress.org/abstract.cfm?URI=oe-20-4-3550 (cit. on p. 207).

[344] S. Hovel et al. “Spin controlled optically pumped vertical cavity surface emitting laser”. In: *Electronics Letters* 41.5 (2005), pp. 251–253. ISSN: 0013-5194. DOI: 10.1049/el:20057675 (cit. on p. 207).

[345] J. Alexandre et al. “Compensation of the residual linear anisotropy of phase in a vertical-external-cavity-surface-emitting laser for spin injection”. In: *Opt. Lett.* 42.3 (2017), pp. 651–654. DOI: 10.1364/OL.42.000651. URL: http://ol.osa.org/abstract.cfm?URI=ol-42-3-651 (cit. on pp. 207, 212).

[346] G. Boéris et al. “Tailoring chirp in spin-lasers”. In: *Applied Physics Letters* 100.12 (2012), p. 121111 (cit. on p. 207).

[347] M. Lindemann et al. “Ultrafast spin-lasers”. In: *Nature* 568.7751 (2019), p. 212 (cit. on p. 207).

[348] A. Laurain et al. “Multiwatt power highly coherent compact single frequency tunable Vertical External Cavity Surface Emitting Semiconductor Laser”. In: *Opt. Express* 18.14 (2010), pp. 14627–14636. DOI: 10.1364/OE.18.014627. URL: http://www.opticsexpress.org/abstract.cfm?URI=oe-18-14-14627 (cit. on p. 207).

[349] A. Garnache, A. Ouvrard, and D. Romanini. “Single-Frequency operation of External-Cavity VCSELs: Non-linear multimode temporal dynamics and quantumlimit”. In: *Opt. Express* 15.15 (2007), pp. 9403–9417. DOI: 10.1364/OE.15.009403. URL: http://www.opticsexpress.org/abstract.cfm?URI=oe-15-15-9403 (cit. on p. 207).

[350] P. S. Zory. *Quantum Well Lasers*. OPTICS AND PHOTONICS SERIES. Academic Press, 1993. ISBN: 9780127818900. URL: https://books.google.fr/books?id=lb-VfmQF8TMC (cit. on p. 207).

[351] N. C. Gerhardt and M. R. Hofmann. "Spin-Controlled Vertical-Cavity Surface-Emitting Lasers". In: *Advances in Optical Technologies* 2012 (2012), pp. 268949–15. URL: http://dx.doi.org/10.1155/2012/268949 (cit. on p. 207).

[352] P. E. Faria Junior et al. "Wurtzite spin lasers". In: *Phys. Rev. B* 95 (11 2017), p. 115301. DOI: 10.1103/PhysRevB.95.115301. URL: https://link.aps.org/doi/10.1103/PhysRevB.95.115301 (cit. on p. 207).

[353] M. Holub and B. T. Jonker. "Threshold current reduction in spin-polarized lasers: Role of strain and valence-band mixing". In: *Phys. Rev. B* 83 (12 2011), p. 125309. DOI: 10.1103/PhysRevB.83.125309. URL: https://link.aps.org/doi/10.1103/PhysRevB.83.125309 (cit. on p. 207).

[354] J. Lee et al. "Spin-lasers: From threshold reduction to large-signal analysis". In: *Applied Physics Letters* 105.4 (2014), p. 042411 (cit. on p. 207).

[355] L. A. Coldren, S. W. Corzine, and M. L. Mashanovitch. *Diode Lasers and Photonic Integrated Circuits*. Wiley Series in Microwave and Optical Engineering. Wiley, 2012. ISBN: 9781118148181. URL: https://books.google.cz/books?id=GBB1kOYONT4C (cit. on pp. 207, 209).

[356] M. Travagnin et al. "Role of optical anisotropies in the polarization properties of surface-emitting semiconductor lasers". In: *Phys. Rev. A* 54 (2 1996), pp. 1647–1660. DOI: 10.1103/PhysRevA.54.1647. URL: http://link.aps.org/doi/10.1103/PhysRevA.54.1647 (cit. on pp. 207, 211).

[357] M. Travagnin et al. "Erratum: Role of optical anisotropies in the polarization properties of surface-emitting semiconductor lasers [Phys. Rev. A **54** , 1647 (1996)]". In: *Phys. Rev. A* 55 (6 1997), pp. 4641–4641. DOI: 10.1103/PhysRevA.55.4641. URL: http://link.aps.org/doi/10.1103/PhysRevA.55.4641 (cit. on pp. 207, 211).

[358] M. P. Van Exter, M. B. Willemsen, and J. P. Woerdman. "Polarization fluctuations in vertical-cavity semiconductor lasers". In: *Phys. Rev. A* 58 (5 1998), pp. 4191–4205. DOI: 10.1103/PhysRevA.58.4191. URL: http://link.aps.org/doi/10.1103/PhysRevA.58.4191 (cit. on p. 207).

[359] M. Sondermann, M. Weinkath, and T. Ackemann. "Polarization switching to the gain disfavored mode in vertical-cavity surface-emitting lasers". In: *IEEE Journal of Quantum Electronics* 40.2 (2004), pp. 97–104. ISSN: 0018-9197. DOI: 10.1109/JQE.2003.821537 (cit. on p. 207).

[360] M. San Miguel, Q. Feng, and J. V. Moloney. "Light-polarization dynamics in surface-emitting semiconductor lasers". In: *Phys. Rev. A* 52 (2 1995), pp. 1728–1739. DOI: 10.1103/PhysRevA.52.1728. URL: http://link.aps.org/doi/10.1103/PhysRevA.52.1728 (cit. on pp. 207, 211, 212).

[361] M. B. Willemsen, M. P. van Exter, and J. P. Woerdman. "Anatomy of a Polarization Switch of a Vertical-Cavity Semiconductor Laser". In: *Phys. Rev. Lett.* 84 (19 2000), pp. 4337–4340. DOI: 10.1103/PhysRevLett.84.4337. URL: http://link.aps.org/doi/10.1103/PhysRevLett.84.4337 (cit. on p. 207).

[362] E. L. Blansett et al. "Ultrafast polarization dynamics and noise in pulsed vertical-cavity surface-emitting lasers". In: *Opt. Express* 9.6 (2001), pp. 312–318. DOI: 10.1364/OE.9.000312. URL: http://www.opticsexpress.org/abstract.cfm?URI=oe-9-6-312 (cit. on p. 207).

[363] T. Ackemann and M. Sondermann. "Characteristics of polarization switching from the low to the high frequency mode in vertical-cavity surface-emitting lasers". In: *Applied Physics Letters* 78.23 (2001), pp. 3574–3576. DOI: 10.1063/1.1375833. URL: http://aip.scitation.org/doi/abs/10.1063/1.1375833 (cit. on p. 207).

[364] M. Holub et al. "Electrically injected spin-polarized vertical-cavity surface-emitting lasers". In: *Applied Physics Letters* 87.9 (2005), p. 091108. DOI: 10.1063/1.2035329. URL: http://aip.scitation.org/doi/abs/10.1063/1.2035329 (cit. on p. 207).

[365] D. Hägele and M. Oestreich. "Comment on Electrically injected spin-polarized vertical-cavity surface-emitting lasers [Appl. Phys. Lett. 87, 091108 (2005)]". In: *Applied Physics Letters* 88.5 (2006), p. 056101. DOI: 10.1063/1.2170134. URL: http://aip.scitation.org/doi/abs/10.1063/1.2170134 (cit. on p. 207).

[366] M. Y. Li et al. "Birefringence controlled room-temperature picosecond spin dynamics close to the threshold of vertical-cavity surface-emitting laser devices". In: *Applied Physics Letters* 97.19 (2010), p. 191114. DOI: 10.1063/1.3515855. URL: http://aip.scitation.org/doi/abs/10.1063/1.3515855 (cit. on p. 207).

[367] M. Herms et al. "Residual strain in annealed GaAs single-crystal wafers as determined by scanning infrared polariscopy, X-ray diffraction and topography". In: *Journal of Crystal Growth* 210.1-3 (2000), pp. 172 –176. ISSN: 0022-0248. DOI: http://dx.doi.org/10.1016/S0022-0248(99)00673-9. URL: http://www.sciencedirect.com/science/article/pii/S0022024899006739 (cit. on p. 207).

[368] J.-L. Yu et al. "Observation of strong anisotropic forbidden transitions in (001) InGaAs/GaAs single-quantum well by reflectance-difference spectroscopy and its behavior under uniaxial strain". In: *Nanoscale Research Letters* 6.1 (2011), p. 210. DOI: 10.1186/1556-276X-6-210. URL: http://dx.doi.org/10.1186/1556-276X-6-210 (cit. on pp. 207, 208, 211).

[369] O. Krebs and P. Voisin. "Giant Optical Anisotropy of Semiconductor Heterostructures with No Common Atom and the Quantum-Confined Pockels Effect". In: *Phys. Rev. Lett.* 77 (9 1996), pp. 1829–1832. DOI: 10.1103/PhysRevLett.77.1829. URL: http://link.aps.org/doi/10.1103/PhysRevLett.77.1829 (cit. on pp. 207, 208).

[370] O. Krebs et al. "Investigations of giant 'forbidden' optical anisotropy in GaInAs - InP quantum well structures". In: *Semiconductor Science and Technology* 12.7 (1997), p. 938. URL: http://stacks.iop.org/0268-1242/12/i=7/a=002 (cit. on p. 208).

[371] S. Cortez, O. Krebs, and P. Voisin. "In-plane optical anisotropy of quantum well structures: From fundamental considerations to interface characterization and optoelectronic engineering". In: *Journal of Vacuum Science & Technology B: Microelectronics and Nanometer Structures Processing, Measurement, and Phenomena* 18.4 (2000), pp. 2232–2241. DOI: 10.1116/1.1305286. URL: http://avs.scitation.org/doi/abs/10.1116/1.1305286 (cit. on p. 208).

[372] S. Cortez, O. Krebs, and P. Voisin. "Breakdown of rotational symmetry at semiconductor interfaces: a microscopic description of valence subband mixing". In: *The European Physical Journal B - Condensed Matter and Complex Systems* 21.2 (2001), pp. 241–250. ISSN: 1434-6036. DOI: 10.1007/s100510170200. URL: http://dx.doi.org/10.1007/s100510170200 (cit. on p. 208).

[373] L. F. Lastras-Martínez et al. "Optical anisotropy of (001)-GaAs surface quantum wells". In: *Phys. Rev. B* 64 (24 2001), p. 245303. DOI: 10.1103/PhysRevB.64.245303. URL: http://link.aps.org/doi/10.1103/PhysRevB.64.245303 (cit. on p. 208).

[374] E. A. Cerda-Méndez et al. "Interfaces in $Ga_xIn_{1-x}As_ySb_{1-y}/Al_xGa_{1-x}As_ySb_{1-y}$ multi-quantum-well heterostructures probed by transmittance anisotropy spectroscopy". In: *Journal of Applied Physics* 98.6 (2005), p. 066107. DOI: 10.1063/1.2058214. URL: http://dx.doi.org/10.1063/1.2058214 (cit. on p. 208).

[375] H. Shen et al. "Optical anisotropy in $GaAs/Al_xGa_{1-x}As$ multiple quantum wells under thermally induced uniaxial strain". In: *Phys. Rev. B* 47 (20 1993), pp. 13933–13936. DOI: 10.1103/PhysRevB.47.13933. URL: http://link.aps.org/doi/10.1103/PhysRevB.47.13933 (cit. on p. 208).

[376] A. Garnache et al. "A new kind of fast quantum-well semiconductor saturable-absorber mirror with low losses for ps pulse generation". In: *International Conference onIndium Phosphide and Related Materials, 2003.* 2003, pp. 247–250. DOI: 10.1109/ICIPRM.2003.1205361 (cit. on p. 208).

[377] M. S. Park et al. "Polarization control of vertical-cavity surface-emitting lasers by electro-optic birefringence". In: *Applied Physics Letters* 76.7 (2000), pp. 813–815. DOI: 10.1063/1.125593. URL: http://dx.doi.org/10.1063/1.125593 (cit. on p. 208).

[378] L. F. Lastras-Martínez et al. "Stress-induced optical anisotropies measured by modulated reflectance". In: *Semiconductor Science and Technology* 19.9 (2004), R35. URL: http://stacks.iop.org/0268-1242/19/i=9/a=R01 (cit. on p. 208).

[379] M. Holub and P. Bhattacharya. "Spin-polarized light-emitting diodes and lasers". In: *Journal of Physics D: Applied Physics* 40.11 (2007), R179–R203. DOI: 10.1088/0022-3727/40/11/r01. URL: https://doi.org/10.1088%2F0022-3727%2F40%2F11%2Fr01 (cit. on p. 210).

[380] A. Gahl, S. Balle, and M. S. Miguel. "Polarization dynamics of optically pumped VCSELs". In: *IEEE Journal of Quantum Electronics* 35.3 (1999), pp. 342–351. ISSN: 0018-9197. DOI: 10.1109/3.748839 (cit. on pp. 211, 212).

[381] I. A. I. Khanin. *Fundamentals of Laser Dynamics*. Cambridge International Science Publishing, 2006. ISBN: 9781904602118. URL: https://books.google.fr/books?id=taAp1uZVdHkC (cit. on pp. 211, 217).

[382] G. Agrawal. "Gain nonlinearities in semiconductor lasers: Theory and application to distributed feedback lasers". In: *IEEE Journal of Quantum Electronics* 23.6 (1987), pp. 860–868 (cit. on p. 211).

[383] S. E. Hodges et al. "Multimode laser model with coupled cavities and quantum noise". In: *J. Opt. Soc. Am. B* 14.1 (1997), pp. 191–199. DOI: 10.1364/JOSAB.14.000191. URL: http://josab.osa.org/abstract.cfm?URI=josab-14-1-191 (cit. on pp. 211, 217).

[384] J. Martin-Regalado et al. "Polarization properties of vertical-cavity surface-emitting lasers". In: *IEEE Journal of Quantum Electronics* 33.5 (1997), pp. 765–783. ISSN: 0018-9197. DOI: 10.1109/3.572151 (cit. on p. 211).

[385] A. Fiore and A. Markus. "Differential Gain and Gain Compression in Quantum-Dot Lasers". In: *IEEE Journal of Quantum Electronics* 43.4 (2007), pp. 287–294. ISSN: 0018-9197. DOI: 10.1109/JQE.2006.890399 (cit. on p. 211).

[386] T. Fördös et al. “Matrix approach for modeling of emission from multilayer spin-polarized light-emitting diodes and lasers”. In: *Journal of Optics* 16.6 (2014), p. 065008. DOI: 10.1088/2040-8978/16/6/065008. URL: https://doi.org/10.1088%2F2040-8978%2F16%2F6%2F065008 (cit. on p. 211).

[387] A. E. Siegman. *Lasers*. University Science Books, 1986 (cit. on p. 211).

[388] J. Frougier et al. “Control of light polarization using optically spin-injected vertical external cavity surface emitting lasers”. In: *Applied Physics Letters* 103.25, 252402 (2013), pp. –. DOI: http://dx.doi.org/10.1063/1.4850676. URL: http://scitation.aip.org/content/aip/journal/apl/103/25/10.1063/1.4850676 (cit. on p. 212).

[389] J. Frougier et al. “Accurate measurement of the residual birefringence in VECSEL: Towards understanding of the polarization behavior under spin-polarized pumping”. In: *Optics express* 23.8 (2015), pp. 9573–9588 (cit. on p. 212).

[390] M. Seghilani. “Highly coherent III-V-semiconductor laser emitting phase-, amplitude- and polarization-structured light for advanced sensing applications: Vortex, SPIN, Feedback Dynamics”. In: *PhD Thesis* (2016) (cit. on p. 212).

[391] A. Garnache et al. “2-2.7μm single frequency tunable Sb-based lasers operating in CW at RT: microcavity and external cavity VCSELs, DFB”. In: *Proc. SPIE* 6184 (2006), 61840N–61840N–15. DOI: 10.1117/12.663448. URL: http://dx.doi.org/10.1117/12.663448 (cit. on p. 212).

[392] Michel I Dyakonov. *Spin physics in semiconductors*. Vol. 1. Springer, 2017 (cit. on p. 213).

[393] S. E. Acosta-Ortiz and A. Lastras-Martínez. “Electro-optic effects in the optical anisotropies of (001) GaAs”. In: *Phys. Rev. B* 40 (2 1989), pp. 1426–1429. DOI: 10.1103/PhysRevB.40.1426. URL: https://link.aps.org/doi/10.1103/PhysRevB.40.1426 (cit. on p. 214).

[394] A. Yariv and Y. Pochi. *Optical electronics in modern communications*. Vol. 1. Oxford University Press, USA, 1997 (cit. on p. 214).

[395] T. Fördös et al. “Eigenmodes of spin vertical-cavity surface-emitting lasers with local linear birefringence and gain dichroism”. In: *Phys. Rev. A* 96 (4 2017), p. 043828. DOI: 10.1103/PhysRevA.96.043828. URL: https://link.aps.org/doi/10.1103/PhysRevA.96.043828 (cit. on p. 215).

[396] M. San Miguel, Q. Feng, and J. V. Moloney. “Light-polarization dynamics in surface-emitting semiconductor lasers”. In: *Phys. Rev. A* 52 (2 1995), pp. 1728–1739. DOI: 10.1103/PhysRevA.52.1728. URL: https://link.aps.org/doi/10.1103/PhysRevA.52.1728 (cit. on p. 217).

[397] T. Fördös et al. “Mueller matrix ellipsometric study of multilayer spin-VCSEL structures with local optical anisotropy”. In: *Applied Physics Letters* 112.22 (2018), p. 221106 (cit. on pp. 218, 221–224).

[398] Z. Vafapour and J. B. Khurgin. “Bandgap engineering and prospects for radiation-balanced vertical-external-cavity surface-emitting semiconductor lasers”. In: *Optics Express* 26 (2018). DOI: /10.1364/OE.26.012985 (cit. on p. 219).

[399] G. E. Jellison and F. A. Modine. “Parameterization of the optical functions of amorphous materials in the interband region”. In: *Applied Physics Letters* 69.3 (1996), pp. 371–373. DOI: 10.1063/1.118064. URL: https://doi.org/10.1063/1.118064 (cit. on pp. 219, 220).

[400] J. Tauc, R. Grigorovici, and A. Vancu. “Optical properties and electronic structure of amorphous germanium”. In: *physica status solidi (b)* 15.2 (1966), pp. 627–637 (cit. on p. 219).

[401] B. Johs et al. “Development of a parametric optical constant model for Hg1- xCdxTe for control of composition by spectroscopic ellipsometry during MBE growth”. In: *Thin Solid Films* 313 (1998), pp. 137–142 (cit. on p. 220).

[402] Y. Fu. *Physical Models of Semiconductor Quantum Devices*. Springer, 2014. ISBN: 978-94-007-7174-1. DOI: /10.1007/978-94-007-7174-1 (cit. on p. 225).

[403] J. Singh. *Electronic and Optoelectronic Properties of Semiconductor Structures*. Cambridge University Press, 2003. ISBN: 9780511805745. DOI: /10.1017/CBO9780511805745 (cit. on p. 225).

[404] J.-L. Yu et al. “Observation of strong anisotropic forbidden transitions in (001) InGaAs/GaAs single-quantum well by reflectance-difference spectroscopy and its behavior under uniaxial strain”. In: *Nanoscale Research Letters* 06 (Mar. 2011). DOI: /10.1186/1556-276X-6-210 (cit. on p. 230).

[405] Y. H. Chen et al. “Interface-related in-plane optical anisotropy in GaAs/AlxGa1-xAs single-quantum-well structures studied by reflectance difference spectroscopy”. In: *Physical Review B* 66 (Nov. 2002). DOI: /10.1103/PhysRevB.66.195321 (cit. on p. 230).

[406] C. G. Tang et al. “Well-width dependence of in-plane optical anisotropy in (001) GaAs/AlGaAs quantum wells induced by in-plane uniaxial strain and interface asymmetry”. In: *Journal of Applied Physics* 105 (2009). DOI: /10.1063/1.3132089 (cit. on p. 230).

[407] J. L. Yu et al. “In-plane optical anisotropy induced by asymmetrically delta-doping in (001) GaAs/AlGaAs quantum wells studied by reflectance difference spectroscopy”. In: *Journal of Applied Physics* 113 (2013). DOI: /10.1063/1.4790577 (cit. on p. 230).

[408] J. L. Yu et al. “In-plane optical anisotropy in GaAsN/GaAs single-quantum well investigated by reflectance-difference spectroscopy”. In: *Journal of Applied Physics* 108 (2010). DOI: /10.1063/1.3457901 (cit. on p. 230).

[409] E. L. Ivchenko. *Optical spectroscopy of semiconductor nanostructures*. Alpha Science Int’l Ltd., 2005 (cit. on pp. 232, 233).

[410] S. Balle. “Simple analytical approximations for the gain and refractive index spectra in quantum-well lasers”. In: *Phys. Rev. A* 57 (2 1998), pp. 1304–1312. DOI: 10.1103/PhysRevA.57.1304. URL: https://link.aps.org/doi/10.1103/PhysRevA.57.1304 (cit. on pp. 233–235).

[411] G. F. Koster. *Properties of the thirty-two point groups*. Vol. 24. The MIT Press, 1963 (cit. on p. 245).

[412] S. B. Radhia et al. “The eight-level k.p model for the conduction and valence bands of InAs, InP, InSb”. In: *Semiconductor Science and Technology* 22.4 (2007), p. 427 (cit. on pp. 249, 261).

[413] G. Mugny et al. “Full-zone k.p parametrization for III-As materials”. In: (2015), pp. 28–31 (cit. on pp. 249, 261).

[414] R. Neffati, I. Saïdi, and K. Boujdaria. “Full-zone kp model for the electronic structure of unstrained GaAs1- x P x and strained Al x In1- x As alloys”. In: *Journal of Applied Physics* 112.5 (2012), p. 053716 (cit. on p. 261).

[415] I. Saïdi, S. Ben Radhia, and K. Boujdaria. “Band parameters of GaAs, InAs, InP, and InSb in the 40-band k.p model”. In: *Journal of Applied Physics* 107.4 (2010), p. 043701 (cit. on p. 261).

[416] M. Cardona, N. E. Christensen, and G. Fasol. "Relativistic band structure and spin-orbit splitting of zinc-blende-type semiconductors". In: *Phys. Rev. B* 38 (3 1988), pp. 1806–1827. DOI: 10.1103/PhysRevB.38.1806. URL: https://link.aps.org/doi/10.1103/PhysRevB.38.1806 (cit. on pp. 278, 284).

[417] D. Y. K. Ko and J. C. Inkson. "Matrix method for tunneling in heterostructures: Resonant tunneling in multilayer systems". In: *Physical Review B* 38 (1988). DOI: /10.1103/PhysRevB.38.9945 (cit. on pp. 291, 294).

[418] C. S. Tang and C. S. Chu. "Coherent quantum transport in the presence of a finite-range transversely polarized time-dependent field". In: *Physica B: Condensed Matter* 292.1 (2000), pp. 127 –135. ISSN: 0921-4526. DOI: https://doi.org/10.1016/S0921-4526(00)00502-0. URL: http://www.sciencedirect.com/science/article/pii/S0921452600005020 (cit. on p. 297).

[419] L. Knopoff. "A matrix method for elastic wave problems". In: *Bulletin of the Seismological Society of America* 54.1 (1964), pp. 431–438 (cit. on p. 299).

[420] R. Pérez-Álvarez and F. García-Moliner. "Transfer matrix, Green functions and related techniques". In: *Universitat Jaume I, Spain* (2004) (cit. on p. 299).

INSTITUT POLYTECHNIQUE DE PARIS

Titre : Méthodes k.p avancées pour la spinorbitronique à base de semi-conducteurs

Mots clés : k.p, spinorbitronique, semi-conducteurs

Résumé : Ce travail de thèse est essentiellement consacré au développement de la théorie de transport tunnel k.p multibandes (14, 30 et 40 bandes) pour une application à la spinorbitronique avec semiconducteur. La spinorbitronique associe généralement les effets de spin et d'orbite, qui par l'intermédiaire du couplage spin-orbite, introduit des propriétés de transport nouvelles comme les effets Hall de spin et les effets tunnel Hall anormal. Celui-ci se caractérise par une déflection de la trajectoire des porteurs polarisés en spin selon la direction transverse de leur flux. D'autres effets caractéristiques concernent i) les mécanismes de transfert de spin ('spin-transfer' ou 'spin-orbit torque') permettant de commuter une aimantation locale par transfert de moment angulaire, généralisant ainsi les processus de transfert de spin ainsi que ii) la conversion spin-charge aux interfaces médiés par les termes Rashba et/ou Dresselhaus. Dans ce cadre, notre théorie de transport tunnel est adaptable aux hétérostructures semiconductrices, magnétiques ou non, traitant d'une simple interface ou de jonctions tunnel. Elle permet de tenir compte de façon fine des interactions spin-orbite de cœur et d'interface (Rashba, d'interface). Elle utilise de façon générale, l'introduction de bandes hautes supplémentaires, dites fantômes, pour traiter les états spurious inhérents à la théorie k.p multibandes. Outre l'introduction de tels états 'fantômes' ne déformant ni la structure électronique, ni le transport polarisé, notre approche utilise la continuité des composantes des fonctions d'onde à chaque interface ainsi que le raccordement des composantes du courant d'onde selon la symétrie particulière des interfaces en considérant soit 1) la continuité des composantes du courant d'onde (extension de la théorie Ben Daniel Duke), 2) les conditions de raccordement correspondant à une symétrie particulière C2v introduisant un certain mélange trous lourds/trous légers dans la bande de valence (conditions d'Ivchenko) ou 3) une discontinuité des bandes p 'hautes'.

Title : Advanced multiband k.p methods for semiconductor-based spinorbitronics

Keywords : k.p, spinorbitronics, semiconductor

Abstract : This thesis is essentially devoted to the development of the multiband k.p tunneling theory (14, 30 and 40 bands) for the applications of spinorbitronic based on semiconductors. Spinorbitronic generally associates to the effects of spin and orbit, which via spin-orbit coupling, introduces new transport properties such as spin Hall effects or anomalous tunnel Hall effects which is characterized by a deflection of the trajectory of the spin-polarized carriers according to the transverse direction of their flux. Other characteristic effects concern : i) the spin-transfer or spin-orbit torque mechanisms, which make it possible to switch a local magnetization by angular momentum transfer, thus generalizing the spin transfer processes as well as ii) spin-charge conversion at interfaces mediated by the Rashba and / or Dresselhaus terms. In this context, our tunnel transport theory is adaptable to semiconductor heterostructures dealing with a simple interface or tunnel junctions. It allows one to take into account in a fine way the spin-orbit interactions within the bulk and at the interface. Besides, our method uses in a general way, the introduction of additional high bands, called ghost-bands, to treat the spurious states in framework of multiband k.p theory. In addition to the introduction of such 'ghost' states, which weakly affect the electronic structure or the polarized transport, our approach uses the matching conditions of the wavefunction and wave current at each interface according to the particular symmetry of the interfaces considering either 1) the continuity of the components of the wavefunction and wave current (extension of the Ben Daniel Duke theory), or 2) the matching conditions corresponding to a particular symmetry C2v at the interface introducing a certain mixture of heavy holes / light holes in the valence band (Ivchenko matching conditions) or 3) a discontinuity of the components of the wavefunctions of "high" bands (Durnev matching conditions).

Institut Polytechnique de Paris
91120 Palaiseau, France